BIOGEOCHEMICAL CONSEQUENCES OF CLIMATE-DRIVEN CHANGES IN THE ARCTIC

EDITED BY: Adam Jerold Reed, Robyn E. Tuerena, Martin Solan and Philippe Archambault

PUBLISHED IN: Frontiers in Environmental Science and Frontiers in Marine Science

frontiers Research Topics

ISSN 1664-8714
ISBN 978-2-88966-967-7
DOI 10.3389/978-2-88966-967-7

About Frontiers

Frontiers is more than just an open-access publisher of scholarly articles: it is a pioneering approach to the world of academia, radically improving the way scholarly research is managed. The grand vision of Frontiers is a world where all people have an equal opportunity to seek, share and generate knowledge. Frontiers provides immediate and permanent online open access to all its publications, but this alone is not enough to realize our grand goals.

Frontiers Journal Series

The Frontiers Journal Series is a multi-tier and interdisciplinary set of open-access, online journals, promising a paradigm shift from the current review, selection and dissemination processes in academic publishing. All Frontiers journals are driven by researchers for researchers; therefore, they constitute a service to the scholarly community. At the same time, the Frontiers Journal Series operates on a revolutionary invention, the tiered publishing system, initially addressing specific communities of scholars, and gradually climbing up to broader public understanding, thus serving the interests of the lay society, too.

Dedication to Quality

Each Frontiers article is a landmark of the highest quality, thanks to genuinely collaborative interactions between authors and review editors, who include some of the world's best academicians. Research must be certified by peers before entering a stream of knowledge that may eventually reach the public - and shape society; therefore, Frontiers only applies the most rigorous and unbiased reviews.
Frontiers revolutionizes research publishing by freely delivering the most outstanding research, evaluated with no bias from both the academic and social point of view. By applying the most advanced information technologies, Frontiers is catapulting scholarly publishing into a new generation.

What are Frontiers Research Topics?

Frontiers Research Topics are very popular trademarks of the Frontiers Journals Series: they are collections of at least ten articles, all centered on a particular subject. With their unique mix of varied contributions from Original Research to Review Articles, Frontiers Research Topics unify the most influential researchers, the latest key findings and historical advances in a hot research area! Find out more on how to host your own Frontiers Research Topic or contribute to one as an author by contacting the Frontiers Editorial Office: frontiersin.org/about/contact

BIOGEOCHEMICAL CONSEQUENCES OF CLIMATE-DRIVEN CHANGES IN THE ARCTIC

Topic Editors:
Adam Jerold Reed, University of Southampton, United Kingdom
Robyn E. Tuerena, Scottish Association For Marine Science, United Kingdom
Martin Solan, University of Southampton, United Kingdom
Philippe Archambault, Laval University, Canada

Citation: Reed, A. J., Tuerena, R. E., Solan, M., Archambault, P., eds. (2021). Biogeochemical Consequences of Climate-Driven Changes in the Arctic. Lausanne: Frontiers Media SA. doi: 10.3389/978-2-88966-967-7

Table of Contents

frontiers in Environmental Science

EDITORIAL
published: 05 May 2021
doi: 10.3389/fenvs.2021.696909

Editorial: Biogeochemical Consequences of Climate-Driven Changes in the Arctic

Adam J. Reed[1*†], *Robyn E. Tuerena*[2†], *Philippe Archambault*[3,4†] *and Martin Solan*[1†]

[1]School of Ocean and Earth Science, National Oceanography Centre Southampton, Waterfront Campus, University of Southampton, Southampton, United Kingdom, [2]Scottish Association for Marine Science, Dunstaffnage, United Kingdom, [3]ArcticNet, Université Laval, Québec, QC, Canada, [4]Québec Océan, Takuvik, Département de Biologie, Université Laval, Québec, QC, Canada

Keywords: arctic, biogeochemistry, climate change, ocean, sediments, organic matter, permafrost

Editorial on the Research Topic

Biogeochemical Consequences of Climate-Driven Changes in the Arctic

OPEN ACCESS

Edited and reviewed by:
Vera I. Slaveykova,
Université de Genève, Switzerland

***Correspondence:**
Adam J. Reed
adam.reed@noc.soton.ac.uk

†ORCID:
Adam J. Reed
orcid.org/0000-0003-2200-5067
Robyn E. Tuerena
orcid.org/0000-0001-7664-840X
Philippe Archambault
orcid.org/0000-0001-5986-6149
Martin Solan
orcid.org/0000-0001-9924-5574

Specialty section:
This article was submitted to Biogeochemical Dynamics, a section of the journal Frontiers in Environmental Science

Received: *18 April 2021*
Accepted: *23 April 2021*
Published: *05 May 2021*

Citation:
Reed AJ, Tuerena RE, Archambault P and Solan M (2021) Editorial: Biogeochemical Consequences of Climate-Driven Changes in the Arctic. Front. Environ. Sci. 9:696909. doi: 10.3389/fenvs.2021.696909

INTRODUCTION

The Arctic Ocean is warming at an unprecedented rate, leading to the loss of multi-year sea ice, and changes to stratification and ocean circulation patterns (Polyakov et al., 2017; Lind et al., 2018; Stroeve and Notz 2018). Increased discharge of freshwater (McClelland et al., 2006) and terrestrial organic matter into Arctic coastal water (Parmentier et al., 2017) further influence the timing of natural cycles. The ecological consequences of these changes manifest in adjusted primary productivity cycles (Lewis et al., 2020), alterations in the quality and quantity of organic matter reaching the seafloor (Krajewska et al., 2017; Stevenson and Abbott 2019; Olivier et al., 2020), benthic biogeochemical cycles (MacDonald et al., 2015; Solan et al., 2020) and the food-web (Yunda-Guarin et al., 2020). Mechanistic understanding of these processes requires continual revision, and in this research topic, we report new findings and emerging insights about how Arctic biogeochemical processes are responding to climate change and altering system dynamics. The contributions received present nuanced perspectives on the role of spatial and temporal variability, the connectivity between terrestrial and marine systems, the context dependency of organic matter degradation, and they highlight some emerging ecological consequences from a range of Arctic locations.

Spatial and Temporal Influences on Biogeochemistry

As sea ice melts, areas of once permanent sea ice are now shifting to seasonal sea ice zones, with concomitant changes in light availability, upper-ocean mixing, and community structure. In this issue, Matthes et al. document the spatial variability of UV and PAR transmission through melting sea ice and conclude that spatial averages in transmission are more representative than single point irradiance measurements used for estimating nutrient availability and, by inference, primary production. Marmillot et al. exploit spatial variations in physiochemical seawater properties to explore its relationship with lipid and fatty acid distributions, and highlight the importance of long-lived subsurface chlorophyll maximum layers in supplying PUFA-rich POM to the food web. Using biogeochemical modelling, Benkort et al. include a sea-ice component for the Barents Sea, which links the dynamics of the sea-ice, pelagic and benthic environments. Their findings indicate the important role of sea-ice algae in influencing the timing and amplitude of pelagic primary and secondary production, and in seeding pelagic diatoms.

Terrestrial–Marine Connectivity

The Arctic Ocean is surrounded by the northernmost regions of the American and Eurasian continents where glaciers and permafrost are decreasing in areal extent (Chadburn et al., 2017). The Arctic basin is unique in that it holds less than 2% of the ocean's volume but receives 10% of global riverine discharge and, therefore, processes occurring in Arctic rivers can have disproportionate consequences for biogeochemical cycling across the wider Arctic Ocean (Holmes et al., 2012). As climate forcing progresses, increases in riverine discharge associated with increases in precipitation and permafrost thaw emphasize land–ocean connectivity. McGovern et al. describe the effects of increased terrestrial riverine input on a fjordal system in Svalbard, and highlight the need for detailed and high resolution sampling to explore biogeochemical and ecological responses over time. Similarly, Juhls et al. describe the dynamics of the Lena River biogeochemistry. Using an unprecedented high temporal frequency of samples, they reveal seasonal changes in the composition and sources of dissolved organic matter (DOM). These new data indicate a shift in subsurface DOM properties towards older sources which are mobilized from within deeper soil horizons and permafrost deposits, raising concerns about positive climatic feedbacks.

Effects of Changing Biogeochemistry on the Ecosystem

Changes to biogeochemical properties in the Arctic can also influence the broader ecosystem, although the mechanistic basis of many of these linkages are poorly understood, and do not always follow expected patterns. O'Daly et al. measure sinking particulate organic carbon during a particularly ice free and warm summer in the Pacific-influenced Arctic. Contrary to expectations, they find high carbon fluxes which suggest the potential for high productivity in a warming Arctic ocean. Meanwhile, using a mesocosm study, Reed et al. investigate the reproductive response of abundant benthic invertebrates to projected temperature and CO_2 concentrations. They show no change in oocyte size frequency, and suggest that the quantity and quality of food, often available *ad libitum* in laboratory experiments, is likely to be an important determinant of physiological responses to projected environmental change.

Organic Matter Degradation

The characteristics and degradability of organic matter has important implications for climate. Jongejans et al. describe the organic matter characteristics in a thermokarst lake in Siberia and postulate on the ecological landscape through time while exploring the degradation of organic matter through permafrost thaw. They find that the organic carbon inventory of thawed permafrost reflects poor deposition, partial mobilization and release as methane from the lake, while the frozen elements of the permafrost indicate that the input signal of the organic matter still exceeds the degradation signal from thaw underneath. Their study indicates that changes in environmental circumstance can have substantive effects on organic matter retention and release. Indeed, Saidi-Mehrabad et al. considers whether or not climatic-induced transitions in state could occur in Arctic regions by examining how soil chemical and microbial parameters operate across the Pleistocene–Holocene boundary. As modern cold-adapted systems near a climatic threshold they conclude that cold soils could transition in ways similar to those seen across the Pleistocene–Holocene boundary with unknown ecosystem consequences.

CONCLUSION

Biogeochemical influences in the Arctic are often studied in the context of seasonality and climate forcing. However, it is now becoming clear that a greater understanding of the temporal influences in biogeochemistry overshadow our knowledge of spatial variations, which may constrain efforts to project regional responses to climate forcing. Previous work has emphasized the importance of primary productivity in controlling Arctic biogeochemistry, but as shown throughout the contributions in this thematic issue, multiple components of the system, from sea ice to seafloor, can have a substantive role in determining system response. It will be important to incorporate this knowledge to identify thresholds and feedbacks, vulnerabilities and surprises, and to improve projections of biogeochemical and wider ecosystem responses to climate change.

AUTHOR CONTRIBUTIONS

AR wrote the first editorial draft. RT, PA, and MS provided editorial suggestions and critical comments for revision. All authors agreed on the final submission.

FUNDING

Supported by "The Changing Arctic Ocean Seafloor (ChAOS)–how changing sea ice conditions impact biological communities, biogeochemical processes, and ecosystems" project (NE/N015894/1 and NE/P006426/1, 2017-2021) and the ARISE project "Can we detect changes in Arctic ecosystems?" (NE/P006310/1) funded by the Natural Environment Research Council (NERC) in the United Kingdom.

REFERENCES

Chadburn, S. E., Burke, E. J., Cox, P. M., Friedlingstein, P., Hugelius, G., and Westermann, S. (2017). An Observation-Based Constraint on Permafrost Loss as a Function of Global Warming. *Nat. Clim Change.* 7 (5), 340–344. doi:10.1038/nclimate3262

Holmes, R. M., McClelland, J. W., Peterson, B. J., Tank, S. E., Bulygina, E., Eglinton, T. I., et al. (2012). Seasonal and Annual Fluxes of Nutrients and Organic Matter from Large Rivers to the Arctic Ocean and Surrounding Seas. *Estuaries and Coasts* 35 (2), 369–382. doi:10.1007/s12237-011-9386-6

Krajewska, M., Szymczak-Żyła, M., and Kowalewska, G. (2017). Algal Pigments in Hornsund (Svalbard) Sediments as Biomarkers of Arctic Productivity and Environmental Conditions. *Pol. Polar Res.* 38, 423–443. doi:10.1515/popore-2017-0025

Lewis, K. M., van Dijken, G. L., and Arrigo, K. R. (2020). Changes in Phytoplankton Concentration Now Drive Increased Arctic Ocean Primary Production. *Science* 369 (6500), 198–202. doi:10.1126/science.aay8380

Lind, S., Ingvaldsen, R. B., and Furevik, T. (2018). Arctic Warming Hotspot in the Northern Barents Sea Linked to Declining Sea-Ice Import. *Nat. Clim Change* 8, 634–639. doi:10.1038/s41558-018-0205-y

Macdonald, R. W., Kuzyk, Z. Z. A., and Johannessen, S. C. (2015). The Vulnerability of Arctic Shelf Sediments to Climate Change. *Environ. Rev.* 23, 461–479. doi:10.1139/er-2015-0040

McClelland, J. W., Déry, S. J., Peterson, B. J., Holmes, R. M., and Wood, E. F. (2006). A Pan-Arctic Evaluation of Changes in River Discharge during the Latter Half of the 20th Century. *Geophys. Res. Lett.* 33, L06715. doi:10.1029/2006gl025753

Olivier, F., Gaillard, B., ThébaultMeziane, J. T., Meziane, T., Tremblay, R., Dumont, D., et al. (2020). Shells of the Bivalve Astarte Moerchi Give New Evidence of a Strong Pelagic-Benthic Coupling Shift Occurring since the Late 1970s in the North Water Polynya. *Phil. Trans. R. Soc. A.* 378, 20190353. doi:10.1098/rsta.2019.0353

Parmentier, F.-J. W., Christensen, T. R., Rysgaard, S., Bendtsen, J., Glud, R. N., Else, B., et al. (2017). A Synthesis of the Arctic Terrestrial and Marine Carbon Cycles under Pressure from a Dwindling Cryosphere. *Ambio* 46, 53–69. doi:10.1007/s13280-016-0872-8

Polyakov, I. V., Pnyushkov, A. V., Alkire, M. B., Ashik, I. M., Baumann, T. M., Carmack, E. C., et al. (2017). Greater Role for Atlantic Inflows on Sea-Ice Loss in the Eurasian Basin of the Arctic Ocean. *Science* 356 (6335), 285–291. doi:10.1126/science.aai8204

Solan, M., Ward, E. R., Wood, C. L., Reed, A. J., Grange, L. J., and Godbold, J. A. (2020). Climate-driven Benthic Invertebrate Activity and Biogeochemical Functioning across the Barents Sea Polar Front. *Phil. Trans. R. Soc. A.* 378, 20190365. doi:10.1098/rsta.2019.0365

Stevenson, M. A., and Abbott, G. D. (2019). Exploring the Composition of Macromolecular Organic Matter in Arctic Ocean Sediments under a Changing Sea Ice Gradient. *J. Anal. Appl. Pyrolysis* 140, 102–111. doi:10.1016/j.jaap.2019.02.006

Stroeve, J., and Notz, D. (2018). Changing State of Arctic Sea Ice across All Seasons. *Environ. Res. Lett.* 13, 103001. doi:10.1088/1748-9326/aade56

Yunda-Guarin, G., Brown, T. A., Michel, L. N., Saint-Béat, B., Amiraux, R., Nozais, C., et al. (2020). Reliance of Deep-Sea Benthic Macrofauna on Ice-Derived Organic Matter Highlighted by Multiple Trophic Markers during Spring in Baffin Bay, Canadian Arctic. *Elem. Sci. Anth* 8, 1. doi:10.1525/elementa.2020.047

Conflict of Interest: The authors declare that the research was conducted in the absence of any commercial or financial relationships that could be construed as a potential conflict of interest.

frontiers in Marine Science

ORIGINAL RESEARCH
published: 26 March 2020
doi: 10.3389/fmars.2020.00183

Spatial Heterogeneity as a Key Variable Influencing Spring-Summer Progression in UVR and PAR Transmission Through Arctic Sea Ice

Lisa C. Matthes[1], C. J. Mundy[1], S. L.-Girard[2], M. Babin[2], G. Verin[2,3] and J. K. Ehn[1]*

[1] Centre for Earth Observation Science, University of Manitoba, Winnipeg, MB, Canada, [2] Takuvik Joint International Laboratory, Université Laval and CNRS (France), Quebec City, QC, Canada, [3] UGA, CNRS, Institut des Géosciences de l'Environnement (IGE), UMR 5001, Grenoble, France

The transmission of ultraviolet (UVR) and photosynthetically available radiation (PAR) through sea ice is a key factor controlling under-ice phytoplankton growth in seasonally ice-covered waters. The increase toward sufficient light levels for positive net photosynthesis occurs concurrently with the sea ice melt progression in late spring when ice surface conditions shift from a relatively homogeneous high-albedo snow cover to a less reflective mosaic of bare ice and melt ponds. Here, we present a detailed dataset on the spatial and temporal progression of transmitted UVR and PAR in relation to changing quantities of snow, sea ice and melt ponds. Data were collected with a remotely operated vehicle (ROV) during the GreenEdge landfast sea ice campaign in June–July 2016 in southwestern Baffin Bay. Over the course of melt progression, there was a 10-fold increase in spatially averaged UVR and PAR transmission through the sea ice cover, reaching a maximum transmission of 31% for PAR, 7% for UVB, and 26% for UVA radiation. The depth under the sea ice experiencing spatial variability in light levels due to the influence of surface heterogeneity in snow, white ice and melt pond distributions increased from 7 ± 4 to 20 ± 6 m over our study. Phytoplankton drifting in under-ice surface waters were thus exposed to variations in PAR availability of up to 43%, highlighting the importance to account for spatial heterogeneity in light transmission through melting sea ice. Consequently, we demonstrate that spatial averages of PAR transmission provided more representative light availability estimates to explain under-ice bloom progression relative to single point irradiance measurements during the sea ice melt season. Encouragingly, the strong dichotomy between white ice and melt pond PAR transmittance and surface albedo permitted a very good estimate of spatially averaged light transmission from drone imagery of the surface and point transmittance measurements beneath different ice surface types.

Keywords: Arctic sea ice, radiative transfer, PAR, UVR, transmittance, spatial variability, ROV, under-ice phytoplankton bloom

OPEN ACCESS

Edited by:
Robyn E. Tuerena, The University of Edinburgh, United Kingdom

Reviewed by:
Lars Chresten Lund-Hansen, Aarhus University, Denmark
LI Zhijun, Dalian University of Technology, China

****Correspondence:***
Lisa C. Matthes
matthesl@myumanitoba.ca

Specialty section:
This article was submitted to Global Change and the Future Ocean, a section of the journal Frontiers in Marine Science

Received: *13 December 2019*
Accepted: *09 March 2020*
Published: *26 March 2020*

Citation:
Matthes LC, Mundy CJ, L.-Girard S, Babin M, Verin G and Ehn JK (2020) Spatial Heterogeneity as a Key Variable Influencing Spring-Summer Progression in UVR and PAR Transmission Through Arctic Sea Ice. Front. Mar. Sci. 7:183. doi: 10.3389/fmars.2020.00183

INTRODUCTION

In the Arctic Ocean, under-ice phytoplankton blooms can contribute significantly to spring primary production and have been documented more frequently in the last decades (e.g., Fortier et al., 2002; Mundy et al., 2009; Arrigo et al., 2014; Assmy et al., 2017; Oziel et al., 2019). During spring, surface nutrient concentrations tend to be replete and the presence of sea ice and meltwater create a low turbulence that favor the growth of diatoms (Arrigo et al., 2014; Neeley et al., 2018; Oziel et al., 2019) and the colonial haptophyte *Phaeocystis pouchetti* (Assmy et al., 2017). The onset of under-ice phytoplankton production is largely triggered by the seasonal increase in transmission of photosynthetically active radiation (PAR, 400–700 nm) through the ice layer to sufficient levels for positive net photosynthesis (Mundy et al., 2014). A study by Horvat et al. (2017) demonstrated that nearly 30% of the ice-covered Arctic Ocean in July permits PAR levels that are sufficient for under-ice algal blooms. However, *in situ* optical measurements beneath the sea ice cover are difficult due to spatial heterogeneity in light propagation caused by differences in snow depth, melt pond coverage, melt pond geometry and depth, ice thickness, and the horizontal distribution of light absorbing ice impurities (Ehn et al., 2008, 2011; Katlein et al., 2015; Light et al., 2015; Lu et al., 2016; Horvat et al., 2020).

Sea ice albedo has been widely studied showing that the decrease in light reflection is not a steady process (Fetterer and Untersteiner, 1998; Ehn et al., 2011; Perovich and Polashenski, 2012; Landy et al., 2014; Diaz et al., 2018). Snow melt and an impermeable ice layer cause surface flooding and thus a rapid decrease in the surface albedo. As melt progresses, the trapped water begins to drain toward flaws and seal breathing holes resulting in a short-term increase in regional albedo due to the emerging white ice (drained bare surface ice layer). In the last stage of melt, surface albedo further decreases with the thinning white ice layer and ice cover until ice break-up. During this surface melt progression, the initiation of melt pond formation is associated with the strongest increase in light levels at the ice bottom (Nicolaus et al., 2012; Zhang et al., 2015). However, the intensified differences in light transmittance through ponded vs. white ice combined with the lateral spreading of radiation within the ice layer create a more complex underwater light field (Frey et al., 2011; Katlein et al., 2016; Massicotte et al., 2018; Matthes et al., 2019). As shown in these studies studying the under-ice light field, vertical radiation transfer can be influenced by higher light transmittance through more transparent near-by structures causing edge effects at the ice bottom and subsurface irradiance maxima. This light attenuation discrepancy affects point measurements of light transmittance under the ice with different surface types and makes regional estimates of under-ice PAR availability for marine primary production estimates difficult. Optical measurements beneath a depth of 5 to 15 m are less affected by spatially heterogenous light transmission due to a more downward directed light propagation, which is only dependent on absorption and scattering processes within the water column (Frey et al., 2011; Katlein et al., 2015; Matthes et al., 2019). Thought from a surface perspective, Perovich (2005) defined this spatial scale of minimal variation in the propagation of solar radiation as the aggregate scale. Following this definition, the depth of spatially transmitted light independence on surface conditions is hereinafter called the "aggregate-scale depth" of light transmission. Knowledge about the impact of the surface melt progression on this depth is still limited.

To capture regional variability of light transmission through sea ice and the underlying water column, remotely operated vehicles (ROVs) equipped with different sensor arrays are more frequently used. ROVs were deployed to perform large-scale irradiance measurements beneath landfast sea ice and moving pack ice in the Arctic Ocean (Nicolaus and Katlein, 2013; Katlein et al., 2015, 2019), West Greenlandic fjord (Lund-Hansen et al., 2018), and in the Weddell Sea (Arndt et al., 2017). The minimized disturbance caused by ROV-based measurements compared to traditional core-based point-sampling methods also enables repeated operations within the same area throughout the melt season (Nicolaus et al., 2012). These measurements can be used to calculate regional estimates of under-ice PAR levels, which are needed in the investigation of the timing of under-ice phytoplankton growth. Large-scale sea-ice coverage sampling also minimizes statistical errors in primary production estimates caused by spatially heterogeneous light propagation (Massicotte et al., 2019). Hence, spatially averaged light transmission could represent a better estimate of light availability as phytoplankton cells often drift at a different rate and direction than that of the sea ice. This is particularly true for the case of a static landfast ice cover overlying a tide-influenced water column. Additionally, area-wide averages of light transmittance were found to cancel out edge effects caused by differences in ice surface reflection of melt ponds and white ice (Ehn et al., 2011; Taskjelle et al., 2017).

Meltwater transport and melt pond evolution at the ice surface has been described to undergo several stages throughout the sea ice spring-summer progression (Eicken et al., 2002; Polashenski et al., 2012; Landy et al., 2014). However, similar studies about the temporal increase in light transmission over the melt season are still sparse. In this paper, we hypothesize that the temporal increase in under-ice PAR and UVR levels follows the stages of melt pond evolution while the spatial heterogeneity of PAR and UVR transmission remains unchanged after the melt pond onset. We further hypothesize that including spatial heterogeneity of light transmission in the calculation of the euphotic zone depth will provide a more accurate estimate to help explain processes influencing development of an under-ice phytoplankton bloom. To quantify the increase of spectral light transmission through sea ice as a function of melt processes, a remotely operated vehicle (ROV) equipped with hyperspectral radiometers was used in June–July 2016 in Southwestern Baffin Bay. Horizontal transects and vertical profiles were repeatedly performed beneath the ice cover with changing quantities of snow, ice, melt ponds and ice algae to calculate average PAR and UVR transmittance and to investigate the interaction of increasing under-ice PAR availability and the initiation of phytoplankton growth. Simultaneously, the impact of the varying ice surface conditions on the scale of spatial variability of surface albedo and light transmission and the aggregate-scale depth are examined.

MATERIALS AND METHODS

Sampling Site

As part of the GreenEdge project in 2016, measurements of spectral irradiance and environmental parameters were performed on level landfast first-year sea ice (67° 28.784′ N, 63° 47.372′ W) near Qikiqtarjuaq, Nunavut, Baffin Bay (**Figure 1**). An undisturbed area east of the ice camp was chosen to repeatedly measure light transmittance through sea ice transitioning from snow-covered to shallow melt ponds and white ice surface conditions between 6 June and 2 July. Snow melt onset had already begun prior to the commencement of our study with daytime air temperatures consistently exceeding 0°C on 3 June followed by melt pond formation on 15 June (Oziel et al., 2019). Sky conditions varied between cloudy with sunny intervals, fully overcast and long periods of fog causing a decrease in incident surface PAR in June compared to the previous month [Figure 2 in Oziel et al. (2019)].

Optical Measurements

Incoming solar irradiance at the sea ice surface, $E_d(\lambda, 0)$, was measured with a visible (VIS) hyperspectral radiometer (wavelength range 350–950 nm with 3.3 nm resolution over 256 channels) and a 4-channel multispectral ultraviolet (UV) radiometer (305, 325, 340, 379 nm; Satlantic HyperOCR and OCR-504 UV, respectively, Sea-Bird Scientific, United States), both with cosine collector and mounted on a tripod 1.5 m above the ice surface. Surface albedo measurements were made with a separate hyperspectral radiometer (wavelength range 320–950 nm with 3.3 nm resolution over 190 channels; Ramses-ACC, TriOS GmbH, Germany) after the under-ice light sampling. Spectral albedo, $\alpha(\lambda)$, was calculated as the ratio of five measurements of downwelling, $E_d(\lambda, 0)$, and upwelling, $E_u(\lambda, 0)$, surface irradiance measured 1 m above the ice surface:

$$\alpha(\lambda) = \frac{E_u(\lambda, 0)}{E_d(\lambda, 0)} \quad (1)$$

Downwelling under-ice irradiance at 2 m water depth, $E_d(\lambda, 2)$, was measured using a remotely operated vehicle (ROV; SeaBotix vLBV300, United States), connected to a surface control unit through a tether cable of 300 m length (**Supplementary Figure S1**). The ROV was equipped with matching VIS and multispectral UV surface radiometers but calibrated for underwater deployment. All sensors were triggered synchronously, and light data was binned to one measurement per second. Also attached to the ROV was a CTD probe (SBE 49 FastCAT, Seabird, United States), an altimeter (resolution: 1 mm, VA500, Valeport, United States) to measure the distance between the vehicle and the ice bottom and a 360 degree action camera (PIXPRO SP360, Kodak, United States) to record ice bottom features. The ROV was launched and recovered through ∼1 m^2 holes and moved along horizontal transects by six thrusters at an average speed of 0.5 m s^{-1}. The average sinking speed for vertical profiles was 0.2 m s^{-1}. An integrated camera system at the front and back of the ROV enabled under-ice navigation along guiding lines. Prior to the field deployment, the weight distribution of ROV attachments were balanced, such that the internally measured pitch and roll of the vehicle never exceeded 7° during under-ice deployments.

To increase the spatial and temporal coverage of sampling, two transects areas were designated as shown in **Figure 2**. The change in spectral light transmission overtime was measured continuously along one 150-m long horizontal transect, called non-destructive (ND) transect, at a water depth of 2 m. No destructive sampling occurred along the ND transect to guarantee an undisturbed ice surface melt progression throughout the sampling period. However, the first 20 m of the transect distance was not used in the data analysis to avoid artificial disturbances of the ice cover caused by the access hole and the ROV set-up procedures. To calculate spectral light transmittance, $T(\lambda)$, surface and under-ice irradiance in the UV and visible spectrum were measured simultaneously during the ROV deployment. Also, along the same transect vertical profiles to a water depth of 50 m were performed at 50, 100, and 150 m distance from the access hole. To navigate the ROV consistently along the transect beneath the fully consolidated ice cover, a clear nylon fishing line was stretched taut beneath the ice through holes at the start and end of the transect and secured using ice screws. Additionally, every 10 m of the line was marked to provide a reference distance for the recorded light data. In total, the ND transect was measured eight times over four weeks. Ice draft, h_I, was measured during each deployment via

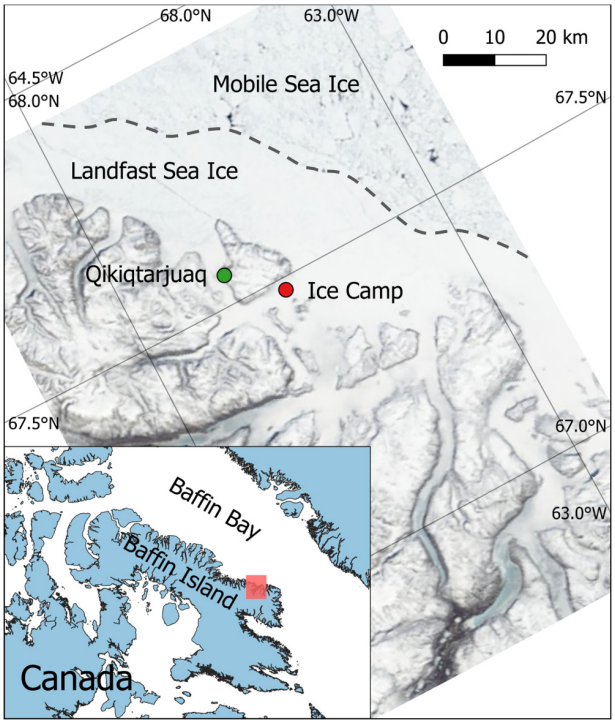

FIGURE 1 | Location of the ice camp as part of the GreenEdge campaign in 2016 on landfast sea ice near Qikiqtarjuaq, Southern Baffin Island, NU, Canada (MODIS image, 13 June 2016).

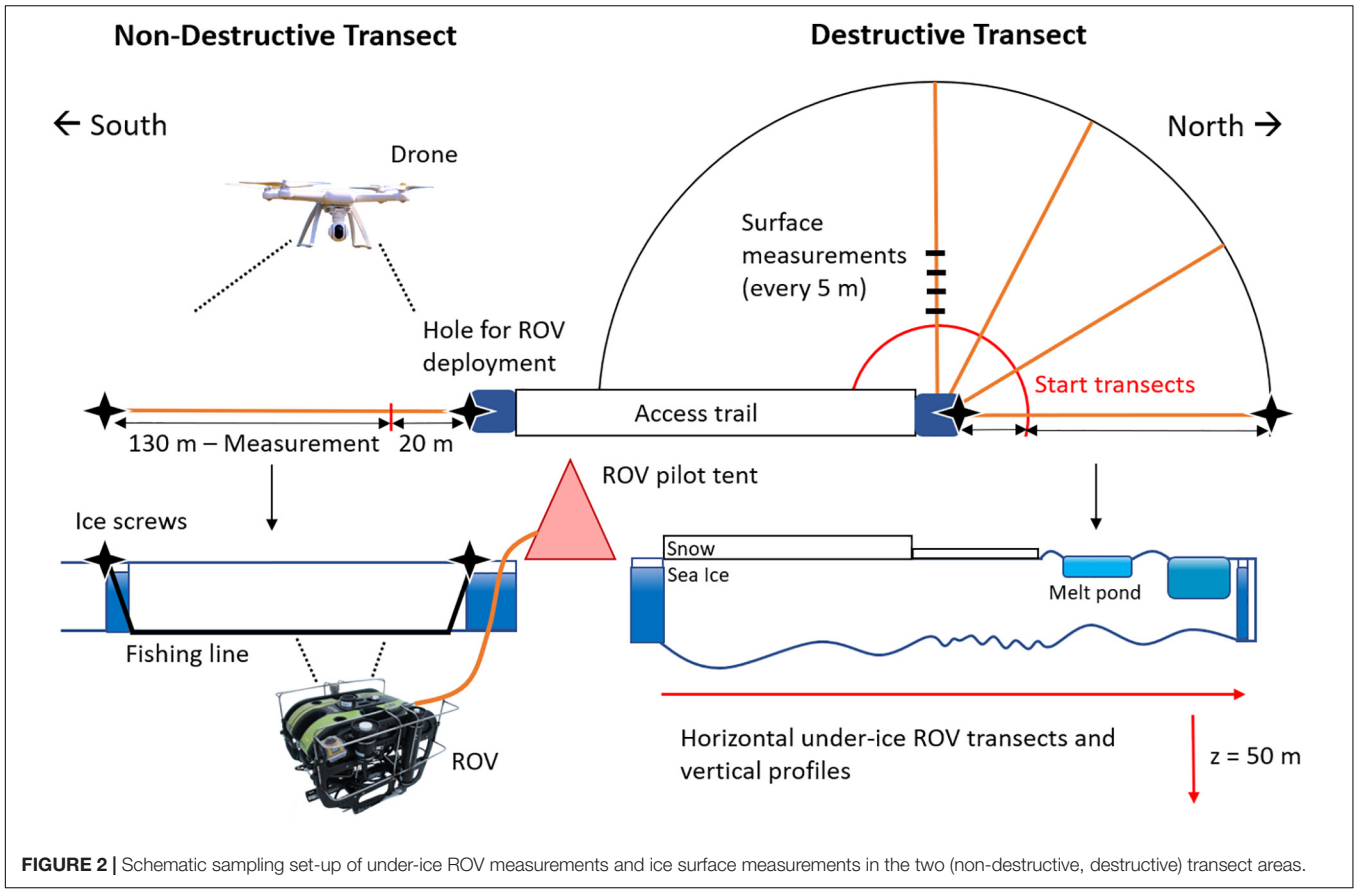

FIGURE 2 | Schematic sampling set-up of under-ice ROV measurements and ice surface measurements in the two (non-destructive, destructive) transect areas.

the ROV altimeter (mounted level with the radiometers) as the difference between the ROV depth (via the ROV CTD that was level with the radiometers) and its distance to the sea ice bottom (**Supplementary Figure S1**). Drilling through the sea ice cover to measure ice thickness was not performed to avoid artificial draining of the sampling area.

At a near-by site, identical under-ice horizontal transects, and vertical profiles were performed to study the spatial variability in light transmission caused by the differences in sea ice surface properties. Along these destructive (D) transects, every ROV deployment was followed by surface measurements. Surface properties such as snow depth, h_S, melt pond depth, h_{MP}, and the height of drained white ice above melt pond surface, h_{BI}, were measured with a ruler every 5 m of the D transect and after the eighth and final ROV deployment along the ND transect. Surface albedo measurements were performed every 10 m when the ice was still snow-covered. After melt ponds had formed, albedo was measured at nine locations along the transect above varying ice surface structures. In total, seven D transects were performed throughout the sampling period with varying snow depth and melt pond coverage.

Changes in surface properties and melt pond coverage within both transect areas were also documented through aerial drone (Phantom 2 Vision +, United States) surveys 90 m above the ice surface. Drone images were used to retrieve information on variability of surface brightness as proxy for surface albedo along the vehicle track. Following the procedure described in Katlein et al. (2015), pixel brightness was derived from the three RGB channels of the attached camera. The intensities of the R, G, and B channels were divided by the maximum value of 255 to gain pixel brightness from a single image of each transect. Brightness values between 0 and 1 were used in the semi-variogram analysis of the spatial variability of surface albedo.

Data Analysis

To estimate length-weighted average albedo, $\overline{\alpha}_{LW}(PAR)$, for the transect area, four replicates were measured for each surface type. Following Perovich (2005), $\overline{\alpha}_{LW}(PAR)$ was calculated for each transect with known melt pond coverage as

$$\overline{\alpha}_{LW} = \alpha_S A_S + \alpha_W A_{WI} + \alpha_{MP} A_{MP} \quad (2)$$

where α is the albedo and A is the area fraction for snow (S), white ice (WI) and melt ponds (MP). Under-ice irradiance data was pre-processed with the radiometers' software ProSoft (Satlantic, United States) to perform dark corrections and immersion correction for all under-ice light measurements due to the larger refractive index of water compared to air. Recorded spectra between 320 and 700 nm were also interpolated to 1-nm steps and converted into quantum irradiance (μmol photons m^{-2} s^{-1}), which is more relevant for biological studies. Irradiance in the UVB spectrum was not interpolated due to the measurement

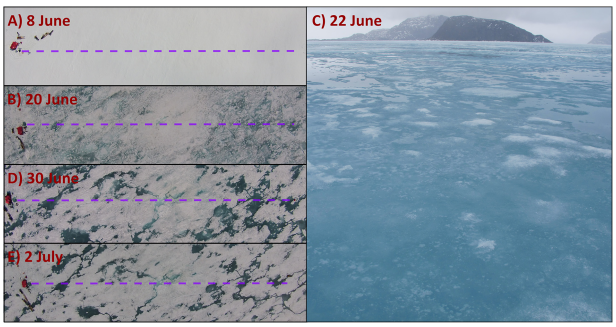

FIGURE 3 | Areal images of sea ice surface conditions along the sampling transects on **(A)** 8 June, **(B)** 20 June, **(C)** 22 June, **(D)** 30 June, and **(E)** 2 July, 2016. The ROV under-ice ND transect is indicated by the purple dashed line.

of a single wavelength (305 nm). Based on the ROV speed, the horizontal resolution of $E_d(\lambda, 2)$ was between 1 and 2 m, while vertical profiles of $E_d(\lambda, z)$ were calculated at 0.2-m steps from 1.6 to 50 m using linear interpolation. Spectral and PAR transmittance, $T(\lambda)$ and $T(PAR)$, respectively, as well as the diffuse vertical attenuation coefficient for downwelling irradiance, $K_d(PAR)$, were calculated as described in Matthes et al. (2019). The vertical attenuation coefficient was calculated as the average of three vertical profiles along each horizontal transect. However, only irradiance spectra from 15 to 50 m were included to avoid the impact of variable light transmission through different surface types of the sea ice cover (Matthes et al., 2019). In order to calculate $T(PAR)$ at the ice/water interface, $K_d(PAR)$ was also used to extrapolate the transmittance data from 2 m water depth to the ice bottom following Ehn et al. (2011). Measured transmittance in the UV spectrum has not been corrected for light attenuation in the water due to irradiance values near the detection limit resulting in uncertainties in the calculation of $K_d(UVR)$. Mean transmittance, $\bar{T}(PAR, UVR)$, was calculated for each horizontal transect as the average of 164 to 1161 coincident measurements of surface and transmitted irradiance spectra. Additionally, to compare methods of calculating mean PAR transmittance of an area, length-weighted average transmittance, $\bar{T}_{LW}(PAR)$, was calculated for each D transect following Taskjelle et al. (2017)

$$\bar{T}_{LW} = \frac{L_P T_P + L_{WI} T_{WI}}{L_P + L_{WI}} \quad (3)$$

where L_P and L_{WI} are the length of the transect covered by melt ponds or white ice, respectively, and T_P and T_{WI} are the corresponding PAR transmittances at four melt ponds and four white ice sites along the transect.

The impact of varying ice surface conditions on the aggregate scale depth was investigated by plotting change in standard deviation, SD, of the three PAR measurements at each depth of the vertical profiles of each sampling day. A difference in SD below the threshold of ± 1 μmol photons m^{-2} s^{-1} was chosen to identify the depth at which the under-ice light field is no longer influenced by spatial differences in light transmission through the ice cover. Repeated irradiance measurements along the ND transect and drone pictures of the same area also enabled a spatial analysis of the change in the scale of variability in surface brightness and PAR transmittance over time. Semi-variogram statistics of these two parameters provided information about the spatial distance (lag) between the first and the next measurement that is no longer correlated with the first measurement. To investigate the length scales of spatial variability the data set, a least square fit of exponential (surface brightness) or gaussian (transmittance) theoretical variograms were used to obtain range values. The range describes the lag distance at which the model reaches 95% of the estimated semi-variance (sill) and thus measurements are spatially independent. Significant changes in the range of surface brightness, a proxy for surface albedo, and PAR transmittance were investigated using linear regression.

RESULTS

Sea Ice Conditions

In June 2016, under-ice irradiance measurements commenced just after snow melt onset (**Figure 3A**). Melt water became visible at the ice surface on 15 June (**Figure 3B**), and field observations showed that the snow cover turned into large melt grain clusters. A rain event on 22 June contributed to a rapidly flooded ice surface (**Figure 3C**). After the rain event, air temperatures decreased leading to snowfall, freezing surface water during the night and a decline in the rate of surface melt. By 27 June, large, but shallow melt ponds had formed that were separated by an elevated and drained white ice surface cover as shown for 30 June in **Figure 3D**. Increased ice surface drainage led to shrinking melt pond sizes and more prominent white ice coverage in the following days (**Figure 3E**).

Snow depth ± standard deviation decreased from 30.1 ± 6.9 cm to 6.5 ± 3.8 cm within the first sampling week leading up to the melt pond onset on 15 June (**Figure 4A**). The initial snow cover was characterized by a high water content forming a 7.3 ± 6.1 cm thick layer of slush at its basis on 9 June. Aerial drone surveys of the D transect showed that melt pond coverage increased from 1.7% on 16 June to a maximum of 52.5% on 22 June (**Figure 4A**). In the following days, melt pond coverage decreased gradually from 26.5% on 30 June to 16.8% on 2 July.

Ice draft decreased over the sampling period from average values of 1.47 ± 0.08 m to 1.24 ± 0.13 m along the ND transect (**Figure 4A**). An average freeboard of 0.09 ± 0.03 m was measured at a near-by area and was within the stated standard deviation of the ice draft along the ROV transects. Temperature and salinity, measured at 2.4 m water depth and averaged for each horizontal ROV transect, shows the seasonal increase in heat content (departure from freezing temperature) and melt water content (**Figure 4B**). Up to 13 June, measured surface water salinity and temperature remained nearly constant at 32.2 and −1.7°C, respectively. After melt pond onset salinity decreased to 31.7, while the difference between the freezing temperature of seawater at −1.7°C and the surface water temperature at −1.3°C on

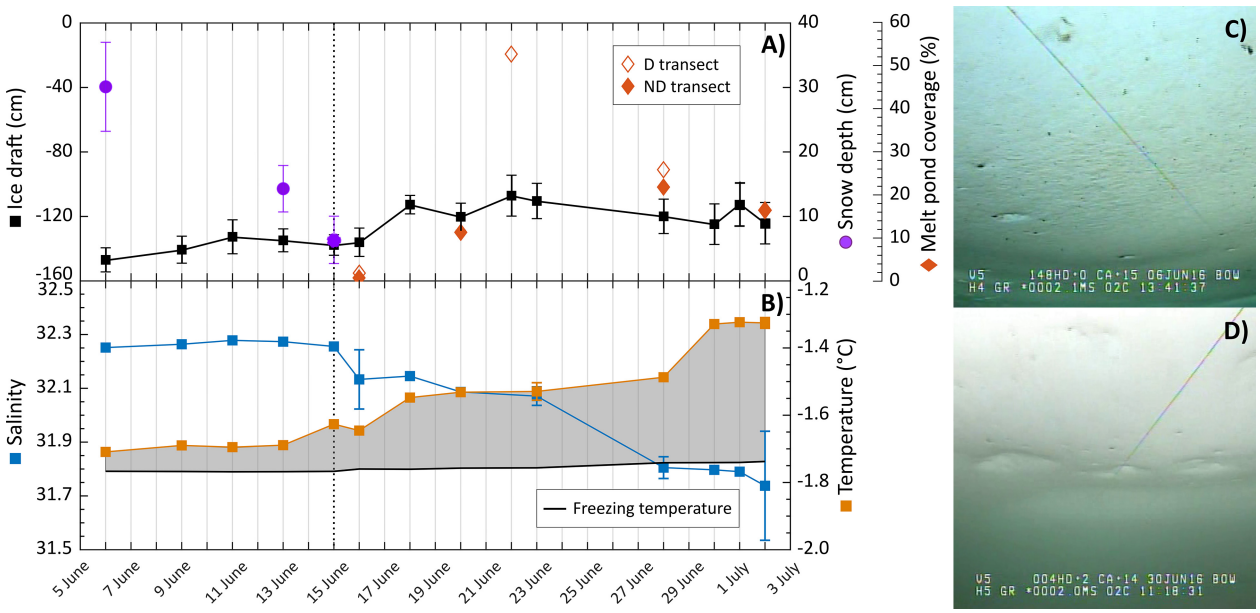

FIGURE 4 | Time series of spatially averaged **(A)** snow depth (purple circles, standard deviation error bars), ice draft (black squares), melt pond coverage (red diamonds), and averaged **(B)** surface water salinity (blue squares), surface water temperature (orange squares), and freezing temperature of seawater for each transect at 2.4-m depth over the sampling period. Images of the ice bottom were taken at 2 m on **(C)** 6 June, and **(D)** 30 June 2016. Melt pond coverage for the transect area is highlighted for D transects (empty diamonds) and ND transect (filled diamonds) after the melt pond onset (dotted line). The shaded area highlights the difference between water and freezing temperature.

2 July increased suggesting a larger energy input associated with solar radiative heating. This warming of the upper water column coincides with an alteration in sea ice bottom topography. Under-ice images taken on 6 June showed a smooth ice bottom with a brown coloration indicating the presence of ice algae and dark aggregates caught in small drainage holes (**Figure 4C** and **Supplementary Video S1**). By the beginning of July, the ice bottom appeared smoother, with larger holes and domes, and without a visible bottom coloration (**Figure 4D**).

PAR and UVR Above and Below Sea Ice Cover

Due to clear sky conditions, incoming radiation was highest in the first half of June (**Table 1**). The second half of June was characterized by several fog events and an increasing cloud cover, which created a diffuse surface light field and reduced surface $E_d(UVA, PAR, 0)$ until the cloud cover decreased again in the beginning of July. Daily incident radiation in the UVB spectrum, $E_d(305nm, 0)$, reached values between 1–3 mmol photons m^{-2} d^{-1} throughout the sampling period. Transmitted UVR and PAR increased with surface melt and varied along each transect (**Table 1**). This spatial variability further increased with the formation of melt ponds at the ice surface. Only at this late melt stage was a very low $E_d(305\ nm, 2)$ of 0.003 µmol photons m^{-2} s^{-1} actually measured at 2 m water depth. In the water column, diffuse vertical attenuation of PAR increased in late June, which was accompanied by an observed decrease in visibility of the guiding lines.

Change in Light Transmission With Surface Melt Progression

Measured surface PAR albedo as well as transmittance of PAR and four wavelengths in the UV spectrum are shown over the sampling period in **Figure 5**. Concurrently with the development of melt ponds, calculated length-weighted $\overline{\alpha}_{LW}(PAR)$ declined from 0.91 for snow-covered ice, to 0.58 after melt pond onset on 15 June (**Figure 5A**). As surface melt progressed, albedo variability increased until distinct melt ponds had formed. From 22 June onward, $\overline{\alpha}_{LW}(PAR)$ stayed relatively consistent between 0.47 and 0.53. Drone images also revealed that the prevailing landfast ice cover compromised a mosaic of smaller and larger ice floes that were frozen together (**Supplementary Figure S2**). This structural component had an impact on the color of melt ponds by creating brighter and darker ponds and thus causing a large range of melt pond albedo from 0.21 to 0.44.

Measured $T(PAR)$ and $T(UVR)$ at the ice bottom are presented as boxplots to display the variability of transmittance along the horizontal transect for each day (**Figures 5B,C**). With the shift in surface conditions from a highly reflective snow cover to a less reflective mosaic of bare ice and melt ponds, light transmission through the ice cover increased by a factor of 30. However, a continuous increase was only observed in the second and third week of June before mean PAR transmittance, $\bar{T}(PAR)$, leveled off to an average of 0.23 ± 0.05 (**Figure 5B**). The observed seasonal progression of light transmittance was split into three stages defined by the state of ice surface melt and the corresponding change in the magnitude and spatial variability of light transmittance:

TABLE 1 | Mean and standard deviation (SD) of incoming UVR and PAR at the sea ice surface, $E_d(0)$, and at 2 m water depth, $E_d(2)$, the daily incident UVR and PAR, and the mean vertical diffuse attenuation coefficient, $K_d(PAR)$, for four days in 2016.

		11 June	20 June	23 June	2 July
	Number of measurements	***n* = 306**	***n* = 356**	***n* = 205**	***n* = 166**
$E_d(PAR, 0)$	Mean (μmol photons m^{-2} s^{-1})	1750.0	681.2	1205.3	1268.1
	SD	111.8	15.5	29.3	53.6
	Daily (mol photons m^{-2} d^{-1})	68.6	29.3	56.5	49.9
$E_d(UVA, 0)$	Mean (μmol photons m^{-2} s^{-1})	154.8	68.3	112.1	115.1
	SD	6.0	1.0	1.7	3.0
	Daily (mol photons m^{-2} d^{-1})	6.4	3.0	5.2	4.7
$E_d(PAR, 2)$	Mean (μmol photons m^{-2} s^{-1})	29.3	108.9	241.6	202.1
	SD	10.6	50.5	99.5	100.2
$E_d(UVA, 2)$	Mean (μmol photons m^{-2} s^{-1})	2.5	11.5	26.2	21.1
	SD	1.0	5.5	10.5	10.4
$K_d(PAR)$	Mean	0.07	0.07	0.10	0.13

Stage I Prior to Melt Pond Onset on 15 June

Only 0.02 ± 0.01 of incoming PAR was transmitted through the snow-covered ice and spatial variability of light transmission did not change noticeably.

Stage II From 15 to 22 June

Once melt water became visible in large stretches at the ice surface, $\bar{T}(PAR)$ increased by an order of magnitude to 0.31 on 22 June, while under-ice irradiance became increasingly variable.

Stage III From 23 June to 2 July

A short snowfall event followed by an enhanced surface melt resulted in discrete areas of white ice and melt pond, defining stage III. PAR transmittance and its spatial variability did not increase further during this stage. In fact, $\bar{T}(PAR)$ measured along the ND transect decreased from 0.23 to 0.16.

The observed large drop in $\bar{T}(PAR)$ measured along the ND transect on 28 June was attributed to the snowfall event. Unfortunately, surface albedo was not measured that day. Repeated measurements along this transects also showed more pronounced transmittance peaks beneath melt ponds while PAR transmittance below white ice became less variable over time (**Supplementary Figure S3**). These high transmittance values of discrete surface ponds became pronounced as outliers in the boxplots after the surface flooding in stage III. The larger areas of white ice transmitting less PAR compared to ponded ice also resulted in a skewed distribution and the median to be less than the calculated mean for most of the days within stage III. On the last sampling day, the variability in measured under-ice PAR levels decreased while $\bar{T}(PAR)$ remained unchanged at 0.20. As shown in the aerial drone image of the sampling area on 2 July (**Figure 4E**), more white ice had emerged at the surface due to ongoing drainage of melt ponds, leading to a drop in the melt pond coverage and a more uniform sea ice surface. It should be noted that the proposed stages of changes in $\bar{T}(PAR)$ are different from the stages of melt pond evolution described elsewhere (Eicken et al., 2002).

For the comparison of measured mean PAR transmittance and length-weighted average transmittance, $\bar{T}_{LW}(PAR)$ was calculated for all D transects. To do so, $T(PAR)$ values of 0.16 to 0.24 beneath white ice and 0.25 to 0.40 beneath ponded ice, measured along four destructive transects, were used. As shown in **Figure 5B**, $\bar{T}(PAR)$ and $\bar{T}_{LW}(PAR)$ were not significantly different ($t(12) = 0.005$, $p = 0.996$) over the sampling period.

The increase in the transmission of one wavelength (305 nm) in the UVB spectrum and three wavelengths (325, 340, and 379 nm) in the UVA spectrum at 2 m is shown for all transects over the sampling period (**Figure 5C**). Beneath snow-covered sea ice in stage I, $\bar{T}(UVA)$, ranged from 0.01 to 0.02, while UVB radiation was not detectable. It is noted that surface and transmitted irradiance were integrated over the UVA wavelength spectrum (320–400 nm) prior to estimating $\bar{T}(UVA)$. With melt pond onset, $\bar{T}(UVA)$ increased to 0.26 by the end of stage II on 22 June. Also, UVB radiation was detectable beneath the ice cover with a $\bar{T}(305\ nm)$ of 0.01. In stage III, transmission of UVA radiation did not increase further, displaying a mean of 0.21 ± 0.05 for D and ND transects. However, $\bar{T}(305\ nm)$ was on average greater during stage III than stage II, reaching a mean value of 0.07 ± 0.06. During stage III, UVR transmittance remained relatively consistent, while the variability in measured under-ice UVR levels decreased. Furthermore, UVR transmission through melt ponds was twice as high than through white ice. $T_{WI}(305\ nm)$ and $T_{MP}(305\ nm)$ ranged from 0.03 to 0.08 and 0.11 to 0.14, respectively. Differences in the transmission of UVA radiation through the two surface types were less pronounced with a $T_{WI}(UVA)$ and $T_{MP}(UVA)$ between 0.16 and 0.24 and 0.22 and 0.35, respectively.

To compare measured transmittance of UVR and PAR at 2 m water depth, boxplots and the spectral shape in the 400 to 700 nm range of three sampling days (11 June, 23 June, 2 July 2016), representing different ice surface types, are shown in **Figure 6**. For all presented days, $\bar{T}(PAR)$ was smaller than $\bar{T}(379\ nm)$ due to a pronounced decrease in transmittance in the 600 to 700 nm wavelength spectrum. Differences between calculated transmittance were smallest beneath snow-covered sea ice with $\bar{T}(379\ nm)$ and $\bar{T}(PAR)$ of 0.2 on 11 June. During stage I, the edges of $T(\lambda)$ were much steeper with a transmittance peak at 512 nm. With melt pond formation, $\bar{T}(379\ nm)$ exceeded

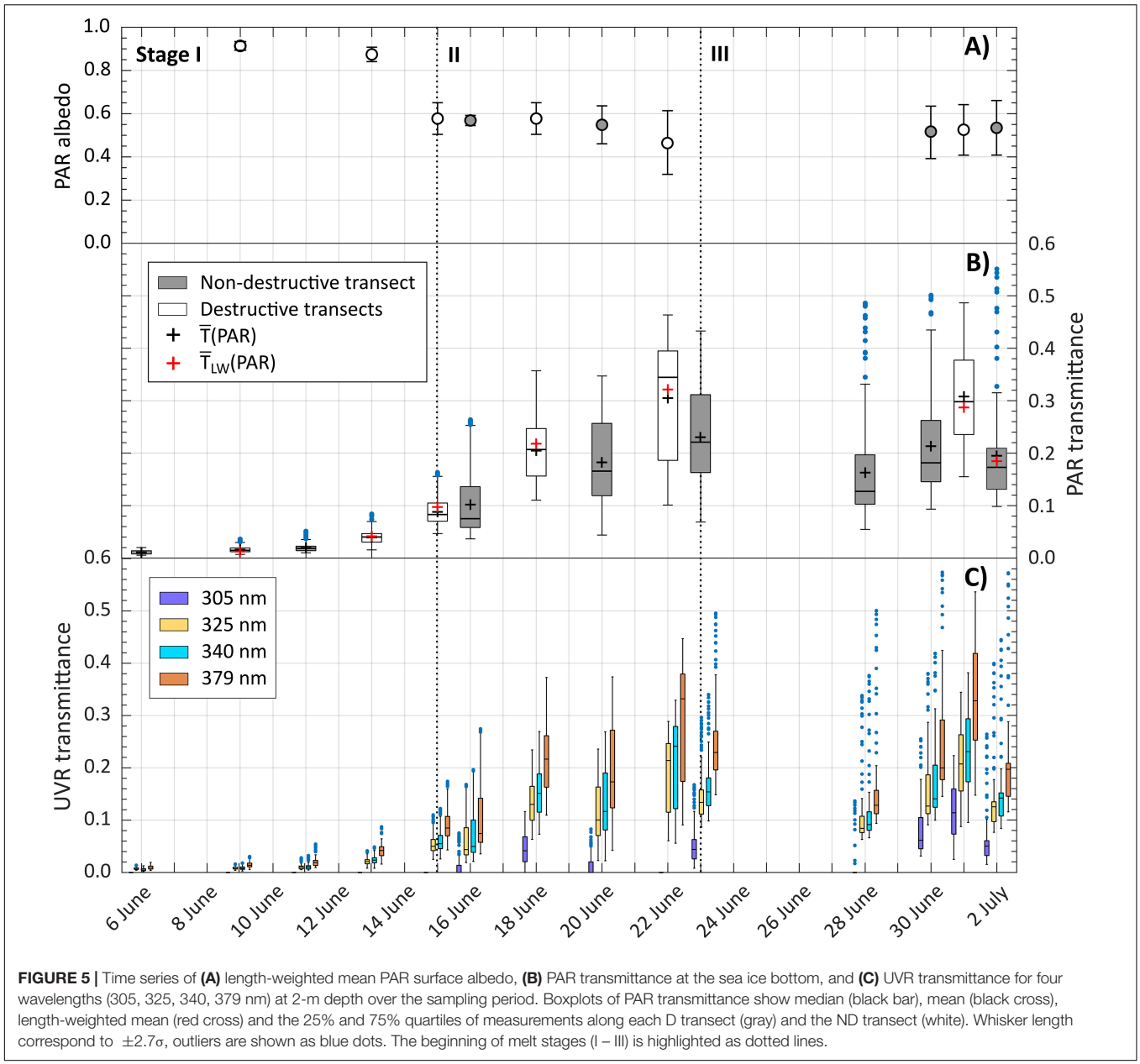

FIGURE 5 | Time series of **(A)** length-weighted mean PAR surface albedo, **(B)** PAR transmittance at the sea ice bottom, and **(C)** UVR transmittance for four wavelengths (305, 325, 340, 379 nm) at 2-m depth over the sampling period. Boxplots of PAR transmittance show median (black bar), mean (black cross), length-weighted mean (red cross) and the 25% and 75% quartiles of measurements along each D transect (gray) and the ND transect (white). Whisker length correspond to $\pm 2.7\sigma$, outliers are shown as blue dots. The beginning of melt stages (I – III) is highlighted as dotted lines.

$\bar{T}(PAR)$ increasingly, while the transmittance peak of the $T(\lambda)$ spectrum shifted toward the blue spectrum at 481 nm during stages II and III.

Spatial Variability of PAR Propagation

The change in spatial variability of ice surface brightness, as a proxy for variability of (PAR), and $T(PAR)$ at the ice bottom was investigated using semi-variances calculated for lag distances over the collected dataset (**Supplementary Figure S4**). Variograms of surface brightness were computed for eight horizontal transects of which aerial drone images were taken, while variograms of $T(PAR)$ were calculated for twelve horizontal transects (**Supplementary Table S1**). The change in variogram range of variability in surface brightness did not follow any trend during the surface melt progression ($R^2 = 0.35$, $p = 0.15$). The computed mean range throughout the sampling period was 3.9 ± 1.8 m and matched well the observed length of melt ponds between 3.7 and 4.4 m along the transects. Similar to surface brightness, no temporal trend was observed in the spatial variability of $T(PAR)$ ($R^2 = 0.07$, $p = 0.47$). However, variability in calculated length scales of $T(PAR)$ was greater, varying between 3.9 and 7.4 m with a mean of 5.4 m.

Aggregate-Scale Depth of Light Transmission

During stage I, the ice surface was still characterized by a snow cover, such that only a small portion of the incident PAR

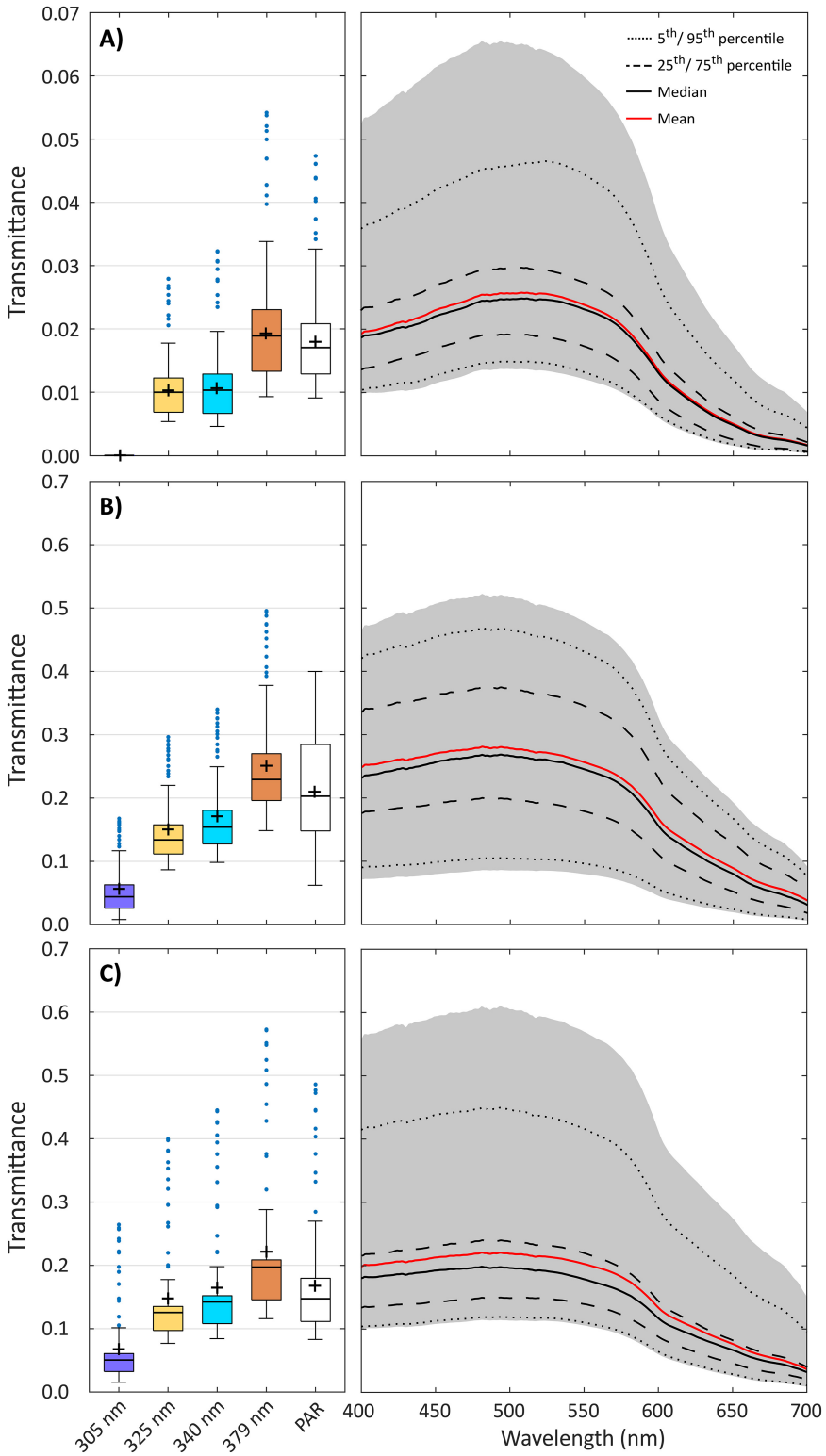

FIGURE 6 | Measured transmittance of UVR (305, 325, 340, 379 nm) and PAR along ND transect at 2-m depth on **(A)** 11 June, **(B)** 23 June, and **(C)** 2 July 2016. Boxplots of UVR and PAR transmittance show median (black bar), mean (cross) and the 25% and 75% quartiles of measurements along each transect. Whisker length correspond to $\pm$ 2.7σ, outliers are shown as blue dots. Spectral irradiance in the PAR spectrum is shown for all single measurements (shaded area) along the same ND transect, and as median (black line), mean (red line), 25th/75th percentiles (dashed line) and 5th/95th percentile (dotted line).

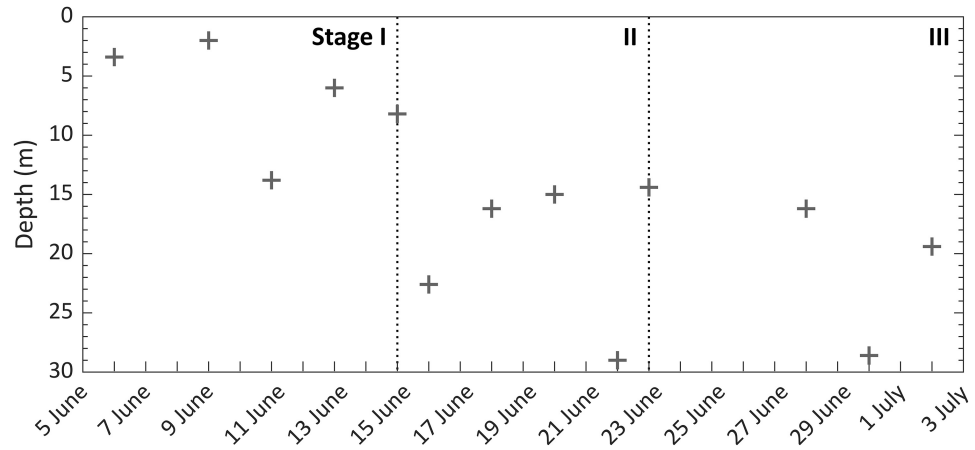

FIGURE 7 | Aggregate scale depth of PAR transmission beneath landfast sea ice over the melt season. The dotted line states the beginning of each melt stage (I–III).

was transmitted to the underlying water column (**Figure 6A**). Vertical PAR profiles were no longer influenced by differences in surface light transmission at relatively shallow water depths between 2.0 and 13.8 m (**Figure 7**). The influence of surface snow and melt pond distribution on the aggregate-scale depth of light transmission increased after the melt pond onset. With the occurrence of melt water at the ice surface during stage II and the formation of a more heterogenous sea ice surface during stage III, the aggregate-scale depth increased to between 14.4 and 29.0 m. This large change in depth was associated with the enhanced differences in transmittance of ponded vs. white ice. A linear regression analysis of the relationship between the aggregate scale depth and several parameters such as $\overline{\alpha}_{LW}(PAR)$, melt pond coverage (%), $\bar{T}(PAR)$ and the mean CV of $\bar{T}(PAR)$ revealed only a significant negative trend of the aggregate-scale depth with $\overline{\alpha}_{LW}(PAR)$ (R^2 = 0.64, p = 0.006). This trend was mainly driven by the large decrease in surface albedo with melt pond onset between 15 and 16 June, when we observed a steep increase in aggregate-scale depth from 8.2 to 22.6 m.

DISCUSSION

Spatio-Temporal Variability of Light Transmission

Smooth first-year ice dominated the landfast ice study site. Our observations lacked features such as pressure ridges or leads. Variogram results revealed that the 130 m transect length was more than an order of magnitude greater than the ∼4 m and ∼5 m range of $\alpha(PAR)$ and $T(PAR)$ transect observations, respectively, for the typical surface features. Therefore, our spatial light transmission analysis is believed to be representative of the light available beneath landfast sea ice. Interestingly, spatial continuity in both $\alpha(PAR)$ and $T(PAR)$ did not follow any temporal trend, even though their averaged ranges matched well with surface features that developed during the melt progression. For example, the 3.9 m average range for surface reflection matched the average melt pond size, whereas the range of $T(PAR)$ was slightly larger at 5.4 m. During stage I and II, snow drifts played an important role in the scale of variability in $T(PAR)$ as ranges of spatial variability in snow distribution patterns on FYI were similar to those of $T(PAR)$ (Iacozza and Barber, 1999). During stage III, observed melt ponds were small in the sampling area, so that measured $\bar{T}(PAR)$ beneath ponds was affected by radiation propagating from the surrounding white ice patches with a mean length of 12.7 m and vice-versa (Ehn et al., 2011). Essentially, scattering by the snow and sea ice diffused the under-ice light field (Matthes et al., 2019), acting to smooth out spatial variability in light transmittance to a longer distance than that of surface melt pond size. Spatial autocorrelation analyses of PAR transmittance through mobile FYI determined even larger ranges between 7 and 30 m which were driven by variations in the ice draft originating from ridges and refrozen leads (Katlein et al., 2015; Lange et al., 2017). In our study, ice draft only varied by a few centimeters along the transect and thus it likely was not a significant factor in influencing the observed spatial variation in transmittance.

Overall, the variability of calculated PAR transmittance along the horizontal transects increased as discrepancy between surface characteristics (ponded vs. white ice) increased (**Figure 5B**). To investigate the relative change in variation of PAR transmittance over time, the coefficient of variation, CV (%), as the ratio of standard deviation and mean was calculated for each transect and averaged for the three melt stages. In stage I, CV of 34 ± 3% was smallest within the sampling period which is related to the small variability in snow depth and the overall low light levels at the ice bottom. The spatial variability increased with the ablation of snow and the exposure of large stretches of less reflective surface melt water. This caused a 15-fold increase in $\bar{T}(PAR)$ and a mean CV of 40 ± 11% in stage II and a mean CV of 43 ± 14% in stage III. However, mean CV was not significantly different between the melt stages ($F_{2,11}$ = 0.876, p = 0.444).

Prior to melt pond onset during stage I of the seasonal progression of light transmittance, measured snow depth and the corresponding low $\bar{T}(PAR)$ were similar to other observations on landfast and mobile FYI in the Canadian Arctic (Iacozza and

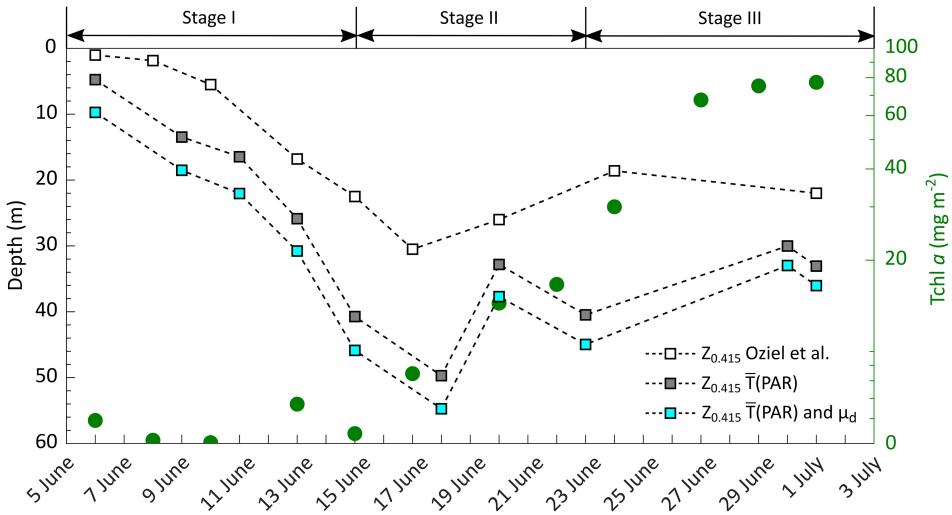

FIGURE 8 | Change in total chlorophyll *a* (Tchl *a*) concentration (green circles) integrated over 100-m water column (Massicotte et al., 2020), and in isolume depth ($z_{0.415}$), extracted from Oziel et al. (2019, white squares), as well as calculated from mean PAR transmittance ($\bar{T}$ (*PAR*), gray squares) and calculated from $\bar{T}$ (*PAR*) and scalar irradiance using an inverse average cosine (μ_d) of 1.4 (blue squares) for each melt stage (I – III) at the ice camp site.

Barber, 1999; Campbell et al., 2015). From the melt pond onset on 15 June, wet patches on the ice surface increased, which led to a rapid increase in $\bar{T}(PAR)$ until maximum transmittance values were reached during the largest spread of surface melt water on 22 June. Another study by Katlein et al. (2019) of the seasonal evolution of light transmission through mobile Arctic sea ice observed a similar increase of integrated $\bar{T}$(320–900nm) from 0.01 through melting snow-covered ice in June to 0.25 through ponded ice in August. Katlein et al. (2019) also note that spatial variability of $\bar{T}$(320–900nm) was highest after the melt pond onset. This widespread ponding in stage II due to the disappearance of snow matches as hypothesized the start of the ice ablation season described elsewhere (Eicken et al., 2002; Polashenski et al., 2012; Landy et al., 2014). In these studies, the second stage of melt pond evolution started with the complete removal of snow and an accelerated ice surface melt. Simultaneously, melt water flowed latterly toward flaws (cracks, seal breathing holes, enlarged brine drainage channels) in the ice surface while the ice was still impermeable. This led to a decrease in melt pond size and an increase in white ice patches and relates to our observed stage III of the seasonal progression of light transmittance. Also, the measured decrease in ice draft (**Figure 4A**), the visible change in ice bottom coloration in the ROV video footage (**Figures 4C,D**) and the change in shape of the transmitted PAR spectrum toward weaker attenuation at 400 and 700 nm (**Figure 6**) indicated a sloughing of bottom ice algae during stage I and II, which contributed to the increase in light transmission. To calculate the increase in $\bar{T}(PAR)$ through this process, $E_d(PAR)$ above the ice algae layer was calculated for 15 June 2016. Following Ehn and Mundy (2013), a $K_d(PAR)$ of 10.45 m^{-1} was used for the ice algae layer that corresponds to the given chlorophyll *a*, chl *a*, concentration extracted from Oziel et al. (2019). Applying Lambert-Beer's law, the loss of the ice algal layer caused an increase of 0.02 in $\bar{T}(PAR)$ which corresponds to a 34% increase relative to $\bar{T}(PAR)$ values during stage I, but much less relative to that of stages II and III. The increase in $\bar{T}(PAR)$ of 0.2 due to snow melt was an order of magnitude higher. Thus, changes in the snow cover played a more important role in spatio-temporal variability of light transmission to the ice bottom compared to differences in ice algal biomass. Following the increased transmittance through the ice cover in stage II after melt pond onset was an observed rise in under-ice surface water temperature by ∼0.2°C (**Figure 4B**). A rapid temperature rise by ∼0.2°C was again observed in stage III concurrent with a rapid increase in phytoplankton biomass (**Figure 8**).

The rapid change in ice surface conditions and the resulting spatial and temporal variations in PAR transmittance through the sea ice underline the importance of continuous irradiance measurements throughout the melt season for the purpose of estimating light availability for under-ice primary production. Area-averaged PAR transmittance values account for increasing spatial variability during sea ice melt progression as also discussed in Massicotte et al. (2019), who investigated the relative error in primary production estimates when averaging a certain number of single-point under-ice light measurements at random locations. The relative error was observed to drop below 10% at 99 under-ice ROV light measurements (Table 3 in Massicotte et al., 2019). However, large scale measurements by autonomous or remotely operated vehicles are expensive and logistically challenging to deploy. Hence, length-weighted mean transmittance, $\bar{T}_{LW}(PAR)$, calculated from measurements beneath melt ponds and white ice combined with aerial surveys by more affordable drones (UAVs) has shown to provide an alternative (Ehn et al., 2011; Taskjelle et al., 2017). Chosen melt ponds and white ice areas for under-ice irradiance measurements should be also sufficiently large to avoid the influence of near-by surface types on the footprint of the deployed radiometer.

Following equation (1) in Nicolaus et al. (2010) we calculated the irradiance sensor bottom-ice footprint size that should encapsulate 95% of incoming light measured at the sensor. We obtained a footprint range of 1 to 2 m for the corresponding range in sensor distance from the ice bottom of 0.4 to 0.8 m, as determined from the ROV-mounted altimeter. It is noted that this footprint size is likely a maximum as the equation assumes an isotropic light field, whereas Matthes et al. (2019) concluded that the under-ice light field is downward directed with a corresponding downwelling average cosine of 0.7. Regardless, with the size of melt pond and white ice patches ranging from 3.7 to 4.4 m and 7.4 to 18.0 m in our study, respectively, our ROV transmittance measurements at the center of these surface patches should not be significantly influenced by stray light from pond/ice edges. In conclusion, a lack of statistical difference between our estimates of $\bar{T}_{LW}(\mathrm{PAR})$ and $\bar{T}(PAR)$ confirm the applicability of this UAV technique for future studies requiring characterization of spatial variability in light transmission estimates through smooth first-year sea ice. Satellite-derived melt pond fraction (Rösel and Kaleschke, 2011; Zege et al., 2015) and surface albedo (Scharien et al., 2007) from optical sensors would allow even further upscaling throughout the summer melt. Although, an application on mobile pack ice would need to include a quantitative assessment of ridges and refrozen leads to account for large variations in ice draft.

Impact of Sea Ice Surface Melt on Aggregate-Scale Depth

Photosynthetically available radiation availability in the upper, ice-covered water column can be estimated from incoming irradiance at the ice surface, the presented mean transmittance and the diffuse vertical attenuation coefficient, $K_d(PAR)$. However, recorded vertical irradiance profiles to derive K_d are greatly influenced within the first meters by the previously discussed differences in light transmittance through the melting snow and ice cover (Frey et al., 2011; Massicotte et al., 2018; Matthes et al., 2019). Our results showed a deepening of the aggregate-scale depth with the formation of melt ponds. During stage I, a snow layer covered the landfast sea ice, causing light transmission to be more diffuse (Matthes et al., 2019) and small variations in the range of transmitted irradiance to the ice-water interface. The resultant mean depth at which spatial irradiance levels were no longer affected by surface variability was 7 ± 4 m. After the formation of melt pond in stage II, spatial heterogeneity of $\bar{T}(PAR)$ and thus the mean aggregate-scale depth increased to 20 ± 6 m. Our observations were in the same range of those reported elsewhere that fall between 5 and 15 m beneath melt pond-covered ice (Frey et al., 2011; Katlein et al., 2015; Matthes et al., 2019).

A correlation between the change in the aggregate-scale depth and sea ice surface properties as well as PAR transmittance was not identified. However, once an under-ice phytoplankton bloom develops, the scattering by phytoplankton may increase the diffusion of the heterogenous transmitted light and, hence, decrease the aggregate-scale depth. This was not observed during our study. In the sampling area, depth-integrated total chlorophyll *a* (Tchl *a*, the sum of chlorophyll *a*, divinyl-chlorophyll *a* and chlorophyllide *a*) concentration reached 77 mg m^{-2} on 1 July over the 100-m water column (Massicotte et al., 2019). This was much less than other observations of under-ice blooms with depth-integrated Tchl *a* concentrations ranging from 450 to 1292 mg m^{-2} (Fortier et al., 2002; Arrigo et al., 2014; Mundy et al., 2014). Arrigo et al. (2014) showed a 3.5-fold increase in light absorption and a 5-fold increase in scattering that was mainly attributable to phytoplankton cells (78%). Scattering by phytoplankton cells has also shown to decrease the degree of anisotropy of the downwelling under-ice radiation field in a radiative transfer model (Pavlov et al., 2017).

Seasonal Increase in UVR Transmission

Radiation in the UV spectrum can inhibit the photosynthetic capacity of phytoplankton (Villafañe et al., 2004) and ice algal communities (McMinn et al., 2005). Previous optical measurements beneath Arctic landfast sea ice recorded a transmittance of 0.01 – 0.02 through bare ice and 0.19 through ponded ice in the UVA (350 – 360 nm) spectral range (Elliott et al., 2015). During our investigation, we showed that UVR transmittance increased significantly with surface melt progression, reaching levels equal to PAR transmittance with $\bar{T}(UVA)$ of 0.19 beneath white ice and 0.30 beneath ponded ice by the end of June. Particularly after melt pond formation, $\bar{T}(379\ nm)$ exceeded $\bar{T}(PAR)$ because the latter is impacted by the high absorption coefficient in the red part of the visible spectrum. However, transmittance at shorter UV wavelengths remained less than $\bar{T}(PAR)$. Laboratory experiments by Perovich and Govoni (1991) demonstrated an increase in the absorption coefficient of snow and ice with decreasing wavelength within the spectrum of 250 to 400 nm, explaining the observed absence of UVB radiation during the early melt stage. However, after melt pond onset, $\bar{T}(305\ nm)$ increased to 0.05 through white ice and 0.11 through ponded ice.

Overall, $\bar{T}(UVR)$ was much larger than previously reported values obtained beneath landfast sea ice in Antarctica (Trodahl and Buckley, 1990) and from radiative transfer modeling for mobile Arctic FYI (Perovich, 2006). This greater transmission highlights the potential ecological significance of UVR transmission measurements during melt season when the spring phytoplankton bloom commences underneath sea ice. Algae in melt pond and in the ice as well as phytoplankton can synthesize mycosporine-like amino acids (MAAs) that act as UV-absorbing sun protection (Uusikivi et al., 2010; Ha et al., 2012; Elliott et al., 2015; Piiparinen et al., 2015). In particular, the study by Elliott et al. (2015) showed a modulation of the MAA concentration of an under-ice phytoplankton bloom with prevailing light conditions and stage of surface melt. Our results show that a significant portion of incoming UVA irradiance, up to 26 μmol photons m^{-2} s^{-1}, was transmitted during the spring melt when an under-ice bloom commenced beneath the ice cover. Incubation experiments of temperate phytoplankton assemblies in winter with radiation regimes of UVR and PAR or PAR only have shown an enhanced carbon fixation rate at UVR levels < 65 μmol photons m^{-2} s^{-1} and significantly lower fixation rates at higher UVR levels (Barbieri et al., 2002). The

authors also concluded that the taxonomic composition and light history of the phytoplankton community plays an important role in the sensitivity of algal cells to UVR. More research is therefore needed on the acclimation and photoprotection of under-ice phytoplankton communities to know if our UVA levels < 26 μmol photons m^{-2} s^{-1} have an impact on the algal communities.

Implications of Spatial Heterogeneity on Nutrient Availability for Under-Ice Phytoplankton Blooms

Several studies have identified the increase in PAR availability and water column stratification associated with melt pond onset as the trigger for under-ice phytoplankton blooms (Arrigo et al., 2014; Mundy et al., 2014; Hill et al., 2018; Oziel et al., 2019). However, the relationship between the sudden change in ice surface properties, the increase in the spatial heterogeneity of PAR transmittance, and the onset of algal growth during the spring melt are still not well understood. **Figure 8** provides an overview of the measured increase in Tchl *a* concentration in the water column (Massicotte et al., 2020) at the ice camp site and the depth of the isolume, $z_{0.415}$, where integrated $PAR_{24h}(z) = 0.415$ mol photons m^{-2} d^{-1}, a threshold used for positive net growth (Boss and Behrenfeld, 2010). The $z_{0.415}$ was extracted from Oziel et al. (2019), and estimated from $\bar{T}(PAR)$ from our study using the same daily incident PAR data and $K_d(PAR)$. It is important to note that irradiance measurements presented in Oziel et al. (2019) were taken beneath snow-covered and later white ice at the same location throughout the entire sampling period. At this site, $T(PAR)$ increased from 0.01 to 0.09 between 6 June and 1 July, 2016. However, our ROV measurements determined $\bar{T}(PAR)$ ranged from 0.01 to 0.31 over the same period (**Figure 5B**).

As **Figure 8** indicates, the initiation of the observed under-ice bloom was directly related to switches in the surface melt stage. During stage I, Tchl *a* concentration accumulated slowly although the $z_{0.415}$ deepened from 5 m to 46 m with the exponential increase over time in PAR transmission (**Figure 5B**). Only after the switch to stage II, Tchl *a* accumulation accelerated within the mixed surface water layer to a depth of 25 m (Oziel et al., 2019). The $z_{0.415}$ calculated from $\bar{T}(PAR)$ reached a greater maximum depth of 50 m compared to a maximum $z_{0.415}$ of 31 m obtained from the white ice point. To further account for the shape of the under-ice light field, under-ice planar irradiance gained from $E_d(PAR, 0)$ and $\bar{T}(PAR)$ was converted to scalar irradiance by using an inverse average cosine of 1.4 (Matthes et al., 2019). Results show an even deeper maximum $z_{0.415}$ of 55 m on 18 June. These differences in calculating $z_{0.415}$ have large implications on the interpretation of nutrient availability for under-ice phytoplankton growth. A deeper $z_{0.415}$ indicates that phytoplankton had access to a much larger nutrient pool than in the previous estimate. Indeed, Oziel et al. (2019) observed an increased nutrient drawdown at 40 m on 23 June, which also matches well with the second inflection point in Tchl *a* accumulation in the beginning of stage III. In the end of stage II, the $z_{0.415}$ shoaled due to the increased light attenuation by the phytoplankton accumulation and remained relatively constant in stage III. By the end of the sampling period, phytoplankton Tchl *a* concentration leveled off at the maximum observed values of 77 mg m^{-2}, likely as a result of the increased light attenuation by the algal cells and depleted nutrients concentrations in the surface water layer during the melt pond period (Oziel et al., 2019).

SUMMARY AND CONCLUSION

In this study, we characterized the seasonal spring progression of the transmission of UVR and PAR, and their spatial variability, in a large landfast sea ice area in southwest Baffin Bay (near the community of Qikiqtarjuaq, Nunavut) throughout the melt season in 2016. Understanding the magnitude of sunlight transmitted through the melting sea ice is of key importance to improve our understanding of the spring phytoplankton bloom. Our objectives were achieved through combined measurements of horizontal transects and vertical profiles of under-ice irradiance using a ROV, and manual and drone-based surveys of ice surface properties. This data set confirms our hypothesis of a close link between the temporal increase in under-ice PAR and UVR levels and the stages of melt pond evolution while the spatial heterogeneity of PAR and UVR transmission remained unchanged after the melt pond onset. The main findings are summarized in points 1–4 below:

1. Our study area was composed of smooth landfast sea ice. Variogram results revealed that the 130 m length of our ROV transects were more than an order of magnitude greater than the 4–5 m length scale of $\alpha(PAR)$ and $T(PAR)$ transect observations for typical surface types. This indicates that our spatial light transmission measurements and statistics were representative of the light available beneath the larger landfast sea ice area.
2. With melt pond formation, spatially averaged PAR transmittance increased from 0.02 to 0.31, while variations in measured under-ice PAR levels increased to up to 43%. This exposed drifting phytoplankton cells to a wide range of light conditions and highlights the importance to accurately capture spatial heterogeneity in light transmission.
3. Melt pond onset on 15 June resulted in a steep increase in aggregate scale depth for under-ice PAR levels from 7 ± 4 to 20 ± 6 m (**Figure 7**). PAR profiles were found to be affected by surface variability to depths of 2.0–13.8 m during stage I prior to melt pond onset, and to depths of 14.4–29.0 m during stages II-III when melt water was visible present on the surface.
4. With progressing surface melt, $\bar{T}(379\ nm)$ exceeded $\bar{T}(PAR)$ due to the high absorption coefficient in the red part of the visible spectrum. Transmittance at shorter UV wavelengths remained less than $\bar{T}(PAR)$. However, after melt pond onset, $\bar{T}(305\ nm)$ increased to 0.05 through white ice and 0.11 through ponded ice.

Monitoring the increasing spatial variability in transmitted light levels even under smooth, melting landfast sea ice pose

challenges in this rapidly changing environment. However, continuous observations on the spatial and temporal progression of transmitted spectral irradiance in relation to the changing quantities of snow, ice and melt ponds has proven to better explain the link between the deepening of the euphotic zone accompanied by an increased nutrient accessibility and the observed increase in the Tchl *a* concentration in this area.

DATA AVAILABILITY STATEMENT

All data are accessible at the Green Edge database (http://www.obs-vlfr.fr/proof/php/GREENEDGE/x_datalist_1.php?xxop=greenedge&xxcamp=icecamp2016).

AUTHOR CONTRIBUTIONS

LM, SL-G, JE, and CM contributed to the conception and design of the manuscript. LM, SL-G, GV, and MB contributed to the acquisition of data. LM, SL-G, CM, and JE contributed to the analysis and interpretation of the presented data. The author and all co-authors drafted and/or revised the article and approved the submitted version for publication.

FUNDING

The Green Edge project is funded by the following French and Canadian programs and agencies: ANR (Contract #111112), CNES (project #131425), IPEV (project #1164), CSA, Fondation Total, ArcticNet, LEFE and the French Arctic Initiative (GreenEdge project). Further funding was provided by the Canadian Space Agency and NSERC Discovery Grants to JE and CM and ABOL-CFI to CM and JE. LM was supported by the University of Manitoba graduate student fellowship. SL-G was funded by a postdoctoral fellowship from NSERC.

ACKNOWLEDGMENTS

This study is a contribution to the Green Edge project which was conducted under the scientific coordination of the Canada Excellence Research Chair on Remote Sensing of Canada's new Arctic frontier and the CNRS & Université Laval Takuvik Joint International laboratory (UMI3376). We specially thank Robert Hodgson, Julien Laliberté and Henri Bitting for their help during the ROV deployment, and P. Massicotte and L. Oziel for their support in the data processing. Our field campaign was successful thanks to the contribution of J. Ferland, G. Massé, D. Christiansen-Stowe and M.-H. Forget from the Takuvik laboratory, F. Pinczon du Sel and E. Brossier from Vagabond. This project would not have been possible without the support of the Hamlet of Qikiqtarjuaq and the members of the community as well as the Inuksuit School and its Principal Jacqueline Arsenault. We further thank the two reviewers for their comments to improve this manuscript.

SUPPLEMENTARY MATERIAL

The Supplementary Material for this article can be found online at: https://www.frontiersin.org/articles/10.3389/fmars.2020.00183/full#supplementary-material

REFERENCES

Arndt, S., Meiners, K. M., Ricker, R., Krumpen, T., Katlein, C., and Nicolaus, M. (2017). Influence of snow depth and surface flooding on light transmission through Antarctic pack ice. *J. Geophys. Res. Oceans* 122, 2108–2119. doi: 10.1002/2016JC012325

Arrigo, K. R., Perovich, D. K., Pickart, R. S., Brown, Z. W., van Dijken, G. L., Lowry, K. E., et al. (2014). Phytoplankton blooms beneath the sea ice in the Chukchi Sea. *Deep Sea Res. Part II Top. Stud. Oceanogr.* 105, 1–16.

Assmy, P., Fernández-Méndez, M., Duarte, P., Meyer, A., Randelhoff, A., Mundy, C. J., et al. (2017). Leads in Arctic pack ice enable early phytoplankton blooms below snow-covered sea ice. *Sci. Rep.* 7:40850. doi: 10.1038/srep40850

Barbieri, E. S., Villafañ, V. E., and Helbling, E. W. (2002). Experimental assessment of UV effects on temperate marine phytoplankton when exposed to variable radiation regimes. *Limnol. Oceanogr.* 47, 1648–1655. doi: 10.4319/lo.2002.47.6.1648

Boss, E., and Behrenfeld, M. (2010). In situ evaluation of the initiation of the North Atlantic phytoplankton bloom. *Geophys. Res. Lett.* 110:18603.

Campbell, K., Mundy, C. J., Barber, D. G., and Gosselin, M. (2015). Characterizing the sea ice algae chlorophyll a–snow depth relationship over Arctic spring melt using transmitted irradiance. *J. Mar. Syst.* 147, 76–84.

Diaz, A., Ehn, J., Landy, J., Else, B., Campbell, K., and Papakyriakou, T. (2018). The energetics of extensive meltwater flooding of level Arctic Sea Ice. *J. Geophys. Res. Oceans* 123, 8730–8748.

Ehn, J. K., and Mundy, C. J. (2013). Assessment of light absorption within highly scattering bottom sea ice from under-ice light measurements: Implications for Arctic ice algae primary production. *Limnol. Oceanogr.* 58, 893–902.

Ehn, J. K., Mundy, C. J., Barber, D. G., Hop, H., Rossnagel, A., and Stewart, J. (2011). Impact of horizontal spreading on light propagation in melt pond covered seasonal sea ice in the Canadian Arctic. *J. Geophys. Res. Oceans* 116:C00G02.

Ehn, J. K., Papakyriakou, T. N., and Barber, D. G. (2008). Inference of optical properties from radiation profiles within melting landfast sea ice. *J. Geophys. Res. Oceans* 113:C09024. doi: 10.1029/2007JC004656

Eicken, H., Krouse, H. R., Kadko, D., and Perovich, D. K. (2002). Tracer studies of pathways and rates of meltwater transport through Arctic summer sea ice. *J. Geophys. Res. Oceans* 107, SHE 22-1–SHE 22-20. doi: 10.1029/2000JC000583

Elliott, A., Mundy, C. J., Gosselin, M., Poulin, M., Campbell, K., and Wang, F. (2015). Spring production of mycosporine-like amino acids and other UV-absorbing compounds in sea ice-associated algae communities in the Canadian Arctic. *Mar. Ecol. Prog. Ser.* 541, 91–104. doi: 10.3354/meps11540

Fetterer, F., and Untersteiner, N. (1998). Observations of melt ponds on Arctic sea ice. *J. Geophys. Res. Oceans* 103, 24821–24835.

Fortier, M., Fortier, L., Michel, C., and Legendre, L. (2002). Climatic and biological forcing of the vertical flux of biogenic particles under seasonal Arctic sea ice. *Mar. Ecol. Prog. Ser.* 225, 1–16.

Frey, K. E., Perovich, D. K., and Light, B. (2011). The spatial distribution of solar radiation under a melting Arctic sea ice cover. *Geophys. Res. Lett.* 38:L22501.

Ha, S.-Y., Kim, Y.-N., Park, M.-O., Kang, S.-H., Kim, H., and Shin, K.-H. (2012). Production of mycosporine-like amino acids of in situ phytoplankton community in Kongsfjorden, Svalbard, Arctic. *J. Photochem. Photobiol. B* 114, 1–14. doi: 10.1016/j.jphotobiol.2012.03.011

Hill, V. J., Light, B., Steele, M., and Zimmerman, R. C. (2018). Light availability and phytoplankton growth beneath Arctic sea ice: Integrating observations and modeling. *J. Geophys. Res. Oceans* 123, 3651–3667.

Horvat, C., Flocco, D., Rees Jones, D. W., Roach, L., and Golden, K. M. (2020). The effect of melt pond geometry on the distribution of solar energy under first-year Sea ice. *Geophys. Res. Lett.* 47:e2019GL085956. doi: 10.1029/2019GL085956

Horvat, C., Jones, D. R., Iams, S., Schroeder, D., Flocco, D., and Feltham, D. (2017). The frequency and extent of sub-ice phytoplankton blooms in the Arctic Ocean. *Sci. Adv.* 3:e1601191. doi: 10.1126/sciadv.1601191

Iacozza, J., and Barber, D. G. (1999). An examination of the distribution of snow on sea-ice. *Atmos. Ocean* 37, 21–51. doi: 10.1080/07055900.1999.9649620

Katlein, C., Arndt, S., Belter, H. J., Castellani, G., and Nicolaus, M. (2019). Seasonal evolution of light transmission distributions through Arctic sea ice. *J. Geophys. Res. Oceans* 124, 5418-5435. doi: 10.1029/2018JC014833

Katlein, C., Arndt, S., Nicolaus, M., Perovich, D. K., Jakuba, M. V., Suman, S., et al. (2015). Influence of ice thickness and surface properties on light transmission through Arctic sea ice. *J. Geophys. Res. Oceans* 120, 5932–5944.

Katlein, C., Perovich, D. K., and Nicolaus, M. (2016). Geometric effects of an inhomogeneous sea ice cover on the under ice light field. *Front. Earth Sci.* 4:6. doi: 10.3389/feart.2016.00006

Landy, J., Ehn, J., Shields, M., and Barber, D. (2014). Surface and melt pond evolution on landfast first-year sea ice in the Canadian Arctic Archipelago. *J. Geophys. Res. Oceans* 119, 3054–3075.

Lange, B. A., Katlein, C., Castellani, G., Fernández-Méndez, M., Nicolaus, M., Peeken, I., et al. (2017). Characterizing Spatial Variability of Ice Algal Chlorophyll a and Net Primary Production between Sea Ice Habitats Using Horizontal Profiling Platforms. *Front. Mar. Sci.* 4:349. doi: 10.3389/fmars.2017.00349

Light, B., Perovich, D. K., Webster, M. A., Polashenski, C., and Dadic, R. (2015). Optical properties of melting first-year Arctic sea ice. *J. Geophys. Res. Oceans* 120, 7657–7675.

Lu, P., Leppäranta, M., Cheng, B., and Li, Z. (2016). Influence of melt-pond depth and ice thickness on Arctic sea-ice albedo and light transmittance. *Cold Reg. Sci. Technol.* 124, 1–10. doi: 10.1016/j.coldregions.2015.12.010

Lund-Hansen, L. C., Juul, T., Eskildsen, T. D., Hawes, I., Sorrell, B., Melvad, C., et al. (2018). A low-cost remotely operated vehicle (ROV) with an optical positioning system for under-ice measurements and sampling. *Cold Reg. Sci. Technol.* 151, 148–155. doi: 10.1016/j.coldregions.2018.03.017

Massicotte, P., Amiraux, R., Amyot, M.-P., Archambault, P., Ardyna, M., Arnaud, L., et al. (2020). Green Edge ice camp campaigns: understanding the processes controlling the under-ice Arctic phytoplankton spring bloom. *Earth Syst. Sci. Data Discuss.* 12, 151–176.

Massicotte, P., Bécu, G., Lambert-Girard, S., Leymarie, E., and Babin, M. (2018). Estimating underwater light regime under spatially heterogeneous Sea Ice in the Arctic. *Appl. Sci.* 8:2693. doi: 10.3390/app8122693

Massicotte, P., Peeken, I., Katlein, C., Flores, H., Huot, Y., Castellani, G., et al. (2019). Sensitivity of phytoplankton primary production estimates to available irradiance under heterogeneous sea-ice conditions. *J. Geophys. Res. Oceans* 124, 5436–5450. doi: 10.1029/2019JC015007

Matthes, L. C., Ehn, J. K., Girard, S. L., Pogorzelec, N. M., Babin, M., and Mundy, C. J. (2019). Average cosine coefficient and spectral distribution of the light field under sea ice: implications for primary production. *Elem Sci Anth.* 7:25. doi: 10.1525/elementa.363

McMinn, A., Ashworth, C., and Ryan, K. (2005). Growth and Productivity of Antarctic Sea Ice Algae under PAR and UV Irradiances. *Bot. Mar.* 42, 401–407. doi: 10.1515/BOT.1999.046

Mundy, C. J., Gosselin, M., Ehn, J., Gratton, Y., Rossnagel, A., Barber, D. G., et al. (2009). Contribution of under-ice primary production to an ice-edge upwelling phytoplankton bloom in the Canadian Beaufort Sea. *Geophys. Res. Lett.* 36:L17601.

Mundy, C. J., Gosselin, M., Gratton, Y., Brown, K., Galindo, V., Campbell, K., et al. (2014). Role of environmental factors on phytoplankton bloom initiation under landfast sea ice in Resolute Passage, Canada. *Mar. Ecol. Prog. Ser.* 497, 39–49.

Neeley, A. R., Harris, L. A., and Frey, K. E. (2018). Unraveling Phytoplankton Community Dynamics in the Northern Chukchi Sea Under Sea-Ice-Covered and Sea-Ice-Free Conditions. *Geophys. Res. Lett.* 45, 7663–7671. doi: 10.1029/2018GL077684

Nicolaus, M., Hudson, S. R., Gerland, S., and Munderloh, K. (2010). A modern concept for autonomous and continuous measurements of spectral albedo and transmittance of sea ice. *Cold Reg. Sci. Technol.* 62, 14–28. doi: 10.1016/j.coldregions.2010.03.001

Nicolaus, M., and Katlein, C. (2013). Mapping radiation transfer through sea ice using a remotely operated vehicle (ROV). *Cryosphere* 7, 763–777. doi: 10.5194/tc-7-763-2013

Nicolaus, M., Katlein, C., Maslanik, J., and Hendricks, S. (2012). Changes in Arctic sea ice result in increasing light transmittance and absorption. *Geophys. Res. Lett.* 39:L24501.

Oziel, L., Massicotte, P., Randelhoff, A., Ferland, J., Vladoiu, A., Lacour, L., et al. (2019). Environmental factors influencing the seasonal dynamics of spring algal blooms in and beneath sea ice in western Baffin Bay. *Elem. Sci. Anth.* 7:34. doi: 10.1525/elementa.372

Pavlov, A. K., Taskjelle, T., Kauko, H. M., Hamre, B., Stephen, H. R., Assmy, P., et al. (2017). Altered inherent optical properties and estimates of the underwater light field during an Arctic under-ice bloom of *Phaeocystis pouchetii*. *J. Geophys. Res. Oceans* 122, 4939–4961. doi: 10.1002/2016JC012471

Perovich, D. K. (2005). On the aggregate-scale partitioning of solar radiation in Arctic sea ice during the Surface Heat Budget of the Arctic Ocean (SHEBA) field experiment. *J. Geophys. Res. Oceans* 110:C03002. doi: 10.1029/2004JC002512

Perovich, D. K. (2006). The interaction of ultraviolet light with Arctic sea ice during SHEBA. *Ann. Glaciol.* 44, 47–52. doi: 10.3189/172756406781811330

Perovich, D. K., and Govoni, J. W. (1991). Absorption coefficients of ice from 250 to 400 nm. *Geophys. Res. Lett.* 18, 1233–1235. doi: 10.1029/91GL01642

Perovich, D. K., and Polashenski, C. (2012). Albedo evolution of seasonal Arctic sea ice. *Geophys. Res. Lett.* 39:L08501. doi: 10.1029/2012GL051432

Piiparinen, J., Enberg, S., Rintala, J.-M., Sommaruga, R., Majaneva, M., Autio, R., et al. (2015). The contribution of mycosporine-like amino acids, chromophoric dissolved organic matter and particles to the UV protection of sea-ice organisms in the Baltic Sea. *Photochem. Photobiol. Sci.* 14, 1025–1038. doi: 10.1039/c4pp00342j

Polashenski, C., Perovich, D., and Courville, Z. (2012). The mechanisms of sea ice melt pond formation and evolution. *J. Geophys. Res. Oceans* 117:C01001. doi: 10.1371/journal.pone.0107452

Rösel, A., and Kaleschke, L. (2011). Comparison of different retrieval techniques for melt ponds on Arctic sea ice from Landsat and MODIS satellite data. *Ann. Glaciol.* 52, 185–191.

Scharien, R. K., Yackel, J. J., Granskog, M. A., and Else, B. G. T. (2007). Coincident high resolution optical-SAR image analysis for surface albedo estimation of first-year sea ice during summer melt. *Remote Sens. Environ.* 111, 160–171. doi: 10.1016/j.rse.2006.10.025

Taskjelle, T., Hudson, S. R., Granskog, M. A., and Hamre, B. (2017). Modelling radiative transfer through ponded first-year Arctic sea ice with a plane-parallel model. *Cryosphere* 11, 2137–2148.

Trodahl, H. J., and Buckley, R. G. (1990). Enhanced ultraviolet transmission of Antarctic sea ice during the austral spring. *Geophys. Res. Lett.* 17, 2177–2179. doi: 10.1029/GL017i012p02177

Uusikivi, J., Vähätalo, A. V., Granskog, M. A., and Sommaruga, R. (2010). Contribution of mycosporine-like amino acids and colored dissolved and particulate matter to sea ice optical properties and ultraviolet attenuation. *Limnol. Oceanogr.* 55, 703–713. doi: 10.4319/lo.2010.55.2.0703

Villafañe, V. E., Barbieri, E. S., and Helbling, E. W. (2004). Annual patterns of ultraviolet radiation effects on temperate marine phytoplankton off Patagonia, Argentina. *J. Plankton Res.* 26, 167–174. doi: 10.1093/plankt/fbh011

Zege, E., Malinka, A., Katsev, I., Prikhach, A., Heygster, G., Istomina, L., et al. (2015). Algorithm to retrieve the melt pond fraction and the spectral albedo of Arctic summer ice from satellite optical data. *Remote Sens. Environ.* 163, 153–164.

Zhang, J., Ashjian, C., Campbell, R., Spitz, Y. H., Steele, M., and Hill, V. (2015). The influence of sea ice and snow cover and nutrient availability on the formation of massive under-ice phytoplankton blooms in the Chukchi Sea. *Deep Sea Res. Part II Top. Stud. Oceanogr.* 118, 122–135. doi: 10.1016/j.dsr2.2015.02.008

Conflict of Interest: The authors declare that the research was conducted in the absence of any commercial or financial relationships that could be construed as a potential conflict of interest.

frontiers in Environmental Science

ORIGINAL RESEARCH
published: 15 May 2020
doi: 10.3389/fenvs.2020.00053

Identifying Drivers of Seasonality in Lena River Biogeochemistry and Dissolved Organic Matter Fluxes

Bennet Juhls[1], Colin A. Stedmon[2], Anne Morgenstern[3], Hanno Meyer[3], Jens Hölemann[4], Birgit Heim[3], Vasily Povazhnyi[5] and Pier P. Overduin[3]*

[1] Department of Earth Sciences, Institute for Space Sciences, Freie Universität Berlin, Berlin, Germany, [2] National Institute of Aquatic Resources, Technical University of Denmark, Copenhagen, Denmark, [3] Helmholtz Centre for Polar and Marine Research, Alfred Wegener Institute, Potsdam, Germany, [4] Helmholtz Centre for Polar and Marine Research, Alfred Wegener Institute, Bremerhaven, Germany, [5] Otto Schmidt Laboratory for Polar and Marine Research, Arctic and Antarctic Research Institute, Saint Petersburg, Russia

OPEN ACCESS

Edited by:
Robyn E. Tuerena, University of Edinburgh, United Kingdom

Reviewed by:
Bin Yang, Beibu Gulf University, China
Nadia Valentina Martínez-Villegas, Instituto Potosino de Investigación Científica y Tecnológica (IPICYT), Mexico

***Correspondence:**
Bennet Juhls
bjuhls@wew.fu-berlin.de

Specialty section:
This article was submitted to Biogeochemical Dynamics, a section of the journal Frontiers in Environmental Science

Received: *26 January 2020*
Accepted: *22 April 2020*
Published: *15 May 2020*

Citation:
Juhls B, Stedmon CA, Morgenstern A, Meyer H, Hölemann J, Heim B, Povazhnyi V and Overduin PP (2020) Identifying Drivers of Seasonality in Lena River Biogeochemistry and Dissolved Organic Matter Fluxes. Front. Environ. Sci. 8:53. doi: 10.3389/fenvs.2020.00053

Warming air temperatures, shifting hydrological regimes and accelerating permafrost thaw in the catchments of the Arctic rivers is affecting their biogeochemistry. Arctic river monitoring is necessary to observe changes in the mobilization of dissolved organic matter (DOM) from permafrost. The Lena River is the second largest Arctic river and 71% of its catchment is continuous permafrost. Biogeochemical parameters, including temperature, electrical conductivity (EC), stable water isotopes, dissolved organic carbon (DOC) and absorption by colored dissolved organic matter (a_{CDOM}) have been measured as part of a new high-frequency sampling program in the central Lena River Delta. The results show strong seasonal variations of all biogeochemical parameters that generally follow seasonal patterns of the hydrograph. Optical indices of DOM indicate a trend of decreasing aromaticity and molecular weight from spring to winter. High-frequency sampling improved our estimated annual fluvial flux of annual dissolved organic carbon flux (6.79 Tg C). EC and stable isotope data were used to distinguish three different source water types which explain most of the seasonal variation in the biogeochemistry of the Lena River. These water types match signatures of (1) melt water, (2) rain water, and (3) subsurface water. Melt water and rain water accounted for 84% of the discharge flux and 86% of the DOC flux. The optical properties of melt water DOM were characteristic of fresh organic matter. In contrast, the optical properties of DOM in subsurface water revealed lower aromaticity and lower molecular weights, which indicate a shift toward an older organic matter source mobilized from deeper soil horizons or permafrost deposits. The first year of this new sampling program sets a new baseline for flux calculations of dissolved matter and has enabled the identification and characterization of water types that drive the seasonality of the Lena River water properties.

Keywords: Lena River, Arctic, DOC, CDOM, optical indices, stable water isotopes

INTRODUCTION

The current warming of the Siberian Arctic (Richter-Menge et al., 2019) is causing intense changes in atmospheric forcing, precipitation, subsurface water storage and runoff from rivers to the Arctic Ocean (Yang et al., 2002; Velicogna et al., 2012; Bintanja and Selten, 2014; Niederdrenk et al., 2016). A number of studies report an increase of runoff from the Eurasian Arctic Rivers (Peterson, 2002; McClelland et al., 2006; Shiklomanov and Lammers, 2009). Of all Arctic Rivers, the Lena River is the second largest in annual discharge. Its annual discharge increased by 15.6% since 1936 (Ye et al., 2003; Shiklomanov, 2010), which may primarily be due to a winter discharge increase by 93% (Tananaev et al., 2016). Furthermore, increasing Lena River temperature (Yang et al., 2002; Liu et al., 2005) leads to more intense thermal erosion along the river shores and the coast of the Laptev Sea (Aré, 1988; Bareiss and Görgen, 2005), warms the surface waters of the central Laptev Sea, and accelerates thawing of newly formed subsea permafrost (Angelopoulos et al., 2019). A change of the river discharge, as well as changes of temperature and biogeochemical properties of river water, can strongly affect the physical state of the Arctic Ocean and marine ecosystems, especially in coastal waters. Increased export of dark, organic-rich river water leads to stronger absorption of sunlight and an increased heat flux, which can, in turn, contribute to sea ice decline (Pegau, 2002; Hill, 2008).

The carbon reservoirs of Arctic river watersheds are currently in transition. Thawing permafrost is releasing previously stored carbon (Schuur et al., 2015; Plaza et al., 2019; Turetsky et al., 2019) and increasing seasonal growth of vegetation (Schuur et al., 2009; Keuper et al., 2012). Both of these processes will increase the particulate and dissolved organic matter flux into rivers and the fluvial flux to coastal waters (Frey and Smith, 2005). Hydrological flow paths will shift toward increased groundwater flow and affect the source and composition of dissolved organic matter (DOM) (Amon et al., 2012). While particulate material is mostly deposited in shelf sea sediments to become mineralised or buried (Charkin et al., 2011; Wegner et al., 2013), dissolved organic matter is exported offshore into the open Arctic Ocean (i.e., Juhls et al., 2019) and approximately 50% is thought to be exported onwards to the Atlantic (Granskog et al., 2012). Most of the DOM transported by the Lena River originates from leaching of surface soils of dominantly boreal forest vegetation (Amon et al., 2012; Kaiser et al., 2017). However, the effect of ongoing permafrost thaw on hydrological pathways will affect DOM fluxes (Freeman et al., 2001; Frey and Smith, 2005). In addition to the amount of DOM, its composition, source and age in the Lena River are expected to change (Amon et al., 2012; Walker et al., 2013; Mann et al., 2016; Wild et al., 2019).

Initiation of the pan-Arctic River sampling programs PARTNERS (2003–2007), Student Partners (2004-2009) and ArcticGRO (since 2009), have provided invaluable insights into the quantitative and qualitative properties of dissolved and particulate matter exported into the Arctic Ocean (Raymond et al., 2007; Holmes et al., 2008; Stedmon et al., 2011; Amon et al., 2012; Mann et al., 2016). Results of PARTNERS and ArcticGRO (Raymond et al., 2007) show that the Lena River contributes 20–29% of the total circumpolar fluvial dissolved organic carbon (DOC) export to the Arctic Ocean. However, reported estimates of annual Lena River DOC fluxes span a wide range between 3.6 Tg C (Gordeev and Kravchishina, 2009) and 7.67 Tg C (Kicklighter et al., 2013). This is likely because the calculation of annual flux is based on a few water samples per year, which are usually taken during open water season (Raymond et al., 2007; Stedmon et al., 2011; Holmes et al., 2012). Such estimates are susceptible to systematic biases: limited sampling can miss seasonal peaks of DOC concentration and lead to subsequent underestimation of the DOC flux (Jollymore et al., 2012). Furthermore, samples from the Lena River are mostly taken in Zhigansk, which is located ∼800 km upstream of the river mouth (**Figure 1**). Little is known about DOM transformation, mineralization and release to the atmosphere on the way from Zhigansk to the river mouth (Amon et al., 2012). In order to identify a trend in DOC flux, it is crucial to reduce uncertainty in the calculated annual flux to below the interannual variability. While most research attention has focused on potential long-term trends of river DOC export (Kicklighter et al., 2013; Tank et al., 2016), seasonal variations of ice break-up and freeze-up timing and the associated discharge, material load and biogeochemistry are also affected by the changing climate and require research attention. Earlier spring ice break-up and later freeze-up in fall result in longer open water and shorter winter flow periods and will have an impact on the annual organic matter flux. Monitoring river water biogeochemistry may provide insights into the progress of this change, since the river water chemistry, measured near its mouth, integrates the changes occurring in the catchment as a whole. DOM fluxes and composition can be expected to change and this will also ultimately influence the fate of terrestrial carbon in the Arctic, including that carbon stored in shelf sediments, mineralised in the Arctic, and exported to the north Atlantic Ocean.

To accurately capture short-term variability and understand how changing climate influences in-river processes that affect organic matter quality and its function in the fluvial ecosystem, it is necessary to monitor water constituents with a high temporal resolution and throughout the whole season (including both open water and ice-covered periods). To characterize fluxes from land to sea, this should be done as close as possible to the river mouth. Such sampling, carried out over multiple years, can enable prediction of future responses of river flux to projected change. The Research Station Samoylov Island provides an opportunity to meet these criteria in the central Lena River Delta as it serves as the basis for regular, frequent and year-round sampling for major biogeochemical parameters. The goal of this study is to better understand and decipher seasonal variations of hydrochemical characteristics and organic matter and its optical properties of the Lena River. We aim to identify how changing water sources drive seasonal changes in fluvial biogeochemistry by putting such a sampling program into place over 1 year at the Research Station Samoylov Island. With this, we provide a basis for future trend analyses and remote sensing studies that may be used to upscale observations from the hydrographic point scale.

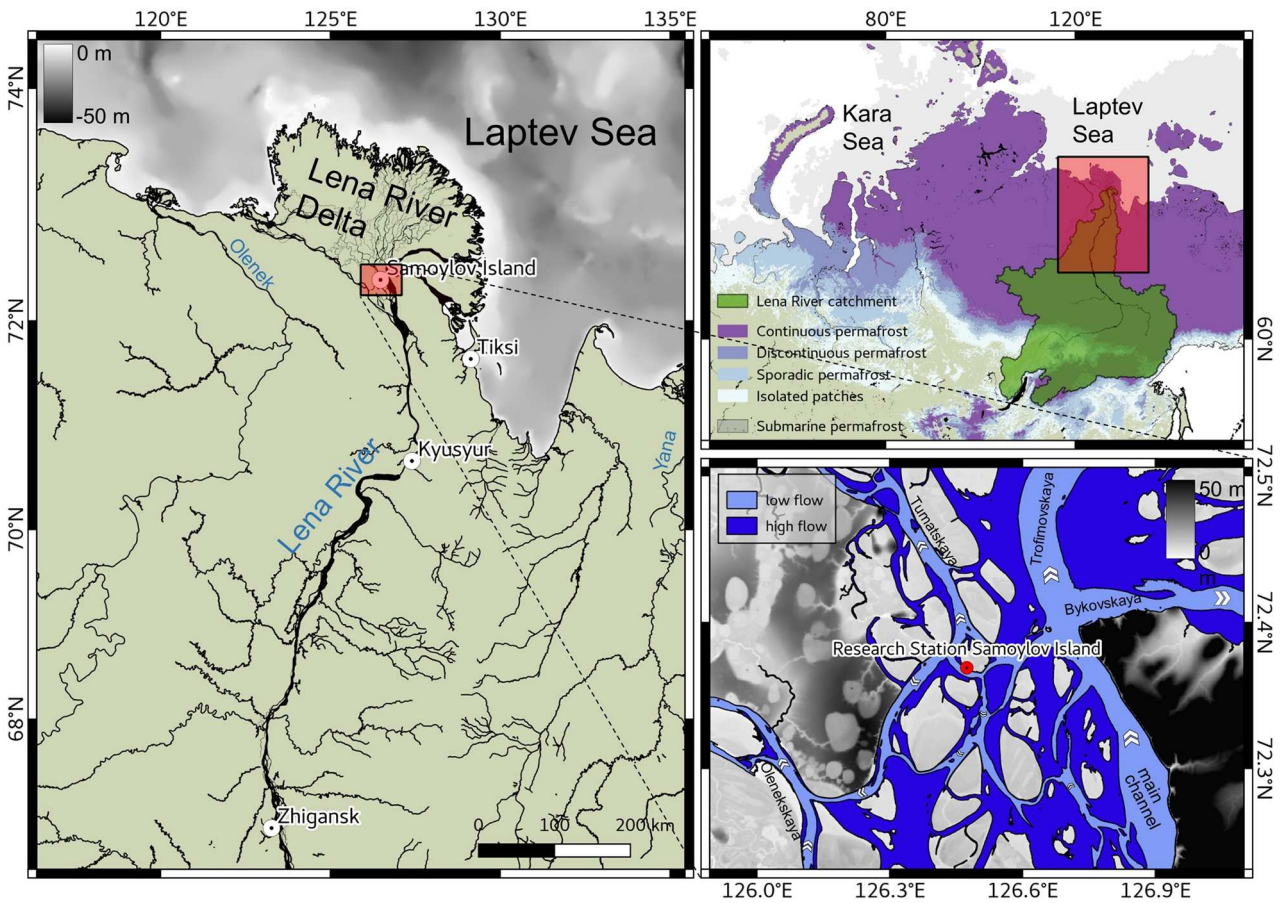

FIGURE 1 | Lena River Delta region. The upper right panel shows an overview map of the study area with permafrost zones (Obu et al., 2019; Overduin et al., 2019). The left panel shows the northern part of the Lena River catchment with the Lena River Delta at the coast of the Laptev Sea. The lower right panel the central Lena River Delta with the location of the Research Station Samoylov Island and the Lena River channels (blue) and flow directions; DEM is based on ArcticDEM (Porter et al., 2018). Dark blue indicates Lena River channels during high flow right after spring ice break-up and light blue indicates Lena River channels during low flow in late summer (based on Sentinel 2 imagery[1]).

MATERIALS AND METHODS

Study Area and Sample Collection

The Lena watershed area (2.61×10^6 km^2) extends ~2,400 km from north to south and is underlain by all types of permafrost: continuous (70.5%), discontinuous (10.6%), sporadic (6.0%), and isolated (7.3%). 5.6% of the watershed, on the northern side of the Lake Baikal, is free of permafrost [numbers calculated using permafrost zones by Obu et al. (2019)]. The catchment is dominantly covered by forest (72.1%) and shrubland (12.5%) (Amon et al., 2012).

We collected water samples from the river surface in the center of the Olenekskaya Channel near Samoylov Island using a pre-rinsed HDPE 1 L bottle (in summer) or a UWITEC 1 L water sampler (under ice) for 1 year beginning in April 2018 (**Figure 1**). The island is located in the central Lena River Delta and hosts a permanently staffed research station (Research Station Samoylov Island), which has been operating since 2013. Additional sample sets with higher temporal resolution, from different years and from Lena River ice, are listed in **Table 1**. During the open water period (28 May 2018 to 22 October 2018), water was sampled from a small boat, and during ice-covered period (until 27 May 2018 and from 23 October 2018), through a hole drilled through the river ice. Two samples during the river ice break-up as well as four samples during the ice freeze-up in October were taken from the shore due to the inaccessibility of a more centered location on the river channel. Water samples were subsampled, filtered and conserved at the research station directly after sampling.

Sampling started on 20 April 2018 at a frequency of ~4 days and is ongoing. For this study, we use a dataset of almost one complete year (until 6 April 2019). For each sample, *in situ* temperature and electrical conductivity (EC) were measured using a hand-held conductivity meter (WTW COND 340I, accuracy ± 0.5%). For all samples, a series of biogeochemical parameters were analyzed (**Table 1**). The EC was additionally re-measured on each sample in the lab using a hand-held

[1]Copernicus Open Access, Hub. Available online at: https://scihub.copernicus.eu/.

TABLE 1 | Sampling period, frequency, sample type and measured parameters of datasets used in this study.

Dataset	Location	Period	Type	Frequency	No. of samples	Parameters
This study	Samoylov Island	20 April 2018–06 April 2019	Water samples	∼ every 4 days	75	DOC, a_{CDOM}, stable H_2O isotopes, cations & anions, EC
This study	Samoylov Island	4 July 2018–15 July 2018	Water samples	2 times per day	23	DOC and a_{CDOM} (using different filter types and filter pore sizes), stable H_2O isotopes, EC
This study	Samoylov Island	4 May 2018	Ice core samples	1 time	1 ice core with 57 subsamples	DOC, a_{CDOM}, stable H_2O isotopes, cations & anions, EC
Eulenburg et al. (2019)	Samoylov Island	22 May 2014–19 June 2014	Water samples	1 to 2 times per day	43	DOC, a_{CDOM}, stable H_2O isotopes, EC
ArcticGRO & Partners; Holmes et al. (2018a,b)	Zhigansk	2002–2019	Water samples	Up to 6 per year	64	DOC, a_{CDOM}, stable H_2O isotopes

conductivity meter (WTW Multilab 540, accuracy ± 0.5%) after transport to Germany. For 11 days, from 4 July 2018 to 15 July 2018, samples were taken at a higher frequency and for additional parameters (**Table 1**).

Discharge

The discharge of the Lena River is monitored by the Russian Federal Service for Hydrometeorology and Environmental Monitoring (Roshydromet) and data are available at www.r-arcticnet.sr.unh.edu (Shiklomanov, 2010; 1936–2009) and www.arcticgreatrivers.org (Shiklomanov et al., 2018, 1999 to present). All discharge data shown in this study were corrected for the distance difference between the gauge station at Kyusyur and water sampling station at Samoylov Island (∼220 km) using a Lena River propagation speed estimate (88 km d^{-1}) from Smith and Pavelsky (2008).

Biogeochemical Parameters

For each sample of the Lena River monitoring program, 1 L of surface river water was collected and subsequently subsampled. For DOC and CDOM absorption (a_{CDOM}), the sample was filtered through a 0.45 µm cellulose acetate filter which had been rinsed with 20 mL sample water. Over 10 days in July 2018, additional filter type and pore size tests for DOC and a_{CDOM} were carried out (**Supplementary Figures 1, 2**). DOC samples were filled into a pre-rinsed 20 mL glass vial and acidified with 25 µL HCl Suprapur (10 M) and stored in the dark at 4°C. After transport, DOC samples were analyzed at the Alfred Wegener Institute Helmholtz Center for Polar and Marine Research (AWI), Potsdam, Germany. DOC concentrations were analyzed using high temperature catalytic oxidation (TOC-VCPH, Shimadzu). Three replicate measurements of each sample were averaged. After every ten samples, a blank (Milli-Q water) and a standard was measured. Eight different commercially available certified standards covered a range between 0.49 mg L^{-1} (DWNSVW-15) and 100 mg L^{-1} (Std. US-QC). The results of standards provided an accuracy better than ± 5%.

a_{CDOM} samples were collected in pre-rinsed 50 mL amber glass bottles that were stored in the dark at 4°C until analysis. a_{CDOM} was measured at the Otto Schmidt Laboratory for Polar and Marine Research (OSL), Saint Petersburg, Russia using a SPECORD 200 spectrophotometer (Analytik Jena) and at the German Research Center for Geosciences (GFZ), Potsdam, Germany using a LAMBDA 950 UV/Vis (PerkinElmer). The median absorbance (A_λ) of three replicate measurements was used to calculate the a_{CDOM} (λ):

$$a_{CDOM}(\lambda) = \frac{2.303 * A_\lambda}{l},$$

where l is the path length (length of cuvette). Fresh Milli-Q water was used as reference. To detect chemical composition and molecular structure of the DOM, two optical indices, SUVA and S275-295, were used. Both indices correlate with aromaticity and molecular weight of bulk DOC (Weishaar et al., 2003; Helms et al., 2008). SUVA (m^2 g C^{-1}) was calculated by dividing the decadal absorption A/l (m^{-1}) at 254 nm by DOC concentration (mg L^{-1}). The spectral slope of $a_{CDOM}(\lambda)$ between 275 and 295 nm (S275–295) is an index for photodegradation (Helms et al., 2008). S275–295 was calculated by fitting a regression for the wavelength ranges 275–295 nm to the exponential function (Helms et al., 2008):

$$a_{CDOM}(\lambda) = a_{CDOM}(\lambda_0) * e^{-S(\lambda - \lambda_0)},$$

where $a_{CDOM}(\lambda_0)$ is the absorption coefficient at reference wavelength λ_0 and S is the spectral slope of $a_{CDOM}(\lambda)$ for the chosen wavelength range.

Water samples for stable isotopes were collected untreated in 10 mL HDPE vials, sealed tightly, stored in the dark at 4°C. Measurements were conducted at the laboratory facility for stable isotopes at AWI Potsdam using a Finnigan MAT Delta-S mass spectrometer equipped with equilibration units for the online determination of hydrogen and oxygen isotopic composition. The data is given as δD and $\delta^{18}O$ values, which is the per

mille difference to standard V-SMOW. The deuterium excess (d-excess) is calculated by:

$$\text{d-excess} = \delta D - 8. * \delta^{18}O.$$

The measurement accuracy for hydrogen and oxygen isotopes was better than ±0.8‰ and ±0.1‰, respectively (Meyer et al., 2000).

Water samples for concentrations of major dissolved components were filtered using a syringe-mounted 0.45 µm CA filter and kept cool and dark until analysis. Concentrations of major anions (SO_4^{2-}, Cl^-, Br^-, F^-, NO^{3-}, and PO_4^{3-}) were determined using ion chromatography (Thermo-Fischer ICS 2100; Weiss, 2001). Total dissolved elemental concentrations (for Al, Ba, Ca, Fe, K, Mg, Mn, Na, P, Si, and Sr) were measured with inductively coupled plasma optical emission spectroscopy (ICP-OES; Perkin Elmer Optima 8300DV; Boss and Fredeen, 1997).

In addition, one ice core (LE08) was drilled on the river channel at Samoylov Island on 4 May 2018 (**Figure 1**). The core was drilled using a Kovacs Mark III and wrapped in HDPE plastic sleeves and stored frozen for transport to AWI Potsdam where further subsampling and analysis were done. The core was retrieved in five pieces with a total length of 144 cm, which was close to the ice thickness measured in the borehole. The ice core was cut into 3 cm slices and analyzed for DOC, $a_{CDOM}(\lambda)$, stable oxygen isotopes, cations and anions following the methods described above.

TABLE 2 | Electrical conductivity (EC) and $\delta^{18}O$ for water source endmember.

Endmember	EC (µS cm^{-1})	$\delta^{18}O$ (‰)
EM1	80	−25
EM2	100	−16
EM3	600	−22

Flux Calculations

For visualization, concentrations (C_d) between sampling dates were linearly interpolated. Then, daily fluxes were calculated by multiplying daily concentrations and the daily discharge (Q_d).

$$\text{Flux}_d = C_d \left(\text{mg L}^{-1}\right) x\, Q_d \left(\text{m}^3\ \text{s}^{-1}\right) x\, 86400\ s,$$

Daily fluxes (Flux_d) were summed for individual periods. The annual heat flux was calculated as in Liu et al. (2005), Yang et al. (2013) to enable inter-annual comparisons. Negative river water temperatures were set to 0°C and the specific heat capacity of water was set constant to 4.184 J g^{-1} °C^{-1}.

Water Source Endmember Calculation

98% of the variability of all measured parameter can be explained by three components (**Supplementary Table 1**). We distinguished three water source fractions using EC and water

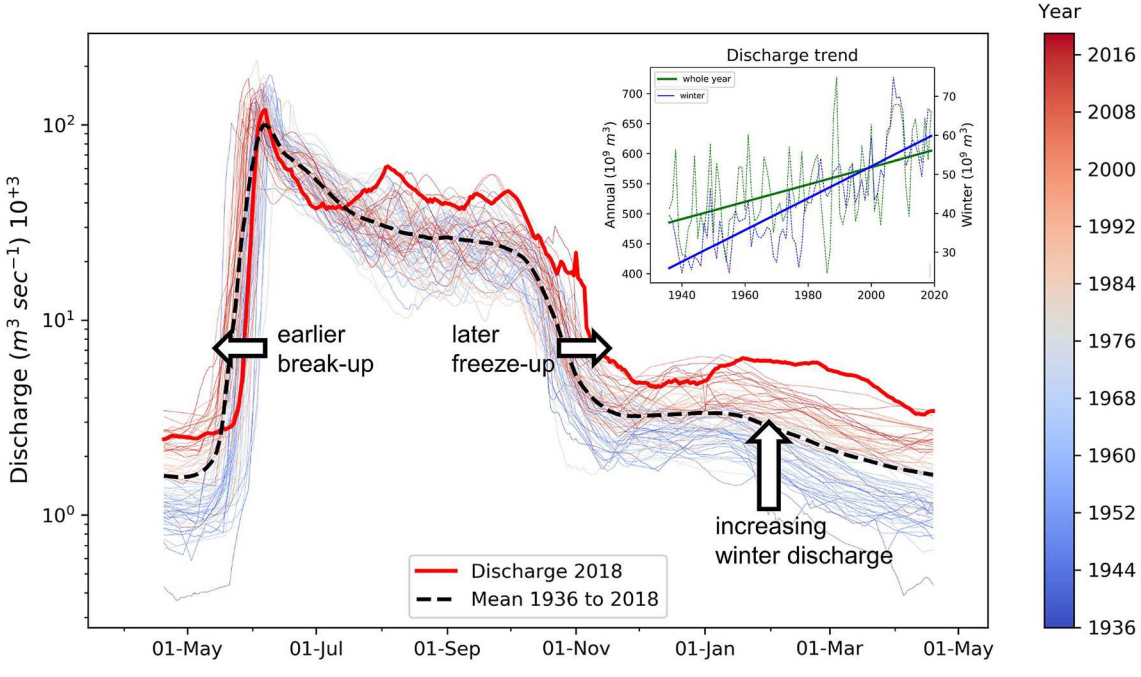

FIGURE 2 | Discharge data from Kyusyur station from 1936 to 2018. Colors from blue to red indicate the year from 1936 to 2018. The red thick solid line shows the year 2018 and the black thick dashed shows the mean of the period from 1936 to 2018. The inset figure shows the discharge flux for the whole year (green) and for November to April (blue). Discharge data: A.I. Shiklomanov (2010) 1939–2008, ArcticGRO 2009–2019.

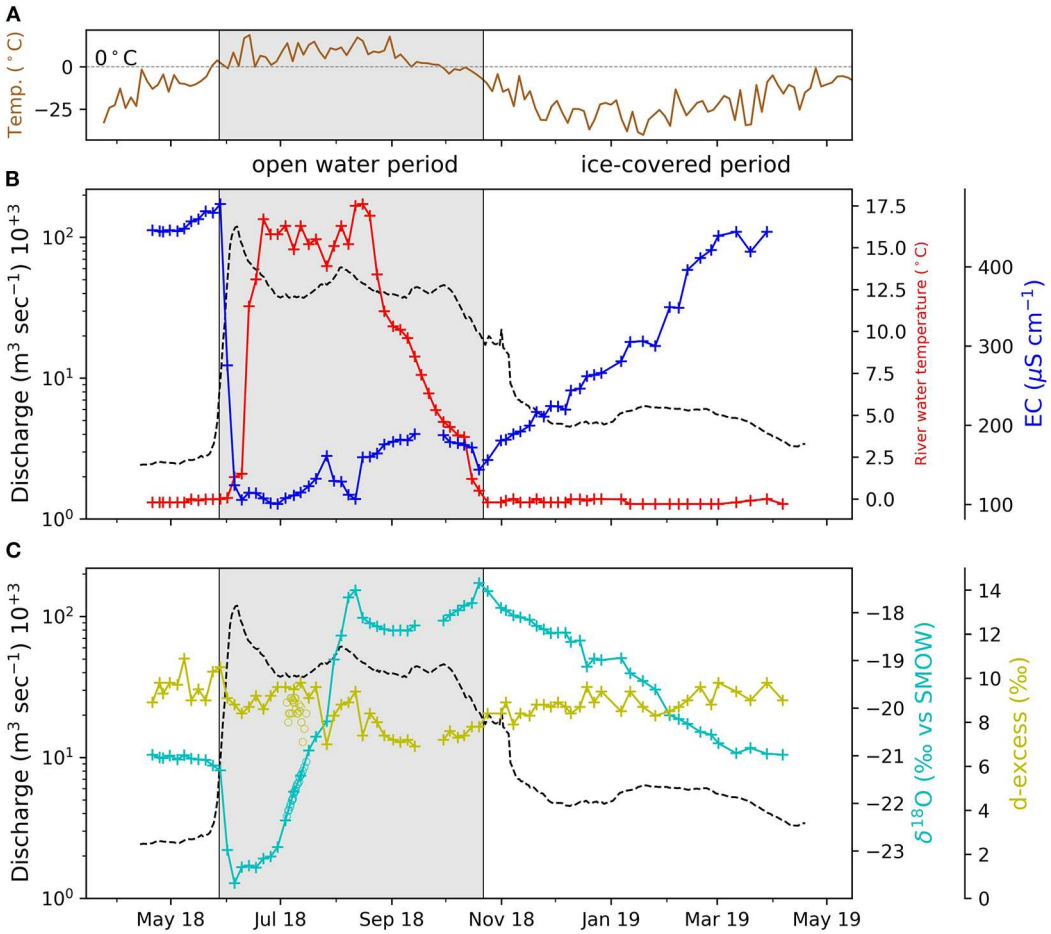

FIGURE 3 | Air temperature, measured **Figure 2** in Tiksi **(A)**, discharge (black dashed line) **(B,C)**, river water temperature and EC **(B)** and $\delta^{18}O$ and d-excess **(C)**. The gray area indicates the period where the Lena River channels around Samoylov Island were not ice covered (dates are based on optical satellite imagery). The EC values are those from measurements made in the laboratory following sampling. Circles in respective colors in **(C)** show high frequency measurements from July 2018.

$\delta^{18}O$ by solving the mass balance equation:

$$f_{EM1} + f_{EM2} + f_{EM3} = 1$$
$$f_{EM1}EC_{EM1} + f_{EM2}EC_{EM2} + f_{EM3}EC_{EM3} = EC$$
$$f_{EM1}\delta^{18}O_{EM1} + f_{EM2}\delta^{18}O_{EM2} + f_{EM3}\delta^{18}O_{EM3} = \delta^{18}O$$

for unknowns, where $f \in [0; 1]$ is the fraction of each water source. We chose endmember for EC and $\delta^{18}O$ values that encompass the overall variability of observed EC and $\delta^{18}O$ (**Table 2**).

RESULTS

The Lena River discharge shows strong seasonality, with low discharge during the ice-covered winter, a spring peak maximum and a moderate summer discharge (**Figure 2**). In some years, additional discharge peaks in late summer and fall occur. Over the period from 1936 to 2018, the Lena River's annual discharge increased (1.44×10^9 m^3 year^{-1}), to a large part driven by the increasing winter (November to April) discharge flux (0.41×10^9 m^3 year^{-1}; **Figure 2** inset). Furthermore, trends are clearly visible in the colors of **Figure 2**, indicating that river ice breaks up earlier and freezes later in the year.

Putting the year 2018 into the long-term context, the winter (November to April) and late summer (August to October) discharge were significantly higher than their 1938–2018 means. The timing and intensity of the 2018 spring discharge peak was close to the long-term median. Summer 2018 was also characterized by multiple higher discharge events, which rise above the long-term mean. The elevated discharge continues into the first 3 months of 2019 (dashed line in **Figures 3B,C**).

Lena River Temperature and Chemistry

During the period when the Lena River is ice-covered, the mean river water temperature below the ice is slightly below 0°C (−0.2 to −0.01°C; **Figure 3A**). During the first days of spring peak discharge, the temperature only marginally increases to 1.5°C. About 2 weeks after the start of spring peak discharge, the temperature rises within 1 week to a relatively stable summer level around 16°C. With decreasing air temperatures in fall,

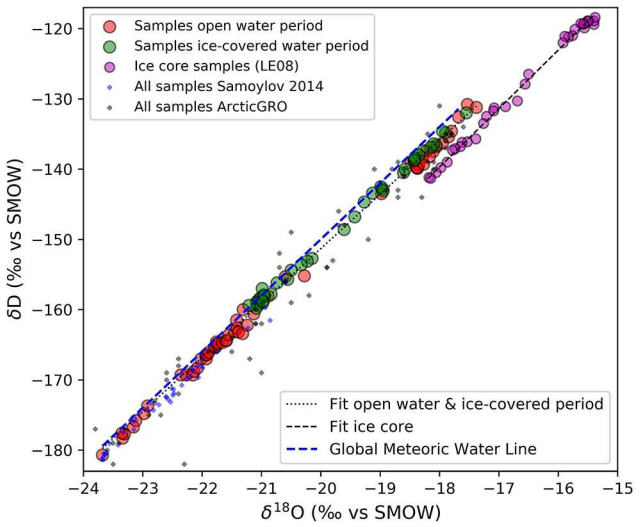

FIGURE 4 | Relationship between $\delta^{18}O$ and δD for open water (red) and ice-covered (green) samples. The black dotted line shows the linear regression of samples from open water period (28 May 2018 to 22 October 2018) and ice-covered period (until 27 May 2018 and from 23 October 2018) combined ($\delta D = 7.73 \times \delta^{18}O + 3.36$). The black dashed line shows the linear regression of ice core samples ($\delta D = 8.33 \times \delta^{18}O + 10.14$). The blue dashed line shows the global meteoric water line after Craig (1961). Additional samples from Samoylov 2014 (blue crosses) and ArcticGRO (gray crosses) include samples from the ice-covered period as well as open water period.

the river temperature gradually decreases and reaches 0°C in mid-October when the Lena River starts to freeze. The highest river water temperature (17.6°C) was recorded on 15. August 2018. The EC drops almost simultaneously with the onset of the spring peak discharge from its annual maximum of 490 µS/cm to its annual minimum of 99 µS/cm. The EC is generally low in summer, and gradually increases during the ice-covered period. The summer discharge peaks coincide with decreases in the EC.

A strong seasonality in river water $\delta^{18}O$ values was observed, ranging between −17.4‰ and −23.7‰ in the sampling period. During late winter, when the Lena River ice thickness reached its maximum (March-April), $\delta^{18}O$ was stable at around −21‰. The lowest $\delta^{18}O$ values (−23.7‰) occurred during the spring freshet in the first days of June, coinciding with the highest discharge. The highest $\delta^{18}O$ (−17.4‰) occurred shortly before freeze-up at the end of October. Similarly high $\delta^{18}O$ (−17.5‰) occurred during the mid-summer discharge peak. With decreasing discharge and freezing of the Lena River and its catchment, $\delta^{18}O$ gradually decreased toward −21‰. d-excess values were highest (+10.9‰) during late winter and lowest (+6.9‰) in late summer. The d-excess of the measurements in July 2018 were about 0.5‰ lower than long-term values. Additional measurements of $\delta^{18}O$ in July 2018 agreed with the long-term measurements.

For all samples in the Lena River dataset, we observed a very strong relationship ($r^2 = 0.996$) between $\delta^{18}O$ and δD (**Figure 4**). The slope of the linear regression is lower (7.73) than the Global Meteoric Water Line (slope GMWL = 8.0), but almost identical to the Local Meteoric Water Line (the slope of the LMWL is 7.6 for 381 event-based samples, and 7.7 for 41 monthly means; Spors, 2018). Lena River ice core samples (LE08) showed overall higher $\delta^{18}O$ and δD than water samples and the regression line showed a clear offset compared to river water samples (**Figure 4**). The slope of the linear regression of ice core samples (8.32) was higher than that of Lena River water. Lena River water samples from 2014 were similarly strongly correlated ($r^2 = 0.987$) and had a similar slope (7.6) compared to the Lena River samples from 2018. Both slopes, from 2014 and 2018, are lower, compared to the GMWL. Ice core samples had higher mean $\delta^{18}O$ and δD values, but with a shift to lower δD for similar $\delta^{18}O$.

The concentrations of most of the major cations and anions correlated with the seasonal variability in EC (**Supplementary Figure 3**). Whereas concentrations of all ions increased during the ice-covered period, the concentration of K behaved differently, with lower values during January and February 2019. During the ice-covered period, Na and Cl^- dominated, while in summer and during the spring discharge peak, Ca and Cl^- and SO_4^{2-} dominated. Whereas concentrations for some species regained over 50% of their late winter concentration during summer (F^-, Si), others did not increase until mid-winter (Na, Ba, Cl^-, Br^-). The end of the open water period was marked by a small decrease in concentration that lasted for almost 2 weeks for all species. Si concentration was hardly affected by precipitation events during the open water period, in contrast to all other measured concentration (for example, the precipitation peak centered at August 20, 2018). Annual fluxes of major ions are presented in **Table 3**. Note that some concentrations fell below analytical detection limits and this prevented a meaningful flux calculation.

Dissolved Organic Carbon (DOC) and Colored Dissolved Organic Matter (CDOM)

Dissolved organic matter in the Lena River varied with the hydrograph, with DOC concentrations ranging from 4.9 to 18.2 mg L^{-1} and $a_{CDOM}(254)$ ranging from 40.8 to 150.92 m^{-1} (**Figure 5A**). Lowest values were observed at the end of winter, right before or with the onset of the spring ice break-up, whereas highest values occurred only a few days later during the spring ice break-up. In summer (July to October) both DOC and $a_{CDOM}(254)$ returned to values near pre-break-up [~6–7 mg L^{-1} DOC and ~44 to 50 m^{-1} $a_{CDOM}(254)$] but then increased during the mid-summer discharge peak from 6.2 to 10.2 mg L^{-1} and from 45.3 to 85.6 m^{-1} $a_{CDOM}(254)$. High frequency sampling during July 2018 agreed closely with the overall pattern from the annual sampling (circles in **Figure 5**).

In winter, DOC and $a_{CDOM}(254)$ increased in response to comparatively minor fluctuations in discharge, with winter maxima of 11.4 mg L^{-1} and 67.8 m^{-1}, respectively. DOC and $a_{CDOM}(254)$ in the river ice had means of 1.04 mg L^{-1} DOC and 0.96 m^{-1} $a_{CDOM}(254)$, with no clear systematic vertical trend down core (**Supplementary Figure 4**).

Two periods with clear correlations between DOC and $a_{CDOM}(254)$ were apparent: one for the open water period (28 May 2018 to 22 Oct. 2018), and another for the rest of the

TABLE 3 | Annual mean values and annual fluxes of Lena River biogeochemical parameter.

	Discharge	Temperature	EC	Heat flux	DOC	$a_{CDOM}(254)$
Annual mean	21173.8 m^3 s^{-1}	4.74°C	250.6 µS cm^{-1}	6.95 × 10^{16} J d^{-1}	8.85 mg L^{-1}	62.8 m^{-1}
Annual flux	690.2 x 10^9 m^3	-	-	25.3 EJ	6.79 Tg	52.1 × 10^{12} m^2

	Ca	K	Mg	Na	Si	Sr	Fl	Cl	SO_4
Annual mean	22.5 mg L^{-1}	0.83 mg L^{-1}	6.69 mg L^{-1}	18.0 mg L^{-1}	3.02 mg L^{-1}	0.19 mg L^{-1}	0.12 mg L^{-1}	26.5 mg L^{-1}	19.2 mg L^{-1}
Annual flux	11.8 Tg	0.45 Tg	3.29 Tg	6.95 Tg	1.59 Tg	0.09 Tg	0.07 Tg	10.2 Tg	8.76 Tg

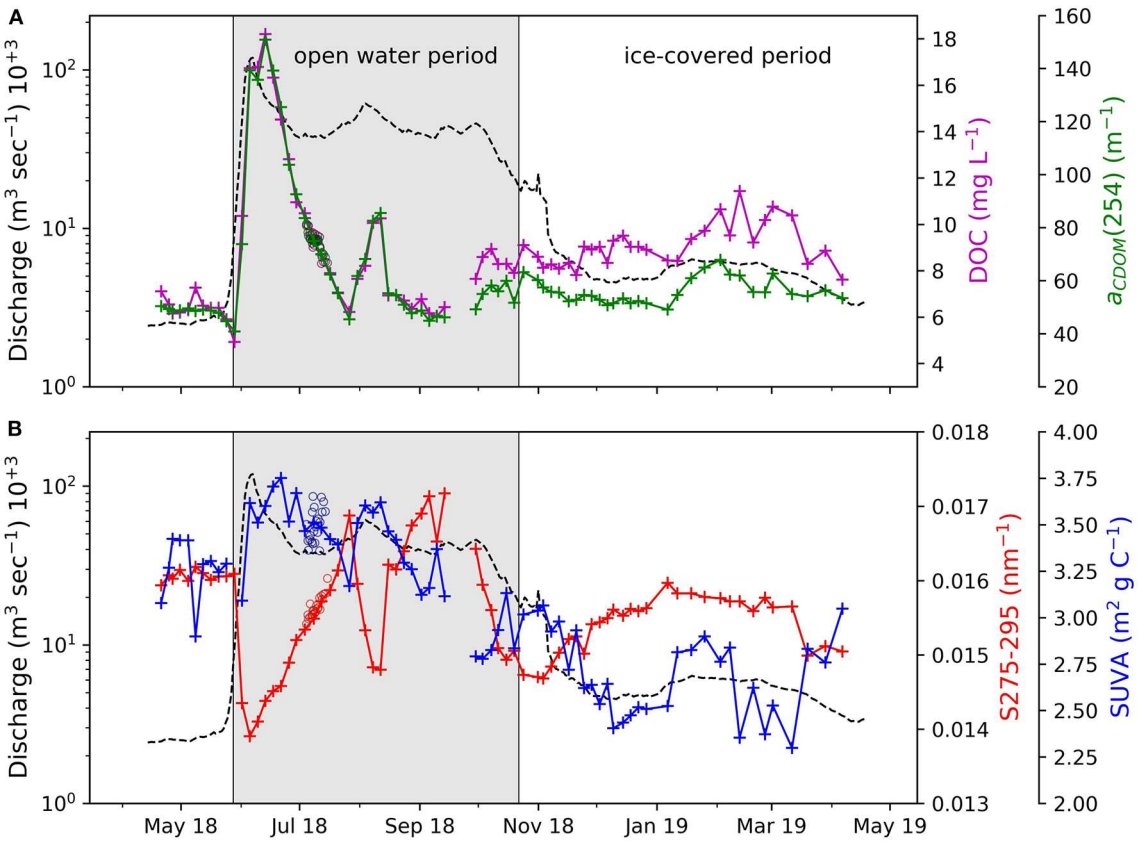

FIGURE 5 | Seasonal variation of DOC and $a_{CDOM}(254)$ **(A)** and S275-295 and SUVA **(B)**. Black dashed line shows the discharge. Circles in respective colors show high frequency measurements from July 2018.

time series, with ice cover. This separation indicates qualitative differences in the river DOM (**Figure 6**). The slope for the $a_{CDOM}(254)$ vs. DOC regression was significantly steeper for the open water period (8.86 m^2 g^{-1}) while the ice covered period had a low slope (2.91 m^2 g^{-1}) and greater intercept. These seasonal qualitative changes were also reflected in S275-295 and SUVA. The lowest slopes (0.0139 nm^{-1}) were measured during the spring ice break-up and the highest during late summer (0.172 nm^{-1}). In winter, during the ice-covered period, S275-295 varied between 0.0147 and 0.0162 nm^{-1}. The SUVA peaked during the spring ice break-up (3.75 m^2 g C^{-1}) and during the early summer discharge peak (3.62 m^2 g C^{-1}) and reached a minimum in late winter (2.3 m^2 g C^{-1}). Beginning at spring ice break-up, SUVA decreased until late winter. In April 2019, almost 2 months before the return of the spring ice break-up, SUVA increased from 2.2 to 3.1 m^2 g C^{-1}.

DOC Flux

We calculated an annual DOC flux of 6.79 Tg C and a discharge flux of 690.2 x 10^9 m^3 for the considered period of 1 year starting 20 April 2019, during which 2.78 Tg C (41% of annual flux) were transported in spring, 3.26 Tg C (48% of annual flux) in summer and 0.75 Tg C in winter (11% of annual flux) (**Supplementary Figure 5**).

Next, we compare the DOC concentration, $a_{CDOM}(254)$ and calculated fluxes of the spring period in 2014 (**Figure 7A**) with

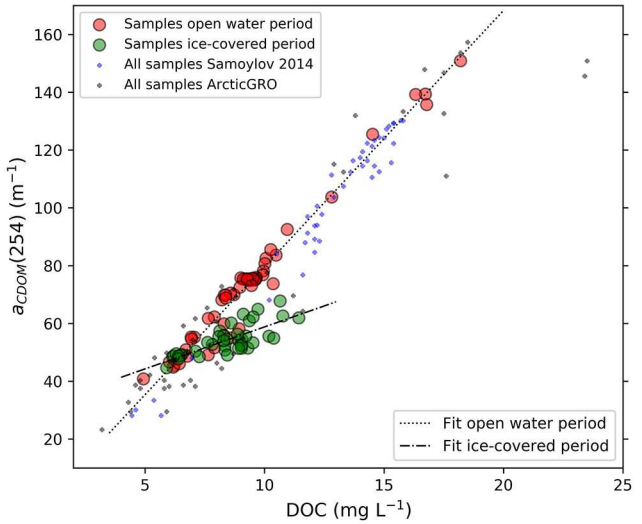

FIGURE 6 | Relationship of Lena River DOC and $a_{CDOM}(254)$ samples. Samples from 2018/19 are shown as circles. Samples from the open water period (28 May 2018 to 22 October 2018) are displayed as red circles, r^2: 0.97, samples from the ice covered period (until 27 May 2018 and from 23 October 2018) as green circles, $r^2 = 0.59$). ArcticGRO data (gray crosses) sampled near Zhigansk ($r^2 = 0.89$, Holmes et al., 2018b) and monitoring data from the 2014 freshet (blue crosses) sampled near Samoylov Island (Samoylov 2014, $r^2 = 0.96$, Eulenburg et al., 2019) are added for comparison. The dotted black line shows the linear regression of the samples from the open water period ($a_{CDOM}(254) = 8.86 \times DOC - 8.98$) and the dashed-dotted black line shows the linear regression of the samples from the ice-covered period ($a_{CDOM}(254) = 2.91 \times DOC + 29.74$).

the hydrologically aligned similar period in 2018 (**Figure 7B**). In 2014, the spring ice break-up discharge peak occurred 6 days earlier than in 2018. Thus, we compare period of similar length in 2018 (29 days) which is shifted 6 days later. In 2014, the discharge flux was 23.3% higher than in 2018, whereas the DOC flux was only 9% higher. This was due to the maximum DOC concentrations being slightly lower in 2014. Both years showed a similar pattern of decreasing DOM concentrations right before the start of the discharge peak followed by a rapid increase of DOM. Right after the discharge reached its maximum, it decreased again rapidly, whereas the DOM concentration remained high and decreased slowly.

DISCUSSION

Drivers of Seasonal Variability in Hydrochemistry and DOM

The Lena River is characterized by a strong seasonality in discharge and its water biogeochemistry and the hydrograph can generally be divided into three periods: the spring ice break-up, summer to fall, and winter. Hence, we compare and contrast these three hydrologically and biogeochemically distinct periods and speculate about the shifts in the provenance of the water and its dissolved load.

(1) **Spring Ice Break-up** is the period when air temperatures are consistently positive in most of the catchment and major parts of the winter-accumulated snow and ice melt. Snowmelt does not occur simultaneously across the whole catchment, but begins in the south and moves northward. About 4 days after the ice break-up of the Lena River, the annual discharge maximum (~120 000 m^3 s^{-1}) is reached. River water temperatures during the first days of the spring discharge peak remain around 0°C, resulting in an export of large volumes of cold water to the Laptev Sea. Simultaneously with the discharge maximum, the water source endmember EM1 peaks (80% on 5 June) and remains the dominant water source until mid-July (**Figure 8**). We identified this endmember as melt water due to the sudden drop of EC (**Figure 3B**), major ions (**Supplementary Figure 3**) as well as $\delta^{18}O$ values (**Figure 3C**). Chosen endmember values for EM1 with low EC (80 µS cm^{-1}) and low $\delta^{18}O$ (−25‰) are characteristic for snow melt water and agree well with reported values (Sugimoto and Maximov, 2012; Spors, 2018; Bonne et al., 2020). With regards to the DOM results it is clear that this pulse has two portions associated with it. The initial input of snow meltwater has low DOM and likely reflects snow not in contact with soil. This results in an initial decrease in DOM in the river which lasts on the order of a week, captured by the high temporal resolution of sampling. This interpretation is supported by the fact that the qualitative measures of DOM (SUVA and S275-295) do not change, essentially reflecting dilution of river water. This is then followed by the discharge maximum, where DOC reaches highest annual concentrations (18.2 mg L^{-1}). In only 2 months (between 2. June 2018 and 2 August 2018), 53.2% (3.62 Tg C) of the total annual DOC flux (6.79 Tg C) is exported to the Laptev Sea. By applying water source fractions, we estimate that 43.3% (2.9 Tg C) of the annual DOC flux is transported with melt water into the river (**Figure 9**). Moreover, melt water accounts for 35% (242×10^9 m^3) of the total annual discharge flux (690.18×10^9 m^3). This volume agrees well with the accumulated snow volume in the Lena River catchment. Using a mean (1988 to 2000) winter peak value of 120 mm as the snow water equivalent in the catchment (Yang et al., 2007), we derive a snow to water equivalent volume of 295.2×10^9 m^3.

With the discharge peak and high DOM concentrations, the quality of the organic matter also changes. Optical indices of DOM (SUVA and S275-295) were comparable to reported values (Walker et al., 2013). The changes occurring during the freshet indicate an organic matter source with high molecular weight and aromaticity (**Figure 5B**) (Weishaar et al., 2003; Helms et al., 2008) which is likely young DOM (Amon et al., 2012). During this period, the frozen ground beneath the snowpack during melt limits infiltration, confining most flow to a thin desiccated organic layer and to overland or snowpack flow. The DOM thus likely originates from modern plant litter, which is washed into the Lena River by the rapid and extensive snowmelt (Amon et al., 2012). Very low S275-295 during the spring ice break-up also suggests the input of fresh DOM.

(2) **Open Water Period in Summer and Fall** is the period during which Lena River water temperatures reach the annual maximum. In this period, the discharge decreases to about half of the spring peak values (40 000 to 60 000 m^3 s^{-1}). The

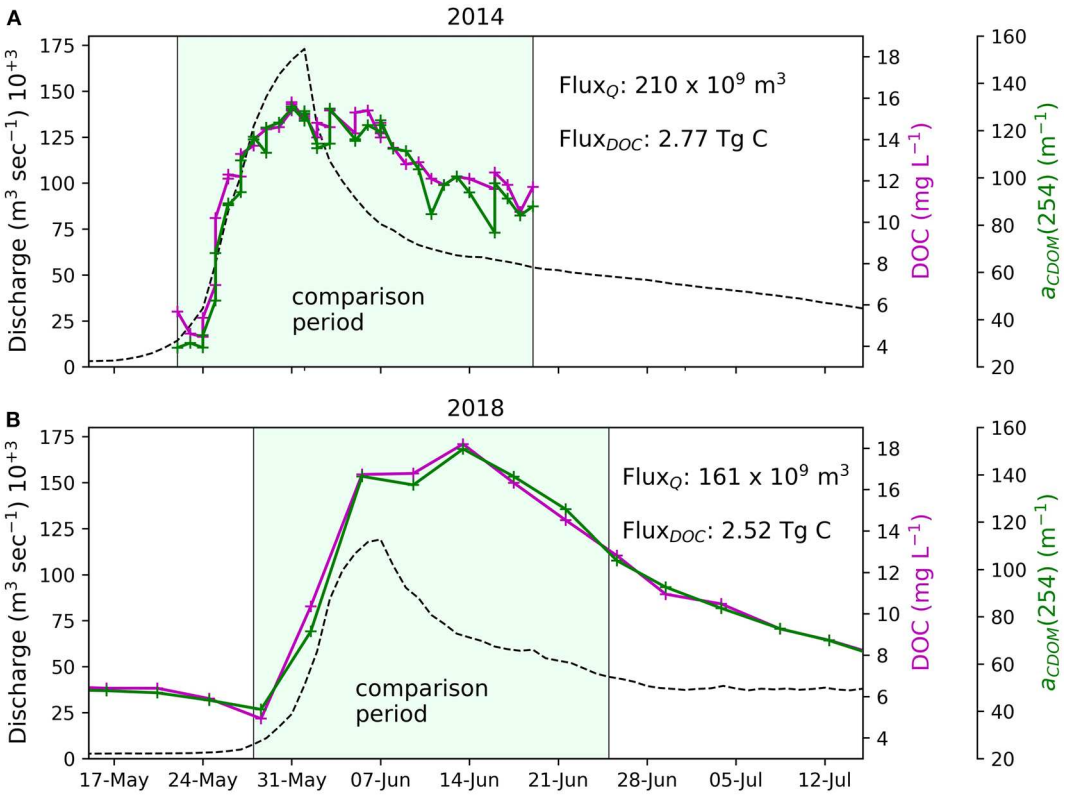

FIGURE 7 | DOC and a_{CDOM}(254) concentrations in 2014 **(A)** and 2018 **(B)**. The 2014 sampling period, was compared to the hydrologically same period in 2018. The flux of discharge (Q) and DOC for the period (29 days) is presented in each panel.

fraction of EM1 (melt-water) decreases and another water source endmember—EM2—becomes dominant. f_{EM2} peaks during the discharge events in summer (82.3% on 11 August and 81.6% on 19 October) (**Figure 8**). At the same time, $\delta^{18}O$ reaches its highest annual values and the EC is dropping. Such high $\delta^{18}O$ and low EC suggest that this end member is meteoric in origin. For these rain-induced discharge maxima, $\delta^{18}O$ and d-excess co-vary. This is likely related to less evaporative fractionation (and thus a higher d-excess), when more moisture is transported to the catchment. On the other hand, the highest evaporative fractionation is observed during the late summer (lowest d-excess). When discharge in summer is low, DOM concentrations are likewise low (~6 mg L^{-1}). During these periods, little DOM is mobilized and transported into the Lena River. In total, rain water accounts for 49.3% (340 x 10^9 m^3) of annual discharge. 42.6% (2.9 Tg C) of DOC is transported by rain water into the Lena River (**Figure 9**).

During the summer period the quality of the DOM changes (lower SUVA, higher S275-295). This could reflect the progress of soil thawing and a deepening active layer. Percolation and the leaching of older and more degraded DOM from deeper in the soil would explain both observations. Changes in SUVA can be linked to changes in source and age of DOM (Stedmon et al., 2011; O'Donnell et al., 2014; Coch et al., 2019) and can indicate the intensity of permafrost degradation within the catchment (Abbott et al., 2014). Furthermore, direct relationships are found between dissolved organic $\delta^{14}C$ and SUVA (Neff et al., 2006; Butman et al., 2012; O'Donnell et al., 2014). Annual maxima in S275-295 during low discharge in summer points toward a higher degree of (photo)-degradation in the river, which can be a result of longer transport time from its source to the sampling station and an exposure of DOM to photodegradation.

There are peaks in DOM concentrations during the distinct rain-induced discharge peaks in summer and fall (**Figure 2**). During these periods, that are likely caused by precipitation events over a large area, more DOM is mobilized from the catchment and transported into the Lena River. The general trend toward older and more degraded DOM is interrupted for those events and DOM similar to that transported by the spring snow melt enters the river. However, during the second strong rain event with peak values of rain water fraction (19 Oct.), higher SUVA values compared to the first summer rain event (11 Aug.) point toward a smaller fraction of young organic material. We suggest that reservoirs of young organic material on the land surface of the Lena River catchment are continuously washed out throughout the summer and thus higher relative fractions of older DOM from deeper soil horizons or permafrost become visible in the water samples. Additionally, rain events cause higher water levels in the Lena River that can re-connect isolated

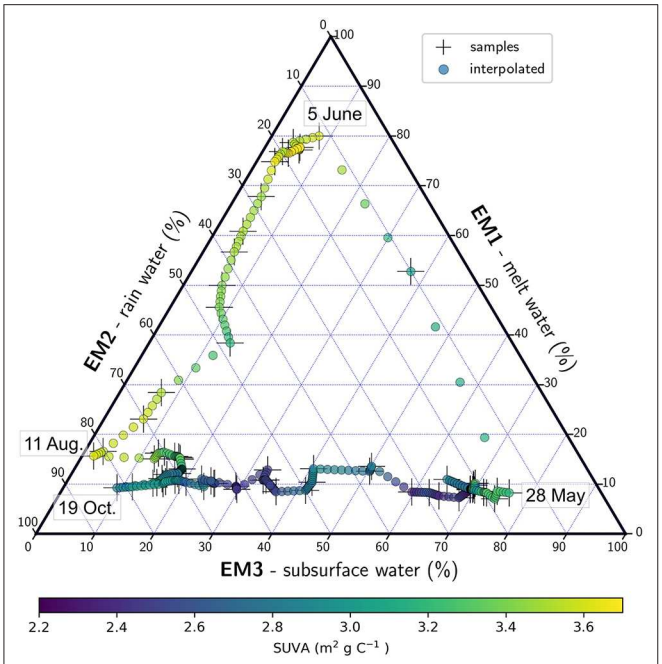

FIGURE 8 | Water source fractions for each sample (cross) and each interpolated day (colored circle) based on EC and stable isotope endmember calculations; Color shows the SUVA. The extreme values of the water source fractions are indicated by dates.

waterbodies and flush lakes, ponds and wetlands. In this way, DOM from phytoplankton production and bleached DOM from standing water bodies can be introduced to the Lena River.

Generally, during the open water period a trend toward lower SUVA and higher S275-295 values is present and continues into the early winter along with a decreasing fraction of rain water. Thus, the amount of fresh and young DOM transported with rain water from the Lena River catchment decreases.

(3) **Winter** is the period when the Lena River is entirely covered with ice and the discharge is low ($<$ 6,000 m^3 s^{-1}) compared to the other seasons and to the annual mean of 21 885 m^3 s^{-1}. During this period, most precipitation in the Lena River catchment accumulates as snow on land and the water level is gradually lowered. The remaining rain water is removed from the hydrological system of the Lena River catchment and the rain water fraction decreases gradually during the first half of the winter (**Figure 8**).

In early March, $\delta^{18}O$ and EC reach a stable level. At this time, the third endmember (EM3) becomes the dominant water source (76.1% on 28 May) (**Figure 8**). We suggest that this water source endmember represents subsurface water such as groundwater, soil and pore water (Abbott et al., 2014), which are the only significant natural water sources in winter, when air temperatures are permanently below 0°C. Subsurface water represents 15.7% (105 x 10^9 m^3) of the annual Lena River water flux. 14.1% (1 Tg C) of the DOC flux was transported with this water during our year of observation (**Figure 9**).

Optical DOM characteristics in winter continue the trend of summer and fall toward older and more degraded DOM until January 2019 when DOM concentrations and SUVA values begin to increase, coincident with a small increase in discharge. During low discharge in winter, a substantial part of the basin outlet discharge originates from the Vilui reservoir (Tananaev et al., 2016), which is regulated by a dam (Viluyskaya HPS) constructed in the 1970s. Changes of DOM concentration and composition may be caused by the higher relative fraction of reservoir water that is released through the Vilui dam. In reservoir water all water sources are pooled throughout the year, leading to DOC concentrations elevated above the otherwise low winter levels. The major increase in long term winter discharge of the Lena River in the late 1970s (**Figure 2**) coincides with the completion of Vilui dam construction and its reaching full capacity (Ye et al., 2003; Tananaev et al., 2016). In late winter, before the spring ice break-up, SUVA increases which likely coincides with first input of fresh DOM from the southern most parts of the catchment, where temperatures begin to rise above 0°C during the day.

Data from the ice core samples suggest that only low concentrations of DOM are incorporated into the river ice. Once the river ice is exported to the Laptev Sea shelf after spring ice break-up, it tends to dilute the shelf waters rather than act as a source of high DOM (Amon et al., 2012). However, patches of high sediment load on the Lena River ice (Fedorova et al., 2015) and the erosion of shorelines during ice jams (van Huissteden, 2020) contribute to the particulate organic matter flux to the Laptev Sea. There is likely a contribution to DOM from dissolution of the transported POM but this is expected to be quantitatively low in comparison to the river load of DOM.

The results presented here show that high frequency sampling reveals subtle changes in water chemistry reflecting the seasonal changes in the hydrology of the Lena River catchment. Most of the intra-annual variation in the Lena River water biogeochemistry can be captured by the 3-component endmember analysis presented here. However, river water at the basin outlet represents an integrated signal from the entire catchment and geographical and temporal variations of biogeochemical signals within the catchment cannot be detected by sampling.

Comparison of Reported DOM Values and Fluxes for the Lena River

Overall, our observed ranges of DOC concentrations and $a_{CDOM}(254)$ agree well with reported values from sampling programs of shorter duration or substantially lower sampling frequency (ArcticGRO and PARTNERS (Holmes et al., 2018a,b); Lena River freshet 2014 (Eulenburg et al., 2019)). ArcticGRO and PARTNERS samples have significantly higher DOC concentrations compared to samples from Samoylov Island in 2014 and 2018. Generally, these samples show a lower r^2 (0.89) of their DOC to $a_{CDOM}(275)$ regression, compared to the dataset shown in this study (r^2 = 0.97). This may indicate either a prominent local influence of anomalous DOM or the impact of analytical differences and different sampling protocols.

A number of studies have reported annual organic carbon fluxes of the Lena River (**Table 4**). Reported values range between 3.6 Tg C (Gordeev and Kravchishina, 2009) and 7.67 Tg C

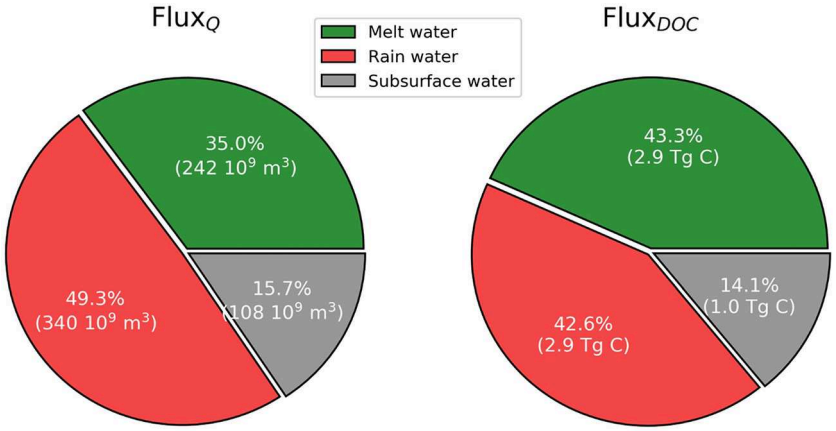

FIGURE 9 | Percentage and absolute fractions of discharge flux ($Flux_Q$) and DOC flux ($Flux_{DOC}$) for each endmember water source.

TABLE 4 | Previously published discharge and DOC fluxes and type of sampling and calculation.

References	Type	Year(s)	Annual discharge flux (10^9 m^3)	Annual DOC flux (Tg C)
Opsahl et al. (1999)	*In situ*	1999	n.a.	4.7
Raymond et al. (2007)	*In situ* + load model	2004	566	5.26
		2005	654	6.39
Gordeev and Kravchishina (2009)	*In situ*	n.a.	n.a.	3.6
Stedmon et al. (2011)	*In situ* + load model	2004 & 2005	615.1	7.27
Holmes et al. (2012)	*In situ* + load model	1999-2008	581	5.68 (varied between 4.1–7.4 Tg C yr^{-1})
Kicklighter et al. (2013)	Terrestrial ecosystem model	1990 - 2006	352	7.67
Wild et al. (2019)	*In situ* + load model	2003 - 2013	n.a.	5.71
This study	*In situ*, long period, high frequency	2018/19	690.18	6.8

(Kicklighter et al., 2013). Variability in DOC flux estimates is likely not only the result of inter-annual variability, but probably also results from differences in sampling frequency, sampling strategy and methods of calculating flux. All of the reported studies are based on a lower number of samples per year and/or on statistical models that are used to pair discharge measurements with concentration (**Table 4**). With statistical models, such as LOADEST (Runkel et al., 2004), estimated daily concentrations can be generated, with which seasonal or annual fluxes can be calculated. Although seasonal changes for the relation of discharge to concentration are taken into account in such models, the very low number of samples is critical and simplifying assumptions can cause systematic biases in flux estimates. Our dataset improves sample frequency and reveals that there is no clear relationship between discharge and DOC concentration. A relationship only persists during spring (r^2 =0.87, not shown). The impact of methodological differences for flux calculations becomes clear when comparing reported DOC flux values for 2004 and 2005 from Raymond et al. (2007) and Stedmon et al. (2011), that are based on precisely the same data but differ by 22.3% (1.46 Tg C). Furthermore, the reported fluxes that used models to relate discharge and DOC concentration tacitly assume that variations in DOC concentration are driven by processes changing the discharge, which is equivalent to a one-component system. Thus, the expected increase of DOC mobilization from degrading and thawing permafrost, which does not significantly affect discharge, cannot be reflected by such models.

The identification of seasonal fluxes by selecting certain time periods (Stedmon et al., 2011; Holmes et al., 2012) throughout different years is a method of addressing this shortcoming but prevents meaningful direct comparisons. The timing of seasonal changes such as the spring ice break-up varies between years and thus influence flux calculations for time periods defined by the calendar. Differences in seasonal fluxes between years (**Supplementary Figure 5**) thus are more likely to show shifts in seasonal timing than in water or dissolved load provenance.

We compared DOC fluxes during the spring discharge peak of 2 years (2014 and 2018). Although the discharge flux between both years differs by 26.4% (4.9 km^3), the difference in DOC flux is not as severe (9.4%). At least for the spring discharge peak, lower discharge is compensated by higher concentrations, which results in a similar flux. This is, however, not the case for summer and fall rain events where high DOC concentrations are triggered by rain that washes organic matter from land surfaces into the Lena River. Thus, recurrence intervals and the

intensity of such rain events dominate inter-annual variability in DOC fluxes.

The high temporal resolution of the sampling program presented in this study improves our ability to capture all seasonal events relevant to organic carbon fluxes, without assuming a relationship between DOC concentration and discharge. Thus, we are confident that our flux calculation can be used as a baseline for future trend analysis of Lena River DOC fluxes and, in particular, for the identification of changing seasonality. Little is known about changes in biogeochemistry between sampling locations further upstream (e.g., Zhigansk) and Samoylov Island. Continuous sampling of both programs (Samoylov sampling and ArcticGRO) will, however, enable future comparative studies.

CONCLUSION

In a warming Arctic, we expect permafrost landscapes to change dramatically. One result will be the remobilization of dissolved matter from permafrost. In particular, the release of dissolved organic carbon is under immense research attention due to its strong potential feedbacks for the climate. By monitoring the biogeochemistry of Arctic river water at the river mouth, we can observe ongoing changes that reflects change at the catchment scale.

In this study, we present 1 year of biogeochemical data from the Lena River, one of the largest Arctic Rivers. We improve on existing studies by sampling at high temporal frequency throughout the whole year. The main drivers that are responsible for the strong seasonality of water discharge and DOC flux were ascribed to three water sources—melt water, rain water and subsurface water. Melt and rain water were found to be the prevailing water sources that transport together 5.8 Tg C dissolved organic matter (85% of annual flux) into the Lena River. Optical DOM indices revealed changing composition and sources of DOM throughout the year. The high resolution sampling also revealed two phases of melt water introduction, with an initial phase of approximately 1 week, during which melt water carries little or no DOM and dilutes river DOM concentrations without altering DOM character, followed by a large pulse of fresher organic matter from the catchment that substantially changes the river DOM characteristics. Future studies including $\delta^{14}C$ measurements of the age of the DOM will enable direct relation of optical DOM indices to the DOM age and the contribution of permafrost thaw as shown in Neff et al. (2006).

The results of this sampling program provide a baseline for future shifts in seasonal variations as well as inter-annual variation of DOM and the chemistry of the Lena River. The annual flux of 6.8 Tg C was calculated without recourse to load models, which are probably the source of discrepancies between existing estimates. Continuous under-ice sampling revealed that high winter DOM concentrations are probably related to the discharge of reservoir water from the Vilui tributary.

This dataset represents the first year of a planned long-term monitoring program at the Research Station Samoylov Island and provides a reference data set against which future change of this large integrative system may be measured. Continuous sampling of Arctic River water will facilitate identification of intra and inter-annual trends during ongoing climate change.

DATA AVAILABILITY STATEMENT

The data sets used here are available online (https://doi.org/10.1594/PANGAEA.913196, https://doi.org/10.1594/PANGAEA.913279).

AUTHOR CONTRIBUTIONS

BJ, PO, and AM initiated the sampling program. BJ and PO designed the study with contributions of all authors. BJ prepared the figures and led the writing of the paper. All authors contributed to the discussion and the editing of the paper.

FUNDING

This research has been supported by Geo. X, the Research Network for Geosciences in Berlin and Potsdam (grant no. SO_087_GeoX). VP was supported from the Ministry of Higher Education and Science of the Russian Federation project RFMEFI61617X0076. This work was supported by funding from the Helmholtz Association in the framework of MOSES (Modular Observation Solutions for Earth Systems). We acknowledge support from the Open Access Publication Initiative of Freie Universität Berlin.

ACKNOWLEDGMENTS

We are grateful to Andrey Astapov, Sergey Volkov, and Ekaterina Abramova who were involved in continuous sampling. We are eminently thankful to Antje Eulenburg for her massive efforts to support this sampling program and the analysis of several parameter shown in this study. Furthermore, we thank the Trofimuk Institute of Petroleum Geology and Geophysics, Siberian Branch of the Russian Academy of Sciences (IPGG SB RAS), Novosibirsk, Russia, for their efforts to run the Research Station Samoylov Island and the team of the Otto Schmidt Laboratory for Polar and Marine Research in St. Petersburg for support in logistics and sample analysis. Furthermore, we thank the logistics of the Alfred Wegener Institute, Potsdam, Germany, specifically Waldemar Schneider and Volkmar Aßmann as well as Luidmila Pestryakova from the Northeastern Federal University (NEFU), Yakutsk, Russia. Projects from the EU Horizon 2020 programme (Nunataryuk, grant no. 773421) and from BMBF-NERC's Changing Arctic Ocean programme (CACOON, NERC grant no. NE/R012806/1, BMBF grant no. 03F0806A) supported discussions within a larger group of experts.

SUPPLEMENTARY MATERIAL

The Supplementary Material for this article can be found online at: https://www.frontiersin.org/articles/10.3389/fenvs.2020.00053/full#supplementary-material

REFERENCES

Abbott, B. W., Larouche, J. R., Jones, J. B., Bowden, W. B., and Balser, A. W. (2014). Elevated dissolved organic carbon biodegradability from thawing and collapsing permafrost. *J. Geophys. Res. Biogeosciences* 119, 2049–2063. doi: 10.1002/2014JG002678

Amon, R. M. W., Rinehart, A. J., Duan, S., Louchouarn, P., Prokushkin, A., Guggenberger, G., et al. (2012). Dissolved organic matter sources in large Arctic rivers. *Geochim. Cosmochim. Acta* 94, 217–237. doi: 10.1016/J.GCA.2012.07.01

Angelopoulos, M., Westermann, S., Overduin, P., Faguet, A., Olenchenko, V., Grosse, G., et al. (2019). Heat and salt flow in subsea permafrost modeled with CryoGRID2. *J. Geophys. Res. Earth Surf.* 124, 920–937. doi: 10.1029/2018JF004823

Aré, F. E. (1988). Thermal abrasion of sea coasts (part I). *Polar Geogr. Geol.* 12:1. doi: 10.1080/10889378809377343

Bareiss, J., and Görgen, K. (2005). Spatial and temporal variability of sea ice in the Laptev Sea: Analyses and review of satellite passive-microwave data and model results, 1979 to 2002. *Glob. Planet. Change* 48, 28–54. doi: 10.1016/j.gloplacha.2004.12.004

Bintanja, R., and Selten, F. M. (2014). Future increases in Arctic precipitation linked to local evaporation and sea-ice retreat. *Nature* 509, 479–482. doi: 10.1038/nature13259

Bonne, J.-L., Meyer, H., Behrens, M., Boike, J., Kipfstuhl, S., Rabe, B., et al. (2020). Moisture origin as a driver of temporal variabilities of the water vapour isotopic composition in the Lena River Delta, Siberia. *Atmos. Chem. Phys. Discuss. Rev*. doi: 10.5194/acp-2019-942

Boss, C. B., and Fredeen, K. J. (1997). *Concepts, Instrumentation, and Techniques in Inductively Coupled Plasma Optical Emission Spectrometry*. Shelton, CT: Perkin Elmer.

Butman, D., Raymond, P. A., Butler, K., and Aiken, G. (2012). Relationships between Δ 14 C and the molecular quality of dissolved organic carbon in rivers draining to the coast from the conterminous United States. *Global Biogeochem. Cycles* 26. doi: 10.1029/2012GB004361

Charkin, A. N., Dudarev, O. V., Semiletov, I. P., Kruhmalev, A. V., Vonk, J. E., Sánchez-García, L., et al. (2011). Seasonal and interannual variability of sedimentation and organic matter distribution in the Buor-Khaya Gulf: the primary recipient of input from Lena River and coastal erosion in the southeast Laptev Sea. *Biogeosciences* 8, 2581–2594. doi: 10.5194/bg-8-2581-2011

Coch, C., Juhls, B., Lamoureux, S. F., Lafrenière, M. J., Fritz, M., Heim, B., et al. (2019). Comparisons of dissolved organic matter and its optical characteristics in small low and high Arctic catchments. *Biogeosciences* 16, 4535–4553. doi: 10.5194/bg-16-4535-2019

Craig, H. (1961). Isotopic variations in meteoric waters. *Science.* 133, 1702–1703. doi: 10.1126/science.133.3465.1702

Eulenburg, A., Juhls, B., and Hölemann, J. A. (2019). Surface water dissolved organic matter (DOC, CDOM) in the Lena River (2014). *PANGAEA*. 16, 2693–2713. doi: 10.1594/PANGAEA.898711

Fedorova, I., Chetverova, A., Bolshiyanov, D., Makarov, A., Boike, J., Heim, B., et al. (2015). Lena Delta hydrology and geochemistry: long-term hydrological data and recent field observations. *Biogeosciences* 12, 345–363. doi: 10.5194/bg-12-345-2015

Freeman, C., Evans, C. D., Monteith, D. T., Reynolds, B., and Fenner, N. (2001). Export of organic carbon from peat soils. *Nature* 412, 785–785. doi: 10.1038/35090628

Frey, K. E., and Smith, L. C. (2005). Amplified carbon release from vast West Siberian peatlands by 2100. *Geophys. Res. Lett.* 32:L09401. doi: 10.1029/2004GL022025

Gordeev, V. V., and Kravchishina, M. D. (2009). "River flux of dissolved organic carbon (DOC) and particulate organic carbon (POC) to the Arctic Ocean: what are the consequences of the global changes?," in *Influence of Climate Change on the Changing Arctic and Sub-Arctic Conditions*, ed J. Nihoul (Dordrecht: Springer Netherlands), 145–160. Available online at: https://www.springer.com/gp/book/9781402094583

Granskog, M. A., Stedmon, C. A., Dodd, P. A., Amon, R. M. W., Pavlov, A. K., de Steur, L., et al. (2012). Characteristics of colored dissolved organic matter (CDOM) in the Arctic outflow in the fram strait: assessing the changes and fate of terrigenous CDOM in the Arctic Ocean. *J. Geophys. Res. Ocean.* 117. doi: 10.1029/2012JC008075

Helms, J. R., Stubbins, A., Ritchie, J. D., Minor, E. C., Kieber, D. J., and Mopper, K. (2008). Absorption spectral slopes and slope ratios as indicators of molecular weight, source, and photobleaching of chromophoric dissolved organic matter. *Limnol. Oceanogr.* 53, 955–969. doi: 10.4319/lo.2008.53.3.0955

Hill, V. J. (2008). Impacts of chromophoric dissolved organic material on surface ocean heating in the Chukchi Sea. *J. Geophys. Res.* 113:C07024. doi: 10.1029/2007JC004119

Holmes, R. M., McClelland, J. W., Peterson, B. J., Tank, S. E., Bulygina, E., Eglinton, T. I., et al. (2012). Seasonal and annual fluxes of nutrients and organic matter from large rivers to the arctic ocean and surrounding seas. *Estuar. Coast.* 35, 369–382. doi: 10.1007/s12237-011-9386-6

Holmes, R. M., McClelland, J. W., Raymond, P. A., Frazer, B. B., Peterson, B. J., and Stieglitz, M. (2008). Lability of DOC transported by Alaskan rivers to the Arctic Ocean. *Geophys. Res. Lett.* 35:L03402. doi: 10.1029/2007GL032837

Holmes, R. M., McClelland, J. W., Tank, S. E., Spencer, R. G. M., and Shiklomanov, A. I. (2018a). *ArcticGRO Absorbance Dataset*. Available online at: https://www.arcticrivers.org/data (accessed January 10, 2020).

Holmes, R. M., McClelland, J. W., Tank, S. E., Spencer, R. G. M., and Shiklomanov, A. I. (2018b). *ArcticGRO Water Quality Dataset*. https://www.arcticrivers.org/data (accessed January 10, 2020).

Jollymore, A., Johnson, M. S., and Hawthorne, I. (2012). Submersible UV-Vis spectroscopy for quantifying streamwater organic carbon dynamics: implementation and challenges before and after forest harvest in a headwater stream. *Sensors* 12, 3798–3813. doi: 10.3390/s120403798

Juhls, B., Paul Overduin, P., Hölemann, J., Hieronymi, M., Matsuoka, A., Heim, B., et al. (2019). Dissolved organic matter at the fluvial-marine transition in the Laptev Sea using *in situ* data and ocean colour remote sensing. *Biogeosciences* 16, 2693–2713. doi: 10.5194/bg-16-2693-2019

Kaiser, K., Canedo-Oropeza, M., McMahon, R., and Amon, R. M. W. (2017). Origins and transformations of dissolved organic matter in large Arctic rivers. *Sci. Rep.* 7:13064. doi: 10.1038/s41598-017-12729-1

Keuper, F., Bodegom, P. M., Dorrepaal, E., Weedon, J. T., Hal, J., Logtestijn, R. S. P., et al. (2012). A frozen feast: thawing permafrost increases plant-available nitrogen in subarctic peatlands. *Glob. Chang. Biol.* 18, 1998–2007. doi: 10.1111/j.1365-2486.2012.02663.x

Kicklighter, D. W., Hayes, D. J., McClelland, J. W., Peterson, B. J., McGuire, A. D., and Melillo, J. M. (2013). Insights and issues with simulating terrestrial DOC loading of Arctic river networks. *Ecol. Appl.* 23, 1817–1836. doi: 10.1890/11-1050.1

Liu, B., Yang, D., Ye, B., and Berezovskaya, S. (2005). Long-term open-water season stream temperature variations and changes over Lena River Basin in Siberia. *Glob. Planet. Change* 48, 96–111. doi: 10.1016/J.GLOPLACHA.2004.12.007

Mann, P. J., Spencer, R. G. M., Hernes, P. J., Six, J., Aiken, G. R., Tank, S. E., et al. (2016). Pan-Arctic trends in terrestrial dissolved organic matter from optical measurements. *Front. Earth Sci.* 4:25. doi: 10.3389/feart.2016.00025

McClelland, J. W., Déry, S. J., Peterson, B. J., Holmes, R. M., and Wood, E. F. (2006). A pan-arctic evaluation of changes in river discharge during the latter half of the 20th century. *Geophys. Res. Lett.* 33:L06715. doi: 10.1029/2006GL025753

Meyer, H., Schönicke, L., Wand, U., Hubberten, H. W., and Friedrichsen, H. (2000). Isotope studies of hydrogen and oxygen in ground ice - Experiences with the equilibration technique. *Isotopes Environ. Health Stud.* 36, 133–149. doi: 10.1080/10256010008032939

Neff, J. C., Finlay, J. C., Zimov, S. A., Davydov, S. P., Carrasco, J. J., Schuur, E. A. G., et al. (2006). Seasonal changes in the age and structure of dissolved organic carbon in Siberian rivers and streams. *Geophys. Res. Lett.* 33, L23401. doi: 10.1029/2006GL028222

Niederdrenk, A. L., Sein, D. V., and Mikolajewicz, U. (2016). Interannual variability of the Arctic freshwater cycle in the second half of the twentieth century in a regionally coupled climate model. *Clim. Dyn.* 47, 3883–3900. doi: 10.1007/s00382-016-3047-1

Obu, J., Westermann, S., Bartsch, A., Berdnikov, N., Christiansen, H. H., Dashtseren, A., et al. (2019). Northern Hemisphere permafrost map based on TTOP modelling for 2000–2016 at 1 km2 scale. *Earth Sci. Rev.* 193, 299–316. doi: 10.1016/j.earscirev.2019.04.023

O'Donnell, J. A., Aiken, G. R., Walvoord, M. A., Raymond, P. A., Butler, K. D., Dornblaser, M. M., et al. (2014). Using dissolved organic matter age and composition to detect permafrost thaw in boreal watersheds of interior

Alaska. *J. Geophys. Res. Biogeosciences* 119, 2155–2170. doi: 10.1002/2014JG002695

Opsahl, S., Benner, R., and Amon, R. M. W. (1999). Major flux of terrigenous dissolved organic matter through the Arctic Ocean. *Limnol. Oceanogr.* 44, 2017–2023. doi: 10.4319/lo.1999.44.8.2017

Overduin, P. P., Schneider von Deimling, T., Miesner, F., Grigoriev, M. N., Ruppel, C., Vasiliev, A., et al. (2019). Submarine permafrost map in the Arctic modeled using 1-D transient heat flux (SuPerMAP). *J. Geophys. Res. Ocean.* 124. doi: 10.1029/2018JC014675

Pegau, W. S. (2002). Inherent optical properties of the central Arctic surface waters. *J. Geophys. Res. C Ocean.* 107:SHE 16-1–SHE 16-7. doi: 10.1029/2000jc000382

Peterson, B. J. (2002). Increasing river discharge to the Arctic Ocean. *Science.* 298, 2171–2173. doi: 10.1126/science.1077445

Plaza, C., Pegoraro, E., Bracho, R., Celis, G., Crummer, K. G., Hutchings, J. A., et al. (2019). Direct observation of permafrost degradation and rapid soil carbon loss in tundra. *Nat. Geosci.* 12, 627–631. doi: 10.1038/s41561-019-0387-6

Porter, C., Morin, P., Howat, I., Noh, M.-J., Bates, B., Peterman, K., et al. (2018). ArcticDEM. *Harvard Dataverse* V1. doi: 10.7910/DVN/OHHUKH

Raymond, P. A., McClelland, J. W., Holmes, R. M., Zhulidov, A. V., Mull, K., Peterson, B. J., et al. (2007). Flux and age of dissolved organic carbon exported to the Arctic Ocean: a carbon isotopic study of the five largest arctic rivers. *Global Biogeochem. Cycles* 21. doi: 10.1029/2007GB002934

Richter-Menge, J., Druckenmiller, M. L., and Jeffries, M. (Eds.). (2019). *2019: Arctic Report Card 2019*. Available online at: https://www.arctic.noaa.gov/Report-Card (accessed December 13, 2019).

Runkel, R. L., Crawford, C. G., and Cohn, T. A. (2004). "Load Estimator (LOADEST): a FORTRAN program for estimating constituent loads in streams and rivers," in *Techniques and Methods Book 4*, Chapter A5, 69. Available online at: http://www.usgs.gov/ (accessed January 22, 2020).

Schuur, E. A. G., McGuire, A. D., Schädel, C., Grosse, G., Harden, J. W., Hayes, D. J., et al. (2015). Climate change and the permafrost carbon feedback. *Nature* 520, 171–179. doi: 10.1038/nature14338

Schuur, E. A. G., Vogel, J. G., Crummer, K. G., Lee, H., Sickman, J. O., and Osterkamp, T. E. (2009). The effect of permafrost thaw on old carbon release and net carbon exchange from tundra. *Nature* 459, 556–559. doi: 10.1038/nature08031

Shiklomanov, A. I. (2010). Observed and naturalized discharge data for large Siberian rivers. Available at: http://www.r-arcticnet.sr.unh.edu/ObservedAndNaturalizedDischarge-Website/ (accessed December 9, 2019).

Shiklomanov, A. I., Holmes, R. M., McClelland, J. W., Tank, S. E., and Spencer., R. G. M. (2018). ArcticGRO Discharge Dataset, Version 2020-01-23. *Arct. Gt. Rivers Obs. Discharge*. Available online at: https://arcticgreatrivers.org/data/

Shiklomanov, A. I., and Lammers, R. B. (2009). Record Russian river discharge in 2007 and the limits of analysis. *Environ. Res. Lett.* 4:045015. doi: 10.1088/1748-9326/4/4/045015

Smith, L. C., and Pavelsky, T. M. (2008). Estimation of river discharge, propagation speed, and hydraulic geometry from space: Lena River, Siberia. *Water Resour. Res.* 44, 1–11. doi: 10.1029/2007WR006133

Spors, S. (2018). *Stable Water Isotope Characteristics of Recent Precipitation from Tiksi and Samoylov Island – Calibration of a Geoscientific Proxy for Northern Siberia* (Bachelor Thesis). University of Potsdam, Potsdam.

Stedmon, C. A., Amon, R. M. W., Rinehart, A. J., and Walker, S. A. (2011). The supply and characteristics of colored dissolved organic matter (CDOM) in the Arctic Ocean: Pan Arctic trends and differences. *Mar. Chem.* 124, 108–118. doi: 10.1016/J.MARCHEM.2010.12.007

Sugimoto, A., and Maximov, T. C. (2012). Study on hydrological processes in Lena River Basin using stable isotope ratios of River water (IAEA-TECDOC—1673). *Monit. Isot. Rivers Creat. Glob. Netw. Isot. Rivers*. 41–49. Available online at: https://www.osti.gov/etdeweb/biblio/21570990

Tananaev, N. I., Makarieva, O. M., and Lebedeva, L. S. (2016). Trends in annual and extreme flows in the Lena River basin, Northern Eurasia. *Geophys. Res. Lett. 43*, 10,764-10,772. doi: 10.1002/2016GL070796

Tank, S. E., Striegl, R. G., McClelland, J. W., and Kokelj, S. V. (2016). Multi-decadal increases in dissolved organic carbon and alkalinity flux from the Mackenzie drainage basin to the Arctic Ocean. *Environ. Res. Lett.* 11:054015. doi: 10.1088/1748-9326/11/5/054015

Turetsky, M. R., Abbott, B. W., Jones, M. C., Walter Anthony, K., Olefeldt, D., Schuur, E. A. G., et al. (2019). Permafrost collapse is accelerating carbon release. *Nature* 569, 32–34. doi: 10.1038/d41586-019-01313-4

van Huissteden, J. (2020). "Permafrost carbon quantities and Fluxes," in *Thawing Permafrost* (Cham: Springer Nature), 179–274. doi: 10.1007/978-3-030-31379-1

Velicogna, I., Tong, J., Zhang, T., and Kimball, J. S. (2012). Increasing subsurface water storage in discontinuous permafrost areas of the Lena River basin, Eurasia, detected from GRACE. *Geophys. Res. Lett.* 39:9403. doi: 10.1029/2012GL051623

Walker, S. A., Amon, R. M. W., and Stedmon, C. A. (2013). Variations in high-latitude riverine fluorescent dissolved organic matter: a comparison of large Arctic rivers. *J. Geophys. Res. Biogeosciences* 118, 1689–1702. doi: 10.1002/2013JG002320

Wegner, C., Bauch, D., Hölemann, J. A., Janout, M. A., Heim, B., Novikhin, A., et al. (2013). Interannual variability of surface and bottom sediment transport on the Laptev Sea shelf during summer. *Biogeosciences* 10, 1117–1129. doi: 10.5194/bg-10-1117-2013

Weishaar, J. L., Aiken, G. R., Bergamaschi, B. A., Fram, M. S., Roger, F., and Mopper, K. (2003). Evaluation of specific ultraviolet absorbance as an indicator of the chemical composition and reactivity of dissolved organic *carbon*. *Environ Sci Technol.* 37, 4702–4708. doi: 10.1021/ES030360X

Weiss, J. (2001). *Ionenchromatographie*. Weinheim: Wiley.

Wild, B., Andersson, A., Bröder, L., Vonk, J., Hugelius, G., McClelland, J. W., et al. (2019). Rivers across the Siberian Arctic unearth the patterns of carbon release from thawing permafrost. *Proc. Natl. Acad. Sci. U.S.A.* 116, 10280–10285. doi: 10.1073/pnas.1811797116

Yang, D., Kane, D. L., Hinzman, L. D., Zhang, X., Zhang, T., and Ye, H. (2002). Siberian Lena River hydrologic regime and recent change. *J. Geophys. Res. Atmos.* 107, 14–10. doi: 10.1029/2002JD002542

Yang, D., Marsh, P., and Shaoqing, G. E. (2013). *Cold and Mountain Region Hydrological Systems Under Climate Change.* IAHS Publ. Available online at: http://www.usgs.gov/ (accessed December 16, 2019).

Yang, D., Zhao, Y., Armstrong, R., Robinson, D., and Brodzik, M.-J. (2007). Streamflow response to seasonal snow cover mass changes over large Siberian watersheds. *J. Geophys. Res.* 112:F02S22. doi: 10.1029/2006JF000518

Ye, B., Yang, D., and Kane, D. L. (2003). Changes in Lena River streamflow hydrology: Human impacts versus natural variations. *Water Resour. Res.* 39. doi: 10.1029/2003WR001991

Conflict of Interest: The authors declare that the research was conducted in the absence of any commercial or financial relationships that could be construed as a potential conflict of interest.

frontiers in Environmental Science

ORIGINAL RESEARCH
published: 21 July 2020
doi: 10.3389/fenvs.2020.00118

n-Alkane Characteristics of Thawed Permafrost Deposits Below a Thermokarst Lake on Bykovsky Peninsula, Northeastern Siberia

Loeka L. Jongejans[1,2], Kai Mangelsdorf[3], Lutz Schirrmeister[1], Mikhail N. Grigoriev[4], Georgii M. Maksimov[4], Boris K. Biskaborn[5], Guido Grosse[1,2] and Jens Strauss[1]*

[1] Section of Permafrost Research, Alfred Wegener Institute, Helmholtz Centre for Polar and Marine Research, Potsdam, Germany, [2] Institute of Geosciences, University of Potsdam, Potsdam, Germany, [3] Section of Organic Geochemistry, GFZ German Research Centre for Geosciences, Potsdam, Germany, [4] Laboratory of General Geocryology, Melnikov Permafrost Institute, Siberian Branch of the Russian Academy of Sciences, Yakutsk, Russia, [5] Section of Polar Terrestrial Environmental Systems, Alfred Wegener Institute Helmholtz Centre for Polar and Marine Research, Potsdam, Germany

OPEN ACCESS

Edited by:
Adam Jerold Reed, University of Southampton, United Kingdom

Reviewed by:
Jianfang Hu, Guangzhou Institute of Geochemistry, CAS, China
Geoffrey Denis Abbott, Newcastle University, United Kingdom

***Correspondence:**
Loeka L. Jongejans
Loeka.jongejans@awi.de

Specialty section:
This article was submitted to Biogeochemical Dynamics, a section of the journal Frontiers in Environmental Science

Received: *04 March 2020*
Accepted: *02 July 2020*
Published: *21 July 2020*

Citation:
Jongejans LL, Mangelsdorf K, Schirrmeister L, Grigoriev MN, Maksimov GM, Biskaborn BK, Grosse G and Strauss J (2020) n-Alkane Characteristics of Thawed Permafrost Deposits Below a Thermokarst Lake on Bykovsky Peninsula, Northeastern Siberia. Front. Environ. Sci. 8:118. doi: 10.3389/fenvs.2020.00118

Rapid permafrost thaw by thermokarst mobilizes previously frozen organic matter (OM) down to tens of meters deep within decades to centuries, leading to microbial degradation and greenhouse gas release. Late Pleistocene ice-rich Yedoma deposits that thaw underneath thermokarst lakes and refreeze after lake drainage are called taberal sediments. Although widespread, these have not been the subject of many studies. To study OM characteristics and degradability in thawed Yedoma, we obtained a 31.5 m long core from beneath a thermokarst lake on the Bykovsky Peninsula, northeastern Siberia. We reported radiocarbon ages, biogeochemical parameters [organic carbon (OC) content and bulk carbon isotopes] and *n*-alkane distributions. We found the most degraded OM in frozen, fluvial sediments at the bottom of the core, as indicated by the lowest *n*-alkane odd-over-even predominance (OEP; 2.2). Above this, the thawed Yedoma sediments had an *n*-alkane distribution typical of emergent vegetation, suggesting a landscape dominated by low-centered polygons. These sediments were OC poor (OC content: 0.8 wt%, 60% of samples < 0.1 wt%), but the OM (OEP$\sim$5.0) was better preserved than in the fluvial sediments. The upper part of the Yedoma reflected a transition to a drier, grass dominated environment. Furthermore, this unit's OM was least degraded (OEP$\sim$9.4). The thermokarst lake that formed about 8 cal ka BP thawed the Yedoma in the talik and deposited Holocene lake sediments containing well-preserved OM (OEP$\sim$8.4) with the highest *n*-alkane concentrations (20.8 $\mu g\ g^{-1}$ sediment). Old, allochthonous OM was found in the thawed Yedoma and frozen fluvial deposits. Using an *n*-alkane endmember model, we identified a mixed OM input in all units. In our study, the thawed Yedoma sediments contained less OC than reported in other studies for still frozen Yedoma. The Yedoma OM was more degraded compared to previous biomarker research on frozen Yedoma. However, this signal is

overprinted by the input signal. The fluvial deposits below the Yedoma contained more OM, but this OM was more degraded, which can be explained by the OM input signal. Continued talik deepening and expansion of this thermokarst lake and others similar to it will expose OM with heterogeneous properties to microbial degradation.

Keywords: Russian Arctic, organic matter degradability, Yedoma deposits, thermokarst lake, talik, molecular biomarkers

INTRODUCTION

Current climate change is causing rapid changes in the Arctic. Accordingly, permafrost deposits are warming and thawing in many regions including Siberia (Biskaborn et al., 2019). Thawing leads to increased microbial decomposition of the previously freeze-locked organic matter (OM) (Mackelprang et al., 2011; Schuur et al., 2015). The amount of organic carbon (OC) that may be mobilized from thawed permafrost sediments is constrained by the OM quantity and quality. Top-down thaw by deepening of the seasonally thawed layer (active layer) largely affects OM in the active layer and near surface permafrost, some of which has already been influenced by early Holocene deeper active layer thaw (French, 1999; Lacelle et al., 2019). Deep permafrost thaw processes, however, such as thermokarst development, may expose OM from Late Pleistocene permafrost deposits to microbial degradation down to tens of meters deep for the first time (Heslop et al., 2019; Turetsky et al., 2020).

Ice-rich, syngenetic Yedoma deposits are late Pleistocene permafrost deposits that are widespread in northern Siberia and Alaska (Schirrmeister et al., 2013) and contain a significant OC pool (Strauss et al., 2013; Hugelius et al., 2014). Yedoma deposits that thaw *in situ* in taliks underneath thermokarst lakes become diagenetically altered due to ice-loss and compaction. Following lake drainage, these talik sediments can refreeze again, after which they are called taberal sediments: *in situ* thawed, diagenetically altered and refrozen sediments (Romanovskii, 1993). Strauss et al. (2013) estimated that about 10% of the Yedoma region is covered by lakes and rivers and 56% by drained lake basins with likely refrozen taberal deposits. After thawing of the Yedoma deposits, anaerobic conditions in the water-logged compacted talik sediments promote methane production (Zimov et al., 1997; Walter et al., 2006). Although spatially widespread, taberal sediments have not been subject of many studies yet and are rarely included in OC storage estimates or studies of OM degradability.

A first estimate of the taberal deposit OC pools suggests ∼114 Gt OC, which is about 25% of the Yedoma domain OC storage (∼398 Gt) (Walter Anthony et al., 2014; Strauss et al., 2017). In several studies, it is also shown that the OM degradability in Yedoma deposits is higher compared to that in Holocene deposits (Knoblauch et al., 2013; Strauss et al., 2015; Jongejans et al., 2018; Stapel et al., 2018). However, the fate of OM in Yedoma deposits affected by thawing and subsequent qualitative and quantitative changes is poorly understood. Various studies indicate that OM from thawed Yedoma becomes partially degraded. For example, Wetterich et al. (2009) found that plant material was further degraded in taberal deposits than in Yedoma deposits in the Dmitry Laptev Strait.

The study of the biomolecules and other OM characteristics can give important insights into OM degradability and could hence greatly improve estimates of permafrost OM mobilization (Andersson and Meyers, 2012; Sánchez-García et al., 2014). A few studies have previously focused on molecular biomarkers in northeastern Siberian permafrost deposits (Zech et al., 2010; Höfle et al., 2013; Strauss et al., 2015; Stapel et al., 2018). In general, the abundance and distribution of *n*-alkanes, which are long-chained, single bonded hydrocarbons, are used as indicator for OM characterization. The length of *n*-alkanes is an indicator for OM source. Long chained *n*-alkanes (>22 carbon atoms) mainly originate from vascular plants, for example in leaf waxes, whereas short chains (12–20 carbon atoms) are produced by bacteria and algae (Killops and Killops, 2013). The ratio of odd to even chains – expressed as carbon preference index (CPI) (Bray and Evans, 1961; Marzi et al., 1993) or odd-over-even predominance (OEP) (Zech et al., 2009; Struck et al., 2019) – is an indicator for OM degradability and decreases with ongoing alteration of the OM. Furthermore, several studies in temperate latitudes showed that relative *n*-alkane proportions can be used to distinguish between vegetation types. *n*-C_{23} and *n*-C_{25} are predominant in aquatic macrophytes and *Sphagnum* mosses (Ficken et al., 1998; Bingham et al., 2010; Bush and McInerney, 2013), *n*-C_{27} and *n*-C_{29} are mainly produced by trees and shrubs, and *n*-C_{31} and *n*-C_{33} mostly derive from grasses and herbs (Zech et al., 2009; Schäfer et al., 2016). Very few comparable studies were carried out for talik or taberal sediments (Romankevich et al., 2017; Ulyantsev et al., 2017).

Thus, for the first time we present molecular biomarker characteristics from Yedoma deposits thawed *in situ* in the talik underneath a thermokarst lake. This study aims to answer the following research questions: (1) what is the sedimentation history of the Yedoma deposits at the study site and (2) what is the OM degradation potential of Yedoma deposits already thawed in a talik?

STUDY AREA

To answer these research questions, we analyzed a 31.5 m long sediment core from sediments underneath Goltsovoye Lake, a thermokarst lake on Bykovsky Peninsula in northeastern Siberia. The Bykovsky Peninsula is a remnant of a former late Pleistocene Yedoma accumulation plane, situated in the foreland of the Kharaulakh Ridge at the Laptev Sea coast (**Figure 1**).

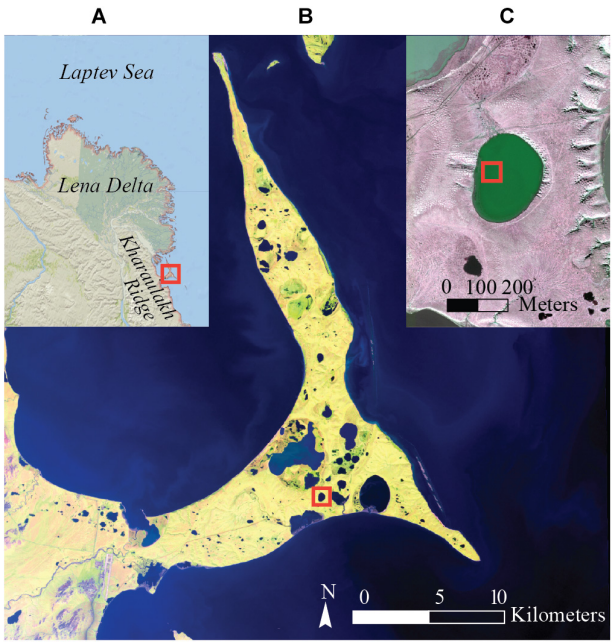

FIGURE 1 | Bykovsky Peninsula in northeastern Siberia. **(A)** Bykovsky Peninsula (red square) at the Laptev Sea coast, southeast of the Lena Delta and east of the Kharaulahk Ridge, **(B)** Goltsovoye Lake (red square) close to southern coast of Bykovsky Peninsula, **(C)** coring location PG2412 and PG2420 (red square; ~20 m apart) in Goltsovoye Lake. Source imagery: (a) ESRI Basemap: National Geographic World Map, (b) ESA Sentinel-2 False Color Composite (11-8-2) acquired 2019-08-03, (c) World View 3 Image acquired 2019-09-02 (©DigitalGlobe).

The area is characterized by continuous permafrost, which reaches depths down to 600 m (Grigoriev, 1960). The modern surface morphology is characterized mainly by Yedoma uplands (up to 45 m a.s.l.) and thermokarst depressions and lakes, as well as thermal erosional valleys (Siegert et al., 2002; Grosse et al., 2007). Nival and slope processes in the nearby Kharaulakh Ridge and *in situ* frost weathering after deposition led to the formation of the Yedoma uplands in the mountain foreland during the late Pleistocene (Schirrmeister et al., 2002a; Strauss et al., 2012). Strong permafrost degradation since the late Pleistocene to early Holocene transition resulted in thermokarst development and thermal erosion of the Yedoma uplands, which characterize the modern relief of the Bykovsky Peninsula (Grosse et al., 2005). The Bykovsky Peninsula is covered by about 14.4% by thermokarst lakes and lagoons while 46.1% are covered by drained thermokarst lake basins (Grosse et al., 2005).

Goltsovoye Lake (71.74515°N, 129.30217°E) is a medium-sized thermokarst lake (dimensions: 630 by 480 m, surface: ~23 ha) located close to the southern coast of the peninsula (**Figure 1**). The lake reaches a water depth of about 5 m and has a talik reaching about 30 m deep (Strauss et al., 2018). It is mainly surrounded by Yedoma deposits that are eroded along the lake shore, and drained thermokarst lake basins which are characterized by ice wedge polygons. Several other thermokarst lakes in the vicinity transitioned to thermokarst lagoons already due to coastal erosion and inundation with sea water, allowing salt water to interact with the former freshwater taliks (Jenrich, 2020).

Previous permafrost research on the Bykovsky Peninsula included cryostratigraphical and cryolithological research on Yedoma and thermokarst-affected deposits (Kunitsky, 1989; Slagoda, 1993; Schirrmeister et al., 2002a,b, 2018; Slagoda, 2004, 2005; Grosse et al., 2007; Romankevich et al., 2017; Ulyantsev et al., 2017). The total organic carbon (TOC) content of Yedoma deposits on the east coast of the Bykovsky Peninsula (Mamontovy Khayata) ranges from 2 to 14 wt%, whereas Holocene cover deposits on top of the Yedoma have a TOC between 2 and 27 wt% (Schirrmeister et al., 2002a). In a transect study in the central part of Bykovsky Peninsula, Fuchs et al. (2018) found mean TOC values of 5.1 ± 4.3 wt% for the upper 3 m on Yedoma uplands consisting of Holocene cover deposits and 7.9 ± 9.0 wt% for drained thermokarst lake basin deposits.

Despite the coastal setting, the modern climate of the Bykovsky Peninsula is rather continental with long, severe winters (September-May) and short, cold summers. The mean air temperature (2000–2016) is −29°C in January and +8°C in July (Tiksi Hydrometeorological Observatory) and the mean annual precipitation is less than 350 mm. Mean ground temperatures reach −9 to −11°C. This region is dominated by moss-grass low shrub tundra and is therefore classified as northern tundra (Treshnikov, 1985).

MATERIALS AND METHODS

Field Work

Field work on the Bykovsky Peninsula was carried out in April 2017 (Strauss et al., 2018). Over the course of 4 days, a 31.5-m long sediment core (PG2412; 71.74515°N, 129.30217°E) was retrieved from the deepest point in Goltsovoye Lake (**Figure 1**), using a URB2-4T drilling rig placed on a truck. The ice cover of the thermokarst lake was 195 cm thick and sediments started at 510 cm from the ice surface. For the depth assignment of the sample material, the water column with the ice cover was included (e.g., see **Figure 2**). Thus, depth measurements started at the ice surface. The core consisted of unfrozen talik sediments (until 3425 cm) and frozen sediments below the talik. The upper few meters of sediment consist of gray silty, fine sand and include plant remains and biogenic shells. Deeper in the core, coarser sandy intervals containing 2-cm-big pebbles alternate with fine sand intervals with large wooden remains. In general, abundant wooden remains and organic-enriched layers were observed between 3665 and 1900 cm. The core material was documented and protected and transported frozen to Potsdam for subsampling. During drilling, core loss happened in the intervals: 3550–3510 cm, 2135–2050 cm and 910–755 cm.

We compare the data from the PG2412 sediment core with the data from a 5 m long sediment core (PG2420; 71.74530°N, 129.30243°E) that was drilled ~20 m away from PG2412, using a UWITEC piston coring system (Strauss et al., 2018; Biskaborn and Sens, 2020). From here on, we will refer to core PG2412 as the long core and PG2420 as the short core.

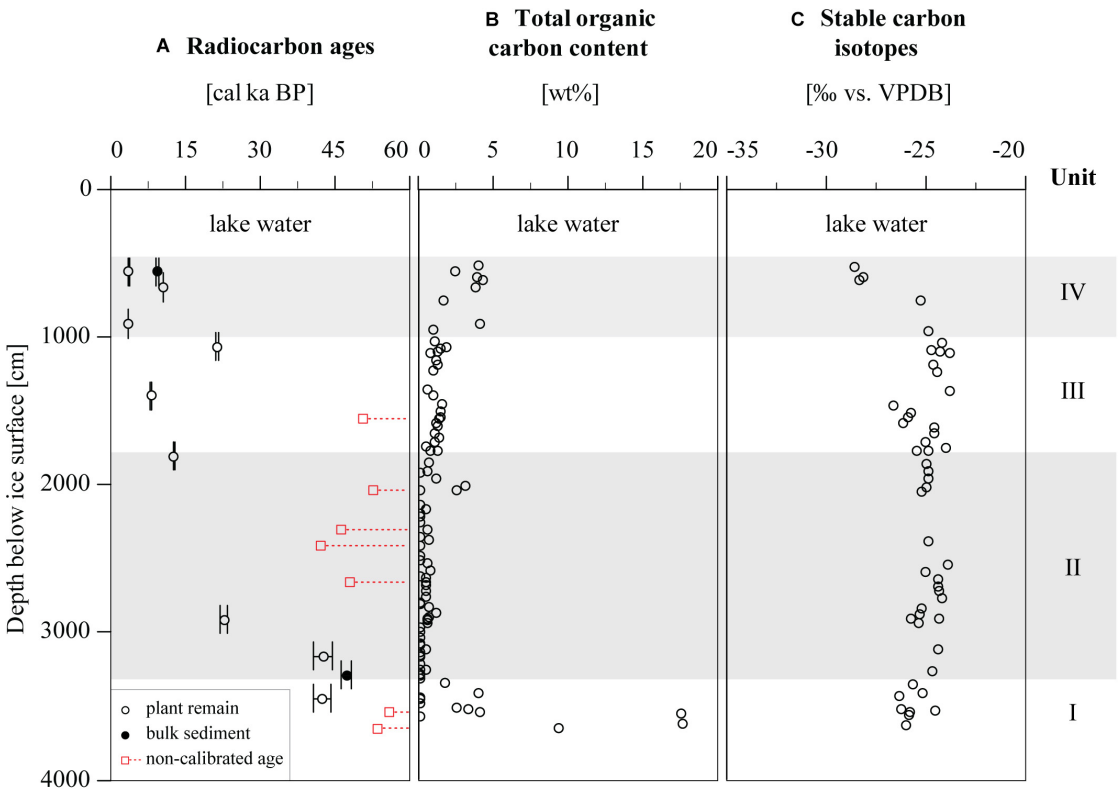

FIGURE 2 | Radiocarbon ages and biogeochemical parameters of Goltsovoye Lake sediment core PG2412. **(A)** Calibrated radiocarbon ages (open circles: plant remains dated, closed circles: bulk sediment dated, red circles: non-calibrated infinite ages), **(B)** total organic carbon content and **(C)** stable carbon isotopes. Units indicated on the right.

Laboratory Analyses

The long core was described in detail and subsampled for laboratory analyses. Pore water was extracted from thawed samples using rhizon soil moisture samples (membrane pore size: 0.12–0.18 μm). The pH and electrical conductivity (μS cm^{-1}) were measured from the pore water. The sediment samples were freeze-dried and the water content was determined based on the weight difference before and after drying.

Eighteen samples were selected for radiocarbon dating from the long core. Macrofossils such as plant (sedges and twigs) and wooden remains were dated using Accelerator Mass Spectrometry in the AWI MICADAS Laboratory in Bremerhaven. For two of the samples, bulk sediment was dated due to the lack of visible macrofossils. Radiocarbon dates were calibrated using the CALIB 7.1 software and the IntCal13 calibration curve, and expressed as calibrated kilo years before present (cal ka BP) (Stuiver et al., 2017).

The grain size distribution of 71 samples from the long core was measured with a laser particle size analyzer (Malvern Mastersizer 3000, <1 mm fraction) after removal of organic material by treating the samples with hydrogen peroxide (30%). The samples were washed, freeze-dried, manually homogenized and sieved (<1 mm fraction measured) before measuring. Here, we show the grain size distribution of the fraction from 0.1 μm to 1 mm.

Homogenized bulk samples (n = 92, sample interval: ∼35 cm) from the long core were analyzed for total nitrogen (TN) and total carbon (TC; Elementar Vario El III), and total organic carbon (TOC; Elementar Vario Max C), which are expressed in weight percentage (wt%). The stable carbon isotopic composition was determined for all samples with TOC values above the detection limit (0.1 wt%). The measured $\delta^{13}C$ (Thermo Fisher Scientific Delta-V-Advantage gas mass spectrometer equipped with a FLASH elemental analyzer EA 2000 and a CONFLO IV gas mixing system) is compared to the standardized Vienna Pee Dee Belemnite (VPDB) and expressed in per mille (‰ vs. VPDB). TOC values below the detection limit were not considered in further calculations.

For the short core, the same methods were used for radiocarbon dating, TOC content and stable carbon isotopes.

Biomarker Analysis

Twenty three samples from the long core were analyzed for lipid biomarkers at the German Research Centre for Geosciences (GFZ) after Schulte et al. (2000). Extraction of OM was done with a Dionex 200 ASE extractor using dichloromethane/methanol (DCM/MeOH, 99:1 v/v, heating phase 5 min, static phase 20 min at 75°C and 5 MPa). The extracts were passed over a sodium sulfate column with n-hexane and four internal standards were added for compound quantification: 5α-androstane, ethylpyrene,

5α-androstan-17-one and erucic acid. Using medium-pressure liquid chromatography (MPLC) after Radke et al. (1980), the extracts were separated into an aliphatic, aromatic and NSO (nitrogen-, sulfur- and oxygen-containing compounds) fraction.

n-Alkanes were measured in the aliphatic fraction using gas chromatography/mass spectrometry (GC-MS; GC Trace GC Ultra and MS DSQ, Thermo Electron Corporation) as described by Jongejans et al. (2018) (capillary column from BPX5, 22 mm × 50 m, 0.25 μm). Compounds were identified and quantified with respect to the internal standards from full scan mass spectra (m/z 50–600 Da, 2.5 scans s^{-1}) using the software XCalibur.

Biomarker Indices

The total lipid concentration of *n*-alkanes is expressed in microgram per gram of sediment (μg g^{-1} sed.) and per gram of TOC (μg g^{-1} TOC).

The average chain length (ACL) of *n*-alkanes provides a measure for the main focus of the *n*-alkane chain length distribution and is used to identify OM source. Long-chain *n*-alkanes are produced by terrestrial higher plants for instance in mosses (*n*-C_{23} and *n*-C_{25}), in leaf waxes (*n*-C_{27} and *n*-C_{29}) and in grasses (*n*-C_{31} and *n*-C_{33}) (e.g., 1998; Zech et al., 2009), whereas short-chain *n*-alkanes are mainly produced by bacteria and algae (Killops and Killops, 2013). The ACL was calculated for *n*-alkanes with carbon number 23–33 according to Equation (1) where *i* is the carbon number (Poynter and Eglinton, 1990).

$$ACL_{23-33} = \frac{\sum i \cdot C_i}{\sum C_i} \quad (1)$$

The CPI and odd-over-even predominance (OEP) indicate the maturity of the OM. High values typically correspond to fresh, undegraded OM, and the ratios decrease with degradation (Bray and Evans, 1961; Marzi et al., 1993). The starting values depend on the composition of the source material. These indices were calculated following Equation (2) (Marzi et al., 1993) and (3) (Zech et al., 2009; Struck et al., 2019), respectively. As both indices are used in other studies, both parameters are presented here.

$$CPI_{23-33} = \frac{\sum \text{odd } C_{23-31} + \sum \text{odd } C_{25-33}}{2 \cdot \sum \text{even } C_{24-32}} \quad (2)$$

$$OEP_{26-33} = \frac{\sum \text{odd } C_{27-33}}{\sum \text{even } C_{26-32}} \quad (3)$$

Schäfer et al. (2016) developed an *n*-alkane endmember model to distinguish between trees and shrubs, and grasses and herbs. It is based on the *n*-alkane ratio (after Equation 4) and the OEP.

$$n-\text{Alkane ratio} = \frac{C_{31} + C_{33}}{C_{27} + C_{31} + C_{33}} \quad (4)$$

In their pilot study, Ficken et al. (2000) proposed the proxy P_{aq} for submerged or floating macrophytes ($P_{aq} > 0.4$) versus emergent ($0.1 < P_{aq} < 0.4$) and terrestrial plant input ($P_{aq} < 0.1$; Equation 5).

$$P_{aq} = \frac{C_{23} + C_{25}}{C_{23} + C_{25} + C_{29} + C_{31}} \quad (5)$$

As this proxy has only been used in tropical and temporal regions, we focus on the trend of the P_{aq} and do not put weight on the proposed ranges. Zheng et al. (2007) developed the proxy P_{wax} to express the share of OM derived from terrestrial plants (Equation 6).

$$P_{wax} = \frac{C_{27} + C_{29} + C_{31}}{\sum \text{odd } C_{23-31}} \quad (6)$$

RESULTS

Based on clustering of the *n*-alkane parameters (see "*n*-Alkane Distributions"), we divided the long core into four units. Unit I ranged from 3665 to 3300 cm, Unit II from 3300 to 1800 cm, Unit III from 1800 to 1000 cm and Unit IV from 1000 to 510 cm. We decided to separate the results and discussion following the statistical clustering of the *n*-alkane parameters. The short core was divided into 3 units from the bottom to the top: Unit A from 1010 to 855 cm, Unit B1 from 855 to 820 cm and Unit B2 from 820 to 510 cm (**Figure 3**).

For both the long and the short core, we describe the radiocarbon ages and biogeochemical parameters (see section "Bulk Sediment"; **Figures 2**, **3**). For the long core, the hydrochemical parameters are characterized (see section "Hydrochemistry"; **Figure 4**), as well as the *n*-alkane parameters (see section "*n*-Alkane Distributions"; **Figure 5**). We further calculated general statistics for all parameters (**Supplementary Table 1**). All reported datasets were published in the open access PANGAEA archive (Biskaborn and Sens, 2020; Jongejans et al., 2020).

Bulk Sediment

Long Core PG2412

The calibrated radiocarbon ages of the macrofossils and bulk sediment of the long core (**Figure 2A**) showed a general trend over depth ranging from 47.5 cal ka BP at 3300 cm to 3.6 cal ka BP at 558 cm (surface sediments) (**Supplementary Table 2**). In Unit I, II and III, seven samples had an infinite age (i.e., below the radiocarbon detection limit; >42.4 to >56.1 ka BP) that could not be calibrated. Unit IV is of Holocene age. The bulk sediment at 558 cm was 5.7 ka older (9.3 cal ka BP) than the macro remains dated from the same sample (3.6 cal ka BP).

In the bottom of the core, the sediments were coarser (**Supplementary Figure 1**). Unit I contained coarse sand and rounded pebbles (up to 2 cm diameter), as well as finer sandy horizons that were mostly layered. The grain size distribution of Unit I and II (up to ∼25 m) was predominantly unimodal indicating fine sand (**Supplementary Figure 1**). Units III and IV had a polymodal grain size distribution and the sediments were mostly very coarse silt to very fine sand.

During the drilling, the talik boundary was located at 3425 cm. Initial temperature data of the borehole (date: 2017-04-23), however, indicated the talik to be ∼32 m deep (Strauss et al., 2018). Unit II, III, and IV were completely unfrozen. The cryostructure below 3425 cm was dominantly pore ice (ice between the organic remains) and partly structureless. Segregated ice was rare (ice lens at 3550 cm, 4 × 0.2 cm; ice band at 3592 cm, 1 cm thick).

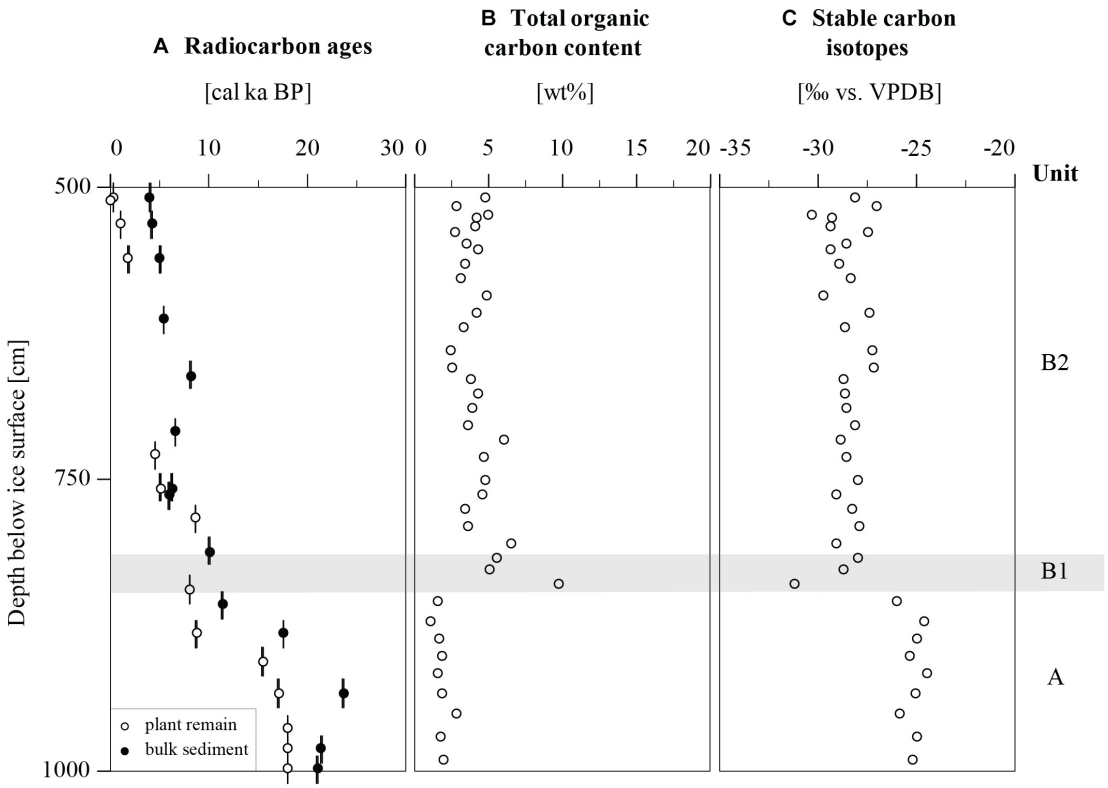

FIGURE 3 | Radiocarbon ages and biogeochemical parameters of Goltsovoye Lake sediment core PG2420. **(A)** Calibrated radiocarbon dates (open circles: plant remains dated, closed circles: bulk sediment dated), **(B)** total organic carbon, and **(C)** stable carbon isotopes. Units indicated on the right.

Unit I was especially enriched in OM. Layers up to 30 cm thick containing twigs, stems, organic layers and lenses, and wooden remains up to 4 cm long in a frozen sandy matrix were found in the interval from 3665 to 3395 cm depth (**Supplementary Figure 2A**). Signs of cryoturbation were present at 3558 to 3555 cm (**Supplementary Figure 2B**). In the lowermost layer (3665-3650 cm), vertically oriented twigs up to 2 cm in length were discovered. Furthermore, organic remains were found from 2173–2311 cm, 1989–2050 cm, 1430–1590 cm, 950–1100, and 510–755 cm. The TOC was highest in the bottom of the core (maximum of 17.8 wt% at 3635 cm) (**Figure 2B**). Unit II and III were very OC poor, but TOC increased again in Unit IV (median: 1.1 wt%). The $\delta^{13}C$ ranged from −28.6‰ vs. VPDB in Unit IV (523 cm) to −23.8‰ vs. VPDB in Unit III (1370 cm) (median: −24.9‰ vs. VPDB).

Short Core PG2420

The short core was dated from 23.8 to 0 cal ka BP (**Figure 3A**) (Biskaborn and Sens, 2020). Unit A was deposited during the late Pleistocene, whereas Unit B1 and B2 were of Holocene age. The radiocarbon ages of Unit A ranged from 23.77 ± 0.06 cal ka BP (bulk sediment at 937 cm) to 11.41 ± 1 cal ka BP (bulk sediment at 860 cm). In Unit B, the samples had radiocarbon ages between 10.10 ± 0.05 cal ka BP (at 815 cm) and recent (at 514 cm, surface sediment). Almost all radiocarbon ages from bulk sediments were older than the respective picked plant remains (except for the sample at 767 cm), with a maximum difference of 8.9 cal ka at 885 cm. However, both profiles show a general depth-related trend to older ages with increasing depth.

The sediments ranged from silty sand in Unit A to clayey silt in Unit B2. Unit B1 was composed of a peat layer. The sediments in Unit A were coarser than in Unit B1 and B2 (Strauss et al., 2018).

The TOC was lowest in Unit A (1.1 wt% at 875 cm), had its maximum in Unit B1 (9.8 wt% at 900 cm), and decreased to ∼4 wt% in Unit B2 (median: 3.6 wt%; **Figure 3B**).

The bulk carbon isotope ratio was highest in Unit A (−24.4 ‰ vs. VPDB at 920 cm) and lowest at the bottom of in Unit B1 (−31.2‰ vs. VPDB at 842 cm). Above, in Unit B2, the bulk $d^{13}C$ signal ranged between −30.3 and −27.0‰ vs. VPDB (median: −28.2‰ vs. VPDB; **Figure 3C**).

Hydrochemistry

The water content of the long core ranged from 10.5 to 65.4 wt% and was highest in Unit I (frozen part) and the upper three samples of Unit IV (sediment surface samples) (median: 17.1 wt%; **Figure 4A**). There was not much variation in Unit II and III. The pH slightly increased from 7.2 in Unit I to 8.7 in Unit II, was relatively constant in Units II and III, but was much lower in the topmost three samples with the minimum of 6.3 at 596 cm (median: 8.2; **Figure 4B**). The electrical conductivity increased from Unit I to Unit II and decreased to the top from Unit III and IV (median: 778 $\mu S\ cm^{-1}$;

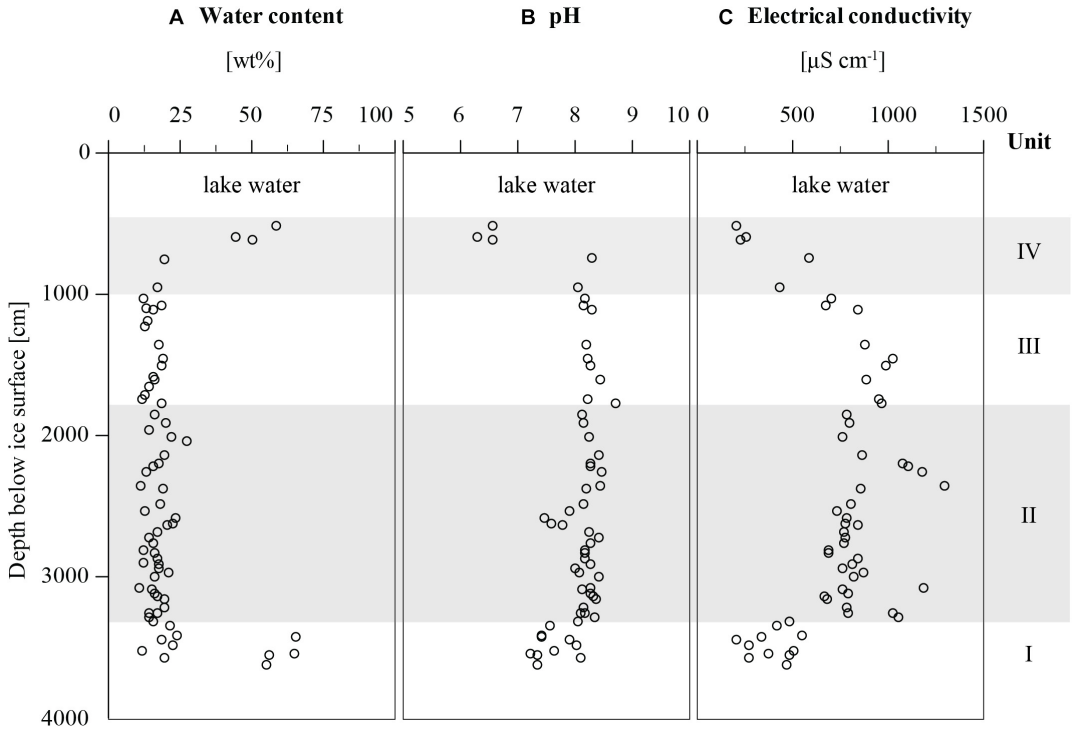

FIGURE 4 | Hydrochemical parameters of Goltsovoye Lake sediment core PG2412. **(A)** Water content, **(B)** pH, and **(C)** electrical conductivity. Units indicated on the right.

Figure 4C). In all hydrochemical parameters, the lowermost and uppermost samples of the core were substantially different from the middle part.

n-Alkane Distributions

The *n*-alkane concentration varied from 0.6 to 20.8 $\mu g\ g^{-1}$ sed. (median: 1.8 $\mu g\ g^{-1}$ sed.; **Figure 5A** and **Supplementary Table 3**). In contrast to the other samples of Unit I (median: 2.1 $\mu g\ g^{-1}$ sed.), the lowermost sample showed a relatively high value (14.3 $\mu g\ g^{-1}$ sed.). In Unit II and III, the *n*-alkane concentrations were generally low (median: 0.9 and 5.3 $\mu g\ g^{-1}$ sed., respectively). In contrast, Unit IV was characterized by higher concentrations (median: 19.3 $\mu g\ g^{-1}$ sed.). The *n*-alkane concentration per gram of TOC primarily increased from the bottom to the top of the core from 50.1 to 581.4 $\mu g\ g^{-1}$ TOC with some stagnation in Unit II and III (median: 367.5 $\mu g\ g^{-1}$ TOC; **Figure 5B** and **Supplementary Table 4**). The sediments were dominated by long-chain *n*-alkanes as indicated by a median ACL_{23-33} of 27.5 (**Figure 5C**), representing the main focus of the *n*-alkane chain length distribution. The ACL increased from the bottom to the top and ranged from 26.5 in Unit I to 28.4 in Unit III. In Unit IV, the values were a bit lower again around 27.8. The CPI and OEP both increased stepwise from Unit I to II and III before they slightly decreased between Units III and IV. Overall, CPI and OEP were between 2.3 and 8.9 (median CPI: 4.8), and 2.2 and 11.0 (median OEP: 5.7), respectively (**Figure 5D**). The *n*-alkane ratio ranged from 0.4 to 0.6 and was slightly higher in Units II and III (**Figure 5E**).

Clustering of the *n*-alkane data revealed four different units, which were also visible in the stepwise changes in the *n*-alkane proxies (**Figure 5**). These units seem to represent environmental changes reflected by different *n*-alkane distributions and were therefore used as subunits of the investigated sediment core (**Figure 5F**). All described *n*-alkane parameters were used as input for the clustering. Clustering was carried out in R v. 3.6.1 using the "chclust" function in package "rioja" with method "coniss."

Odd-carbon number chains dominated the *n*-alkane distributions of all samples. The dominating chain varied between mid- and long-chain *n*-alkanes (**Supplementary Figure 3**). Unit I was dominated by *n*-C_{23} and *n*-C_{25}. Unit II and III were dominated by either *n*-C_{27} or *n*-C_{29}. The upper samples from Unit III (1158 and 1070 cm) were dominated by *n*-C_{31} and Unit IV again by *n*-C_{27}.

In order to see how the odd chains varied over depth with respect to each other, we calculated the relative *n*-alkane concentration per gram TOC for the odd chains C_{23-33} (**Figure 6**). The *n*-C_{33} was least abundant and showed a relatively constant depth profile. The *n*-C_{27} and *n*-C_{29} *n*-alkanes were most abundant. The relative concentration of *n*-C_{23} and *n*-C_{25} decreased upwards in the core, whereas *n*-C_{31} generally increased upwards.

The P_{aq} and P_{wax} were strongly negatively correlated (Pearson correlation index $r = -0.995$, $p < 0.01$; **Figure 7**). The P_{aq}

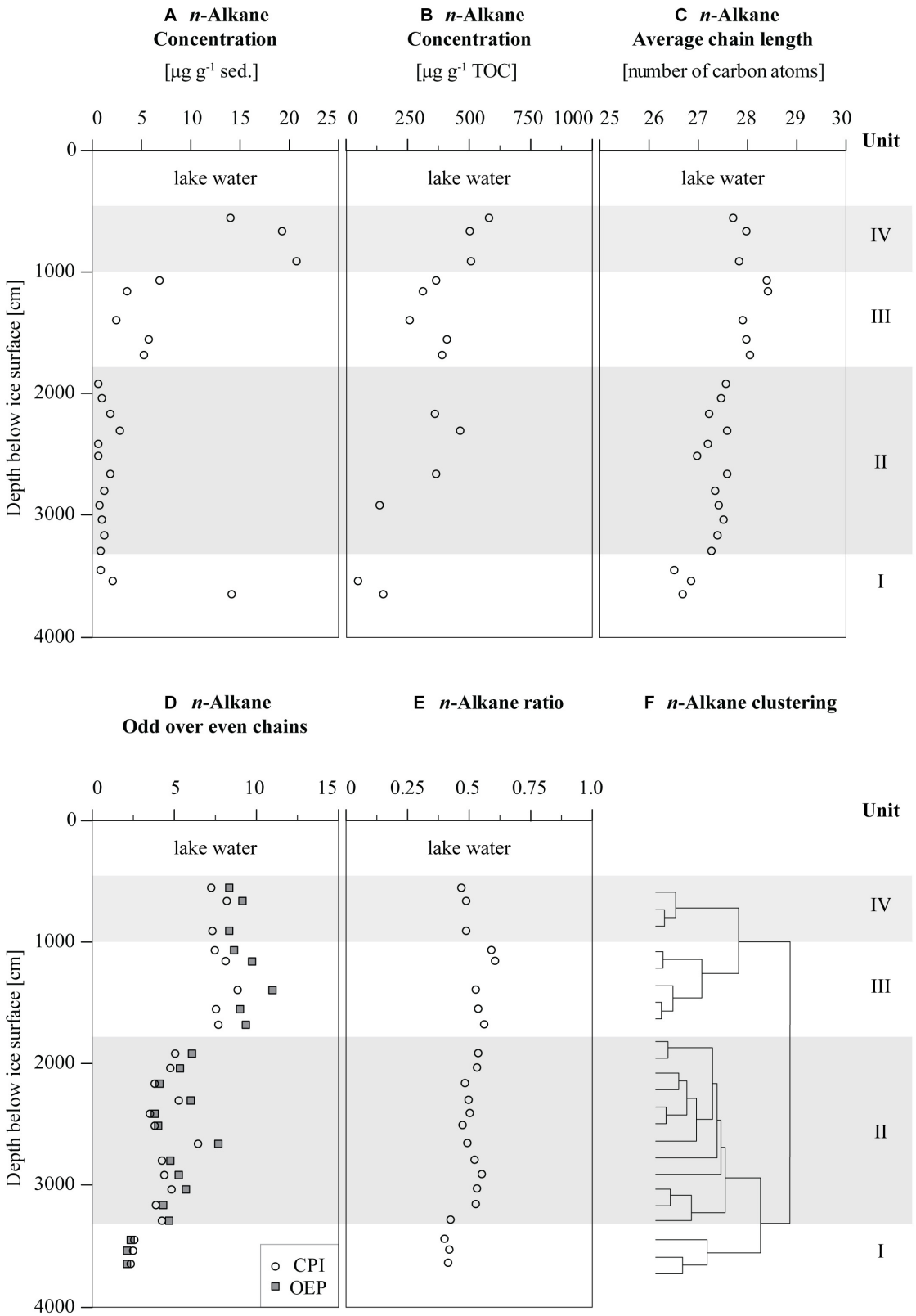

FIGURE 5 | *n*-Alkane parameters of Goltsovoye Lake sediment core PG2412. **(A)** *n*-Alkane concentration per gram sediment, **(B)** *n*-alkane concentration per gram organic carbon (note: samples with TOC < 0.1 wt% not shown), **(C)** *n*-alkane average chain length, **(D)** *n*-alkane carbon preference index (CPI) and odd-over-even predominance (OEP; gray squares), **(E)** *n*-alkane ratio (after Schäfer et al., 2016), and **(F)** *n*-alkane clustering. Units indicated on the right.

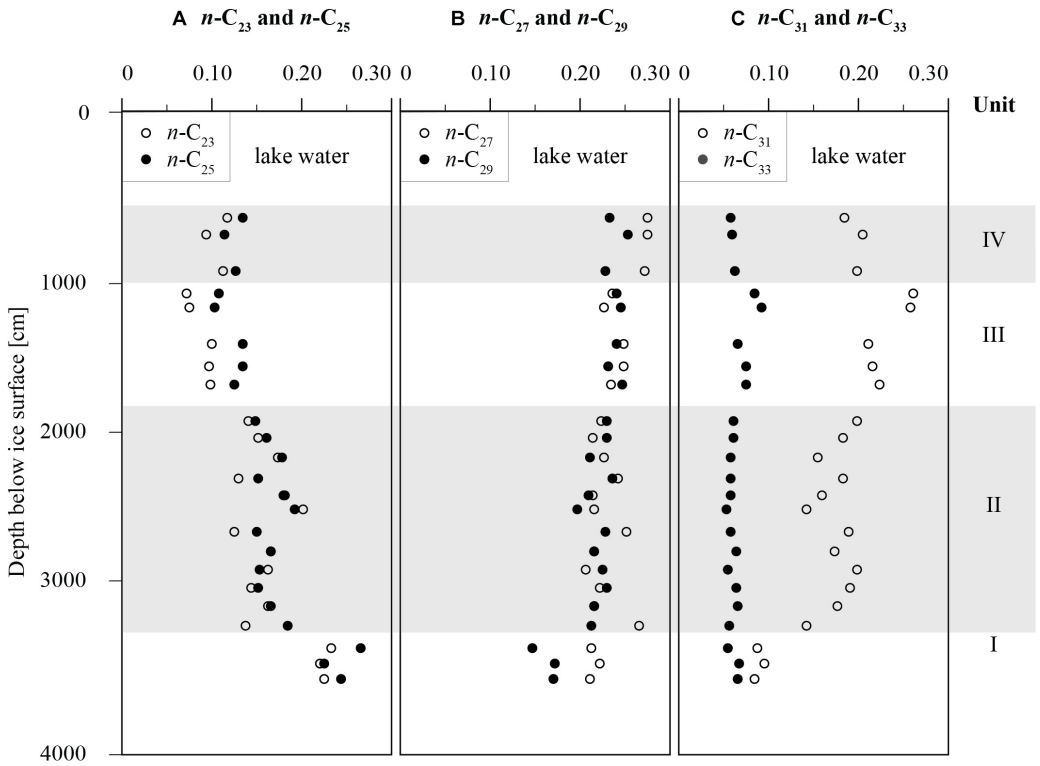

FIGURE 6 | Relative concentration of odd chain *n*-alkanes of Goltsovoye Lake sediment core PG2412. **(A)** n-C_{23} (open circles) and n-C_{25} (closed circles), **(B)** n-C_{27} (open circles) and n-C_{29} (closed circles) and **(C)** n-C_{31} (open circles) and n-C_{33} (closed circles). Example of formula for n-C_{23}: n-C_{23}/(n-C_{23} + n-C_{25} + n-C_{27} + n-C_{29} + n-C_{31} + n-C_{33}). Units indicated on the right.

decreased with depth with a maximum of 0.68 in Unit I and a minimum of 0.26 in Unit III (median: 0.41).

DISCUSSION

Depositional History at the Study Site

In the following, we discuss the sedimentation and post-depositional history of permafrost and lacustrine deposits on Bykovsky Peninsula based on sediment and biomarker parameters observed in our cores.

Generally, it should be noted that age reversals in the sediment core suggest that old organic material has been remobilized in the thermokarst lake environment, i.e., due to thaw and erosion of surrounding permafrost outcrops along the lake shore, which is typical for such dynamic environments (Lenz et al., 2016). Accordingly, the radiocarbon concentrations of bulk samples represent a mixture of reworked particulate organic matter and fresh organic material from the ecosystem at the time of deposition, causing bulk radiocarbon dates to be offset toward older ages compared to dated plant samples (see also Gaglioti et al., 2014).

The sedimentary record in our core starts with fluvial sediments that were deposited during the early Weichselian (see section "Unit I – Early Weichselian fluvial sedimentation"), after which Yedoma sedimentation took place (see sections "Unit II – Yedoma Deposition in Wetland Landscapes Dominated by Low-Centered Polygons" and "Unit III/Unit A – Yedoma Deposition Under Cold-Dry Conditions During the Late Weichselian"). During the Holocene, a thermokarst lake formed, which thawed the Yedoma sediments and allowed the deposition of lacustrine sediments (see section "Unit IV/Unit B – Holocene Thermokarst Lake Formation and Lacustrine Sedimentation"). The estimated talik depth based on the core field description following the drilling (3425 cm) was about 2 m deeper than the talik defined by the 0°C boundary based on the borehole temperature measurements (∼32 m). This inconsistency is caused by drilling heat that has slightly warmed the sediments in the core, making it challenging to visually identify the frozen-unfrozen boundary in the core during the field description. Temperature data from the lake from 1984 indicated that the talik was about 30 m deep (Grigoriev, 1993), which is similar to our findings.

The homogeneous water contents across all units of the long sediment core, with the exception of the uppermost and lowermost samples, suggest that variations are due to potential changes in pore space. The higher OM content in some samples of the fluvial unit may have led to a higher water content, although Strauss et al. (2012) found that the TOC content was too low to affect the total absolute water content of frozen Yedoma substantially. Nevertheless, higher TOC values can be a reason for the increasing water contents toward the top of the core.

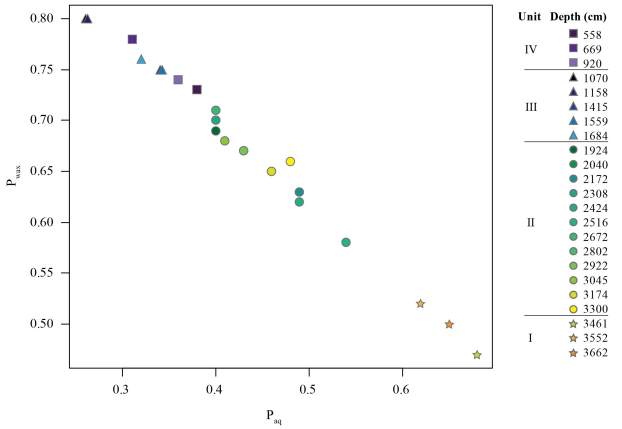

FIGURE 7 | *n*-Alkane proxies for aquatic (P_{aq}) vs. terrestrial (P_{wax}) plant input of Goltsovoye Lake sediment core PG2412. Unit I: orange stars, Unit II: green circles, Unit III: blue triangles, Unit IV: purple squares.

The electrical conductivity is low (**Figure 4**), reflecting a meteoric source for pore waters in interaction with sediment. The electrical conductivity variations over depth might be explained by variation in solid phase surface area: low in Unit I and high in Unit II, leading to lower concentrations in the thawed Unit I and dissolution of mineral material in Unit II. The upwardly decreasing conductivity in Units III and IV suggests a combination of interactions with the solid phase and diffusive exchange with lake water, which has a conductivity of around 200 µS/cm (Strauss et al., 2018). The EC values in the pore water of the Yedoma sediments (669–1301 µS cm^{-1}, median: 812 µS cm^{-1}) are comparable to thawed Yedoma sediments studied in the Ivashkina Lagoon (Schirrmeister et al., 2018). They found that the EC of water extracts from undisturbed Yedoma sediments at the Mamontovy Khayata were an order of magnitude lower.

Unit I – Early Weichselian Fluvial Sedimentation

The coarser sediments and the presence of rounded pebbles in Unit I and the lower part of Unit II, point to a strong fluvial influence. Significant differences in the biogeochemistry (**Figure 8**) and hydrochemistry between Unit I and II (TOC: $p < 0.05$, $\delta^{13}C$: $p < 0.01$, water content: $p < 0.01$, pH: $p < 0.01$ and EC: $p < 0.01$) corroborates a different source material. Previous studies found fluvial sediments underneath the Yedoma deposits on the Bykovsky Peninsula (Slagoda, 1993; Siegert et al., 2002; Grosse et al., 2007; Schirrmeister et al., 2008b), similar to sites in the Lena Delta (Schirrmeister et al., 2003; Wetterich et al., 2008) and on Cape Mamontov Klyk at the western Laptev Sea coast (Schirrmeister et al., 2008a). On the Bykovsky Peninsula, the meandering paleo-Lena River deposited fluvial sediments during the early Weichselian period (100–50 ka BP) (Kunitsky, 1989; Slagoda, 1993, 2004, 2005; Wetterich et al., 2008). The two infinite ages we found in Unit I at 3662 and 3552 cm and the coarse fluvial material suggest that Unit I underneath Goltsovoye Lake has likely formed as part of a regional fluvial depositional environment of the early Weichselian.

The transport and input of allochthonous organic material (large organic remains and driftwood; **Supplementary Figure 2**) by the paleo-river also explains the high variability and the high values of TOC and *n*-alkane concentrations (g^{-1} sed.) in Unit I compared to Unit II (**Figures 8A,C**). The CPI and OEP are lowest in Unit I (median: 2.5 and 2.2) and significantly lower than in Unit II ($p < 0.01$ and $p < 0.05$, respectively; **Figures 8E,F**), which reflects the strong OM degradation before and during the transport. The organic-rich woody layers in Unit I most likely did not originate from *in situ* growing trees, but are considered an accumulation of fluvial transported driftwood material from further south.

The *n*-alkane composition is substantially different in Unit I compared to the units above, as can be seen in the proportion of *n*-C_{23}, *n*-C_{27} and *n*-C_{29} and *n*-C_{31} (**Supplementary Figure 4**). Unit I is enriched in *n*-C_{23} and has the lowest concentration of *n*-C_{27} + *n*-C_{29} and *n*-C_{31}. The relative abundance of the shorter chains *n*-C_{23} and *n*-C_{25} are highest in Unit I (**Figure 6**). Furthermore, the P_{aq}, representing aquatic OM contents, is highest (>0.6) and the P_{wax}, representing terrestrial OM, lowest (∼0.5) (**Figure 7**) in Unit I compared to the other units. Also, the ACL_{23-33}, indicating the main focus of the *n*-alkane distribution, is lowest (∼26.7) in this unit (**Figure 5C**). The tendency of long chain *n*-alkanes with lower carbon numbers point to the presence of OM from submerged or floating macrophytes (Ficken et al., 2000), which fits to an aquatic environment in a fluvial regime.

Unit II – Yedoma Deposition in Wetland Landscapes Dominated by Low-Centered Polygons

In the finer, thawed sediments of Unit II (**Supplementary Figure 1**), four of the radiocarbon ages were infinite (**Figure 2A**). Age reversals could point to either reworked sediments or the incorporation of older organic matter. However, in Yedoma sediments, reworking of sediments is not usual due to the syngenetic freezing upon sedimentation. Soil movement as a result of cryoturbation is often restricted to tens of centimeter (Kaiser et al., 2007), while larger cryoturbation patterns sometimes are observed in particular settings. Reworking after *in situ* thawing of the sediments in the talik can happen due to volume loss after melting of ice. Such partial reworking of Yedoma upon thaw underneath lakes was previously described by Farquharson et al. (2016). However, there are no substantial differences in biogeochemical, hydrochemical and *n*-alkane parameters between samples with finite and infinite ages. Also, the incorporation of allochthonous ancient OM in Yedoma deposits is common (Vasil'chuk and Vasil'chuk, 2017; Jongejans et al., 2018) and hence the most likely explanation of the age reversals in this unit.

The sediments in Unit II are generally OC poor (median TOC: 0.6 wt% and 18 samples with TOC < 0.1 wt%; **Figure 2B**). The low TOC content of the sediments likely results from a combination of OM poor deposition as well as partial OM decomposition after thawing of the sediments. The relatively low CPI and OEP (median: 4.3 and 5.0) reveal partly degraded OM.

The changes in *n*-alkane distribution (**Supplementary Figure 3**) and relative *n*-alkane concentration (**Figure 6**) over

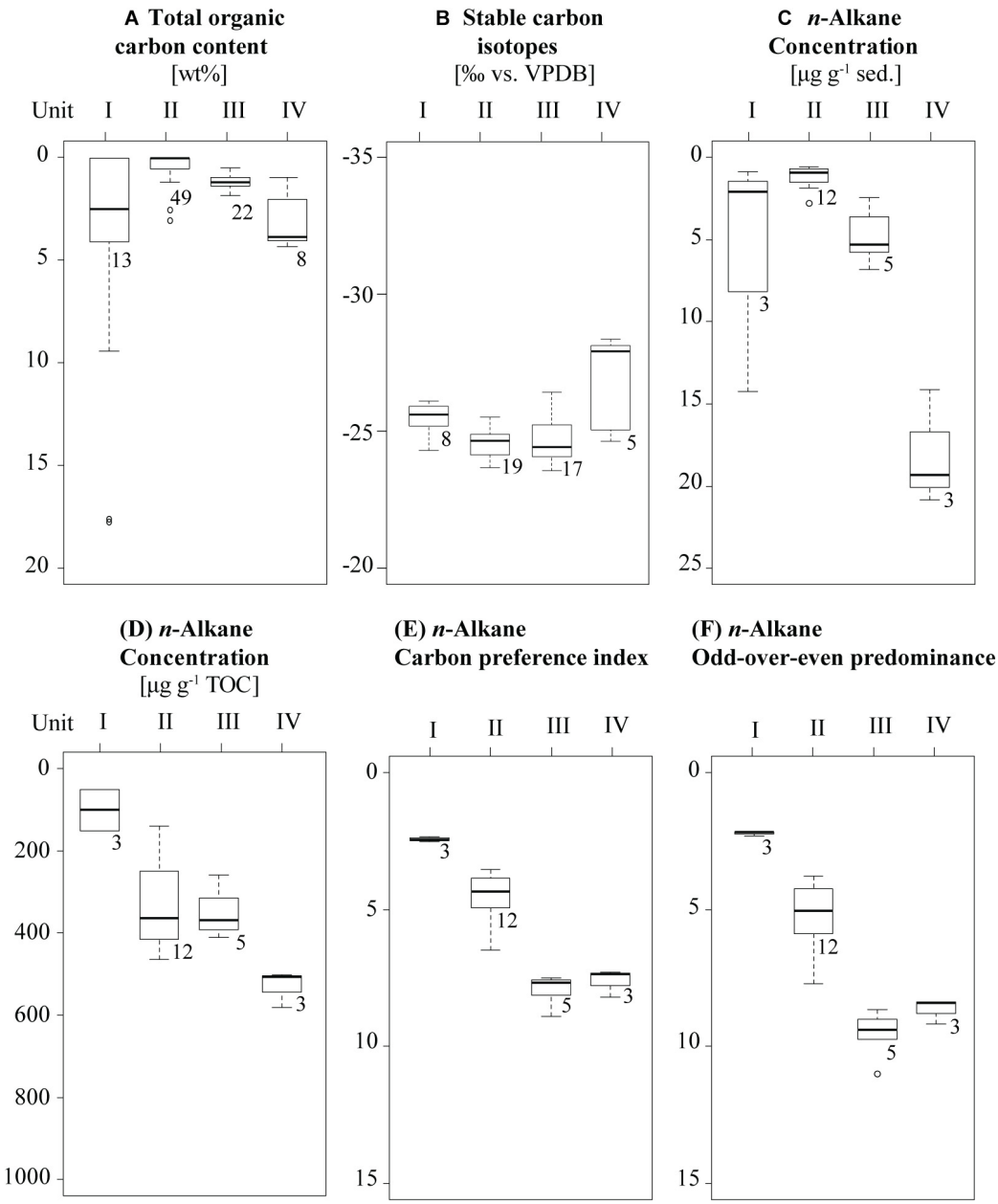

FIGURE 8 | Box-whisker plots of biogeochemical and biomarker parameters of Goltsovoye Lake sediment core PG2412. **(A)** Total organic carbon content, **(B)** stable carbon isotopes, **(C)** *n*-alkane concentration per g sed., **(D)** *n*-alkane concentration per g TOC, **(E)** *n*-alkane carbon preference index, and **(F)** *n*-alkane odd-over-even predominance. Samples sorted according to *n*-alkane clustering. Box-whisker plots according to Tukey with outliers outside of 1.5 interquartile range (IQR). IQR = Q_3-Q_1, range between upper and lower quartiles. Numbers denote sample count.

depth indicates different OM sources. A lower P_{aq} (0.4–0.5) and higher P_{wax} (0.6–0.7) compared to Unit I (**Figure 7**) and slightly increased ACL_{23-33} values (**Figure 5C**) indicate the presence of emergent macrophytes. The relative large proportion of *n*-C_{23} and *n*-C_{25} in Unit I and II (**Figure 6**) is often found in *Sphagnum* mosses (Ficken et al., 1998; Bingham et al., 2010; Bush and McInerney, 2013). The presence of moss points to wet conditions and thus, these findings indicate a wet environment with shallow-water plant species. Therefore, we interpret this unit as a low-centered polygon environment, whereby water accumulates in the centers of the polygons (Liljedahl et al., 2016). The Yedoma deposition in Unit II could correspond to the relatively wetter conditions of the Kargin Interstadial (Schirrmeister et al., 2002b).

In their study of methane emissions from low-center polygons in the Lena Delta, Kutzbach et al. (2004) found that the amount of methane released relied heavily on the microrelief

of the polygons. Small changes in microrelief led to different hydrologic conditions, thereby influencing the aeration status, OM content and vegetation cover. Also, the water table relative to the roots influences the aeration status. Especially vascular plants can form major pathway for methane transport into the atmosphere. The wetland conditions of the low-centered polygon environment of Unit II probably has led to substantial methane emission in the past.

Unit III/Unit A – Yedoma Deposition Under Cold-Dry Conditions During the Late Weichselian

Unit III of the long sediment core corresponds to Unit A of the short core. Unit III contains one infinite age (at 1559 cm; **Figure 3**) and the dated sample at 1070 cm, which gained a late Pleistocene (MIS 2) age (21.39 ± 0.27 cal ka BP) is older than the general radiocarbon age trend, indicating the presence of reworked or eroded material in this sample. Unit A was deposited during the same period. The age difference between the bulk sediment and the picked plant remains in the short core points to a considerable amount of reworked particulate carbon from the surrounding environment.

The biogeochemical parameters are similar for Units III (median TOC: 1.15 wt%, median $\delta^{13}C$: −24.6‰ vs. VPDB; **Figure 2**) and Unit A (median TOC: 1.7 wt%, median $\delta^{13}C$: −25.0‰ vs. VPDB; **Figure 3**). The multimodal grain size distribution of Unit III (**Supplementary Figure 1**) suggests that multiple transport, accumulation and re-sedimentation processes were involved in the formation, which is in agreement with previous studies of Yedoma deposits (Schirrmeister et al., 2008b; Strauss et al., 2012).

The lower part of Unit III is dominated by *n*-C_{27} and *n*-C_{29} and the upper part (at 1158 and 1070 cm) by *n*-C_{31} suggesting a transition to a grass/herb dominated environment (**Supplementary Figure 3** and **Figure 6**) (Zech et al., 2009; Schäfer et al., 2016). In this interval, also the ACL_{23-33} is shifted to the highest values (**Figure 5C**). The P_{aq} proxy shows the lowest value (below 0.34) and the P_{wax} the highest (above 0.75) (**Figure 7**). These findings point to a less aquatic and drier environment, which could correspond to the cold and dry steppe-like tundra that characterized the late Weichselian and the Last Glacial Maximum. This is in agreement with paleo-ecological data from the Mamontovy Khayata Yedoma cliff at the east coast of Bykovsky Peninsula from this period (Schirrmeister et al., 2002b). The TOC and *n*-alkane concentration (g^{-1} sed.) are significantly higher than in the unit below ($p < 0.01$) (**Figures 8A,C**). The CPI and OEP show maxima at the top of Unit III (median: 7.7 and 9.4; **Figures 8E,F**), indicating that this material shows a low level of degradation.

Few other studies focus on *n*-alkane concentrations in Siberian Yedoma sediments. The Yedoma sediments from this study (Unit II and III; 138–2455 μg g^{-1} TOC) have *n*-alkane concentrations comparable to the data from other studied Yedoma deposits in the Ivashkina Lagoon (267–1199 μg g^{-1} TOC) (Ulyantsev et al., 2017), on the Buor Khaya Peninsula (387–1715 μg g^{-1} TOC) (Strauss et al., 2015) and at the cliff of Sobo Sise in the Lena Delta (176–639 μg g^{-1} TOC) (Neubauer, 2016) (**Figure 9A**).

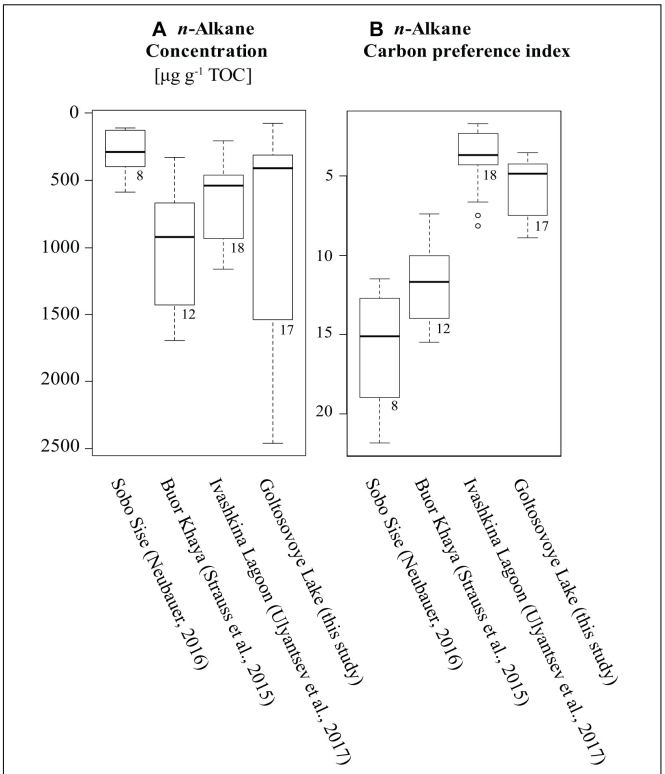

FIGURE 9 | Box-whisker plots of biomarker parameters from Siberian Yedoma studies. **(A)** *n*-Alkane concentration and **(B)** *n*-alkane carbon preference index. Box-whisker plots according to Tukey with outliers outside of 1.5 IQR. Numbers denote sample count.

Unit IV/Unit B – Holocene Thermokarst Lake Formation and Lacustrine Sedimentation

Unit IV of the long sediment core corresponds to Unit B of the short core. Unit B1 consists of a peat layer (**Figure 3**). Likely, this basal peaty layer formed during a wetland phase prior to the lake phase and therefore represents the transition to a thermokarst lake. The thickness of the peaty layer of Unit B1 (35 cm) suggests an extended wetland phase. Similar to other young thermokarst lakes (Kessler et al., 2012; Walter Anthony et al., 2018), talik growth and expansion into the previously deposited late Pleistocene Yedoma deposits certainly thawed the Yedoma OM, resulting in high methane production also underneath Goltsovoye Lake. With subsequent lake basin deepening due to subsidence of the thawing ice-rich permafrost, contemporary lake mud containing *in situ* produced OM and reworked old OC from the surrounding slopes accumulated, similarly to other thermokarst lakes in northern Siberia (Biskaborn et al., 2013b; Schleusner et al., 2015).

The radiocarbon age of the peat layer (848 cm depth) is 8 ± 0.05 cal ka BP (**Figure 3**) and probably indicates that thermokarst lake formation started around 8000 years BP. The total thaw depth (talik depth ∼32 m, altitude difference between lake and Yedoma uplands ∼20 m) of ∼52 m is relatively shallow for 8000 years of thermokarst development (M. Angelopoulos, personal communication, 2020). Previous talik modeling studies

of Alaskan thermokarst lakes showed faster talik growth rates for lakes in North America (e.g., Ling and Zhang, 2003; West and Plug, 2008; Kessler et al., 2012; Creighton et al., 2018). However, talik growth could be slowed by characteristics of Siberian Yedoma, such as its higher ice volume in these sediments or the presence of bedfast ice during an extended shallow lake phase (<2 m).

In the long core, the transition from a dry and cold, grass-dominated landscape to a thermokarst lake lies between Unit III and Unit IV. The biogeochemical parameters of Unit IV (median TOC: 3.9 wt%, $\delta^{13}C$: −28.2‰ vs. VPDB; **Figure 2**) are very similar to Unit B (median TOC: 4.2 wt%, median $\delta^{13}C$: −28.6‰ vs. VPDB; **Figure 3**). We found substantial differences between Unit III and IV for the TOC ($p < 0.01$), $\delta^{13}C$ ($p < 0.05$) and the *n*-alkane concentration ($p < 0.05$) (**Figure 8**). Also, the TOC and stable carbon isotope ratio are significantly different between Unit A and B in the short core ($p < 0.01$). The sediments of Unit IV have a higher TOC compared to the thawed Yedoma sediments, which is characteristic for lake sediments with input of lake primary production (Walter Anthony et al., 2014; Jongejans et al., 2018). This is also suggested by the relatively high CPI and OEP in Unit IV (median: 7.3 and 8.4) compared to the lower units.

The dominating *n*-alkane chain in Unit IV is *n*-C_{27} (**Supplementary Figure 3**). The ACL, *n*-alkane ratio, P_{wax}, CPI and OEP are lower in Unit IV compared to Unit III (**Figure 8**) and P_{aq} is partly a bit higher. The OM in this unit is likely a mixture derived from primary production in the thermokarst lake and from thawing permafrost surrounding the lake. As found in other thermokarst lake systems, the lake primary productivity is largely influenced by local thermal erosion, surrounding depositional characteristics and drainage processes strongly affecting hydrochemistry and water level (e.g., Biskaborn et al., 2013a; Lenz et al., 2016).

Organic Matter Degradation

The state of OM degradability of Yedoma and other deposits underneath Goltsovoye Lake can be assessed with the *n*-alkane proxies. In thermokarst-affected Yedoma uplands, the previously undisturbed sediments thaw from the top downwards and therefore, the sediments closer to the surface are expected to have been exposed to thawed conditions for the longest time. Intuitively, one would expect the most degraded OM in the top sediments and the least degraded OM in the bottom sediments of the core. However, based on the CPI and OEP parameters, we found an opposite trend with the furthest degraded OM in the deepest part of the core (**Figures 5D**, **8E,F**). As described above, the OM incorporated into the sediments underneath Goltsovoye Lake accumulated under different environmental conditions. Both the OM origin and the depositional conditions have an effect on the CPI and OEP values. Different OM origin and composition lead to different starting values of the parameters for the deposited OM (see for comparison **Figure 9B**) and different environmental conditions can lead to different degradation levels during deposition. Since the OEP and CPI, as well as the *n*-alkane concentrations and the ACL, show stepwise changes from unit to unit, we interpret the CPI and OEP profiles to be still dominated by the OM input and the degradation level of the time of deposition was largely preserved, rather than being overprinted by the thaw process underneath the thermokarst lake. Thus, the higher terrestrial character (highest P_{wax}) of the OM in Unit III might have caused the highest CPI and OEP values in this core interval, while high degradation of presumably reworked material in the fluvial deposits of Unit I might have led to the lowest values in this core sequence. Overall, the CPI and OEP values still indicate relatively less degraded OM material at least for the Units IV and III and partly also for Unit II.

Romankevich et al. (2017) and Ulyantsev et al. (2017) studied *n*-alkane parameters of a 38-m-long sediment core from the Ivashkina Lagoon (**Figures 9A,B**), about 3 km east of the Goltsovoye Lake. They found alluvial sands in the bottom (38–22 m), containing highly altered OM (median CPI: 2.7) (Romankevich et al., 2017), which is in line with our findings. In the Yedoma sediments overlying these sands (22–3 m), they distinguished changes in sediment and OM source, as well as burial conditions. In the middle part of the core (∼21–13 m), the OM was enriched in *n*-C_{29} and *n*-C_{31}, and intermediate bulk CPI values (median: 3.8) could point to microbial degradation. Less-degraded material was found in the upper 5 m of the sediment core. Generally, their interpretation corresponds to our findings. Our *n*-alkane concentration does not differ significantly in the Ivashkina Yedoma deposits compared to the Goltsovoye Yedoma deposits. However, the OM in the Ivashkina deposits is further degraded (CPI: $p < 0.01$, **Figure 9B**).

We plotted the *n*-alkane ratio of our samples against the OEP (**Figure 10**). The samples clearly plot according to the *n*-alkane cluster units with lowest OEP and *n*-alkane ratio in Unit I and maxima in Unit III. Schäfer et al. (2016) calculated degradation lines for grasses and herbs (orange dashed line) and for deciduous trees and shrubs (green dashed line) based on the data from their study in Central Europe and that of Zech et al. (2013) of eastern Germany. The degradation lines are based on (1) the degradation of the organic material, which is indicated by the OEP, and (2) the vegetation type, which is indicated by the *n*-alkane ratio. We fitted a logarithmic function to the data of this study (purple dashed line). From this, we argue that the OM in our study contains a mixture of long and mid-chain *n*-alkanes. Due to the lack of typical deciduous trees and shrubs on the Bykovsky Peninsula, the presence of the *n*-C_{27} alkanes has to be explained by a different source. Using this endmember model is a first-order approximation to decipher a general pattern. First, one cannot assume a similar plant composition in Arctic regions compared to temperate regions. Second, some plant genera such as *Artemisia* or *Sphagnum*, have been found to have a dominance of the *n*-C_{29} alkane, thereby 'mimicking' deciduous trees and shrubs (Ficken et al., 1998; Struck et al., 2019). Third, lake aquatic organisms can contribute to mid-chain alkanes (*n*-C_{21} to *n*-C_{27}), which also leads to the overestimation of the presence of trees and shrubs (Ficken et al., 2000). Finally, samples with poorly preserved OM (low OEP values) can be difficult to interpret, as the degradation signal may have altered the *n*-alkane patterns (Struck et al., 2018). Even though this endmember model does not seem to reflect the OM source patterns in our samples, it does show a mixed character of the OM. Furthermore, this is

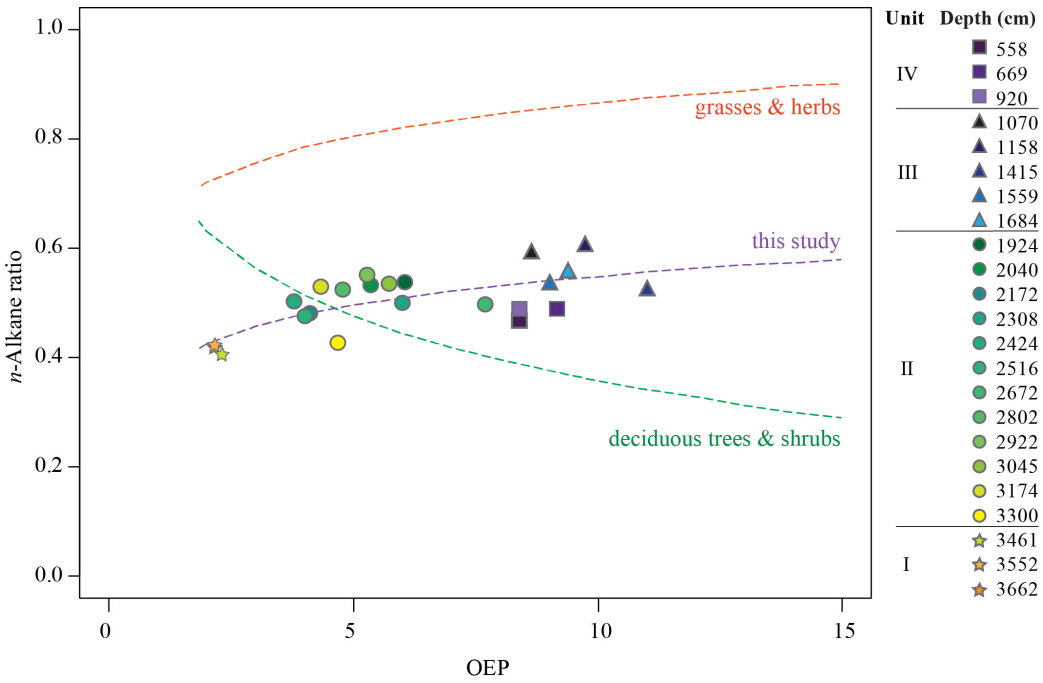

FIGURE 10 | *n*-Alkane endmember model of Goltsovoye Lake sediment core PG2412. Degradation line for grasses and herbs [dashed orange; $y = 0.09*\ln(OEP) + 0.66$] and deciduous trees and shrubs [dashed green; $y = 0.17*\ln(OEP) + 0.75$] after Zech et al. (2013) and Schäfer et al. (2016). Fitted line for this study [dashed purple; $y = 0.08*\ln(OEP) + 0.37$]. *n*-Alkane ratio: $(n\text{-}C_{31} + n\text{-}C_{33})/(n\text{-}C_{27} + n\text{-}C_{31} + n\text{-}C_{33})$. Unit I: orange stars, Unit II: green circles, Unit III: blue triangles, Unit IV: purple squares.

the first time this endmember model has been applied to Arctic sediments samples. More calibrations studies should be carried out to test this promising method for OM characterization studies in Arctic sediments.

In our study, the frozen fluvial sediments below the thawed Yedoma deposits had higher TOC values than in the thawed Yedoma, but this OM at the very bottom of the core also showed a higher level of degradation. The TOC content of the thawed Yedoma deposits is relatively low (median TOC: 0.8 wt% and 22 samples with TOC below detection limit) compared to previous research of still frozen Yedoma on the Bykovsky Peninsula that reported TOC values of 1.2 to 14 wt% (e.g., Schirrmeister et al., 2002a; Strauss et al., 2020). Furthermore, compared to Yedoma deposits on the Buor Khaya Peninsula and the Yedoma cliff of Sobo Sise (median CPI: 11.7 and 15.2, respectively), a degradation signal of the Yedoma OM is traceable (**Figure 9B**). As we have no information about the detailed OM characteristics of undisturbed Yedoma deposits of the study area, we argue that the OM signal of these thawed Yedoma deposits is a mixture of a source signal and a degradation signal of OM thaw and partial microbial decomposition after talik formation. Still, we find that for our biomarker proxies, the OM input signal exceeds the degradation signal in this study.

Continued thermokarst lake growth of Goltsovoye Lake will lead to further talik deepening and thus thawing of more sediments as well as erosion of surrounding sediments into the lake. Walter et al. (2006) showed that methane release at the lake margins accounted for the largest portion of methane release from thermokarst lakes. As we took our sediment core from the deepest point of the lake, the sediments likely have been thawed the longest time for this lake, while sediments nearer to the shore would have been exposed to thaw only more recently. Our study highlights that thawed deposits underneath a thermokarst lake vary in the OM composition and degradability and that this is primarily a result of OM origin and depositional environment, and less of permafrost thaw history. To understand future responses of further permafrost thaw and to assess the greenhouse gas emission potential, more knowledge is needed about the OM characteristics of the permafrost deposits. A direct comparison of thawed and still frozen Yedoma OM from nearby sites would be useful to better understand the impacts of thaw and microbial decomposition. The applied study of *n*-alkanes proves to be very useful in identifying OM sources, level of degradation and assessment of the depositional environment. Further research using other biogeochemical assessments such as those based on amino acids (Hutchings et al., 2019), *Sphagnum*-derived phenols (Abbott et al., 2013) and pectin-like polysaccharides as well as C/N burial profiles (Schellekens et al., 2015) would also be valuable.

CONCLUSION

Our study of OM degradation in thermokarst-affected permafrost sediments in an ice-rich Yedoma permafrost landscape relied on a unique set of two drilling cores from beneath a thermokarst

lake in northeastern Siberia. Using *n*-alkane indices, we were able to distinguish four depositional units for the frozen and thawed sediments underneath Goltsovoye Lake on Bykovsky Peninsula. The lowest sediments (36.6-33 m) are of fluvial origin and were deposited prior to Yedoma formation. Their OM is characterized by a high degradation level and a relatively large share of aquatic OM (e.g., macrophytes). Yedoma formation started in a relatively wet, low-centered polygon landscape (33-18 m) with low amounts of but largely less degraded OM. Subsequently, *n*-alkane indices indicate a transition to a drier environment during the peak period of the Last Glacial Maximum (18-10 m) that was partly grass dominated (12 to 10 m). Furthermore, the OM in this sediment interval shows a low level of degradation. In the middle Holocene, a thermokarst lake formed and deposited lacustrine sediments (10-5.1 m), accompanied by talik formation that subsequently thawed the previously accumulated ice-rich Yedoma deposits. These lake sediments exhibit a higher TOC and *n*-alkane concentrations compared to the Yedoma sediments below.

Both the Yedoma deposits and the fluvial deposits contain old allochthonous OM. Moreover, using the *n*-alkane endmember model, we found a mixed input of the OM in all units. In the thawed Yedoma sediments, less OC was found compared to frozen Yedoma deposits reported elsewhere, suggesting a combination of OC poor deposition and partial mobilization of OC and release as methane from the thermokarst lake talik. Higher OC contents were found in the frozen fluvial sediments below the Yedoma deposits. However, using the *n*-alkane parameters, we found a trend toward increasingly degraded OM in these sediments in the bottom of the core. Overall, the *n*-alkane proxies suggest that the input signal of the OM still exceeds the degradation signal from thaw underneath the lake and that these parameters can still provide valuable information on the origin, degradation level and deposition conditions of the deposited OM.

DATA AVAILABILITY STATEMENT

All datasets generated for this study are available on PANGAEA.

AUTHOR CONTRIBUTIONS

JS, GG, and MG developed the overall coring plans for the Bykovsky Peninsula field campaign. JS, MG, GM, LS, BB, and GG conducted the field work. LJ and JS developed the study design for biomarker analysis of the core. LJ and BB performed the laboratory analyses and led the data interpretation for the long (PG2412) and short (PG2420) sediment cores, respectively. All co-authors contributed with their specific expertise to data interpretation and provided feedback to the manuscript. LJ led the writing of the manuscript.

FUNDING

LJ was funded by a doctoral stipend from the German Federal Environmental Foundation (DBU). This study was carried out within the ERC Project PETA-CARB (#338335) and a NERC-BMBF grant (project CACOON, grant no. 03F0806A). MG and GM were funded by the Russian Foundation for Basic Research (#18-05-70091 and #18-45-140057). The Alfred Wegener Institute Helmholtz Centre for Polar and Marine Research (AWI) and the Germany Research Centre for Geosciences (GFZ) provided funding for the expedition.

ACKNOWLEDGMENTS

We thank the Hydrobase Tiksi, Arctica GeoZentr, Stanislav Ostreldin, Waldemar Schneider, and Sergey Pravkin for their logistic contribution to the field expedition Bykovsky 2017. We thank Dirk Wagner (GFZ) for supporting the expedition. We thank the MICADAS Team at AWI Bremerhaven for dating the radiocarbon samples. We thank Paul Overduin for discussing the hydrochemical results and for providing comments to the manuscript, and we thank Michael Angelopoulos for discussing the thermokarst lake talik results. We also thank Angélique Opitz, Dyke Scheidemann, Jonas Sernau, Mirjam Sens (AWI), Cornelia Karger, and Anke Sobotta (GFZ) for their support and assistance in the lab.

SUPPLEMENTARY MATERIAL

The Supplementary Material for this article can be found online at: https://www.frontiersin.org/articles/10.3389/fenvs.2020.00118/full#supplementary-material

REFERENCES

Abbott, G. D., Swain, E. Y., Muhammad, A. B., Allton, K., Belyea, L. R., Laing, C. G., et al. (2013). Effect of water-table fluctuations on the degradation of *Sphagnum* phenols in surficial peats. *Geochim. Cosmochim. Acta* 106, 177–191. doi: 10.1016/j.gca.2012.12.013

Andersson, R. A., and Meyers, P. A. (2012). Effect of climate change on delivery and degradation of lipid biomarkers in a Holocene peat sequence in the Eastern European Russian Arctic. *Org. Geochem.* 53, 63–72. doi: 10.1016/j.orggeochem.2012.05.002

Bingham, E. M., McClymont, E. L., Väliranta, M., Mauquoy, D., Roberts, Z., Chambers, F. M., et al. (2010). Conservative composition of *n*-alkane biomarkers in *Sphagnum* species: implications for palaeoclimate reconstruction in ombrotrophic peat bogs. *Org. Geochem.* 41, 214–220. doi: 10.1016/j.orggeochem.2009.06.010

Biskaborn, B. K., Herzschuh, U., Bolshiyanov, D., Savelieva, L., Zibulski, R., and Diekmann, B. (2013a). Late Holocene thermokarst variability inferred from diatoms in a lake sediment record from the Lena Delta, Siberian Arctic. *J. Paleolimnol.* 49, 155–170. doi: 10.1007/s10933-012-9650-1

Biskaborn, B. K., Herzschuh, U., Bolshiyanov, D. Y., Schwamborn, G., and Diekmann, B. (2013b). Thermokarst processes and depositional events in a tundra lake, northeastern Siberia. *Permafr. Periglac. Process.* 24, 160–174. doi: 10.1002/ppp.1769

Biskaborn, B. K., and Sens, M. (2020). *Biogeochemical And Radiocarbon Data Of Sediment Core PG2420*. Bykovsky Peninsula: Great Lake Publishing.

Biskaborn, B. K., Smith, S. L., Noetzli, J., Matthes, H., Vieira, G., Streletskiy, D. A., et al. (2019). Permafrost is warming at a global scale. *Nat. Commun.* 10:264. doi: 10.1038/s41467-018-08240-4

Bray, E. E., and Evans, E. D. (1961). Distribution of *n*-paraffins as a clue to recognition of source beds. *Geochim. Cosmochim. Acta* 22, 2–15. doi: 10.1016/0016-7037(61)90069-2

Bush, R. T., and McInerney, F. A. (2013). Leaf wax *n*-alkane distributions in and across modern plants: implications for paleoecology and chemotaxonomy. *Geochim. Cosmochim. Acta* 117, 161–179. doi: 10.1016/j.gca.2013.04.016

Creighton, A. L.-T., Parsekian, A. D., Angelopoulos, M., Jones, B. M., Bondurant, A. C., Engram, M., et al. (2018). Transient electromagnetic surveys for the determination of talik depth and geometry beneath thermokarst lakes. *J. Geophys. Res. Solid Earth* 123, 9310–9323. doi: 10.1029/2018JB016121

Farquharson, L., Anthony, K. W., Bigelow, N., Edwards, M., and Grosse, G. (2016). Facies analysis of yedoma thermokarst lakes on the northern Seward Peninsula, Alaska. *Sediment. Geol.* 340, 25–37. doi: 10.1016/j.sedgeo.2016.01.002

Ficken, K. J., Barber, K. E., and Eglinton, G. (1998). Lipid biomarker, δ13C and plant macrofossil stratigraphy of a Scottish montane peat bog over the last two millennia. *Org. Geochem.* 28, 217–237. doi: 10.1016/S0146-6380(97)00126-125

Ficken, K. J., Li, B., Swain, D., and Eglinton, G. (2000). An *n*-alkane proxy for the sedimentary input of submerged/floating freshwater aquatic macrophytes. *Org. Geochem.* 31, 745–749. doi: 10.1016/S0146-6380(00)00081-4

French, H. M. (1999). Past and present permafrost as an indicator of climate change. *Polar Res.* 18, 269–274. doi: 10.3402/polar.v18i2.6584

Fuchs, M., Grosse, G., Strauss, J., Günther, F., Grigoriev, M., Maximov, G. M., et al. (2018). Carbon and nitrogen pools in thermokarst-affected permafrost landscapes in Arctic Siberia. *Biogeosciences* 15, 953–971. doi: 10.5194/bg-15-953-2018

Gaglioti, B. V., Mann, D. H., Jones, B. M., Pohlman, J. W., Kunz, M. L., and Wooller, M. J. (2014). Radiocarbon age-offsets in an arctic lake reveal the long-term response of permafrost carbon to climate change. *J. Geophys. Res. Biogeosciences* 119, 1630–1651. doi: 10.1002/2014JG002688

Grigoriev, M. (1993). *Cryomorphogenesis of the Lena River Mouth Area*. Novosibirsk: Siberian Branch.

Grigoriev, N. (1960). The temperature of permafrost in the Lena delta basin-deposit conditions and properties of the permafrost in Yakutia. *Yakutsk* 2, 97–101.

Grosse, G., Schirrmeister, L., Kunitsky, V., Rachold, V., Grigoriev, M. N., and Hubberten, H.-W. (2005). "Volumetric balance of ice complex deposits at Bykovsky Peninsula (NE Siberia), using field data, remote sensing and digital elevation models," in *Proceedings of the 2nd European Conference on Permafrost*, Potsdam.

Grosse, G., Schirrmeister, L., Siegert, C., Kunitsky, V. V., Slagoda, E. A., Andreev, A. A., et al. (2007). Geological and geomorphological evolution of a sedimentary periglacial landscape in Northeast Siberia during the late quaternary. *Geomorphology* 86, 25–51. doi: 10.1016/j.geomorph.2006.08.005

Heslop, J. K., Anthony, K. M. W., Grosse, G., Liebner, S., and Winkel, M. (2019). Century-scale time since permafrost thaw affects temperature sensitivity of net methane production in thermokarst-lake and talik sediments. *Sci. Total Environ.* 691, 124–134. doi: 10.1016/j.scitotenv.2019.06.402

Höfle, S., Rethemeyer, J., Mueller, C. W., and John, S. (2013). Organic matter composition and stabilization in a polygonal tundra soil of the Lena Delta. *Biogeosciences* 10, 3145–3158. doi: 10.5194/bg-10-3145-2013

Hugelius, G., Strauss, J., Zubrzycki, S., Harden, J. W., Schuur, E. A. G., Ping, C.-L., et al. (2014). Estimated stocks of circumpolar permafrost carbon with quantified uncertainty ranges and identified data gaps. *Biogeosciences* 11, 6573–6593. doi: 10.5194/bg-11-6573-2014

Hutchings, J. A., Bianchi, T. S., Kaufman, D. S., Kholodov, A. L., Vaughn, D. R., and Schuur, E. A. G. (2019). Millennial-scale carbon accumulation and molecular transformation in a permafrost core from Interior Alaska. *Geochim. Cosmochim. Acta* 253, 231–248. doi: 10.1016/j.gca.2019.03.028

Jenrich, M. (2020). *Thermokarst Lagoons - Carbon Pools and Panarctic Distribution*. Master thesis, University of Potsdam, Potsdam.

Jongejans, L. L., Mangelsdorf, K., and Strauss, J. (2020). n-Alkanes, total organic carbon content, radiocarbon ages, grain size distribution, biogeochemical and hydrochemical parameters of sediment core beneath thermokarst lake Goltsovoye Lake on the Bykovsky Pensinula, northeastern Siberia. *PANGAEA*. doi: 10.1594/PANGAEA.919811

Jongejans, L. L., Strauss, J., Lenz, J., Peterse, F., Mangelsdorf, K., Fuchs, M., et al. (2018). Organic matter characteristics in yedoma and thermokarst deposits on Baldwin Peninsula, west Alaska. *Biogeosciences* 15, 6033–6048. doi: 10.5194/bg-15-6033-2018

Kaiser, C., Meyer, H., Biasi, C., Rusalimova, O., Barsukov, P., and Richter, A. (2007). Conservation of soil organic matter through cryoturbation in arctic soils in Siberia. *J. Geophys. Res. Biogeosciences* 112:258. doi: 10.1029/2006JG000258

Kessler, M. A., Plug, L. J., and Walter Anthony, K. M. (2012). Simulating the decadal- to millennial-scale dynamics of morphology and sequestered carbon mobilization of two thermokarst lakes in NW Alaska. *J. Geophys. Res. Biogeosciences* 117:1796. doi: 10.1029/2011JG001796

Killops, S. D., and Killops, V. J. (2013). "5.1.2 General differences between major groups of organisms," in *Introduction to Organic Geochemistry*, (Somerset: Wiley), 167.

Knoblauch, C., Beer, C., Sosnin, A., Wagner, D., and Pfeiffer, E.-M. (2013). Predicting long-term carbon mineralization and trace gas production from thawing permafrost of Northeast Siberia. *Glob. Change Biol.* 19, 1160–1172. doi: 10.1111/gcb.12116

Kunitsky, V. V. (1989). *Kriolitologiya Nizo'ev Leny (Cryolithology ofthe Lower LENA)*. Yakutsk: Permafrost Institute Press.

Kutzbach, L., Wagner, D., and Pfeiffer, E.-M. (2004). Effect of microrelief and vegetation on methane emission from wet polygonal tundra, Lena Delta, Northern Siberia. *Biogeochemistry* 69, 341–362. doi: 10.1023/B:BIOG.0000031053.81520.db

Lacelle, D., Fontaine, M., Pellerin, A., Kokelj, S. V., and Clark, I. D. (2019). Legacy of holocene landscape changes on soil biogeochemistry: a perspective from paleo-active layers in Northwestern Canada. *J. Geophys. Res. Biogeosci.* 124, 2662–2679. doi: 10.1029/2018JG004916

Lenz, J., Jones, B. M., Wetterich, S., Tjallingii, R., Fritz, M., Arp, C. D., et al. (2016). Impacts of shore expansion and catchment characteristics on lacustrine thermokarst records in permafrost lowlands. Alaska Arctic Coastal Plain. *Arktos* 2:25. doi: 10.1007/s41063-016-0025-0

Liljedahl, A. K., Boike, J., Daanen, R. P., Fedorov, A. N., Frost, G. V., Grosse, G., et al. (2016). Pan-Arctic ice-wedge degradation in warming permafrost and its influence on tundra hydrology. *Nat. Geosci.* 9, 312–318. doi: 10.1038/ngeo2674

Ling, F., and Zhang, T. (2003). Numerical simulation of permafrost thermal regime and talik development under shallow thaw lakes on the Alaskan Arctic Coastal Plain. *J. Geophys. Res. Atmos.* 108:3014. doi: 10.1029/2002JD003014

Mackelprang, R., Waldrop, M. P., DeAngelis, K. M., David, M. M., Chavarria, K. L., Blazewicz, S. J., et al. (2011). Metagenomic analysis of a permafrost microbial community reveals a rapid response to thaw. *Nature* 480, 368–371. doi: 10.1038/nature10576

Marzi, R., Torkelson, B. E., and Olson, R. K. (1993). A revised carbon preference index. *Org. Geochem.* 20, 1303–1306. doi: 10.1016/0146-6380(93)90016-5

Neubauer, D. (2016). *Characterization Of Organic Matter Stored In Yedoma And Thermokarst Permafrost*. Master thesis, Freie Universität, Berlin.

Poynter, J., and Eglinton, G. (1990). "14. Molecular composition of three sediments from hole 717c: the Bengal fan," in *Proceedings of the Ocean Drilling Program: Scientific Results*, College Station, TX.

Radke, M., Willsch, H., and Welte, D. H. (1980). Preparative hydrocarbon group type determination by automated medium pressure liquid chromatography. *Anal. Chem.* 52, 406–411. doi: 10.1021/ac50053a009

Romankevich, E. A., Vetrov, A. A., Belyaev, N. A., Sergienko, V. I., Semiletov, I. P., Sukhoverkhov, S. V., et al. (2017). Alkanes in quaternary deposits of the Laptev Sea. *Dokl. Earth Sci.* 472, 36–39. doi: 10.1134/S1028334X17010093

Romanovskii, N. (1993). *Fundamentals of Cryogenesis Of Lithosphere*. Moscow: Moscow University Press.

Sánchez-García, L., Vonk, J. E., Charkin, A. N., Kosmach, D., Dudarev, O. V., Semiletov, I. P., et al. (2014). Characterisation of three regimes of collapsing arctic ice complex deposits on the SE laptev sea coast using biomarkers and dual carbon isotopes. *Permafr. Periglac. Process.* 25, 172–183. doi: 10.1002/ppp.1815

Schäfer, I. K., Lanny, V., Franke, J., Eglinton, T. I., Zech, M., Vysloužilová, B., et al. (2016). Leaf waxes in litter and topsoils along a european transect. *Soil* 2, 551–564. doi: 10.5194/soil-2-551-2016

Schellekens, J., Bindler, R., Martínez-Cortizas, A., McClymont, E. L., Abbott, G. D., Biester, H., et al. (2015). Preferential degradation of polyphenols from *Sphagnum* - 4-Isopropenylphenol as a proxy for past hydrological conditions in *Sphagnum*-dominated peat. *Geochim. Cosmochim. Acta* 150, 74–89. doi: 10.1016/j.gca.2014.12.003

Schirrmeister, L., Froese, D., Tumskoy, V., Grosse, G., and Wetterich, S. (2013). "Yedoma: late pleistocene ice-rich syngenetic permafrost of Beringia," in *Encyclopedia of Quaternary Science*, eds S. A. Elias, C. J. Mock, and J. Murton (Amsterdam: Elsevier), doi: 10.1016/B978-0-444-53643-3.00106-0

Schirrmeister, L., Grigoriev, M. N., Strauss, J., Grosse, G., Overduin, P. P., Kholodov, A., et al. (2018). Sediment characteristics of a thermokarst lagoon in the northeastern Siberian Arctic (Ivashkina Lagoon, Bykovsky Peninsula). *Arktos* 4:13. doi: 10.1007/s41063-018-0049-8

Schirrmeister, L., Grosse, G., Kunitsky, V., Magens, D., Meyer, H., Dereviagin, A., et al. (2008a). Periglacial landscape evolution and environmental changes of Arctic lowland areas for the last 60 000 years (western Laptev Sea coast, Cape Mamontov Klyk). *Polar Res.* 27, 249–272. doi: 10.1111/j.1751-8369.2008.00067.x

Schirrmeister, L., Kunitsky, V. V., Grosse, G., Kuznetsova, T. V., Derevyagin, A. Y., Wetterich, S., et al. (2008b). "The yedoma suite of the Northeastern Siberian shelf region characteristics and concept of formation," in *Proceedings of the Ninth International Conference on Permafrost*, Fairbanks.

Schirrmeister, L., Grosse, G., Schwamborn, G., Andreev, A., Meyer, H., Kunitsky, V. V., et al. (2003). Late Quaternary history of the accumulation plain north of the chekanovsky ridge (Lena Delta, Russia) - a multidisciplinary approach. *Polar Geogr.* 27, 277–319. doi: 10.1080/789610225

Schirrmeister, L., Siegert, C., Kunitzky, V. V., Grootes, P. M., and Erlenkeuser, H. (2002a). Late quaternary ice-rich permafrost sequences as a paleoenvironmental archive for the Laptev Sea region in northern Siberia. *Int. J. Earth Sci.* 91, 154–167. doi: 10.1007/s005310100205

Schirrmeister, L., Siegert, C., Kuznetsova, T., Kuzmina, S., Andreev, A., Kienast, F., et al. (2002b). Paleoenvironmental and paleoclimatic records from permafrost deposits in the Arctic region of Northern Siberia. *Quat. Int.* 89, 97–118. doi: 10.1016/S1040-6182(01)00083-0

Schleusner, P., Biskaborn, B. K., Kienast, F., Wolter, J., Subetto, D., and Diekmann, B. (2015). Basin evolution and palaeoenvironmental variability of the thermokarst lake E l'gene-K yuele, Arctic Siberia. *Boreas* 44, 216–229. doi: 10.1111/bor.12084

Schulte, S., Mangelsdorf, K., and Rullkötter, J. (2000). Organic matter preservation on the Pakistan continental margin as revealed by biomarker geochemistry. *Org. Geochem.* 31, 1005–1022. doi: 10.1016/S0146-6380(00)00108-X

Schuur, E. A. G., McGuire, A. D., Schädel, C., Grosse, G., Harden, J. W., Hayes, D. J., et al. (2015). Climate change and the permafrost carbon feedback. *Nature* 520:171. doi: 10.1038/nature14338

Siegert, C., Schirrmeister, L., and Babiy, O. (2002). The sedimentological, mineralogical and geochemical composition of late Pleistocene deposits from the ice complex on the Bykovsky peninsula, northern Siberia. *Polarforsch.* 70, 3–11.

Slagoda, E. A. (1993). *Genesis i Mikrostroenie Kriolitogennykh Otlozhenii Bykovskogo Polyostrova i Ostrova Muoastakh [Genesis and Microstructure Of Cryolithogenic Deposits At The Bykovsky Peninsula and the Muostakh Island]*. Ph.D. thesis, Permafrost Institute Yakutsk, Yakutsk.

Slagoda, E. A. (2004). *Kriogennye Otlozheniya Primorskoi Ravninymorya Laptebykh: Litologiya I Mikromorfologiya [CryolithogenicDeposits of the Laptev Sea Coastal Plain: Lithology and Micromorphology]*. Tyumen: Express Printing Center.

Slagoda, E. A. (2005). "Cryogenic structure and genesis of late cenozoicwatershed formations at the primorsky mountain range adjacent to the Bykovsky Peninsula, Laptev Sea, Russia," in *2nd European Conference on Permafrost*, Potsdam, Germany, 23–24.

Stapel, J. G., Schwamborn, G., Schirrmeister, L., Horsfield, B., and Mangelsdorf, K. (2018). Substrate potential of last interglacial to holocene permafrost organic matter for future microbial greenhouse gas production. *Biogeosciences* 15, 1969–1985. doi: 10.5194/bg-15-1969-2018

Strauss, J., Boike, J., Bolshiyanov, D. Y., Grigoriev, M. N., El-Hajj, H., Morgenstern, A., et al. (2018). *Russian-German Cooperation: Expeditions to Siberia in 2017*. Bremerhaven: Alfred Wegener Institute for Polar and Marine Research.

Strauss, J., Laboor, S., Schirrmeister, L., Grosse, G., Fortier, D., Hugelius, G., et al. (2020). *Yedoma and Thermokarst Site Characteristics From Sample Analysis, 1998-2016, Alaska (US), Northern Siberia (RU)*. Bremerhaven: Alfred Wegener Institute for Polar and Marine Research.

Strauss, J., Schirrmeister, L., Grosse, G., Fortier, D., Hugelius, G., Knoblauch, C., et al. (2017). Deep Yedoma permafrost: a synthesis of depositional characteristics and carbon vulnerability. *Earth Sci. Rev.* 172, 75–86. doi: 10.1016/j.earscirev.2017.07.007

Strauss, J., Schirrmeister, L., Grosse, G., Wetterich, S., Ulrich, M., Herzschuh, U., et al. (2013). The deep permafrost carbon pool of the yedoma region in Siberia and Alaska. *Geophys. Res. Lett.* 40, 6165–6170. doi: 10.1002/2013GL058088

Strauss, J., Schirrmeister, L., Mangelsdorf, K., Eichhorn, L., Wetterich, S., and Herzschuh, U. (2015). Organic-matter quality of deep permafrost carbon - a study from Arctic Siberia. *Biogeosciences* 12, 2227–2245. doi: 10.5194/bg-12-2227-2015

Strauss, J., Schirrmeister, L., Wetterich, S., Borchers, A., and Davydov, S. P. (2012). Grain-size properties and organic-carbon stock of Yedoma ice complex permafrost from the Kolyma lowland, northeastern Siberia. *Glob. Biogeochem. Cycles* 26:2011GB004104. doi: 10.1029/2011GB004104

Struck, J., Bliedtner, M., Strobel, P., Schumacher, J., Bazarradnaa, E., and Zech, R. (2019). Leaf wax *n*-alkane pattern and compound-specific δ13C of plants and topsoils from semi-arid Mongolia. *Biogeosciences Discuss.* 2019, 1–23. doi: 10.5194/bg-2019-251

Struck, J., Roettig, C. B., Faust, D., and Zech, R. (2018). Leaf waxes from aeolianite-paleosol sequences on Fuerteventura and their potential for paleoenvironmental and climate reconstructions in the arid subtropics. *EG Quat. Sci. J.* 66, 109–114. doi: 10.5194/egqsj-66-109-2018

Stuiver, M., Reimer, P. J., and Reimer, R. W. (2017). *CALIB 14C Calibration Program*. Available online at: http://calib.org/calib/ (accessed December 13, 2017).

Treshnikov, A. (1985). *Atlas Arktiki [Atlas of the Arctic]*. Available online at: https://www.worldcat.org/title/atlas-arktiki/oclc/14694389 (accessed February 15, 2020).

Turetsky, M. R., Abbott, B. W., Jones, M. C., Anthony, K. W., Olefeldt, D., Schuur, E. A. G., et al. (2020). Carbon release through abrupt permafrost thaw. *Nat. Geosci.* 13, 138–143. doi: 10.1038/s41561-019-0526-0

Ulyantsev, A. S., Romankevich, E. A., Bratskaya, S. Yu, Prokuda, N. A., Sukhoverkhov, S. V., Semiletov, I. P., et al. (2017). Characteristic of quaternary sedimentation on a shelf of the Laptev Sea according to the molecular composition of *n*-alkanes. *Dokl. Earth Sci.* 473, 449–453. doi: 10.1134/S1028334X17040158

Vasil'chuk, Y. K., and Vasil'chuk, A. C. (2017). Validity of radiocarbon ages of *Siberian yedoma*. *Geol. Res. J.* 13, 83–95. doi: 10.1016/j.grj.2017.02.004

Walter, K. M., Zimov, S. A., Chanton, J. P., Verbyla, D., and Chapin, F. S. (2006). Methane bubbling from Siberian thaw lakes as a positive feedback to climate warming. *Nature* 443, 71–75. doi: 10.1038/nature05040

Walter Anthony, K., Schneider von Deimling, T., Nitze, I., Frolking, S., Emond, A., Daanen, R., et al. (2018). 21st-century modeled permafrost carbon emissions accelerated by abrupt thaw beneath lakes. *Nat. Commun.* 9:3262. doi: 10.1038/s41467-018-05738-9

Walter Anthony, K. M., Zimov, S. A., Grosse, G., Jones, M. C., Anthony, P. M. III, Chapin, F. S., et al. (2014). A shift of thermokarst lakes from carbon sources to sinks during the holocene epoch. *Nature* 511, 452–456. doi: 10.1038/nature13560

West, J. J., and Plug, L. J. (2008). Time-dependent morphology of thaw lakes and taliks in deep and shallow ground ice. *J. Geophys. Res. Earth Surf.* 113:697. doi: 10.1029/2006JF000696

Wetterich, S., Kuzmina, S., Andreev, A. A., Kienast, F., Meyer, H., Schirrmeister, L., et al. (2008). Palaeoenvironmental dynamics inferred from late quaternary permafrost deposits on Kurungnakh Island, Lena Delta, Northeast Siberia, Russia. *Quat. Sci. Rev.* 27, 1523–1540. doi: 10.1016/j.quascirev.2008.04.007

Wetterich, S., Schirrmeister, L., Andreev, A., Pudenz, M., Plessen, B., Meyer, H., et al. (2009). Eemian and Late Glacial/holocene palaeoenvironmental records from permafrost sequences at the dmitry laptev strait (NE Siberia, Russia). *Palaeogeogr. Palaeoclimatol. Palaeoecol.* 279, 73–95. doi: 10.1016/j.palaeo.2009.05.002

Zech, M., Andreev, A., Zech, R., Müller, S., Hambach, U., Frechen, M., et al. (2010). Quaternary vegetation changes derived from a loess-like permafrost palaeosol

sequence in northeast Siberia using alkane biomarker and pollen analyses. *Boreas* 393, 540–550. doi: 10.1111/j.1502-3885.2009.00132.x

Zech, M., Buggle, B., Leiber, K., Marković, S., Glaser, B., Hambach, U., et al. (2009). Reconstructing Quaternary vegetation history in the Carpathian Basin, SE-Europe, using *n*-alkane biomarkers as molecular fossils: problems and possible solutions, potential and limitations. *EG Quat. Sci. J.* 58, 148–155. doi: 10.3285/eg.58.2.03

Zech, M., Krause, T., Meszner, S., and Faust, D. (2013). Incorrect when uncorrected: reconstructing vegetation history using *n*-alkane biomarkers in loess-paleosol sequences - a case study from the saxonian loess region, Germany. *Quat. Int.* 296, 108–116. doi: 10.1016/j.quaint.2012.01.023

Zheng, Y., Zhou, W., Meyers, P. A., and Xie, S. (2007). Lipid biomarkers in the Zoigê-Hongyuan peat deposit: indicators of holocene climate changes in West China. *Org. Geochem.* 38, 1927–1940. doi: 10.1016/j.orggeochem.2007.06.012

Zimov, S. A., Voropaev, Y. V., Semiletov, I. P., Davidov, S. P., Prosiannikov, S. F., Chapin, F. S., et al. (1997). North siberian lakes: a methane source fueled by pleistocene carbon. *Science* 277, 800–802. doi: 10.1126/science.277.5327.800

Conflict of Interest: The authors declare that the research was conducted in the absence of any commercial or financial relationships that could be construed as a potential conflict of interest.

frontiers in Environmental Science

ORIGINAL RESEARCH
published: 19 August 2020
doi: 10.3389/fenvs.2020.00133

Permafrost Microbial Community Structure Changes Across the Pleistocene-Holocene Boundary

*Alireza Saidi-Mehrabad[1], Patrick Neuberger[1], Morteza Hajihosseini[2], Duane Froese[3] and Brian D. Lanoil[1]**

[1] Department of Biological Sciences, University of Alberta, Edmonton, AB, Canada, [2] School of Public Health, University of Alberta, Edmonton, AB, Canada, [3] Department of Earth and Atmospheric Sciences, University of Alberta, Edmonton, AB, Canada

Despite the presence of well-documented changes in vegetation and faunal communities at the Pleistocene-Holocene transition, it is unclear whether similar shifts occurred in soil microbes. Recent studies do not show a clear connection between soil parameters and community structure, suggesting permafrost microbiome-climate studies may be unreliable. However, the majority of the permafrost microbial ecological studies have been performed only in either Holocene- or Pleistocene-aged sediments and not on permafrost that formed across the dramatic ecosystem reorganization at the Pleistocene-Holocene transition. In our study, we used permafrost recovered in proximity to the Pleistocene-Holocene transition subsampled under strict sterile conditions developed for ancient DNA studies. Our ordination analyses of microbial community composition based on 16S RNA genes and chemical composition of the soil samples resulted into two distinct clusters based on whether they were of late Pleistocene or Holocene age, while samples within an epoch were more similar than those across the boundary and did not result in age based separation. Between epochs, there was a statistically significant correlation between changes in OTU composition and soil chemical properties, but only Ca and Mn were correlated to OTU composition within Holocene aged samples; furthermore, no chemical parameters were correlated to OTU composition within Pleistocene aged samples. Thus, the results indicate that both soil chemical and microbial parameters are fairly stable until a threshold, driven by climate change in our study, is crossed, after which there is a shift to a new steady state. Modern anthropogenic climate change may lead to similar transitions in state for soil biogeochemical systems and microbial communities in Arctic regions.

Keywords: permafrost, microbial community, Pleistocene-Holocene, climate change, soil physicochemical parameters

OPEN ACCESS

Edited by:
Adam Jerold Reed,
University of Southampton,
United Kingdom

Reviewed by:
Pernille Bronken Eidesen,
The University Centre in Svalbard,
Norway
Jianfang Hu,
Guangzhou Institute of Geochemistry,
CAS, China
Lyle Whyte,
McGill University, Canada

****Correspondence:***
Brian D. Lanoil
lanoil@ualberta.ca

Specialty section:
This article was submitted to Biogeochemical Dynamics, a section of the journal Frontiers in Environmental Science

Received: *04 April 2020*
Accepted: *16 July 2020*
Published: *19 August 2020*

Citation:
Saidi-Mehrabad A, Neuberger P, Hajihosseini M, Froese D and Lanoil BD (2020) Permafrost Microbial Community Structure Changes Across the Pleistocene-Holocene Boundary. Front. Environ. Sci. 8:133. doi: 10.3389/fenvs.2020.00133

INTRODUCTION

The Pleistocene – Holocene transition was accompanied by rapid, extensive global climate and ecosystem changes (Barnosky et al., 2004; Guthrie, 2006). These rapid changes forced the Earth system to cross a climate threshold causing a major transition in terrestrial biosphere and pedogenesis from one stable state to another stable state and coincided with extinction of megafauna, reorganization of plant communities, and accompanying changes in soil chemistry

and sedimentation (Alley et al., 2003; Steffen et al., 2018; Lacelle et al., 2019). At high latitudes, these changes may be preserved in relict permafrost (Shapiro and Cooper, 2003; Froese et al., 2009; Gaglioti et al., 2016). These natural biological and chemical archives have been used to reconstruct late Quaternary paleoclimate (Porter et al., 2019), vegetation (Willerslev et al., 2014), and faunal communities (Haile et al., 2009; Lorenzen et al., 2011). Despite the presence of well-documented changes in vegetation and faunal community structure across the Pleistocene-Holocene transition (Guthrie, 2006; Mann et al., 2016), it is still unclear whether these changes were associated with concomitant restructuring of soil microbial communities.

Recent studies have shown that the main factors governing microbial community structure in permafrost appear to be the age of the samples (Mackelprang et al., 2017; Burkert et al., 2019; Liang et al., 2019), ice content (Burkert et al., 2019), dispersal limitation and physical/thermodynamic constraints (Bottos et al., 2018), with little to no correlation with soil chemical parameters. For example, one recent study indicated that microbes within three Pleistocene-aged permafrost chronosequences changed in composition in response to increasing age, with a corresponding increase in survival strategies (Mackelprang et al., 2017). These correlations suggest that these environmental pressures, arising from harsh permafrost conditions, select for a subset of species and that the community structure deviates from the community present at the time the permafrost was formed (Willerslev et al., 2004; Kraft et al., 2015; Mackelprang et al., 2017; Liang et al., 2019). However, another study performed on two Pleistocene-aged permafrost samples of a similar age but differing origins (lake-alluvial sediments and Yedoma/ice complex sediments) indicated the presence of two distinct microbial communities, which were formed in response to differing environmental settings and not due to the age of the samples alone (Rivkina et al., 2016). As a result, it is not clear whether relict permafrost microbial communities provide a window into past soil microbial communities, or are the strict remnants of selective pressures of the permafrost environment, or some combination of the two.

In this study, we selected samples on either side of the Pleistocene-Holocene transition from a permafrost core extracted from central Yukon, a part of Eastern Beringia. The permafrost of Eastern Beringia contains exceptional proxy records of climate change (Froese et al., 2009). Furthermore, the Pleistocene-Holocene transition zone preserved in Eastern Beringian permafrost is prominent in the core stratigraphy, allowing for detailed microbiological and soil physicochemical analyses (Porter et al., 2019). The core in this study was collected about 1.5 m adjacent to, and shares stratigraphy with a well-dated and chemically and physically characterized core spanning the last ca. 16,000 years (Davies et al., 2018; Porter et al., 2019).

MATERIALS AND METHODS

Permafrost Coring Location and Analysis of the Soil Texture

The topography of our sampling site (DHP174-13L) along with the paleoenvironmental setting, stratigraphy and coring strategies were described previously (Davies et al., 2018; Porter et al., 2019). We obtained a 3.97 m long permafrost core (called DHL_16, collected in May 2016) about 1.5 m lateral to the core reported by Porter et al. (2019). Three intervals from depths of 174–210, 296–319, and 327–365 cm (termed DHL_16_1, DHL_16_2, and DHL_16_3 in this manuscript, respectively) were selected from the DHL_16 core for microbiological and chemical analyses. We were careful to sample near the Pleistocene-Holocene transition zone while avoiding the transition zone itself to minimize any effects of water migration in the paleoactive layer [detailed in Porter et al. (2019) for the stable isotopes of the pore waters in that study]. Active layer (or seasonally thawed soils) can allow water leaching from the paleo-surface to deeper depths (<∼50 cm at this site today) and result in mixing of the surface water, potentially impacting microbial and edaphic properties. We used the depleted water isotopes to provide further support that the waters (and thus the microbes) have not been mobilized since they froze (detailed in Porter et al., 2019).

The core stratigraphy, reported by Davies et al. (2018) and Porter et al. (2019), documents three prominent units that are readily recognized in both cores: units 1, 2, and 3 from the bottom of the core to the surface. The youngest unit sampled, corresponding to unit 3 of Porter et al. (2019) consists of peat (sampled interval 174–210 cm; DHL_16_1) and dates to the early Holocene (∼8–10.5 k cal yr BP), whereas DHL_16_2 and DHL_16_ 3 are loessal silts (eolian silt) (sampled at 296–319 cm and 327–365 cm respectively) both associated with the late Pleistocene (∼14.3–15 k cal yr BP, and ∼15–16 k cal yr BP, respectively), based on the age model of Porter et al. (2019). At the site, the peat/silt boundary was determined to be at 244 cm (which was dated to ∼10.5 k cal yr BP, **Supplementary Figure S1**). These three selected intervals were vertically cut into 1/3 and 2/3 subsections with the aid of a masonry saw. The 2/3 sections were used for DNA extraction, while the 1/3 sections were used for chemical analyses (Saidi-Mehrabad et al., 2020).

Soil textures of Holocene-aged samples from 210 cm depth and Pleistocene-aged samples from 296 cm depth were examined and photographed under 4.5× and 67× magnifications of a zoom stereomicroscope (Olympus-Life Sciences SZ61, Japan). These two depths were near the 244 cm peat/silt boundary. Samples were allowed to thaw and dry at 70°C in a table top oven for 48 h prior to microscopy.

Permafrost Edaphic Parameter Analysis

Selected intervals of DHL_16_1, DHL_16_2, and DHL_16_3 were sub-sectioned for soil chemical analysis based on a previously described method (Saidi-Mehrabad et al., 2020). Briefly, the 1/3 core sections were cut into 1 cm^3 cubes with a hand saw in a 4°C cold room for measuring the basic chemical parameters of these samples, including organic carbon (OC), pH and gravimetric water content (GW) (Saidi-Mehrabad et al., 2020). Total carbon (TC) and total nitrogen (TN) were measured from 0.5 g of subsections based on a dry combustion method with the aid of an Elemental Analyzer (EA 4010; Costech International Strumatzione, Italy) (Sparks et al., 1996). Nitrate/nitrite (NO^-_3/NO_2^-) was analyzed using ∼

5 g of soil material with a colorimetric diazo coupling method by a SmartChem Discrete Wet Chemistry analyzer (model 200, Westco Scientific, United States) (Maynard et al., 1993). Ammonium (NH_4^+) was measured from 0.5 g of subsections based on a colorimetric Berthelot protocol (Maynard et al., 1993). Electrical conductivity (EC) was measured at 1:5 soil:water (w/v) ratio, calibrated at 20°C with 0.01M KCl solution (Hardie and Doyle, 2012) using an EC500 ExStik® II conductivity measuring device (EXTECH instruments, United States). Dissolved metals were extracted from 0.5 g of sample by HNO_3/HCl digestion and measured via inductively coupled plasma-optical emission spectroscopy (iCAP6300, Thermofisher Scientific, Canada) (Skoog et al., 2007).

DNA Extraction and Sequencing

Prior to DNA extraction the 2/3 sections associated with the DHL_16_1, DHL_16_2, and DHL_16_3 intervals were cut into ∼6 × 3.5 × 2.5 cm rectangular pieces (n = 16) and the exterior of these rectangles were painted with a total of 3×10^8 cells/ml of *Escherichia coli* (*E. coli*) (strain DH10B) suspended in 50 ml of 1 × PBS using a 25 mm paintbrush (Saidi-Mehrabad et al., 2020). The *E. coli* strain used in our contamination monitoring procedure harbored a mNeonGreen-expressing and ampicillin-resistant pBAD/His B vector, which allowed us to trace the contamination at a much smaller levels via direct PCR targeting the vector or macro-photography of the glowing mNeonGreen protein under 470 nm wavelength (Saidi-Mehrabad et al., 2020). All rectangular pieces were decontaminated by the combination of bleach washing and scraping under sterilize conditions designed for ancient DNA analysis in a class 1000 clean lab with no history of sample processing (Saidi-Mehrabad et al., 2020). Genomic DNA was extracted from a total of ∼10 g of homogenized thawed soil at room temperature from each 6 cm subsection using a modified ZymoBIOMICS DNA Microprep kit (Zymo Research, United States) protocol (Saidi-Mehrabad et al., 2020). DNA concentration was measured with a Qubit dsDNA HS Assay Kit according to manufacturer's protocol (Thermofisher Scientific, Canada). The extracted DNA was tested for the presence of the biological tracer used in our contamination monitoring procedure via PCR (performed in triplicate and in a variety of dilutions) as described previously (Saidi-Mehrabad et al., 2020). We were unable to obtain sufficient DNA devoid of the contamination tracer for sequencing from DHL_16_3 sub-sections, as a result, these samples were excluded from further molecular analysis (**Supplementary Figure S2**). Thus, a total of six segments, three from DHL_16_1 (174–179, 179–184, and 189–194 cm) and three from DHL_16_2 (296–301, 305–310, and 314–319 cm), passed our quality control steps (Saidi-Mehrabad et al., 2020) for microbial community analysis.

Clean genomic DNA extracted from the permafrost samples, a lab-constructed mock community (**Supplementary Figure S3**), and DNA extraction blanks (**Supplementary Table S1**) were sequenced based on the V4 region of the 16S rRNA genes by using standard Earth Microbiome Project (EMP) primers 515F and 806R (Caporaso et al., 2011). The platform used by the commercial sequencing provider (Microbiome Insights, Canada) was an Illumina MiSeq machine using a 250-bp paired-end kit (V2 500-cycle PE Chemistry; Illumina, United States). No additional library preparation kits were used, as the libraries were constructed in a single PCR step. Generated sequences were demultiplexed via bcl2fastq2 2.20 according to Illumina guidelines (Illumina, United States).

Quality Control of Raw Sequences and OTU Construction

A combination of USEARCH 10.0.240 (Edgar, 2010) and Mothur 1.39.5 (Schloss et al., 2009) pipelines were utilized for analyzing the sequences. USEARCH was used to merge the reads and to form contigs based on the criteria recommended in USEARCH 10 manual for analyzing sequences generated from the V4 region of the 16S rRNA genes. Mothur was used to merge the raw reads into a single merge file and to normalize the reads to the lowest read counts via random subsampling. OTU picking, chimera, and universal singleton checks were performed with the UPARSE pipeline via *de novo*/greedy heuristic algorithm (Edgar, 2013). The threshold used for OTU clustering was 97% similarity. Constructed OTUs were mapped to taxonomy via SINTAX algorithm by using a trained V4 16S rRNA RDP (v16; 13k sequences) database (Cole et al., 2014; Edgar, 2016). The confidence level cut-off at each taxonomic level was set to 0 to prevent data loss. In addition to the bootstrap values obtained from SINTAX algorithm, the taxonomic identity of the sequences were manually investigated via Basic Local Alignment Search Tool (BLAST) in the NCBI database (Altschul et al., 1990). All strains detected in the blank controls, Eukarya, Archaea species and *Cyanobacteria*/Chloroplast (termed anomalous sequences) were removed from downstream community analyses (**Supplementary Table S2**).

In summary, 98.1% of the reads passed the filtering Q score parameters (with expected error < 1.0) and resulted in 87843 filtered reads. Of these, 11417 reads were unique (de-replicated) and 8287 were singletons (72.6%). OTU counts were rarified to 1768 sequences per sample by random subsampling. UPARSE picked 778 OTUs, with 612 OTUs assigned to domain Bacteria via SINTAX after removal of anomalous sequences. Despite a relatively small number of OTUs and sample size, the constructed rarefaction curve demonstrated enough sampling depth for downstream diversity analyses (**Supplementary Figure S4**). Raw sequences obtained in this study have been archived in NCBI Sequence Read Archive under the ascension number of PRJNA607368, and BioSample accession of SAMN14130768.

Community Analysis

All the statistical computations that utilized the R language were performed in R Studio environment 1.1.442. The soil parameters were $\log_{10}$ (x + 1) transformed and were later used to create a variable matrix for PcOrd version 6.22 (Wild Blueberry Media, Inc., United States) and a Phyloseq 1.16.2 object for alpha and beta diversity analyses (McMurdie and Holmes, 2013). The possible differences in OTU structure between groups were calculated with Bray-Curtis dissimilarity matrix and clustering was calculated based on average linkage in PcOrd version 6.22. Results were visualized in a principal coordinate analysis biplot

(PCoA) and statistical support for differences between groups was calculated with the aid of Multi-Response Permutation Procedure (MRPP) with 999 randomized permutation tests in PcOrd version 6.22 (Mielke et al., 1976). The coefficient of determination of chemical parameters to sample groups (Holocene or Pleistocene) were assessed based on the "envfit" function of vegan ver 2.4-2 package with max $p < 0.05$ and 999 permutation tests (Oksanen et al., 2007). Differences in chemical composition between samples were visualized in a principal component biplot (PCA). Samples were clustered based on average linkage and statistical significance between clusters were assessed based on MRPP in PcOrd version 6.22 (Mielke et al., 1976). The shared and unique OTUs between and within clusters detected in PCoA analysis were investigated with a co-occurrence network test based on a maximum ecological distance of 0.8 and distance matrix of Jaccard by the aid of Phyloseq 1.16.2 package (McMurdie and Holmes, 2013). To assess which taxa were significantly differentially abundant in Pleistocene and Holocene groups, the DESeq2 differential abundance method (Love et al., 2014) with a threshold of 0.01 and $p < 0.05$ was used on the top 10 dominant phyla within all samples combined (microbiomeSeq package 0.1). In order to assess the sequence similarity of the Pleistocene- and Holocene-aged bacteria to published bacteria, each representative sequence of an OTU was compared to publicly available sequences via BLAST in NCBI (standard nucleotide (nr/nt) database). Uncultured/environmental sample sequences were excluded from our search criteria. The top sequence hit similarity values for each individual group were averaged and compared with each other. The possible effect of epoch-based separation on the relationship between soil chemistry and changes in OTU structure were investigated using a negative binomial many-generalized linear model (ManyGLM) (Warton et al., 2012). The model performed multiple random re-samplings via Monte Carlo algorithm to investigate many correlated variables while considering the strong mean-variance relationship due to the presence of rare species and high zero inflation (Warton, 2011; Warton et al., 2012). The statistical significance of this model was based on Wald's test, which employed a generalized estimating equations approach (Warton et al., 2012). The model was executed with the mvabund 4.0.1 package (Wang et al., 2012). This model was also used to assess the differential abundance of OTUs shared between Pleistocene- and Holocene-aged samples with the same criteria described above.

Live/Dead Microscopy Assay

The viability assay was performed with a Live/Dead BacLight Bacterial Viability Kit (Invitrogen Thermo Fisher, Canada) and a DM RXA fluorescence microscope (Leica Microsystems, Germany). The viable cells were enumerated via green fluorescence at 470 nm excitation and the dead cells were enumerated via red fluorescence at 530 nm excitation. A 36 cm section from DHL_16_1 and a 23 cm section from DHL_16_2 were cut, homogenized and subsampled in quadruplicate as representative Holocene and Pleistocene samples, respectively. For each replicate subsample, 15 fields of view were counted under both wavelengths and the resulting $n = 60$ mean observation was used to calculate the abundance and live/dead proportion of the cells. The detailed protocol is available in the supporting information.

RESULTS

The Holocene-aged permafrost sediments had properties distinct from Pleistocene-aged permafrost sediments, matching the descriptions of Fraser and Burn (1997) and Kotler and Burn (2000). The most noticeable difference was Holocene sediments were dominated by peat, while Pleistocene sediments were comprised of silty loess with frozen rare lenses of ice and largely lacking visible plant remains (**Supplementary Figures S2A–D**). No clear differences in texture were observed for samples within each epoch (**Supplementary Figure S2**). The presence of well-preserved plant macroremains from the peat suggest a relatively uninterrupted aggradation of permafrost with the plant material since the time of deposition, and that the permafrost of our sampling region formed syngenetically, or as the surface aggraded, without signs of previous thaw; this is also reflected by the water isotopes from these cores reported by Porter et al. (2019).

All measured chemical parameters differed significantly between Pleistocene and Holocene sediments (**Tables 1**, **2** and **Supplementary Figures S1, S5**). Similar to texture, none of the measured chemical parameters showed statistically significant changes within epochs. Holocene samples had significantly higher organic carbon ($p < 0.001$), nitrate/nitrite ($p < 0.01$), water ($p < 0.01$), and total nitrogen ($p < 0.01$) as well as significantly lower metals ($p < 0.05$), electrical conductivity ($p < 0.05$), and pH ($p < 0.001$) than Pleistocene samples (**Tables 1**, **2**).

In addition to dramatic changes in soil composition and chemistry, there was significantly higher cell viability and cell abundance in Holocene samples than in Pleistocene samples, with ∼8 fold higher viable cells ($p < 0.001$), ∼2 fold fewer dead cells ($p < 0.001$) and ∼2 fold higher total cells ($p < 0.001$) (**Figure 1**). Direct microscopic cell counts demonstrated Holocene samples had a total of 1.12×10^7 ($\pm 4.44 \times 10^6$) cells g^{-1} of wet soil, with 84% viable cells and 16% non-viable cells. Pleistocene samples had a total of 6.47×10^6 ($\pm 9.57 \times 10^5$) cells g^{-1} of wet soil, with 17% viable cells and 83% non-viable cells (**Figure 1**).

Overall microbial diversity based on 16S rRNA genes was either not significantly different between Holocene and Pleistocene samples (as measured by observed OTUs, Shannon diversity index, Chao1 richness estimator, Simpson evenness, and Fisher's alpha diversity index), or the statistical support for differences was weak (as for the Mann–Whitney U test) (**Supplementary Table S3**). In a PCoA biplot, composite Holocene and Pleistocene samples demonstrated a dramatic dissimilarity in OTU composition. The microbial communities formed two clusters based on epoch; there was no clear differentiation within the epoch-based groups (**Figure 2**). Similar to soil texture, chemistry and cell abundance, each epoch-based cluster had a unique set of OTUs not present in the

TABLE 1 | Basic soil edaphic parameters of the selected segments for microbial analysis.

Epoch	Depth (cm)	OC[1c**] (±SD)	TC[1c*] (±SD)	TN[1c*] (±SD)	GW[1c*] (±SD)	pH** (±SD)	NO_3^-/NO_2^{-d*} (±SD)	EC[e*] (±SD)	NH_4^{+d*} (±SD)
H[a]	174–179	95 (3)	47 (4)	1 (0.2)	92 (0.8)	3.7 (0.06)	0.9 (0.12)	370 (55)	15.5 (3.2)
H	179–184	96 (0.4)	48 (3.6)	1 (0.2)	90 (1.4)	3.7 (0.08)	1 (0.1)	405 (5)	19 (2.8)
H	189–194	96 (0.7)	45 (0.6)	0.8 (0.05)	91 (1.8)	3.73 (0.03)	1.18 (0.01)	342 (22)	21 (0.07)
P[b]	296–301	22 (16)	7 (0.9)	0.6 (0.07)	77 (18)	6 (0.15)	0.1 (0.01)	671 (186)	136 (24)
P	305–310	16 (12)	7 (1)	0.5 (0.08)	62 (18)	6.46 (0.04)	0.1 (0.1)	701 (150)	90 (41)
P	314–319	6 (0.3)	5 (1.4)	0.4 (0.1)	45 (6.2)	6.71 (0.16)	0.3 (0.04)	1106 (422)	90 (42)

*Segments 174–194 cm were associated with Holocene aged DHL_16_1 core and 296–319 cm were associated with Pleistocene aged DHL_16_2 core. **$p < 0.001$, *$p < 0.01$. (±SD), standard deviation. 1 OC, organic carbon; TC, total carbon; TN, total nitrogen; GW, gravimetric water content; EC, electrical conductivity. [a]H, Holocene age, [b]Pleistocene age, [c]% (w/w), [d]mg/kg, [e]μ S/cm.*

TABLE 2 | Measured dissolved metals of the selected segments for microbial analysis.

Epoch	Depth (cm)	Ca[c*] (±SD)	Cu[d*] (±SD)	Fe[c*] (±SD)	K[c*] (±SD)	Mg[c*] (±SD)	Mn[d*] (±SD)	Zn[d*] (±SD)	Na[d*] (±SD)	P[c*] (±SD)	S[c**] (±SD)
H[a]	174–179	0.23 (0.07)	18.26 (11.7)	0.33 (0.19)	0.02 (0.01)	0.05 (0.02)	19.51 (0.5)	21 (5)	129 (69)	0.02 (0.0)	0.17 (0.006)
H	179–184	0.27 (0.13)	9 (1.25)	0.19 (0.3)	0.02 (0.0)	0.05 (0.02)	18.33 (1.08)	22 (6)	109 (40)	0.02 (0.004)	0.16 (0.03)
H	189–194	0.4 (0.02)	9.65 (2)	0.32 (0.03)	0.01 (0.001)	0.08 (0.007)	19 (2)	28 (2)	146 (12)	0.02 (0.0)	0.12 (0.01)
P[b]	296–301	0.83 (0.08)	68 (30)	1.7 (0.24)	0.13 (0.01)	0.5 (0.07)	153 (57)	137 (9.4)	224 (15)	0.09 (0.0)	0.22 (0.02)
P	305–310	0.8 (0.03)	82 (9.5)	1.71 (0.02)	0.14 (0.03)	0.47 (0.03)	136 (33)	139 (12)	261 (66)	0.09 (0.002)	0.21 (0.03)
P	314–319	1.60 (1)	62 (19)	1.96 (0.22)	0.13 (0.006)	0.75 (0.34)	194 (47)	148 (1.4)	261 (65)	0.1 (0.01)	0.16 (0.02)

*Segments 174–194 cm were associated with Holocene aged DHL_16_1 core and 296–319 cm were associated with Pleistocene aged DHL_16_2 core. *$p < 0.01$, **$p < 0.05$. (±SD), standard deviation. [a]Holocene age, [b]Pleistocene age, [c]%(w/w), [d]mg/kg.*

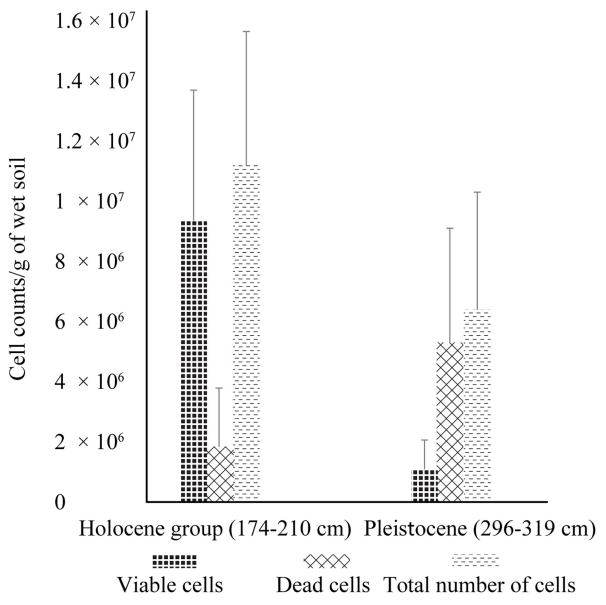

FIGURE 1 | Live/dead cell counts of Holocene and Pleistocene aged samples. Error bars represent one standard deviation from the mean ($n = 60$ mean observation). For this experiment, samples from 174–210 cm ($n = 4$) and 296–319 cm ($n = 4$) were selected to investigate cell viability in Holocene aged and Pleistocene aged soils. These depths were selected based on their close proximity to the Pleistocene-Holocene transition zone of 244 cm. The statistical significance (Student's *t*-test) of fold change in cell counts from Holocene to Pleistocene is as follows: fold change in viable cells ($p < 0.001$), fold change in dead cells ($p < 0.001$), and fold change in total cells ($p < 0.001$).

other epoch, which are probably selected by the environmental condition of each permafrost soil. The OTUs within and between epochs demonstrated that of 336 OTUs within Holocene samples, 84.5% were unique to this group (which we termed core Holocene OTUs, 284 OTUs), and only 15.5% were shared with the Pleistocene group (which we termed Pleistocene-Holocene shared, 52 OTUs) (**Supplementary Figure S6**). Similarly, of a total of 328 OTUs within the Pleistocene cluster, 84.1% of the OTUs were unique to this group (which we termed core Pleistocene OTUs, 276 OTUs), and only 15.8% of the OTUs were in Pleistocene-Holocene shared group (**Supplementary Figure S6**). The three dominant OTUs that formed the top 30% of the composite Pleistocene and Holocene samples were associated with the Pleistocene-Holocene shared group. In general, OTUs found within this cluster were slightly more dominant in Pleistocene samples (52.1%) than Holocene samples (47.8%).

Core Pleistocene and Holocene sequences were individually compared to the standard reference DNA sequence database in NCBI via BLAST. The average percent similarity of core Pleistocene OTU 16S rRNA gene sequences to published bacterial sequences was 92.1% (±0.05%; $n = 276$ OTUs) in comparison to Holocene OTUs, which was 97.5% (±0.03%; $n = 284$ OTUs) ($p < 0.001$). Since the average of the 16S rRNA gene sequence similarity value of Pleistocene OTUs were less than the 97% identity boundary between unknown and known species (Stackebrandt and Goebel, 1994), they are uncharacterized and are more different from extant bacterial communities in databases than are Holocene OTUs. Pleistocene-Holocene shared OTUs ($n = 52$) demonstrated similarity to characterized strains

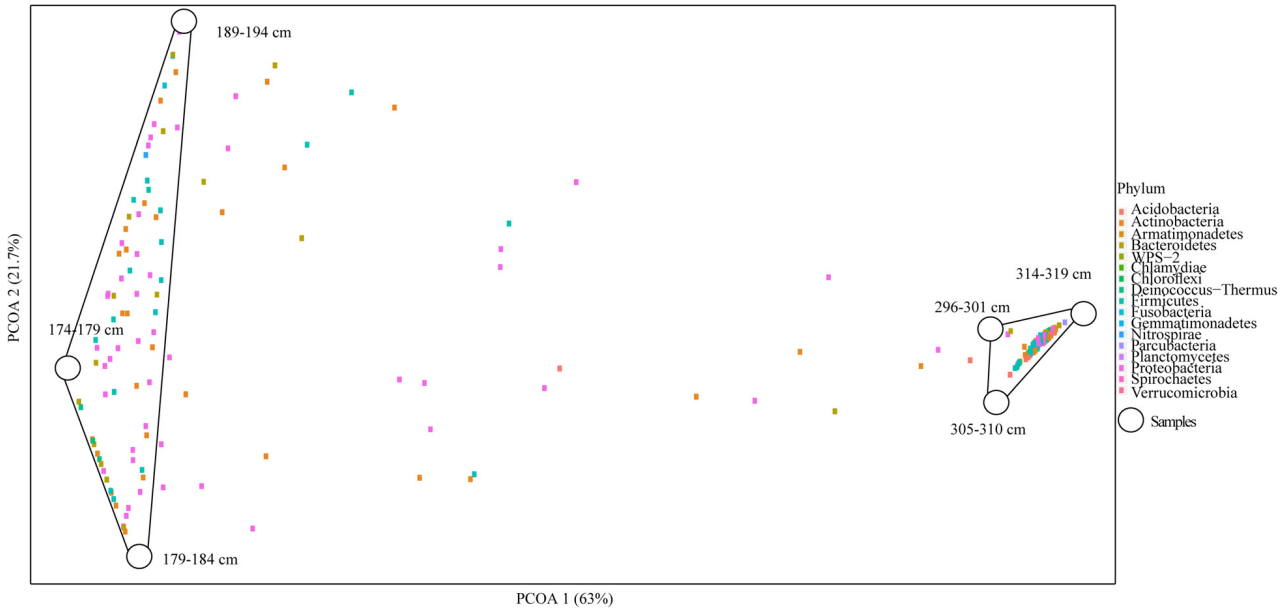

FIGURE 2 | PCoA biplot of the OTU composition in Holocene (n = 3) and Pleistocene (n = 3) aged samples. Combined Axis 1 (PCOA1) and Axis 2 (PCOA2) components explained a total of 84.7% of the dissimilarity between the clusters in the system (p = 0.022). Samples 174–179, 179–184, 189–194 cm formed the Holocene cluster (8–10 k cal yr BP) and 296–301, 305–310, 314–319 cm formed the Pleistocene aged cluster (14–15 k cal yr BP). In the ordination space, samples (5 cm segments of DHL_16-1 and 2) have been shown with white circles and OTUs with colored squares. Colors of OTUs represent their taxonomic identity at the phylum level.

similar to that for the Holocene OTUs (97.3% ± 0.05%) ($p > 0.05$) and not Pleistocene OTUs ($p < 0.001$).

Differential abundance analysis of the top 10 dominant phyla in composite Holocene and Pleistocene samples identified five phyla (Actinobacteria, Acidobacteria, Proteobacteria, Deinococcus-Thermus and Fusobacteria) as the main drivers of differences in taxonomy ($p < 0.001$) between Pleistocene and Holocene samples (**Supplementary Figures S7, S8**). In composite Holocene samples, 94% of the sequences fell within the Proteobacteria (56%), Actinobacteria (17%), Firmicutes (15%), and Bacteroidetes (5%) (**Figure 3**). Deinococcus-Thermus and Fusobacteria were part of the core Holocene samples and together constituted 3.58% of the community. On the other hand, 98% of the composite Pleistocene sequences were Actinobacteria (43%), Firmicutes (24%), Proteobacteria (16%), Acidobacteria (8%), and Bacteroidetes (6%). A similar distinction in taxonomic composition between composite Holocene and Pleistocene samples was also evident at the class level (**Supplementary Figure S9**). In the Pleistocene-Holocene shared group, 98% of the OTUs were associated with Proteobacteria (88%), Actinobacteria (8%), Firmicutes (2%) and Bacteroidetes (1%) respectively (**Supplementary Figure S10a**). Although these OTUs were shared between Pleistocene and Holocene samples the abundance of these OTUs were significantly different between epochs ($p < 0.001$) (**Supplementary Figure S10b**).

To test for possible correlation between epoch-based separation of the microbial community structure and changes in soil chemical parameters, a ManyGLM model was utilized. The ManyGLM indicated that within the composited Holocene samples, only Ca and Mn had a statistically significant correlation ($p < 0.05$) to the core OTUs. The other 20 measured variables, including depth of the samples, did not show any significant relationship to the core OTUs (**Table 3**). Within Pleistocene samples, no significant correlation was found between core OTUs and any measured variable, including depth of the samples. However, between the Pleistocene and Holocene groups, there was a clear correlation between shift in epoch, changes in soil chemical parameters and reorganization in core OTU compositions (**Table 3**).

DISCUSSION

The perennially frozen nature of permafrost prevents movement of entrapped bacteria, creating a dispersal limitation. Furthermore, it is a challenging environment in terms of energy and nutrient availability (thermodynamic constraints) and damage to cells (physical constraints) (Mackelprang et al., 2017; Bottos et al., 2018; Burkert et al., 2019; Liang et al., 2019). Therefore, permafrost creates an environmental filter that only allows species resistant to these effects to survive, dramatically changing the composition of the community (Mackelprang et al., 2017; Bottos et al., 2018). Furthermore, these effects are compounded with time, further shifting the communities as the permafrost ages (Mackelprang et al., 2017). Hence, it is not clear if the surviving community members can be used as a paleoenvironmental tool.

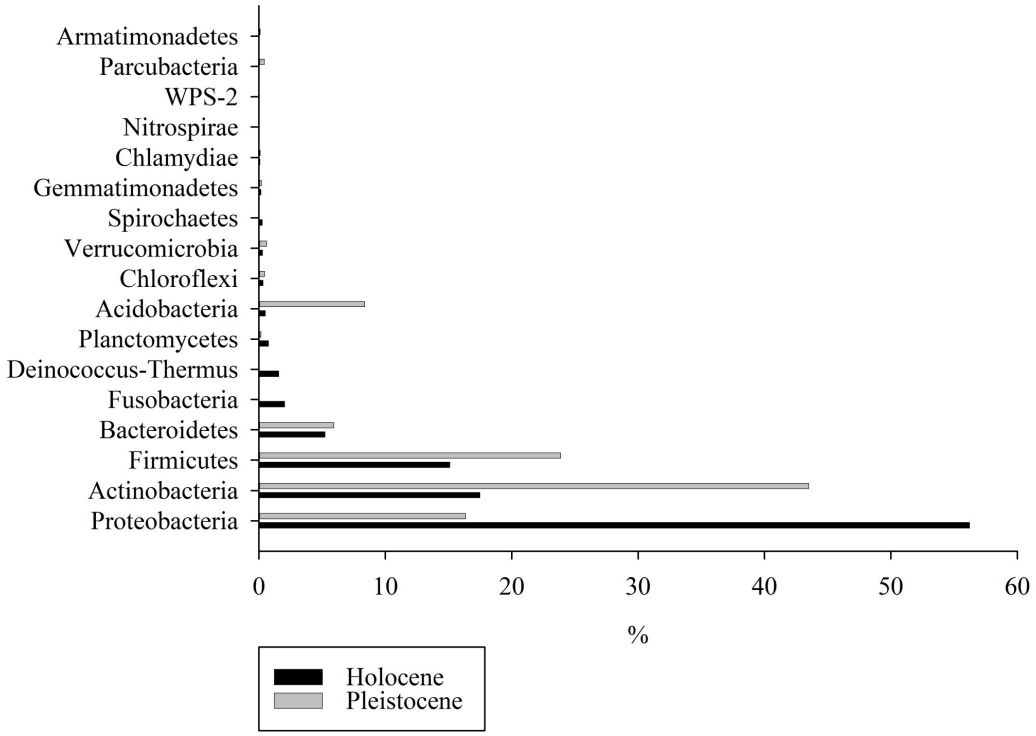

FIGURE 3 | Relative abundance analyses of the OTUs detected in Holocene-aged and Pleistocene-aged permafrost samples at the phylum level.

Most previous studies of permafrost microbial community structure or community-level function have been conducted on permafrost chronosequences from a single epoch (e.g., Mackelprang et al., 2011, 2017; Hultman et al., 2015). Therefore, it is not known whether there is a shift in the permafrost microbial community structure close to the Pleistocene-Holocene transition. We observed dramatic differences in soil chemistry and OTU composition in samples from either side of the Pleistocene-Holocene transition (**Figure 2**, **Supplementary Figures S1, S5, S6**, and **Tables 1**, **2**). A small number of OTUs (n = 52) that were able to persist despite the dramatic change during the Pleistocene-Holocene transition and the permafrost freezing-filtering effect were shared among the Pleistocene and Holocene samples (Pleistocene-Holocene shared group; **Supplementary Figure S6**). However, their abundance differed dramatically between epochs (**Supplementary Figure S10b**). No significant differences were observed between samples within an epoch (despite a difference in age between the samples). The lack of clear observable correlations between chemistry and microbiology within epochs is consistent with prior observations (e.g., Mackelprang et al., 2017; Bottos et al., 2018).

Based on our data, microbial community structure within an epoch is relatively stable over time, likely due to physiological flexibility and community stability of the microbial community (Shade et al., 2013). Thus, the environmental filter of the frozen and isolated conditions in the permafrost creates a strong selection pressure on microbial communities that are initially similar. Any relatively small signal of microbial community differences at the time of formation are lost. However, once the system surpasses a threshold, both chemical and microbial parameters rapidly shift to a new stable state. Some OTUs are able to persist, despite the dramatic change during the Pleistocene-Holocene transition and the permafrost freezing filtering effect, and were shared among the Pleistocene and Holocene samples (Pleistocene-Holocene shared group; **Supplementary Figure S6**) (Mandakovic et al., 2018). This scenario resembles the threshold hypothesis (also known as the tipping point hypothesis) (Scheffer et al., 2001), wherein a critical threshold exists in a system beyond which perturbations cause extensive changes (called "catastrophic" by Scheffer et al., 2001) and the system shifts from one stable state to another (Allison and Martiny, 2008; Shade et al., 2012; Mikkelson et al., 2016). Many paleoclimatic records indicate that the Pleistocene-Holocene transition was rapid and caused the climate system to cross a threshold, triggering a rapid transition to a warmer Holocene climate (Alley et al., 2003; Guthrie, 2006; Boers et al., 2018). Such an abrupt change is consistent with our ManyGLM model (**Table 2**), which did not detect any statistically significant correlation between OTU composition and soil chemical parameters within an epoch, with the exception of weak statistical support for correlations with Mn and Ca in Holocene samples (**Table 2**). However, between epochs, the ManyGLM model indicated a statistically significant change in microbial community structure and chemical profile (**Table 2**). Hence, we hypothesize that both soil chemical and microbial parameters were relatively stable until a threshold was reached at the Pleistocene-Holocene

TABLE 3 | The probability values calculated based on Wald's generalized estimating equation in the context of a negative binomial many generalized linear model (ManyGLM).

Measured Variables	Holocene	Pleistocene	Between Epoch
Depth	0.605	0.184	0.009*
TC[a]	0.394	0.32	0.021*
TN[a]	0.219	0.444	0.005**[c]
$NO3^-/NO2^-$	0.531	0.385	0.012*
$NH4^+$	0.151	0.072	0.003**
EC[a]	0.391	0.494	0.021*
pH	0.081	0.294	0.014*
H2O	0.379	0.226	0.044*
OC[a]	0.469	0.287	0.033*
Ca	0.039*[b]	0.349	0.022*
Cu	0.417	0.225	0.016*
Fe	0.3	0.505	0.027*
K	0.108	0.604	0.032*
Mg	0.12	0.271	0.014*
Mn	0.037*	0.567	0.016*
Zn	0.165	0.383	0.014*
Na	0.435	0.596	0.031*
P	0.074	0.239	0.008**
S	0.097	0.672	0.003**

[a] *TC, total carbon; TN, total nitrogen; EC, electric conductivity; OC, organic carbon.* [b] *$*p < 0.05$,* [c] *$**p < 0.01$. Within an epoch, degrees of freedom remaining after fitting each variable was 1 and degrees of freedom attributed to each variable was also 1. Between epochs, degrees of freedom remaining after fitting each variable was 4 and degrees of freedom attributed to each variable was 1.*

transition, after which there was a drastic shift to a new set of chemical and microbial parameters.

One implication of the threshold hypothesis described above is that it may explain why some decades-long *in situ* soil warming experiments have shown little or no change in microbial community structure (e.g., Kuffner et al., 2012), while lab-based incubations have shown dramatic shifts in community structure in a matter of days (e.g., Mackelprang et al., 2011). This difference between field and lab outcomes is likely because field-based studies generally involve moderate heating of the surface active layer of soil and thus do not strongly affect the underlying permafrost. In these experiments, microbes are able to gradually acclimate to moderate warming and the community resists shifts in composition (Allison and Martiny, 2008; Bradford et al., 2008; Rousk et al., 2012; Metcalfe, 2017). In contrast, in laboratory-based experiments, small amounts of permafrost thaw rapidly in response to increased temperature, leading to significant changes in the physicochemical parameters of the soil (Vonk et al., 2015) accompanied by dramatic changes in microbial community structure (e.g., Mackelprang et al., 2011; Schostag et al., 2019). Even changes at subzero temperatures in laboratory microcosms have been reported to alter microbial community structure (Tuorto et al., 2014).

Changes in OTU and chemical composition between epochs were accompanied by major changes in taxonomy (**Supplementary Figures S7, S8**). Proteobacteria-related species were dominant in Holocene samples, whereas Actinobacteria-related species dominated Pleistocene samples (**Figure 3** and **Supplementary Figures S7, S8**). Species associated with phyla Proteobacteria and Actinobacteria are the most dominant species in soil worldwide (Janssen, 2006), including cold environments such as permafrost (e.g., Gittel et al., 2014; Zhang et al., 2016). Although phylogeny cannot be used to directly infer physiology and broad taxonomic groups (such as phyla) can include organisms with many different physiological features, strains affiliated with Actinobacteria have been characterized as oligotrophs adapted to nutrient-poor environments, while strains associated with Proteobacteria have been characterized as copiotrophs adapted to carbon-rich systems (De Vries and Shade, 2013; Itcus et al., 2018). Competition for nutrients among species associated with these two phyla have been reported (Goldfarb et al., 2011). According to a recent revision in environmental filtering theory, abiotic factors initially select certain strains, and then the second phase of selection pressure occurs based on species competition for resources (Freedman and Zak, 2015; Kraft et al., 2015). Hence, competition for resources could be a major consequence of threshold-crossing events, which might drastically alter ecosystem services, in particular when Pleistocene-aged permafrost thaws and releases the entrapped microorganisms to the surrounding environment due to climate warming (Castro et al., 2010; De Vries and Shade, 2013; Strauss et al., 2017; Schostag et al., 2019). Based on metatranscriptome analysis of frozen permafrost, Coolen and Orsi (2015) demonstrated a shift in microbial community structure from Firmicutes, Acidobacteria, Actinobacteria and Proteobacteria dominant community to a Firmicutes, Bacteroidetes, and Euryarchaeota dominant community upon thaw. Permafrost thaw in their study was in parallel in increase in complex biopolymer degradation, translation and biogenesis transcripts, indicating a general increase in microbial activity (Coolen and Orsi, 2015).

Another, less likely, scenario to explain the microbial community shift between epochs is the effect of the relict extracellular DNA on our diversity analyses. In this scenario, relict preserved DNA released from dead cells differs between Holocene and Pleistocene samples and bias increases with relict DNA pool size (similar to Carini et al., 2016). Within the Pleistocene samples, 83% of the enumerated cells were non-viable and Holocene samples had ∼8 fold higher viable cells (**Figure 1**). Hence, it is possible that relict DNA might be an important factor in epoch based separation of Holocene and Pleistocene microbial community structure. However, this scenario seems unlikely for two reasons. First, Burkert et al. (2019) did not find a significant change in microbial community structure after removal of relict DNA preserved within Beringian permafrost. Second, Lennon et al. (2018) reported a minimal effect of relict DNA on estimates of microbial alpha diversity as long as the species abundance distribution of the relict and intact DNA pools are equivalent. Hence, since our alpha diversity indices did not indicate any statistically significant variation between epochs (**Supplementary Table S3**), the species abundance distribution of the relict and intact DNA are likely equivalent. However, it is not possible to fully exclude this scenario.

CONCLUSION

Anthropocene warming in the western Arctic exceeds the dramatic warming associated with the Early Holocene thermal maximum, and arguably represents the warmest temperatures of the last ca. 14,000 years (Porter et al., 2019). As a result fragile cold-adapted systems have been predicted to be near a threshold- similar to the Pleistocene-Holocene transition (Miller et al., 2010). Similar changes observed in this study might occur in modern cold soils, which could alter ecosystem services with unknown consequences. The single core and six samples from this study only represent a snap shot of the effects of dramatic climate change on microbial population dynamics across the Pleistocene-Holocene transition at one location. Future investigations should focus on different types of permafrost-affected regions with different terrain types or different permafrost stratigraphy, both at microbial community and functional levels. It is yet to be seen if our findings are more generally representative of the microbial community dynamics across the Pleistocene-Holocene transition at a pan-Arctic scale. If our threshold hypothesis is supported by more regional studies in diverse settings, it may provide a framework for a better understanding of potential changes in important archaeal and bacterial functional guilds, which could in turn improve climate models by predicting microbial responses in a warmer world.

Also, we noticed that the bacteria entrapped in Pleistocene aged permafrost are distantly related to the known reference sequences, this suggest that the microbial members of the Eastern Beringian permafrost are mainly unknown. Future research demands to isolate these strains and study them at a phylogenetic and genome levels for possible biotechnological applications or for expanding our knowledge regarding bacterial evolution/succession over geologically meaningfully timescales.

DATA AVAILABILITY STATEMENT

The datasets presented in this study can be found in online repositories. The names of the repository/repositories and accession number(s) can be found below: https://www.ncbi.nlm.nih.gov/genbank/, PRJNA607368; https://www.ncbi.nlm.nih.gov/, SAMN14130768.

AUTHOR CONTRIBUTIONS

AS-M collected the samples, performed the experiments, analyzed the data, and wrote the manuscript. PN performed the experiments. MH performed and analyzed the statistical tests. DF and BL designed the project, obtained the funding, and aided with the interpretation of the data. All the authors reviewed and edited the manuscript.

FUNDING

This research was funded by the NSERC Discovery Grants (BL and DF) and NSERC Northern Research Supplements (DF) and ArcticNet project 2019-13 (BL). A Yukon Scientists and Explorers License was acquired from the Yukon Government for coring the permafrost samples.

ACKNOWLEDGMENTS

We would like to acknowledge Dr. Lauren Davies for assistance with radiocarbon dating and chronology of the cores, and Sasiri Bandara, Casey Buchanan, and Joseph Young for assisting us in sampling. We would like to extend our thanks to the University of Alberta (UANRA grant), the Polar Knowledge Canada (NSTP grant), and the Alberta Innovates Technology (AITF) for their student financial support. In addition, we would like to thank Dr. Martin Sharp, Dr. Alberto Reyes, Dr. Derek MacKenzie, and Ashley Gilliland for their insightful comments, support, and allowing us to use their labs.

SUPPLEMENTARY MATERIAL

The Supplementary Material for this article can be found online at: https://www.frontiersin.org/articles/10.3389/fenvs.2020.00133/full#supplementary-material

REFERENCES

Alley, R. B., Marotzke, J., Nordhaus, W. D., Overpeck, J. T., Peteet, D. M., Pielke, R. A., et al. (2003). Abrupt climate change. *Science* 299, 2005–2010.

Allison, S. D., and Martiny, J. B. (2008). Resistance, resilience, and redundancy in microbial communities. *PNAS* 105, 11512–11519. doi: 10.1073/pnas.0801925105

Altschul, S. F., Gish, W., Miller, W., Myers, E. W., and Lipman, D. J. (1990). Basic local alignment search tool. *J. Mol. Biol.* 215, 403–410.

Barnosky, A. D., Koch, P. L., Feranec, R. S., Wing, S. L., and Shabel, A. B. (2004). Assessing the causes of late Pleistocene extinctions on the continents. *Science* 306, 70–75. doi: 10.1126/science.1101476

Boers, N., Ghil, M., and Rousseau, D. D. (2018). Ocean circulation, ice shelf, and sea ice interactions explain Dansgaard–Oeschger cycles. *PNAS* 115, E11005–E11014.

Bottos, E. M., Kennedy, D. W., Romero, E. B., Fansler, S. J., Brown, J. M., Bramer, L. M., et al. (2018). Dispersal limitation and thermodynamic constraints govern spatial structure of permafrost microbial communities. *FEMS Microbiol. Ecol.* 94:fiy110.

Bradford, M. A., Davies, C. A., Frey, S. D., Maddox, T. R., Melillo, J. M., Mohan, J. E., et al. (2008). Thermal adaptation of soil microbial respiration to elevated temperature. *Ecol. Lett.* 11, 1316–1327. doi: 10.1111/j.1461-0248.2008.01251.x

Burkert, A., Douglas, T. A., Waldrop, M. P., and Mackelprang, R. (2019). Changes in the active, dead, and dormant microbial community structure across a Pleistocene permafrost chronosequence. *Appl. Environ. Microbiol.* 85: e02646-18.

Caporaso, J. G., Lauber, C. L., Walters, W. A., Berg-Lyons, D., Lozupone, C. A., Turnbaugh, P. J., et al. (2011). Global patterns of 16S rRNA diversity at a depth of millions of sequences per sample. *PNAS* 108, 4516–4522. doi: 10.1073/pnas.1000080107

Carini, P., Marsden, P. J., Leff, J. W., Morgan, E. E., Strickland, M. S., and Fierer, N. (2016). Relic DNA is abundant in soil and obscures estimates of soil microbial diversity. *Nat. Microbiol.* 2, 1–6.

Castro, H. F., Classen, A. T., Austin, E. E., Norby, R. J., and Schadt, C. W. (2010). Soil microbial community responses to multiple experimental climate change drivers. *Appl. Environ. Microbiol.* 76, 999–1007. doi: 10.1128/aem.02874-09

Cole, J. R., Wang, Q., Fish, J. A., Chai, B., McGarrell, D. M., Sun, Y., et al. (2014). Ribosomal Database Project: data and tools for high throughput rRNA analysis. *Nucleic Acids Res.* 42, D633–D642.

Coolen, M. J., and Orsi, W. D. (2015). The transcriptional response of microbial communities in thawing Alaskan permafrost soils. *Front. Microbiol.* 6:197. doi: 10.3389/fmicb.2015.00197

Davies, L. J., Appleby, P., Jensen, B. J., Magnan, G., Mullan-Boudreau, G., Noernberg, T., et al. (2018). High-resolution age modelling of peat bogs from northern Alberta, Canada, using pre-and post-bomb ^{14}C, ^{210}Pb and historical cryptotephra. *Quat. Geochronol.* 47, 138–162. doi: 10.1016/j.quageo.2018.04.008

De Vries, F. T., and Shade, A. (2013). Controls on soil microbial community stability under climate change. *Front. Microbiol.* 4:265. doi: 10.3389/fmicb.2013.00265

Edgar, R. (2016). SINTAX: a simple non-Bayesian taxonomy classifier for 16S and ITS sequences. *BioRxiv* [Preprint]. doi: 10.1101/074161

Edgar, R. C. (2010). Search and clustering orders of magnitude faster than BLAST. *Bioinformatics* 26, 2460–2461. doi: 10.1093/bioinformatics/btq461

Edgar, R. C. (2013). UPARSE: highly accurate OTU sequences from microbial amplicon reads. *Nat. Methods* 10:996. doi: 10.1038/nmeth.2604

Fraser, T. A., and Burn, C. R. (1997). On the nature and origin of "muck" deposits in the Klondike area, Yukon Territory. *Can. J. Earth Sci.* 34, 1333–1344. doi: 10.1139/e17-106

Freedman, Z., and Zak, D. R. (2015). Soil bacterial communities are shaped by temporal and environmental filtering: evidence from a long-term chronosequence. *Environ. Microbiol.* 17, 3208–3218. doi: 10.1111/1462-2920.12762

Froese, D. G., Zazula, G. D., Westgate, J. A., Preece, S. J., Sanborn, P. T., Reyes, A. V., et al. (2009). The Klondike goldfields and Pleistocene environments of Beringia. *GSA Today* 19, 4–10. doi: 10.1130/gsatg54a.1

Gaglioti, B. V., Mann, D. H., Jones, B. M., Wooller, M. J., and Finney, B. P. (2016). High-resolution records detect human-caused changes to the boreal forest wildfire regime in interior Alaska. *Holocene* 26, 1064–1074. doi: 10.1177/0959683616632893

Gittel, A., Bárta, J., Kohoutová, I., Mikutta, R., Owens, S., Gilbert, J., et al. (2014). Distinct microbial communities associated with buried soils in the Siberian tundra. *ISME* 8, 841–853. doi: 10.1038/ismej.2013.219

Goldfarb, K. C., Karaoz, U., Hanson, C. A., Santee, C. A., Bradford, M. A., Treseder, K. K., et al. (2011). Differential growth responses of soil bacterial taxa to carbon substrates of varying chemical recalcitrance. *Front. Microbiol.* 2:94. doi: 10.3389/fmicb.2011.00094

Guthrie, R. D. (2006). New carbon dates link climatic change with human colonization and Pleistocene extinctions. *Nature* 441, 207–209. doi: 10.1038/nature04604

Haile, J., Froese, D. G., MacPhee, R. D., Roberts, R. G., Arnold, L. J., Reyes, A. V., et al. (2009). Ancient DNA reveals late survival of mammoth and horse in interior Alaska. *PNAS* 106, 22352–22357. doi: 10.1073/pnas.0912510106

Hardie, M., and Doyle, R. (2012). *Measuring Soil Salinity In Plant Salt Tolerance 2012*. Totowa, NJ: Humana Press.

Hultman, J., Waldrop, M. P., Mackelprang, R., David, M. M., McFarland, J., Blazewicz, S. J., et al. (2015). Multi-omics of permafrost, active layer and thermokarst bog soil microbiomes. *Nature* 521, 208–212. doi: 10.1038/nature14238

Itcus, C., Pascu, M. D., Lavin, P., Perşoiu, A., Iancu, L., and Purcarea, C. (2018). Bacterial and archaeal community structures in perennial cave ice. *Sci. Rep.* 8, 1–4.

Janssen, P. H. (2006). Identifying the dominant soil bacterial taxa in libraries of 16S rRNA and 16S rRNA genes. *Appl. Environ. Microbiol.* 72, 1719–1728. doi: 10.1128/aem.72.3.1719-1728.2006

Kotler, E., and Burn, C. R. (2000). Cryostratigraphy of the Klondike "muck" deposits, west-central Yukon Territory. *Can. J. Earth Sci.* 37, 849–861. doi: 10.1139/e00-013

Kraft, N. J., Adler, P. B., Godoy, O., James, E. C., Fuller, S., and Levine, J. M. (2015). Community assembly, coexistence and the environmental filtering metaphor. *Funct. Ecol.* 29, 592–599. doi: 10.1111/1365-2435.12345

Kuffner, M., Hai, B., Rattei, T., Melodelima, C., Schloter, M., Zechmeister-Boltenstern, S., et al. (2012). Effects of season and experimental warming on the bacterial community in a temperate mountain forest soil assessed by 16S rRNA gene pyrosequencing. *FEMS. Microbiol. Ecol.* 82, 551–562. doi: 10.1111/j.1574-6941.2012.01420.x

Lacelle, D., Fontaine, M., Pellerin, A., Kokelj, S. V., and Clark, I. D. (2019). Legacy of holocene landscape changes on soil biogeochemistry: a perspective from paleo-active layers in Northwestern Canada. *J. Geophys. Res. Biogeol.* 124, 2662–2679.

Lennon, J. T., Muscarella, M. E., Placella, S. A., and Lehmkuhl, B. K. (2018). How, when, and where relic DNA affects microbial diversity. *Am. Soc. Microbiol.* 9:e00637-18.

Liang, R., Lau, M., Vishnivetskaya, T., Lloyd, K. G., Wang, W., Wiggins, J., et al. (2019). Predominance of anaerobic, spore-forming bacteria in metabolically active microbial communities from ancient Siberian permafrost. *Appl. Environ. Microbiol.* 85:e00560-19.

Lorenzen, E. D., Nogués-Bravo, D., Orlando, L., Weinstock, J., Binladen, J., Marske, K. A., et al. (2011). Species-specific responses of Late Quaternary megafauna to climate and humans. *Nature* 479, 359–364.

Love, M. I., Huber, W., and Anders, S. (2014). Moderated estimation of fold change and dispersion for RNA-seq data with DESeq2. *Genome. Biol.* 15:550.

Mackelprang, R., Burkert, A., Haw, M., Mahendrarajah, T., Conaway, C. H., Douglas, T. A., et al. (2017). Microbial survival strategies in ancient permafrost: insights from metagenomics. *ISME* 11, 2305–2318. doi: 10.1038/ismej.2017.93

Mackelprang, R., Waldrop, M. P., DeAngelis, K. M., David, M. M., Chavarria, K. L., Blazewicz, S. J., et al. (2011). Metagenomic analysis of a permafrost microbial community reveals a rapid response to thaw. *Nature* 480, 368–371. doi: 10.1038/nature10576

Mandakovic, D., Rojas, C., Maldonado, J., Latorre, M., Travisany, D., Delage, E., et al. (2018). Structure and co-occurrence patterns in microbial communities under acute environmental stress reveal ecological factors fostering resilience. *Sci. Rep.* 8:5875.

Mann, P. J., Spencer, R. G., Hernes, P. J., Six, J., Aiken, G. R., Tank, S. E., et al. (2016). Pan-Arctic trends in terrestrial dissolved organic matter from optical measurements. *Front. Earth Sci.* 4:25. doi: 10.3389/feart.2016.00025

Maynard, D. G., Kalra, Y. P., and Crumbaugh, J. A. (1993). *Nitrate and Exchangeable Ammonium Nitrogen. Soil Sampling and Methods of Analysis*. Washington, DC: Lewis Publishers.

McMurdie, P. J., and Holmes, S. (2013). Phyloseq: an R package for reproducible interactive analysis and graphics of microbiome census data. *PLoS One* 8:e61217. doi: 10.1371/journal.pone.0061217

Metcalfe, D. B. (2017). Microbial change in warming soils. *Science* 358, 41–42. doi: 10.1126/science.aap7325

Mielke, P. W. Jr., Berry, K. J., and Johnson, E. S. (1976). Multi-response permutation procedures for a priori classifications. *Commun. Stat Theor.* 5, 1409–1424. doi: 10.1080/03610927608827451

Mikkelson, K. M., Lozupone, C. A., and Sharp, J. O. (2016). Altered edaphic parameters couple to shifts in terrestrial bacterial community structure associated with insect-induced tree mortality. *Soil Biol. Biochem.* 95, 19–29. doi: 10.1016/j.soilbio.2015.12.001

Miller, G. H., Alley, R. B., Brigham-Grette, J., Fitzpatrick, J. J., Polyak, L., Serreze, M. C., et al. (2010). Arctic amplification: can the past constrain the future? *Quat. Sci. Rev.* 29, 1779–1790. doi: 10.1016/j.quascirev.2010.02.008

Oksanen, J., Kindt, R., Legendre, P., O'Hara, B., Stevens, M. H., Oksanen, M. J., et al. (2007). The vegan package. *Commun. Ecol. Package* 10, 631–637.

Porter, T. J., Schoenemann, S. W., Davies, L. J., Steig, E. J., Bandara, S., and Froese, D. G. (2019). Recent summer warming in northwestern Canada exceeds the Holocene thermal maximum. *Nat. Commun.* 10, 1–10.

Rivkina, E., Petrovskaya, L., Vishnivetskaya, T., Krivushin, K., Shmakova, L., Tutukina, M., et al. (2016). Metagenomic analyses of the late Pleistocene permafrost–additional tools for reconstruction of environmental conditions. *Biogeosciences* 13, 2207–2219. doi: 10.5194/bg-13-2207-2016

Rousk, J., Frey, S. D., and Bååth, E. (2012). Temperature adaptation of bacterial communities in experimentally warmed forest soils. *Glob. Change Biol.* 18, 3252–3258. doi: 10.1111/j.1365-2486.2012.02764.x

Saidi-Mehrabad, A., Neuberger, P., Cavaco, M., Froese, D., and Lanoil, B. D. (2020). Optimization of subsampling, decontamination, and DNA extraction of difficult peat and silt permafrost samples. *bioRxiv* [Preprint]. doi: 10.1101/2020.01.02.893438

Scheffer, M., Carpenter, S., Foley, J. A., Folke, C., and Walker, B. (2001). Catastrophic shifts in ecosystems. *Nature* 413, 591–596. doi: 10.1038/35098000

Schloss, P. D., Westcott, S. L., Ryabin, T., Hall, J. R., Hartmann, M., Hollister, E. B., et al. (2009). Introducing mothur: open-source, platform-independent, community-supported software for describing and comparing microbial communities. *Appl. Environ. Microbiol.* 75, 7537–7541. doi: 10.1128/aem.01541-09

Schostag, M., Priemé, A., Jacquiod, S., Russel, J., Ekelund, F., Jacobsen, C. S. (2019). Bacterial and protozoan dynamics upon thawing and freezing of an active layer permafrost soil. *ISME.* 13, 1345–1359. doi: 10.1038/s41396-019-0351-x

Shade, A., Caporaso, J. G., Handelsman, J., Knight, R., and Fierer, N. (2013). A meta-analysis of changes in bacterial and archaeal communities with time. *ISME* 7:1493. doi: 10.1038/ismej.2013.54

Shade, A., Peter, H., Allison, S. D., Baho, D., Berga, M., Bürgmann, H., et al. (2012). Fundamentals of microbial community resistance and resilience. *Front. Microbiol.* 3:417. doi: 10.3389/fmicb.2012.00417

Shapiro, B., and Cooper, A. (2003). Beringia as an ice age genetic museum. *Quat. Res.* 60, 94–100. doi: 10.1016/s0033-5894(03)00009-7

Skoog, D. A., Holler, F. J., and Crouch, S. R. (2007). *Atomic Emission Spectrometry: Chapter 10 in Principles of Instrumental Analysis*, 6th Edn. Belmont, CA: Saunders College Publication.

Sparks, D. L., Page, A. L., Helmke, P. A., Loeppert, R. H., Soltanpour, P. N., Tabatabai, M. A., et al. (1996). *Methods of Soil Analysis, part 3, Chemical Methods*. Madison: SSSA.

Stackebrandt, E., and Goebel, B. M. (1994). A place for DNA DNA reassociation and 16S rRNA sequence analysis in the present species definition in bacteriology. *Int. J. Syst. Evol. Microbiol.* 44, 846–849. doi: 10.1099/00207713-44-4-846

Steffen, W., Rockström, J., Richardson, K., Lenton, T. M., Folke, C., Liverman, D., et al. (2018). Trajectories of the earth system in the anthropocene. *PNAS* 115, 8252–8259.

Strauss, J., Schirrmeister, L., Grosse, G., Fortier, D., Hugelius, G., Knoblauch, C., et al. (2017). Deep Yedoma permafrost: a synthesis of depositional characteristics and carbon vulnerability. *Earth Sci. Rev.* 172, 75–86. doi: 10.1016/j.earscirev.2017.07.007

Tuorto, S. J., Darias, P., McGuinness, L. R., Panikov, N., Zhang, T., Häggblom, M. M., et al. (2014). Bacterial genome replication at subzero temperatures in permafrost. *ISME* 8, 139–149. doi: 10.1038/ismej.2013.140

Vonk, J. E., Tank, S. E., Bowden, W. B., Laurion, I., Vincent, W. F., Alekseychik, P., et al. (2015). Reviews and syntheses: effects of permafrost thaw on Arctic aquatic ecosystems. *Biogeosciences* 12, 7129–7167. doi: 10.5194/bg-12-7129-2015

Wang, Y. I., Naumann, U., Wright, S. T., and Warton, D. I. (2012). mvabund–an R package for model-based analysis of multivariate abundance data. *Methods. Ecol. Evol.* 3, 471–474. doi: 10.1111/j.2041-210x.2012.00190.x

Warton, D. I. (2011). Regularized sandwich estimators for analysis of high-dimensional data using generalized estimating equations. *Biometrics* 67, 116–123. doi: 10.1111/j.1541-0420.2010.01438.x

Warton, D. I., Wright, S. T., and Wang, Y. (2012). Distance-based multivariate analyses confound location and dispersion effects. *Methods. Ecol. Evol.* 3, 89–101. doi: 10.1111/j.2041-210x.2011.00127.x

Willerslev, E., Davison, J., Moora, M., Zobel, M., Coissac, E., Edwards, M. E., et al. (2014). Fifty thousand years of Arctic vegetation and megafaunal diet. *Nature* 506, 47–51.

Willerslev, E., Hansen, A. J., Rønn, R., Brand, T. B., Barnes, I., Wiuf, C., et al. (2004). Long-term persistence of bacterial DNA. *Curr. Biol.* 14, R9–R10.

Zhang, B., Wu, X., Zhang, G., Li, S., Zhang, W., Chen, X., et al. (2016). The diversity and biogeography of the communities of Actinobacteria in the forelands of glaciers at a continental scale. *Environ. Res. Lett.* 11:054012.

Conflict of Interest: The authors declare that the research was conducted in the absence of any commercial or financial relationships that could be construed as a potential conflict of interest.

frontiers in Marine Science

ORIGINAL RESEARCH
published: 08 September 2020
doi: 10.3389/fmars.2020.542563

Terrestrial Inputs Drive Seasonality in Organic Matter and Nutrient Biogeochemistry in a High Arctic Fjord System (Isfjorden, Svalbard)

Maeve McGovern[1,2,3], Alexey K. Pavlov[4,5], Anne Deininger[1,6], Mats A. Granskog[7], Eva Leu[4], Janne E. Søreide[3] and Amanda E. Poste[1]**

[1] Norwegian Institute for Water Research, Oslo, Norway, [2] Department of Arctic and Marine Biology, UiT: The Arctic University of Norway, Tromsø, Norway, [3] University Centre in Svalbard, Longyearbyen, Norway, [4] Akvaplan-niva, Fram Centre, Tromsø, Norway, [5] Institute of Oceanology, Polish Academy of Sciences, Sopot, Poland, [6] Center for Coastal Research, University of Agder, Kristiansand, Norway, [7] Norwegian Polar Institute, Fram Centre, Tromsø, Norway

OPEN ACCESS

Edited by:
Susana Agusti, King Abdullah University of Science and Technology, Saudi Arabia

Reviewed by:
Maria Lund Paulsen, Aarhus University, Denmark
Rainer M. W. Amon, Texas A&M University, United States

***Correspondence:**
Maeve McGovern
maeve.mcgovern@niva.no
Amanda E. Poste
amanda.poste@niva.no

Specialty section:
This article was submitted to Global Change and the Future Ocean, a section of the journal Frontiers in Marine Science

Received: *13 March 2020*
Accepted: *17 August 2020*
Published: *08 September 2020*

Citation:
McGovern M, Pavlov AK, Deininger A, Granskog MA, Leu E, Søreide JE and Poste AE (2020) Terrestrial Inputs Drive Seasonality in Organic Matter and Nutrient Biogeochemistry in a High Arctic Fjord System (Isfjorden, Svalbard). Front. Mar. Sci. 7:542563. doi: 10.3389/fmars.2020.542563

Climate-change driven increases in temperature and precipitation are leading to increased discharge of freshwater and terrestrial material to Arctic coastal ecosystems. These inputs bring sediments, nutrients and organic matter (OM) across the land-ocean interface with a range of implications for coastal ecosystems and biogeochemical cycling. To investigate responses to terrestrial inputs, physicochemical conditions were characterized in a river- and glacier-influenced Arctic fjord system (Isfjorden, Svalbard) from May to August in 2018 and 2019. Our observations revealed a pervasive freshwater footprint in the inner fjord arms, the geochemical properties of which varied spatially and seasonally as the melt season progressed. In June, during the spring freshet, rivers were a source of dissolved organic carbon (DOC; with concentrations up to 1410 μmol L^{-1}). In August, permafrost and glacial-fed meltwater was a source of inorganic nutrients including $NO_2 + NO_3$, with concentrations 12-fold higher in the rivers than in the fjord. While marine OM dominated in May following the spring phytoplankton bloom, terrestrial OM was present throughout Isfjorden in June and August. Results suggest that enhanced land-ocean connectivity could lead to profound changes in the biogeochemistry and ecology of Svalbard fjords. Given the anticipated warming and associated increases in precipitation, permafrost thaw and freshwater discharge, our results highlight the need for more detailed seasonal field sampling in small Arctic catchments and receiving aquatic systems.

Keywords: climate change, coastal biogeochemistry, dissolved organic matter, freshwater inputs, glacier runoff, light climate, permafrost, land-ocean interactions

INTRODUCTION

Recent climate change driven increases in air temperature and precipitation are changing the timing, magnitude and geochemical nature of freshwater runoff with unknown implications for Arctic coastal waters. The observed changes in climate have been distinct in the high-Arctic Svalbard archipelago (e.g., Adakudlu et al., 2019; van Pelt et al., 2019) where marine and

land-terminating glaciers are shrinking in size (van Pelt et al., 2019) and where the upper layer of permafrost, where large amounts of organic carbon are stored (Tarnocai et al., 2009) is warming (Grosse et al., 2016; Biskaborn et al., 2019), and active layer depth is increasing (Christiansen et al., 2005). Together with increased precipitation and freshwater discharge (Peterson et al., 2002; McClelland et al., 2006; Adakudlu et al., 2019), the thawing terrestrial cryosphere is expected to lead to the mobilization and transport of dissolved and particulate organic and inorganic matter from Arctic watersheds to coastal waters (Parmentier et al., 2017).

In central Svalbard, snowmelt typically occurs in June (van Pelt et al., 2016) alongside high river discharge (Hodson et al., 2016). The permafrost active layer is deepest in August (Christiansen et al., 2005), a typically low discharge period (Hodson et al., 2016) when glacial-meltwater has higher residence time in the catchment. Seasonal changes in catchment hydrology have implications for the transport and bioavailability of carbon and nutrients in glacial meltwater on Svalbard (Nowak and Hodson, 2015; Koziol et al., 2019) and elsewhere in the Arctic (Neff et al., 2006; Holmes et al., 2008; Spencer et al., 2008). For example, carbon delivered during spring freshet in Alaskan rivers is more labile compared to aged, microbially reworked carbon delivered later in the summer (Holmes et al., 2008). While seasonal changes in river physicochemistry have been well documented for the Great Arctic rivers (e.g., Holmes et al., 2011), seasonal data from small Arctic catchments are scarce, making it difficult to assess potential impacts on receiving near-shore and coastal waters.

Arctic fjord estuaries are biogeochemical hotspots for the cycling of organic matter (OM) (Bianchi et al., 2020) and burial of carbon (Smith et al., 2015; Bianchi et al., 2018). The fate of terrestrial materials in the marine system is linked to physical and biological processes in the water column. Flocculation and sedimentation at the land-ocean interface (Meslard et al., 2018), and photodegradation and mineralization can act to remove OM from the water column while uptake by coastal biota can integrate terrestrial OM into the marine food-web (Parsons et al., 1989; Harris et al., 2018). Turbid freshwater plumes can also stratify the water column and inhibit nutrient-rich deep water renewal (Torsvik et al., 2019), while also rapidly attenuating light critical for photosynthesis (Murray et al., 2015; Holinde and Zielinski, 2016; Pavlov et al., 2019), with implications for the autotrophic: heterotrophic balance in nearshore areas (Wikner and Andersson, 2012). Despite the rapid warming documented in the high Arctic (IPCC, 2014; Adakudlu et al., 2019), little is known regarding how these changes will affect the quantity and quality of materials transported to and through near-shore, fjord and coastal systems and thus their potential impacts on local and regional biogeochemical cycles (Parmentier et al., 2017).

To address these knowledge gaps, we studied the impacts of inputs from marine terminating glaciers and rivers on light, stratification, nutrient and OM dynamics in Isfjorden (Svalbard). To evaluate seasonal changes in runoff and associated impacts (snow melt vs. glacial melt/permafrost erosion), we targeted three stages of the melt season (1) pre-freshet in May, (2) spring freshet in June, and (3) late-summer runoff in August. Specifically, we aimed to identify the spatial and seasonal response in fjord physicochemical conditions and OM characteristics and evaluate how these might change with the future projected changes in freshwater runoff on Svalbard.

MATERIALS AND METHODS

Sampling Location

Fieldwork took place in 2018 and 2019 in Isfjorden, the largest fjord system on the West coast of Spitsbergen, Svalbard (**Figures 1a,b**). Isfjorden exchanges waters with the west Spitsbergen shelf, where the West Spitsbergen Current (WSC) and the Spitsbergen Polar Current (SPC) bring Atlantic and Arctic waters, which enter the fjord along the southern shore and exit the fjord along the northern coastline (Nilsen et al., 2016; **Figure 1c**). Isfjorden has several fjord arms (e.g., Fraser et al., 2018). Tempelfjorden and Billefjorden and the northern side of Isfjorden have marine terminating glaciers, which are absent from the southern side of Isfjorden, including Adventfjorden (**Figure 1b**). Of the sampled fjord arms, only Billefjorden has a shallow sill (50 m) at the entrance, which typically inhibits water mass exchange with adjacent (or central) parts of Isfjorden (Nilsen et al., 2008). The intrusion of warm and saline Atlantic water from the WSC (Fraser et al., 2018) facilitates the melting of Svalbard glaciers (Luckmann et al., 2015). In turn, runoff from glaciers and rivers contribute to estuarine circulation in the fjord (Torsvik et al., 2019). The rivers sampled in this study have catchments ranging from (55–725 km^2) in size with varying degrees of glacial cover (10–51%; pers. com. Guerrero, 2019).

Sample Collection and Processing

In 2018, samples were collected in May (10th–11th), June (18th–24th), and August (16th–24th), from a total of 17 different stations in Isfjorden along gradients from rivers and glaciers to the outer fjord (**Figure 1a**). The number of stations sampled each month varied due to presence of ice in May (**Figure 1a**), when additional fjord transect stations were sampled at the land-fast ice edge in the fjord arms, and where the innermost stations were not accessible. In 2019, the same sampling techniques were used in Adventfjorden with a higher spatial resolution, during June (15th–17th) and August (7th–9th; **Figure 1b**). Samples were collected from 8 stations in Adventfjorden as well as 2 rivers (Adventelva and Longyearelva). At each fjord station, water samples were collected from up to 5 depths (surface, 2 m, 5 m, 15 m, and 30 m) depending on station depth.

In both sampling years, a CTD profiler (SD204, SAIV A/S or Seabird SBE 911) was used to collect vertical profiles of salinity, temperature and chlorophyll fluorescence. Secchi depth was measured and light measurements were made using optical sensors. In 2018, a PAR cosine-corrected sensor was used to obtain vertical profiles of photosynthetically active radiation (PAR, 400–700 nm) while in 2019, TrioS Ramses ACC-VIS hyperspectral radiometers (one for profiling, one as a surface reference) were used to obtain downwelling planar irradiance profiles. At all stations, water was collected from the surface and 15 m using a Niskin bottle. At stations shallower than 17 m,

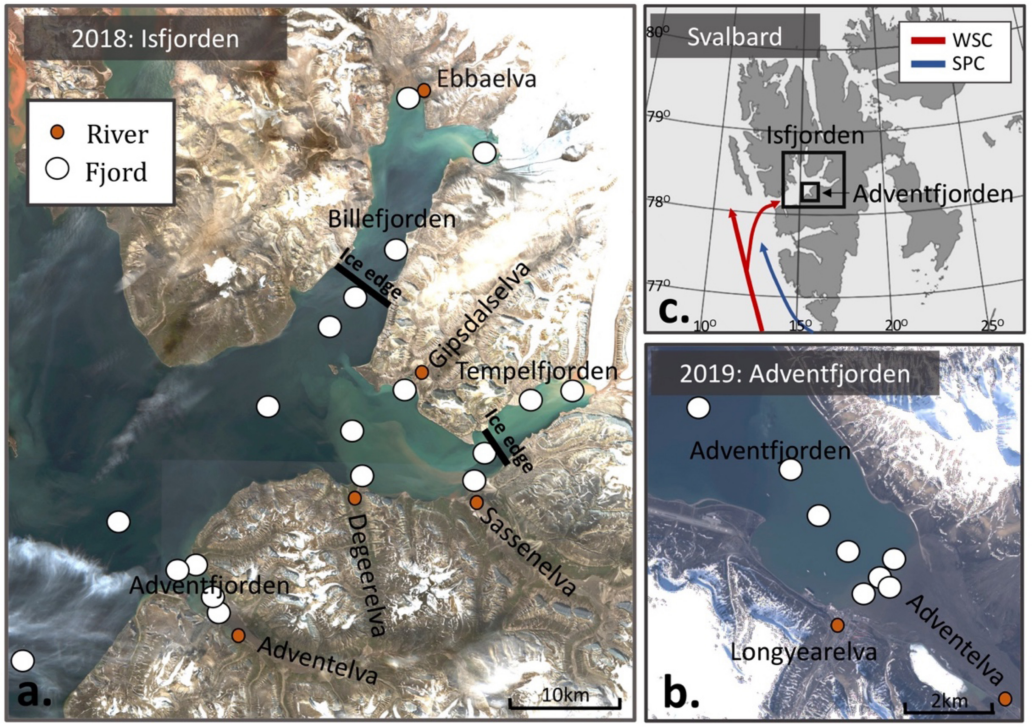

FIGURE 1 | (a) Station map of Isfjorden (sampled in 2018), and **(b)** Adventfjorden (sampled in 2019), superimposed on satellite images taken from the same week as sampling [August 20, 2018 and June 14th, 2019; Sentinel-2 (https://scihub.copernicus.eu/)]. The location of the ice edge in May 2018, when land-fast ice covered the inner fjord arms, is indicated in black. **(c)** Map of Svalbard with the West Spitsbergen Current (WSC) and Spitsbergen Polar Current (SPC) depicted in red and blue respectively.

water was collected from the surface and from 2 m above the bottom. A multiparameter sensor (Hanna instruments, HI 98195) and handheld turbidity meter (Thermo Scientific Eutech TN-100) were used in the field to record temperature, salinity, pH, conductivity and turbidity for each sample in a well-mixed bucket of sample water immediately after collection. Water was collected directly from the Niskin bottle into 20 liter jugs for further processing at the University Centre in Svalbard (UNIS).

Samples for analysis of dissolved organic carbon (DOC), dissolved nutrients [ammonium (NH_4), phosphate (PO_4), nitrite + nitrate ($NO_2 + NO_3$), and silica (SiO_2)] were filtered through 0.2 μm polycarbonate membrane filters and preserved with 4M H_2SO_4 (final concentration of 1% by volume) in 100 mL pre-cleaned amber glass bottles (DOC) or 100 mL acid-washed HDPE bottles (dissolved nutrients). Samples were stored in the dark at 4°C until analysis. For characterization of chromophoric dissolved organic matter (cDOM), water was filtered through 0.2 um polycarbonate filters and stored in 100 mL amber glass bottles in the dark at 4°C. To determine the concentration of suspended particulate matter (SPM), water was filtered onto pre-combusted and pre-weighed glass fiber filters (Whatman GF/F, nominal pore size 0.7 μm). For particulate organic carbon (POC) and particulate nitrogen (PartN) and analysis of stable carbon and nitrogen isotopes (SIA), up to 1.5L of water was filtered onto pre-combusted 25 mm GF/F filters. Particulate phosphorus (PartP) and chlorophyll *a* (Chla) samples were filtered onto a non-combusted GF/F filters. All filters were stored frozen at −20°C until analysis.

Laboratory Analyses

Nutrient, DOC, and PartP analyses were carried out at the Norwegian Institute for Water Research (NIVA, Oslo, Norway) using standard and accredited methods (as described in Kaste et al., 2018). Filters for SPM were dried and reweighed to determine SPM concentrations. Chlorophyll *a* was determined fluorometrically on a Turner 10-AU fluorometer after methanol extraction (Parsons, 2013). Pheophytin was measured on the same samples following acidification with 3 drops of 1M HCl. Stable isotope analysis of particulate organic matter (POM) was carried out at the University of California, Davis (UC Davis Stable Isotope Facility, United States). For PartN, filters were dried and packed into tin capsules for analysis. For POC, filters were fumigated for 24–48 h in a desiccator with concentrated HCl to remove inorganic carbonates prior to encapsulation. $\delta^{13}C$, $\delta^{15}N$, as well as total C and N content were measured using an elemental analyzer interfaced to an isotope ratio mass spectrometer. Run-specific standard deviations at UC Davis were ± 0.09‰ for ^{13}C and 0.05‰ for ^{15}N in 2018 and ± 0.08‰ for ^{13}C and 0.05‰ for ^{15}N in 2019. Stable carbon and nitrogen isotope values are presented using delta notation, relative to international standards (Vienna PeeDee Belemnite for C, and atmospheric N for nitrogen) (Peterson

and Fry, 1987). For analysis of cDOM properties (**Table 1**), absorbance was measured at 1 nm intervals across a wavelength range of 200–900 nm with a Perkin-Elmer Lambda 40P UV/VIS Spectrophotometer using a cuvette with a 5 cm path-length. Absorbance values were blank corrected (Milli-Q) and the average absorbance from 700–900 nm was subtracted from the spectra to correct for possible absorption offset (Helms et al., 2008). Values were converted to Naperian absorption coefficients by multiplying the raw absorbance values by 2.303 and dividing by the pathlength (m) (Hu et al., 2002). Spectral slopes (S) (**Table 1**), which serve as proxies for the composition and source of DOM, with steeper $S_{275-295}$ and increasing slope ratio (S_R; $S_{275-295}$:$S_{350-400}$) indicative of marine, low molecular weight OM (Helms et al., 2008), were calculated from the spectral absorption data. Meanwhile, specific UV absorbance at 254 nm ($SUVA_{254}$), which is positively related to aromaticity of DOM (Weishaar et al., 2003), was calculated by dividing absorbance at 254 nm by the DOC concentration (Weishaar et al., 2003).

Light and Stratification

Spectral irradiance obtained using TriOS Ramses ACC-VIS sensors in 2019 was integrated over the PAR range (400–700 nm). The diffuse attenuation coefficient K_d(PAR) (m-1) was calculated in the top 1 m using the following equation (Kirk, 2010), which assumes the exponential attenuation of light with depth (Beer's Law):

$$K_d(\mathrm{PAR}) = \frac{1}{Z} \ln\left(\frac{E_d(\mathrm{PAR}, 0)}{E_d(\mathrm{PAR}, Z)}\right)$$

where Ed(PAR, 0) and Ed(PAR, Z) represent the downwelling irradiance just below the surface and at depth Z, respectively.

The euphotic depth (Z_{eu}) was calculated as 1% of surface values (just below the water surface) based on irradiance profiles. In cases when Z_{eu} exceeded the station depth, light profiles were extrapolated using the best exponential fit to estimate Z_{eu}.

Freshwater content (FWC) relative to a salinity of 34.7 in the top 10 m was calculated from CTD profiles at all stations using the following equation (Proshutinsky et al., 2009):

$$\mathrm{FWC} = \int_z^0 \frac{\mathrm{Sref} - \mathrm{S}}{\mathrm{Sref}} \mathrm{dz}$$

The reference salinity, S_{ref} is taken as 34.7, which represents the boundary between surface waters and advected waters in Isfjorden (Nilsen et al., 2008). S is the water salinity at depth z. Change in FWC is a measure of how much liquid freshwater has accumulated or been lost from the ocean column bounded by the 34.7 isohaline. In this study, FWC in the surface layer is used as an indicator of degree of freshwater influence in Isfjorden. In addition, a difference in salinity (dS) between the surface and 10 m is used as a simple indicator of water column stratification at the time of sampling.

Data Analysis

All statistical analyses were carried out using R (version 3.4.3, R Core Team, 2017). Temperature-Salinity (TS) diagrams were made using the PlotSvalbard package (Vihtakari, 2019). Water mass determinations were made based on Nilsen et al. (2008); Surface waters (SW) = Sal < 34, T > 1°C, intermediate waters (IW) = 34 < Sal < 34.7, T > 1°C, Atlantic waters (AW) = Sal > 34.9, T > 3°C), transformed Atlantic water (TAW) = Sal > 34.7, T > 1°C, Arctic water (ArW) = 34.4 < Sal < 34.8, −1.5 > T < 1°C, winter cooled

TABLE 1 | Optical characteristics of cDOM based on absorption spectra.

DOM absorption metric	Equation	Interpretation	References
a_{CDOM} (375)	Absorption coefficient (a) at 375 nm	Quantity of cDOM	Stedmon and Markager, 2001
$SUVA_{254}$	a_{CDOM} (254):DOC	Indicates aromaticity of DOM (humic content)	Weishaar et al., 2003
$S_{275-295}$	Non-linear slope of absorption between 275 and 295 nm	High = Marine, Low = Terrestrial	Helms et al., 2008
$S_{350-400}$	Non-linear slope of absorption between 350 and 400 nm	High molecular weight and aromaticity	Helms et al., 2008
S_R	Slope ratio $S_{275-295}$:$S_{350-400}$	Low molecular weight and aromaticity	Helms et al., 2008

TABLE 2 | Key water chemistry parameters (averages ± SD) of river water, fjord surface water (SW), and fjord advected water (AdW) samples from 2018 to 2019 for each month.

Month	Sample	*n*	SPM (mg L^{-1})	$NO_2 + NO_3$ (μmol L^{-1})	PO_4 (μmol L^{-1})	DOC (μmol L^{-1})	POC (μmol L^{-1})	δ^{13}C-POC (‰)
May	River	1	110.5	3.27	0.06	980	205.65	−26.5
	Fjord SW	7	27.1 (± 9.2)	0.36 (± 0.14)	0.11 (± 0.03)	206 (± 170)	28.5 (± 11.0)	−24.0 (± 0.8)
	Fjord AdW	20	32.3 (± 6.8)	0.88 (± 0.96)	0.18 (± 0.07)	161 (± 127)	29.5 (± 5.8)	−23.8 (± 0.8)
June	River	7	348.5 (± 288.0)	7.78 (± 2.56)	0.04 (± 0.03)	604 (± 550)	549.4 (± 604.6)	−26.5 (± 1.1)
	Fjord SW	48	29.4 (± 7.5)	1.27 (± 1.39)	0.44 (± 0.67)	196 (± 193)	41.8 (± 24.2)	−26.2 (± 2.1)
	Fjord AdW	7	26.1 (± 3.5)	0.55 (± 0.26)	0.17 (± 0.05)	139 (± 139)	25.4 (± 11.0)	−27.4 (± 1.3)
August	River	7	170.0 (± 91.6)	12.03 (± 7.45)	0.56 (± 0.67)	43 (± 19)	789.1 (± 1412.5)	−26.5 (± 1.0)
	Ford SW	44	46.5 (± 41.7)	0.93 (± 2.06)	0.22 (± 0.09)	71 (± 17)	65.4 (± 99.9)	−26.4 (± 0.8)
	Fjord AdW	14	24.2 (± 11.3)	0.72 (± 0.45)	0.26 (± 0.07)	77 (± 11)	19.1 (± 8.1)	−27.3 (± 0.9)

A complete overview of measured parameters can be found in ***Supplementary Table S1****.*

water (WCW) = Sal > 34.74, T < −0.5°C) and local water (LW) = T < 1°C. For **Table 2**, discrete waters samples are grouped by fjord surface water (salinity < 34.7) and fjord advected water (salinity ≥ 34.7). Spearman rank correlations were used to evaluate relationships between water chemistry parameters and salinity (**Supplementary Figure S1**).

Redundancy analysis (RDA) was performed on scaled data using the vegan package (Oksanen et al., 2018) to test whether terrestrial inputs explain variation in water chemistry parameters as well as the source and quality of OM. Explanatory variables included salinity, turbidity, temperature and sampling month. To avoid overestimation of the explained variation, constraining variables were selected using forward model selection with a double-stopping criterion (Blanchet et al., 2008). For the water chemistry RDA, salinity, turbidity, temperature and sampling month were chosen via forward selection and all explained a significant amount of variation. For the organic matter RDA, turbidity was not significant, and instead salinity, temperature and sampling month were chosen for the RDA model.

RESULTS

Freshwater Inputs and Seasonal Water Mass Transformation

In May, sampling took place when land-fast ice still covered much of inner Billefjorden and Tempelfjorden (**Figure 1**). Of the six rivers sampled in this study, only one (Adventelva) was running in May, and the water column at all sampling stations comprised of WCW and LW (**Figure 2**). In June and August, freshwater input from all of the rivers, as well as glacial melt and diffuse runoff along the coast, resulted in extensive freshening of surface waters in both years (**Figure 2**). This freshening was accompanied by increased stratification (based on dS) and fresh water content (FWC) between the surface and 10 m in June and August (**Figures 3A,B**). Riverine and glacial inputs delivered high concentrations of SPM to nearshore waters in Isfjorden (**Figure 3D**), resulting in turbid freshwater plumes associated with increased light attenuation, and thus a decreased depth of the euphotic zone (Z_{eu}) in affected areas of the fjord (**Figure 3C**). Meanwhile, in the deeper waters, the intrusion of cold saline ArW and warmer saline TAW from the shelf was observed at the outer Isfjorden stations in June and August (**Figure 2**).

Runoff as a Source of Carbon and Nutrients to Fjord Waters

River samples had high concentrations of carbon early in the melt season (**Figure 4A**). In May, the DOC concentration in Adventelva was 980 μmol L^{-1}. In June, DOC in Adventelva was much lower (40 μmol L^{-1}) while the other rivers sampled had concentrations ranging from 670 to 1410 μmol L^{-1} (average 604 ± 550 μmol L^{-1}; **Table 2**). All rivers had much lower concentrations of DOC in August, similar to those of Adventelva in June (range: 30–80 μmol L^{-1}; average: 43 ± 19 μmol L^{-1}). POC was also highly variable between rivers (**Figure 4B**) and was much higher than concentrations observed for advected water

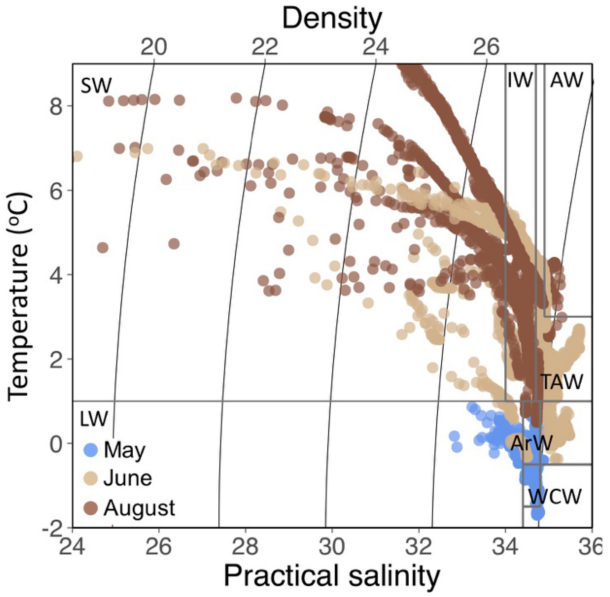

FIGURE 2 | TS diagram based on all CTD profiles by sampling month. Water masses were determined using categories specific to Isfjorden (Nilsen et al., 2008).

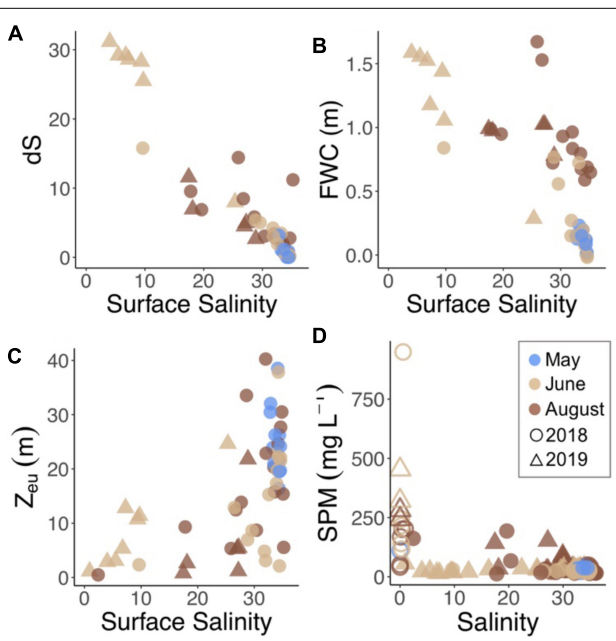

FIGURE 3 | (A) Difference in salinity (dS) between surface and 10 m, **(B)** fresh water content (FWC) between surface and 10 m, **(C)** depth of euphotic zone (Z_{eu}), and **(D)** suspended particulate matter (SPM) by year (symbol) and month (color). River samples are further distinguished by open symbols.

(**Table 2**). Results of δ^{13}C-POC (**Figure 4C**) indicate that marine phytoplankton dominated the particulate matter pool in May during the spring phytoplankton bloom (δ^{13}C: −23.9 ± 0.8‰). Meanwhile, terrestrial carbon dominated POC in June (δ^{13}C:

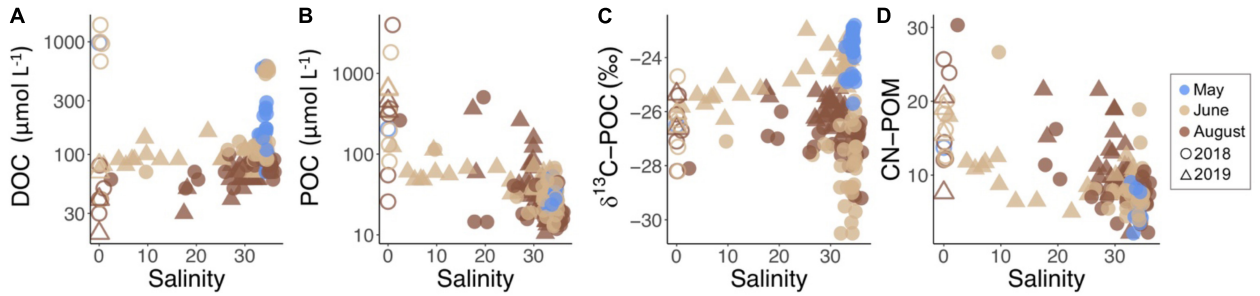

FIGURE 4 | Concentrations of **(A)** DOC, **(B)** POC, and **(C)** δ^{13}C-POC and **(D)** CN ratio of POM vs. salinity for each water sample by year (symbol) and month (color). River samples are further distinguished by open symbols.

-26.4 ± 2.0‰) and August (δ^{13}C: -26.6 ± 0.9‰) at all fjord sampling locations. CN ratios (**Figure 4D**) increased from May to June to August in both the rivers and the water column and decreased across the salinity gradient.

Concentrations of $NO_2 + NO_3$ and SiO_2 were highest in the river samples and decreased across the salinity gradient (**Figure 5**). These nutrients had high spatial and seasonal variability in Isfjorden with increasing concentrations from May to August at the near-shore stations (**Figure 5**). In May, 2018, sampling occurred during the end of the spring bloom. Concentrations of $NO_2 + NO_3$ in surface waters averaged 0.36 ± 0.14 µmol L^{-1} in SW, and 0.88 ± 0.96 µmol L^{-1} in AdW (**Table 2**). In June and August, nutrient concentrations were more strongly related to freshening when rivers and glaciers were a source of dissolved (**Figure 5A**) and particulate (**Figure 5D**) nitrogen (N) to Isfjorden. The partitioning of the N pool between particulate and dissolved phases also varied along the freshwater-marine gradient. In June and August, partN made up 60 ± 23 and 53 ± 28% of the total N pool in river samples and 30 ± 8 and 28 ± 14% in fjord SW and 23 ± 12 and 21 ± 12% of the total N pool in AdW respectively.

Rivers were also a source of phosphorus (P) in August (**Figure 5B** and **Table 2**). Mean concentrations of PO_4 were 0.56 ± 0.67 µmol L^{-1} in river water samples, 0.22 ± 0.09 in fjord SW and 0.26 ± 0.07 µmol L^{-1} in AdW. Rivers had high concentrations of partP in both June and August, which were exponentially higher than concentrations in Fjord SW (**Figure 5E**). Similar to N, P concentrations were higher in the particulate fraction in rivers, but then partitioned more toward the dissolved phase across the salinity gradient. In June and August, partP made up 97 ± 3 and 70 ± 26% of total P in river samples and 38 ± 20 and 42 ± 23% in fjord SW and 19 ± 10 and 19 ± 11% of total P in AdW respectively.

DOM Properties

Seasonal changes in DOM properties overwhelmed spatial differences within the fjord. In May, steep spectral slopes ($S_{275-295}$) and high S_R (**Figure 6**) indicated marine-derived, low molecular weight mDOM in the fjord. In both June and August, DOM properties in fjord waters were consistent between river and glacier-influenced parts of the fjord where low $S_{275-295}$ values indicated the dominance of terrestrially derived OM (**Figure 6**). However, despite terrestrial OM dominating in both freshwater-influenced months, there was a distinct difference between tDOM in June and August, largely driven by differing concentrations of $a_{CDOM}(375)$ and slope ratio (S_R). The higher levels of $a_{CDOM}(375)$ and $S_{350-400}$ in June indicated that terrestrial cDOM dominated the DOM pool at all fjord stations. High concentrations of DOC in several high salinity samples in the outer fjord in June (**Figure 4A**) were accompanied by low values of δ^{13}C (**Figure 4D**), high $S_{350-400}$ (**Figure 6D**), and low S_R (**Figure 6E**) values similar to river samples (**Figure 6F**). Meanwhile, in August, DOM properties reflected a terrestrial (low $S_{275-295}$), aromatic (high $SUVA_{254}$) source of DOM, which was of low molecular weight (high S_R; **Figure 6E**) across all fjord stations.

Results of redundancy analysis illustrated the importance of salinity, turbidity, sampling month and temperature in explaining variation in water chemistry parameters and sampling month, temperature and salinity for explaining variation in OM source and quality in both sampling years (**Figure 7**). Of the constraining variables, salinity and turbidity explained 31% of the total variation in the water chemistry parameters while sampling month explained the greatest amount of variation in the OM dataset (19% of the total variation; **Figure 7**).

DISCUSSION

We observed seasonal changes in organic matter properties and water column structure from May to August along the terrestrial to marine gradient (**Figure 8**). Changes in water column structure can be attributed to two main drivers: freshwater discharge from land and the advection of Atlantic and Arctic water masses from the shelf into the fjord (**Figure 2**). In Isfjorden, the main source of freshwater is from melting marine-terminating glaciers, and river runoff sustained by land-terminating glacial meltwater and snow melt (Nilsen et al., 2008). Meanwhile, TAW and AW, largely driven by local wind conditions, enter the fjord in the deep and subsurface waters from the shelf. These two endmembers (terrestrial inputs and marine advected water) as well as local autochthonous production, represent the main sources of OM and inorganic nutrients to Isfjorden. The terrestrial endmember, represented here by river samples,

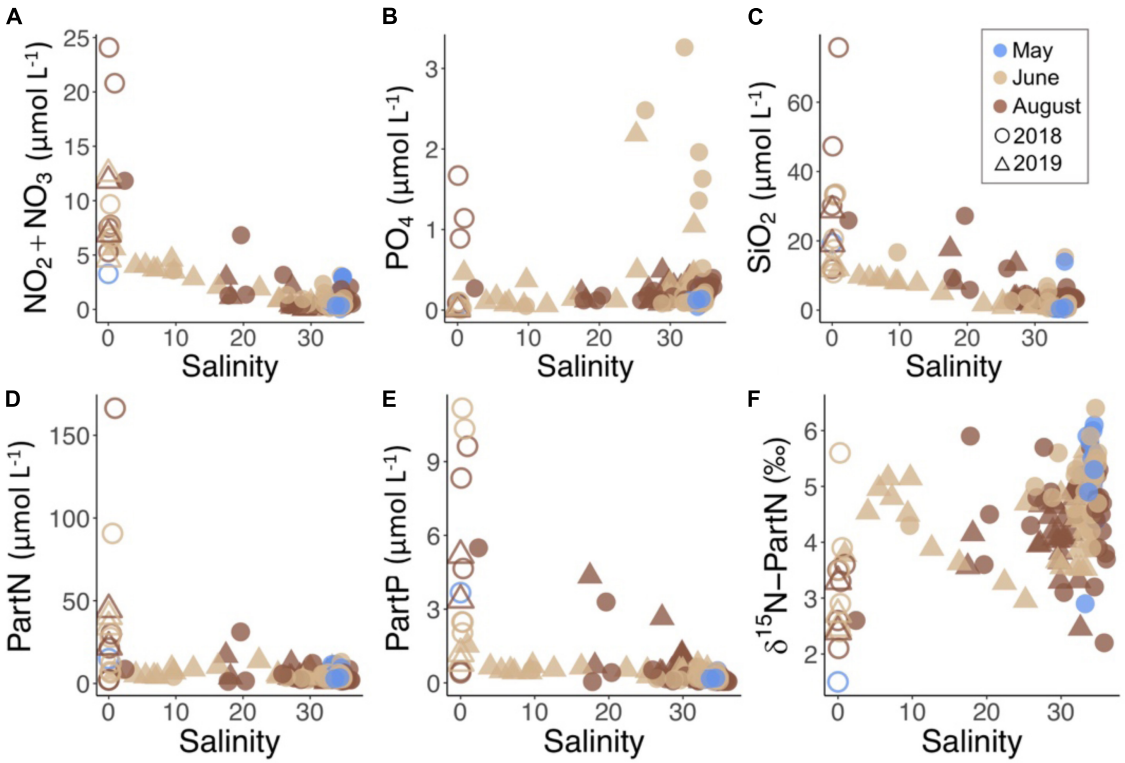

FIGURE 5 | Concentrations of dissolved nutrients **(A)** NO_2 + NO_3, **(B)** PO_4, **(C)** SiO_2 and particulate nutrients **(D)** particulate nitrogen (PartN), **(E)** particulate phosphorus (PartP), and **(F)** δ^{15}N-PartN vs. salinity for each water sample by year (symbol) and month (color). River samples are further distinguished by open symbols.

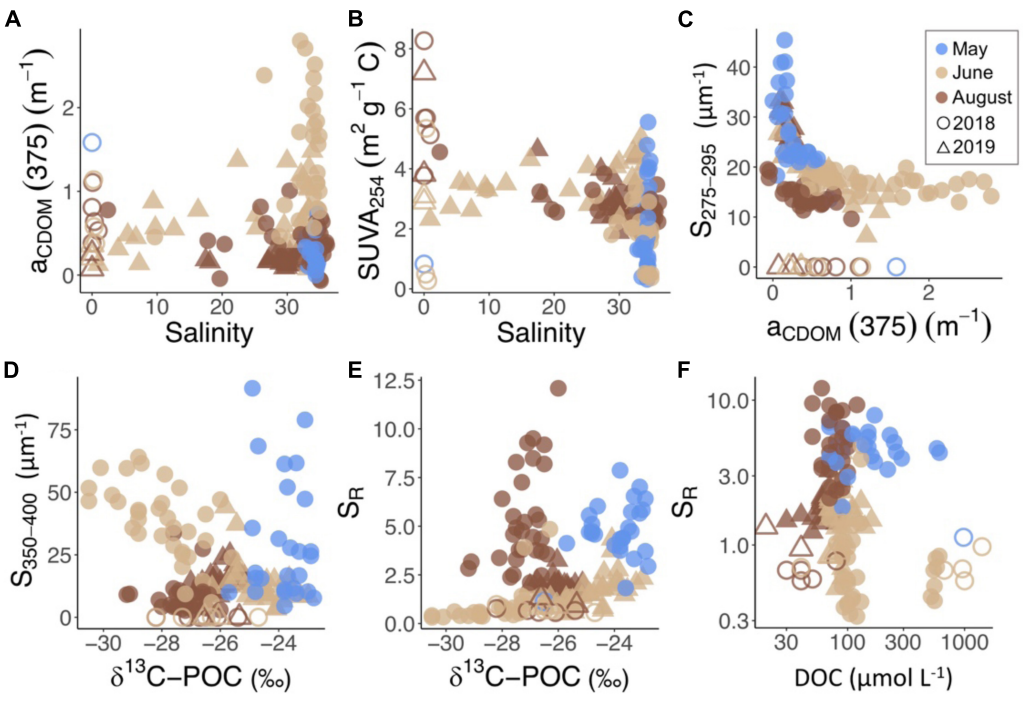

FIGURE 6 | cDOM absorption characteristics including **(A)** a_{CDOM}(375) and **(B)** $SUVA_{254}$ vs. salinity, **(C)** $S_{275-295}$ vs. a_{CDOM}(375) and **(D)** $S_{350-400}$ and **(E)** slope ratio (S_R) vs. δ^{13}C-POC and **(F)** S_R vs. DOC for all water samples by year (symbol) and month (color). River samples are further distinguished by open symbols.

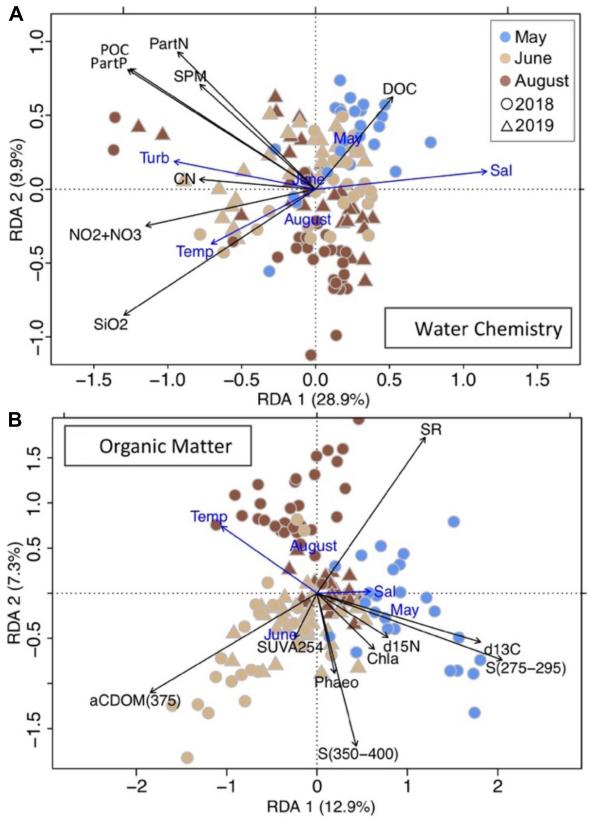

FIGURE 7 | Redundancy analyses (RDA) of **(A)** water chemistry parameters constrained by salinity, turbidity, temperature and sampling month (in blue), and **(B)** organic matter properties constrained by salinity, temperature and sampling month (in blue). Response variables unrelated to main axes ($p > 0.05$) are not shown.

shifted seasonally, with high DOC concentrations in June and high dissolved nutrient ($NO_2 + NO_3$ and PO_4) concentrations measured in August. Thus, from the spring phytoplankton bloom in May to spring freshet in June and late-season melt in August, we observed strong seasonal changes in nutrients and OM properties in the fjord, with potential implications for coastal biogeochemistry and carbon pathways. The fate of these terrestrial carbon and nutrients in the marine system is likely linked to the physical effects of freshwater, including light attenuation and stratification, as well as the bioavailability of the delivered terrestrial material to marine biological communities.

River Water Chemistry Changes Seasonally

Seasonal variation in river water chemistry from May through August reflects changing flow paths in the catchments. River samples collected during the spring freshet in May/June had concentrations of DOC similar to values observed during spring freshet for permafrost dominated catchments in the Siberian and North American Arctic (Holmes et al., 2011; Amon et al., 2012), and much higher than observations from glacier-dominated catchments elsewhere on Svalbard (Zhu et al., 2016) and in Greenland (Paulsen et al., 2017). In fact, concentrations in Sassenelva (a river draining a permafrost-rich valley; **Figure 1**) in June reached 1400 μmol L^{-1} while samples from Gipsdalselva and Ebbaelva (both heavily glaciated catchments) were as high as 670 and 1000 μmol L^{-1}, respectively. Adventelva was the only river with low concentrations of DOC in June (40 μmol L^{-1}), but this river was flowing already in May, with a DOC concentration of 980 μmol L^{-1} at that time (**Table 2**), confirming that the melt progression occurred earlier in Adventdalen. These high concentrations of riverine DOC draining into Isfjorden in June are consistent with other studies in the Arctic that show that approximately half of Arctic river DOC flux occurs during snow melt (Finlay et al., 2006) and high flow events (Rember and Trefry, 2004; Raymond et al., 2007; Raymond and Saiers, 2010; Coch et al., 2018) when surficial and shallow flow paths (Barnes et al., 2018) and high catchment connectivity (Johnston et al., 2019) help to flush modern, plant-derived OM (Feng et al., 2013) into aquatic systems. Permafrost also plays an important role in mobilization and transport of DOC from C-rich surface soils during snowmelt by sustaining near surface water tables and inhibiting deep percolation (Carey, 2003). Moreover, high discharge periods lead to reduced residence time in the catchment, reducing the potential for processing of DOC during transport from the catchment to coastal areas (Koch et al., 2013; Raymond et al., 2016). Thus, the high concentrations of DOC and increased cDOM observed throughout fjord surface waters in June is likely a result of increased transport of terrestrial OM during the spring freshet.

On Svalbard, late-season run-off is driven by glacial melt (Nowak and Hodson, 2015), which was characterized by much lower concentrations of DOC, but higher concentrations of N and P. Decreases in DOC post-freshet has also been found for the Yukon river (Striegl et al., 2005) and Siberian rivers (Neff et al., 2006) as flow paths deepen. Depending on the geology of the catchment, deeper flow paths can potentially drain nutrient-rich mineral soils, transporting N and P to aquatic systems (Barnes et al., 2018). Alternatively, microbial processes, including nitrification, on catchment glaciers have also been linked to N and P -rich meltwater (Hodson et al., 2004; Telling et al., 2011; Wadham et al., 2016). It is estimated that approximately half of glacially exported N is sourced from microbial activity within glacial sediments at the surface and bed of the ice, doubling N fluxes in runoff (Wadham et al., 2016). However, both glacial and soil-derived nutrients may also be heavily sediment bound (P; Hodson et al., 2004), or retained in the catchment through further microbial processing or uptake by terrestrial vegetation (N; Nowak and Hodson, 2015). Even so, concentrations of $NO_2 + NO_3$ in our river samples (sampled close to the river outlet) reached 24 μmol L^{-1} in August, with estuary surface waters still high at 11.8 μmol L^{-1}. Concentrations of PO_4 were also high, reaching 1.7 μmol L^{-1} in river samples in August. These concentrations are higher than concentrations measured from AW advected from the shelf (maximum of 2 μmol L^{-1} for $NO_2 + NO_3$ and 0.4 μmol L^{-1} for PO_4 in this study, but other observations from Svalbard show 6–11 μmol L^{-1} for N and 0.8 μmol L^{-1} for P (Chierici et al., 2019; Halbach et al., 2019). While SiO_2 has been associated with glacial meltwater

from contact with silica-rich bedrock in Isfjorden (Fransson et al., 2015), Kongsfjorden (Halbach et al., 2019) and Greenland fjords (Meire et al., 2016; Kanna et al., 2018; Hendry et al., 2019), N and P have been linked primarily to advected deep water. In contrast to glacial meltwaters in Kongsfjorden (Halbach et al., 2019) and Greenland (Paulsen et al., 2017), the rivers sampled in our study had comparably high concentrations of N and P in addition to SiO_2. While these increased solute concentrations were observed during a relatively low discharge period, the extensive freshwater presence in the fjord in late summer and associated physical effects on the water column could enhance their importance for biological processes.

Physical Effects of Freshwater Runoff Indirectly Affect Fate of Terrestrial OM in Surface Waters

The physical effects of freshwater and suspended sediments associated with glacial and riverine inputs have implications for the fate of terrestrial OM in the marine system. When river inputs meet the coast, the slowing of the current can cause large particles, including sediment-associated particulate nutrients, to settle out of the water column. In addition, increased salinity causes flocculation and sedimentation of finer particles and dissolved components (Sholkovitz, 1976). These processes are reflected in the exponential decrease in SPM, carbon and nutrients from rivers to estuary stations observed in this study. In the Adventelva estuary, this has been known to lead to the rapid removal of 25% of the suspended sediments from surface waters to the benthos, where hyperpycnal flows transport sediment along the bottom (Zajączkowski, 2008). Despite these losses, concentrations of nutrients in terrestrially influenced surface waters were higher than in subsurface fjord waters, which suggests that these nutrients could support excess coastal production.

Freshwater runoff to surface waters combined with warm, saline water masses transported from the shelf in the deeper waters resulted in seasonally increasing stratification throughout Isfjorden in 2018 and 2019 (**Figure 5**). As noted in previous studies, strong stratification weakens vertical mixing of the water column and in extreme cases can prevent bottom water renewal (Boone et al., 2017; Torsvik et al., 2019), which can lead to nutrient limitation, especially when nutrients from advected deep waters are important (Bergeron and Tremblay, 2014; Coupel et al., 2015; Yun et al., 2016; Holding et al., 2019). However, in this study, surface waters were influenced by nutrient-rich terrestrial runoff, so the stratification could be an effective physical barrier keeping these nutrients suspended in the euphotic zone, and thus available for primary production. While the fresh surface layer was very thin (and very fresh) in June, mixing of this layer with deeper water can occur through tidal or wind action (Cottier et al., 2010). In August, the fresh surface layer had mixed with the upper water column, resulting in a higher FWC. The deeper mixed layer in August is likely important for the biological utilization of the associated terrestrial nutrients delivered during this period.

High concentrations of SPM are not unusual for coastal waters influenced by runoff from heavily glaciated catchments, where these particles rapidly attenuate light needed for photosynthesis (Murray et al., 2015; Pavlov et al., 2019). In this study, the shallowest mean euphotic depth was observed at estuary stations, where the rapid attenuation of light (max $K_{d\ PAR}$ in the top 1 m was 5.40 m^{-1}) resulted in euphotic depths of just over 5 m in June, and 1.55 m in August. Meanwhile, the finer particles, which can remain suspended and, in some cases, can be transported several kilometers from the meltwater plumes (Cowan and Powell, 1991; Meslard et al., 2018), are likely responsible for the far-reaching effects on light attenuation, which reached the fjord transect stations in June. At outer fjord stations, the lowest mean K_d(PAR) was 0.27–0.38 m^{-1} in August, which is comparable to K_d(PAR) values previously reported in surface waters of WSC in autumn (Pavlov et al., 2015). These corresponded to mean Z_{eu} exceeding 25–30 m. Thus, in August, increased FWC but reduced turbidity may allow for increased photodegradation of terrestrial OM in surface waters. Thus, the fate of transported terrestrial OM is closely tied to the physical effects of terrestrial runoff. Terrestrial carbon and nutrients can be exported to the sediments when reaching the marine system, or transported further out into the fjord where they are largely confined to the mixed layer due to stratification and could potentially be photodegraded or utilized for primary production where turbidity is low enough that sufficient light is available.

Seasonal Changes in Source and Quality of Organic Matter in Isfjorden

The fate of terrestrial OM in the coastal system is also linked to its nutritional value and bioavailability for microbial communities. The seasonality in OM composition observed in this study is linked to the progression from a spring phytoplankton bloom (before spring freshet) to impacts of terrestrial inputs, the geochemical nature of which shifted from freshet to late summer. These seasonal changes, in both the rivers and the fjord, had strong effects on the quality and quantity of DOM throughout the entire fjord and provide insights into the potential for processing of terrestrial carbon in the water column.

In May, the quantity and quality of OM is related to the spring phytoplankton bloom. Monthly chlorophyll *a* concentrations measured in outer Adventfjorden in 2018 confirm that the spring bloom occurred in early May, roughly a week before the sampling for this study was carried out (Nyeggen, 2019). While the spring bloom was over in the nearshore stations (low concentrations of N and Chl *a*), the outer fjord stations were characterized by high abundances of *Phaeocystis* (pers. com; Dąbrowska, 2020). High $\delta^{13}C$ values indicate that POC was dominated by marine phytoplankton, and DOM properties (**Table 1**) also reflect a predominantly marine source of OM. The high $S_{275-295}$ and S_R (Helms et al., 2008) indicate that this freshly produced marine mDOM is of low molecular weight, and is presumably quite bioavailable to bacterial communities. This is in line with a recent study in Isfjorden which highlighted the importance of marine OM, and ice algae for bacterial production following the spring phytoplankton bloom (Holding et al., 2017).

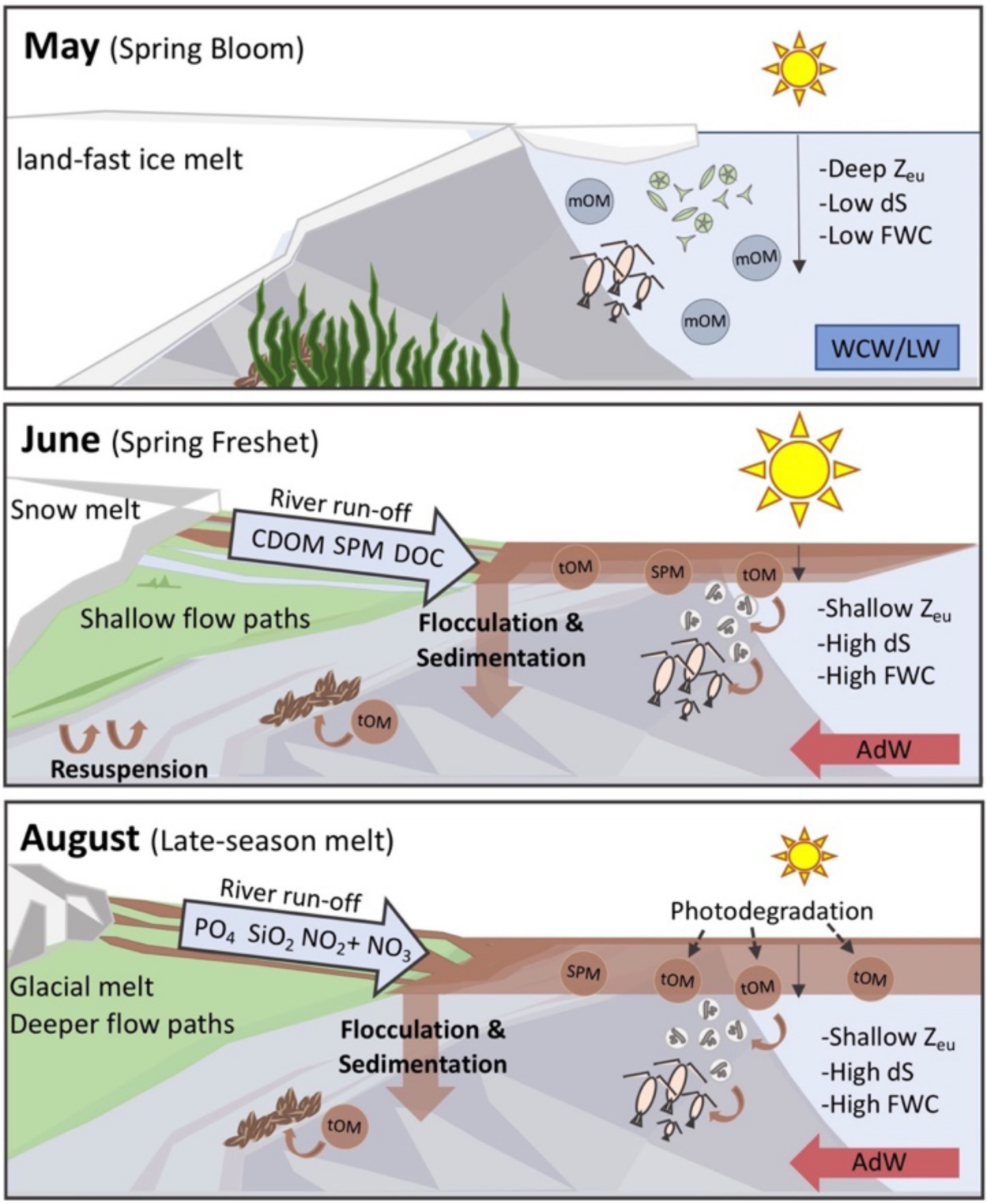

FIGURE 8 | A conceptual diagram summarizing main findings and future perspectives. In May, ice still covered the inner fjord arms of Isfjorden and marine OM (mOM) was present throughout the water column following the spring phytoplankton bloom, when there was a deep euphotic zone (Z_{eu}). The spring freshet in June was a source of terrestrial DOC and SPM to Isfjorden, and while some of these materials were removed from the water column through flocculation and sedimentation, terrestrial OM (tOM) was observed throughout the highly stratified (dS) and turbid fjord surface waters. In August, glacier-fed rivers with deeper flowpaths were a source of nutrients including nitrogen and phosphorus to Isfjorden. Surface waters also had increased fresh water content (FWC) and degraded OM dominated throughout the fjord in August.

Meanwhile, in June, terrestrially derived OM dominated surface waters throughout the fjord. High DOC concentrations in the rivers in June were found alongside increased $a_{CDOM}(375)$ at all fjord stations, even for more saline samples collected from the outer fjord. Results of stable isotope analysis confirm that the POM at the highly turbid estuary and glacier stations was dominated by terrestrial particles. In fact, terrestrially derived POC was present even in the outer fjord. Surprisingly, while δ^{13}C-POC values from river samples ranged from −24 to −28 ‰, estuary and outer fjord stations had values as low as −30.5 ‰ in June, 2018. Studies in Kongsfjorden have also reported similarly low δ^{13}C values for POC (Kędra et al., 2012; Calleja et al., 2017; Jain et al., 2019), which no clear explanation. We suggest that the low δ^{13}C-POC values here could represent the finer organic fraction of terrestrial POC transported farther from glacial fronts and river outlets, or the transport of material from diffuse runoff, coastal erosion and sediment resuspension in the nearshore (Zajączkowski, 2008). While the outer fjord stations were further from the glacier fronts and river outlets, they were still in close proximity to shore (**Figure 1**). The low δ^{15}N values of PartN also imply a terrestrial source of POM (**Figure 5F**). DOM absorption properties for these outer fjord samples with low δ^{13}C-POC further support a terrestrial origin for OM at these sites. As also observed in Kongsfjorden (Calleja et al., 2017), low δ^{13}C values were found alongside steep spectral slopes at the longer wavelengths ($S_{350-400}$) and low S_R (**Figure 6**), both indications of high molecular weight terrestrial material (Weishaar et al., 2003; Helms et al., 2008). On the other hand, Jain et al. (2019), suggest that low δ^{13}C values can also be observed for marine POC on Svalbard, where increased lipids (which are depleted in ^{13}C) due to the presence of cryophytes in the water column, lead to lower δ^{13}C values in the POM. While cryptophytes and other lipid-rich plankton were present in the water column in June, 2018 (pers. com. Dąbrowska, 2020), no relationship was found between lipid content of POM and δ^{13}C values for POC in our dataset (M. McGovern, unpublished data).

In August, river runoff is driven by glacial meltwater, which was characterized by low DOC concentrations, similar to concentrations found in Bayelva in Kongsfjorden (Zhu et al., 2016). DOM absorption characteristics of these samples reflected a terrestrial yet highly aromatic (high $SUVA_{254}$) source of DOM (Weishaar et al., 2003). While a high proportion of ancient, glacial OM can be quite labile (Hood et al., 2009) and thus an important resource for microbial processing as glaciers recede, our study indicates that for Isfjorden, terrestrial OM mobilized during freshet (high concentrations of presumably modern, plant-derived DOM from surficial flowpaths), may be more important when considering coastal processes. In fjord surface waters, DOM absorption characteristics in August indicate that while the DOM was terrestrial (and humic), it was also of low molecular weight. Low S_R values in August are consistent with previously observed changes in DOM properties associated with photochemical or microbial processing in the marine environment (Moran et al., 2000; Granskog et al., 2012; Asmala et al., 2018). In fact, the decrease in $SUVA_{254}$ from river to fjord in August, and in $S_{350-400}$ from June to August in surface waters indicate that photochemical degradation of terrestrial OM, presumably from freshet, could be largely responsible for the observed changes in S_R from June to August (Hansen et al., 2016). This photochemical alteration of DOM from larger molecules to smaller labile photoproducts impacts the potential cycling of DOM (Hansen et al., 2016) in Isfjorden, as it could lead to the removal of DOM by volatilization or microbial utilization (Wetzel et al., 1995; Moran and Zepp, 1997). This is in line with the rapid photodegradation of freshet OM to a more bioavailable form readily remineralized by microbial communities in the Mackenzie delta (Gareis and Lesack, 2018) and Kolyma river basin (Mann et al., 2012), and thus may represent an important pathway driving remineralization of terrestrial OM delivered to Isfjorden during freshet.

Future Perspectives

With air temperatures projected to increase upwards of 10°C by 2100, Svalbard, which is covered by more than 53% glaciers (Nuth et al., 2013), is facing rapid changes (Adakudlu et al., 2019), and the effects are already evident. Pronounced glacier mass loss, changes in precipitation patterns, permafrost warming, and subsequent increases in freshwater runoff have been documented in the last decades (Adakudlu et al., 2019; Błaszczyk et al., 2019; van Pelt et al., 2019) and are expected to continue during this century. The results of this study highlight the spatial and seasonal variability in riverine runoff as a source of OM and inorganic nutrients to Isfjorden, and suggest that in Svalbard, terrestrial DOC inputs could be systematically underestimated due to lack of field sampling during freshet, or following increasingly frequent intense rainfall events (Adakudlu et al., 2019). Since these high DOC concentrations in the river samples are likely due to the flushing of vegetative layer with snow melt, this young terrigenous carbon is presumably semi-bioavailable to fjord microbial communities (Raymond et al., 2007). Moreover, expected increases in vegetative biomass (Myneni et al., 1997; Ju and Masek, 2016) will likely enhance DOC export during periods of high discharge while further permafrost degradation will likely lead to increased POC (Guo and Macdonald, 2006) and nutrient export later in the summer. Higher sediment loads in rivers across the Arctic, including in Adventelva tributaries (Bogen and Bønsnes, 2003) are also expected due to increased erosion with amplified discharge (Syvitski, 2002). Thus, expected future changes in Arctic catchments paired with increased runoff will likely lead to enhanced land-ocean connectivity and increased transport of carbon, nutrients and SPM to coastal areas (**Figure 8**).

In Svalbard fjords, changes in the timing and geochemical nature of freshwater inputs are occurring alongside increases in Atlantic water advection (Spielhagen et al., 2011), and the disappearance of sea-ice (Muckenhuber et al., 2016) and associated ice algae. Thus, increased freshwater inputs are likely to both limit marine production as the turbid melt season may eventually overlap with the spring phytoplankton bloom, while also providing a potential terrestrial carbon subsidy to marine food-webs. With greener catchments and reductions in sea-ice, terrestrial carbon could become increasingly important for coastal zooplankton and benthos, especially in heavily impacted parts of the fjord where increased light attenuation could limit

phytoplankton and macroalgal growth. However, more detailed characterization of the terrestrial DOM pool both seasonally and also between glacial and riverine/permafrost sources is required to better predict the fate of terrestrial material in the marine system. If bioavailable, terrestrial OM can provide heterotrophic bacteria with substrate that allows them to outcompete phytoplankton for nutrients (Sipler et al., 2017), driving shifts in lower food-web structure (Joli et al., 2018; Kellogg et al., 2019) and autotrophic: heterotrophic balance (Wikner and Andersson, 2012). Thus, increasingly persistent and turbid freshwater plumes could lead to changes in basal production, food-web structure and carbon balance in Isfjorden and other Arctic areas facing enhanced land-ocean connectivity (**Figure 8**).

While it's evident that terrestrial inputs have profound physical, chemical and biological implications for the fjord, these freshwater plumes are highly variable in space and time. The spatial extent of freshwater plumes is driven by freshwater discharge, the Coriolis effect, tides, ice cover, and the wind direction and strength (Granskog et al., 2005; Forwick et al., 2010). Observed changes in extent and duration of sea ice in Isfjorden (Muckenhuber et al., 2016), and the expected future reduction in sea ice, will also affect the spatial extent of freshwater plumes (Granskog et al., 2005), especially in spring in combination with earlier snow melt (Adakudlu et al., 2019). However, considering the strong explanatory power of turbidity when constraining physicochemical parameters for both sampling years, our results indicate that the use of ocean color data from satellite or airborne platforms has great potential for assessing and quantifying the spatial extent and associated impacts of terrestrial inputs on coastal surface waters. However, the importance of seasonality for constraining OM quality and quantity also emphasizes the need for high temporal resolution data to capture seasonal changes as well as dynamic local events in the catchments and water column.

CONCLUSION

Seasonality in the magnitude and geochemistry of terrestrial inputs drive strong gradients in light availability, nutrient concentrations, and DOM properties in Isfjorden (**Figure 8**). Large differences between glacial rivers and marine surface water concentrations indicate that flocculation and sedimentation is an efficient removal pathway for particulate and dissolved carbon and nutrients associated with riverine and glacial SPM. Despite high removal at the land-ocean interface, terrestrial OM was observed throughout Isfjorden's surface waters in June and August. The physical effects of freshwater on the water column, including retention of terrestrial carbon and nutrients within the euphotic zone due to stratification, may indicate that riverine OM and inorganic nutrients are particularly biologically relevant in coastal systems where vertical mixing is limited during the most productive season. Seasonal shifts in optical properties of DOM further suggest that the photodegradation of terrestrial OM delivered during the spring freshet could lead to increased bioavailability for microbial communities. Climate-change driven increases in freshwater discharge can be expected to lead to increased suspended sediment loads, and the mobilization and transport of terrestrial carbon and nutrients from thawing and greening watersheds, with important implications for future Arctic coastal ecosystems.

DATA AVAILABILITY STATEMENT

The datasets generated for this study are available on request to the corresponding author.

AUTHOR CONTRIBUTIONS

AEP and MM developed the study design. MM, JS, AEP, and AD carried out fieldwork in 2018 and 2019. AKP performed calculations of K_d, FWC, and dS. MM analyzed the data, made the figures, and wrote the manuscript with contributions from all co-authors. All authors contributed to the article and approved the submitted version.

FUNDING

This research was supported by the Norwegian Research Council (TerrACE; project number: 268458), the Fram Center Flagship "Fjord and Coast" grant (FreshFate; project number 132019), and the Svalbard Science Forum's Arctic Field Grant (RIS number: 10914).

ACKNOWLEDGMENTS

We thank Espen Lund and Emelie Skogsberg for running the cDOM samples and the NIVA lab (especially Anne Luise Ribeiro and Tina Brytensen) for water chemistry analyses. We would like to thank the students and fellow scientists who helped us with the fieldwork including Uta Brandt, Nathalie Carrasco, Ulrike Dietrich, Cathrine Gundersen, Sverre Johansen, Hannah Miller, Sarah Nelson, Emelie Skogsberg, Liv Sletten, Tobias Vonnahme, and Emilie Hernes Vereide. We also thank Laura de Steur for a discussion about freshwater content calculations. Additional gratitude goes to UNIS logistics and the crew of the RV *Helmer Hansen* and *Clione* for their help during the field campaigns.

SUPPLEMENTARY MATERIAL

The Supplementary Material for this article can be found online at: https://www.frontiersin.org/articles/10.3389/fmars.2020.542563/full#supplementary-material

REFERENCES

Adakudlu, M., Andresen, J., Bakke, J., Beldring, S., Benestad, R., Bilt, W., et al. (2019). *Climate in Svalbard 2100 – A Knowledge Base for Climate Adaptation*. Norway: Norwegian Environmental Agency.

Amon, R., Rinehart, A., Duan, S., Louchouarn, P., Prokushkin, A., Guggenberger, G., et al. (2012). Dissolved organic matter sources in large arctic rivers. *Geochim. Cosmochim. Acta* 94, 217–237. doi: 10.1016/j.gca.2012.07.015

Asmala, E., Haraguchi, L., Markager, S., Massicotte, P., Riemann, B., Staehr, P. A., et al. (2018). Eutrophication leads to accumulation of recalcitrant autochthonous organic matter in coastal environment. *Glob. Biogeochem. Cycles* 32, 1673–1687. doi: 10.1029/2017GB005848

Barnes, R. T., Butman, D. E., Wilson, H. F., and Raymond, P. A. (2018). Riverine export of aged carbon driven by flow path depth and residence time. *Environ. Sci. Technol.* 52, 1028–1035. doi: 10.1021/acs.est.7b04717

Bergeron, M., and Tremblay, J.-E. (2014). Shifts in biological productivity inferred from nutrient drawdown in the southern Beaufort Sea (2003–2011) and the northern Baffin Bay (1997–2011), Canadian Arctic. *Geophys. Res. Lett.* 41, 3979–3987. doi: 10.1002/2014GL059649

Bianchi, T. S., Arndt, S., Austin, W. E. N., Benn, D. I., Bertrand, S., Cui, X., et al. (2020). Fjords as aquatic critical zones (ACZs). *Earth Sci. Rev.ews* 203:103145. doi: 10.1016/j.earscirev.2020.103145

Bianchi, T. S., Cui, X., Blair, N. E., Burdige, D. J., Eglinton, T. I., and Galy, V. (2018). Centers of organic carbon burial and oxidation at the land-ocean interface. *Organ. Geochem.* 115, 138–155. doi: 10.1016/j.orggeochem.2017.09.008

Biskaborn, B. K., Smith, S. L., Noetzli, J., Matthes, H., Vieira, G., Streletskiy, D. A., et al. (2019). Permafrost is warming at a global scale. *Nat. Commun.* 10:264. doi: 10.1038/s41467-018-08240-4

Blanchet, F. G., Legendre, P., and Borcard, D. (2008). Forward selection of explanatory variables. *Ecology* 89, 2623–2632. doi: 10.1890/07-0986.1

Błaszczyk, M., Ignatiuk, D., Uszczyk, A., Cielecka-Nowak, K., Grabiec, M., Jania, J. A., et al. (2019). Freshwater input to the Arctic fjord Hornsund (Svalbard). *Polar Res.* 38:3506. doi: 10.33265/polar.v38.3506

Bogen, J., and Bønsnes, T. E. (2003). Erosion and sediment transport in high arctic rivers, Svalbard. *Polar Res.* 22, 175–189. doi: 10.1111/j.1751-8369.2003.tb00106.x

Boone, W., Rysgaard, S., Kirillov, S., Dmitrenko, I., Bendtsen, J., Mortensen, J., et al. (2017). Circulation and fjord-shelf exchange during the ice-covered period in young sound-Tyrolerfjord, Northeast Greenland (74° N). *Estuar. Coast. Shelf Sci.* 194, 205–216. doi: 10.1016/j.ecss.2017.06.021

Calleja, M. L., Kerhervé, P., Bourgeois, S., Kędra, M., Leynaert, A., Devred, E., et al. (2017). Effects of increase glacier discharge on phytoplankton bloom dynamics and pelagic geochemistry in a high Arctic fjord. *Prog. Oceanogr.* 159, 195–210. doi: 10.1016/j.pocean.2017.07.005

Carey, S. K. (2003). Dissolved organic carbon fluxes in a discontinuous permafrost subarctic alpine catchment. *Permafrost Periglac. Process.* 14, 161–171. doi: 10.1002/ppp.444

Chierici, M., Vernet, M., Fransson, A., and Børsheim, K. Y. (2019). Net community production and carbon exchange from winter to summer in the Atlantic water inflow to the Arctic Ocean. *Front. Mar. Sci.* 6:528. doi: 10.3389/fmars.2019.00528

Christiansen, H. H., French, H. M., and Humlum, O. (2005). Permafrost in the Gruve-7 mine, Adventdalen, Svalbard. *Norwegian J. Geogr.* 59, 109–115. doi: 10.1080/00291950510020592

Coch, C., Lamoureux, S. F., Knoblauch, C., Eischeid, I., Fritz, M., Obu, J., et al. (2018). Summer rainfall dissolved organic carbon, solute, and sediment fluxes in a small Arctic coastal catchment on Herschel Island (Yukon Territory, Canada). *Arctic Sci.* 4, 750–780. doi: 10.1139/as-2018-0010

Cottier, F. R., Nilsen, F., Skogseth, R., Tverberg, V., Skarðhamar, J., and Svendsen, H. (2010). Arctic fjords: a review of the oceanographic environment and dominant physical processes. *Geol. Soc. Lond. Spec. Publ.* 344, 35–50. doi: 10.1144/SP344.4

Coupel, P., Ruiz-Pino, D., Sicre, M. A., Chen, J. F., Lee, S. H., Schiffrine, N., et al. (2015). The impact of freshening on phytoplankton production in the Pacific Arctic Ocean. *Prog. Oceanogr.* 131, 113–125. doi: 10.1016/j.pocean.2014.12.003

Cowan, E. A., and Powell, R. D. (1991). "Ice-proximal sediment accumulation rates in a temperate glacial fjord, southeastern Alaska," in *Glacial Marine Sedimentation: Paleoclimatic Significance*, eds J. B. Anderson and G. M. Ashley (Boulder, CO: Geological Society America), 61–73. doi: 10.1130/spe261-p61

Dąbrowska, A. M. (2020). *Institute of Oceanology, Polish Academy of Sciences Sopot, Poland*. Spring: Personal communication.

Feng, X., Vonk, J. E., Van Dongen, B. E., Gustafsson, Ö, Semiletov, I. P., Dudarev, O. V., et al. (2013). Differential mobilization of terrestrial carbon pools in Eurasian Arctic river basins. *Proc. Natl. Acad. Sci. U.S.A.* 110, 14168–14173. doi: 10.1073/pnas.1307031110

Finlay, J., Neff, J., Zimov, S., Davydova, A., and Davydov, S. (2006). Snowmelt dominance of dissolved organic carbon in high-latitude watersheds: implications for characterization and flux of river DOC. *Geophys. Res. Lett.* 33:L10401. doi: 10.1029/2006GL025754

Forwick, M., Vorren, T. O., Hald, M., Korsun, S., Roh, Y., Vogt, C., et al. (2010). Spatial and temporal influence of glaciers and rivers on the sedimentary environment in Sassenfjorden and Tempelfjorden, Spitsbergen. *Geol. Soc. Lond. Spec. Publ.* 344, 163–193. doi: 10.1144/sp344.13

Fransson, A., Chierici, M., Nomura, D., Granskog, M. A., Kristiansen, S., Martma, O., et al. (2015). Effect of glacial drainage water on the CO2 system and ocean acidification state in an Arctic tidewater-glacier fjord during two contrasting years. *J. Geophys. Res. Ocean.* 120, 2413–2429. doi: 10.1002/2014JC010320

Fraser, N. J., Skogseth, R., Nilsen, F., and Inall, M. E. (2018). Circulation and exchange in abroad Arctic fjord using glider-based observations. *Polar Res.* 37:1485417. doi: 10.1080/17518369.2018.1485417

Gareis, J. A., and Lesack, L. F. (2018). Photodegraded dissolved organic matter from peak freshet river discharge as a substrate for bacterial production in a lake-rich great Arctic delta. *Arctic Sci.* 4, 557–583. doi: 10.1139/as-2017-0055

Granskog, M. A., Ehn, J., and Niemelä, M. (2005). Characteristics and potential impacts of under-ice river plumes in the seasonally ice-covered Bothnian Bay (Baltic Sea). *J. Mar. Syst.* 53, 187–196. doi: 10.1016/j.jmarsys.2004.06.005

Granskog, M. A., Stedmon, C. A., Dodd, P. A., Amon, R. M., Pavlov, A. K., de Steur, L., et al. (2012). Characteristics of colored dissolved organic matter (CDOM) in the Arctic outflow in the Fram Strait: assessing the changes and fate of terrigenous CDOM in the Arctic Ocean. *J. Geophys. Res. Oceans* 117:C12021. doi: 10.1029/2012JC008075

Grosse, G., Goetz, S., McGuire, A. D., Romanovsky, V. E., and Schuur, E. A. (2016). Changing permafrost in a warming world and feedbacks to the Earth system. *Environ. Res. Lett.* 11:040201. doi: 10.1088/1748-9326/11/4/040201

Guerrero, J. L. (2019). *Norwegian Institute for Water Research*. Oslo: Personal communication related to Isfjorden catchments.

Guo, L., and Macdonald, R. W. (2006). Source and transport of terrigenous organic matter in the upper Yukon River: evidence from isotope (d13C,D14C, and d15N) composition of dissolved, colloidal, and particulate phases. *Glob. Biogeochem. Cycles* 20:GB2011. doi: 10.1029/2005GB002593

Halbach, L., Assmy, P., Vihtakari, M., Hop, H., Duarte, P., Wold, A., et al. (2019). Tidewater glaciers and bedrock characteristics control the phytoplankton growth environment in an Arctic fjord. *Front. Mar. Sci.* 6:254. doi: 10.3389/fmars.2019.00254

Hansen, A. M., Kraus, T. E. C., Pellerin, B. A., Fleck, J. A., Downing, B. D., Bergamaschi, and B. A. (2016). Optical properties of dissolved organic matter (DOM): effects of biological and photolytic degradation. *Limnol. Oceanogr.* 61, 1015–1032. doi: 10.1002/lno.10270

Harris, C. N., McTigue, N. D., McClelland, J. W., and Dunton, K. H. (2018). Do high Arctic coastal food webs rely on a terrestrial carbon subsidy? *Food Webs* 15, 2352–2496.

Helms, J. R., Stubbins, A., Ritchie, J. D., Minor, E. C., Kieber, D. J., and Mopper, K. (2008). Absorption spectral slopes and slope ratios as indicators of molecular weight, source, and photobleaching of chromophoric dissolved organic matter. *Limnol. Oceanogr.* 53, 955–969. doi: 10.4319/lo.2008.53.3.0955

Hendry, K. R., Huvenne, V. A. I., Robinson, L. F., Annett, A., Badger, M., Jacobel, A. W., et al. (2019). The biogeochemical impact of glacial meltwater from Southwest Greenland. *Prog. Oceanogr.* 176:102126. doi: 10.1016/j.pocean.2019.102126

Hodson, A., Mumford, P., and Lister, D. (2004). Suspended sediment and phosphorus in proglacial rivers: bioavailability and potential impacts upon the P status of ice-marginal receiving waters. *Hydrol. Process.* 18, 2409–2422. doi: 10.1002/hyp.1471

Hodson, A., Nowak, A., and Christiansen, H. (2016). Glacial and periglacial floodplain sediments regulate hydrologic transfer of reactive iron to a high arctic fjord. *Hydrol. Process.* 30, 1219–1229. doi: 10.1002/hyp.10701

Holding, J. M., Duarte, C. M., Delgado-Huertas, A., Soetaert, K., Vonk, J. E., Agustí, S., et al. (2017). Autochthonous and allochthonous contributions of organic carbon to microbial food webs in Svalbard fjords. *Limnol. Oceanography* 62, 1307-1323. doi: 10.1002/lno.10526

Holding, J. M., Markager, S., Juul-Pedersen, T., Paulsen, M. L., Moller, E. F., Meire, L., et al. (2019). Seasonal and spatial patterns of primary production in a high-latitude fjord affected by Greenland Ice Sheet run-off. *Biogeosciences* 16, 3777–3792. doi: 10.5194/bg-16-3777-2019

Holinde, L., and Zielinski, O. (2016). Bio-optical characterization and light availability parameterization in Uummannaq Fjord and Vaigat-Disko Bay (West Greenland). *Ocean Sci.* 12, 117–128. doi: 10.5194/os-12-117-2016

Holmes, R. M., McClelland, J. W., Peterson, B. J., Tank, S. E., Bulygina, E., Eglinton, T. I., et al. (2011). Seasonal and annual fluxes of nutrients and organic matter from large rivers to the Arctic Ocean and surrounding seas. *Estuar. Coasts* 35, 369–382. doi: 10.1007/s12237-011-9386-6

Holmes, R. M., McClelland, J. W., Raymond, P. A., Frazer, B. B., Peterson, B. J., and Stieglitz, M. (2008). Lability of DOC transported by Alaskan rivers to the Arctic Ocean. *Geophys. Res. Lett.* 35:L03402. doi: 10.1029/2007GL032837

Hood, E., Fellman, J., Spencer, R. G. M., Hernes, P. J., Edwards, R., D'Amore, D., et al. (2009). Glaciers as a source of ancient and labile organic matter to the marine environment. *Nature* 462, 1044–1047. doi: 10.1038/nature08580

Hu, C., Muller-Karger, F. E., and Zepp, R. G. (2002). Absorbance, absorption coefficient, and apparent quantum yield: a comment on common ambiguity in the use of these optical concepts. *Limnol. Oceanogr.* 47, 1261–1267. doi: 10.4319/lo.2002.47.4.1261

IPCC (2014). "Climate change 2014: synthesis report," in *Proceedings of the Contribution of Working Groups I, II and III to the Fifth Assessment Report of the Intergovernmental Panel on Climate Change[Core Writing Team]*, eds R. K. Pachauri and L. A. Meyer (Geneva: IPCC).

Jain, A., Krishnan, K. P., Singh, A., Thomas, F. A., Begum, N., Tiwari, M., et al. (2019). Biochemical composition of particles shape particle-attached bacterial community structure in a high Arctic fjord. *Ecol. Indic.* 102, 581–592. doi: 10.1016/j.ecolind.2019.03.015

Johnston, S. E., Bogard, M. J., Rogers, J. A., Butman, A., Striegl, R. G., Dornblaser, et al. (2019). Constraining dissolved organic matter sources and temporal variability in a model sub-Arctic lake. *Biogeochemistry* 146, 271–292. doi: 10.1007/s10533-019-00619-9

Joli, N., Gosselin, M., Ardyna, M., Babin, M., Onda, D. F., Tremblay, J. E., et al. (2018). Need for focus on microbial species following ice melt and changing freshwater regimes in a Janus Arctic Gateway. *Sci. Rep.* 8:9405. doi: 10.1038/s41598-018-27705-6

Ju, J., and Masek, J. G. (2016). The vegetation greenness trend in Canada and US Alaska from 1984–2012 Landsat data. *Remote Sens. Environ.* 176, 1–16. doi: 10.1016/j.rse.2016.01.001

Kanna, N., Sugiyama, S., Ohashi, Y., Sakakibara, D., Fukamachi, Y., and Nomura, D. (2018). Upwelling of macronutrients and dissolved inorganic carbon by a subglacial freshwater driven plume in Bowdoin Fjord, northwestern Greenland. *J. Geophys. Res. Biogeosci.* 123, 1666–1682. doi: 10.1029/2017jg004248

Kaste, Ø, Skarbøvik, E., Greipsland, I., Gundersen, C. B., Austnes, K., Skancke, L. B., et al. (2018). *The Norwegian River Monitoring Programme–Water Quality Status and Trends 2017. NIVA-Repport M-no* 1168. Norway: Miljødirektoratet.

Kędra, M., Kuliński, K., Walkusz, W., and Legeżyńska, J. (2012). The shallow benthic food web structure in the high Arctic does not follow seasonal changes in the surrounding environment. *Estuar. Coast. Shelf Sci.* 114, 183–191. doi: 10.1016/J.ECSS.2012.08.015

Kellogg, C. T. E., McClelland, J. W., Dunton, K. H., and Crump, B. C. (2019). Strong seasonality in arctic estuarine microbial food webs. *Front. Microbiol.* 10:2628. doi: 10.3389/fmicb.2019.02628

Kirk, J. T. O. (2010). *Light and Photosynthesis in Aquatic Ecosystems*. Cambridge: Cambridge University Press.

Koch, J. C., Runkel, R. L., Striegl, R., and McKnight, D. M. (2013). Hydrologic controls on the transport and cycling of carbon and nitrogen in a boreal catchment underlain by continuous permafrost. *J. Geophys. Res. Biogeo.* 118, 698–712. doi: 10.1002/jgrg.20058

Koziol, K. A., Moggridge, H. L., Cook, J. M., and Hodson, A. J. (2019). Organic carbon fluxes of a glacier surface: a case study of Foxfonna, a small Arctic glacier. *Earth Surf. Process. Landf.* 44, 405–416. doi: 10.1002/esp.4501

Luckmann, A., Benn, D. I., Cottier, F., Bevan, S., Nilsen, F., and Inall, M. (2015). Calving rates at tidewater glaciers vary strongly with oceantemperature. *Nat. Comm.* 6:8566. doi: 10.1038/ncomms9566

Mann, P. J., Davydova, A., Zimov, N., Spencer, R. G. M., Davydov, S., Bulygina, E., et al. (2012). Controls on the composition and lability of dissolved organic matter in Siberia's Kolyma River basin. *J. Geophys. Res.* 117:G01028. doi: 10.1029/2011jg001798

McClelland, J. W., Déry, S. J., Peterson, B. J., Holmes, R. M., and Wood, E. F. (2006). A pan-arctic evaluation of changes in river discharge during the latter half of the 20th century. *Geophys. Res. Lett.* 33:L06715. doi: 10.1029/2006gl025753

Meire, L., Mortensen, J., Rysgaard, S., Bendtsen, J., Boone, W., Meire, P., et al. (2016). Spring bloom dynamics in a subarctic fjord influenced by tidewater outlet glaciers (Godthåbsfjord, SW Greenland). *J. Geophys. Res. Biogeosci.* 121, 1581–1592. doi: 10.1002/2015JG003240

Meslard, F., Bourrin, F., Many, G., and Kerhervé, P. (2018). Suspended particle dynamics and fluxes in an Arctic fjord (Kongsfjorden, Svalbard). *Estuar. Coast. Shelf Sci.* 204, 212–224. doi: 10.1016/j.ecss.2018.02.020

Moran, M. A., Sheldon, W. M. Jr., and Zepp, R. G. (2000). Carbon loss and optical property changes during long-term photochemical and biological degradation of estuarine dissolved organic matter. *Limnol. Oceanogr.* 45, 1254–1264. doi: 10.4319/lo.2000.45.6.1254

Moran, M. A., and Zepp, R. G. (1997). Role of photoreactions in the formation of biologically labile compounds from dissolved organic matter. *Limnol. Oceanogr.* 42, 1307–1316. doi: 10.4319/lo.1997.42.6.1307

Muckenhuber, S., Nilsen, F., Korosov, A., and Sandven, S. (2016). Sea ice cover in Isfjorden and Hornsund, Svalbard (2000–2014) from remote sensing data. *Cryosphere* 10, 149–158. doi: 10.5194/tc-10-149-2016

Murray, C., Markager, S., Stedmon, C. A., Juul-Pedersen, T., Sejr, M. K., and Bruhn, A. (2015). The influence of glacial melt water on bio-optical properties in two contrasting Greenlandic fjords. *Estuar. Coast. Shelf Sci.* 163, 72–83. doi: 10.1016/j.ecss.2015.05.041

Myneni, R. B., Keeling, C. D., Tucker, C. J., Asrar, G., and Nemani, R. R. (1997). Increased plant growth in the northern high latitudes from 1981-1991). *Nature* 386, 698–701. doi: 10.1038/386698a0

Neff, J. C., Finaly, J. C., Zimov, S. A., Davydov, S. P., Carrasco, J. J., Schuur, E. A. G., et al. (2006). Seasonal changes in the age and structure of dissolved organic carbon in Siberian rivers and streams. *Geophy. Res. Lett.* 33:L10401. doi: 10.1029/2006GL028222

Nilsen, F., Cottier, F., Skogseth, R., and Mattsson, S. (2008). Fjord-shelf exchanges controlled by ice and brine production: the interannual variation of Atlantic Water in Isfjorden, Svalbard. *Contin. Shelf Res.* 28, 1838–1853. doi: 10.1016/j.csr.2008.04.015

Nilsen, F., Skogseth, R., Vaardal-Lunde, J., and Inall, M. (2016). A simple shelf circulation model: intrusion of Atlantic Water on the West Spitsbergen Shelf. *J. Phys. Oceanogr.* 46, 1209–1230. doi: 10.1175/jpo-d-15-0058.1

Nowak, A., and Hodson, A. (2015). On the biogeochemical response of a glacierized High Arctic watershed to climate change: revealing patterns, processes and heterogeneity among micro-catchments. *Hydrol. Process.* 29, 1588–1603. doi: 10.1002/hyp.10263

Nuth, C., Kohler, J., König, M., von Deschwanden, A., Hagen, J. O., and Kääb, A. (2013). Decadal changes from a multi-temporal glacier inventory of Svalbard. *Cryosphere* 7, 1603–1621. doi: 10.5194/tc-7-1603-2013

Nyeggen, M. U. (2019). *Seasonal Zooplankton Dynamics in Svalbard Coastal Waters: The Shifting Dominance of Mero- and Holoplankton and Timing of Reproduction in Three Species of Copepoda*. Master thesis. Bergen: University of Bergen.

Oksanen, J., Blanchet, F. G., Friendly, M., Kindt, R., Legendre, P., McGlinn, D., et al. (2018). *vegan: Community Ecology Package. R Package Version 2.5-2. 2018*.

Parmentier, F. J. W., Christensen, T. R., Rysgaard, S., Bendtsen, J., Glud, R. N., Else, B., et al. (2017). A synthesis of the arctic terrestrial and marine carbon cycles under pressure from a dwindling cryosphere. *Ambio* 46, S53–S69. doi: 10.1007/s13280-016-0872-8

Parsons, T. R. (2013). *A Manual of Chemical & Biological Methods for Seawater Analysis*. Kent: Elsevier.

Parsons, T. R., Webb, D. G., Rokeby, B. E., Lawrence, M., Hopkey, G., and Chiperzak, D. (1989). Autotrophic and heterotrophic production in the Mackenzie River/Beaufort Sea estuary. *Polar Biol.* 9, 261–266. doi: 10.1007/bf00263774

Paulsen, M. L., Nielsen, S. E. B., Müller, O., Møller, E. F., Stedmon, C. A., Juul-Pedersen, T., et al. (2017). Carbon bioavailability in a high arctic fjord influenced by glacial meltwater, NE Greenland. *Front. Mar. Sci.* 4:176. doi: 10.3389/fmars.2017.00176

Pavlov, A. K., Granskog, M. A., Stedmon, C. A., Ivanov, B. V., Hudson, S. R., and Falk-Petersen, S. (2015). Contrasting optical properties of surface waters across the Fram Strait and its potential biological implications. *J. Mar. Syst.* 143, 62–72. doi: 10.1016/j.jmarsys.2014.11.001

Pavlov, A. K., Leu, E., Hanelt, D., Bartsch, I., Karsten, U., Hudson, S. R., et al. (2019). "The underwater light climate in Kongsfjorden and its ecological implications," in *The Ecosystem of Kongsfjorden, Svalbard*, eds H. Hop and C. Wiencke (Cham: Springer International Publishing), 137–170. doi: 10.1007/978-3-319-46425-1_5

Peterson, B. J., and Fry, B. (1987). Stable isotopes in ecosystem studies. *Annu. Rev. Ecol. Syst.* 18, 293–320. doi: 10.1146/annurev.es.18.110187.001453

Peterson, B. J., Holmes, R. M., McClelland, J. W., Vörösmarty, C. J., Lammers, R. B., Shiklomanov, A. I., et al. (2002). Increasing river discharge to the Arctic Ocean. *Science* 298, 2171–2173. doi: 10.1126/science.1077445

Proshutinsky, A., Krishfield, R., Timmermans, M.-L., Toole, J., Carmack, E., McLaughlin, F., et al. (2009). Beaufort gyre freshwater reservoir: state and variability from observations. *J. Geophys. Res. Oceans* 114:C00A10. doi: 10.1029/2008jc005104

R Core Team (2017). *R: A Language and Environment for Statistical Computing*. Vienna: R Foundation for Statistical Computing.

Raymond, P., Saiers, J., and Sobczak, W. (2016). Hydrological and biogeochemical controls on watershed dissolved organic matter transport: pulse-shunt concept. *Ecology* 97, 5–16. doi: 10.1890/14-1684.1

Raymond, P. A., McClelland, J. W., Holmes, R. M., Zhulidov, A. V., Mull, K., Peterson, B. J., et al. (2007). Flux and age of dissolved organic carbon exported to the Arctic Ocean: a carbon isotopic study of the five largest arctic rivers. *Glob. Biogeochem. Cycles* 21:GB401. doi: 10.1029/2007gb002934

Raymond, P. A., and Saiers, J. E. (2010). Event controlled DOC export from forested watersheds. *Biogeochemistry* 100, 197–209. doi: 10.1007/s10533-010-9416-7

Rember, R. D., and Trefry, J. H. (2004). Increased concentrations of dissolved trace metals and organic carbon during snowmelt in rivers of the Alaskan Arctic. *Geochim. Cosmochim. Acta* 68, 477–489. doi: 10.1016/s0016-7037(03)00458-7

Sholkovitz, E. R. (1976). Flocculation of dissolved organic and inorganic matter during the mixing of river water and seawater. *Geochim. Cosmochim. Acta* 40, 831–845. doi: 10.1016/0016-7037(76)90035-1

Sipler, R. E., Kellogg, C. T. E., Connelly, T. L., Roberts, Q. N., Yager, P. L., and Bronk, D. A. (2017). Microbial community response to terrestrially derived dissolved organic matter in the coastal Arctic. *Front. Microbiol.* 8:1018. doi: 10.3389/fmicb.2017.01018

Smith, R. W., Bianchi, T. S., Allison, M., Savage, C., and Galy, V. (2015). High rates of organic carbon burial in fjord sediments globally. *Nat. Geosci.* 8, 450–U446. doi: 10.1038/ngeo2421

Spencer, R. G. M., Aiken, G. R., Wickland, K. P., Striegl, R. G., and Hernes, P. J. (2008). Seasonal and spatial variability in dissolved organic matter quantity and composition from the Yukon River basin, Alaska. *Glob. Biogeochem. Cycles* 22:GB4002. doi: 10.1029/2008gb003231

Spielhagen, R. F., Werner, K., Sørensen, S. A., Zamelczyk, K., Kandiano, E., Budeus, G., et al. (2011). Enhanced modern heat transfer to the arctic by warm atlantic water. *Science* 331, 450–453. doi: 10.1126/science.1197397

Stedmon, C., and Markager, S. (2001). The optics of chromophoric dissolved organic matter (CDOM) in the Greenland Sea: an algorithm for differentiation between marine and terrestrially derived organic matter. *Limnol. Oceanogr.* 46, 2087–2093. doi: 10.4319/lo.2001.46.8.2087

Striegl, R. G., Aiken, G. R., Dornblaser, M. M., Raymond, P. A., and Wickland, K. P. (2005). A decrease in discharge-normalized DOC export by the Yukon River during summer through autumn. *Geophys. Res. Lett.* 32:L21413. doi: 10.1029/2005GL024413

Syvitski, J. P. M. (2002). Sediment discharge variability in Arctic rivers: implications for a warmer future. *Polar Res.* 21:323. doi: 10.3402/polar.v21i2.6494

Tarnocai, C., Canadell, J. G., Schuur, E. A. G., Kuhry, P., Mazhitova, G., and Zimov, S. (2009). Soil organic carbon pools in the northern circumpolar permafrost region. *Glob. Biogeochem. Cycles* 23:GB2023. doi: 10.1029/2008gb003327

Telling, J., Anesio, A. M., Tranter, M., Irvine-Fynn, T., Hodson, A., Butler, C., et al. (2011). Nitrogen fixation on Arctic glaciers, Svalbard. *J. Geophys. Res. Biogeosci.* 116:G03039. doi: 10.1029/2010jg001632

Torsvik, T., Albretsen, J., Sundfjord, A., Kohler, J., Sandvik, A. D., Skarðhamar, J., et al. (2019). Impact of tidewater glacier retreat on the fjord system: modeling present and future circulation in Kongsfjorden, Svalbard. *Estuar. Coast. Shelf Sci.* 220, 152–165. doi: 10.1016/j.ecss.2019.02.005

van Pelt, W., Pohjola, V. A., Pettersson, R., Marchenko, S., Kohler, J., Luks, B., et al. (2019). A long-term dataset of climatic mass balance, snow conditions, and runoff in Svalbard (1957-2018). *Cryosphere* 13, 2259–2280. doi: 10.5194/tc-13-2259-2019

van Pelt, W. J. J., Pohjola, V. A., and Reijmer, C. H. (2016). The changing impact of snow conditions and refreezing on the mass balance of an idealized Svalbard Glacier. *Front. Earth Sci.* 4:102. doi: 10.3389/feart.2016.00102

Vihtakari, M. (2019). *PlotSvalbard: PlotSvalbard – Plot Research Data From Svalbard on Maps. Rpackage version* 0.8.5.

Wadham, J. L., Hawkings, J., Telling, J., Chandler, D., Alcock, J., O'Donnell, E., et al. (2016). Sources, cycling and export of nitrogen on the Greenland Ice Sheet. *Biogeosciences* 13, 6339–6352. doi: 10.5194/bg-13-6339-2016

Weishaar, J. L., Aiken, G. R., Bergamaschi, B. A., Fram, M. S., Fujii, R., and Mopper, K. (2003). Evaluation of specific ultraviolet absorbance as an indicator of the chemical composition and reactivity of dissolved organic carbon. *Environ. Sci. Technol.* 37, 4702–4708. doi: 10.1021/es030360x

Wetzel, R. G., Hatcher, P. G., and Bianchi, T. S. (1995). Natural photolysis by ultraviolet irradiance of recalcitrant dissolved organic matter to simple substrates for rapid bacterial metabolism. *Limnol. Oceanogr.* 40, 1369–1380. doi: 10.4319/lo.1995.40.8.1369

Wikner, J., and Andersson, A. (2012). Increased freshwater discharge shifts the trophic balance in the coastal zone of the northern Baltic Sea. *Glob. Chang. Biol.* 18, 2509–2519. doi: 10.1111/j.1365-2486.2012.02718.x

Yun, M. S., Whitledge, T. E., Stockwell, D., Son, S. H., Lee, J. H., Park, J. W., et al. (2016). Primary production in the Chukchi Sea with potential effects of freshwater content. *Biogeosciences* 13, 737–749. doi: 10.5194/bg-13-737-2016

Zajączkowski, M. (2008). Sediment supply and fluxes in glacial and outwash fjords, Kongsfjorden and Adventfjorden, Svalbard. *Polish Polar Res.* 29, 59–72.

Zhu, Z., Wu, Y., Liu, S., Wenger, F., Hu, J., Zhang, J., et al. (2016). Organic carbon flux and particulate organic matter composition in Arctic valley glaciers: examples from the Bayelva River and adjacent Kongsfjorden. *Biogeosciences* 13, 975–987. doi: 10.5194/bg-13-975-2016

Conflict of Interest: The authors declare that the research was conducted in the absence of any commercial or financial relationships that could be construed as a potential conflict of interest.

frontiers in Environmental Science

ORIGINAL RESEARCH
published: 10 November 2020
doi: 10.3389/fenvs.2020.548013

On the Role of Biogeochemical Coupling Between Sympagic and Pelagic Ecosystem Compartments for Primary and Secondary Production in the Barents Sea

Déborah Benkort[1], Ute Daewel[1], Michael Heath[2] and Corinna Schrum[1,3]*

[1] Helmholtz-Zentrum Geesthacht, Centre for Materials and Coastal Research, Geesthacht, Germany, [2] Department of Mathematics and Statistics, University of Strathclyde, Glasgow, United Kingdom, [3] Institute of Oceanography, Center for Earth System Research and Sustainability, University of Hamburg, Hamburg, Germany

OPEN ACCESS

Edited by:
Robyn E. Tuerena, Scottish Association For Marine Science, United Kingdom

Reviewed by:
William Gerald Ambrose Jr., Coastal Carolina University, United States
Andrew Mcminn, University of Tasmania, Australia

***Correspondence:**
Déborah Benkort
deborah.benkort@hzg.de;
deborah.benkort@gmail.com

Specialty section:
This article was submitted to Biogeochemical Dynamics, a section of the journal Frontiers in Environmental Science

Received: *01 April 2020*
Accepted: *16 October 2020*
Published: *10 November 2020*

Citation:
Benkort D, Daewel U, Heath M and Schrum C (2020) On the Role of Biogeochemical Coupling Between Sympagic and Pelagic Ecosystem Compartments for Primary and Secondary Production in the Barents Sea. Front. Environ. Sci. 8:548013. doi: 10.3389/fenvs.2020.548013

Primary production in the Arctic marine system is principally due to pelagic phytoplankton. In addition, sea-ice algae also make a contribution and play an important role in food web dynamics. A proper representation of sea-ice algae phenology and the linkage with the pelagic and benthic systems is needed, so as to better understand the ecosystem response to warming and shrinking ice cover. Here we describe the extension of the biogeochemical model ECOSMO II to include a sympagic system in the model formulation, illustrated by implementation in the Barents Sea. The new sympagic system formulation includes four nutrients (NO_3, NH_4, PO_4, and SiO_2), one functional group for sea-ice algae and one detritus pool, and exchanges with the surface ocean layer. We investigated the effects of linkage between the three systems (sympagic, pelagic, and benthic) on the ecosystem dynamic; the contribution of the ice algae to total primary production; and how the changes in ice coverage will affect the lower trophic level Arctic food-web dynamics. To solve the scientific and technical challenges related to the coupling, the model was implemented in a 1D application of the General Ocean Turbulence Model (GOTM). Results showed that the model simulated the seasonal pattern of the sympagic components realistically when compared to the current knowledge of the Barents Sea. Our results show that the sympagic system influences the timing and the amplitude of the pelagic primary and secondary production in the water column. We also demonstrated that sea-ice algae production leads to seeding of pelagic diatoms and an enhancement of the zooplankton production. Finally, we used the model to explain how the interaction between zooplankton and ice algae can control the pelagic primary production in the Barents Sea.

Keywords: biogeochemical model, primary and secondary production, Barents Sea, zooplankton grazing impact, sea-ice algae

INTRODUCTION

The Arctic Ocean is one of the environments experiencing the most severe changes due to ongoing climate change (Anisimov and Fitzharris, 2001; Bennett et al., 2015), exemplified by the extent of summer sea ice retreat (Stroeve and Notz, 2018). The current rate of decrease in summer ice cover is estimated to be 13.5% (Peng and Meier, 2018) per decade, with commensurate changes in ice thickness (Lindsay and Schweiger, 2015). Forecasts predict an Arctic Ocean completely free of ice within 30 years (Wang and Overland, 2012) and possibly by 2030 (Diebold and Rudebusch, 2019). These factors all contribute to an earlier exposure of the ocean surface to the atmosphere in spring and ice-free conditions over a longer season (Stroeve et al., 2012; Meier, 2017). All of these changes impact on the physical and ecological characteristic of the Arctic Ocean (Darnis et al., 2012), and its role in the air-sea interface interaction (Cottier et al., 2017; McPhee, 2017).

Sea ice is an essential component of Arctic ecosystems, acting both as a physical barrier to light, wind and dispersion (Clark et al., 2017; Bouchard et al., 2018), and as a substrate for living organisms. The presence of ice modifies and influences exchanges between the atmosphere and the water column such as nutrient deposition, wind stress, water mixing, and light availability, which in turn affects primary production. Moreover, sea ice represents a habitat for a rich microorganism community, mainly composed of microalgae (Thomas, 2017). Ice algae communities play an important role in Arctic ecosystems by contributing to primary production. Sympagic production contributes 3–25%, and in some regions such as the central Arctic, more than 50% of the total primary production (Legendre et al., 1992; Gosselin et al., 1997; Kohlbach et al., 2016). Ice algae also represent a valuable resource for zooplankton grazers, such as copepods (Runge and Ingram, 1991; Leu et al., 2011), amphipods (Werner, 1997), or krill (Stretch et al., 1988; Kohlbach et al., 2017a). In the Arctic shelves, ice algae can also be a key resource early in the season for benthic organisms when they settle to the seabed after ice melt (Søreide et al., 2013; Schollmeier et al., 2018). Ice algae are important for the phenology of pelagic and benthic organisms which rely on this additional energy source for reproduction and growth in spring (McMahon et al., 2006; Søreide et al., 2010), and have a key role in the benthic communities' structure and dynamic (Kohlbach et al., 2019).

An especially productive Arctic region is the Barents Sea (Sakshaug et al., 2009). In the Barents Sea, sea-ice algae can locally represent around 20% of the total primary production (Hegseth, 1998). However, winter sea ice extent in the Barents Sea has substantially decreased especially since around 1990 (Årthun et al., 2012). Impacts of the sea ice decrease on the primary and secondary production phenology and amplitude remain poorly understood in the Arctic and in the Barents Sea. Some studies already highlight a potential mismatch between ice algae production and zooplankton production and suggest important consequences for the reproduction of copepods (Leu et al., 2011; Dezutter et al., 2019). For example, the reproduction of *Calanus glacialis* has been found to coincide with the spring ice algae bloom while hatching of eggs coincides with the phytoplankton bloom (Søreide et al., 2010). In the Barents Sea around 80% of zooplanktonic biomass consists of copepod species, of which most, such as *C. glacialis* and *Calanus finmarchicus*, can actively feed on sea-ice algae attached to the ice (Runge and Ingram, 1988, 1991), as well as on ice algae released to the water column during the melting process (Michel et al., 1996). While living ice algae cells are important for the zooplankton, dead cells are of relevance for benthic organisms. Few ice algae can survive in the water column and most of them are rapidly exported to the sea floor after ice melt where they contribute to benthic production (Ambrose et al., 2005; Juul-Pedersen et al., 2008; Boetius et al., 2013). Rich in polyunsaturated fatty acids, ice algae represent a valuable food for benthos and play a key role in the detritivorous feed web (McMahon et al., 2006; Sun et al., 2007). For example, Søreide et al. (2013) showed that benthos principally uses particulate organic matter originating from ice algae in the Svalbard region and highlighted that changes in the ice algae production can affect the pelagic and benthic systems. In this context it is essential to thoroughly understand sea-ice algae phenology and its linkage with the pelagic and benthic ecosystems when aiming to identify future changes in the Arctic ecosystem.

Because the Arctic is an extreme environment, *in situ* observations are not readily available and are often limited to the spring-summer season. Under these circumstances numerical models become a tool of choice for studies covering large spatial and temporal scales. In the last 20 years, there have been important improvements in the modeling of sea ice biogeochemistry (Steiner et al., 2016; Vancoppenolle and Tedesco, 2017). First models were developed and parametrized in a 1D framework focusing on specific locations (Arrigo et al., 1993; Lavoie et al., 2005) and particular processes, for example, the complex brine dynamic and nutrient exchange across the ice-ocean interface (Vancoppenolle et al., 2010). These 1D studies were supported by improvements in understanding of the biogeochemistry and dynamic of the Arctic ecosystem (Yakubov et al., 2019). The studies highlighted instances where ice algae could seed pelagic phytoplankton growth and modify the timing of pelagic primary production (Jin et al., 2006, 2007; Tedesco and Vichi, 2010), and how ice algae could control pelagic phytoplankton biomass by competing for nutrients in the surface water (Mortenson et al., 2017). Subsequently, sea ice modeling has been extended to a 3D framework simulating large-scale primary production in the whole Arctic basin (Deal et al., 2011) or more regional area such as the Hudson Bay System (Sibert et al., 2010). In spite of these recent improvements in the biogeochemical modeling, the linkages between the sympagic, pelagic and benthic systems are still poorly represented.

In order to improve knowledge and understanding of the linkage between the sympagic, pelagic and benthic ecosystems, we present here an enhanced version of the biogeochemical model ECOSMO II (Daewel and Schrum, 2013) implemented for the Barents Sea, to include a fully coupled sympagic system. With recent developments of the ECOSMO-E2E (Daewel et al., 2019), the model will then later allow us to explore ecosystem dynamic including predators such as fishes and macrobenthos. These two components (fish and macrobenthos) are dependent

on high-quality sea-ice algae food source (Sun et al., 2009; Søreide et al., 2013) and should be linked to the sympagic system to accurately represent Arctic ecosystem dynamic. We used the model in a 1D application to comparatively assess three characteristic regions of the Barents Sea and investigated (1) the importance of linkages between the pelagic and the sympagic systems for ecosystem dynamics; (2) the relative contribution of the ice algae on the total primary and secondary production; and (3) how variability in ice coverage affects Arctic food-web dynamics.

MATERIALS AND METHODS

We present here a new version of the ECOSMO II (Daewel et al., 2019) model including a new sympagic (sea-ice biogeochemistry) module and its application to the Barents Sea region. The biogeochemical model was built with the Fortran-based Framework for Aquatic Biogeochemical Models (FABM) (Bruggeman and Bolding, 2014) in order to facilitate coupling to the physical model described below (section *Physical model and forcing data*). Here we work in a 1D numerical framework, which allows model parameterization, verification, sensitivity tests to study process level with a low computation effort without add complex hydrodynamic processes. Therefore, this approach neglects horizontal transport and only take into account vertical exchange processes.

Model Description

Physical Model and Forcing Data

Physical processes in the water column are calculated by the 1D General Ocean Turbulence Model (GOTM) (Burchard et al., 1999). The simulation resolves the profiles of velocities, temperature, salinity, turbulent mixing, and transport of ecosystem state variables in 50 vertical layers. The physical environment affects the ecosystem dynamics, while an ecosystem feedback to the physics, e.g., heating or albedo is switched off. Photosynthetically available radiation is calculated based on the ecosystem tracers in water and ice as described below. At the surface, the model is forced with atmospheric conditions from the NCEP-R2 reanalysis [NCEP-DOE AMIP-II Reanalysis (R-2); Kanamitsu et al., 2002], and sea ice thickness, sea ice concentration and snow thickness are prescribed from a hindcast simulation with the HYCOM (HYbrid Coordinate Ocean Model) (Bleck, 2002) using a setup based on a model version described in Samuelsen et al. (2015). Tidal currents are prescribed M2 and S2 components of the horizontal velocity in order to parameterize tidal mixing and a spring-neap cycle. Tidal variability of the sea surface elevation is neglected for the present study. Physical conditions are initialized from the World Ocean Atlas v2013 (Boyer et al., 2013), which is also used for a filtered restoring of salinities to the climatological conditions in order to parameterize horizontal fluxes of fresh water. The ecosystem model dynamics are coupled with the FABM framework (Bruggeman and Bolding, 2014) into the 1D model, integrated with a third-order Runge–Kutta ODE solver (Schober et al., 2014), and transported in the vertical due to sinking, vertical advection, and turbulent mixing. The 1D model framework provides a consistent scheme for the analysis of ice-ocean ecosystem exchange fluxes, while horizontal triggers are included only through nudging of salinities and forcing with ice conditions.

Biogeochemical Sea Ice Processes

The ECOSMO II model (Schrum et al., 2006; Daewel and Schrum, 2013), including pelagic and benthic biological and geochemical components, has been adapted here for the Arctic ecosystem. One of the most important characteristics of the Arctic ecosystem is the presence of a sea ice cover and the associated microbial communities, forming a sympagic system (Thomas, 2017). To make the existing ecosystem model applicable to the Arctic, a sympagic system model is required that allows online coupling to the existing model for the pelagic and benthic systems. To achieve this, we added six state variables to the original ECOSMO II model framework, accounting for: one sea-ice algae functional group (*IA*), four nutrients variables (phosphate PO_4, nitrate NO_3, ammonium NH_4, and silicate SiO_2), and one detritus variable (ID) (**Figure 1**).

Arctic sea ice supports a highly diverse microbial community (Arrigo, 2014; Thomas, 2017). Many species of algae bloom in succession throughout the annual season (Hegseth, 1992; Ambrose et al., 2005). Several studies have emphasized the dominance of diatoms (Werner et al., 2007), especially *Nitzschia frigida* and *Melosira arctica* (Horner and Alexander, 1972; Gosselin et al., 1997). However, the ECOSMO II model represents functional groups instead of species, and the entire ice algae community approach is represented by a single state variable. Following the assumption that diatoms are dominant in the system, the group processes are parametrized for diatom species.

Similar to the pelagic environment, ice algae dynamics are influenced by various abiotic and biotic factors such as temperature, salinity, light, nutrients, and consumption by microorganisms (Arrigo et al., 1993; Werner, 1997; Arrigo, 2014; Galindo et al., 2017; Oziel et al., 2019). The rate of change in the ice algae biomass is calculated as follows:

$$\frac{\partial IA}{\partial t} = \sigma\,[IA] - \mathrm{M}\,[IA] - G\,[IA] + G_{\mathrm{ice\_flux}}[IA] \qquad (1)$$

where *IA* is the sea-ice algae biomass in mgC m^{-2}. The first term in Eq. 1 represents the gross primary production of ice algae, the second and third term account for the loss of ice algae and the fourth term parametrizes the exchange between ice and water column. The ice algae growth σ depends on the ambient temperature and salinity of brine in the cracks and channels in the ice and can be limited by light and nutrient. We assume a single limiting factor approach rather than multiplicative limitation, such that the specific growth rate is given by:

$$\sigma\,[IA] = \left(\sigma_{\max} \times\ f_T \times f_S \times \min\left(N_{\lim},\ L_{\lim}\right)\right) \times\ [IA] \qquad (2)$$

Where $\sigma_{\max}$ is the maximum growth rate (**Table 1**). f_T and f_S are respectively, the temperature and salinity dependence of the sea-ice algae growth, and $N_{\lim}$ and $L_{\lim}$ account for nutrient and light limitation respectively. Laboratory experiments have

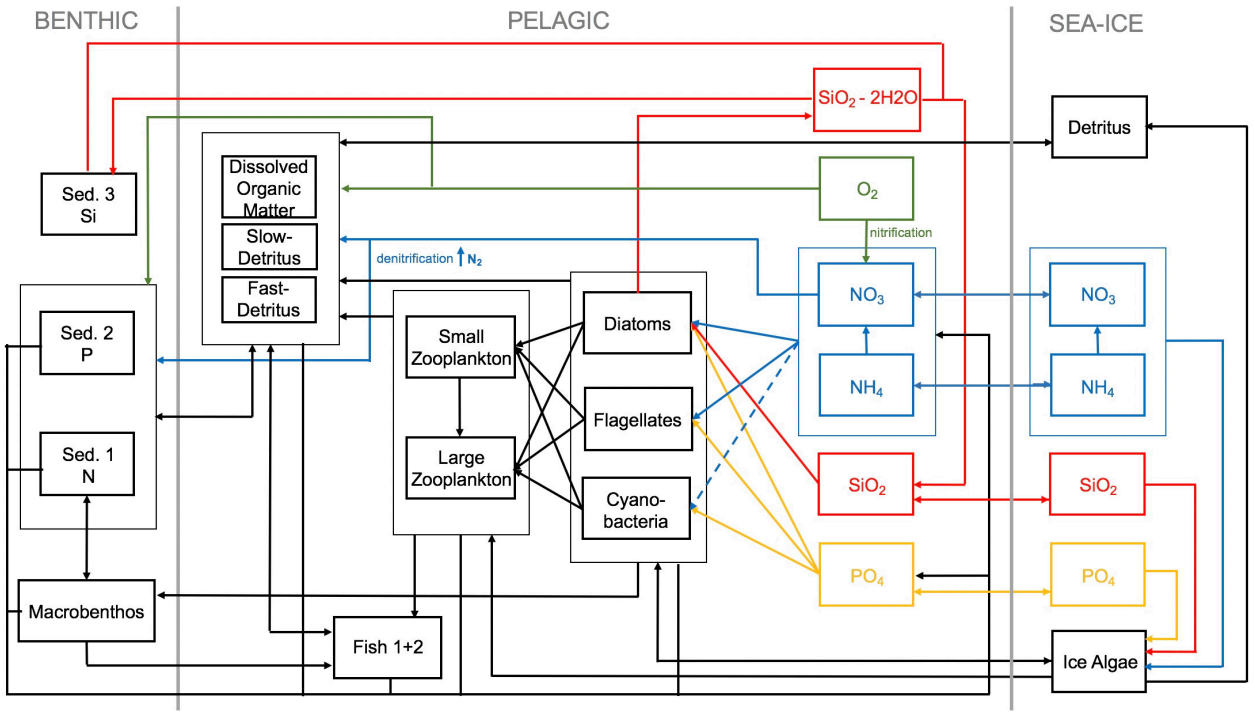

FIGURE 1 | Schematic diagram of the coupled sea-ice ocean model ECOSMO-E2E. The three system (benthic, pelagic, and sympagic) are included. Sed. 1, nitrate/carbon sediment pool; Sed. 2, phosphate sediment pool; Sed. 3, silicate sediment pool.

shown that algal growth is influenced by these two factors especially when salinities reach high values in the brine (Arrigo and Sullivan, 1992). According to Vancoppenolle and Tedesco (2017) temperature and salinity dependencies are expressed as following:

$$f_T = e^{r_g \times T} \tag{3}$$

TABLE 1 | List of parameters, corresponding description, and units used in the model for ice algae dynamic.

Abbreviation	Definition	Value	Units
σ_{max}	Maximum growth rate	0.86	day^{-1}
r_g	Temperature sensitivity coefficient	0.0633	$°C^{-1}$
$K_{s(N)}$	Half-saturation constant for nitrogen	1.6	mmol N m^{-3}
$K_{s(Si)}$	Half-saturation constant for silicate	3.9	mmol Si m^{-3}
$K_{s(P)}$	Half-saturation constant for phosphorus	0.24	mmol P m^{-3}
α_p	Photosynthesis efficiency	0.08	mgC (mgchl $a)^{-1}$ h^{-1} (Einst m^{-1} $s^{-1})^{-1}$
P_m	Maximum photosynthetic rate	0.28	mgC (mgchl $a)^{-1}$ h^{-1}
rM	Ice algae mortality rate	0.05	day^{-1}
rG	Grazing rate	0.086	day^{-1}
f_{dia}	Fraction of diatom which survive inside the ice	0.50	Unitless

$$f_S = e^{-\left(2.16 - 8.310^{-5} \times S^{2.11} - 0.55 \times \ln(S)\right)^2} \tag{4}$$

The terms T and S are, respectively, the ambient temperature in °C and salinity, r_g is the temperature sensitivity coefficient (**Table 1**). The availability of light and nutrients are the two main factors limiting the ice algae growth with different seasonal relevance (during the polar night in winter for light, and during the summer season for nutrients). The ice algae growth is therefore limited by the four nutrients (NO_3, NH_4, PO_4, and SiO_2) following a Monod-formulation (Monod, 1949). Even though nutrient stoichiometry inside the ice algae is known to be variable, we assume a fixed Redfield stoichiometry (Vancoppenolle and Tedesco, 2017; Selz et al., 2018).

$$N_{\lim} = \frac{N_i}{N_i + K_{S_{(i)}}} \tag{5}$$

where N_i is the concentration of a specific nutrient (NO_3, NH_4, PO_4, and SiO_2) in the sea ice in mmol m^{-2}, and $K_s(i)$ is the half-saturation constant of the nutrient. *Ks* values for each nutrient are taken from Sarthou et al. (2005) (see **Table 1**). Light limitation follows a hyperbolic tangent function as described in previous studies (Lavoie et al., 2005; Tian, 2006; Castellani et al., 2017):

$$L_{\lim} = 1 - e^{\frac{\alpha_p \, PAR}{Pm}} \tag{6}$$

where *PAR* (photosynthetically active radiation) is the light available for ice algal photosynthesis, α_p is the photosynthetic

efficiency and P_m is the maximum photosynthetic rate. Values and units for α and P_m (**Table 1**) are taken from Castellani et al. (2017).

The second term in Eq. 1 correspond to the mortality loss term in mgC m^{-2}. Loss of ice algae includes losses due to lysis, exudation and respiration and is given as a constant loss rate, *rM* (**Table 1**; Lavoie et al., 2005; Vancoppenolle and Tedesco, 2017).

$$M\,[IA] = rM \times [IA] \tag{7}$$

The third term in Eq. 1 refers to the loss of ice algae by zooplankton grazing. Little is known about the grazing on ice algae, but observational evidence highlights the importance of carbon pathways from ice algae to zooplankton in Arctic ecosystems (Michel et al., 1996). Even though ice algae can be grazed inside the ice matrix (Gradinger et al., 1999), Michel et al. (2002) concludes that the ice grazing constitutes only a minor proportion of the ice algae loss. Therefore we consider grazing by pelagic grazers only following previous modeling approaches assuming a constant uptake rate by pelagic grazers, *rG* (**Table 1**; Lavoie et al., 2005; Tedesco, 2014).

$$G\,[IA] = rG \times [IA] \tag{8}$$

This simplified consideration of zooplankton grazing is justifiable as ice algae concentrations are generally relatively low and, during the ice algae bloom, ice algae constitute almost the only food source for zooplankton in the model and prey selectivity can be neglected.

The fourth term in Eq. 1 refers to the exchange at the sea ice/ocean interface and it depends on rate of change of sea ice thickness $\frac{dH_i}{dt}$.This term is positive during sea-ice growth and negative during sea ice melt.

$$\begin{aligned} G_{\text{ice\_flux}}\,[IA] &= \max\left(0.0,\ \frac{dH_i}{dt}\right) \times \max\left(0.0,\ f_{\text{dia}} \times \text{Dia}\ \right) \times \frac{\rho_{\text{ice}}}{\rho_{\text{water}}} \\ &+\ \min\left(0.0,\ \frac{dH_i}{dt}/H_i\right) \times \max\left(0.0,\ \ [IA]\right) \end{aligned} \tag{9}$$

where Dia is diatom concentration in mgC m^{-3}, and ρ_{ice} and ρ_{water} the density of ice and sea water respectively. Even though the sympagic and the pelagic diatom communities feature some similarities they are different in structure. It has been shown that the main source of the ice algae communities stem from the water column, the benthic system and the sea ice itself, but the origin, the amount and the seasonality of the ice algae origin is still unclear (Kauko et al., 2018). It seems, however, sensible to consider that not all the algae entrapped during sea ice formation are adapted to survive inside the sea ice. Therefore, we advance the assumption that the quantity of algae entering in the sympagic system is controlled by a factor f_{dia} (Table1), corresponding to the fraction of algae which continue to develop after being entrapped in the ice. As pelagic algae are not the only source of ice algae in the sea ice, we fixed a minimum threshold of ice algae in the ice (0.01 mgC m^{-2}), to avoid a complete depletion during winter and to decrease the delay of the ice algae bloom at spring. The remaining part does not survive and contributes directly to the sea-ice detritus pool. Because of the lack of observations and knowledge, we arbitrary set this value at 0.5, after a sensitivity analysis (see section "Results: Role of Sympagic System: Implementation, Verification and Sensitivity").

TABLE 2 | List of parameters, corresponding description, and units used in the model for nutrients dynamic.

Abbreviation	Definition	Value	Units
e	Brine fraction in the sea ice layer	0.5	Unitless
K_{wi}	Molecular diffusion coefficient	4.7×10^{-8}	$m^2\ s^{-1}$
ρ_{ice}	Density of sea ice	900	kg m^{-3}
ρ_{water}	Density of seawater	1026	kg m^{-3}
v_n	Half-saturation constant for preferential uptake of nitrate	0.2	mmol N m^{-3}
r_{nit}	Nitrification rate	0.01	day^{-1}
ε_D	D remineralization rate	0.01	day^{-1}
ε_{Si}	SiO_2 remineralization rate	0.01	day^{-1}

The rate of change in the ice detritus biomass is calculated as follows:

$$\frac{\partial ID}{\partial t} = M\,[IA] - (\varepsilon_D \times [ID]) \ +\ G_{\text{ice\_flux}}[ID] \tag{10}$$

where *ID* is the sea-ice detritus biomass in mgC m^{-2}. The first term in Eq. 10 represents the loss of ice algae, the second term account for the remineralization process, with a constant remineralization rate ε_D (**Table 2**). The third term parametrizes the exchange between ice and water column.

As for ice algae, the exchange at the sea ice/ocean interface and it depends on rate of change of sea ice thickness $\frac{dH_i}{dt}$.This term is positive during sea-ice growth and negative during sea ice melt.

$$\begin{aligned} G_{\text{ice\_flux}}\,[ID] &= \max\left(0.0,\ \frac{dH_i}{dt}\right) \times \max\left(0.0,\ D_f\ \right) \times \frac{\rho_{\text{ice}}}{\rho_{\text{water}}} \\ &+\ \max\left(0.0,\ \frac{dH_i}{dt}\right) \times \max\left(0.0,\ (1-f_{\text{dia}}) \times \text{Dia}\ \right) \times \frac{\rho_{\text{ice}}}{\rho_{\text{water}}} \\ &+\ \min\left(0.0,\ \frac{dH_i}{dt}/H_i\right) \times \max\left(0.0,\ \ [ID]\right) \end{aligned} \tag{11}$$

where D_f is fast sinking detritus concentration in mgC m^{-3}.

Nutrient Dynamics

Inside sea ice, biological communities exist within a complex network of brine channels, extending into the ice layer, with brine volume varying according to the thermohaline characteristics of the ice. Brine volumes are at maximum in the first few centimeters from the ice-ocean interface (Arrigo, 2014; Thomas, 2017), and this is mainly where biological activity is concentrated (Tedesco, 2014). In this present study, we follow an approach suggested in earlier modeling studies (Arrigo et al., 1993; Duarte et al., 2015). Thus, instead of considering a complex brine network dynamic, we assume a bottom layer with biological activity with about 5 cm thickness. The relative brine volume *e* in this layer is assumed to be 50% ($e = 0.5$) as suggested by Duarte et al. (2015).

The ice-ocean interface is a dynamic area where exchanges of salt, organic, and inorganic material occur between the two systems (sympagic and pelagic), determining the salinity and nutrient, detritus, and algae concentrations in the sea ice and the water body below. Exchanges occur due to convection, diffusion, ice formation, and ice melting processes (Vancoppenolle et al.,

2010; Arrigo, 2014). In the absence of biological activity, it is customary to consider the dynamics of the majority of macro-elements in sea ice following the same dynamical changes as salinity. Meaning that, during the formation of sea ice crystalline lattice impurities and salt are not entrapped in the structure and nutrients and other components are as well rejected in the brines network where they will exchange with the water underneath.

The bulk formulation N_i^{bk} for each of the aforementioned types of nutrients i is characterized as follows (Belém, 2002; Vancoppenolle et al., 2010):

$$N_i^{bk} = e \times N_i^{br} \tag{12}$$

where N_i^{br} is the nutrient content for nutrient i in the brine (mmol m^{-2}) and e is the brine volume fraction (**Table 2**). Ammonia is an exception to this rule, being entrapped in the crystalline lattice of the ice and expelled to the brine channels (Weeks, 2010; Vancoppenolle et al., 2013). Therefore, the brine concentration of ammonia, unlike the other nutrients, is equal to the bulk mass of ammonia. The rate of change of the respective nutrients in the brine is described as Duarte et al. (2015):

$$\frac{\partial N_{NO_3}^{br}}{\partial t} = Br_{\text{flux}} + G_{\text{ice\_flux}} - \sigma\,[IA]\; p_{NO_3} \frac{\left[N_{NO_3}^{br}\right]}{[N_{NO_3}^{br}] + [N_{NH_4}^{br}]} + r_{nit}[N_{NH_4}^{br}] \tag{13}$$

$$\frac{\partial N_{NH_4}^{br}}{\partial t} = Br_{\text{flux}} + G_{\text{ice\_flux}} - \sigma\,[IA]\;\left(1 - p_{NO_3}\right) \frac{\left[N_{NO_3}^{br}\right]}{[N_{NO_3}^{br}] + [N_{NH_4}^{br}]} - r_{nit}[N_{NH_4}^{br}] + \varepsilon_D[D] \tag{14}$$

$$\frac{\partial N_{SiO_2}^{br}}{\partial t} = Br_{\text{flux}} + G_{\text{ice\_flux}} - \sigma\,[IA] + \varepsilon_{Si}[D] \tag{15}$$

$$\frac{\partial N_{PO_4}^{br}}{\partial t} = Br_{\text{flux}} + G_{\text{ice\_flux}} - \sigma\,[IA] + \varepsilon_D[D] \tag{16}$$

The first terms in Eqs 13–16 represent the nutrient transport at the interface due to the diffusion mechanism.

$$Br_{\text{flux}} = e \times K_{wi} \times \frac{\partial N_i^{br}}{\partial z} \tag{17}$$

where K_{wi} is the molecular diffusion coefficient (Jin et al., 2006; **Table 2**) and dN_i^{br}/dz is the vertical gradient of the respective nutrient at the ice-ocean interface. The second terms G_{ice_flux} in Eqs 13–16 are either the entrapment of dissolved matter in the ice due to the congelation of water process or the release of nutrients during the ice melt. This entrapment/melting acts on the nutrient bulk. It is defined following the relationship defined as follows (Tedesco and Vichi, 2014):

$$G_{\text{ice\_flux}} = \max\left(0.0,\ \frac{dH_i}{dt}\right) \times \max\left(0.0,\ N_i^w\right) \times \frac{\rho_{\text{ice}}}{\rho_{\text{water}}} \times e + \min\left(0.0,\ \frac{dH_i}{dt}/H_i\right) \times \max\left(0.0,\ N_i^{bk}\right) \tag{18}$$

where N_i^w is the water concentration of nutrient i (mmol m^{-3}). For ammonium, during the congelation process the quantity is not divided by the brine fraction due to the entrapment into the crystalline lattice as well in the brine. The third terms of the Eqs 13–16 are the uptake of nutrients by ice algae. Here p_{NO3} in Eqs 13 and 14 differentiate the uptake of nitrate from that of ammonium based on Mortenson et al. (2017):

$$p_{NO_3} = \frac{\nu_n}{\nu_n + [N_{NH_4}^{br}]} \tag{19}$$

where ν_n is the half-saturation constant for preferential uptake of nitrate (**Table 2**). The fourth terms in Eqs 13 and 14 are the nitrification rate, which is fixed as constant here (**Table 2**). The last terms in Eqs 14–16 represent the remineralization process from the detritus pool in sea ice. The remineralization rate is constant (**Table 2**).

Biogeochemical Pelagic Modifications

The ocean biogeochemical model ECOSMO includes 13 state variables describing three nutrient cycles (NO_3, NH_4, SiO_2, and PO_4), two phytoplankton groups (diatoms, flagellates), two zooplankton groups (mesozooplankton and microzooplankton), oxygen, biogenic opal, detritus (fast and slow), and dissolved organic matter. In the here used setup, the benthic system is included in the model formulation consisting of three state variables, of which each corresponds to a respective nutrient pool in the sediment (nitrogen, silicate, and phosphate). Model equations and parameterization are described in detail elsewhere (Daewel and Schrum, 2013; Daewel et al., 2019). To study the Arctic system and the sympagic-pelagic-benthic interactions, some changes have been made. These changes are explained in the section below. In particular we split the detritus group into a fast (D_f) and a slow (D_s) sinking class. Similar to diatom entrapment into sea ice, during the melting phase not all the ice algae are transferred to the diatom pool but only a fraction, corresponding to the surviving algae. The same fraction f_{dia} as for the entrapment is used. The remaining part is added to the fast sinking detritus pool. Additionally, the sea-ice detritus is released into the fast sinking detritus pool in the water column during ice melt. The reaction equations for two detritus groups are given as:

$$R_{D_f} = (1 - a_{\text{dom}})\, R_{D_f}^{+} - R_{D_f}^{-} + \left[\lambda_{s2d} C_{SE_1} - \lambda_{d2s} C_{D_f}/dz\right]_{z=\text{bottom}} \tag{20}$$

$$R_{D_f}^{+} = G_{\text{ice\_flux}}[ID] \tag{21}$$

$$R_{D_f}^{-} = \sum_{i=1}^{2} C_{Z_i} G_i \left(C_{D_f}\right) + \varepsilon_D\,(T)\, C_{D_f} \tag{22}$$

$$R_{D_s} = (1 - a_{\text{dom}})\, R_{D_s}^{+} - R_{D_s}^{-} + \left[\lambda_{s2d} C_{SE_1} - \lambda_{d2s} C_{D_s}/dz\right]_{z=\text{bottom}} \tag{23}$$

TABLE 3 | List of parameters, corresponding description, and units used in the model for pelagic dynamic.

Abbreviation	Definition	Value	Units
$m_{P_{1/2/3}}$	$P_{1/2/3}$ mortality rates	0.05/0.08/0.08	day^{-1}
$m_{Z_{1/2}}$	$Z_{1/2}$ mortality rates	0.2/0.1	day^{-1}
γ_1	Assimilation efficiency, grazing on $P_{1/2/3}$, Z_1	0.75	Unitless
γ_2	Assimilation efficiency, grazing on $D_{f,s}$	0.30	Unitless
ε_D	$D_{f,s}$ remineralization rate	$\varepsilon_D(T) = 0.006\left(1 + 20\left(\frac{T^2}{T_{ref}^2+T^2}\right)\right)$	Unitless
T_{ref}	$D_{f,s}$ remineralization reference temperature	13	°C
a_{dom}	Fraction of dissolved organic matter from detritus	0	Unitless
λ_{s2d}	Resuspension rate if $\tau < \tau_{crit}$	25	day^{-1}
λ_{d2s}	Sedimentation rate if $\tau \geq \tau_{crit}$	3.5	$m\ day^{-1}$
T_{lim}	Temperature dependency relationship coefficient	0.0582	$°C^{-1}$

$$R_{D_s}^{+} = (1-\gamma_1)\left(\sum_{i=1}^{2} C_{Z_i}\sum_{j=2}^{2} G_i\left(C_{P_j}\right) + G_2\left(C_{Z_1}\right)\right) + (1-\gamma_2)\sum_{i=1}^{2} C_{Z_i} G_i\left(C_{D_s}\right) + \sum_{j=1}^{2} m_{P_j} C_{P_j} + \sum_{i=1}^{2} m_{Z_i} C_{Z_i} \quad (24)$$

$$R_{D_s}^{-} = \sum_{i=1}^{2} C_{Z_i} G_i\left(C_{D_s}\right) + \varepsilon_D(T)\, C_{D_s} \quad (25)$$

where, T is the temperature in °C and z the depth in m. C_X is biomass of the state variable of the X in mgC m^{-3}, where X represents P_j [phytoplankton group with j = 1, 2 denotes the phytoplankton type (1: diatom, 2: flagellate)]; Z_i [zooplankton group with i = 1, 2 denotes the zooplankton type (1: micro-, 2: meso-zooplankton] and SE_1 is the sediment group representing the sediment carbon pool. $G_{i-1,2}$ is the zooplankton grazing rate. A sensitivity analysis (not included in the results) on the different sinking speed for the fast sinking detritus group showed that a sinking speed of 50 m d^{-1} leads to the best representation of the ecosystem dynamics. This value has also been chosen in earlier modeling studies by Lavoie et al. (2005) and Mortenson et al. (2017). The parameters values for Eqs 18–23 are given in **Table 3**. Additionally, we added a temperature dependence to the phytoplankton growth rate following an exponential function as described by Eppley (1972):

$$f_T = e^{T_{\lim} \times T} \quad (26)$$

where, T is the ambient temperature in°C and T_{lim} is the reference temperature (**Table 3**).

Light

Light is one major factor controlling growth of both sea-ice algae and phytoplankton in the water column. Light that penetrates in and through the ice reaching the sea-ice algal communities depends on the snow and ice thickness following the Beer–Lambert law as Castellani et al. (2017):

$$I\left(H_{\text{ice}}, H_{\text{snow}}\right) = I_0\left(1 - \alpha_{(\text{ice, snow})}\right) C_0 e^{-k_{\text{ice}}H_{\text{ice}} - k_{\text{snow}}H_{\text{snow}}} \quad (27)$$

where I_0 is the shortwave incoming solar radiation, α is the albedo of the surface component ice or snow, C_0 is the fraction of incoming radiation absorbed in the first centimeters of snow or ice layer, k_{ice} and k_{snow} are the ice and snow attenuation coefficient respectively and H_{ice} and H_{snow} are the ice and snow thickness, respectively. All parameter values and units are referred in **Table 4**.

Light available for phytoplankton in the water column below the ice depends on the snow and ice thickness but also on the ice algae concentration. In a given grid cell, however, the available light for primary production in the water column is additionally determined by what fraction of the area is covered by ice A (Slagstad et al., 2015). Light intensity reaching the water column below ice is expressed as:

$$I\left(H_{\text{ice}}, H_{\text{snow}}, Z_{\text{bot}}\right) = I_0\left(1 - \alpha_{(\text{ice,snow})}\right) C_0 e^{-k_{\text{ice}}H_{\text{ice}} - k_{\text{snow}}H_{\text{snow}} - k_{\text{ia}}Z_{\text{bot}}[IA]} \quad (28)$$

where Z_{bot} is the thickness of the biologically active bottom sea ice layer. The total light available in a grid cell is then given by:

$$I_{\text{tot}} = A \times I\left(H_i, H_s, Z_{\text{bot}}\right) + (1 - A) \times I_0 \quad (29)$$

TABLE 4 | List of parameters, corresponding description, and units used in the model for light calculation (most of parameters values come from Castellani et al., 2017).

Abbreviation	Definition	Value	Units
α_i	Albedo for ice	0.70	Unitless
α_s	Albedo for snow	0.81	Unitless
C_0	Surface transmission parameter	0.30	Unitless
k_i	Ice attenuation coefficient	1.50	m^{-1}
k_s	Snow attenuation coefficient	5.00	m^{-1}
k_{ia}	Constant of attenuation coefficient due to algae	3.00	m^{-1}
Z_{bot}	Bottom layers thickness	0.05	m

Numerical Experiments and Sensitivity Analysis

With the 1D model setup we performed numerical experiments to understand primary and secondary production in the Barents Sea. Even though the Barents Sea is one of the most productive areas in the Arctic Ocean it features a high spatial variability in ecosystem productivity with less production in the northern than in the southern areas (Sakshaug, 1997; Dalpadado et al., 2014). To address the spatial dynamics, we ran simulations at three separate locations (**Figure 2**) that differ in ice dynamics and environmental conditions. The southernmost station was located in an area where the ocean is free of ice all year round (SBS: 39.25 E; 71.41 N). A second station in the center of the Barents Sea (MBS: 38.58 E; 76.44 N) represents the area with a seasonal cycle in ice coverage where the ocean is free of ice during late summer. The third station represented the area with year-round ice coverage, located in the northern Barents Sea (NBS: 35 E; 81.6 N). All the simulations were performed with a 30 min time step and daily means were provided for analysis. As initial concentration for the modeled state variables for ice algae, diatom, flagellate, microzooplankton, mesozooplankton, and two detritus pools very small values were chosen (0.0, 0.1, 0.1, 0.01, 0.01, and 0.05 mgC m^{-2}, respectively) for all three stations. The state variables for nitrate, ammonium, phosphate, and silicate were initialized based on observed winter concentrations in the central Barents Sea (Reigstad et al., 2002; Sakshaug et al., 2009) (10.5, 2, 0.8, and 4.5 mmol m^{-3}).

We performed three sets of scenarios to evaluate the primary and secondary production in the Barents Sea area at different spatial and temporal scale. The first set of experiments was designed to understand the response of the pelagic production system to implementation of the sympagic ecosystem dynamics in the model. These scenarios were run at MBS location during 1997. In this first set of experiments, we ran the same setup (i) including all the biogeochemical components and interaction between the sympagic and the pelagic systems (fullBGC scenario), (ii) neglecting the biogeochemical interaction between the sympagic and the pelagic system but including the sea ice physics (noBGC scenario), and (iii) neglecting the sea ice completely (noICE scenario), which allowed us to dissociate the role of the sea ice presence itself and the role of the sea ice biogeochemistry on the pelagic system. This last experiment also explores the ice free environment, which is expected in the next decades considering climate induced sea ice retreat (Onarheim and Årthun, 2017).

The second set of scenario experiments described the spatial variability of the primary and secondary production at three stations (NBS, MBS, and SBS) following a north-south gradient.

The third set of scenario experiments addressed the interannual variability of the primary and secondary production at the MBS station. We ran each simulation for a 10 years' time period (1990–1999), where the first 2 years were considered as spin-up period and were disregarded for analysis.

Since the Arctic ecosystem is difficult to access and data on parameters relevant for the sympagic ecosystem are sparse, we additionally performed a sensitivity study to investigate the models' response to some of the most uncertain parameters in the ice-ecosystem formulation. The proportion of phytoplankton entrapped in the ice during freezing determines the initialization of the sea-ice algae and thus consequently ice algae biomass but is hardly measurable and thus difficult to identify. Some evidence shows that ice algae stem from different sources (multi-year ice, pelagic system, benthic system; Syvertsen, 1991; Ratkova and Wassmann, 2005; Werner et al., 2007; Olsen et al., 2017). But it remains unclear how much exactly originates from the pelagic system and finally survives inside the ice. On the other hand, the proportion of ice algae released into the water during the sea ice melt contributes to the algal biomass in the water column and can be used by zooplankton as a valuable food source (Michel et al., 1996; Søreide et al., 2006, 2013). Moreover, some studies highlight the potential of some ice algae species to seed phytoplankton production during the ice melt (Haecky et al., 1998; Galindo et al., 2014; Szymanski and Gradinger, 2016). Through a sensitivity analysis, we evaluated the impact of the amount of phytoplankton entrapped in sea ice on ice algae phenology and, of the amount of ice algae released to the pelagic system on the primary and secondary production. We ran four scenarios for this experiment:

1. control run: 100% of diatoms entrapped is transferred into the ice algae pool and 100% of ice algae is release to the diatom pool;
2. 75% of the diatoms entrapped are transferred to the ice algae pool while the remaining 25% are transferred to the ice detritus pool and, 75% of the ice algae released are transferred in the diatoms pool while the remaining 25% are transferred to the pelagic fast sinking detritus pool;
3. where the proportion of algae:detritus is 50:50%;
4. where the proportion of algae:detritus is 25:75%.

The main assumption of the 1D modeling approach described here is that lateral advection in both the ice and water layers is negligible compared to other fluxes. We used forcing data retrieved from outputs of a 3D hydrodynamic model – which includes advection – to define the seasonality of temperature, vertical mixing, and ice properties. However, the 1D model itself does account for net lateral fluxes of state variables at the given location. This limitation does not invalidate the approach as deployed in this article for exploring hypotheses on the linkage between sympagic-pelagic-benthic systems provided the deployment locations are chosen carefully to avoid areas with strong horizontal gradients in the model variables so that advection is of secondary importance. However, it could become an issue for interpretation of responses to climate change. Climate warming is not only accompanied by loss of sea ice, but also by changes in wind patterns, water mass characteristics and circulation (Skagseth et al., 2020). These could change net horizontal fluxes, especially of ice at our study sites in the Barents Sea (Kimura and Wakatsuchi, 2001; Koenigk et al., 2009; Kwok, 2009). Hence advection could become a significant term in the rate of change of ice algae biomass at model locations. Thus, in the next step of our work we will apply the model in a fully coupled 3D biological-physical model to account for the dynamics nature of the system. This will additionally account for sea ice

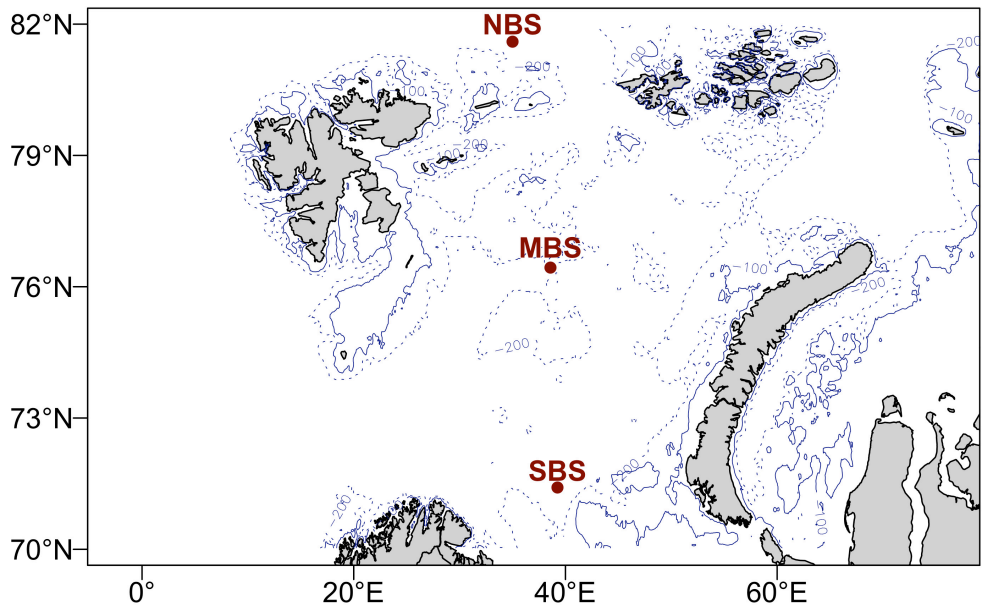

FIGURE 2 | Map of the Barents Sea area. Red dots indicate the three stations where environmental forcing are extracted to run experimental simulation. NBS means north Barents Sea station, MBS means central Barents Sea station, and SBS means south Barents Sea station.

dynamic forced by the atmospheric conditions, which has clear implications for both sympagic as well as pelagic productivity.

RESULTS AND DISCUSSION

Role of Sympagic System: Implementation, Verification, and Sensitivity

In **Figure 3** we show the seasonal variations of estimated ice algae dynamics (fullBGC scenario) and the related external and internal properties. The results show that ice algae growth started slowly at the beginning of March as soon as sufficient light became available (**Figure 3E**), and prevailed until mid-June when biomass started to decrease (**Figure 3C**) controlled by both ice melting (**Figures 3A,B**) and grazing by pelagic zooplankton. The ice algae growth dynamic was characterized by three blooms. The two first occurred in early and mid-May, both followed by a sharp decrease of biomass due to two melting events, generating a strong ice algae release (**Figure 3B**). A third bloom, which was the most important, occurred in mid-June (**Figure 3C**), during which the biomass increased up to 378 mgC m^{-2} with a maximum daily ice algae production rate about 89 mgC m^{-2} d^{-1}. Our biomass estimates were consistent with data from field measurement in the Barents Sea area (69–620 mgC m^{-2}; Tamelander et al., 2009) and in the Arctic region (3–460 mgC m^{-2}; Gosselin et al., 1997). The results on daily ice algae production rate, however, appear to be higher than measured production rates in the northern Barents sea (0.16–55 mgC m^{-2} d^{-1}; Hegseth, 1998; McMinn and Hegseth, 2007). On the other hand, our results showed low biomass of ice algae when compared with data from Rózañska et al. (2009) and Fernández-Méndez et al. (2018), who reported ice algae biomasses up to 2250 mgC m^{-2}, indicating that our model might underestimate ice algae biomass. The abiotic environment (e.g., light, ice, and snow thickness) strongly influences the daily ice algae production rate. These environmental conditions vary strongly in the Barents Sea both spatially and temporally, which can explain these differences between model results and observations, particularly since our environmental forcing is only representative for one specific location. Moreover, we only consider ice algae originating from entrapment of pelagic algae, which neglecting ice algae advection from other area. As this provide a relatively small quantity of algae it impacts the growth of biomass and might explain the slow growth between March and May, and the potentially too low ice algae biomass. Nonetheless, over the large existing range of measured and simulated production rates (from 0.16 to 100 mgC m^{-2} d^{-1}; Clasby et al., 1973; Mortenson et al., 2017) our simulated values are well in the range of previously reported production rates and our daily production rates appear acceptable.

The simulated ice algae bloom dynamic was not nutrient limited in our scenario (**Figure 3E**), even though the silicate concentration decreased sharply during the bloom event, it never became limiting (**Figures 3D,E**). Our simulations show two strong melt events during the ice algae bloom period which removed a substantial amount of ice algae biomass from the ice, which also reduced the nutrient requirements in the ice. In addition, the ice bottom layer at the ocean interface is highly dynamic and nutrients can be replenished by convective mixing (Vancoppenolle et al., 2010). This is in compliance with findings from Werner et al. (2007), who showed that ice algae do not appear to be limited by nutrients in the Barents Sea. The

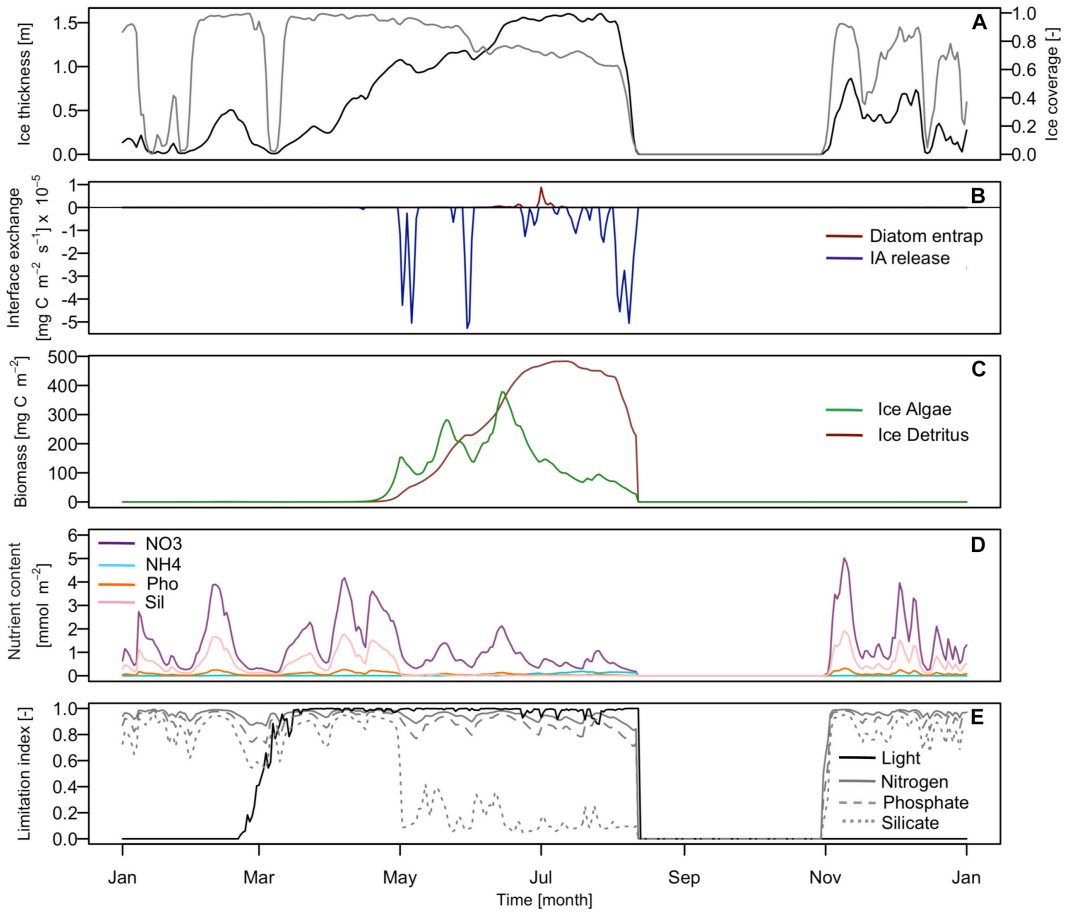

FIGURE 3 | Seasonal variation in the environmental forcing **(A)** of ice thickness (black) and ice coverage (gray) in 1997; **(B)** diatoms/ice algae flux at the ice-ocean interface. (Red line represents the quantity of diatoms entrap into the sympagic system and the blue line represents the quantity of ice algae released into the pelagic system.); **(C)** the ice algae (green) and detritus in ice (red) biomass; **(D)** integrated nutrient content in the sea ice: nitrate (NO_3: purple), ammonium (NH_4: light green), phosphate (Pho: orange), and silicate (Sil: pink); **(E)** light (black) and nutrients (gray) ice algae growth limitation index. Nitrogen (solid), phosphate (dashed), and silicate (dotted) are represented.

Barents Sea is a shallow area and is significantly influenced by winds and tidal mixing (Sundfjord et al., 2007). Hence nutrients are abundant and not generally a limiting factor for ice algae as also shown by Tamelander et al. (2009). The total annual production of the simulated ice algae was about 2.44 gC m^{-2}, which represented about 3.8% of the total primary production. This fraction is in the lower part of the range of the observations previously reported for the whole Arctic (3–57%; Gosselin et al., 1997). According to Sakshaug (1997) and Hegseth (1998) who reported estimated total annual production respectively around 6 and 7% of the total primary production in the northern Barents Sea, our total production estimation appeared to be slightly underestimated but reasonable.

In order to assess the role of the sympagic system on the overall ecosystem dynamics, we performed three numerical experiments to separate the impacts of the physical and biological forcing. The results are presented in **Figure 4** for the fullBGC (**Figures 4A,D,G,J**), the noBGC (**Figures 4B,E,H,K**) and the noICE scenario (**Figures 4C,F,I,L**). Scenario explanations are given the methods section. The results highlight how the sympagic system generates important changes in the whole ecosystem by modifying the phytoplankton and zooplankton phenology.

What we generally can see is that implementing ice biogeochemistry in the model formulation strongly impacts the dynamics of the pelagic ecosystem, both with respect to magnitude and timing of the different components. Most importantly, we found major differences in the dynamics of diatoms and zooplankton. In the fullBGC scenario, when the sympagic system was fully implemented, the model estimated two diatom blooms during the season (**Figure 4A**), while only one spring bloom was simulated in noBGC. The first bloom occurred in July in both scenarios, partly under ice, when the ice coverage started to decrease, allowing better light conditions in the water column. In case of fullBGC, this bloom was not limited by nutrients but instead controlled by zooplankton grazing (**Figures 4G,J**). In the noBGC scenario, on the other hand, this first diatom bloom developed until silicate became limiting. The

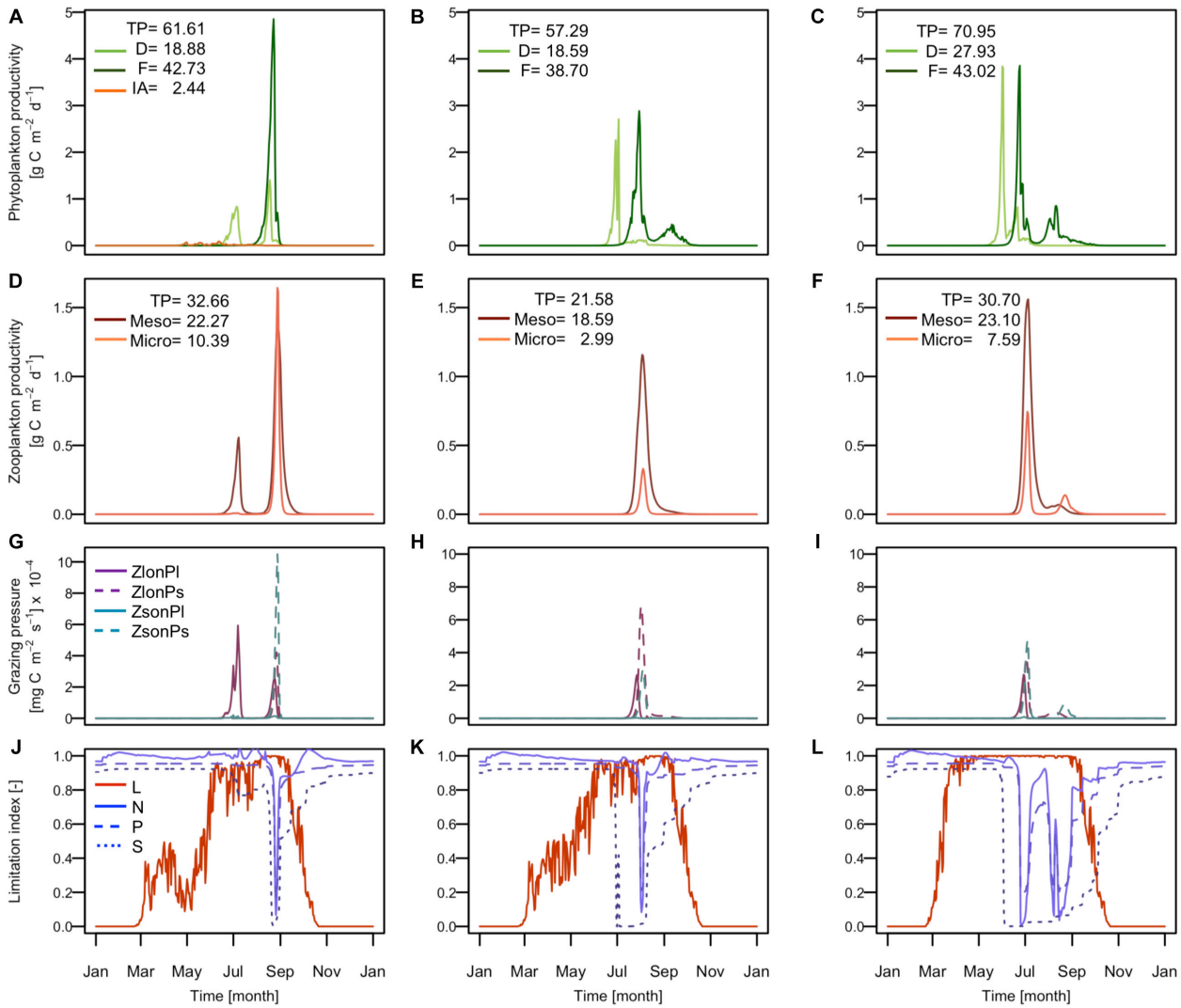

FIGURE 4 | Simulated sympagic and pelagic primary and secondary production, predation pressure of zooplankton on phytoplankton and nutrient and light growth limitation in the surface layer (4 m depth) for full coupling experiment **(A,D,G,J)**, physical coupling experiment **(B,E,H,K)**, and free ice experiment **(C,F,I,L)**. Time series of **(A–C)** primary production rates of ice algae (IA: orange), diatoms (D: light green), and flagellates (F: dark green), **(D–F)** secondary production rates of mesozooplankton (Meso: dark red) and microzooplankton (Micro: orange), **(G–I)** grazing rates of large and small zooplankton on large and small phytoplankton, and **(J–L)** growth limitation index for light (solid orange), nitrogen (solid blue), phosphate (dashed blue), and silicate (dotted blue). In the legend **(A–F)** are indicated the annual production in gC m^2 for total pelagic production (TP), diatoms (D), flagellates (F), ice algae (IA), mesozooplankton (Meso), and microzooplankton (Micro). In the legend **(G–I)** are indicated large zooplankton grazing rate on large phytoplankton (ZlonPl), large zooplankton grazing rate on small phytoplankton (ZlonPs), small zooplankton grazing rate on large phytoplankton (ZsonPl), and small zooplankton grazing rate on small phytoplankton (ZsonPs). In the legend **(J–L)** are indicated light limitation (L), nitrogen limitation (N), phosphate limitation (P), and silicate limitation (S) at the surface layer.

major process leading to this difference was that generally the zooplankton benefits from feeding on ice algae prior to the first diatom bloom, leading to relatively high zooplankton biomasses early in the season (**Figure 4D**). Consequently, zooplankton and phytoplankton maximum biomass occurred at the same time (**Figures 4A,D**), which systematically modified the overall system dynamics. Therefore, silicate remained in the water column allowing a second diatom bloom in August during full open water condition following the ice break-up. Zooplankton grazing on ice algae, in the ice and in the water column just after being released, appears one of the most important links between the pelagic and sympagic component of the ecosystem leading in our results to a general increase in zooplankton biomass. This important link has earlier been reported on the basis of field observations (Stretch et al., 1988; Runge and Ingram, 1991; Werner, 1997; Juul-Pedersen et al., 2008). Observations indicate that the grazing on ice algae is partly used by female copepods to mature their gonads and produce eggs (Søreide et al., 2010; Durbin and Casas, 2014). In this case, there is an increase in biomass due to egg production. But because eggs do not feed directly on phytoplankton during their development and only participate in phytoplankton consumption later in the season after hatching,

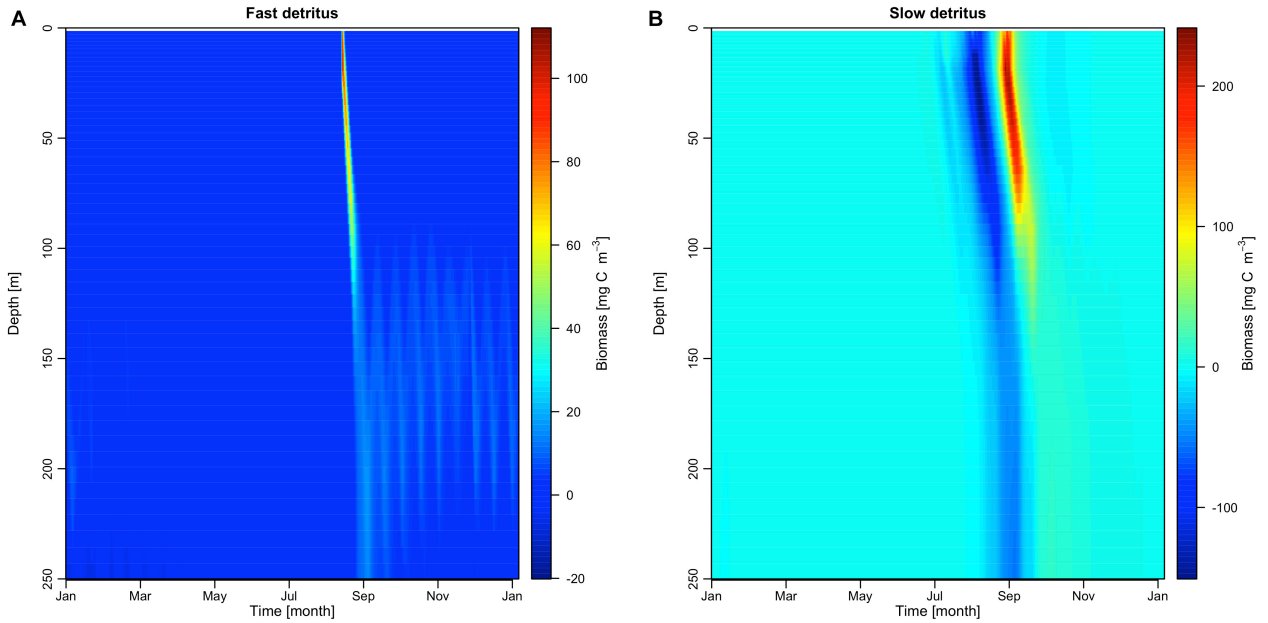

FIGURE 5 | Vertical profile of difference in biomass concentration between full coupling experiment and physical coupling experiment for the fast sinking rate detritus group **(A)** and the slow sinking rate detritus group **(B)**.

the control of our first phytoplankton bloom by the zooplankton grazing could potentially be overestimated. More investigations are necessary here to accurately understand the direct role of ice algae on zooplankton dynamics and vice versa. Nonetheless, the interaction between the pelagic zooplankton and ice algae remains an important process as it determines the fitness of these zooplankton species and includes other species that use ice algae such as amphipods and krill.

The flagellate bloom occurred after the ice break-up at the same time as the second diatoms bloom (**Figure 4A**) but with a much higher biomass. Flagellates generally dominated the primary production with a total annual production about 42.73 gC m^{-2}, which represent around two thirds of the total pelagic primary production (61.61 gC m^{-2}). Previous studies estimated annual primary production for the Barents Sea to be between 20 and 200 gC m^{-2}, depending on the area, with estimates around 76 gC m^{-2} in the central Barents Sea (Luchetta et al., 2000; Sakshaug et al., 2009), which supports our model estimates. The high flagellate biomass results from the fact that the diatoms are mainly controlled by zooplanktonic grazing. This leads to relatively high nutrient concentrations (**Figure 4J**) and consequently allows a strong flagellate bloom in the fall. Also, for mesozooplankton a second maximum follows the spring maximum in July and is closely related to the diatom dynamics. Microzooplankton, on the other hand, followed the flagellate's dynamic with a unique peak by the end of summer. Mesozooplankton dominated the secondary production.

In **Figure 5**, we showed differences between the fullBGC and the noBGC scenario in the vertical biomass profiles of the two detritus groups (**Figure 5A**: fast and **Figure 5B**: slow sinking rate). These results indicate a lower biomass of slow sinking detritus during summer (**Figure 5B**) when the sympagic system is coupled to the pelagic ecosystem, related to a smaller summer diatom bloom in the fullBGC scenario. This was followed by a second strong detritus production in autumn, which was exported to the benthic system in late autumn, and which corresponds to the strong flagellate production. Direct export of ice algae to the benthic system happened at the end of summer when ice melts. We observed a contribution of the fast sinking detritus group in September with a slightly higher export to the benthic system in the fullBGC scenario compared to the noBGC scenario (**Figure 5A**). It has already been shown that ice algae contributes to the export of matter to the benthos due to the fast sinking rate and it represents a valuable resource for benthic organisms early in the season (Søreide et al., 2013; Schollmeier et al., 2018). Due to the forcing data we used, the simulated ice break-up occurred late in the season at mid-June and we did not observe a spring contribution of ice algae to the benthos as was showed in previous studies (Boetius et al., 2013; Szymanski and Gradinger, 2016). However, our results pointed out that the ice algae are exported rapidly to the benthos and earlier than the phytoplankton in the productive season (**Figure 5**). In addition, our results highlight the indirect contribution to detritus export by changes in zooplankton dynamics (**Figure 5B**). Because of the feeding process on ice algae, zooplankton developed earlier and participated in an increase in the slow sinking detritus biomass. The results indicate temporal changes on the export of detritus biomass to the benthic system when sympagic biogeochemistry is included. The sympagic system therefore does not only play a role in pelagic dynamics but also influences both the amplitude and timing of detritus export to the benthic system. Here, we additionally hypothesize that the indirect contribution due to

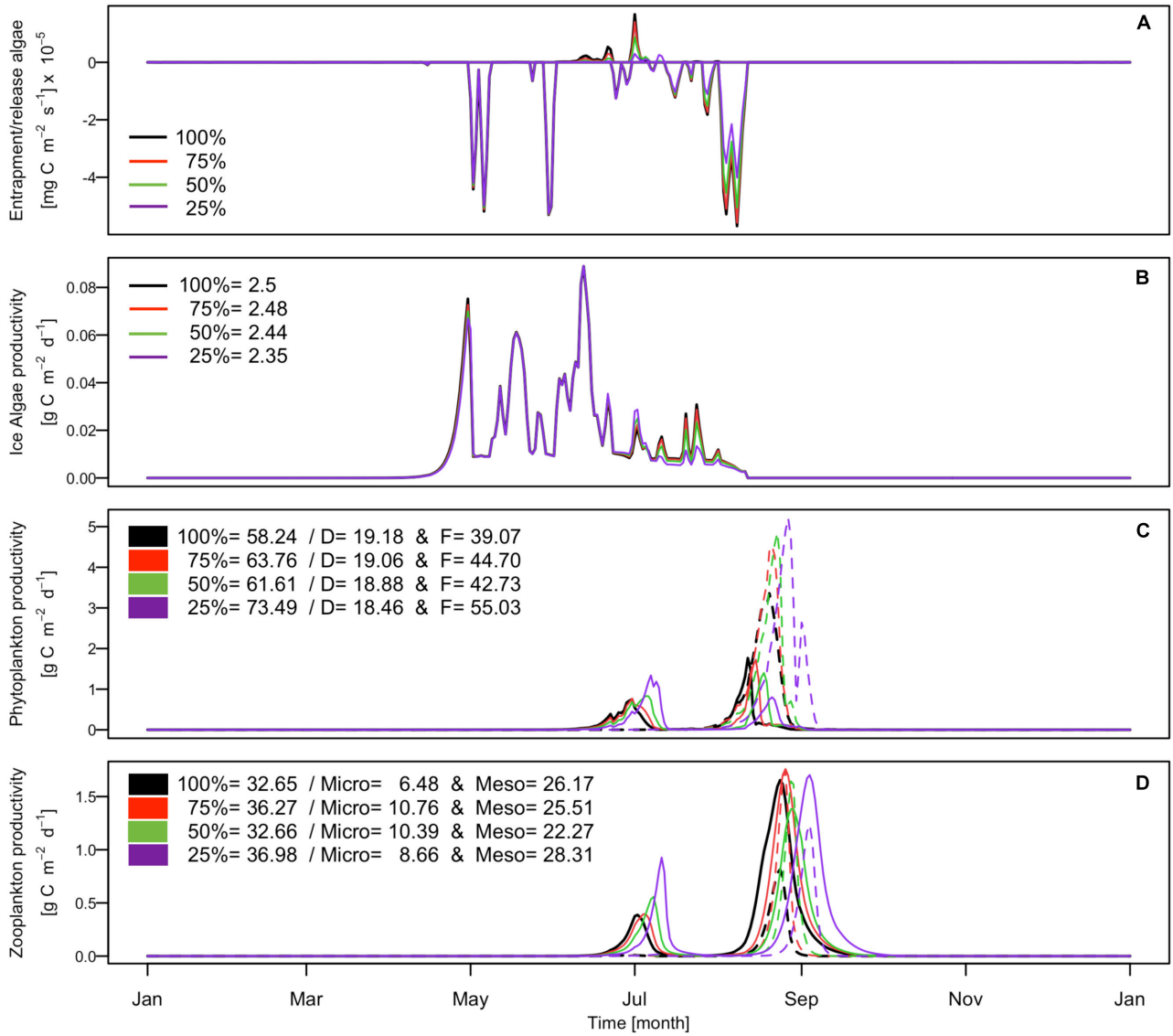

FIGURE 6 | Simulated time series of **(A)** diatoms/ice algae flux at the ice-ocean interface; **(B)** production rates of ice algae; **(C)** production rates of phytoplankton including diatoms (D: solid line) and flagellates (F: dashed line), and **(D)** production rates of zooplankton including mesozooplankton (Meso: solid line) and microzooplankton (Micro: dashed line). Black color presents result for the 100% experiment, red color for the 75% experiment, green color for the 50% experiment, and purple color the 25% experiment. In the legend **(B–D)** are indicated the annual production in gC m^{-2} for ice algae, phytoplankton including diatoms production (D) and flagellates production (F) and zooplankton including microzooplankton (Micro) and mesozooplankton (Meso).

the zooplankton feeding on the ice algae is as important for the timing and magnitude of material export to the benthic system.

The noICE scenario shows similar dynamics to the noBGC scenario. The main difference observed is an earlier onset of spring bloom production with about one-month time difference (**Figures 4B,C**). This is due to the absence of ice cover leading to sufficient light conditions earlier in the year (**Figures 4K,L**). The other major difference is the increase of the total annual primary and secondary productivity in the noICE scenario. The structure of the ecosystem groups does not change between these two scenarios suggesting that the presence of ice only as a physical barrier does not seem to influence pelagic ecosystem functioning. Differences between fullBGC and noICE scenarios, i.e., earlier primary production and higher primary production, reflect changes expected for the Arctic region regarding an ice decrease. These changes are further discussed in the section *Spatial variability in the Barents Sea, environmental drivers and ecosystem dynamics.*

Results of the sensitivity analysis (**Figures 6A,B**) showed that the proportion of phytoplankton entrapped in the ice influenced slightly the total ice algae production with a change of about 0.25 gC m^{-2} y^{-1} between the 100 and 25% numerical experiments, which represent a decrease of about 10% for an entrapment proportion decrease of 75%. The sensitivity

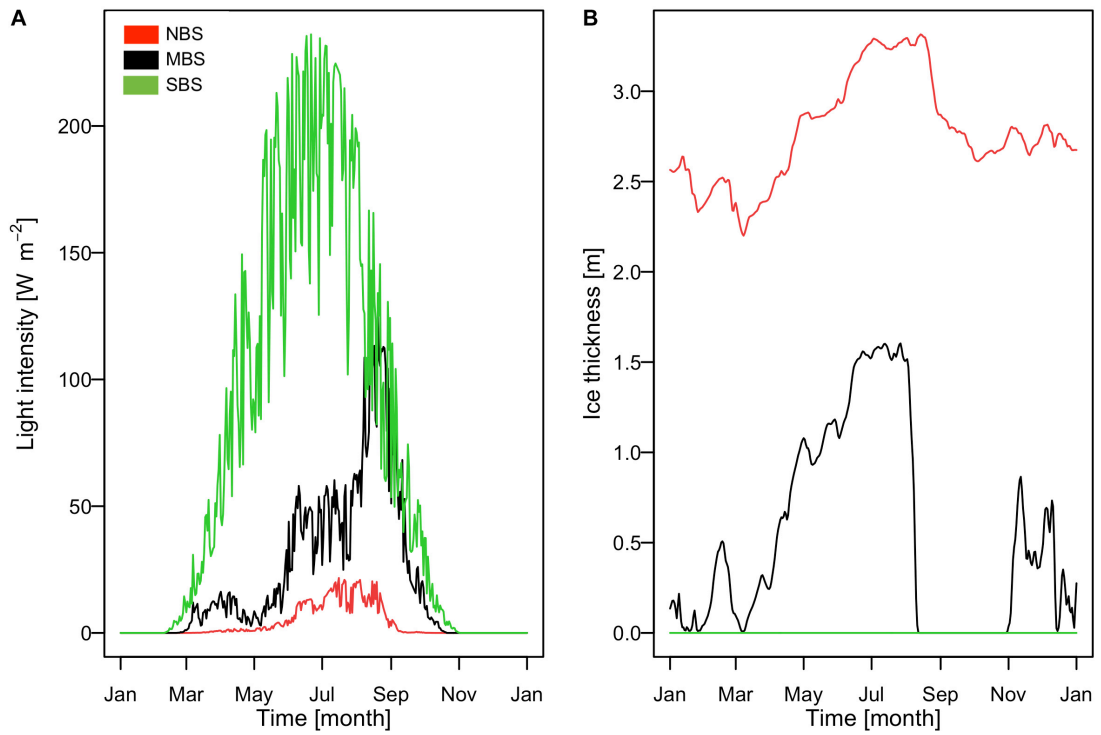

FIGURE 7 | Simulated time series of **(A)** light intensity (W m^{-2}) at the ocean surface (includes ice and ice algae attenuation) and **(B)** extracted sea ice thickness (m) forcing. Black color presents result for the central Barents Sea station over the 1997, red color for the north Barents Sea station over the 1997, and green color for the south Barents Sea station over the 1997.

experiments did not indicate any changes in ice algae production in terms of timing and amplitude of the maximum growth rate. This principally resulted from the minimum threshold implemented in our model to allow a minimum proportion of ice algae to survive during winter in the ice when conditions are not favorable for growth. This assumption was made because the fate and origin of ice algae during winter remains poorly understood. Different hypotheses were suggested previously including the existence of resting cysts or spores, metabolism adaptation to low light, facultative heterotrophy, or origin of algae in the ice from nearby multi-year ice (Syvertsen, 1991; Niemi et al., 2011; Kauko et al., 2018). Even though the total amount of ice primary production changed only slightly, we found that the magnitude of the initial bloom in May was decreased by almost 50% when only 25% of the entrapped algae were used for production.

Although variations in phytoplankton entrapment did not show a prominent effect on the sympagic production, the modeled pelagic system showed a clear response to the amount of ice algae released into the sympagic system during ice melt (**Figures 6C,D**). First, our results indicate that released ice algae seeded the diatoms blooms, both under ice and during the ice break-up. This is one of the main assumptions made in our approach. The hypotheses about the ice algae seeding are divergent and controversially discussed in the scientific community, because evidence is not clear. Some field samplings highlight that ice algae contribute to the start of the phytoplankton bloom, due to some species overlapping in both the sympagic and pelagic communities (Haecky et al., 1998; Lizotte, 2001; Mangoni et al., 2009). Contradictory field studies have indicated that ice and pelagic algae communities are distinct and that ice algae apparently do not seed phytoplankton blooms (Riebesell et al., 1991; Mundy et al., 2014). Our results showed that, under the condition of ice algae seeding, the proportion of ice algae released into the diatom pool has consequences for the phenology of the diatoms, with an earlier peak biomass the more ice algae are released. This consequently also results in a modified phenology of the secondary production. The maximum difference in peak bloom timing for the two most extreme experiments (100 and 25%) was about 1 week, both for the under-ice bloom and the late summer bloom. The results thereby showed that the peak production occurred later the less important the ice algae seeding is for the overall diatom biomass. This estimated change in diatom phenology systematically modified the primary producers' dynamics. The associated environmental conditions, such as temperature, ice cover, and available light, in the water column change slightly within this 1-week period. This influences the growth rate of the diatoms such that, although the seeding of diatoms was lower, it led to a shorter bloom with higher peak biomass. After the ice break-up flagellates developed quickly, limiting the diatom bloom. Because ice algae seed the diatom blooms it allowed them to bloom earlier at the ice break-up. Therefore, the smaller the ice algae release is, the weaker the second bloom and the greater the flagellate's production. The difference in total

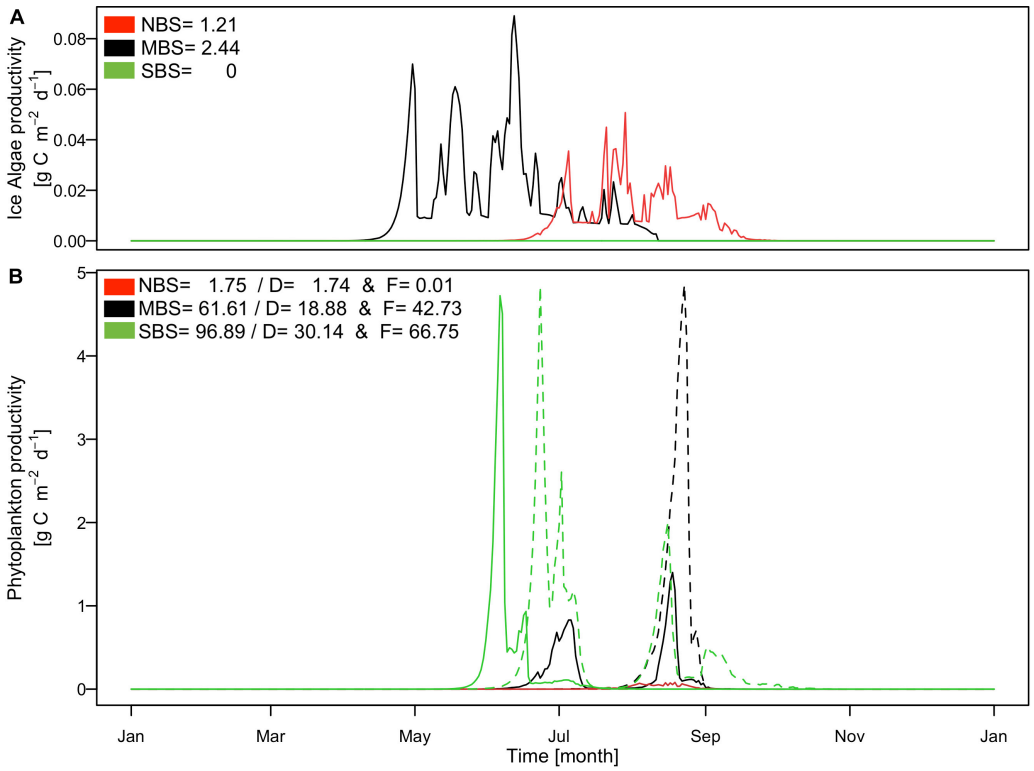

FIGURE 8 | Simulated time series of **(A)** production rates of ice algae; **(B)** production rates of phytoplankton including diatoms (D: solid line) and flagellates (F: dashed line). Black color presents result for the central Barents Sea station over the 1997, red color for the north Barents Sea station over the 1997, and green color for the south Barents Sea station over the 1997. In the legend **(A,B)** are indicated the annual production in gC m^{-2} for ice algae and phytoplankton including diatoms production (D) and flagellates production (F).

flagellate production between the 100 and 25% experiments was an increase of 40.8%. In light of our results and also model results published by Tedesco et al. (2012) and Jin et al. (2007) ice algae seeding appears to be a key process in the Arctic marine ecosystem dynamics and further investigations should be done in order to decrease uncertainties about this process. Especially as Lizotte (2001) highlighted, climate change can alter and modify algae communities and consequently potentially change the contribution of ice algae to the phytoplankton bloom.

The sensitivity analysis again highlights the importance of clarifying the current parameterization of sympagic components and the exchanges with the pelagic components underneath. Despite ice algae representing a small proportion of the total primary production, we showed that its contribution to the phenology of all the pelagic groups is significant. The results also suggest important changes in the Arctic pelagic structure of planktonic communities might be related to ice algae changes, as already suggested before for copepods in an earlier study (Tedesco et al., 2019). Indeed, there is evidences that females of *C. finmarchicus* and *C. glacialis*, when barely out of diapause, benefit from feeding on ice algae to maturate their gonads and produce eggs (Hirche and Kosobokova, 2003; Søreide et al., 2010; Leu et al., 2011). Although, the factors of entry and exit in a diapause state remain not well identified, some evidence about a mismatch between the presence of individuals at the surface and algal bloom have already been highlighted, showing significant consequences for fitness and next generations of these species (Dezutter et al., 2019). Diapause behavior is not yet a part of our model formulation and should be integrated in future work to identify more accurately the planktonic phenology in the Arctic system as modeling work of Pourchez (2018) showed for the Beaufort Sea. We previously discussed a possible model artifact of zooplankton controlling the first phytoplankton bloom due to an earlier growing phase feeding on ice algae. If we consider that a significant zooplankton biomass migrates from the bottom to the surface at springtime, it seems realistic that such a grazing control takes place. It could also help to explain the second phytoplankton bloom in autumn, when naturally zooplankton migrates back to the bottom and relieves the grazing pressure (Pourchez, 2018). Identification of these key parameters becomes all the more urgent in the context of rapid climate change in order to properly understand and manage the near future Arctic ecosystem.

Spatial Variability in the Barents Sea, Environmental Drivers and Ecosystem Dynamic

The Barents Sea area exhibits strong seasonal contrasts as well as high spatial variability, as illustrated in **Figure 7** regarding the

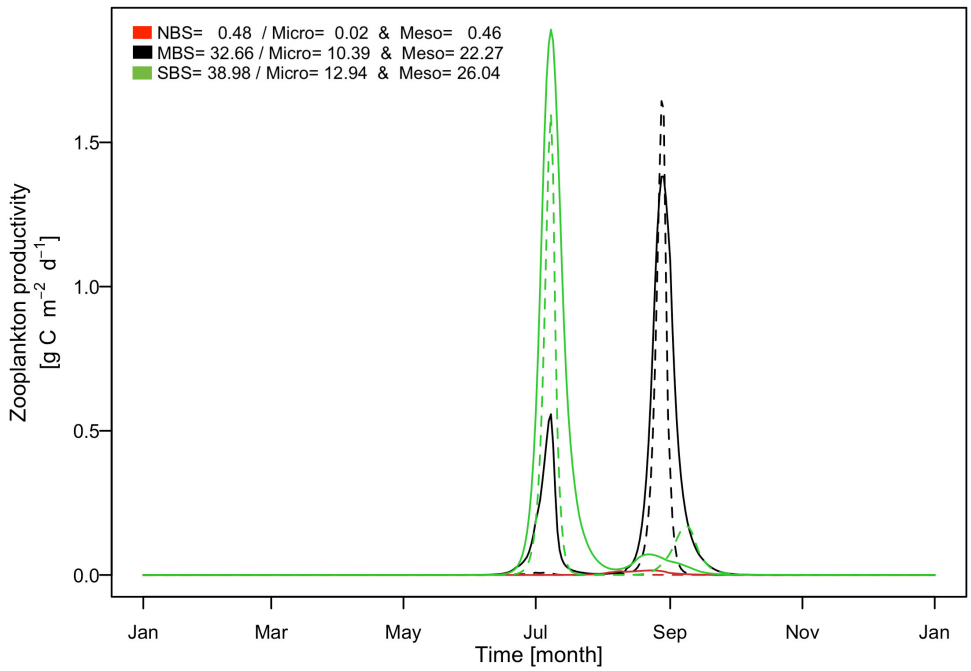

FIGURE 9 | Simulated time series of production rates of zooplankton including mesozooplankton (solid line) and microzooplankton (dashed line). Black color presents result for the central Barents Sea station over the 1997, red color for the north Barents Sea station over the 1997, and green color for the south Barents Sea station over the 1997. In the legend are indicated the annual production in gC m^{-2} for zooplankton including microzooplankton (Micro) and mesozooplankton (Meso).

light availability at the ocean surface (**Figure 7A**) and the sea ice thickness (**Figure 7B**). This high variability in environmental conditions results in very different ecosystem dynamics and follows mainly a south-north gradient related to temperature and ice cover (**Figures 8**, **9**). For the northernmost station (NBS), which is covered by ice all year round, our results showed the lowest productivity, with a total annual primary production of 2.86 gC m^{-2} yr$^{-1,}$ while at the central and southernmost location our model estimated 64.05 gC m^{-2} yr^{-1} and 96.89 gC m^{-2} yr^{-1}, respectively (**Figure 8**). This was due to the presence of a thick ice coverage in the north leading to low light availability at the ice-ocean interface. Our results are consistent with field observations provided by Sakshaug et al. (2009), who estimated that primary production varied from <20 to 200 gC m^{-2} yr^{-1} over the Barents Sea. Even though ice algae production was relatively small in the north when compared to the central Barents Sea area, it was more important for the overall productivity in the region representing around 42% of the total primary production at this location. In contrast, in the central Barents Sea the ice algae accounted only for 3.8% of the overall primary production (**Figure 8A**). Light conditions not only determined the magnitude but also the phenology of the productivity resulting in an onset of spring diatom bloom in the beginning of June in the southern Barents Sea, beginning of July in the central Barents Sea, and middle of August in the northern station (**Figure 8B**). A second diatom bloom developed only in the central Barents Sea area in the middle of August when ice break-up allowed more favorable light conditions. Flagellates bloomed twice (end of June and beginning of August) in the south, whereas in the central Barents Sea only one bloom occurred in the middle of August. Environmental conditions at the northern location are generally not favorable for primary production and flagellates were outcompeted by diatoms. In contrast, flagellates dominated the primary production in the south and central part of the Barents Sea by around two thirds.

TABLE 5 | Annual production of ice algae, phytoplankton (diatom + flagellate), and zooplankton (microzooplankton + mesozooplankton) for the central Barents Sea station over the 7 years simulated (1992–1998).

Year	Annual ice algae production (gC m^{-2} y^{-1})	Annual phytoplankton production (gC m^{-2} y^{-1})	Annual zooplankton production (gC m^{-2} y^{-1})
1992	0 (0%)	80.31	40.58
1993	2.23 (4.35%)	48.98	23.19
1994	1.55 (2.40%)	63.05	33.56
1995	0.80 (0.83%)	95.92	49.76
1996	1.81 (3.33%)	52.51	27.92
1997	2.44 (3.81%)	61.61	32.66
1998	2.49 (6.76%)	34.33	13.61

For mesozooplankton and microzooplankton the seasonal dynamics followed closely phytoplankton blooms (**Figure 9**). Thereby, in the south zooplankton were mainly concentrated at the beginning of July following the diatoms and first flagellate blooms and slightly developed at the fall. In the north, only very little mesozooplankton developed in August following the

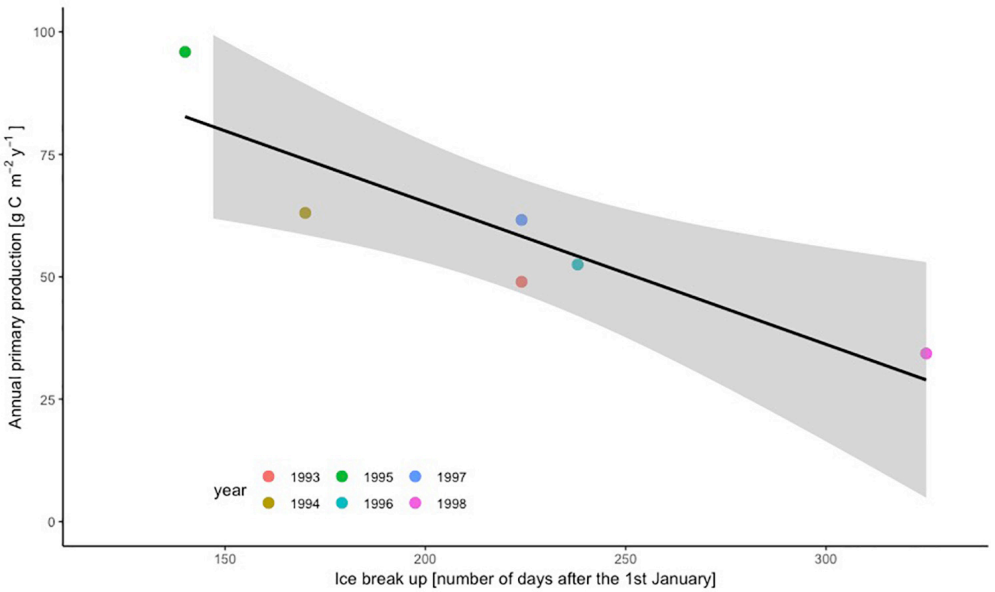

FIGURE 10 | Relationship between annual primary production and ice break-up timing for the 7 years simulated at the central Barents Sea station. Values (p = 0.0159, R^2 adjusted = 0.75).

diatom bloom. In the central area the seasonal dynamics were very different featuring two major zooplankton peaks in July and September, respectively. Contrary to the phytoplankton phenologies our results indicated that no phenological shift occurred in secondary production between the southern and the central Barents Sea location. The reason was that the zooplankton also feeds on ice algae allowing an increase in zooplankton biomass even before the pelagic diatom bloom starts and therefore promoting an early peak in zooplankton biomass.

Another interesting emergent result is that although primary production in the south was around 30% higher than in the central Barents Sea, the zooplankton annual total production was not significantly different between these two regions suggesting a more efficient trophic transfer from phytoplankton to zooplankton, again caused by the feeding process of zooplankton on ice algae.

Going from north to south in the Barents Sea may also be indicative of the Barents Sea ecosystem through time. Considering the expected sea ice retreat in the light of climate change during the next decades in the Barents Sea, we can expect a change toward a more southern ecosystem in terms of structure and functioning. This means an increase in primary production for the central Barents Sea and an increase of both primary and secondary productions for the northernmost regions. Previous modeling studies have already highlighted the potential increase of primary production in the Arctic and in the Barents Sea due to climate change and sea ice reduction and support our study results (Arrigo et al., 2008; Holt et al., 2016). Because the Arctic ecosystem structure has a relatively low complexity with few key players (Darnis et al., 2012), changes in the sea ice extent and ecosystem can greatly affect the whole Arctic food-web structure and functioning. As an example, according to the modeling study of Suprenand et al. (2018) important changes in zooplankton have already happened in the Beaufort Sea, and suggest greater changes in the marine ecosystem will occur in the next decades due to the sea ice decrease and temperature increase presently ongoing. Several species directly or indirectly depend on the ice algae, especially female *Calanus* for the eggs production as already discussed before.

Interannual Variability Pattern of Primary and Secondary Production

An additionally performed multi-year simulation experiment in the central Barents Sea highlights the interannual variability in this area (Sakshaug et al., 2009) with respect to magnitude and seasonality in primary and secondary production (**Table 5**). Within the simulated 7 year time period total annual primary production varied in the range of 34.33–95.92 gC m^{-2} y^{-1}, with associated response in secondary production, which varies in the range of 13.61–49.76 gC m^{-2} y^{-1}. Over these years the ice algae production represented always less than 10% of the total annual primary production also with strong interannual variation. The results indicated that years with long ice seasons, but thin ice thickness were the most productive for the ice algae (e.g., 1998). Our results did not demonstrate a clear and recurring seasonal pattern over the years due to the high variability of the ice cover dynamic. We can highlight the existence of a relationship between the length of the ice season and productivity of the ecosystem, which was already described by Rysgaard et al. (1999), showing a clear linear relationship between the annual pelagic primary production and length of productive open water period. **Figure 10** shows clearly how the timing of the ice break-up

drives the magnitude of the primary production. It becomes evident that the earlier in the season the ice breaks up, the higher the total annual primary production, which is consistent with findings by Arrigo and van Dijken (2015). This result also implies an increase of the total primary production in the next decade with the decrease of sea ice coverage and thickness and with a shorter period of ice coverage. This trend is already ongoing and observed in the Barents Sea and the other Arctic Seas (Frey et al., 2018) and is expected to be extended northward in future. Our results however suggested that the maximum productivity did not occur in an ice-free year, but rather during a year showing thin ice coverage and an early ice break-up, as it happens in 1995. This finding indicates that primary production in the Barents Sea may not necessarily increase under upcoming ice-free conditions but could even decrease especially in areas with seasonal sea ice dynamics. Additional numerical experiments in a 3D context will help to explore this pattern further with respect to regional scales. Previous modeling work from Holt et al. (2016) agreed with the heterogeneous effects of the climate change and ice retreat on the Barents Sea productivity and showed for instance that, in contrast to the northern and north-eastern Barents Sea, in the coastal southern Barents Sea production is expected to decrease.

CONCLUSION

The overarching objective of our modeling approach was to understand the linkage between sympagic and pelagic ecosystem components by implementing a sympagic component to the biogeochemical model ECOSMO. We used the model in 1D at different locations in the Barents Sea ecosystem and analyzed spatial and interannual differences in ecosystem dynamics. The sympagic model component was based on previous developments (Lavoie et al., 2005; Tedesco and Vichi, 2014; Castellani et al., 2017; Vancoppenolle and Tedesco, 2017) and meant to improve the ECOSMO model performance in the Arctic ecosystem. In general, our results showed that the simulated seasonality of the sympagic components were realistic and in line with the current knowledge of the Barents Sea ecosystem. Compared to earlier model applications, our study specifically highlighted the strong interactions between the sympagic and the pelagic ecosystems. Most importantly, we could show that the ice algae play an important role for zooplankton phenology as it allows zooplankton biomass growth prior to the onset of the pelagic spring bloom. This process consequently determines the whole ecosystem structure as the zooplankton impacts the amplitude and the timing of the pelagic primary and secondary production. Additional relevant processes are the timing of the ice break-up and that ice algae production determine the phenologies of phytoplankton through seeding. Therefore, we propose that a fully coupled pelagic-sympagic ecosystem is a prerequisite to simulate the Arctic Ocean ecosystem and its changes correctly.

Exchange processes at the ice-ocean interface remain still poorly understood and our sensitivity analyses showed that the parametrization of these processes is a key component for our understanding of the Arctic ecosystem dynamics. With our approach we also found that the proportion of ice algae released and surviving in the pelagic system had an effect on the phytoplankton and zooplankton dynamics. Consequently, slight changes in the ice dynamic can disturb the whole structure of the present Arctic system and can modify phenologies not only of phytoplankton but also all the others species closely related of the ice algae, such as zooplankton (Werner, 1997; Søreide et al., 2010; Kohlbach et al., 2017a), fish (Kohlbach et al., 2017b; Steiner et al., 2019), or bird (Ramírez et al., 2017; Cusset et al., 2019). As an example, Polar cod (*Boreogadus saida*) is a central key species of the Arctic ecosystem and it is closely related to the ice algae especially during their larval development feeding on amphipods, which directly grazed on ice algae and sometimes directly feeding on ice algae itself (Gilbert et al., 1992; Kohlbach et al., 2017b). A decrease in the ice coverage will consequently affect the life cycle of Polar cod, by either creating a mismatch situation with the ice algae or changing the diet of larval Polar cod. We should expect changes in the Polar cod distribution in the next decades, with migration northward, and potentially an extension of the capelin population to replace the Polar cod as already suggested by Hop and Gjøsæter (2013) in the Barents Sea and Steiner et al. (2019) in the Western Canadian Arctic. Moreover, we can expect important change in the abundance and distribution of the predators feeding on both Polar cod and capelin. This example demonstrates, that further numerical experiments including higher trophic level of the marine ecosystem and coupling in a 3D framework will allow us to further explore these hypotheses.

Due to the harsh environmental conditions the Arctic remains a poorly sampled ecosystem leaving many uncertainties in the understanding of its ecosystem functioning. In the context of rapid climate changes, collaborative work becomes even more urgent to fill the knowledge gaps and improve our understanding of the Arctic system in order to establish sustainable management plan in the next decades.

DATA AVAILABILITY STATEMENT

The raw data supporting the conclusions of this article will be made available by the authors, without undue reservation.

AUTHOR CONTRIBUTIONS

DB performed and analyzed the biogeochemical model simulations. DB and UD wrote the main manuscript. All authors discussed the results and implications and participated in the manuscript improvement at all stages.

FUNDING

This work was jointly funded by the UK Research and Innovation Natural Environment Research Council (NERC)

and the German Federal Ministry of Education and Research (BMBF).

ACKNOWLEDGMENTS

This work resulted from the MiMeMo projects (NE/R012571/1 and NE/R012679/1), part of the Changing Arctic Ocean program. We acknowledge particularly Richard Hofmeister for his valuable help on the model designing and programming process. We also acknowledge colleagues from the MiMeMo project, HZG institute and from the BEPSII (Biogeochemical Exchange Processes at the Sea-Ice Interfaces) for the useful discussions and comments. We are thankful for the insightful comments of the two reviewers and the editor.

REFERENCES

Ambrose, W. G., von Quillfeldt, C., Clough, L. M., Tilney, P. V. R., and Tucker, T. (2005). The sub-ice algal community in the Chukchi sea: large- and small-scale patterns of abundance based on images from a remotely operated vehicle. *Polar Biol.* 28, 784–795. doi: 10.1007/s00300-005-0002-8

Anisimov, O., and Fitzharris, B. (2001). "Polar Regions (Arctic and Antarctic). In Climate change 2001: Impacts, adaptation and vulnerability," in *Contribution of Working Group II to the Third Assesment Report of the Intergovernmental Panel on Climate Change*, ed. K. S. White, (Cambridge: Cambridge University Press), 801–842.

Arrigo, K. R. (2014). Sea Ice Ecosystems. *Ann. Rev. Mar. Sci.* 6, 439–467. doi: 10.1146/annurev-marine-010213-135103

Arrigo, K. R., Kremer, J. N., and Sullivan, C. W. (1993). A simulated Antarctic fast ice ecosystem. *J. Geophys Res.* 98, 6929–6946. doi: 10.1029/93JC00141

Arrigo, K. R., and Sullivan, C. W. (1992). The influence of salinity and temperature covariation on the photophysiological characteristics of antarctic sea ice microalgae. *J. Phycol.* 28, 746–756. doi: 10.1111/j.0022-3646.1992.00746.x

Arrigo, K. R., van Dijken, G., and Pabi, S. (2008). Impact of a shrinking Arctic ice cover on marine primary production. *Geophys. Res. Lett.* 35:L19603. doi: 10.1029/2008GL035028

Arrigo, K. R., and van Dijken, G. L. (2015). Continued increases in arctic ocean primary production. *Prog. Oceanogr* 136, 60–70. doi: 10.1016/j.pocean.2015.05.002

Årthun, M., Eldevik, T., Smedsrud, L. H., Skagseth, Ø, and Ingvaldsen, R. B. (2012). Quantifying the influence of atlantic heat on barents sea ice variability and retreat. *J. Clim.* 25, 4736–4743. doi: 10.1175/JCLI-D-11-00466.1

Belém, A. L. (2002). *Modeling Physical and Biological Processes in Antarctic Sea Ice. Dissertation thesis*. Bremen: Universitat Bremen.

Bennett, J. R., Shaw, J. D., Terauds, A., Smol, J. P., Aerts, R., Bergstrom, D., et al. (2015). Polar lessons learned: long-term management based on shared threats in Arctic and Antarctic environments. *Front. Ecol. Environ.* 13:316–324. doi: 10.1890/140315

Bleck, R. (2002). An oceanic general circulation model framed in hybrid isopycnic-Cartesian coordinates. *Ocean Model.* 4, 55–88. doi: 10.1016/S1463-5003(01)00012-9

Boetius, A., Albrecht, S., Bakker, K., Bienhold, C., Felden, J., and Fernández-Méndez, M. (2013). Export of algal biomass from the melting arctic sea ice. *Science* 339, 1430. doi: 10.1126/science.1231346

Bouchard, C., Geoffroy, M., LeBlanc, M., and Fortier, L. (2018). Larval and adult fish assemblages along the Northwest Passage: the shallow Kitikmeot and the ice-covered Parry Channel as potential barriers to dispersal. *Arct. Sci.* 4, 781–793. doi: 10.1139/as-2018-0003

Boyer, T. P., Antonov, J. I., Baranova, O. K., Coleman, C., Garcia, H. E., and Grodsky, A. (2013). "World Ocean Database 2013," in *NOAA Atlas NESDIS 72*, eds S. Levitus, and A. Mishonov, (Silver Spring, MD: National Oceanographic Data Center), 209. doi: 10.7289/V5NZ85MT

Bruggeman, J., and Bolding, K. (2014). A general framework for aquatic biogeochemical models. *Environ. Model. Softw.* 61, 249–265. doi: 10.1016/j.envsoft.2014.04.002

Burchard, H., Bolding, K., and Villarreal, M. R. (1999). *GOTM, A General Ocean Turbulence Model. Theory, Implementation And Test Cases*. Greece: Space Applications Institute,.

Castellani, G., Losch, M., Lange, B. A., and Flores, H. (2017). Modeling Arctic sea-ice algae: physical drivers of spatial distribution and algae phenology. *J. Geophys. Res. Ocean.* 122, 7466–7487. doi: 10.1002/2017JC012828

Clark, G. F., Stark, J. S., Palmer, A. S., Riddle, M. J., and Johnston, E. L. (2017). The roles of sea-ice, light and sedimentation in structuring shallow antarctic benthic communities. *PLoS One* 12:e0168391. doi: 10.1371/journal.pone.0168391

Clasby, R. C., Horner, R., and Alexander, V. (1973). An in situ method for measuring primary productivity of arctic sea ice algae. *J. Fish Res. Board Can.* 30, 835–838. doi: 10.1139/f73-139

Cottier, F., Steele, M., and Nilsen, F. (2017). *Sea ice and Arctic Ocean Oceanography*. Hoboken, NJ: John Wiley &Sons, 197–215. doi: 10.1002/9781118778371.ch7

Cusset, F., Fort, J., Mallory, M., Braune, B., Massicotte, P., and Massé, G. (2019). Arctic seabirds and shrinking sea ice: egg analyses reveal the importance of ice-derived resources. *Sci. Rep.* 9:15405. doi: 10.1038/s41598-019-51788-4

Daewel, U., and Schrum, C. (2013). Simulating long-term dynamics of the coupled North Sea and Baltic Sea ecosystem with ECOSMO II: model description and validation. *J. Mar. Syst.* 119, 30–49. doi: 10.1016/j.jmarsys.2013.03.008

Daewel, U., Schrum, C., and Macdonald, J. (2019). Towards End-2-End modelling in a consistent NPZD-F modelling framework (ECOSMOE2E_vs1.0*):* application to the North Sea and Baltic Sea. *Geosci. Model Dev. Discuss.* 2019, 1–40. doi: 10.5194/gmd-2018-239

Dalpadado, P., Arrigo, K. R., Hjøllo, S. S., Rey, F., Ingvaldsen, R. B., Sperfeld, E., et al. (2014). Productivity in the barents sea–response to recent climate variability. *PLoS One* 9:e095273. doi: 10.1371/journal.pone.0095273

Darnis, G., Robert, D., Pomerleau, C., Link, H., Archambault, P., Nelson, R. J., et al. (2012). Current state and trends in Canadian Arctic marine ecosystems: II. *Heterotrophic food web, pelagic-benthic coupling, and biodiversity*. *Clim. Change* 115, 179–205. doi: 10.1007/s10584-012-0483-8

Deal, C., Jin, M., Elliott, S., Hunke, E., Maltrud, M., and Jeffery, N. (2011). Large-scale modeling of primary production and ice algal biomass within arctic sea ice in 1992. *J. Geophys, Res. Ocean* 116, 148–227. doi: 10.1029/2010JC006409

Dezutter, T., Lalande, C., Dufresne, C., Darnis, G., and Fortier, L. (2019). Mismatch between microalgae and herbivorous copepods due to the record sea ice minimum extent of 2012 and the late sea ice break-up of 2013 in the Beaufort Sea. *Prog. Oceanogr.* 173, 66–77. doi: 10.1016/j.pocean.2019.02.008

Diebold, F. X., and Rudebusch, G. D. (2019). *Probability Assessments Of An Ice-Free Arctic: Comparing Statistical And Climate Model Projections*. PIER Working Paper No. 20-001, University of Pennsylvania, Philadelphia, PA. doi: 10.2139/ssrn.3513025

Duarte, P., Assmy, P., Hop, H., Spreen, G., Gerland, S., and Hudson, S. R. (2015). The importance of vertical resolution in sea ice algae production models. *Mar. J. Syst.* 145, 69–90. doi: 10.1016/j.jmarsys.2014.12.004

Durbin, E. G., and Casas, M. C. (2014). Early reproduction by Calanus glacialis in the Northern Bering Sea: the role of ice algae as revealed by molecular analysis. *J. Plankton Res.* 36, 523–541. doi: 10.1093/plankt/fbt121

Eppley, R. W. (1972). Temperature and phytoplankton growth in the sea. *Fish. Bull.* 70, 1063–1085.

Fernández-Méndez, M., Olsen, L. M., Kauko, H. M., Meyer, A., Rösel, A., and Merkouriadi, L. (2018). Algal hot spots in a changing Arctic Ocean: sea-ice ridges and the snow-ice interface. *Front. Mar. Sci.* 5:75. doi: 10.3389/fmars.2018.00075

Frey, K. E., Comiso, J. C., Cooper, L. W., Grebmeier, J. M., and Stock, L. V. (2018). "Arctic ocean primary productivity: The response of marine algae to climate warming and sea ice decline," in *Arctic Report Card Update* 2018, eds E. Osborne, J. Richter-Menge, and M. Jeffries, (Washingdon, DC: NOAA).

Galindo, V., Gosselin, M., Lavaud, J., Mundy, C. J., Else, B., Ehn, J., et al. (2017). Pigment composition and photoprotection of Arctic sea ice algae during spring. *Mar. Ecol. Prog. Ser.* 585, 49–69. doi: 10.3354/meps12398

Galindo, V., Levasseur, M., Mundy, C. J., Tremblay, J.-E., Scarratt, M., Gratton, Y., et al. (2014). Biological and physical processes influencing sea ice, under-ice algae, and dimethylsulfoniopropionate during spring in the Canadian Arctic Archipelago. *J. Geophys. Res. Ocean.* 119, 3746–3766. doi: 10.1002/2013JC009497

Gilbert, M., Fortier, L., Ponton, D., and Drolet, R. (1992). Feeding ecology of marine fish larvae across the Great Whale River plume in seasonally ice-covered southeastern Hudson Bay. *Mar. Ecol. Prog. Ser. Oldend.* 84, 19–30.

Gosselin, M., Levasseur, M., Wheeler, P. A., Horner, R. A., and Booth, B. C. (1997). New measurements of phytoplankton and ice algal production in the Arctic Ocean. *Deep. Res. Part II Top. Stud. Oceanogr.* 44, 1623–1644. doi: 10.1016/S0967-0645(97)00054-4

Gradinger, R., Friedrich, C., and Spindler, M. (1999). Abundance, biomass and composition of the sea ice biota of the Greenland Sea pack ice. *Deep Sea Res. Part II Top. Stud. Oceanogr.* 46, 1457–1472. doi: 10.1016/S0967-0645(99)00030-2

Haecky, P., Jonsson, S., and Andersson, A. (1998). Influence of sea ice on the composition of the spring phytoplankton bloom in the northern Baltic Sea. *Polar Biol.* 20, 1–8. doi: 10.1007/s003000050270

Hegseth, E. N. (1992). Sub-ice algal assemblages of the Barents Sea: species composition, chemical composition, and growth rates. *Polar Biol.* 12, 485–496. doi: 10.1007/BF00238187

Hegseth, E. N. (1998). Primary production of the northern Barents Sea. *Polar Res.* 17, 113–123. doi: 10.1111/j.1751-8369.1998.tb00266.x

Hirche, H.-J., and Kosobokova, K. (2003). Early reproduction and development of dominant calanoid copepods in the sea ice zone of the Barents Sea—need for a change of paradigms? *Mar. Biol.* 143, 769–781. doi: 10.1007/s00227-003-1122-8

Holt, J., Schrum, C., Cannaby, H., Daewel, U., Allen, I., Artioli, Y., et al. (2016). Potential impacts of climate change on the primary production of regional seas: a comparative analysis of five European seas. *Prog. Oceanogr.* 140, 91–115. doi: 10.1016/j.pocean.2015.11.004

Hop, H., and Gjøsæter, H. (2013). Polar cod (*Boreogadus saida*) and capelin (*Mallotus villosus*) as key species in marine food webs of the Arctic and the Barents Sea. *Mar. Biol. Res.* 9, 878–894. doi: 10.1080/17451000.2013.775458

Horner, R., and Alexander, V. (1972). Algal populations in Arctic sea ice: an investigation of heterotrophy. *Limnol. Oceanogr.* 17, 454–458. doi: 10.4319/lo.1972.17.3.0454

Jin, M., Deal, C., Wang, J., Alexander, V., Gradinger, R., and Saitoh, S.-I. (2007). Ice-associated phytoplankton blooms in the southeastern Bering Sea. *Geophys. Res. Lett.* 34, 94–8276. doi: 10.1029/2006GL028849

Jin, M., Deal, C. J., Wang, J. K., Shin, H., Tanaka, N., Whitledge, T. E., et al. (2006). Controls of the landfast ice–ocean ecosystem offshore Barrow, Alaska. *Ann. Glaciol.* 44, 63–72. doi: 10.3189/172756406781811709

Juul-Pedersen, T., Michel, C., Gosselin, M., and Seuthe, L. (2008). Seasonal changes in the sinking export of particulate material under first-year sea ice on the Mackenzie Shelf (western Canadian Arctic). *Mar. Ecol. Prog. Ser.* 353, 13–25. doi: 10.3354/meps07165

Kanamitsu, M., Ebisuzaki, W., Woollen, J., Yang, S.-K., Hnilo, J. J., Fiorino, M., et al. (2002). NCEP–DOE AMIP-II Reanalysis (R-2). *Bull. Am. Meteorol. Soc.* 83, 1631–1644. doi: 10.1175/BAMS-83-11-1631

Kauko, H. M., Olsen, L. M., Duarte, P., Peeken, I., Granskog, M. A., Johnsen, G., et al. (2018). Algal colonization of young arctic sea ice in spring. *Front. Mar. Sci.* 5:199. doi: 10.3389/fmars.2018.00199

Kimura, N., and Wakatsuchi, M. (2001). Mechanisms for the variation of sea ice extent in the Northern Hemisphere. *Geophys, J., Res. Ocean.* 106, 31319–31331. doi: 10.1029/2000jc000739

Koenigk, T., Mikolajewicz, U., Jungclaus, J. H., and Kroll, A. (2009). Sea ice in the Barents Sea: seasonal to interannual variability and climate feedbacks in a global coupled model. *Clim. Dyn.* 32, 1119–1138. doi: 10.1007/s00382-008-0450-2

Kohlbach, D., Ferguson, S. H., Brown, T. A., and Michel, C. (2019). Landfast sea ice-benthic coupling during spring and potential impacts of system changes on food web dynamics in Eclipse Sound, Canadian Arctic. *Mar. Ecol. Prog. Ser.* 627, 33–48.

Kohlbach, D., Graeve, M., Lange, B. A., David, C., Peeken, I., and Flores, H. (2016). The importance of ice algae-produced carbon in the central Arctic Ocean ecosystem: food web relationships revealed by lipid and stable isotope analyses. *Limnol. Oceanogr.* 61, 2027–2044. doi: 10.1002/lno.10351

Kohlbach, D., Lange, B. A., Schaafsma, F. L., David, C., Vortkamp, M., Graeve, M., et al. (2017a). Ice algae-produced carbon is critical for overwintering of antarctic krill Euphausia superba. *Front. Mar. Sci.* 4:310. doi: 10.3389/fmars.2017.00310

Kohlbach, D., Schaafsma, F. L., Graeve, M., Lebreton, B., Lange, B. A., David, C., et al. (2017b). Strong linkage of polar cod (Boreogadus saida) to sea ice algae-produced carbon: evidence from stomach content, fatty acid and stable isotope analyses. *Prog. Oceanogr.* 152, 62–74. doi: 10.1016/j.pocean.2017.02.003

Kwok, R. (2009). Outflow of Arctic Ocean sea ice into the Greenland and Barent Seas: 1979-2007. *Clim. J.* 22, 2438–2457. doi: 10.1175/2008JCLI2819.1

Lavoie, D., Denman, K., and Michel, C. (2005). Modeling ice algal growth and decline in a seasonally ice-covered region of the Arctic (Resolute Passage, Canadian Archipelago). *J. Geophys. Res. Ocean* 110:C11009. doi: 10.1029/2005JC002922

Legendre, L., Ackley, S. F., Dieckmann, G. S., Gulliksen, B., Horner, R., and Hoshiai, T. (1992). Ecology of sea ice biota. *Polar Biol.* 12, 429–444. doi: 10.1007/BF00243114

Leu, E., Søreide, J. E., Hessen, D. O., Falk-Petersen, S., and Berge, J. (2011). Consequences of changing sea-ice cover for primary and secondary producers in the European Arctic shelf seas: timing, quantity, and quality. *Prog. Oceanogr.* 90, 18–32. doi: 10.1016/j.pocean.2011.02.004

Lindsay, R., and Schweiger, A. (2015). Arctic sea ice thickness loss determined using subsurface, aircraft, and satellite observations. *Cryosphere* 9, 269–283. doi: 10.5194/tc-9-269-2015

Lizotte, M. P. (2001). The contributions of sea ice algae to antarctic marine primary production1. *Am. Zool.* 41, 57–73. doi: 10.1093/icb/41.1.57

Luchetta, A., Lipizer, M., and Socal, G. (2000). Temporal evolution of primary production in the central Barents Sea. *J. Mar. Syst.* 27, 177–193. doi: 10.1016/S0924-7963(00)00066-X

Mangoni, O., Saggiomo, M., Modigh, M., Catalano, G., Zingone, A., and Saggiomo, V. (2009). The role of platelet ice microalgae in seeding phytoplankton blooms in Terra Nova Bay (Ross Sea. Antarctica): a mesocosm experiment. *Polar Biol.* 32, 311–323. doi: 10.1007/s00300-008-0507-z

McMahon, K. W., Ambrose, W. G. Jr, Johnson, B. J., Sun, M.-Y., Lopez, G. R., Clough, L. M., et al. (2006). Benthic community response to ice algae and phytoplankton in Ny Alesund. *Svalbard. Mar. Ecol. Prog. Ser.* 310, 1–14. doi: 10.3354/meps310001

McMinn, A., and Hegseth, E. N. (2007). Sea ice primary productivity in the northern Barents Sea, spring 2004. *Polar Biol.* 30, 289–294. doi: 10.1007/s00300-006-0182-x

McPhee, M. G. (2017). *The Sea Ice–Ocean Boundary Layer*. Hoboken, NJ: John Wiley & Sons, Ltd, 138–159. doi: 10.1002/9781118778371.ch5

Meier, W. N. (2017). *Losing Arctic Sea Ice: Observations of the Recent Decline and the Long-Term Context*. Hoboken, NJ: John Wiley & Sons, Ltd, 290–303. doi: 10.1002/9781118778371.ch11

Michel, C., Legendre, L., Ingram, R. G., Gosselin, M., and Levasseur, M. (1996). Carbon budget of sea-ice algae in spring: evidence of a significant transfer to zooplankton grazers. *J. Geophys. Res. Ocean.* 101, 18345–18360. doi: 10.1029/96JC00045

Michel, C., Nielsen, T. G., Nozais, C., and Gosselin, M. (2002). Significance of sedimentation and grazing by ice micro-and meiofauna for carbon cycling in annual sea ice (northern Baffin Bay). *Aquat. Microb. Ecol.* 30, 57–68. doi: 10.3354/ame030057

Monod, J. (1949). The growth of bacterial cultures. *Annu. Rev. Microbiol.* 3, 371–394. doi: 10.1146/annurev.mi.03.100149.002103

Mortenson, E., Hayashida, H., Steiner, N., Monahan, A., Blais, M., Gale, M. A., et al. (2017). A model-based analysis of physical and biological controls on ice algal and pelagic primary production in Resolute Passage. *Elem. Sci. Anth.* 5:39. doi: 10.1525/elementa.229

Mundy, C., Gosselin, M., Gratton, Y., Brown, K., Galindo, V., Campbell, K., et al. (2014). Role of environmental factors on phytoplankton bloom initiation under landfast sea ice in Resolute Passage. *Canada. Mar. Ecol. Prog. Ser.* 497, 39–49. doi: 10.3354/meps10587

Niemi, A., Michel, C., Hille, K., and Poulin, M. (2011). Protist assemblages in winter sea ice: setting the stage for the spring ice algal bloom. *Polar Biol.* 34, 1803–1817. doi: 10.1007/s00300-011-1059-1

Olsen, L. M., Laney, S. R., Duarte, P., Kauko, H. M., Fernández-Méndez, M., Mundy, C. J., et al. (2017). The seeding of ice algal blooms in Arctic pack ice:

the multiyear ice seed repository hypothesis. *J. Geophys. Res. Biogeosci.* 122, 1529–1548. doi: 10.1002/2016JG003668

Onarheim, I. H., and Årthun, M. (2017). Toward an ice-free Barents Sea. *Geophys. Res. Lett.* 44, 8387–8395. doi: 10.1002/2017GL074304

Oziel, L., Massicotte, P., Randelhoff, A., Ferland, J., Vladoiu, A., and Lacour, L. (2019). Environmental factors influencing the seasonal dynamics of spring algal blooms in and beneath sea ice in western Baffin Bay. *Elem. Sci. Anthr. Univ. Calif. Press* 7:34. doi: 10.1525/elementa.372

Peng, G., and Meier, W. N. (2018). Temporal and regional variability of Arctic sea-ice coverage from satellite data. *Ann. Glaciol.* 59, 191–200. doi: 10.1017/aog.2017.32

Pourchez, A. (2018). *Impact de la Diapause sur la Dynamique de Communautés Planctonique dans un Écosystème Arctique Numérique*. Master's thesis. Quebec, QL: Universté Laval.

Ramírez, F., Tarroux, A., Hovinen, J., Navarro, J., Afán, I., Forero, M. G., et al. (2017). Sea ice phenology and primary productivity pulses shape breeding success in Arctic seabirds. *Sci. Rep.* 7:4500. doi: 10.1038/s41598-017-04775-6

Ratkova, T. N., and Wassmann, P. (2005). Sea ice algae in the White and Barents seas: composition and origin. *Polar Res.* 24, 95–110. doi: 10.3402/polar.v24i1.6256

Reigstad, M., Wassmann, P., Wexels Riser, C., Øygarden, S., and Rey, F. (2002). Variations in hydrography, nutrients and chlorophyll a in the marginal ice-zone and the central Barents Sea. *Mar, J., Syst.* 38, 9–29. doi: 10.1016/S0924-7963(02)00167-7

Riebesell, U., Schloss, I., and Smetacek, V. (1991). Aggregation of algae released from melting sea ice: implications for seeding and sedimentation. *Polar Biol.* 11, 239–248. doi: 10.1007/BF00238457

Rózańska, M., Gosselin, M., Poulin, M., Jm, W., and Michel, C. (2009). Influence of environmental factors on the development of bottom ice protist communities during the winter–spring transition. *Mar. Ecol. Prog. Ser.* 386, 43–59. doi: 10.3354/meps08092

Runge, J. A., and Ingram, R. G. (1988). Underice grazing by planktonic, calanoid copepods in relation to a bloom of ice microalgae in southeastern Hudson Bay. *Limnol. Oceanogr.* 33, 280–286. doi: 10.4319/lo.1988.33.2.0280

Runge, J. A., and Ingram, R. G. (1991). Under-ice feeding and diel migration by the planktonic copepods *Calanus glacialis* and *Pseudocalanus minutus* in relation to the ice algal production cycle in southeastern Hudson Bay. *Canada. Mar. Biol.* 108, 217–225. doi: 10.1007/BF01344336

Rysgaard, S., Nielsen, T. G., and Hansen, B. W. (1999). Seasonal variation in nutrients, pelagic primary production and grazing in a high-Arctic coastal marine ecosystem. Young Sound, Northeast Greenland. *Mar. Ecol. Prog. Ser.* 179, 13–25. doi: 10.3354/meps179013

Sakshaug, E. (1997). Biomass and productivity distributions and their variability in the Barents Sea. *ICES Mar. J. Sci.* 54, 341–350. doi: 10.1006/jmsc.1996.0170

Sakshaug, E., Johnsen, G. H., and Kovacs, K. M. (2009). *Ecosystem Barents Sea, Tapir*. Cambridge, MA: Academic Press.

Samuelsen, A., Hansen, C., and Wehde, H. (2015). Tuning and assessment of the HYCOM-NORWECOM V2.1 biogeochemical modeling system for the North Atlantic and Arctic oceans. *Geosci. Model Dev.* 8, 2187–2202. doi: 10.5194/gmd-8-2187-2015

Sarthou, G., Timmermans, K. R., Blain, S., and Tréguer, P. (2005). Growth physiology and fate of diatoms in the ocean: a review. *J. Sea Res.* 53, 25–42. doi: 10.1016/j.seares.2004.01.007

Schober, M., Duvenaud, D. K., and Hennig, P. (2014). Probabilistic ODE solvers with Runge-Kutta means. *Adv. Neural Inf. Process. Syst.* 2014, 739–747.

Schollmeier, T., Oliveira, A. C. M., Wooller, M. J., and Iken, K. (2018). Tracing sea ice algae into various benthic feeding types on the Chukchi Sea shelf. *Polar Biol.* 41, 207–224. doi: 10.1007/s00300-017-2182-4

Schrum, C., Alekseeva, I., and St John, M. (2006). Development of a coupled physical–biological ecosystem model ECOSMO: part I: model description and validation for the North Sea. *J. Mar. Syst.* 61, 79–99. doi: 10.1016/j.jmarsys.2006.01.005

Selz, V., Saenz, B. T., van Dijken, G. L., and Arrigo, K. R. (2018). Drivers of Ice Algal Bloom Variability between 1980 and 2015 in the Chukchi Sea. *J. Geophys. Res. Ocean* 123, 7037-7052. doi: 10.1029/2018JC014123

Sibert, V., Zakardjian, B., Saucier, F., Gosselin, M., Starr, M., and Senneville, S. (2010). Spatial and temporal variability of ice algal production in a 3D ice – ocean model of the Hudson Bay, Hudson Strait and Foxe Basin system Spatial and temporal variability of ice algal production in a 3D ice – ocean model of the Hudson Bay, Hudson Strait. *Polar Res.* 29, 353–378. doi: 10.3402/polar.v29i3.6084

Skagseth, Ø, Eldevik, T., Årthun, M., Asbjørnsen, H., Lien, V. S., and Smedsrud, L. H. (2020). Reduced efficiency of the Barents Sea cooling machine. *Nat. Clim. Change* 10, 661–666. doi: 10.1038/s41558-020-0772-6

Slagstad, D., Wassmann, P. F. J., and Ellingsen, I. (2015). Physical constrains and productivity in the future Arctic Ocean. *Front. Mar. Sci.* 2:85. doi: 10.3389/fmars.2015.00085

Søreide, J. E., Carroll, M. L., Hop, H., Ambrose, W. G. Jr., Hegseth, E. N., and Falk-Petersen, S. (2013). Sympagic-pelagic-benthic coupling in Arctic and Atlantic waters around Svalbard revealed by stable isotopic and fatty acid tracers. *Mar. Biol. Res.* 9, 831–850. doi: 10.1080/17451000.2013.775457

Søreide, J. E., Hop, H., Carroll, M. L., Falk-Petersen, S., and Hegseth, E. N. (2006). Seasonal food web structures and sympagic–pelagic coupling in the European Arctic revealed by stable isotopes and a two-source food web model. *Prog. Oceanogr.* 71, 59–87. doi: 10.1016/j.pocean.2006.06.001

Søreide, J. E., Leu, E., Berge, J., Graeve, M., and Falk-Petersen, S. (2010). Timing of blooms, algal food quality and Calanus glacialis reproduction and growth in a changing Arctic. *Glob. Chang Biol.* 16, 3154–3163. doi: 10.1111/j.1365-2486.2010.02175.x

Steiner, N., Deal, C., Lannuzel, D., Diane, L., François, M., and Lisa, A. (2016). What sea-ice biogeochemical modellers need from observers. *Elem. Sci. Anth.* 4:000084. doi: 10.12952/journal.elementa.000084

Steiner, N. S., Cheung, W. W. L., Cisneros-Montemayor, A. M., Drost, H., Hayashida, H., Hoover, C., et al. (2019). Impacts of the changing ocean-sea ice system on the key forage fish arctic cod (Boreogadus Saida) and subsistence fisheries in the western canadian arctic—evaluating linked climate. ecosystem and economic (CEE) Models. *Front. Mar. Sci.* 6:179. doi: 10.3389/fmars.2019.00179

Stretch, J. J., Hamner, P. P., Hamner, W. M., Michel, W. C., Cook, J., and Sullivan, C. W. (1988). Foraging behavior of Antarctic krill Euphausia superba on sea ice microalgae. *Mar. Ecol. Prog. Ser* 44, 131–139.

Stroeve, J., and Notz, D. (2018). Changing state of Arctic sea ice across all seasons. *Environ. Res. Lett.* 13:103001.

Stroeve, J. C., Serreze, M. C., Holland, M. M., Kay, J. E., Malanik, J., and Barrett, A. P. (2012). The Arctic's rapidly shrinking sea ice cover: a research synthesis. *Clim. Change* 110, 1005–1027. doi: 10.1007/s10584-011-0101-1

Sun, M.-Y., Carroll, M. L., Ambrose, W. G., Clough, L. M., Zou, L., and Lopez, G. R. (2007). Rapid consumption of phytoplankton and ice algae by Arctic soft-sediment benthic communities: evidence using natural and 13C-labeled food materials. *J. Mar, Res.* 65, 561–588. doi: 10.1357/002224007782689094

Sun, M.-Y., Clough, L. M., Carroll, M. L., Dai, J., Ambrose, W. G., and Lopez, G. R. (2009). Different responses of two common Arctic macrobenthic species (Macoma balthica and Monoporeia affinis) to phytoplankton and ice algae: will climate change impacts be species specific? *Exp, J., Mar. Bio. Ecol.* 376, 110–121. doi: 10.1016/j.jembe.2009.06.018

Sundfjord, A., Fer, I., Kasajima, Y., and Svendsen, H. (2007). Observations of turbulent mixing and hydrography in the marginal ice zone of the Barents Sea. *Geophys, J., Res. Ocean* 112:C05008. doi: 10.1029/2006JC003524

Suprenand, P. M., Ainsworth, C. H., and Hoover, C. (2018). Ecosystem model of the entire beaufort sea marine ecosystem: a temporal tool for assessing food-web structure and marine animal populations from 1970 to 2014. *Marine Science Faculty Publications* 261.

Syvertsen, E. E. (1991). Ice algae in the Barents Sea: types of assemblages, origin, fate and role in the ice-edge phytoplankton bloom. *Polar Res.* 10, 277–288. doi: 10.1111/j.1751-8369.1991.tb00653.x

Szymanski, A., and Gradinger, R. (2016). The diversity, abundance and fate of ice algae and phytoplankton in the Bering Sea. *Polar Biol.* 39, 309–325. doi: 10.1007/s00300-015-1783-z

Tamelander, T., Reigstad, M., Hop, H., and Ratkova, T. (2009). Ice algal assemblages and vertical export of organic matter from sea ice in the Barents Sea and Nansen Basin (Arctic Ocean). *Polar Biol.* 32:1261. doi: 10.1007/s00300-009-0622-5

Tedesco, L. (2014). *Modelling Coupled Physical-Biogeochemical Processes in Ice-Covered Oceans*. Ph.D. dissertation. University of Bologna.

Tedesco, L., and Vichi, M. (2010). *BFM-SI: A New Implementation of the Biogeochemical Flux Model in Sea Ice*. CMCC Research Paper No. 81, University Ave, Rochester, NY.

Tedesco, L., and Vichi, M. (2014). Sea ice biogeochemistry: a guide for modelers. *PLoS One* 9:e89217. doi: 10.1371/journal.pone.0089217

Tedesco, L., Vichi, M., and Scoccimarro, E. (2019). Sea-ice algal phenology in a warmer Arctic. *Sci. Adv.* 5:eaav4830. doi: 10.1126/sciadv.aav4830

Tedesco, L., Vichi, M., and Thomas, D. N. (2012). Process studies on the ecological coupling between sea ice algae and phytoplankton. *Ecol. Model.* 226, 120–138. doi: 10.1016/j.ecolmodel.2011.11.011

Thomas, D. N. (2017). *Sea ice*. Hoboken, NJ: John Wiley & Sons.

Tian, R. C. (2006). Toward standard parameterizations in marine biological modeling. *Ecol. Model.* 193, 363–386.

Vancoppenolle, M., Goosse, H., de Montety, A., Fichefet, T., Tremblay, B., and Tison, J.-L. (2010). Modeling brine and nutrient dynamics in Antarctic sea ice: the case of dissolved silica. *Geophys. J. Res. Ocean* 115, 148–227. doi: 10.1029/2009JC005369

Vancoppenolle, M., Meiners, K. M., Michel, C., Laurent, B., Frédéric, B., and Gauthier, C. (2013). Role of sea ice in global biogeochemical cycles: emerging views and challenges. *Quat. Sci. Rev.* 79, 207–230. doi: 10.1016/j.quascirev.2013.04.011

Vancoppenolle, M., and Tedesco, L. (2017). *Numerical Models of Sea Ice Biogeochemistry*. Hoboken, NJ: John Wiley & Sons, 492–515. doi: 10.1002/9781118778371.ch20

Wang, M., and Overland, J. E. (2012). A sea ice free summer Arctic within 30 years: n update from CMIP5 models. *Geophys. Res. Lett.* 39:18501. doi: 10.1029/2012GL052868

Weeks, W. F. (2010). *On Sea Ice*. Fairbanks, AL: University of Alaska Press.

Werner, I. (1997). Grazing of Arctic under-ice amphipods on sea-ice algae. *Mar. Ecol. Prog. Ser.* 160, 93–99. doi: 10.3354/meps160093

Werner, I., Ikävalko, J., and Schünemann, H. (2007). Sea-ice algae in Arctic pack ice during late winter. *Polar Biol.* 30, 1493–1504. doi: 10.1007/s00300-007-0310-2

Yakubov, S., Wallhead, P., Protsenko, E., Yakushev, E., Pakhomova, S., and Brix, H. (2019). A 1-dimensional sympagic–pelagic–benthic transport model (SPBM): coupled simulation of ice, water column, and sediment biogeochemistry, suitable for arctic applications. *Water* 11:1582. doi: 10.3390/w11081582

Conflict of Interest: The authors declare that the research was conducted in the absence of any commercial or financial relationships that could be construed as a potential conflict of interest.

frontiers in Marine Science

ORIGINAL RESEARCH
published: 19 November 2020
doi: 10.3389/fmars.2020.548931

Extraordinary Carbon Fluxes on the Shallow Pacific Arctic Shelf During a Remarkably Warm and Low Sea Ice Period

Stephanie H. O'Daly[1], Seth L. Danielson[1], Sarah M. Hardy[1], Russell R. Hopcroft[1], Catherine Lalande[2], Dean A. Stockwell[3] and Andrew M. P. McDonnell[1]*

[1] College of Fisheries and Ocean Sciences, University of Alaska Fairbanks, Fairbanks, AK, United States, [2] Amundsen Science, Université Laval, Québec, QC, Canada, [3] Institute of Marine Sciences, University of Alaska Fairbanks, Fairbanks, AK, United States

The shallow Pacific Arctic shelf has historically acted as an effective carbon sink, characterized by tight benthic pelagic coupling. However, the strength of the biological carbon pump in the Arctic has been predicted to weaken with climate change due to increased duration of the open-water period for primary production, enhanced nutrient limitation, and increased pelagic heterotrophy. In order to gain insights into how the biological carbon pump is functioning under the recent conditions of extreme warming and sea ice loss on the Pacific Arctic shelf, we measured sinking particulate organic carbon (POC) fluxes with drifting and moored sediment traps, as well as rates of primary production and particle-associated microbial respiration during June 2018. In Bering Shelf/Anadyr Water masses, sinking POC fluxes ranged from 0.8 to 2.3 g C m^{-2} day^{-1}, making them among the highest fluxes ever documented in the global oceans. Furthermore, high export ratios averaging 82% and low rates of particle-associated microbial respiration also indicated negligible recycling of sinking POC in the water column. These results highlight the extraordinary strength of the biological carbon pump on the Pacific Arctic shelf during an unusually warm and low-sea ice year. While additional measurements and time are needed to confirm the ultimate trajectory of these fluxes in response to ongoing climate change, these results do not support the prevailing hypothesis that the strength of the biological carbon pump in the Pacific Arctic will weaken under these conditions.

Keywords: carbon cycling, particulate organic carbon, Bering and Chukchi Sea Shelves, marine particles, marine snow, Arctic, climate change, biological carbon pump

OPEN ACCESS

Edited by:
Robyn E. Tuerena, Scottish Association For Marine Science, United Kingdom

Reviewed by:
Henry Ruhl, Monterey Bay Aquarium Research Institute (MBARI), United States
Mark Andrew Stevenson, Newcastle University, United Kingdom

****Correspondence:***
Stephanie H. O'Daly
shodaly2@alaska.edu;
stephanie.odaly@outlook.com

Specialty section:
This article was submitted to Global Change and the Future Ocean, a section of the journal Frontiers in Marine Science

Received: *04 April 2020*
Accepted: *27 October 2020*
Published: *19 November 2020*

Citation:
O'Daly SH, Danielson SL, Hardy SM, Hopcroft RR, Lalande C, Stockwell DA and McDonnell AMP (2020) Extraordinary Carbon Fluxes on the Shallow Pacific Arctic Shelf During a Remarkably Warm and Low Sea Ice Period. Front. Mar. Sci. 7:548931. doi: 10.3389/fmars.2020.548931

INTRODUCTION

Arctic marine systems are currently undergoing rapid and profound changes due to the effects of climate change, including reduced sea ice extent, earlier sea ice retreat, protracted ice-free seasons, warming air and ocean temperatures, and shifts in currents and water column stratification (Vaughan et al., 2013; Richter-Menge et al., 2019). These environmental changes have recently

Abbreviations: ACW, Alaska Coastal Waters; ASGARD, Arctic Shelf Growth, Advection, Respiration, and Deposition rate experiments project; BSAW, Bering Shelf/Anadyr Waters; PN, particulate nitrogen; POC, particulate organic carbon.

accelerated on the Pacific Arctic's Bering and Chukchi Sea shelves (Stabeno and Bell, 2019; Huntington et al., 2020; Thoman et al., 2020). During 2017 and 2018, bottom water temperatures in the Bering Sea were 3°C higher than the 2005–2016 baseline (Stabeno and Bell, 2019), and the four lowest maximum sea ice extents since 1979 in the Bering and Chukchi Seas have occurred after 2015 (Fetterer et al., 2017). Cascading impacts on the regional ecosystems, biogeochemical cycles, climate, and human communities on and around the Pacific Arctic shelf are expected, although the nature and magnitude of these impacts remain largely speculative (Carroll and Carroll, 2003; Grebmeier, 2012; Moore and Stabeno, 2015; Stabeno and Bell, 2019).

The shallow Pacific Arctic shelf, averaging 50 m depth, has historically acted as a strong sink of carbon (Bates, 2006; Chen and Borges, 2009). Water movement on these shelves is generally northward carrying different water masses of Pacific origin into the Arctic (Pickart et al., 2016; Danielson et al., 2017), with a significant seasonal modulation (Woodgate et al., 2015) (see **Supplementary Figure 1** for visualization of currents). This region is also characterized by a strong biological carbon pump having pelagic primary productivity (Walsh et al., 1989; Springer and McRoy, 1993), sedimentation (Naidu et al., 2004), and benthic productivity (Grebmeier and McRoy, 1988; Grebmeier and McRoy, 1989) rates that are all amongst the highest measured in any marine system. When light is sufficient, pelagic primary productivity may reach up to 16 g C m^{-2} day^{-1} and 470–840 g C m^{-2} $year^{-1}$ (Walsh et al., 1989; Springer and McRoy, 1993) due to elevated nutrient concentrations (5–20 μM) (Danielson et al., 2017) advected into the region with the Anadyr current from deep Pacific upwelling (Walsh et al., 1989; Springer and McRoy, 1993). The spring phytoplankton bloom is typically dominated by large, rapidly sinking sympagic or pelagic diatoms (Springer and McRoy, 1993; Gradinger, 1999, 2009) that contributed to an annual particulate organic carbon (POC) flux of up to 145 g C m^{-2} $year^{-1}$ near Hanna Shoal (Lalande et al., 2020) and likely facilitate substantial carbon burial in sediments. Similar to other Arctic shelves (Grebmeier and Barry, 1991), total organic carbon on the Pacific Arctic shelf averages 1% and reaches up to 2% in surface layers (Grebmeier and McRoy, 1989; Grebmeier and Barry, 1991; Bluhm and Gradinger, 2008). This active biological carbon pump supports large populations of benthic-feeding pelagic seabirds and marine mammals (Bluhm and Gradinger, 2008; Moore and Kuletz, 2019), many of which are important to Indigenous communities that rely on subsistence hunting (Hovelsrud et al., 2008).

The strength of the biological carbon pump in the Arctic is predicted to weaken with climate change due to increased duration of the open-water period for primary production and enhanced nutrient limitation (Piepenburg, 2005; Wassmann and Reigstad, 2011; Grebmeier, 2012). Warmer waters could increase metabolic rates of pelagic grazers and heterotrophic bacteria and potentially favor smaller phytoplankton and faster-growing grazers that more rapidly recycle organic matter within the water column (Wassmann and Reigstad, 2011; Neeley et al., 2018). Additionally, increased frequency of storms could increase mixing and efflux of carbon dioxide (Hauri et al., 2013; Slats et al., 2019). If these predictions prove accurate, such mechanisms could accelerate feedback processes on the services supported by the biological carbon pump. While the effects of changing ice conditions and warming water on production on the Pacific Arctic shelf have been investigated for many years (Lee et al., 2012; Arrigo et al., 2014; Hill et al., 2018), few studies have directly measured pathways within the biological carbon pump (Fukuchi et al.,1993; Lalande et al., 2020). As part of the Arctic Shelf Growth, Advection, Respiration, and Deposition rate experiments (ASGARD) project, we measured the strength and efficiency of the biological carbon pump by directly quantifying and comparing rates of primary productivity, sinking POC flux, and microbial respiration associated with trap-collected sinking particulate matter during June of 2018 on the Pacific Arctic Shelf. This study occurred after the winter with the lowest maximum sea ice extent on record and in a prolonged time of abnormally warm water (Stabeno and Bell, 2019; Danielson et al., 2020; Huntington et al., 2020). These unique environmental conditions, described in detail in Huntington et al. (2020), provided an opportunity to test the prevailing hypothesis that the biological carbon pump will decrease in strength with climate change (Piepenburg, 2005; Wassmann and Reigstad, 2011; Grebmeier, 2012).

MATERIALS AND METHODS

Hydrography Sampling

All cruise operations were performed on the R/V *Sikuliaq*. The CTD unit consisted of a Seabird SBE16plus unit coupled with WetLabs fluorometer and transmissometer. A Satlantic SUNA V2 instrument was also mounted to the rosette to measure nitrate. To characterize the water mass at each station, surface salinity and temperature data were retrieved from the CTD profiles at each station, then plotted on a temperature–salinity (T/S) diagram.

Drifting Sediment Trap Sampling

A standard Lagrangian-type surface-tethered drifting sediment trap (KC Denmark model number 28.200) was used to collect sinking particles (Moran et al., 2012) at seven locations (**Figure 1**). Two of the four tubes contained a removable clear-bottomed cup filled with 250 mL of viscous polyacrylamide gel. The cups were fitted with a thin sloping ramp to funnel all sinking particles into the gel within the cup and prevent particles from settling between the inside of the tube and the outside of the cup. All four tubes were filled with chilled (0°C) filtered seawater (0.3 μm) collected in Niskin bottles from the same depth and station at which the drifting sediment trap was deployed. The remaining two tubes collected sinking particles in bulk, maintaining *in situ* chemistry as much as possible. The trap array was deployed at 30 m below the surface at each station, estimated to correspond to the bottom of the euphotic zone, for 3–12 h depending on the timing of other cruise operations (**Table 1**). We used the same depth for consistency and to reduce issues of resuspension by sampling too close to the seafloor. The drifting sediment trap was fitted with an ARGOS beacon and a go-Tele GPS tracker unit to track its real-time location.

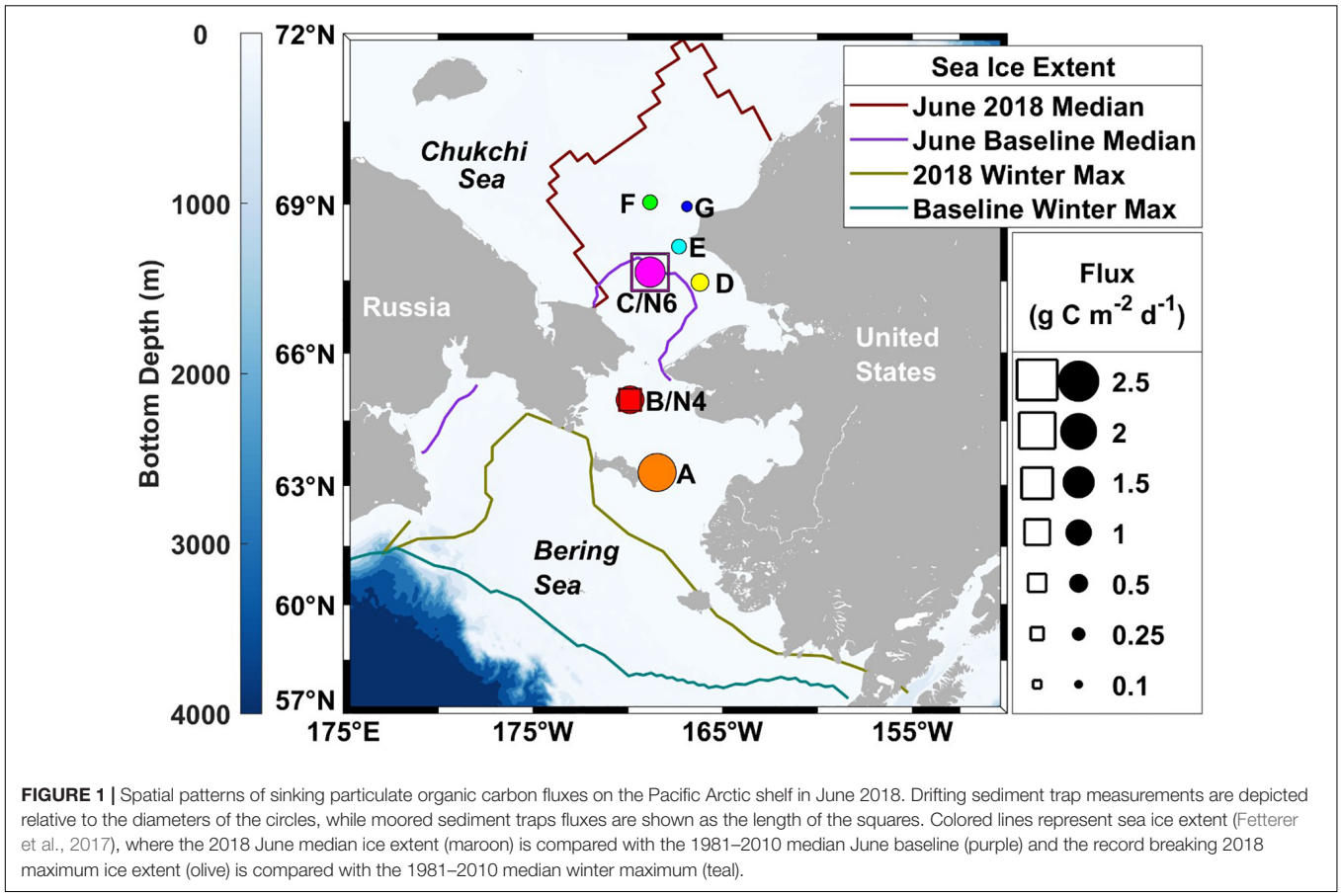

FIGURE 1 | Spatial patterns of sinking particulate organic carbon fluxes on the Pacific Arctic shelf in June 2018. Drifting sediment trap measurements are depicted relative to the diameters of the circles, while moored sediment traps fluxes are shown as the length of the squares. Colored lines represent sea ice extent (Fetterer et al., 2017), where the 2018 June median ice extent (maroon) is compared with the 1981–2010 median June baseline (purple) and the record breaking 2018 maximum ice extent (olive) is compared with the 1981–2010 median winter maximum (teal).

TABLE 1 | Location and duration of drifting sediment trap deployments 30 m below the sea surface in 2018.

Station name	ASGARD station name	Bottom depth (m)	Latitude deploy (degrees decimal minute)	Longitude deploy (degrees decimal minute)	Date and time of deployment (M/DD HH:MM UTC)	Date and time of recovery (M/DD HH:MM UTC)	Total time of deployment
A	CBE1	41	63° 18.1′	−168° 27.0′	6/07 15:05	6/08 2:40	11h 35m
B	DBO2.4	50	64° 58.6′	−169° 52.8′	6/11 10:59	6/11 17:29	6h 40m
C	DBO3.8	50	67° 40.4′	−168° 50.1′	6/14 23:10	6/15 4:52	5h 42m
D	IL4	42	67° 28.3′	−166° 12.5′	6/13 11:57	6/13 20:44	8h 47m
E	DBO3.3	49	68° 11.1′	−167° 18.6′	6/15 19:30	6/15 22:55	3h 25m
F	CL3	51	69° 2.1′	−168° 49.4′	6/16 19:41	6/17 0:10	4h 29m
G	CL1	46	68° 57.3′	−166° 53.8′	6/17 21:18	6/18 2:20	5h 2m

Flux Rate Measurements

Sinking particles collected in the drifting sediment trap were used to determine POC fluxes. Once the trap was recovered, the following steps were performed as quickly as possible in an environmental chamber that fluctuated in temperature from 3 to 5°C in order to maintain as close to *in situ* conditions for particle-associated microbes as possible. Overlying water was siphoned using a vacuum pump down to a boundary layer above the settled particles at the bottom of all four tubes. In the two bulk particle collection tubes, the material that remained in the tubes after siphoning was quantitatively split into four subsamples using a Folsom plankton splitter. Three subsamples were used for triplicate analytical flux measurements. These subsamples were filtered onto pre-combusted 25-mm Whatman GF/F filters and placed in a dehydrator at 60°C for 12 h. Once dried, the filters were sealed in Petri dishes until further analysis (See section "Elemental POC/PN/δ^{13}C/δ^{15}N Analysis" for details). Particulate organic carbon values were converted to daily fluxes depending on the deployment period and the collecting area (g C m^{-2} day^{-1}).

Respiration Rate Measurements

One subsample from each of the two drifting sediment trap tubes was used to estimate particle-associated microbial respiration rates. This material was homogenized by swirling the container and pipetted with a wide-bore pipette into eight replicate

2-mL glass vials (Batch PSTS-1721-01) fitted with Pre-Sens Oxygen Optode Sensor Spots (Regensburg, Germany) per drifting sediment trap tube, totaling 16 experimental samples. Filtered seawater controls were obtained from a Niskin bottle closed at 30 m depth during a CTD cast upon recovery of the drifting sediment trap. Water for the control samples was filtered (0.3 μm) to remove particles and particle-associated microbes. The filtrate was pipetted into eight replicate vials that were identical to the experimental vials. All 24 vials were checked for air bubbles, and vials were then placed inside a sealable, clear, plastic water-bath and placed on top of a PreSens SDR SensorDish Reader The water-bath was located inside a dimly lit cold room that varied from 3–5°C and connected to a Fisherbrand Isotemp 500LCSU Circulator, now referred to as a chiller, which maintained temperature at precisely 4.0°C during the incubation. The concentration of oxygen in each vial and temperature in the incubation chamber were recorded every 30 s for the duration of the incubation using PreSens – Sensor Dish Reader Version 4 Software. Incubations lasted for between 3 and 12 h. After the incubations, the remaining material from each vial was filtered onto individual GF/F filters and treated the same as the flux measurement samples.

A few modifications were made to the methods used for measuring particle-associated microbial respiration rates during the course of the study in order to try to improve the accuracy of our measurements. During the first incubation at station A, a low-oxygen micro-environment formed around the sensor spot, located at the bottom of the vial. For all subsequent incubations, the entire incubation chamber was repeatedly inverted for 5 s every 3 min to mix the sample. Additionally, we noticed the concentration of oxygen increased over time in a few of the experimental samples (i.e., at stations A, C, and E), suggesting photosynthetic activity. During the last two incubations at stations F and G, a black cloth was used to cover the incubation chamber in order to prevent any light from reaching the samples, theoretically preventing light reactions associated with photosynthesis. However, it should be noted that dark reactions associated with photosynthesis can continue for several hours after the removal of light in cold water.

The data recorded by the PreSens software were downloaded and analyzed using the following steps in Matlab 2017a computing software. Data collected before the incubation temperature stabilized were trimmed so that only the time during which the incubation temperature remained stable was analyzed. The first 188 min of data after temperature stabilization was used to determine respiration rates. Linear regression analysis was performed on the oxygen concentration data from each vial. The average and standard deviation of the eight replicate control slopes ($r_{control}$) was taken, and for each of the two experimental samples. Then the average slopes for each of the experimental incubations were averaged together and the error was propagated (r_{exp}). We calculated the carbon-specific particle-associated microbial respiration rate (R_PAM) using a 117:170 organic carbon to oxygen molar respiratory quotient ($V_{OC:O2}$), assuming a one to one relationship with organic carbon degradation and carbon dioxide production (Anderson and Sarmiento, 1994), an incubation volume (vol) of 2 mL, and the final concentration of POC at the end of the incubation ([POC]) (Eq. 1).

$$\text{R\_PAM} = \frac{\left(r_{exp} - r_{control}\right) \times \text{vol} \times V_{OC:O2}}{[\text{POC}]} \quad (1)$$

The average R_PAM ± 1 standard deviation was compared with those from other studies (Ploug and Jorgensen, 1999; Ploug and Grossart, 2000; Iversen and Ploug, 2010; Collins et al., 2015; McDonnell et al., 2015; Belcher et al., 2016a,b) at different locations.

Sinking Particle Visualization

Collecting particles in polyacrylamide gel kept sinking particles intact and allowed for particle imaging and identification (Ebersbach and Trull, 2008; McDonnell and Buesseler, 2010; Durkin et al., 2015). The contents of the cups were photographed within 6 h of sediment trap recovery using a 42.4 MP digital camera equipped with a 90 mm macro-lens and a flash unit. A length to pixel relationship was determined for each image in Adobe Photoshop CS6. These samples were used to qualitatively determine sinking particle type.

Primary Productivity Rate Measurements

^{13}C-^{15}N dual-isotope tracer technique was used to measure integrated rates of primary productivity at the seven stations following a standard protocol (Dugdale and Goering, 1967; Hama et al., 1983). For primary productivity rate measurements, water was collected at six depths corresponding to the 100, 50, 30, 12, 5, and 1% light levels. The 1% light level is estimated to be the minimum amount of light necessary for photosynthesis to occur, i.e., the bottom of the euphotic zone. The incubations lasted between 4 and 7 h, and measurements were extrapolated to daily production by adjusting to total daylight for each incubation site. At the end of the experiment, contents in each incubation bottle were filtered onto pre-combusted GF/F filters and frozen at −80°C until further analysis. These depth-specific rates were then integrated over the entire depth of the euphotic zone to determine total water column primary productivity rates in units of g C m^{-2} day^{-1}.

Elemental POC/PN/$\delta^{13}C$/$\delta^{15}N$ Analysis

All dried or frozen GF/F filters were processed in the Alaska Stable Isotope Facility at the University of Alaska Fairbanks's Water and Environmental Research Center. Filters were acidified with 10% hydrochloric acid for 24 h to remove particulate inorganic carbon (PIC). The filters were pelletized in tin cups. Stable isotope data were obtained using continuous-flow isotope ratio mass spectrometry. Stable isotope ratios were reported in δ notation as parts per thousand (‰) deviation from the international standards VPDB (carbon) and air (nitrogen). Typically, instrument precision was <0.2‰.

Moored Sediment Trap Sampling

Two 24-cup Hydro-Bios sediment traps were moored at stations B south of Bering Strait (trap depth 37 m, bottom depth 49 m) and C north of Bering Strait (trap depth 35 m, bottom depth

50 m) from June 2017 to June 2018 (see **Table 2** and **Figure 1** for location of traps). Sample cups were filled with a hypersaline (salinity 38) 5% formalin solution in filtered seawater to preserve samples during and after deployment (Lalande et al., 2020). The carousel rotated at pre-programmed intervals ranging from seven to 40 days.

As the trap at station B was recovered before the end of its rotation, the material in the last open cup was excluded from analysis. Subsamples from each cup were filtered onto pre-combusted (500°C overnight) GF/F filters (0.7 μm), exposed to 1 N hydrochloric acid overnight for removal of inorganic carbon, and dried at 60°C overnight before encapsulation for POC measurements (Lalande et al., 2020). Particulate organic carbon measurements were conducted on a Perkin Elmer CHNS 2400 Series II elemental analyzer. Particulate organic carbon measurements were converted to daily flux rates depending on the open cup duration of each sample.

Instruments measuring physical and biological parameters in tandem with sinking POC flux were deployed on the moorings at stations B and C. A 300 kHz RDI workhorse ADCP measured bottom current velocity ∼5 m off the seafloor at each site. Lowpass-filtered bottom current velocity were plotted overlaid with a 12-h smoothing. A Seabird SBE16plus unit coupled with a Wetlabs fluorometer measured temperature, salinity and fluorescence at 27 m at station B and 25 m at station C.

Remote Sensing

Daily sea ice concentrations were retrieved from the National Snow and Ice Data Center satellite records for the deployment period at both mooring sites (Fetterer et al., 2017). Wind velocity was obtained from modeled wind reanalysis for the deployment period at both mooring sites (European Centre for Medium-Range Weather Forecasts, 2019). Twenty-four hour smoothing was performed on wind data.

RESULTS

Environmental Conditions

Sea surface temperatures ranged from 1 to 10°C during the ASGARD expedition in June 2018, with the warmest water temperature above 8°C observed south of Nome and west of Norton Sound. These warm waters were characteristically fresher, with salinities ranging from 30 to 30.5, consistent with Alaska Coastal Water (ACW) characteristics and a shift to wind direction from the south (see **Supplementary Figure 1** for a map depicting regional currents in the study area). Wind speed ranged from 0 to 36 kt during the course of the cruise as measured by a vessel-mounted anemometer corrected for ship motion. Throughout the water column, temperatures ranged from −0.5 to 10°C and salinities ranged from 30 to 33.5. Chlorophyll fluorescence ranged from 0 to 15 $\mu g\ L^{-1}$ while nitrate concentration ranged from 0 to 20 $\mu mol\ L^{-1}$ and was highest along the northernmost Cape Lisburne line. SUNA-derived nitrate concentration measurements were confirmed with bottle-derived nitrate concentration measurements. Sea ice was absent during the cruise. A salinity of 31 delimited stations A, B, and C into the Bering Shelf/Anadyr Waters (BSAW) (salinity > 31) and stations D, E, F, and G into ACW waters (salinity < 31) (**Figure 2**).

Drifting Sediment Trap Flux Rate Measurements

The depth of the water column varied little at our seven stations, ranging from 41 to 51 m and averaging 47 m, 17 m deeper than the drifting sediment traps sampling depths at 30 m (1% Photosynthetically Active Radiation (PAR)). The actual 1% PAR varied from between 16 and 30 m, except for station F having a 1% PAR reaching 38 m (**Table 3**). The overall average depth of the euphotic zone was 26 m, comparable to POC export measurements at 30 m. Sinking POC fluxes were high (up to 2.2 g C m^{-2} day^{-1}) but spatially variable. Bering Shelf/Anadyr Waters were associated with higher fluxes (1.2–2.2 g C m^{-2} day^{-1}) at stations A, B, and C, while lower fluxes (0.2–0.5 g C m^{-2} day^{-1}) were characteristic of ACW at stations D, E, F, and G (**Figure 2**). For stations in the BSAW, sinking particles consisted mostly of aggregated diatoms and viable diatom cells while the ACW stations contained more diverse particles including fecal pellets, zooplankton, and diatom cells (**Figure 3**).

The particulate nitrogen (PN) flux ranged from 0.03 to 0.47 g N m^{-2} day^{-1}. Both the highest and lowest PN flux were measured in the ACW (**Table 3**). PN flux was slightly, though not significantly, higher in the BSAW (0.27 g N m^{-2} day^{-1}) than in the ACW (0.15 g N m^{-2} day^{-1}). Delta ^{13}C ranged from −24.03 to −19.94‰ with no clear distinction in $\delta^{13}C$ values between the ACW and BSAW. Both the least negative and most negative $\delta^{13}C$ values were located at stations in the ACW. A similar pattern was true for $\delta^{15}N$ values with values ranging from 5.63 to 8.5‰. There was no spatial pattern in $\delta^{15}N$ values and both the highest and lowest $\delta^{15}N$ values were found in stations in the ACW.

Respiration Rate Measurements

Overall carbon specific particle-associated microbial respiration ranged from −13.7 to 12.8% day^{-1} (**Table 4**). Negative

TABLE 2 | Location and duration of moored sediment traps.

Station name	Trap name	Sampling period	Trap depth (m)	Bottom depth (m)	Latitude (degrees decimal minute)	Longitude (degrees decimal minute)
B	N4	June 26, 2017 to June 08, 2018	37	49	64° 55. 7′	−169° 55.1′
C	N6	June 17, 2017 to June 08, 2018	35	50	67° 40.2′	−168° 44.7′

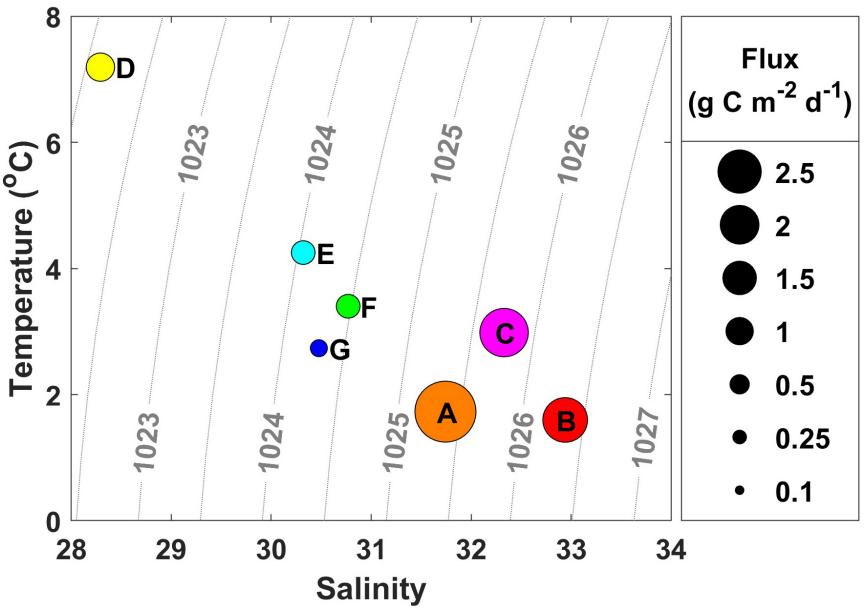

FIGURE 2 | Water mass characteristics from each station where drifting sediment traps were deployed. The size of the circle is indicative of the amount of particulate organic carbon (POC) flux, labeled with station name. Warmer, fresher water characteristic of Alaska Coastal Water (ACW) has lower flux values compared with cooler, more saline water characteristic of Bering Shelf/Anadyr Water (BSAW), which has higher flux values.

TABLE 3 | Particulate organic carbon (POC) flux, primary productivity, and export ratios at seven stations in the Bering and Chukchi seas at drifting sediment trap sites.

Station Name	Water Mass	Bottom Depth (m)	Euphotic Zone Depth (m)	POC flux (g C m^{-2} day^{-1})	Primary Productivity (g C m^{-2} day^{-1})	Export Ratio	PN (g N m^{-2} day^{-1})	δ13-C of sinking material (‰)	δ15-N of sinking material (‰)
A	BSAW	41	16	2.20 ± 0.19	4.24	0.52 ± 0.05	0.40 ± 0.04	−21.08 ± 0.10	7.51 ± 0.49
B	BSAW	50	24	1.18 ± 0.10	0.87	1.36 ± 0.12	0.21 ± 0.02	−20.27 ± 0.06	6.23 ± 0.50
C	BSAW	50	24	1.39 ± 0.07	2.15	0.65 ± 0.05	0.21 ± 0.01	−19.94 ± 0.92	6.71 ± 0.29
D	ACW	42	26	0.48 ± 0.03**	0.48	1.00 ± 0.07	0.47 ± 0.03**	−19.55 ± 0.04**	7.20 ± 1.43**
E	ACW	49	30	0.34 ± 0.03	0.74	0.45 ± 0.04	0.06 ± 0.01	−21.64 ± 0.43	7.37 ± 0.17
F	ACW	51	38*	0.34 ± 0.05	0.33	1.02 ± 0.14	0.05 ± 0.01	−22.30 ± 0.15	5.63 ± 0.28
G	ACW	46	24	0.17 ± 0.00	0.23	0.75 ± 0.06	0.03 ± 0.00	−24.03 ± 0.53	8.50 ± 1.12

Drifting sediment trap sampled at 30 m depth. BSAW, Bering Shelf/Anadyr Waters; ACW, Alaska Coastal Waters.
**Euphotic zone depth deeper than 30 m, the depth of the drifting sediment trap deployment.*
***Outlier of 3 standard deviations higher than other 3 replicates removed from analysis*
Pacific Arctic's extraordinary carbon fluxes.

carbon specific particle-associated microbial respiration indicates net respiration of carbon while positive values indicate net production of carbon. Five of the seven stations had carbon specific particle-associated microbial respiration that were indistinguishable from zero where carbon specific particle-associated microbial respiration could not be distinguished from free living microbial respiration. The two respiration measurements that were distinguishable from zero were from stations B (−13.7 ± 10.5% day^{-1}) and C (12.8 ± 6.7% day^{-1}), both of which are in BSAW. Therefore, all carbon specific particle-associated microbial respiration from stations in ACW were indistinguishable from zero. Average carbon specific particle-associated microbial respiration from BSAW stations (3.1 ± 14.6% day^{-1}, average ± 1 standard deviation), ACW stations (1.7 ± 2.9% day^{-1}), as well as all stations combined (2.3 ± 8.7% day^{-1}) were indistinguishable from zero. Additionally, there was no statistical difference in carbon specific particle-associated microbial respiration between the ACW and BSAW.

Primary Productivity Rate Measurements

Primary productivity rates were spatially variable with an overall range of 0.23–4.24 g C m^{-2} day^{-1}. Station A had the highest rate of primary productivity and had the highest fluorescence signal of the seven stations (full depth CTD profiles are shown in **Supplementary Figure 2**). Here, a slight chlorophyll-a maximum of 10 mg m^{-3} fluorescence was present at 5 m depth and the water column was well-mixed. More pronounced, though lower chlorophyll-*a* maximums occurred at stations C

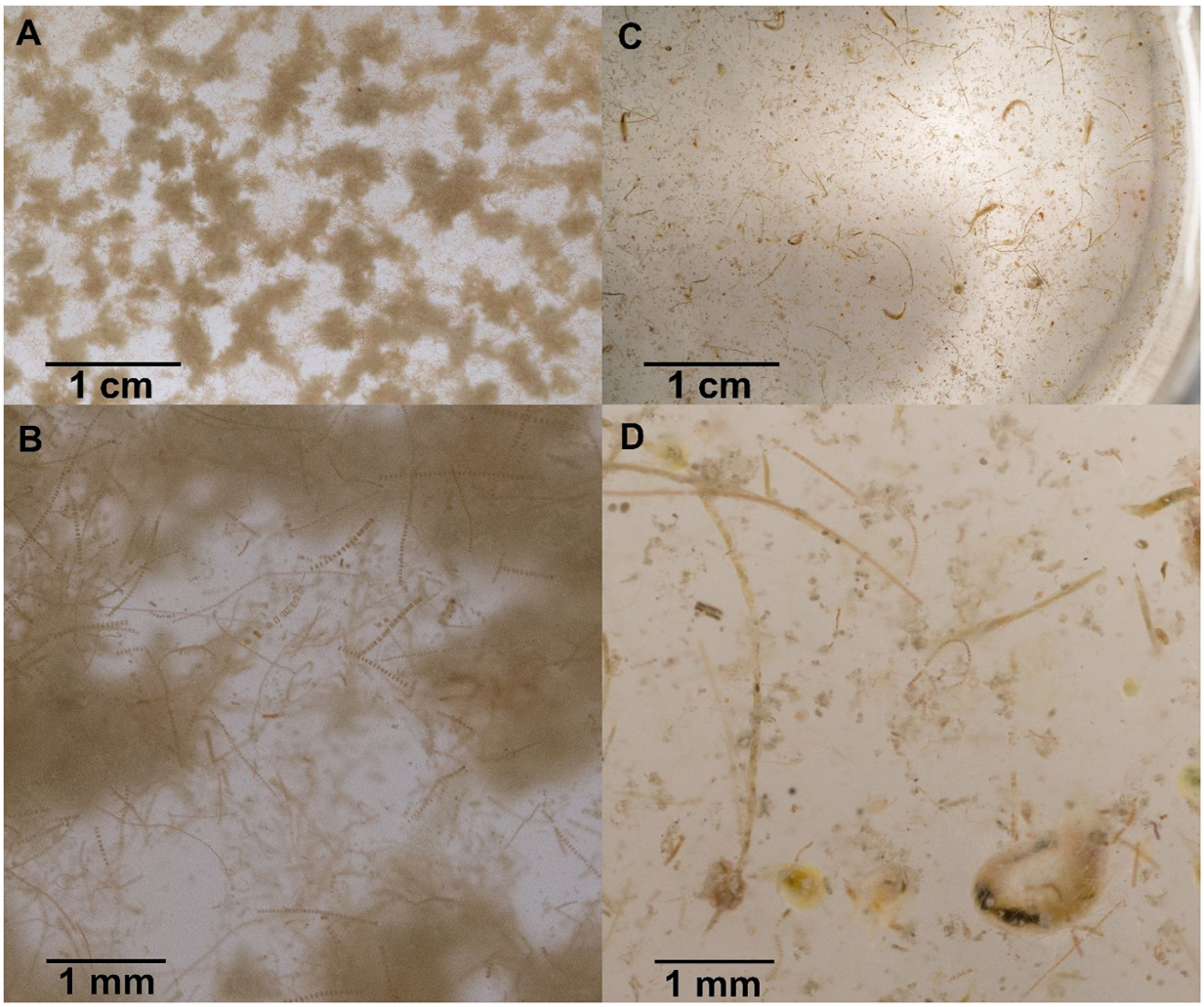

FIGURE 3 | Sinking particles collected in polyacrylamide gel traps at station A **(A,B)** and station D **(C,D)**. Sinking particles at station A are characteristic of Bering Shelf/Anadyr Water stations and consist exclusively of fluffy aggregates made of diatoms and viable diatom chains. Sinking particles at station D are characteristic of Alaska Coastal Water stations and consist of a more diverse set of particles, including fecal pellets, zooplankton swimmers, as well as still viable and senescent diatoms.

TABLE 4 | Particle-associated microbial respiration rates and carbon specific rates for sinking material.

Station Name	Water Mass	r_exp (μmol O_2 m^{-1} L^{-1})	r_control (μmol O_2 m^{-1} L^{-1})	r_PAM (μmol O_2 m^{-1} L^{-1})	R_PAM (% day^{-1})
A	BSAW	−0.215 ± 0.120	−0.076 ± 0.086	−0.139 ± 0.147	10.3 ± 24.0
B	BSAW	***−0.073 ± 0.070***	0.017 ± 0.018	***−0.090 ± 0.072***	***−13.7 ± 10.5***
C	BSAW	***0.087 ± 0.044***	−0.001 ± 0.009	***0.088 ± 0.045***	***12.8 ± 6.7***
D	ACW	0.048 ± 0.024	***0.030 ± 0.012***	0.018 ± 0.027	−0.9 ± 5.7
E	ACW	0.019 ± 0.032	−0.001 ± 0.010	0.020 ± 0.033	4.3 ± 8.0
F	ACW	0.007 ± 0.041	***−0.009 ± 0.008***	0.016 ± 0.042	4.2 ± 9.5
G	ACW	−0.008 ± 0.032	−0.003 ± 0.008	−0.005 ± 0.033	−0.8 ± 7.5

Significant rates in bold and italicized. A total of 188 min were analyzed treating all 16 experimental sample as replicates and the final carbon value used to calculate the per carbon rate. r_exp, experimental respiration rate ± 1 SD; r_control, control respiration rate ± 1 SD; r_PAM, particle-associated microbial respiration rate ± 1 SD, R_PAM; carbon specific particle-associated microbial respiration rate ± 1 SD, BSAW; Bering Shelf/Anadyr Waters; ACW, Alaska Coastal Waters.

(30 m) and F (38 m). Station F had the deepest 1% PAR depth of 38 m, co-occurring with the chlorophyll-a maximum, but had the second lowest rate of primary productivity of 0.34 g C m^{-2} day^{-1}. Overall, primary productivity was higher in the BSAW (0.87–4.24 g C m^{-2} day^{-1}) than in the ACW (0.23–0.74 g C m^{-2} day^{-1}). All three stations in the BSAW had

less stratified water columns, while all four stations in the ACW had more stratified water columns.

Export Ratios

Export ratios are a metric that characterizes the efficiency of the biological carbon pump, calculated using Eq. 2.

$$\text{export ratio} = \frac{\text{flux}}{\text{primary productivity}} \quad (2)$$

Higher export ratios indicate a more efficient biological carbon pump and lower ones less efficient. Export ratios ranged from 0.45 to 1.36 with the lowest export ratio observed at station E and the highest at station B (**Table 3**). There was no significant difference in export ratios between water masses (BSAW: 0.84 ± 0.45 and ACW: 0.81 ± 0.27 mean $\pm$ 1 SD). Three stations (B, D, and F) had export ratios at or above 1 and the overall study average export ratio was 0.82 ± 0.32 (mean $\pm$ 1 SD).

Moored Sediment Trap Time Series Flux Rate Measurements

Moored sediment trap-derived POC fluxes provide independent measures to compare with the fluxes observed with drifting sediment trap sampling. Drifting sediment trap sampling at stations B and C took place three and six days following the end of the moored sediment trap sampling, respectively. Particulate organic carbon fluxes of 0.8 and 1.2 g C m^{-2} day^{-1} at station B and 2.3 and 1.4 g C m^{-2} day^{-1} at station C were obtained with the moored and drifting sediment traps, respectively (**Table 3** and **Figure 4**).

At station B, POC fluxes were generally low (<0.25 g C m^{-2} day^{-1}) from June through October 2017 with brief periods of elevated POC fluxes (0.6–1.3 g C m^{-2} day^{-1}) occurring around the same time as peaks in fluorescence (**Figure 5**). Particulate organic carbon fluxes increased along with wind speed during November and December 2017 (0.9–1.4 g C m^{-2} day^{-1}), decreased during January 2018, and remained relatively low (<0.65 g C m^{-2} day^{-1}) when sea ice was present from January through late April 2018. Fluorescence remained low from mid-October 2017 through April 2018. Sea ice melted at the end of April 2018 and the highest POC fluxes were observed about one month later during late May 2018 (1.5 g C m^{-2} day^{-1}).

At station C, high POC fluxes were recorded from June to mid-July 2017 (1.2–1.7 g C m^{-2} day^{-1}), followed by a period of low POC fluxes from mid-July through mid-October 2017 (<0.5 g C m^{-2} day^{-1}) (**Figure 5**). Spikes in fluorescence occurred sporadically from June until early October 2017. Particulate organic carbon fluxes increased starting in mid-October 2017 and were elevated throughout November and December 2017 (0.9–1.2 g C m^{-2} day^{-1}). Particulate organic carbon flux dramatically decreased when sea ice formed during January 2018. A period of low POC fluxes was observed between January and May 2018 (<0.5 g C m^{-2} day^{-1}), while sea ice was consistently present. The highest POC fluxes were measured at the beginning of June 2018 (2.3 g C m^{-2} day^{-1}), at the same time as the highest peaks of fluorescence soon after sea ice retreated from this station.

The moored sediment trap time series indicates that POC flux had recently peaked at station B before drifting sediment trap sampling took place during early June 2018, but was likely at or near the period of peak annual flux at station C (**Figure 5**). The composition of the material collected in the moored sediment trap samples during June 2018 indicated the occurrence of a pelagic phytoplankton bloom at station B, reflected by the export of the exclusively pelagic centric diatoms *Chaetoceros* spp. and *Thalassiosira* spp. that usually dominate spring blooms on Arctic shelves (Degerlund and Eilertsen, 2010; Lalande et al., 2019). Diatom fluxes, composed of several pennate and centric diatom groups, were nearly three times higher at station C than at station B, reflecting a large diatom bloom.

DISCUSSION

The overall objectives of this study were to characterize the strength and efficiency of the biological carbon pump on the Pacific Arctic shelf during a warm, low-ice year in order to shed light on potential current and future changes in carbon cycling in this region. We addressed this by considering three major aspects of relevance: primary productivity, sinking POC flux, and particle-associated microbial respiration during June of 2018.

Regional Spatial Trends

The largest distinction of regional spatial trends occurred between the two water masses present in this region (ACW and BSAW). Consistent with previous studies, the ACW was warmer and fresher with lower nutrients than the BSAW during June 2018 (Walsh et al., 1989; Springer and McRoy, 1993). Both regions were warmer than normal for this time of year and had experienced much less sea ice than normal (Danielson et al., 2020; Huntington et al., 2020).

We measured consistently lower POC flux rates in ACW than BSAW. These results support the previously untested hypothesis that POC fluxes would be higher in the BSAW compared to ACW (Grebmeier and McRoy, 1989). This distinction in primary productivity and POC flux between the ACW and BSAW could partially be attributed to differences in stratification between these regions; we found a less stratified water column in the BSAW, which could contribute to nutrient input to the surface and allow for higher primary productivity rates. Well-mixed water could also help facilitate POC mixing out of the euphotic zone, however it is more likely that this material could be brought back up to the surface through the same mechanism. The differences in primary productivity and POC flux cannot be fully explained by differences in water column stratification. The two regions were characterized by different types of sinking particles: more uniform aggregated diatoms and viable diatoms were found in the BSAW, while more processed material like fecal pellets and zooplankton were found in the ACW in addition to living diatoms. This distinction suggests more processing of POC by zooplankton or heterotrophic bacteria in the ACW. However, there was no difference in export ratio or particle-associated microbial respiration between

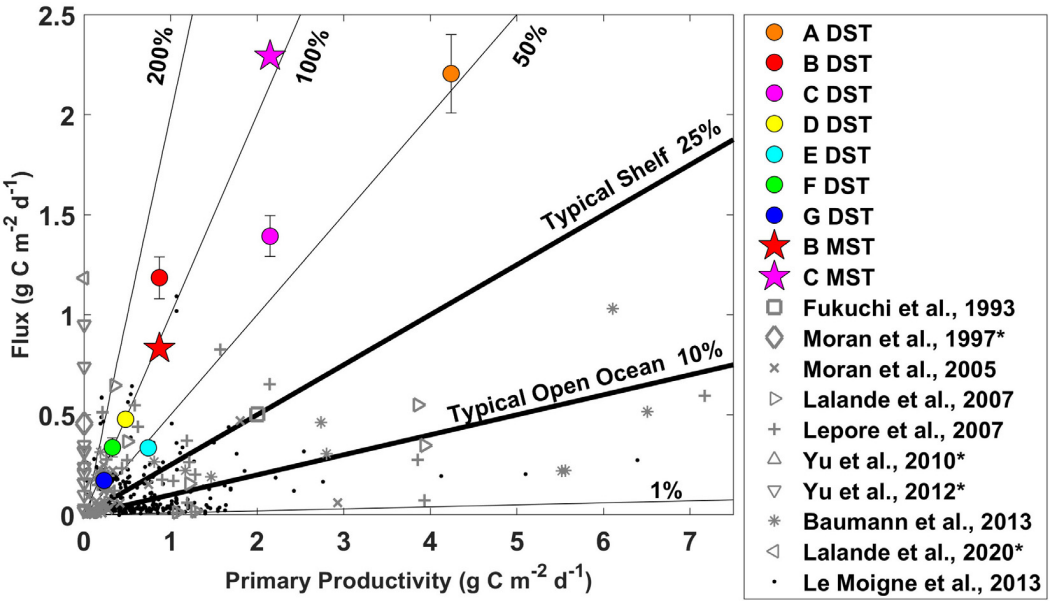

FIGURE 4 | Sinking particulate organic carbon fluxes and primary productivity rates with contours of the export ratio between these two parameters measured during June 2018 on the Pacific Arctic shelf. The circles represent flux measurements from the drifting sediment trap. The stars represent the final flux measurement from the moored sediment traps (values plotted against the same primary productivity rates). Gray markers provide regional (Fukuchi et al., 1993; Moran et al., 1997, 2005; Lalande et al., 2007, 2020; Lepore et al., 2007; Yu et al., 2010, 2012; Baumann et al., 2013) and black markers global context (Le Moigne et al., 2013). *No corresponding productivity data with Moran et al., 1997 (Moran et al., 1997), Yu et al. (2010, 2012), and Lalande et al., 2020 (Lalande et al., 2020).

the two water masses, indicating that POC fluxes are mostly regulated by primary production rates rather than heterotrophic processing. The spatially uniform particle associated microbial respiration rates we measured do not support the postulation that the ACW would have higher particle-associated microbial respiration rates (Andersen, 1988; Grebmeier and Barry, 1991). Nonetheless, the higher primary productivity and POC fluxes in the BSAW demonstrate a stronger biological carbon pump in the BSAW region.

PN, $\delta^{13}C$, and $\delta^{15}N$ values were not significantly different between the BSAW and the ACW. Higher PN in sinking material are associated with more nutritious food for the benthos (Grebmeier et al., 1988). Less negative $\delta^{13}C$ values tend to indicate a larger influence of ice algae or a marine signature while more negative $\delta^{13}C$ values tend to indicate a more coastal or terrigenous signature (Wooller et al., 2007). Larger $\delta^{15}N$ values were associated with material that is higher on the food chain (i.e., secondary and tertiary producers), while lower $\delta^{15}N$ values are associated with material lower on the food chain (i.e., primary producers) (Post, 2002).

The ACW had lower primary productivity than the BSAW. This regional pattern has been well described previously (Walsh et al., 1989; Springer and McRoy, 1993) and is attributed to the lower nutrient concentrations in ACW compared with BSAW (Danielson et al., 2017). Primary productivity values in both water masses fell within a typical range for these regions (Lee et al., 2007; Arrigo et al., 2014; Hill et al., 2018). However, a primary productivity rate of 16 g C m^{-2} day^{-1} has been previously observed in the Pacific Arctic Shelf (Walsh et al., 1989; Springer and McRoy, 1993), much higher than what we measured and what is typically measured. If these higher production rates were associated with export ratios similar to what we observed here, then the associated fluxes would be even more remarkable than the values we observed with the DSTs and MSTs during this study.

Stations with higher rates of primary productivity tended to have higher rates of POC flux. However, there was not a perfect relationship between primary productivity and POC flux, which caused some variations in the export ratios. The stations with export ratios over 1 and the high average export ratio indicate an extremely efficient biological carbon pump or temporal or spatial decoupling between primary production and flux.

While the dominant regional patterns were associated with water masses, we also expected some patterns falling along a latitudinal gradient. It is difficult to separate the signal of water mass from latitude because most of the stations that were classified as BSAW were located south of the stations classified as ACW. We found higher daily primary productivity rates and POC fluxes at the southern stations in the BSAW than at the northern stations in the ACW. The annual POC flux was higher at station C (215 g C m^{-2} $year^{-1}$) than at station B (204 g C m^{-2} $year^{-1}$), indicating an increase in POC flux with latitude. However, an annual POC flux lower than these (145 g C m^{-2} $year^{-1}$) was measured at about 200 miles north of our study area (Lalande et al., 2020). Drifting sediment trap sampling at more stations in the southern portion of the ACW and moored sediment trap sampling in the ACW are needed to better

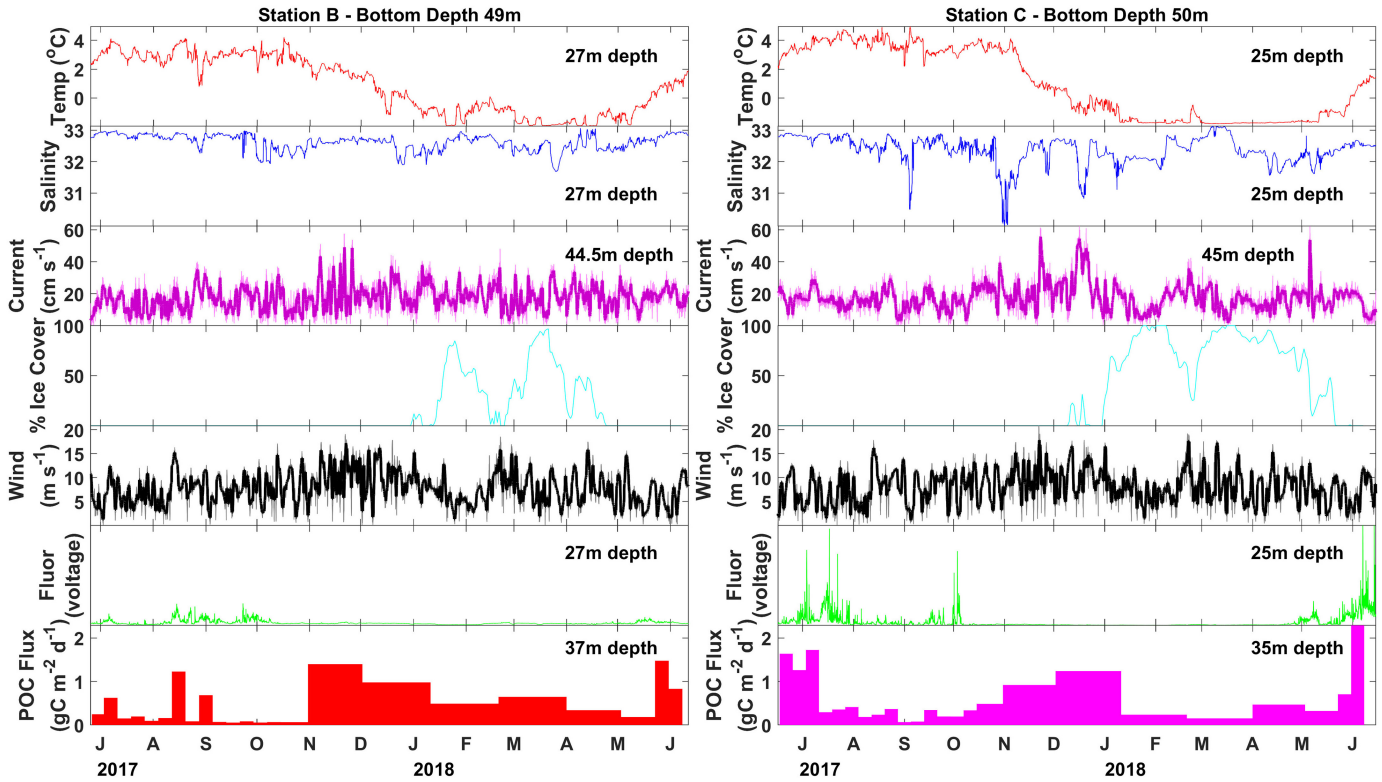

FIGURE 5 | Particulate organic carbon flux (colored bars) measured with moored sediment traps at stations N4 and N6 between June 2017 and June 2018. Sea ice percent cover (cyan line) taken from NSIDC satellite records (Fetterer et al., 2017). Wind velocity (black line) taken from modeled wind reanalysis (European Centre for Medium-Range Weather Forecasts, 2019). Twenty-four hour smoothing is shown with the thick black line. Lowpass-filtered current velocity (magenta line) taken from AD, with 12 h smoothing shown with the thick magenta line, temperature (red line), salinity (blue line), fluorescence (green line) taken from seabird SBE16plus unit coupled with a WetLabs fluorometer on each of the moorings.

tease apart the differences associated with latitude and water mass in this region.

The annual pattern of POC flux shows some latitudinal distinction between the more northern station C and the more southern station B. The peak annual flux occurred during early June 2018 at station C, while the peak annual flux occurred a couple of weeks earlier at station B (late May 2018). The spring peak flux was higher at station C (2.3 g C m^{-2} day^{-1}) compared to station B (1.5 g C m^{-2} day^{-1}). Increased POC flux measurements occurred in the absence of peaks in fluorescence at both stations from November 2017 to January 2018 strongly suggesting episodic resuspension events during fall. Particulate organic carbon fluxes decreased in the presence of sea ice, reducing wind mixing and resuspension. This is particularly evident at station C under higher sea ice concentrations. It is likely that these fall high flux events do not represent increased net flux, as they are likely partly the result of material that previously fell to the seafloor being resuspended and collected in the moored sediment trap again.

Role of Heterotrophy in the Water Column

Bacterial production largely controls how much exported POC reaches the seafloor and might increase in Arctic waters under more acidic, warmer, and lower-ice conditions (Garneau et al., 2009; Vaqué et al., 2019), which could result in higher pelagic community carbon demand (Sala et al., 2010). One factor that has received a lot of thought for the Pacific Arctic shelf region is how a reduction in ice algae relative to to pelagic phytoplankton as primary producers might impact the benthic-pelagic coupling, with the prediction that smaller pelagic phytoplankton will have slower sinking rates and will therefore be more likely to be consumed by zooplankton or bacteria in the water column, resulting in less material reaching the seafloor (Carroll and Carroll, 2003; Grebmeier, 2012; Moore and Stabeno, 2015). A slower particle sinking rate will give more time for bacteria to both colonize and degrade sinking particles. In our study, we mostly collected pelagic diatoms in the drifting sediment traps rather than species associated with ice. However, our direct measurements of microbial respiration rates associated with sinking particles were mostly indistinguishable from zero. This is not unprecedented in high latitude regions (McDonnell et al., 2015).

Conducting a comparison of measured particle-associated microbial respiration rates from around the globe, we found that particle-associated microbial respiration generally decreases with increasing latitude (**Figure 6**). In our study, the rate of particle-associated microbial respiration was 2% day^{-1} on average, with a 95% confidence interval ranging from −24.2 to 34.3% day^{-1}. Given the shallow nature of the Pacific Arctic shelf (20 m average distance from base of euphotic zone to seafloor) and rapid sinking velocity of material caught in the traps (greater than 100 m day^{-1}), even under the fastest respiration rate (−24.2% day^{-1}) we calculated that less than 5% of the exported organic carbon would be remineralized within the water column before being deposited on the seafloor. Considering our conservative estimates, the true consumption is likely much smaller than this value. We conclude that particle-associated microbial respiration does not play a large role in recycling POC below the euphotic zone in this region, implying that most of the material that is exported from the euphotic zone will likely reach the shallow seafloor.

One mitigating factor in how much organic matter is deposited on the seafloor is the role zooplankton and free-living heterotrophic microbes play in consuming organic matter in the water column. Historically, zooplankton have not consumed large proportions of organic matter in the water column (Ashjian et al., 2003; Campbell et al., 2009; Hopcroft et al., 2010; Kitamura et al., 2017; Lalande et al., 2020), but it is possible they may play a larger role in the future. One study from just north of our study area found that primary production rates were similar to free-living community microbial respiration rates during the summer, indicating a large proportion of primary production could be consumed by free-living microbes (Cota et al., 1996). High export ratios in the present study point to zooplankton and free-living heterotrophic microbes playing a small role in consuming organic matter within the euphotic zone. It is possible that zooplankton and bacteria may play a larger role in consuming POC later in the summer. We suggest measuring export ratios and particle associated microbial respiration rates in August on the Pacific Arctic shelf to answer this remaining question.

Comparison of Drifting and Moored Sediment Trap POC Fluxes

The POC flux measurements measured with the drifting and moored traps at stations B and C, while of similar magnitude, were not the same. Many factors potentially caused variations between POC flux values obtained with drifting and moored traps. One reason is the different sampling times as POC fluxes may have changed on time scales much shorter than three or six days. In addition, the moored sediment trap measured flux over eight days, while the drifting sediment traps measured flux for six and a half hours and station B and five and a half hours at station C. If there is a diurnal cycle in flux regulated by zooplankton or phytoplankton it can be captured in the drifting sediment trap sampling and masked in the moored sediment trap sampling. Our study took place on a shallow Arctic shelf over the summer solstice. It is unlikely there was a diurnal cycle of primary production due the nearly 24 h of sunlight that were present. Additionally, due to the shallowness of the shelf, zooplankton in this region are not know to exhibit diel vertical migration (Ashjian et al., 2003; Campbell et al., 2009). It is unlikely that any differences in POC flux are a result of any changes in flux as a diurnal cycle, and, if present, are likely due to changes in the rate of primary production controlled by variable cloud cover and nutrient availability. Finally, the locations of the moored sediment trap and drifting sediment trap sampling did not perfectly overlap, although the drifting sediment traps were deployed within half a mile of the moored sediment traps.

Even if the sampling of these two traps perfectly overlapped in time and space, it is unlikely that they would produce the same

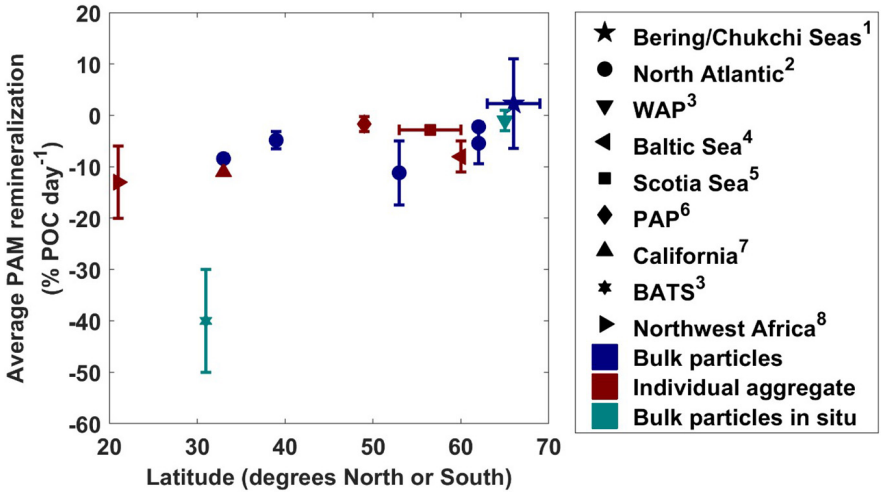

FIGURE 6 | Average particle-associated microbial respiration rates (with one standard deviation plotted as vertical error bars) from this study along with previous measurements at other latitudes. Symbols colored with navy indicate bulk particle respiration measurements, teal indicate measurements taken with RESPIRE *in situ* incubator, and maroon indicate rates measured from individual aggregates. WAP, Western Antarctic Peninsula; PAP, Porcupine Abyssal Plain; BATS, Bermuda Atlantic Time Series. Measurements were taken from this study[1], Collins et al. (2015)[2], McDonnell et al. (2015)[3], Ploug and Grossart (2000)[4], Belcher et al. (2016a)[5], Belcher et al. (2016b)[6], Ploug and Jorgensen (1999)[7], and Iversen and Ploug (2010)[8].

POC flux values. One reason is because the moored sediment traps sample with a Eulerian framework, being moored in one location sampling various water masses as they flow, while drifting sediment traps sample with a Lagrangian approach, staying with one parcel of water and sampling it continuously as it moves with the currents. Another reason is that each of these trap designs have their own individual biases. In high current environments moored sediment traps can tilt to the side, affecting the collection of sinking particles. However, no tilt occurred at stations B and C based on CTD data. In contrast, drifting sediment traps may reduce the vertical shear in high current environments by floating freely within the water column. Additionally, we minimized other hydrodynamic concerns by using a bungee to dampen surface motion, tubes with a high aspect ratio, and bottom weighted tubes to keep them upright (Butman et al., 1986; Nodder et al., 2001, Buesseler et al., 2007). However, sinking POC flux may be incorrectly measured with drifting sediment traps because the tubes are open during deployment and recovery, contrary to the moored sediment traps (Buesseler et al., 2007). This source of error is minimized by deploying the drifting sediment traps at a shallow depth (i.e., 30 m).

With these sources of error, it is helpful to have two independent measurements of POC flux using different methods. The overall range of POC flux values in June 2018 was 1.48 to 2.29 g C m^{-2} day^{-1} with the moored sediment traps and 0.17 to 2.20 g C m^{-2} day^{-1} with the drifting sediment traps. Comparable maximum flux magnitudes from these two different methods minimize the concerns of collection biases common with sediment traps and provide some supporting evidence of the validity of POC fluxes of this magnitude.

Comparing POC Flux, Primary Productivity, and Export Ratios

Primary productivity rates, sinking flux, and export ratios were compared with previous measurements from the same study area (Fukuchi et al., 1993; Moran et al., 1997; Yu et al., 2010, 2012; Lalande et al., 2020), the broader Bering and Chukchi shelf system (Moran et al., 2005; Lalande et al., 2007; Lepore et al., 2007; Baumann et al., 2013), the greater Arctic area (**Supplementary Table 1**), and from a global compilation (Le Moigne et al., 2013; **Figure 4**, and **Supplementary Figure 2**). The upper range of our POC flux measurements (2.2 g C m^{-2} day^{-1} from drifting sediment trap and 2.3 g C m^{-2} day^{-1} from moored sediment trap) was unprecedentedly high compared to other measurements in this region and among the highest recorded in the surrounding areas, the broader Arctic, and globally.

Five previous studies report particulate flux estimates for the Bering and Chukchi shelves (Fukuchi et al., 1993; Moran et al., 1997; Yu et al., 2010, 2012; Lalande et al., 2020), two based on sediment trap measurements. A moored sediment trap deployed (36 m water depth, 49 m bottom depth) from late June to late September 1988, about 500 miles south of Bering Strait, measured flux ranging from 253 to 654 mg C m^{-2} day^{-1} (Fukuchi et al., 1993). More recently, a moored sediment trap deployed (37 m water depth, 45 m bottom depth) from August 2015 to July 2016, about 200 miles north of our most northern stations on the Chukchi shelf, measured POC fluxes ranging from 72 to 1184 mg C m^{-2} day^{-1} (Lalande et al., 2020). An estimate of 456 mg C m^{-2} day^{-1} (36 m water depth, 49 m bottom depth) was calculated using the $^{234}Th/^{238}U$ disequilibrium method on the Chukchi Sea shelf in August 1994 (Moran et al., 1997). Yu et al. (2010) measured a POC flux value of 243.8 mg C m^{-2} day^{-1}

(40 m water depth, 50 m bottom depth) using the $^{234}Th/^{238}U$ disequilibrium method sometime between July and September on the Chukchi shelf within the bounds of our study area. Finally, during a study on the Chukchi shelf from July to September, a POC flux measurement of 951.1 mg C m^{-2} day^{-1} (30 m water depth, 40 m bottom depth) was made using the $^{234}Th/^{238}U$ disequilibrium method within the bounds of and to the north of our study area (Yu et al., 2012). We selected the peak annual POC flux value from Lalande et al. (2020) and the flux measurement from Moran et al. (1997) and Yu et al. (2010, 2012) and plotted them directly on the y-axis indicating no known corresponding primary productivity value (**Figure 4**). The spatial extent of these studies are shown along with that of this study in **Supplementary Figure 3**. It should be noted that the $^{234}Th/^{238}U$ disequilibrium method for calculating sinking POC flux has its own biases, especially in areas with non-steady state flux events and advection and dispersion processes (Buesseler et al., 2007), such as on a shallow Arctic shelf. The measurements of POC flux we made in this study were the same or higher than previous measurements made in this region.

We expanded our region of comparison to include the Bering and Chukchi shelf breaks. Particulate organic carbon flux has been estimated more frequently on the Bering and Chukchi shelf breaks, with a maximum flux value at the base of the euphotic zone of 1.381 g C m^{-2} day^{-1} reported slightly south of our study area on the Bering Sea shelf break (40 m water depth, >125 m bottom depth) in July 2010 (**Figure 6**; Baumann et al., 2013). Additionally, our average regional flux for the BSAW, 1.59 ± 0.54 g C m^{-2} day^{-1} (mean ± 1 SD) is much higher than previous average regional flux estimates from the shelf breaks just north and south of this region, which range from 34 mg C m^{-2} day^{-1} (50 m water depth, bottom depth average 1275 m, May and June sampling period) to 376 mg C m^{-2} day^{-1} (50 m water depth, bottom depth average 838 m, May and June sampling period) (Moran et al., 2005, 2012; Lalande et al., 2007; Lepore et al., 2007; Baumann et al., 2013). Although individual measurements of export ratios approaching 1 are somewhat common (Lepore et al., 2007; Baumann et al., 2013), our average export ratio of 0.82 ± 0.32 (mean ± 1 SD) is very high. These observations illustrate the exceptional efficiency and strength of the biological carbon pump in the shallow Pacific Arctic shelf and shelf breaks.

Sinking POC flux and primary productivity values were also compared with a global review of POC flux measurements obtained using the $^{234}Th/^{238}U$ disequilibrium method (Le Moigne et al., 2013). We plotted all values with both POC flux and primary productivity rate measurements from Le Moigne et al. (2013), along with previous measurements from the broader Pacific shelf system, and our specific study area with the values we measured in this study from the drifting sediment traps and the last values of POC flux from the moored sediment traps (**Figure 4**). When available, sinking POC flux measurements at the base of the euphotic zone were selected, a metric shown to be comparable at sites with different bottom and euphotic zone depths (Buesseler et al., 2020). From this analysis, it is evident that the primary productivity rates from this study mostly fall within the upper range of what has been measured in this region before. Flux measurements at the BSAW stations (0.8–2.3 g C m^{-2} day^{-1}) are very high compared to what has been measured previously (0–1.4 g C m^{-2} day^{-1}).

In addition to the global review by Le Moigne et al. (2013), we compiled POC fluxes, primary productivity rates, and export ratios from other high latitude studies. The results of this review can be found in **Supplementary Table 1**. We categorized the studies by region, including the Baffin Bay, Baltic Sea, Barents Sea, Beaufort Sea, Bering Sea, Canadian Archipelago, Chukchi Sea, Fram Strait, Greenland Sea, Hudson Bay, Kara Sea, Labrador Sea, Laptev Sea, North Atlantic, North Sea, White Sea, as well as the high Arctic. We considered studies that measured sinking POC flux rates using drifting, moored, or neutrally buoyant sediment traps, marine snow catchers, or $^{234}Th/^{238}U$ disequilibrium. When possible, we selected samples from as close to the euphotic zone as possible. Primary productivity rates ranged from 0 to 2.6 g C m^{-2} day^{-1} and export ratios ranged from 0.03 to 1.67. These ranges are consistent with the primary productivity and export ratios measured in this study. Out of 79 studies, only nine measured rates of POC flux greater than 1 g C m^{-2} day^{-1} that were measured in the Baffin Bay (Michel et al., 2002), the Barents Sea (Andreassen and Wassmann, 1998; Olli et al., 2002; Lalande et al., 2008; Gustafsson et al., 2013), the Bering Sea (Baumann et al., 2013), the Beaufort Sea (Amiel and Cochran, 2008), the Chukchi Sea (Lalande et al., 2020), and the North Atlantic (Buesseler et al., 1992). The highest POC flux measurement of 2.5 g C m^{-2} day^{-1} was measured in the Beaufort Sea near the Makenzie River drainage in June at 50 m depth and 230 m water depth (Amiel and Cochran, 2008). The second highest POC flux measurement of 1.5 g C m^{-2} day^{-1} was measured in the Barents Sea in May at 30 m depth and 239 m bottom depth (Olli et al., 2002). We also selected some studies of POC flux from known high productivity and/or high flux regions from around the world (**Supplementary Table 2**). These POC flux values ranged from 1 to 620 mg C m^{-2} day^{-1}. Two POC flux values recorded in the present study were among the highest ever recorded at the base of the euphotic zone (2.20 g C m^{-2} day^{-1} at station A with a drifting sediment trap and 2.29 g C m^{-2} day^{-1} at station C with a moored sediment trap). With individual flux values from different methods at different stations ranking among the highest ever recorded, it is clear that the Pacific Arctic shelf exported a massive amount of organic carbon out of the euphotic zone, even in an anomalously warm year with low sea ice.

Limitations and Implications

Even with strong efforts in place to study the processes on the Pacific Arctic Shelf with the ASGARD program, there is still a lack of available data. While POC flux and water column oceanographic measurements are being obtained more frequently with moored sediment traps, temporally overlapping primary productivity rate measurements are not often available, notably later in the summer or earlier in the spring, when production is highest. Previous primary productivity measurements obtained later in the summer (Springer and McRoy, 1993; Lee et al., 2007; Hill et al., 2018) may no longer be representative of current conditions. Additionally, particle-associated microbial respiration rates are likely variable

throughout the spring, summer and fall and therefore cannot be extrapolated beyond spring. Therefore, there are still many unknowns regarding how the Pacific Arctic is responding and will respond to climate change. It is possible that only after many years of consistently warm and low-ice conditions changes in the strength and efficiency of the biological carbon pump on the Pacific Arctic shelf will become apparent.

It has been hypothesized that the strength of the biological carbon pump in the Arctic may weaken with climate change due to increased duration of the open-water period for primary production and enhanced nutrient limitation (Piepenburg, 2005; Wassmann and Reigstad, 2011; Grebmeier, 2012). Warmer waters have been predicted to increase metabolic rates of pelagic grazers and heterotrophic bacteria and potentially favor smaller phytoplankton and faster-growing grazers that more rapidly recycle organic matter within the water column (Wassmann and Reigstad, 2011; Neeley et al., 2018). We postulate that high nutrient concentrations, the shallow nature of the Pacific Arctic shelf, and the large-celled, fast-sinking phytoplankton that dominate pelagic productivity create conditions unique to this Arctic shelf (Springer and McRoy, 1993; Gradinger, 2009). Nutrients are unlikely to become more limited, especially in the BSAW, because of the consistent influx of the Anadyr Current, which is nutrient replete from Pacific upwelling. High nutrient concentrations favor large-cell phytoplankton (Li et al., 2009). Therefore, it is possible the Pacific Arctic shelf will not experience as dramatic of a shift from large cells to small cells with warming conditions when compared to other Arctic shelves. Finally, the Pacific Arctic shelf is shallower than most other Arctic shelves (averaging only 50 m deep). It will never take very long for sinking material leaving the euphotic zone to reach the seafloor, as it only has to sink about 20 m. Even if there is some increased heterotrophy in zooplankton or bacteria or decrease in cell size, the shallow nature of the shelf will allow for a higher proportion of organic matter to reach the seafloor than over deeper shelves, such as the Canadian Arctic Archipelago and European Arctic shelf. Increased frequency of storms are predicted with a changing Arctic (Slats et al., 2019). This could have major implications for the long-term carbon storage that historically has occurred on the Pacific Arctic shelf. Hauri et al. (2013) found that significant portions of carbon once thought to be stored in sediments on the Chukchi shelf are mixed up during fall storms. Given these features, we speculate that this system may retain strong coupling between the pelagic and benthic realms, continue to support highly productive pelagic and benthic ecosystems, and act as a strong sink for atmospheric carbon dioxide, possibly mediated by increased frequency of fall and winter storms. If these results prove to be a sustained feature of the rapidly changing Pacific Arctic, the biological carbon pump could represent an important element of resilience for regional ecosystems and biogeochemical cycles.

CONCLUSION

Measurements from both drifting and moored sediment traps indicate that fluxes of sinking POC on the Pacific Arctic shelf in June 2018 ranged from 0.8 to 2.3 g C m^{-2} day^{-1} in BSAW, making them amongst the highest fluxes ever documented in the global oceans. This region was also characterized by high export ratios and low rates of particle associated microbial respiration. These observations indicate that the biological carbon pump on the Pacific Arctic shelf is exceptionally strong and efficient despite a recent multi-year shift to warmer and relatively ice-free conditions (Fetterer et al., 2017; Stabeno and Bell, 2019; Danielson et al., 2020; Huntington et al., 2020). While the majority of the fluxes we observed during June 2018 were unprecedented relative to the limited number of historical flux measurements from this region, the data are still insufficient to determine whether functioning of the biological carbon pump has changed significantly relative to earlier, colder, and ice-replete years. Nonetheless, our observations do not provide supporting evidence for the common prediction that a weaker biological carbon pump and increased pelagic heterotrophy will prevail on the Pacific Arctic's continental shelves under future change.

DATA AVAILABILITY STATEMENT

The datasets generated for this study section can be found in the DataONE system (doi: 10.24431/rw1k46v).

AUTHOR CONTRIBUTIONS

SO, SD, SH, RH, DS, and AM: conceptualization. SD, SH, RH, DS, and AM: funding acquisition and project administration. SO, RH, CL, DS, and AM: methodology. SO, SD, CL, DS, and AM: investigation and formal analysis. SD, SH, and AM: supervision. SO and RH: software. SO: data visualization, writing-original draft. SO, SD, SH, RH, CL, DS, and AM: writing-reviewing and editing.

FUNDING

Research funded by the NPRB (Grant A91-00a, A91-88 and A91-99a to SD, SH, RH, AM, and DS).

ACKNOWLEDGMENTS

We thank Captain and crew of the R/V Sikuliaq as well as all collaborators in the ASGARD project, for making this project possible. Additionally, we thank S. B. Moran for the use of the drifting sediment traps, the Alaska Stable Isotope Facility for technical support and analytical assistance (University of Alaska, Fairbanks), and the two reviewers for their constructive comments. NPRB Publication Number "ArcticIERP-40".

SUPPLEMENTARY MATERIAL

The Supplementary Material for this article can be found online at: https://www.frontiersin.org/articles/10.3389/fmars.2020.548931/full#supplementary-material

REFERENCES

Amiel, D., and Cochran, J. K. (2008). Terrestrial and marine POC fluxes derived from 234Th distributions and δ13C measurements on the Mackenzie Shelf. *J. Geophys. Res.* 113:C03S06. doi: 10.1029/2007JC004260

Andersen, P. (1988). The quantitative importance of the "Microbial loop" in the marine pelagic: a case study for the North Bering/Chukchi Sea. *Arch. Hydrobiol. Bieh.* 31, 243–251.

Anderson, L. A., and Sarmiento, J. L. (1994). Redfield ratios of remineralization determined by nutrient data-analysis. *Global Biogeochem. Cycles* 8, 65–80. doi: 10.1029/93GB03318

Andreassen, I. J., and Wassmann, P. (1998). Vertical flux of phytoplankton and particulate biogenic matter in the marginal ice zone of the Barents Sea in May 1993. *Mar. Ecol. Prog. Ser.* 170, 1–14. doi: 10.3354/meps170001

Arrigo, K. R., Perovich, D. K., Pickart, R. S., Brown, Z. W., van Dijken, G. L., Lowry, K. E., et al. (2014). Phytoplankton blooms beneath the sea ice in the Chukchi sea. *Deep Sea Res. II* 105, 1–16. doi: 10.1016/j.dsr2.2014.03.018

Ashjian, C. J., Campbell, R. C., Welch, H. E., Butler, M., and Van Keuren, D. (2003). Annual cycle in abundance, distribution, and size in relation to hydrography of important copepod species in the western Arctic Ocean. *Deep Sea Res. I* 50, 1235–1261. doi: 10.1016/S0967-0637(03)00129-8

Bates, N. R. (2006). Air-sea CO_2 fluxes and the continental shelf pump of carbon in the Chukchi Sea adjacent to the Arctic Ocean. *J. Geophys. Res. Ocean* 111, 1–21. doi: 10.1029/2005JC003083

Baumann, M. S., Moran, S. B., Lomas, M. W., Kelly, R. P., and Bell, D. W. (2013). Seasonal decoupling of particulate organic carbon export and net primary production in relation to sea-ice at the shelf break of the eastern Bering Sea: Implications for off-shelf carbon export. *J. Geophys. Res. Ocean* 118, 5504–5522. doi: 10.1002/jgrc.20366

Belcher, A., Iversen, M., Giering, S., Riou, V., Henson, S. A., Berline, L., et al. (2016a). Depth-resolved particle-associated microbial respiration in the northeast Atlantic. *Biogeosciences* 13, 4927–4943. doi: 10.5194/bg-13-4927-2016

Belcher, A., Iversen, M., Manno, C., Henson, S. A., Tarling, G. A., and Sanders, R. (2016b). The role of particle associated microbes in remineralization of fecal pellets in the upper mesopelagic of the Scotia Sea, Antarctica. *Limnol. Oceanogr.* 61, 1049–1064. doi: 10.1002/lno.10269

Bluhm, B. A., and Gradinger, R. R. (2008). Regional variability in food availability. *Ecol. Appl.* 18, S77–S96. doi: 10.1890/06-0562.1

Buesseler, K. O., Bacon, M. P., Livingston, H. D., and Cochrant, K. (1992). Carbon and nitrogen export during the JGOFS North Atlantic Bloom experiment estimated from ^{234}Th: ^{238}U disequilibria. *Deep. Sea Res.* 39, 1115–1137. doi: 10.1016/0198-0149(92)90060-7

Buesseler, K. O., Boyd, P. W., Black, E. E., and Siegel, D. A. (2020). Metrics that matter for assessing the ocean biological carbon pump. *Proc. Natl. Acad. Sci. U.S.A.* 117, 9679–9687. doi: 10.1071/pnas.1918114117

Buesseler, K. O., Chen, M., Harada, K., Gustafsson, O., Trull, T., Rutgers van der Loeff, M., et al. (2007). An assessment of the use of sediment traps for estimating upper ocean particle fluxes. *J. Mar. Res.* 65, 345–416. doi: 10.1357/002224007781567621

Butman, C. A., Grand, W. D., and Stolzenback, K. D. (1986). Predictions of sediment trap biases in turbulent flows, a theoretical analysis based on observations from the literature. *J. Mar. Res.* 44, 601–644. doi: 10.1357/002224086788403024

Campbell, R. G., Sherr, E. B., Ashjian, C. J., Plourde, S., Sherr, B. F., Hill, V., et al. (2009). Mesozooplanktotn prey preference and grazing impact in the western Arctic Ocean. *Deep Sea Res. II* 56, 1274–1289. doi: 10.1016/j.dsr2.2008.10.027

Carroll, M. L., and Carroll, J. (2003). "The arctic seas," in *Biogeochemistry of Marine Systems*, eds K. D. Black and G. B. Shimmield (Boca Raton, FL: CRC Press), 127–156.

Chen, C. A., and Borges, A. V. (2009). Reconciling opposing views on carbon cycling in the coastal ocean: continental shelves as sinks and near-shore ecosystems as sources of atmospheric CO_2. *Deep Sea Res. II* 56, 578–590. doi: 10.1016/j.dsr2.2008.12.009

Collins, J. R., Edwards, B. R., Thamatrakoln, K., Ossolinski, J. E., Ditullio, G. R., Bidle, K. D., et al. (2015). The multiple fates of sinking particles in the North Atlantic Ocean. *Glob. Biogeochem. Cycles* 29, 1471–1494. doi: 10.1002/2014GB005037

Cota, G. F., Pomeroy, L. R., Harrison, W. G., Jones, E. P., Peters, F., Sheldon, W. M., et al. (1996). Nutrients, primary production and microbial heterotrophy in the southeastern Chukchi Sea: arctic summer nutrient depletion and heterotrophy. *Mar. Ecol. Prog. Ser.* 135, 247–258. doi: 10.3354/meps135247

Danielson, S. L., Ahkinga, O., Ashjian, C., Basyuk, E., Cooper, L. W., Eisner, L., et al. (2020). Manifestation and consequences of warming and latered heat fluxes over the Bering and Chukchi Sea continental shelves. *Deep Sea Res. II* 177:104781. doi: 10.1016/j.dsr2.2020/104781

Danielson, S. L., Eisner, L., Ladd, C., Mordy, C., Sousa, L., and Weingartner, T. J. (2017). A comparison between late summer 2012 and 2013 water masses, macronutrients, and phytoplankton standing crops in the northern Bering and Chukchi Seas. *Deep Sea Res. II* 135, 7–26. doi: 10.1016/j.dsr2.2016.05.024

Degerlund, M., and Eilertsen, H. C. (2010). Main species characteristics of phytoplankton spring blooms in NE Atlantic and Arctic waters (68-80° N). *Estuar. Coasts* 33, 242–269. doi: 10.1007/s12237-009-9167-7

Dugdale, R. C., and Goering, J. J. (1967). Uptake of new and regenerated forms of nitrogen in primary productivity. *Limnol. Oceanogr.* 12, 196–206. doi: 10.4319/lo.1967.12.2.0196

Durkin, C. A., Estapa, M. L., and Buesseler, K. O. (2015). Observations of carbon export by small sinking particles in the upper mesopelagic. *Mar. Chem.* 175, 72–81. doi: 10.1016/j.marchem.2015.02.011

Ebersbach, F., and Trull, T. W. (2008). Sinking particle properties from polyacrylamide gels during the KErguelen Ocean and Plateau compared Study (KEOPS): zooplankton control of carbon export in an area of persistent natural iron inputs in the Southern Ocean. *Limnol. Oceanogr.* 53, 212–224. doi: 10.4319/lo.2008.53.1.0212

European Centre for Medium-Range Weather Forecasts (2019). Updated Monthly. ERA5 Reanalysis (0.25 Degree Latitude-Longitude Grid). Research Data Archive at the National Center for Atmospheric Research, Computational and Information Systems Laboratory. Reading: European Centre for Medium-Range Weather Forecasts.

Fetterer, F., Knowles, K., Meier, W. N., Savoie, M., and Windnagel, A. K. (2017). *Updated Daily. Sea Ice Index, Version 3*. Boulder, CO: National Snow and Ice Data Center.

Fukuchi, M., Sasaki, H., Hattori, H., Matsuda, O., Tanimura, A., Handa, N., et al. (1993). Temporal variability of particulate flux in the northern Bering Sea. *Cont. Shelf Res.* 13, 693–704. doi: 10.1016/0278-4343(93)90100-C

Garneau, M. È, Vincent, W. F., Terrado, R., and Lovejoy, C. (2009). Importance of particle-associated bacterial heterotrophy in a coastal Arctic ecosystem. *J. Mar. Syst.* 75, 185–197. doi: 10.1016/j.jmarsys.2008.09.002

Gradinger, R. (1999). Vertical fine structure of the biomass and composition of algal communities in Arctic pack ice. *Mar. Biol.* 133, 745–754. doi: 10.1007/s002270050516

Gradinger, R. (2009). Sea-ice algae: major contributors to primary production and algal biomass in the Chukchi and Beaufort Seas during May/June 2002. *Deep Sea Res. II* 56, 1201–1212. doi: 10.1016/j.dsr2.2008.10.016

Grebmeier, J. M. (2012). Shifting patterns of life in the Pacific Arctic and Sub-Arctic seas. *Ann. Rev. Mar. Sci.* 4, 63–78. doi: 10.1146/annurev-marine-120710-100926

Grebmeier, J. M., and Barry, J. P. (1991). The influence of oceanographic processes on pelagic-benthic coupling in polar regions?: a benthic perspective. *J. Mar. Syst.* 2, 495–518. doi: 10.1016/0924-7963(91)90049-z

Grebmeier, J. M., and McRoy, C. P. (1988). Pelagic-benthic coupling on the shelf of the northern Bering and Chukchi Seas. I. Food supply and source and benthic biomass. *Mar. Ecol. Prog. Ser.* 48, 57–67. doi: 10.3354/meps053079

Grebmeier, J. M., and McRoy, C. P. (1989). Pelagic-benthic coupling on the shelf of the northern Bering and Chukchi Seas. III. Benthic food supply and carbon cycling. *Mar. Ecol. Prog. Ser.* 53, 93–100.

Grebmeier, J. M., McRoy, C. P., and Feder, H. M. (1988). Pelagic-benthic coupling on the shelf of the northern Bering and Chukchi Seas. I. Food supply and source and benthic biomass. *Mar. Ecol. Prog. Ser.* 48, 57–67. doi: 10.3354/meps053079

Gustafsson, Ö, Larsson, U., Andersson, P., Gelting, J., and Roos, P. (2013). An assessment of upper ocean carbon and nitrogen export fluxes on the boreal continental shelf: a 3-year study in the open Baltic Sea comparing sediment

traps, 234Th proxy, nutrient, and oxygen budgets. *Limnol. Oceanogr. Methods* 11, 495–510. doi: 10.4319/lom.2013.11.495

Hama, T., Miyazaki, T., Ogawa, Y., Iwakuma, T., Takahashi, M., Otsuki, A., et al. (1983). Measurement of photosynthetic production of a marine phytoplankton population using a stable 13C isotope. *Mar. Biol.* 73, 31–36. doi: 10.1007/BF00396282

Hauri, C., Winsor, P., Juranek, L. W., McDonnell, A. M. P., Takahashi, T., and Mathis, J. T. (2013). Wind-driven mixing causes a reduction in the strength of the continental shelf carbon pump in the Chukchi Sea. *Geophys. Res. Lett.* 40, 5932–5936. doi: 10.1002/2013GL058267

Hill, V., Ardyna, M., Lee, S. H., and Varela, D. E. (2018). Decadal trends in phytoplankton production in the Pacific Arctic region from 1950 to 2012. *Deep Sea Res. II* 152, 82–94. doi: 10.1016/j.dsr2.2016.12.015

Hopcroft, R. R., Kosobokova, K. N., and Pinchuk, A. I. (2010). Zooplankton community patterns in the Chukchi Sea during summer 2004. *Deep Sea Res. II* 57, 27–39. doi: 10.1016/j.dsri.2009.08.003

Hovelsrud, G. K., Mckenna, M., and Huntington, H. P. (2008). Marine mammal harvests and other interactions with humans. *Ecol. Appl.* 18, 135–147. doi: 10.1890/06-0843.1

Huntington, H. P., Danielson, S. L., Wiese, F. K., Baker, M., Boveng, P., Citta, J. J., et al. (2020). Evidence suggests potential transformation of the Pacific Arctic ecosystem is underway. *Nat. Clim. Chang.* 10, 342–348. doi: 10.1038/s41558-020-0695-2

Iversen, M. H., and Ploug, H. (2010). Ballast minerals and the sinking carbon flux in the ocean: carbon-specific respiration rates and sinking velocity of marine snow aggregates. *Biogeosciences* 7, 2613–2624. doi: 10.5194/bg-7-2613-2010

Kitamura, M., Amakasu, K., Kikuchi, T., and Nishino, S. (2017). Seasonal dynamics of zooplankton in the southern Chukchi Sea revealed from acoustic backscattering strength. *Cont. Shelf Res.* 133, 47–58. doi: 10.1016/j.csr.2016.12.009

Lalande, C., Grebmeier, J. M., Hopcroft, R. R., and Danielson, S. L. (2020). Annual cycle of export fluxes of biogenic matter near Hanna Shoal in the northeast Chukchi Sea. *Deep Sea Res. II* 177:104730. doi: 10.1016/j.dsr2.2020.104730

Lalande, C., Lepore, K., Cooper, L. W., Grebmeier, J. M., and Moran, S. B. (2007). Export fluxes of particulate organic carbon in the Chukchi Sea: a comparative study using 234Th/238U disequilibria and drifting sediment traps. *Mar. Chem.* 103, 185–196. doi: 10.1016/j.marchem.2006.07.004

Lalande, C., Moran, S. B., Wassmann, P., Grebmeier, J. M., and Cooper, L. W. (2008). 234Th-derived particulate organic carbon fluxes in the northern Barents Sea with comparison to drifting sediment trap fluxes. *J. Mar. Syst.* 73, 103–113. doi: 10.1016/j.marsys.2007.09.004

Lalande, C., Nöthig, E. M., and Fortier, L. (2019). Algal export in the arctic ocean in times of global warming. *Geophys. Res. Lett.* 46, 5959–5967. doi: 10.1029/2019GL083167

Le Moigne, F. A. C., Henson, S. A., Sanders, R. J., and Madsen, E. (2013). Global database of surface ocean particulate organic carbon export fluxes diagnosed from the 234Th technique. *Earth Syst. Sci. Data* 5, 295–304. doi: 10.5194/essd-5-295-2013

Lee, S. H., Joo, H. M., Liu, Z. L., Chen, J. F., and He, J. F. (2012). Phytoplankton productivity in the newly opened waters of the Western Arctic Ocean. *Deep Sea Res II* 81-84, 18–27. doi: 10.1016/j.dsr2.2011.06.005

Lee, S. H., Whitledge, T. E., and Kang, S. H. (2007). Recent carbon and nitrogen uptake rates of phytoplankton in Bering Strait and the Chukchi Sea. *Cont. Shelf Res.* 27, 2231–2249. doi: 10.1016/j.csr.2007.05.009

Lepore, K., Moran, S. B., Grebmeier, J. M., Cooper, L. W., Lalande, C., Maslowski, W., et al. (2007). Seasonal and interannual changes in particulate organic carbon export and deposition in the Chukchi Sea. *J. Geophys. Res. Ocean* 112, 1–14. doi: 10.1029/2006JC003555

Li, W. K., McLaughlin, F. A., Lovejoy, C., and Carmack, E. C. (2009). Smallest algae thrive as the arctic ocean freshens. *Science* 326:539. doi: 10.1126/science.1179798

McDonnell, A. M. P., and Buesseler, K. O. (2010). Variability in the average sinking velocity of marine particles. *Limnol. Oceanogr.* 55, 2085–2096. doi: 10.4319/lo.2010.55.5.2085

McDonnell, A. M. P., Boyd, P. W., and Buesseler, K. O. (2015). Effects of sinking velocities and microbial respiration rates on the attenuation of particulate carbon fluxes through the mesopelagic zone. *Glob. Biogeochem. Cycles* 29, 175–193. doi: 10.1002/2014GB004935

Michel, C., Nielsen, T. G., Nozais, C., and Gosselin, M. (2002). Significance of sedimentation and grazing by ice micro- and meiofauna for carbon cycling in annual sea ice (northern Baffin Bay). *Aquat. Microb. Ecol.* 30, 56–68. doi: 10.3354/ame030057

Moore, S. E., and Kuletz, K. J. (2019). Marine birds and mammals as ecosystem sentinels in and near distributed biological observatory regions: an abbreviated review of published accounts and recommendations for integration to ocean observatories. *Deep Sea Res. II* 162, 211–217. doi: 10.1016/j.dsr2.2018.09.004

Moore, S. E., and Stabeno, P. J. (2015). Synthesis of arctic research (SOAR) in marine ecosystems of the Pacific Arctic. *Prog. Oceanogr.* 136, 1–11. doi: 10.1016/j.pocean.2015.05.017

Moran, S. B., Ellis, K. M., and Smith, J. N. (1997). 234Th/238U disequilibrium in the central Arctic ocean: implications for particulate organic carbon export. *Deep Sea Res. II* 44, 1593–1606. doi: 10.1016/S0967-0645(97)00049-0

Moran, S. B., Kelly, R. P., Hagstrom, K., Smith, J. N., Grebmeier, J. M., Cooper, L. W., et al. (2005). Seasonal changes in POC export flux in the Chukchi Sea and implications for water column-benthic coupling in Arctic shelves. *Deep Sea Res. II* 52, 3427–3451. doi: 10.1016/j.dsr2.2005.09.011

Moran, S. B., Kelly, R. P., Iken, K., Mathis, J. T., Lomas, M. W., and Gradinger, R. (2012). Seasonal succession of net primary productivity, particulate organic carbon export, and autotrophic community composition in the eastern Bering Sea. *Deep Sea Res. II* 65-70, 84–97. doi: 10.1016/j.dsr2.2012.02.011

Naidu, A. S., Cooper, L. W., Grebmeier, J. M., Whitledge, T. E., and Hameedi, M. J. (2004). "The continental margin of the north Bering-Chukchi Sea: concentrations, sources, fluxes, accumulation and burial rates of organic carbon," in *The Organic Carbon Cycle in the Arctic Ocean*, eds R. Stein and R. W. Macdonald (Heidelberg: Springer-Verlag), 193–203. doi: 10.1007/978-3-642-18912-8

Neeley, A. R., Harris, L. A., and Frey, K. E. (2018). Unraveling phytoplankton community dynamics in the Northern Chukchi Sea under sea-ice-covered and sea-ice-free conditions. *Geophys. Res. Lett.* 45, 7663–7671. doi: 10.1029/2018GL077684

Nodder, S. D., Charette, M. A., Waite, A. M., Trull, T. W., Boyd, P. W., Zeldis, J., et al. (2001). Particulate transformations and export flux during an *in situ* iron-stimulated bloom in the Southern Ocean. *Geophys. Res. Lett.* 28, 2409–2412. doi: 10.1029/2001GL013008

Olli, K., Riser, C. W., Wassmann, P., Ratkova, T., Arashkevich, E., and Pasternak, A. (2002). Seasonal variation in vertical flux of biogenic matter in the marginal ice zone and the central Barents Sea. *J. Mar. Syst.* 38, 189–204. doi: 10.1016/S0924-7963(02)00177-X

Pickart, R. S., Moore, G. W. K., Chongyuan, M., Bahr, F., Nobre, C., and Weingartner, T. J. (2016). Circulation of winter water on the Chukchi shelf in early summer. *Deep Sea Res. II* 130, 56–75. doi: 10.1016/j.dsr2.2016.05.001

Piepenburg, D. (2005). Recent research on Arctic benthos: common notions need to be revised. *Polar Biol.* 28, 733–755. doi: 10.1007/s00300-005-0013-5

Ploug, H., and Grossart, H. P. (2000). Bacterial growth and grazing on diatom aggregates: respiratory carbon turnover as a function of aggregate size and sinking velocity. *Limnol. Oceanogr.* 45, 1467–1475. doi: 10.4319/lo.2000.45.7.1467

Ploug, H., and Jorgensen, B. (1999). A net-jet flow system for mass transfer and microsensor studies of sinking aggregates. *Mar. Ecol. Prog. Ser.* 176, 279–290. doi: 10.3354/meps176279

Post, D. M. (2002). Using stable isotopes to estimate trophic position: models, methods and assumptions. *Ecology* 83, 703–718. doi: 10.1890/0012-9658(2002)083[0703:usitet]2.0.co;2

Richter-Menge, J., Druckenmiller, M. L., and Jeffries, M., (eds). (2019). *Arctic Report Card 2019*. https://www.arctic.noaa.gov/Report-Card

Sala, M. M., Arrieta, J. M., Boras, J. A., Duarte, C. M., and Vaqué, D. (2010). The impact of ice melting on bacterioplankton in the Arctic Ocean. *Polar Biol.* 33, 1683–1694. doi: 10.1007/s00300-010-0808-x

Slats, R., Oliver, C., Bahnke, R., Bell, H., Miller, A., Pungowiyi, D., et al. (2019). *Voices from the Front Lines of a Changing Bering Sea. Arctic Report Card 2019*.

Available online at: http://www.arctic.noaa.gov/Report-Card (accessed January 2, 2020).

Springer, A. M., and McRoy, C. P. (1993). The paradox of pelagic food webs in the northern Bering Sea-III. Patterns of primary production. *Cont. Shelf Res.* 13, 575–599. doi: 10.1016/0278-4343(93)90095-F

Stabeno, P. J., and Bell, S. W. (2019). Extreme conditions in the bering Sea (2017-2018): record-breaking low sea-ice extent. *Geophys. Res. Lett.* 46, 8952–8959. doi: 10.1029/2019gl083816

Thoman, R. L., Bhatt, U. S., Bieniek, P. A., Brettschneider, B. R., Brubaker, M., Danielson, S. L., et al. (2020). The record low Bering Sea ice extent in 2018: context, impacts, and an assessment of the role of anthropogenic climate change. *Bull. Am. Meteorol. Soc.* 101, S53–S58. doi: 10.1175/BAMS-D-19-0175.1

Vaqué, D., Lara, E., Arrieta, J. M., Holding, J., Sà, E. L., Hendriks, I. E., et al. (2019). Warming and CO_2 enhance arctic heterotrophic microbial activity. *Front. Microbiol.* 10:494. doi: 10.3389/fmicb.2019.00494

Vaughan, D. G., Comiso, J. C., Allison, I., Carrasco, J., Kaser, G., Kwok, R., et al. (2013). "Observations: Cryosphere," in *Climate Change 2013: The Physical Science Basis. Contribution of Working Group I to the Fifth Assessment of the Intergovernmental Panel on Climate Change*, eds T. F. Stocker, D. Qin, G.-K. Plattner, M. Tignor, S. K. Allen, J. Boschung, et al. (Cambridge: Cambridge University Press), 317–382. doi: 10.1017/CBO9781107415324.012

Walsh, J. J., McRoy, C. P., Coachman, L. K., Goering, J. J., Nihoul, J. J., Whitledge, T. E., et al. (1989). Carbon and nitrogen cycling within the Bering/Chukchi Seas: source regions for organic matter effecting AOU demands of the Arctic Ocean. *Prog. Oceanogr.* 22, 277–359. doi: 10.1016/0079-6611(89)90006-2

Wassmann, P., and Reigstad, M. (2011). Future Arctic Ocean seasonal ice zones and implications for pelagic-benthic coupling. *Oceanography* 24, 220–231. doi: 10.5670/oceanog.2011.74

Woodgate, R. A., Stafford, K. M., and Prahl, F. G. (2015). A synthesis of year-round interdisciplinary mooring measurements in the Bering Strait (1990-2014) and the RUSALCA years (2004-2011). *Oceanography* 28, 46–67. doi: 10.5670/oceanog.2015.57

Wooller, M. J., Zazula, G. D., Edwards, M., Froese, D. G., Boone, R. D., Parker, C., et al. (2007). Stable carbon isotope compositions of eastern beringian grasses and sedges: investigating their potential as paleoenvironmental indicators. *Arctic Antarct. Alpine Res.* 39, 318–331. doi: 10.1657/1523-0430(2007)39[318:scicoe]2.0.co;2

Yu, W., Chen, L., Cheng, J., He, J., Yin, M., and Zeng, Z. (2010). 234Th-derived particulate organic carbon export flux in the western Arctic Ocean. *Chin J. Oceanog. Limnol.* 28, 1146–1151. doi: 10.1007/s00343-010-9933-1

Yu, W., He, J., Li, Y., Lin, W., and Chen, L. (2012). Particulate organic carbon export fluxes and validation of steady state model of 234Th export in the Chukchi Sea. *Deep Sea Res. II* 81–84, 63–71. doi: 10.1016/j.dsr2.2012.03.003

Conflict of Interest: The authors declare that the research was conducted in the absence of any commercial or financial relationships that could be construed as a potential conflict of interest.

frontiers in Environmental Science

ORIGINAL RESEARCH
published: 23 December 2020
doi: 10.3389/fenvs.2020.538635

Environmental and Biological Determinants of Algal Lipids in Western Arctic and Subarctic Seas

Vincent Marmillot[1]*, *Christopher C. Parrish*[2]*, *Jean-Éric Tremblay*[1], *Michel Gosselin*[3] and *Jenna F. MacKinnon*[2]

[1] Département de Biologie, Université Laval, Québec City, QC, Canada, [2] Department of Ocean Sciences, Memorial University of Newfoundland, St. John's, NL, Canada, [3] Institut des Sciences de la mer de Rimouski, Université du Québec à Rimouski, Rimouski, QC, Canada

The Arctic is undergoing numerous environmental transformations. As a result of rising temperatures and additional freshwater inputs, ice cover is changing, with profound impacts on organisms at the base of food webs and consequently on the entire Arctic ecosystem. Indeed, phytoplankton not only provide energy as lipids, but also essential fatty acids (EFA) that animals cannot synthesize and must acquire in their diet. Omega-3 (ω3) and omega-6 (ω6) polyunsaturated fatty acids (PUFA) are essential for the healthy development and function of organisms. The high energy potential of monounsaturated fatty acids (MUFA) is of particular importance in cold waters, and various fatty acids including saturated fatty acids (SFA) are involved in organismal responses to environmental stressors. Yet relatively little is known of how variability or change in physicochemical seawater properties (e.g., temperature, light, salinity, pH and nutrients) may affect lipid synthesis in polar environments, either directly, by altering algal physiology, or indirectly, by promoting shifts in phytoplankton species composition. Here we investigated these two possibilities by sampling along a 3,000-km transect spanning 28 degrees of latitude across the subarctic and Arctic domains of Canada. The taxonomic composition of phytoplankton mainly drove the FA profiles measured in particulate organic matter (POM). Strong, positive correlations between 16:1ω7 and diatoms were observed while the proportion of PUFA and ω6 FA increased with flagellate abundance. Among specific FAs, eicosapentaenoic acid (EPA; 20:5ω3) was positively correlated with diatoms but the expected relationship between docosahexaenoic acid (DHA; 22:6ω3) and dinoflagellates was not observed. Decreasing pH had a negative effect on EPA and MUFA proportions, and DHA proportions tended to decrease with higher temperature. These two effects were primarily driven by differences in phytoplankton assemblage composition. Overall, the results of this geographically extensive study provide new information into the use of lipid markers and the ecological determinants of FA synthesis in the North. It also highlights the importance of long-lived subsurface chlorophyll maximum layers in supplying PUFA-rich POM to the food web and suggests that this situation may persist despite ongoing changes in the physical environment.

Keywords: lipids, phytoplankton, ω3 FA, ω6 FA, Arctic, taxonomy, environment

OPEN ACCESS

Edited by:
Adam Jerold Reed, University of Southampton, United Kingdom

Reviewed by:
Mark Andrew Stevenson, Newcastle University, United Kingdom
Olesia Nikolaevna Makhutova, Institute of Biophysics of Federal Research Center "Krasnoyarsk Science Center" of Siberian Branch of Russian Academy of Sciences, Russia

***Correspondence:**
Vincent Marmillot
vincent.marmillot.1@ulaval.ca
Christopher C. Parrish
cparrish@mun.ca

Specialty section:
This article was submitted to Biogeochemical Dynamics, a section of the journal Frontiers in Environmental Science

Received: *27 February 2020*
Accepted: *30 November 2020*
Published: *23 December 2020*

Citation:
Marmillot V, Parrish CC, Tremblay J-É, Gosselin M and MacKinnon JF (2020) Environmental and Biological Determinants of Algal Lipids in Western Arctic and Subarctic Seas. Front. Environ. Sci. 8:538635. doi: 10.3389/fenvs.2020.538635

INTRODUCTION

Phytoplankton account for nearly half of global primary production (Field et al., 1998) and their productivity is often greatest at high latitudes (Huston and Wolverton, 2009). In seasonally ice-free waters of the Arctic Ocean, the timing of phytoplankton blooms is usually controlled by light, while nutrient availability dictates the magnitude of annual net primary production (Tremblay and Gagnon, 2009; Tremblay et al., 2015). In addition to the total amount of primary production, the quantity and type of lipids synthesized by phytoplankton are crucial for the health and function of polar food webs, as well as for humans who consume marine foods (Lemire et al., 2015). Specific fatty acids (FA) can also be used as markers of taxonomic composition and tracers of food source in consumers (Dalsgaard et al., 2003). Since phytoplankton are the major organisms able to produce essential FA *de novo* in sufficient quantities, several studies have focused on the environmental controls of primary production and fatty acid (FA) synthesis in unicellular algae. These characteristics were found to be influenced by a host of factors in addition to light and nutrients, including physicochemical variables (e.g., salinity, temperature, pH), geographical parameters (e.g., latitude, seasonality) and taxonomic composition (Leu et al., 2006; Galloway and Winder, 2015). In addition to their crucial roles in nutrition and health, the carbon-rich FA synthesized by phytoplankton, once incorporated into zooplankton, may substantially contribute to oceanic carbon sequestration via their vertical migrations (Jónasdóttir et al., 2015).

De novo FA synthesis is a complex process starting with acetyl-CoA and involving fatty acid synthase for carbon chain elongation resulting in a 16-carbon molecule (i.e., palmitic acid, 16:0) that corresponds to the most common FA. In addition to other elongations that may occur to form longer carbon chains, some reactions lead to unsaturation of FAs by inserting a double bond between the carbons. Beyond this first unsaturation, other double bonds can be inserted into the carbon chain resulting in the synthesis of polyunsaturated FA (PUFA) (Parrish, 2009). Specific types of PUFA, such as α-linolenic acid (ALA; 18:3ω3), eicosapentaenoic acid (EPA; 20:5ω3), docosahexaenoic acid (DHA; 22:6ω3), linoleic acid (LA; 18:2ω6) and arachidonic acid (ARA; 20:4ω6), better known as ω3 FA and ω6 FA essential fatty acids (EFA), are synthesized almost exclusively by primary producers and certain bacteria. Animals must acquire these vital molecules from their diet (Parrish, 2009). As Budge et al. (2006) pointed out, FA are rarely found in their free form in nature and are mainly incorporated into more complex molecules constituting different lipid classes with diversified metabolic functions (Guschina and Harwood, 2009; Gladyshev et al., 2013). In this regard, it is useful to distinguish between polar (e.g., phospholipids) and non-polar lipids. Phospholipids (PL) are major components of biological membranes and, with sterols (ST), play a major role in organismal responses to environmental change by acting as a semi-permeable and selective barrier (Guschina and Harwood, 2009). Non-polar lipids such as triacylglycerols (TAG) are used for energy storage (Gurr et al., 2002) and are especially crucial in polar regions where the growing season is short (Falk-Petersen et al., 2000; Leu et al., 2015).

Given the key role of microbial organisms in supplying the entire food web with lipids and essential fatty acids in particular, it appears vital to better understand how multiple environmental factors act or interact to influence algal lipid profiles and the extent to which these profiles will either subsist or be altered in the future Arctic. The Arctic Ocean is experiencing the greatest and most rapid environmental change on Earth (IPCC, 2014). Projections suggest that sea surface temperatures will keep rising, that the extent and thickness of sea ice will continue to decline, and that freshwater loading and ocean acidification will further increase in this ocean. The manifestations and biological impacts of these changes are likely to differ across different sectors (Langen et al., 2018) and a recent study showed that primary production has either declined, not changed or increased in specific areas (Lewis et al., 2020), presumably due to a shifting balance between processes that reinforce vertical stratification and those that promote mixing and nutrient replenishment in surface waters. These changes are also likely to induce shifts in the taxonomic composition of bacterial and phytoplankton assemblages, thereby altering the lipid composition of particulate organic matter (POM), and may cause a mismatch between primary and secondary production as a consequence of early, seasonal sea-ice retreat (Leu et al., 2011).

It is generally accepted that low temperature favors greater proportions of unsaturated FAs (Guschina and Harwood, 2009) that maintain the membrane fluidity necessary for several physiological processes (e.g., permeability, photosynthesis, respiration; Harwood, 1998). Several studies reported inverse relationships between temperature and unsaturation levels or the proportions of EPA, DHA and total PUFA (Tatsuzawa and Takizawa, 1995; Thompson, 1996; Zhu et al., 1997; Jiang and Gao, 2004). The effect of irradiance, which fluctuates widely in polar environments, has also been extensively studied (Thompson et al., 1990; Henriksen et al., 2002; Leu et al., 2006). Negative relationships between unsaturation proportion and light intensity seem to be the norm. For example, the proportion of storage lipids, ω3 FA and EPA were shown to increase with decreasing light, while proportions of polar lipids and saturated FA (SFA) such as 16:0 were found to increase with light (Thompson et al., 1990; Mock and Kroon, 2002; Fábregas et al., 2004). Greater unsaturation and proportions of PUFA under low light presumably serve to boost the efficiency of photosynthesis by increasing membrane fluidity and electron flow.

Abbreviations: AIC, Akaike information criterion; ALA, α-linolenic acid; AMPL, acetone-mobile polar lipids; ARA, arachidonic acid; BFATM, bacterial fatty acid trophic marker; BB, Baffin Bay; BS, Beaufort Sea; DHA, docosahexaenoic acid; EFA, essential fatty acid; EPA, eicosapentaenoic acid; FA, fatty acid; FAME, fatty acid methyl ester; FATM, fatty acid trophic marker; FFA, free fatty acid; FID, flame ionization detector; LS, Labrador Sea; MUFA, monounsaturated fatty acid; NS, Nares Strait; NW, Northwest Passage; PAR, photosynthetically available radiation; PCA, Principal Component Analysis; PL, phospholipid; POM, particulate organic matter; PUFA, polyunsaturated fatty acid; SCM, subsurface chlorophyll maximum; SFA, saturated fatty acid; SID, numbers of days elapsed between the date of 50% sea ice declined and sampling date; ST, sterol; SUR, surface; TAG, triacylglycerol; TLC, thin layer chromatography; ω3, omega-3 fatty acid; ω6, omega-6 fatty acid.

The magnitude of primary production and therefore overall lipid synthesis are highly conditioned by nutrient availability in the ocean. Nitrogen and, to a lesser extent, iron (as in the Southern Ocean for example) are often considered to be the main elements limiting primary production (Moore et al., 2013). For the Arctic, Tremblay and Gagnon (2009) showed a strong correlation between initial nitrate concentration at the onset of phytoplankton blooms and the magnitude of annual primary production. In cultures, low nitrate availability was shown to induce reduced cell division rates while increasing the proportion of storage lipids (e.g., triacylglycerol or TAG) (Pruvost et al., 2009; Rodolfi et al., 2009; Sobczuk and Chisti, 2010), and nitrogen limitation also reduces unsaturation through a shift from polar lipids to saturated storage lipids. However, responses to nutrient limitation vary considerably among species (Reitan et al., 1994). A high variability of responses is also observed in studies testing the effect of pH or pCO_2. While Thompson (1996) showed that high CO_2 concentrations decreased unsaturation, Leu et al. (2013) found positive correlations between PUFA proportions and pCO_2 and attributed these responses to a decline in the relative contribution of diatoms to the phytoplankton assemblage. This notion is in agreement with the metanalysis of Galloway and Winder (2015), who showed that taxonomic composition (e.g., chlorophytes, cryptophytes, cyanobacteria, diatoms, dinoflagellates, and haptophytes) is the main determinant of lipid profiles and differences in essential FA composition among laboratory cultures (Galloway and Winder, 2015).

Faced with rapid climate change, the multiplicity of lipid responses observed in previous studies, and the fact that most of these studies were performed on monospecific laboratory cultures, our primary objective was to assess how physicochemical conditions affect the lipid composition of natural phytoplankton assemblages along macro-ecological environmental gradients. Here we did so by sampling across a 3,000-km stretch of ocean that traversed several distinct oceanographic regions of the western Arctic and subarctic. Beyond the major influence of taxonomy, which can be expected from prior studies, we also expected to see secondary effects of physicochemical variables on the assemblages present. Since the temperature of surface waters generally decreases poleward, we hypothesized that PUFA and EFA proportions should correlate positively with latitude and negatively with temperature. We also hypothesized that PUFA proportions in POM should increase with nutrient availability and the time elapsed since ice break-up (a surrogate for the seasonal maturity of the system). The reverse should be observed for SFA and TAG proportions. A second objective of the study was to identify fatty acid markers of specific phytoplankton groups and assess if they differ from those previously established in other environments.

MATERIALS AND METHODS

Survey Area

Sampling was conducted with the Canadian icebreaker CCGS Amundsen from 29 July to October 2, 2016 (**Figure 1**). The 44 stations were spread out across Baffin Bay (29 July - 3 August and 26–28 September), Nares Strait (6–16 August), the Northwest Passage (4 August and 17–24 August and 18–25 September), the Beaufort Sea (28 August - 5 September) and the Labrador Sea (1–2 October). According to the general ocean circulation pattern, different water masses influence the overall sampling area. The western parts of Baffin Bay and the Labrador Sea are exposed to cold and relatively fresh waters descending from the high Arctic, such as the Baffin Island Current and the Labrador Current (Tremblay et al., 2018). These two currents carry predominantly Pacific-derived waters that previously transited across the Beaufort Sea and enter the Canadian Archipelago via Nares Strait and the Northwest Passage's Barrow Strait and Lancaster Sound. By contrast, Atlantic waters enter the survey area around the southern tip of Greenland and propagate northward with the West Greenland Current along the eastern edges of the Labrador Sea and Baffin Bay eventually crossing to the west. Most of the sampling stations were located in relatively shallow waters but regional differences in average bottom depths were present, with shelf stations of the Labrador sea (153 ± 13 m) and Northwest Passage (204 ± 26 m) being shallower than stations in the Beaufort Sea (352 ± 70 m), Nares Strait (476 ± 31 m) and Baffin Bay (489 ± 42 m).

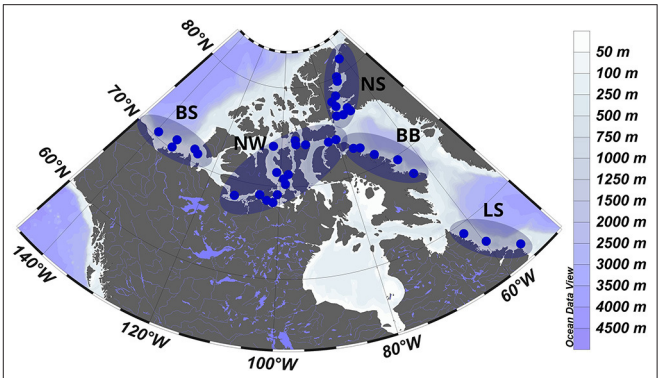

FIGURE 1 | Locations of the sampling stations in different oceanographic regions [Beaufort Sea (BS), Northwest Passage (NW), Nares Strait (NS), Baffin Bay (BB), and Labrador Sea (LS)] of the Canadian Arctic from 29 July to 2 October 2016.

Sampling

At each station, sensors mounted on a rosette sampler provided detailed vertical profiles of temperature and salinity (Sea-Bird SBE-911 CTD), nitrate (*in-situ* Ultraviolet Spectrometer, ISUS, Satlantic), dissolved oxygen (Seabird SBE-43, calibrated onboard against Winkler titrations: Martin et al., 2010), photosynthetically available radiation (PAR, 400–700 nm; Biospherical Instruments QDP2300) and chlorophyll fluorescence (Seapoint). The latter was used to determine the depth of the subsurface chlorophyll maximum (SCM) for sampling purposes. Water was collected at the surface (SUR) and at the SCM with 12-L Niskin bottles mounted on the rosette.

The pH of seawater was measured at 25°C with a spectrophotometer using red phenol (433 and 558 nm) and cresol

purple (434 and 578 nm) according to Robert-Baldo et al. (1985), Clayton and Byrne (1993), and Millero et al. (2009). Total alkalinity was measured by potentiometric titration combined with pH electrodes and dilute HCl (0.02 M) as a titrant. We used CO2sys (Lewis and Wallace, 1998) to convert pH measurements into *in situ* pH and pCO_2 by using alkalinity, temperature and salinity data. Note that pH measurements were not performed in the Beaufort Sea. Subsamples for nutrient determinations were pre-filtered on GF/F filters and the concentrations of phosphate (PO_4^{3-}) and nitrate (NO_3^-) were analyzed fresh with a Bran-Luebbe auto-analyzer 3 using colorimetric methods adapted from Hansen and Koroleff (1999). The detection limit was 0.03 μM for phosphate and nitrate. Sea-ice concentrations provided by AMSR-E/AMSR2 and SSMI (Brodzik and Stewart, 2016; Meier et al., 2018; Earth Observing System Data and Information System, EOSDIS) were used to estimate the date when sea ice had declined by 50% and to calculate the numbers of days elapsed between this date and sampling time for each station (hereafter abbreviated as SID for Sea Ice Decline).

For each station and the two sampling depths, a 200-ml aliquot of seawater was preserved with acidic Lugol's and stored at 4°C in the dark for taxonomic analysis of phytoplankton phylum, class and species. Particulate organic matter (POM) for lipid analysis was collected by filtering 3 L of seawater through 47-mm GF/C filters. The filters were stored in pre-burned aluminum foil at −80°C until analysis at the home laboratory. The carbon content of different phytoplankton groups was estimated from visual counting and sizing of cells under visible light microscopy (Lund et al., 1958; Utermöhl, 1958; Menden-Deuer and Lessard, 2000). The database produced by the HELCOM Phytoplankton Expert Group was used to calculate the biovolume of single cells, which was multiplied by the number of cells to get total biovolume. Following Menden-Deuer and Lessard (2000) we converted the biovolume to carbon quantity using conversion factors i.e., pg C $cell^{-1} = 0.288 \times Vol^{0.811}$ for diatoms, pg C $cell^{-1} = 0.760 \times Vol^{0.819}$ for dinoflagellates and pg C $cell^{-1} = 0.216 \times Vol^{0.939}$ for other groups such as chlorophyte, chrysophyte, dictyochophyte, cryptophyte, euglenophyte, prasinophyte, prymnesiophyte, unidentified flagellates, raphidophyte, heterotrophic group, choanoflagellate, ciliates, and others (i.e., unidentified cells and cysts).

Lipid Extraction

Each filter collected was put in lipid clean vials with 4 ml of chloroform, flushed with nitrogen and sealed with Teflon tape before storage at −20°C. Lipids were extracted with chloroform:methanol:water (1:2:1) following Folch et al. (1957) as modified by Parrish (1999). Filters were ground using a rod, sonicated and centrifuged three times in order to extract lipid layers (lower) with two Pasteur pipettes (double pipetting). Lipid extracts were stored at −20°C in 2 ml vials capped under N_2 and sealed with Teflon tape until further analyses.

Lipid Classes

We used thin-layer chromatography with flame ionization detection (TLC-FID, Mark V Iatroscan, Iatron Laboratories) to determine lipid classes (Parrish, 1987). We spotted extracts on silica gel-coated Chromarods and we used a three-stage development system to separate lipid classes. The first and second hexane-based developments separated triacylglycerol (TAG) sterol (ST) and free fatty acid (FFA). Then more polar systems separated acetone-mobile polar lipid (AMPL) and phospholipid (PL). Nine Sigma Chemical Inc saturated standards ranging in polarity from nonadecane to dipalmitoyl phosphatidylcholine were used for FID calibration via Peak Simple software (version 4.54).

Derivatization and Fatty Acids

Extracts were put in lipid clean vials where we added a mixture of H_2SO_4-MeOH prior to heating at 100°C for 1 h. We then added 1.5 ml of hexane and removed the upper layer containing lipids. Samples were dried under N_2 prior to resuspension and storage at −20°C until fatty acid methyl ester (FAME) analyses by GC-FID (Budge and Parrish, 1998, 1999).

Data Reporting and Statistical Analyses

In the Results section, deviations from mean values are reported as ± one standard error. Since the overall lipid content of organisms is proportional to their biomass, relationships between FA proportions and the taxonomic composition of phytoplankton were explored using the contribution of different groups to total phytoplankton carbon (μg C L^{-1}). However, relationships between physicochemical variables and assemblage composition were established using the numerical contribution of different groups to total cell counts (cells L^{-1}) in order to avoid propagating possible errors associated with the carbon biomass estimation. To simplify the text, use of the words "abundance" or "carbon" after a taxonomic group (e.g., diatom carbon) hereafter designates the relative contribution of this group to total phytoplankton counts or carbon. Considering that a major portion of water-column phytoplankton biomass occurs within the SCM layer during summer and fall in our study area (Martin et al., 2010, 2013), our analyses of FA composition focused on this layer. Nonetheless, surface data were considered in order to refine interpretations and differences between the two sampling layers were examined using paired *t*-tests. ANOVA and multivariate PERMANOVA were used to test for differences between oceanographic regions (i.e., Beaufort Sea, Northwest Passage, Nares Strait, Baffin Bay, and Labrador Sea).

Given the complexity of the data set obtained, different statistical approaches were employed to explore relationships between physicochemical variables, taxonomic composition and FA profiles. In the search for the best variables explaining FA proportions, the Akaike information criterion (AICc) was used first to rank different possible models and test for interactions between variables. While highly useful, the AICc analysis excludes stations with incomplete datasets (e.g., pH in the Beaufort Sea) and possibly overemphasizes significant relationships for variables with the greatest availability. The AICc scores (not shown) were therefore used as initial guidance in the selection of generalized linear models (where the slopes of regression models were defined by β), break-point regression models or multiple regression models with linear or quadratic terms. For conciseness, only the statistical parameters

of regressions that do not already appear in the supplement will be detailed in the main text. Finally, distance-based redundancy analysis (dbRDA) based on a Chi squared distance resemblance matrix and multivariate plots were used to visualize the overall structure of the dataset using R (R Core Team, 2020), RStudio (RStudio Team, 2020) and PRIMER-e software. Methods such as the Grubbs test (R package Outliers; Komsta, 2011) were used to identify statistical outliers in the dataset.

RESULTS

Across the survey area, water temperature at the SCM was confined to a narrow range (−1.55–1.75°C, −0.36 ± 0.14°C on average) and was not related to latitude although significant differences ($p_{perm} < 0.05$) were found between sampling regions (**Supplementary Figure 1** and **Supplementary Tables 1.1**, **1.2**). The highest (1.44 ± 0.45°C) and lowest (−0.67 ± 0.36°C) average values occurred in the Labrador Sea and in Baffin Bay, respectively. The SCM depth also varied significantly between regions ($p_{perm} \leq 0.001$). The deepest and shallowest ones were observed in the Beaufort Sea (mean = 46 ± 4.55 m) and the Labrador Sea (mean = 23 ± 3.36 m), respectively, consistent with a strong positive relationship between SCM depth and longitude ($r^2 = 0.42$, $p < 0.001$). Salinity was negatively correlated with longitude ($r^2 = 0.13$, $p < 0.01$), indicating a greater presence of freshwater in the western part of the survey area. SCM depth did not correlate with latitude, sampling date or SID. The pH ranged from 8.01 to 8.23 (8.11 ± 0.01 on average) at the SCM and significant regional differences were found ($p_{perm} \leq 0.001$), with relatively low average values in the Northwest Passage and the Labrador Sea (8.07 ± 0.01 and 8.08 ± 0.02, respectively), and higher ones in Baffin Bay and Nares Strait (8.13 ± 0.01 and 8.15 ± 0.01, respectively). Overall, pH showed a strong negative relationship with longitude ($r^2 = 0.27$, $p < 0.01$) and a weak positive one with latitude ($r^2 = 0.13$, $p < 0.05$). Average nitrate concentrations (2.01 ± 0.29 μM) and PAR levels (2.01 ± 0.63 μE m^{-2} s^{-1}) at the time of sampling were both generally low and did not exhibit significant differences between regions (PERMANOVA). Instantaneous PAR levels correlated negatively with latitude ($r^2 = 0.14$, $p < 0.01$) but not with SCM depth, sampling date nor SID. With the exception of nutrient concentrations, the range of values for abiotic variables was often larger at the surface than at the SCM (see **Supplementary Table 1**) and paired *t*-tests revealed significant differences ($p < 0.05$) between the two depths for temperature, salinity, PAR, nitrate and phosphate.

When averaged over the entire sampling area, phytoplankton assemblages at the SCM were numerically dominated by diatoms (38.0 ± 4.3% of centrics and 5.1 ± 0.9% of pennates) and unidentified flagellates (18.6 ± 1.7%), followed by prymnesiophytes (8.9 ± 1.8%), dinoflagellates (4.8 ± 0.4%), choanoflagellates (3.5 ± 0.6%) and chrysophytes (1.6 ± 0.4%) (**Figure 2A**). The sum of all these groups minus the diatoms and dinoflagellates accounted for 32.6 ± 2.9 % of total cell counts and is hereafter referred to as "flagellates." Minor identified taxa represented 4.4% and included cryptophytes (1.5%), prasinophytes (1.1%), ciliates (0.67%), dictyochophytes (0.48%), heterotrophic species (0.36%, mainly composed of *Leucocryptos marina*, *Meringosphaera mediterranea*, and *Telonema* sp.), raphidophytes (0.27%), euglenophytes (0.02%), and chlorophytes (0.003%). Other groups comprised small unrecognized cells and cysts that collectively accounted for 15.1% of total counts. Some differences emerged in the relative importance of taxonomic groups when considering carbon biomass (μg C L^{-1}) instead of cell counts (cells L^{-1}); dinoflagellates and ciliates contributions increased at the expense of unidentified flagellates and prymnesiophytes while the contribution of centric diatoms remained stable (see **Supplementary Table 2** for details).

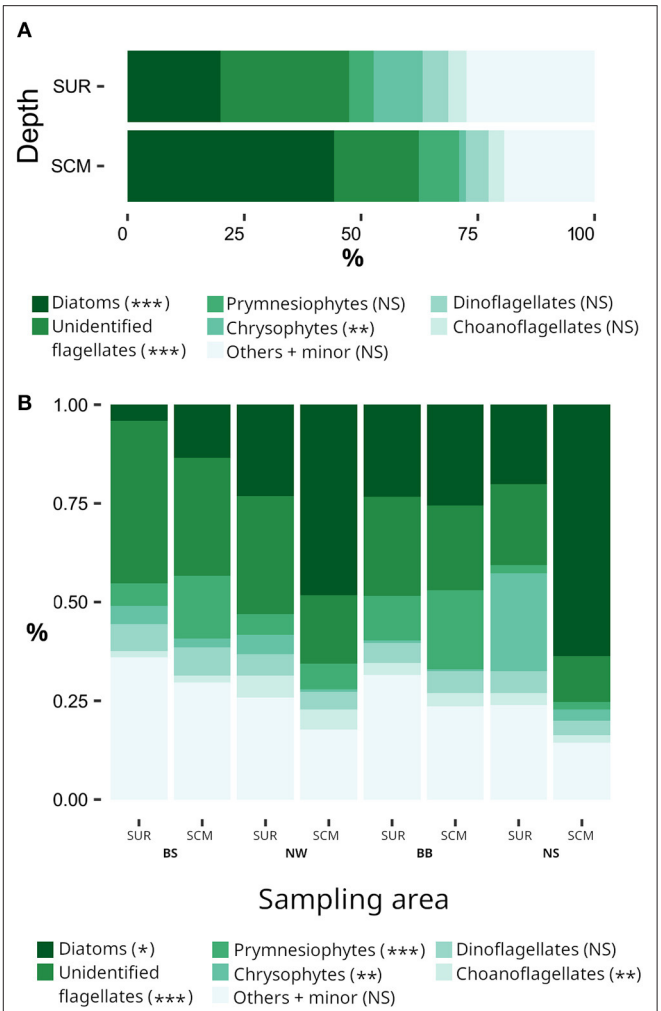

FIGURE 2 | Contributions of the main phytoplankton groups to total cell abundance **(A)** at the surface (SUR) and at the subsurface chlorophyll maximum (SCM) depth and **(B)** in the different oceanographic regions of the Canadian Arctic. No taxonomic data are available for the Labrador Sea. The PERMANOVA results are defined by $^{***}p_{perm} < 0.001$; $^{**}p_{perm} < 0.01$; $^{*}p_{perm} \leq 0.05$; NS, not significant. The "Others + minor" group is composed of unidentified cells and cysts and prasinophytes, cryptophytes, dictyochophytes, heterotrophic taxa, raphidophytes, euglenophytes, and chlorophytes. In **(A)** the PERMANOVA results compare the SUR and SCM depth while in **(B)** the PERMANOVA results compare regions.

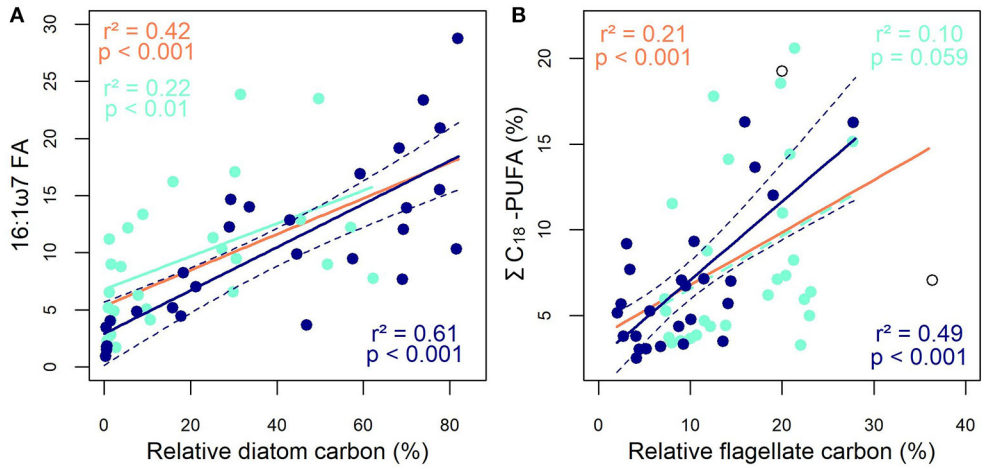

FIGURE 3 | Relationships between **(A)** the 16:1ω7 FA proportion and the relative carbon biomass of diatoms and between **(B)** the ΣC_{18}-PUFA proportion and the relative carbon biomass of flagellates. The dark-blue symbols, lines and text represent the subsurface chlorophyll maximum (SCM), the turquoise symbols, lines and text represent the surface (SUR) while the orange lines and text represent the SCM and SUR data combined. The dashed dark-blue line represents the 95% confidence interval and open circles represent outliers in the SCM dataset (Grubbs test, $p < 0.05$).

On average, the total number of cells was 1.8 × higher at the SCM than at the surface and the difference was similar in terms of carbon content (1.9 ×). The same occurred for relative abundance of diatoms but it was the reverse for unidentified flagellates, chrysophytes and prasinophytes. Finally the proportions of prymnesiophytes, dinoflagellates, and choanoflagellates were similar at the two sampling depths (**Figure 2A**).

Differences in the taxonomic composition of phytoplankton assemblages between regions are shown in **Figure 2B**. Among the major cell groups at the SCM, the relative abundances of diatoms and flagellate were the most spatially variable between regions ($p_{perm} < 0.01$). Regional differences were also observed for prasinophytes and a few other groups ($p_{perm} < 0.05$; **Supplementary Tables 3.1**, **3.2**) but not for dinoflagellates. The same patterns were observed when considering carbon biomass, except for cryptophytes which exhibited significant regional contrasts (**Supplementary Tables 3.1**, **3.2**).

Next, we sought the most robust FA trophic markers (hereafter FATM) of different phytoplankton groups at the SCM. The relationship between diatoms and palmitoleic acid (16:1ω7, **Figure 3A**) gave the strongest correlation between a specific FA and the relative contribution of a phytoplankton group. FA ratios such as 16:1ω7/16:0 and $\Sigma C_{16}/\Sigma C_{18}$ or Σ16:1/Σ18:1 were also highly correlated with diatom carbon (**Supplementary Table 4**). Moreover, proportions of MUFA, 14:0, *i*15:0, 16:0, 16:3ω4, or EPA ($r^2 = 0.11$) correlated positively with diatom carbon. Conversely, flagellate carbon at the SCM was negatively correlated with the proportions of 16:1ω7 ($r^2 = 0.25$, $p < 0.01$), EPA ($r^2 = 0.23$, $p < 0.01$) and MUFA ($r^2 = 0.16$, $p < 0.05$). The proportions of ω6 FA ($r^2 = 0.24$), overall PUFA ($r^2 = 0.31$), 18:4ω1 ($r^2 = 0.44$) and the ΣC_{18}-PUFA in particular ($r^2 = 0.49$) were positively correlated with flagellate carbon (**Figure 3B**). It follows that the latter was negatively correlated with the ΣC_{16}:ΣC_{18} ratio ($r^2 = 0.25$, $p < 0.01$), underlining high ΣC_{18} proportions in flagellates and high ΣC_{16} proportions in diatoms. A similar negative trend was found between dinoflagellates and ΣC_{16}:ΣC_{18} ($r^2 = 0.22$, $p < 0.01$). However, we did not find significant relationships between dinoflagellate carbon and previously identified FATM of this group such as DHA or OTA (18:4ω3). Overall, the strong correlations observed here (e.g., diatoms and 16:1ω7, flagellates and ΣC_{18}-PUFA) at the SCM were much weaker when the analyses were based on SUR data alone or a combination of all SCM and SUR data (**Figure 3**).

Despite the regional contrasts in taxonomic composition (**Figure 2**) and the strong correlations between specific taxonomic groups and FATM (**Figure 3**), the lipid profiles of POM at the SCM were relatively stable across regions in terms of FA composition and lipid classes (i.e., TAG, ST, PL and AMPL). According to the PERMANOVA, MUFA was the only lipid group that showed significant differences between regions (**Figure 4**). The ANOVA performed to elucidate these differences identified the proportions of diatoms ($p < 0.01$), flagellates and dinoflagellates ($p < 0.05$) as the primary cause since the interaction terms between sampling region and taxonomic composition were not significant. However, when using longitude and latitude instead of regional divisions, spatial trends in the lipid composition of POM at the SCM became apparent. Diatom FATM (e.g., 16:1ω7, ΣC_{16}, Σ16:1/Σ18:1) were positively correlated with latitude (see **Supplementary Table 5** for details), consistent with the northward increase in relative diatom abundance ($r^2 = 0.23$, $p < 0.01$) to the detriment of flagellates ($r^2 = 0.29$, $p < 0.01$). Significant trends were also found between the longitude as an independent variable and the relative diatom abundance ($\beta = -0.53$, $r^2 = 0.15$, $p < 0.05$), diatom FATM (e.g., 16:1ω7, see **Supplementary Table 5**) and also the sum of known bacterial FA markers (i.e., denoted

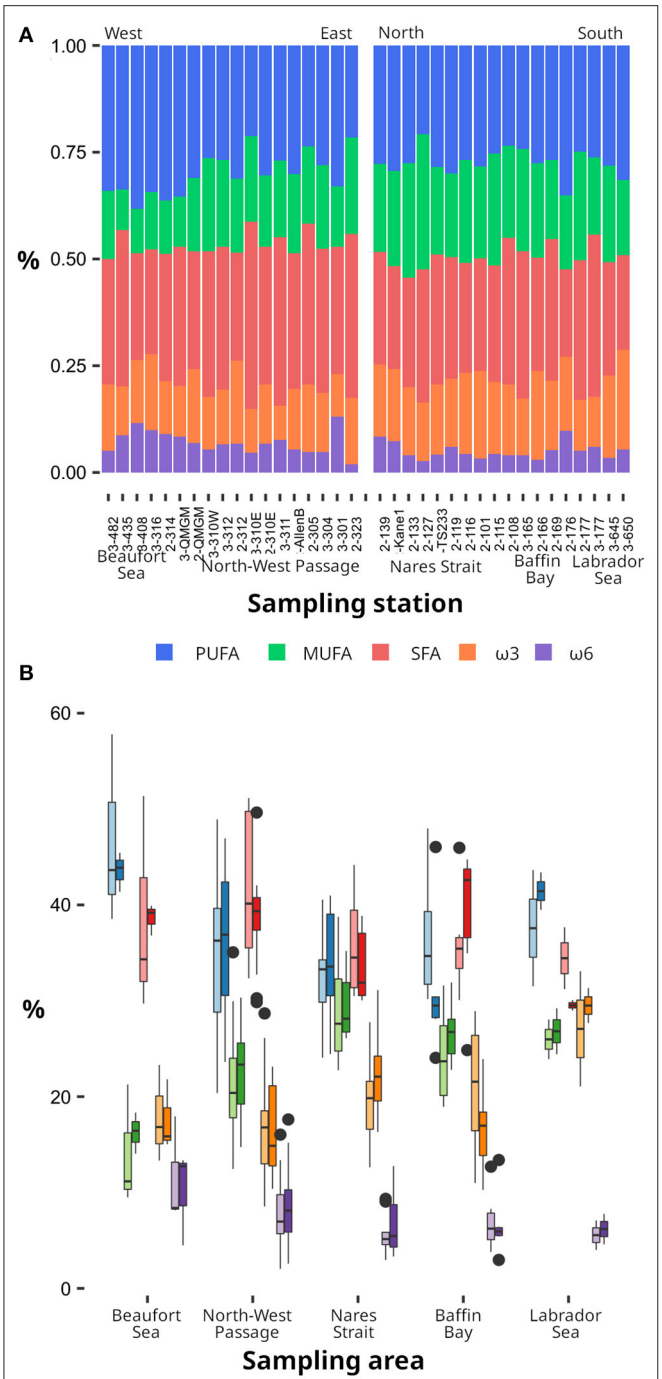

FIGURE 4 | Relative contribution of PUFA, MUFA, SFA, ω3, and ω6 fatty acids in particulate organic matter **(A)** along a longitudinal transect from the Beaufort Sea to the Northwest Passage (left) and a latitudinal transect from Nares Strait to the Labrador Sea (right), and **(B)** in the different oceanographic regions. In **(A)** the mean values (i.e., at the SUR and SCM) are represented while in **(B)**, the light shades represents the SUR and the dark shades represent the SCM.

ΣBFATM and including *i*15:0, *αi*15:0, 15:0, 15:1, *i*16:0, *ai*16:0, *i*17:0, *ai*17:0, 17:0, 17:1, and 18:1ω6). This implies a general westward decrease in diatoms and bacteria coincident with the decline in pH and salinity noted above.

Several relationships emerged between the proportions of different FAs, FATM or taxonomic groups and abiotic variables at the SCM. Firstly, the vertical position of the SCM had a significant impact on the proportions of EPA ($r^2 = 0.10$) and MUFA ($r^2 = 0.20$), which all tended to decrease as the SCM deepened while ΣC_{18}-PUFA increased ($r^2 = 0.19$; see **Supplementary Table 5** for details). Two of the relationships observed between FAs and abiotic variables are highlighted in **Figure 5**, which shows decreasing proportions of ω6 FA with increasing salinity (**Figure 5A**) and a positive correlation between EPA proportion and pH (**Figure 5B**). Temperature was one of the few variables that significantly, but weakly, correlated with DHA proportion. Indeed, negative correlations were found between temperature and DHA ($r^2 = 0.11$) or ΣC_{18}-PUFA ($r^2 = 0.09$). Warming was also associated with rising proportions of ΣBFATM ($r^2 = 0.21$) and dinoflagellates ($r^2 = 0.12$, $p < 0.05$) and the latter was positively correlated with the SID index ($r^2 = 0.23$, $p < 0.001$). SFA proportion correlated positively with the concentrations of nitrate ($r^2 = 0.14$) and phosphate ($r^2 = 0.11$) but numerous other FAs were negatively correlated with phosphate concentration [particularly diatom FATM such as 16:1ω7 ($r^2 = 0.09$), MUFA ($r^2 = 0.19$) and EPA ($r^2 = 0.09$)]. With respect to lipid classes, the only significant relationship observed was between the proportion of TAG and pH ($\beta = 21.09$, $r^2 = 0.11$, $p < 0.05$).

Based on AICc model selections, stepwise multiple linear regressions were employed to better tease out the respective effects of abiotic factors and taxonomy (on a carbon basis) on lipid profiles. The best single variable explaining PUFA proportions at the SCM was flagellate carbon and the coefficient of determination was highest when considering a quadratic model ($r^2 = 0.42$, $p < 0.001$) instead of a linear one ($r^2 = 0.31$, $p < 0.01$). Only the latter was improved by the inclusion of salinity, sampling depth, phosphate or SID ($r^2 = 0.37$ −0.43, $p < 0.01$) as a second independent variable. By contrast, the PUFA or MUFA proportion was explained nearly equally by diatom carbon ($r^2 = 0.20$, $p < 0.05$), sampling depth ($r^2 = 0.20$, $p < 0.01$) or phosphate concentration ($r^2 = 0.19$, $p < 0.01$) and a linear model combining diatoms and phosphate provided the highest coefficient of determination ($r^2 = 0.49$, $p < 0.01$). Note that phosphate and SCM depth were not used together in the same models because they were significantly correlated (Pearson, $p < 0.001$). Nutrient concentrations such as nitrate and phosphate were the only variables explaining some of the variability in SFA proportion ($r^2 = 0.14$, $p < 0.01$, and $r^2 = 0.11$, $p < 0.05$ respectively). We were unable to explain any of the variability in the proportions of overall ω3-FA and ARA; however, when considering specific ω3-EFA such as EPA, the best single explanatory variable was diatom carbon ($r^2 = 0.11$, $p < 0.05$; **Figure 6A**). The coefficient of determination was improved with a quadratic model ($r^2 = 0.26$, $p < 0.05$) and the best multiple linear model included latitude as a second independent variable ($r^2 = 0.48$, $p < 0.01$; **Figure 6B**). Seawater temperature and sampling date were the only variables that explained some of the variability in DHA. Finally ω6 FA variability was mainly explained with flagellate carbon ($r^2 = 0.24$, $p < 0.01$). Here again, predictive power was increased with a quadratic model ($r^2 = 0.28$,

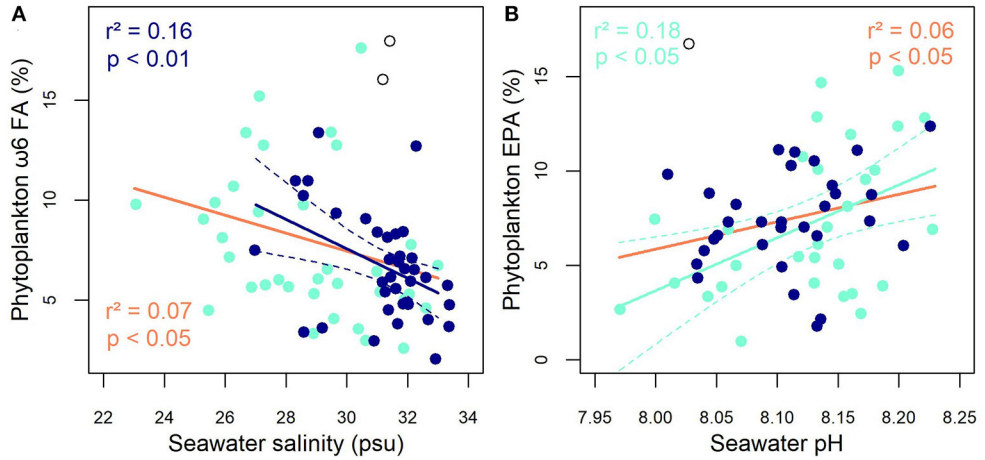

FIGURE 5 | Significant relationships between **(A)** ω6-FA proportion and salinity, and **(B)** EPA proportion and seawater pH. The dark-blue symbols, lines and text represent the subsurface chlorophyll maximum (SCM), the turquoise symbols, lines and text represent the surface (SUR) and the orange lines and text represent the SCM and SUR combined. The dashed line represents the 95% confidence interval and open circles represent outliers in the SCM dataset (Grubbs test, $p < 0.05$).

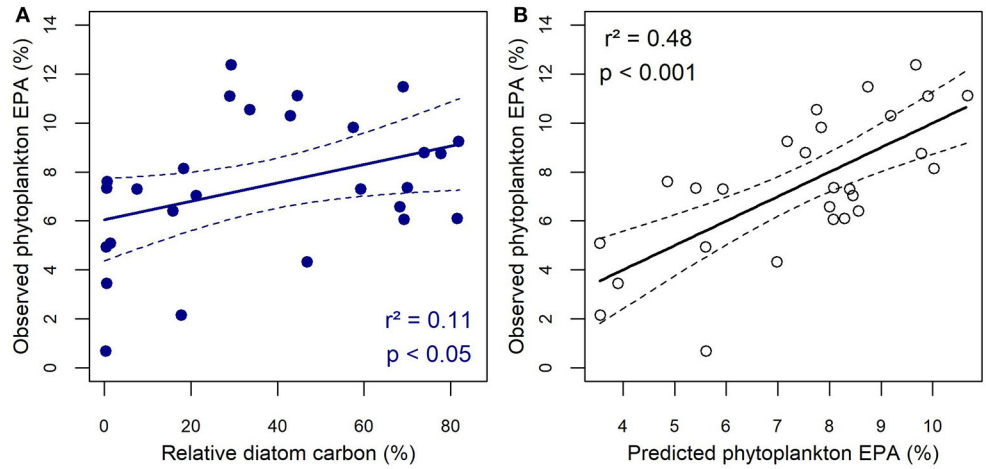

FIGURE 6 | Relationship between the relative contribution of EPA measured in particulate organic matter at the SCM and **(A)** the relative carbon biomass of diatoms and **(B)** the EPA contribution predicted by a multiple regression model that includes diatom carbon and latitude as independent variables. The dashed lines represent the 95% confidence interval.

$p < 0.01$) and the inclusion of a second independent variable, in this case SID ($r^2 = 0.36$, $p < 0.01$) or pH ($r^2 = 0.33$, $p < 0.05$).

Figure 7 presents a dbRDA with the major variables explored in this study and highlights the similarities and contrasts between the SCM and SUR. For both depths, EPA, pH, latitude and phosphate concentration are the main contributors to the first axis. Other major contributors are MUFA at the SCM and ω3 FA at SUR. Differences between the two depths are greater for the second axis. Salinity, nitrate concentration and to a lesser extent taxonomic composition are important contributors to this axis at the SCM, while FAs such as PUFA, ω6 FA, SFA and also carbon from flagellates are the main contributors at SUR. These differences imply that the choice of explanatory models made previously for the SCM should not be considered as systematically valid for each depth. Furthermore, we also plotted the scores of PCA axes 1 and 2 against FA and taxonomy variables in order to explore general multivariate trends. While new relevant correlations did not emerge with this approach, it underscored the major structuring effect of taxonomy on the dataset. Indeed, flagellate carbon was significantly correlated with the scores of PCA axes 1 and 2 at the SCM. It was the same for PC-2 scores at the SUR or a combination of SUR and SCM (**Supplementary Figure 2**).

The effects of environmental variables and taxonomy on PUFA, MUFA and SFA proportions at SUR where similar to those at the SCM, with the best explanatory models including flagellate carbon and salinity for PUFA ($r^2 = 0.30$, $p < 0.01$) while diatom carbon and phosphate mainly explained MUFA variations ($r^2 =$

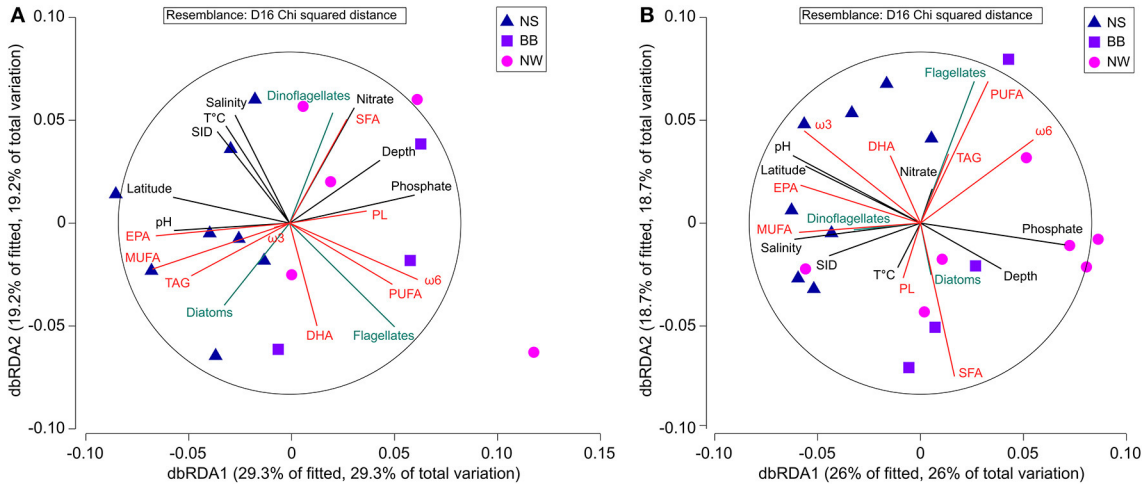

FIGURE 7 | Distance based Redundancy Analysis of lipid composition (red arrows), phytoplankton taxonomy (in term of carbon, blue arrows) and abiotic variables (black arrows) at **(A)** the subsurface chlorophyll maximum and **(B)** the surface. The blue triangles represent data from Nares Strait (NS), the purple squares represents Baffin Bay (BB) and pink circles represent the Northwest Passage (NW).

0.49, $p < 0.001$). Nitrate concentration explained some of the variance in SFA at SUR ($r^2 = 0.09$, $p < 0.05$), but flagellate carbon was the best single predictor ($r^2 = 0.15$, $p < 0.05$) and the coefficient of determination increased with the inclusion of pH ($r^2 = 0.31$, $p < 0.01$). For ω3 FA, none of the variability could be explained at the SCM whereas pH ($r^2 = 0.16$, $p < 0.05$), salinity ($r^2 = 0.16$, $p < 0.01$), and nutrients such as phosphate ($r^2 = 0.24$, $p < 0.01$) and nitrate ($r^2 = 0.13$, $p < 0.05$) had a significant effect at SUR. Including diatom carbon along with pH in a multiple model resulted in the highest coefficient of determination ($r^2 = 0.32$, $p < 0.05$). For EPA, pH was the best single explanatory variable at SUR ($r^2 = 0.18$, $p < 0.05$) but including diatom carbon did not improve the coefficient of determination like as it did at the SCM. In further contrast to the SCM, none of the variability in this DHA could be explained at SUR with the exception of sampling date. Finally the proportion of ω6 FA at SUR was best explained by phosphate concentration and the inclusion of flagellate carbon increased the coefficient of determination ($r^2 = 0.30$, $p < 0.05$). As above, we were unable to explain any ARA variability.

In rare cases, FA responses to abiotic variables at SUR were opposite to those described previously at the SCM. For instance, the proportions of SFA decreased with rising nitrate concentration at SUR ($r^2 = 0.09$, $p < 0.05$). In other cases, relationships observed at one depth held when data from the other depth were pooled, but this generally decreased the coefficient of determination (**Figures 3**, **5**; **Supplementary Tables 4, 5**). Finally, combining SUR and SCM data gave rise to new but weak relationships, including a positive correlation between flagellates and DHA ($r^2 = 0.06$) and a negative one between flagellates and salinity ($r^2 = 0.07$, $p < 0.05$) and also between ALA and depth ($r^2 = 0.16$) or temperature ($r^2 = 0.13$) and finally between sampling date and specific FA ratios such as DHA/EPA ($r^2 = 0.11$) or ω3/ω6 FA ($r^2 = 0.07$).

DISCUSSION

Most prior investigations of the influence of physicochemical factors on phytoplankton lipid composition were based on monospecific cultures of freshwater and marine algae (Guschina and Harwood, 2009). While some general trends emerge from this literature, the results are inconsistent among species, and given the sudden and often strong perturbations employed, cannot be transposed directly to natural communities (Galloway and Winder, 2015). Thus, we considered how multiple environmental drivers or stressors impact lipid synthesis across environmental gradients spanning large spatial scales allowing shifts in assemblage composition as well as local algal acclimation or adaptation. The results presented suggest that physicochemical factors can strongly influence FA composition of marine phytoplankton, even at large scales. Interpreting this is not straightforward since it may occur through changes in assemblage composition or as a direct physiological impact on algae. The following aims to disentangle these possibilities. In addition, our results partly confirm literature-based expectations for FATM that can be used to identify phytoplankton groups. This analysis also produced intriguing results that we explore below. We conclude the discussion by considering how the results may influence carbon cycling with respect to the phenology and vertical partitioning of primary production in the Pacific-influenced sector of the Arctic Ocean.

Fatty Acid Markers

Our results confirm that previously identified diatom FATM, such as the specific FAs 14:0 (myristic) and 16.1ω7 (**Supplementary Table 4**), as well as the FA ratios 16:1ω7/16:0 and $\Sigma C_{16}/\Sigma C_{18}$ (Pepin et al., 2011; Parrish, 2013), are valid over a large portion of the western Arctic. Based on correlation analyses, 16:1ω7 and Σ16:1/Σ18:1 can be considered as the

most robust diatom markers in this region. Proportions of EPA and diatoms were correlated at the SCM but, surprisingly, not at the surface. This could be explained by differences in taxonomic composition between SUR and SCM as well as differences in environmental stability between the two layers. The overall proportion of diatoms was halved at the SUR while the proportion of flagellates doubled (**Figure 2**; **Supplementary Table 2**) and was composed of different taxa with distinct FATM (**Supplementary Table 4**). For example, the chrysophytes that were included in the flagellate group were positively correlated with EPA proportion, which might partially mask the relationship between diatoms and EPA. As well, unidentified cell abundances, whose counts were higher than diatoms at the SUR (**Supplementary Table 2**), may have influenced the relationship with EPA. Relatively frequent or pronounced environmental fluctuations at SUR in terms of pH, salinity or temperature may also blur the relationship since algae may often modulate the degree of FA unsaturation in order to adjust membrane fluidity in changing environments (Tatsuzawa et al., 1996; Bigogno et al., 2002; Los et al., 2013). In this respect, the SCM is generally sheltered within the pycnocline and thus tends to maintain relatively stable physicochemical conditions over time (Martin et al., 2010; Schiffrine et al., 2020). This creates a setting in which the influence of phytoplankton assemblage composition on lipid profiles is less prone to be obscured by short-term physiological responses to fluctuating temperature, salinity, pH or light. While the sampling scheme used here precluded an assessment of the recent light history of algal cells at a given station, phytoplankton at the surface experience daily fluctuations in absolute irradiance that are 5-fold larger than those experienced at a depth corresponding to 20% of incident light, for instance.

Flagellates were the second major taxonomic group in our study and their presence was associated with elevated proportions of ΣC_{18}-PUFA, PUFA and ω6 FA but not with 20:4ω6 (ARA) as previously reported by Connelly et al. (2014). Experimental work with heterotrophic freshwater flagellates showed that different species have contrasted lipid profiles (Véra et al., 2001), suggesting that specific FATM may be more or less present depending on the actual assemblage composition. Since coarse groupings are typically employed due to the difficulty of identifying flagellates to the lowest taxonomic rank with light microscopy, the disparity between our study and Connelly et al. (2014) might be due to unresolved differences in dominant species. Future work would benefit from improved identification of key flagellates and their FATM using laboratory cultures or a combination of molecular tools (Lovejoy et al., 2006), electron microscopy and signature pigments with field samples (Coupel et al., 2015).

Surprisingly, our results did not confirm expected relationships between the contribution of dinoflagellate carbon and known FATM for this group, including DHA, 18:5ω3, or 18:4ω3 (OTA). However, as described by Kelly and Scheibling (2012), the literature supporting the use of DHA as a dinoflagellate marker is based mostly on laboratory cultures with few species (Mansour et al., 1999; Usup et al., 2008). It follows that the lack of correlation observed here for a cold polar environment might be due to the presence of different species. It might also be caused by a bias resulting from the estimation of biovolume prior to the calculation of carbon biomass. Here, the shape of dominant dinoflagellate genera such as *Gyrodinium* and *Gymnodinium* were considered as flattened ellipsoid (Olenina et al., 2006), which possibly induced an overestimation of dinoflagellate carbon relative to other groups. Finally, the potential contribution of dinoflagellates to DHA could be masked by the dominance of other DHA-rich taxa such as cryptophytes (Peltomaa et al., 2018) given low contributions of dinoflagellates.

Abiotic Factors and Taxonomy

The decrease in ΣC_{18}-PUFA and DHA with rising temperature at the SCM is consistent with the literature since PUFA are used to counteract the adverse effect of cold temperatures on membrane fluidity (Hixson and Arts, 2016). These correlations are weak however, which may be related to the very narrow range of temperatures observed at the SCM (**Supplementary Table 1**). Despite the much broader temperature range at SUR, this variable had no apparent effect on PUFA at this depth. It did however explain some of the variability in 20:1ω11 and 22:5ω6, although we have no physiological rationale to propose for these relationships (**Supplementary Table 5**). The contrast in PUFA response between the SCM and SUR suggests that other factors superseded the influence of temperature at the surface (e.g., daily light cycle) or that algae do not invest in the adjustment of membrane fluidity in the presence of rapid temperature fluctuations (e.g., such as daily or hourly temperature changes at SUR due to weather and solar radiation). Another noteworthy effect of temperature was on ΣBFATM at the SCM, suggesting that warming increases the contribution of bacteria to total microbial biomass and production. This is consistent with bacterial production increasing with temperature in the Arctic Ocean which may reduce vertical carbon export and the contribution of this ocean to the global CO_2 sink (Vaqué et al., 2019).

The increase in ΣBFATM with rising pH contrasts with the experimental results of Vaqué et al. (2019), who reported that bacterial production increased with higher pCO_2. However, the highest pCO_2 used by the authors was 5 times higher than the pCO_2 value corresponding to the lowest *in-situ* pH observed in our study, which could therefore partly explain the difference. In addition, the aggregated ΣBFATM variable that we used was composed of different FA previously used as distinct bacterial FATM (Parrish, 2013). Based on the observation that small variations in pH differentially affect distinct components of bacterial assemblages (Krause et al., 2012), the contrast in results might be due to a difference in the taxonomic composition of dominant bacteria although in our study, only two significant and positive relationships were found between pH and specific bacterial FATM (i.e., *i*15:0 and *ai*17:0).

For phytoplankton, a few expectations concerning the effect of pH on the lipid profiles of individual species can be derived from prior laboratory studies with single cultures. One study found that low pH can adversely affect the degree of lipid unsaturation and reduce membrane fluidity in a green alga (Tatsuzawa et al.,

1996), and another showed a negative effect of low pH on total lipid content and the PUFA/SFA ratio in a centric diatom (Rossoll et al., 2012). These responses, if they occur at all in natural settings, were overridden by other factors or community-level processes since the overall proportions of PUFA or unsaturated FA in POM did not correlate with pH. Prior community-level studies simulating future scenarios of low pH (minimum of 7.51) in experimental mesocosms found weak effects on the overall proportion of essential polyunsaturated FA in phytoplankton (Leu et al., 2013; Bermúdez et al., 2016) but reported shifts in the relative contribution of diatoms (Leu et al., 2013) or in the cell size of dominant taxa (Sommer et al., 2015). Knowing that the most abundant diatoms in our study were *Chaetoceros* species (with an apical length of 5–10 μm) while the most abundant flagellates measured 2–5 μm in diameter, the increased dominance of the latter at low pH might be linked to a differential positive effect of elevated pCO_2 on small cells (Bermúdez et al., 2016).

We surmise that in our study the influence of phytoplankton assemblage composition superseded the effect of pH on FA profiles since pH was related positively to the diatom FATMs 16:1ω7, ΣC_{16}, $\Sigma C_{16}/\Sigma C_{18}$, MUFA, and EPA (**Supplementary Table 5**) and inversely to relative flagellate abundance or flagellate FATM such as ΣC_{18}; **Supplementary Table 4**. While this implies a declining proportion of diatoms with decreasing pH, significant correlations between pH and the relative contribution of diatoms to carbon were not found here. This raises the possibility that phytoplankton carbon, when estimated using a series of assumptions, might be a less robust indicator of the contribution of different algal groups to biomass than FATM or that the latter are directly influenced by pH. These hypotheses would have to be tested in the laboratory with cultures of ecologically-relevant species. The fact that pH slightly improved the coefficient of determination of multiple linear regressions of several FA proportions at SUR (e.g., ω3 FA and MUFA) suggests that a direct physiological influence on algal cells cannot be excluded, although it would require membrane reconfiguration to be caused by relatively small or transient changes in seawater pH.

Most studies report increasing proportions of saturated FA under nutrient limitation (Siron et al., 1989; Yongmanitchai and Ward, 1991; Reitan et al., 1994) which has been attributed to an increase in neutral lipids such as TAG and composed mainly of saturated or monounsaturated FA (Parrish and Wangersky, 1987). By either pooling data from the SUR and the SCM or considering the latter only, our analysis revealed a surprising positive relationship between saturated FA proportion and nitrate concentration (**Supplementary Table 5**), which is opposite to the frequently observed increase of TAG in nutrient-limited diatoms (Alonso et al., 2000; Lynn et al., 2000). However, the positive relationship became negative when using data from the surface only, where high irradiance and low nutrient concentrations typical of late to post-bloom conditions occurred (**Supplementary Figure 1**). This pattern is consistent with the literature (Grosse et al., 2019; Jónasdóttir, 2019) and suggests that light-limited growth forestalls the influence of variable nitrate at the SCM.

Since nitrate is considered as the limiting element in the study area (e.g., Tremblay and Gagnon, 2009) and since phosphate remained in excess in samples where nitrate was depleted (**Supplementary Table 1.2**), it may seem surprising to see that phosphate concentration was strongly and positively correlated with ΣC_{18}, ΣC_{18}-PUFA, or ω6 FA at SUR and negatively correlated with 16:1ω7, $\Sigma C_{16}/\Sigma C_{18}$, ΣMUFA, and EPA at the SCM. However, the fact that ω6 FA and ΣC_{18}-PUFA were also positively correlated with flagellate carbon whereas 16:1ω7, $\Sigma C_{16}/\Sigma C_{18}$, ΣMUFA, and EPA were positively correlated with diatom carbon (**Supplementary Table 4**) suggests that phosphate is the dependent variable here and merely marks progress in the productive season and phytoplankton succession. The negative relationship found between phosphate and SID at SUR ($r^2 = 0.08$, $p < 0.05$) and the positive ones between phosphate and the date of sea ice melt at SUR ($r^2 = 0.30$, $p < 0.001$), SCM ($r^2 = 0.09$, $p < 0.05$) and for both datasets pooled ($r^2 = 0.10$, $p < 0.01$) are in agreement with the previous interpretation. However, correlations are weak, suggesting other influences are important.

It is noteworthy that EPA was the only single FA for which pH alone explained more variability than any other variable at SUR ($r^2 = 0.18$, $p < 0.05$). While a positive correlation also existed between pH and salinity ($r^2 = 0.16$, $p < 0.001$), the lack of relationship between EPA and the latter suggests a causal role for pH at this depth. At the SCM, EPA accounted for 42.5% of total ω3 FA on average and correlated positively with diatom FATM but not with pH nor salinity when all stations were considered. An attempt to remove the influence of taxonomy at this depth produced a surprising result. Upon keeping only the stations ($n = 12$) where diatom carbon contributed more than 55% of phytoplankton carbon (range 55 to 82%, see **Figure 3**), salinity was the only abiotic factor explaining a decrease in EPA ($r^2 = 0.37$, $p < 0.05$). Similar or even stronger negative correlations were found with ω3 FA ($r^2 = 0.59$, $p < 0.01$), PUFA ($r^2 = 0.37$, $p < 0.05$) and the PUFA/SFA ratio ($r^2 = 0.44$, $p < 0.05$) but not with DHA nor ω6 FA. For the surface, a grouping of diatoms such as the one made for the SCM was not achievable given the data spread but when considering stations ($n = 14$) where diatom carbon contributed between 0 and 10% of phytoplankton carbon, phosphate concentration and pH were the only physicochemical variables correlating with any specific FA or FA group we focused on in this study. At these fourteen stations, pH positively correlated with ω3 FA ($r^2 = 0.69$, $p < 0.01$) while phosphate correlated negatively with ω3 FA ($r^2 = 0.53$, $p < 0.01$) or EPA ($r^2 = 0.32$, $p < 0.01$), and positively with ω6 FA ($r^2 = 0.48$, $p < 0.01$). Although our 1-year sampling in various environments did not reveal significant differences in taxonomic composition with respect to sampling date or SID, previous studies have shown changes in phytoplankton assemblage composition over several years (Li et al., 2009; Coupel et al., 2015). In keeping with the notion that phosphate is a relatively robust indicator of seasonal maturity, the last correlations suggest that the assemblage composition of flagellates evolves during the productive season and progressively shifts toward ω3 FA-rich species.

In addition to the potential taxonomic shift, the above analysis of diatom and flagellate-dominated stations suggests

that salinity can trigger physiological responses. A previous experimental study with the diatom *Nitzschia laevis* showed that EPA proportions were highest at an intermediate salinity of 20 g L^{-1} but reduced at low (10 g L^{-1}) or high (30 g L^{-1}) salinities (Chen et al., 2008). This is consistent with our results and suggests the existence of an optimum salinity window in which EPA production is maximized in diatoms. Galloway and Winder (2015) later showed that this pattern also holds for long-chain EFA (which include ω3 and ω6 FA) in diatoms but not in other taxonomic groups. The authors found indeed that FA profiles either do not respond or vary linearly and positively or negatively with salinity. Such group-specific responses, when combined with the positive effect of salinity on the flagellates possibly explains why ω6 FA increase with salinity at SUR, while ω3 FA decrease at the SCM where diatoms dominate.

Despite environmental differences between SUR and SCM in terms of nutrient availability, PAR, temperature or salinity, the overall FA composition of POM did not differ between the two depths, except for MUFA. Elevated proportions of MUFA at the surface are consistent with an increase in neutral lipids under nutrient-limited conditions, although significant depth-related differences in TAG or PL proportion were not observed. The lack of differences in overall lipid composition between the surface and the SCM is unexpected given the differences observed by Leu et al. (2006) during the spring bloom in a fjord. Over the large spatial scales considered here, the vertical similarity of lipid profiles might simply arise from different drivers acting differently on distinct algal groups in each layer and resulting in convergent FA profiles. For instance, a greater proportion of flagellates inducing elevated proportions of ALA at SUR could be offset by low irradiance inducing a higher proportion of EPA at the SCM (Khotimchenko and Yakovleva, 2005) thereby reducing possible differences in overall ω3 FA and PUFA between the two depths. The same mechanism also potentially masks intra-depth differences. For instance, higher nutrient limitation at SUR resulting in an increased SFA proportion might be counterbalanced by higher PUFA proportions caused by an increase in flagellates. This might result in an apparent relatively invariant PUFA/SFA ratio. These offsets caused by species or group-specific responses within phytoplankton assemblages underscore the difficulties of extrapolating the results of monospecific culture studies found in the literature to the natural environment.

While our study focused on snapshots of lipid profiles at many different sites, integrating measurements of the absolute quantity of lipids throughout the entire phytoplankton succession encompassing the spring bloom and subsequent SCM development would be useful to fully assess the implication of our results for grazers and the food web. Yet the long duration (3 months from the end of July to the beginning of October) and broad geographical scope of our study (3,000 km) somehow captured a portion of this succession. Overall, sampling started in the southern part of Baffin Bay, moved north to Nares Strait, then west to the Beaufort Sea through the Northwest Passage prior, finally returning to Baffin Bay and the Labrador Sea (**Figure 1**). As a consequence, the SID (number of days elapsed between sea ice decline and sampling date, a surrogate for the degree of seasonal development) and latitude variables covaried to some extent and teasing apart their respective impacts is difficult. Nevertheless, latitude explained a larger portion of the variability in PUFA, MUFA, ALA, OTA and the EPA/DHA ratio than SID (**Supplementary Table 5**), which improved the coefficient of determination of some multiple regressions. Finally, as many variables co-varied, we elected to note weaker, but significant relationships (and the inclusion of these variable in multiple regressions models) since this could provide useful guidance for future studies or experiments.

Perspective

Prior studies of algal lipids in cold temperate waters and the Atlantic sector of the Arctic ocean showed that the spring diatom bloom in the upper euphotic zone is the major source of PUFA-rich lipids (Parrish et al., 2005; Leu et al., 2006). However, in several regions of the Pacific-influenced Arctic and sub-Arctic (e.g., Beaufort Sea, Northwest Passage and the western parts of Baffin Bay and the Labrador Sea), the enhanced vertical stratification caused by freshwater inputs curtails nutrient replenishment during winter and leads to a relatively modest and short-lived surface bloom in spring or early summer (Tremblay et al., 2015). A major if not larger portion of annual POM synthesis therefore occurs in the subsurface during the following weeks and months (e.g., Martin et al., 2010, 2013), resulting in a distinct phenology of FA production and food availability that we now explore.

In Kongsfjorden (Svalbard), Leu et al. (2006) showed that PUFA proportions declined from a maximum of 45%, 2 weeks before the diatom-dominated bloom reached peak biomass, to 28% when the bloom ended (overall average of 31.5% for the time course during 2003). Here, PUFA proportions averaged 35.7 ± 1.2% at the SCM, and the mean contributions of ω6 FA (18.9 ± 0.83%) and ω3 FA (53.3 ± 1.98% of PUFA) to PUFA were higher than in Kongsfjorden despite the fact that sampling occurred *ca* 2 months (median SID value) after ice break up (and presumably followed the end of the surface bloom by a month at least). Phytoplankton biomass at the SCM ranged from 16 to 371 μg C L^{-1} (122 ±15 μg C L^{-1} on average) and was comparable to or higher than in Kongsfjorden during the spring bloom (5–150 μg C L^{-1}). These comparisons indicate that subsurface phytoplankton layers are a quantitatively major and seasonally persistent source of high-quality POM across the large domain surveyed here. Since warming and the ongoing rise in freshwater loading generally increase vertical stratification in the Arctic Ocean, the SCM is likely to become even more crucial as a source of POM and nutritious lipids to the food web in some areas, whereas episodic upwelling (Tremblay et al., 2011) or mixing (Lewis et al., 2020) can foster the reverse in other areas.

The decline in PUFA proportion observed by Leu et al. (2006) during the course of the bloom in Kongsfjorden was partly attributed to a transition from diatoms to flagellates. This contrasts with our observation where flagellate carbon at the SCM was positively correlated with PUFA, ω6 FA and DHA. One likely explanation for this difference is that the communities we sampled between 29 July and 2 October represented more advanced stages of seasonal succession (see above discussion

of SUR communities with < 10% contributions of diatoms) relative to the communities sampled *ca* 2–3 weeks after the peak of the spring bloom in Kongsfjorden. In addition, the algae sampled in the short-lived SCM there exhibited signs of senescence, which also contrasts with the observation that SCM communities in Baffin Bay, the North West Passage and the Beaufort Sea retain high photosynthetic efficiency throughout summer and early fall (Martin et al., 2010, 2013). In terms of PUFA, our results imply that the phytoplankton biomass decline in the upper euphotic zone after the initial bloom is mitigated by protracted diatom production at the SCM, and also by a rising contribution of flagellates as the season progresses and biomass eventually declines.

This second mitigating process may prove especially important for food web resiliency in the Canada Basin, where small-sized flagellates have partially replaced large-sized phytoplankton (Li et al., 2009; Coupel et al., 2015). This analysis also suggests that the looming threat of a temporal mismatch between primary and secondary production due to early ice break-up in the Arctic Ocean (e.g., Leu et al., 2011) is a greater cause of concern in the Atlantic sector than in the Pacific-influenced domain.

Any projection of future changes in FA profiles for the Arctic Ocean is subject to considerable uncertainty since the combined effects of the different growth factors affected by climate change on a given algal group or species may be neutral, additive, synergistic or antagonistic (e.g., Gao et al., 2019). It is nevertheless likely that the transition from diatoms to flagellates will continue given expected trends of further warming, freshening and acidification for the Arctic Ocean (e.g., Bellerby et al., 2018). Based on prior experimental or field studies, this combination of trends should favor small-sized algae over diatoms (Gao et al., 2019). The direct, apparent effects of physicochemical variables on the FA profiles of the mixed communities sampled here were generally weak and secondary in the multiple regressions. As previously mentioned, straightforward interpretations of these emergent effects are difficult since they result from the various responses of all constituents in the community. Nevertheless, our finer analysis of SUR data focusing on flagellate-dominated stations (i.e., where diatoms accounted for < 10% of phytoplankton carbon) suggest that the surface communities are unlikely to be modulated by salinity, temperature or nitrate but potentially by pH. Conversely, the FA profiles of diatom-dominated communities at the SCM might respond primarily to changes in salinity in the Pacific-influenced Arctic. In this case, further reductions in salinity can be expected to have a positive effect on overall PUFA proportions (as long as salinity does not drop below 20 g L^{-1}). However, since the effect of salinity differs depending on the specific EFA considered (e.g., negative correlations with EPA or ω3 FA and non-significant relationships with DHA or ω6 FA), ongoing environmental changes could result in significant modification of specific FA ratios considered as indicators of food quality (e.g., DHA/EPA, ω3/ω6 FA) in terms of reproductive success and growth for grazers and other consumers higher up the food chain (Milke et al., 2004; Arendt et al., 2005).

CONCLUSION

Our extended temporal and spatial sampling scheme combined post-bloom conditions at the surface with nutrient-rich conditions at the SCM, covering a broad range of growth settings. Results confirmed the applicability of previously identified fatty acid trophic markers of diatoms and flagellates to several sectors of the western Arctic but indicate that other FATM should provisionally be considered unreliable, notably for dinoflagellates (DHA, OTA, 18:5ω3) and flagellates (ARA). The analyses underscored that the main effect of physicochemical, environmental factors on the lipid composition of POM in western Arctic seas is indirect and results from taxonomic variability and succession, especially at the SCM. This observation further extends to the field the conclusion of a prior compilation of laboratory studies showing that taxonomy is generally the major single driver of FA profiles. At the SCM, the highest proportions of overall PUFA and ω6 FA were caused by a rising proportion of flagellates as the growth season progressed, with secondary influences of salinity, phosphate and SID. Increases in MUFA and EPA proportions were driven by increasing contributions of diatoms, with secondary influences of phosphate and latitude. Among all the independent variables considered, none emerged as a significant predictor of ω3 FA variability at the SCM. By contrast, the SUR dataset showed a greater direct influence of environmental variables such as the effect of pH on ω3 FA and EPA. With the exception of DHA, none of the variability in the proportions of different FA groups (e.g., SFA, MUFA, PUFA, EPA, ω3 FA, and ω6 FA) could be related to temperature, which for the SCM is possibly due to the narrow range of temperatures encountered. For SUR, where the range was broader, the lack of correlation suggests that the dominant phytoplankton are either well-acclimated to ambient temperatures and do not respond to the rapid fluctuations (i.e., daily or hourly) found in this layer.

Among the relationships explored, the highest coefficients of determination (r^2) were 0.69, 0.59, and 0.53, with several other values being in the 0.30–0.40 range or much lower. While this can be considered as significant progress given the high complexity and large geographical scope of our data set, it implies that a large portion of the variance in FA profiles remains to be explained in natural settings. Refinements in the estimation of carbon content for different phytoplankton groups and species as well as an improved resolution of taxonomic composition using a variety of complementary techniques would certainly help in future studies. Diatoms are important providers of POM for Arctic food webs by virtue of both the high biomasses attained by this group and the quality of their FA. We propose that in several sectors of the perennially stratified Pacific-influenced western Arctic, the protracted seasonal persistence of diatoms at the SCM plays a role that is similar or perhaps even more crucial than the spring bloom does in other areas where relatively deep vertical mixing occurs in winter (i.e., the Atlantic sector). While an experimental study investigating the effect of ocean acidification on FA profiles in a natural setting produced insightful results (e.g., Leu et al., 2013), additional studies simulating the development of high diatom biomasses under both surface and SCM conditions and

different combinations of physicochemical forcing's would be useful. Our results for diatom-dominated stations suggest that salinity may play an important but previously overlooked role in affecting their FA profiles. Although flagellates typically exhibit relatively low biomass, this group was also associated with high-quality POM in our study area and we hypothesize that this quality increases as seasonal succession progresses. Overall, the analyses presented here suggest that the production of PUFA-rich phytoplankton in the Beaufort Sea, the Northwest Passage and the western sectors of Baffin Bay and the Labrador Sea is likely to persist in the near future.

DATA AVAILABILITY STATEMENT

The datasets presented in this study can be found online: https://dataverse.scholarsportal.info/dataset.xhtml?persistentId=doi:10.5683/SP2/RQR8LN.

AUTHOR CONTRIBUTIONS

VM conducted the field sampling, performed the laboratory and statistical analysis, and wrote the manuscript. J-ÉT and CP created the project, designed the sampling, and revised the manuscript. JM performed some lipid analyses. MG provided samples for taxonomic data and revised the manuscript. All authors contributed to the article and approved the submitted version.

FUNDING

This work was supported by a grant from the Natural Sciences and Engineering Research Council of Canada (NSERC) to J-ÉT and CP via the strategic network CHONe (Canadian Healthy Oceans Network), a grant from the Sentinel North program of the Canada First Research Excellence Fund to J-ÉT (project BriGHT), and a grant from the network center of excellence ArcticNet to J-ÉT and MG. This work contributes to the scientific programs of the FRQNT strategic cluster Québec-Océan and the Institut Nordique du Québec.

ACKNOWLEDGMENTS

We are grateful to the officers and crew of NGCC Amundsen, to Jonathan Gagnon, Gabrièle Deslongchamps, and Jeanette Wells for technical support, Pascal Guillot for CTD data processing, Sylvie Lessard for phytoplankton identification and enumeration, and also to the contributors of free or open source software (CRAN-R, Ocean Data View, LibreOffice, Inkscape and Linux community).

SUPPLEMENTARY MATERIAL

The Supplementary Material for this article can be found online at: https://www.frontiersin.org/articles/10.3389/fenvs.2020.538635/full#supplementary-material

REFERENCES

Alonso, D. L., Belarbi, E. H., Fernández-Sevilla, J. M., Rodríguez-Ruiz, J., and Grima, E. M. (2000). Acyl lipid composition variation related to culture age and nitrogen concentration in continuous culture of the microalga *Phaeodactylum tricornutum*. *Phytochemistry* 54, 461–471. doi: 10.1016/S0031-9422(00)00084-4

Arendt, K. E., Jónasdóttir, S. H., Hansen, P. J., and Gärtner, S. (2005). Effects of dietary fatty acids on the reproductive success of the calanoid copepod *Temora longicornis*. *Mar. Biol.* 146, 513–530. doi: 10.1007/s00227-004-1457-9

Bellerby, R., Anderson, L. G., Osborne, E., Steiner, N., Pipko, I., Cross, J., et al. (2018). "Arctic ocean acidification: an update," in *AMAP Assessment* 2018: *Arctic Ocean Acidification*. [Tromsø: Arctic Monitoring and Assessment Programme (AMAP)], 5–14.

Bermúdez, J. R., Riebesell, U., Larsen, A., and Winder, M. (2016). Ocean acidification reduces transfer of essential biomolecules in a natural plankton community. *Sci. Rep.* 6:27749. doi: 10.1038/srep27749

Bigogno, C., Khozin-Goldberg, I., and Cohen, Z. (2002). Accumulation of arachidonic acid-rich triacylglycerols in the microalga *Parietochloris incisa* (Trebuxiophyceae, Chlorophyta). *Phytochemistry* 60, 135–143. doi: 10.1016/S0031-9422(02)00037-7

Brodzik, M. J., and Stewart, J. S. (2016). *Near-Real-Time SSM/I-SSMIS EASE-Grid Daily Global Ice Concentration and Snow Extent, Version 5*. Boulder, CO: NASA National Snow and Ice Data Center Distributed Active Archive Center

Budge, S. M., Iverson, S. J., and Koopman, H. N. (2006). Studying trophic ecology in marine ecosystems using fatty acids: A primer on analysis and interpretation. *Mar. Mammal Sci.* 22, 759–801. doi: 10.1111/j.1748-7692.2006.00079.x

Budge, S. M., and Parrish, C. C. (1998). Lipid biogeochemistry of plankton, settling matter and sediments in Trinity Bay, Newfoundland. *II. Fatty acids. Org. Geochem.* 29, 1547–1559. doi: 10.1016/S0146-6380(98)00177-6

Budge, S. M., and Parrish, C. C. (1999). Lipid class and fatty acid composition of *Pseudo-nitzschia multiseries* and *Pseudo-nitzschia pungens* and effects of lipolytic enzyme deactivation. *Phytochemistry* 52, 561–566. doi: 10.1016/S0031-9422(99)00241-1

Chen, G. Q., Jiang, Y., and Chen, F. (2008). Salt-induced alterations in lipid composition of the diatom *Nitzschia laevis* (*Bacillariophyceae*) under heterotrophic culture condition. *J. Phycol.* 44, 1309–1314. doi: 10.1111/j.1529-8817.2008.00565.x

Clayton, T. D., and Byrne, R. H. (1993). Spectrophotometric seawater pH measurements: total hydrogen ion concentration scale calibration of m-cresol purple and at-sea results. *Deep Sea Res.* 40, 2115–2129. doi: 10.1016/0967-0637(93)90048-8

Connelly, T. L., Deibel, D., and Parrish, C. C. (2014). Trophic interactions in the benthic boundary layer of the Beaufort Sea shelf, Arctic Ocean: combining bulk stable isotope and fatty acid signatures. *Prog. Oceanogr.* 120, 79–92. doi: 10.1016/j.pocean.2013.07.032

Coupel, P., Matsuoka, A., Ruiz-Pino, D., Gosselin, M., Marie, D., Tremblay, J.-É., et al. (2015). Pigment signatures of phytoplankton communities in the Beaufort Sea. *Biogeosciences* 12, 991–1006. doi: 10.5194/bg-12-991-2015

Dalsgaard, J., St. John, M., Kattner, G., Müller-Navarra, D., and Hagen, W. (2003). Fatty acid trophic markers in the pelagic marine environment. *Adv. Mar. Biol.* 46, 225–340. doi: 10.1016/S0065-2881(03)46005-7

Fábregas, J., Maseda, A., Domínguez, A., and Otero, A. (2004). The cell composition of *Nannochloropsis* sp. changes under different irradiances in semicontinuous culture. *World J. Microb. Biot.* 20, 31–35. doi: 10.1023/B:WIBI.0000013288.67536.ed

Falk-Petersen, S., Hop, H., Budgell, W. P., Hegseth, E. N., Korsnes, R., Løyning, T. B., et al. (2000). Physical and ecological processes in the marginal ice zone of the northern Barents Sea during the summer melt period. *J. Mar. Syst.* 27, 131–159. doi: 10.1016/S0924-7963(00)00064-6

Field, C. B., Behrenfeld, M. J., Randerson, J. T., and Falkowski, P. (1998). Primary production of the biosphere: integrating terrestrial and oceanic components. *Science* 281, 237–240. doi: 10.1126/science.281.5374.237

Folch, J., Lees, M., and Sloane Stanley, G. H. (1957). A simple method for the isolation and purification of total lipids from animal tissues. *J. Biol. Chem.* 226, 497–509.

Galloway, A. W. E., and Winder, M. (2015). Partitioning the relative importance of phylogeny and environmental conditions on phytoplankton fatty acids. *PLoS ONE* 10:e0130053. doi: 10.1371/journal.pone.0130053

Gao, K., Beardall, J., Häder, D. P., Hall-Spencer, J. M., Gao, G., and Hutchins, D. A. (2019). Effects of ocean acidification on marine photosynthetic organisms under the concurrent influences of warming, UV radiation, and deoxygenation. *Front. Mar. Sci.* 6:322. doi: 10.3389/fmars.2019.00322

Gladyshev, M. I., Sushchik, N. N., and Makhutova, O. N. (2013). Production of EPA and DHA in aquatic ecosystems and their transfer to the land. *Prostag. Oth. Lipid M.* 107, 117–126. doi: 10.1016/j.prostaglandins.2013.03.002

Grosse, J., Brussaard, C. P. D., and Boschker, H. T. S. (2019). Nutrient limitation driven dynamics of amino acids and fatty acids in coastal phytoplankton. *Limnol. Oceanogr.* 64, 302–316. doi: 10.1002/lno.11040

Gurr, M. I., Harwood, J. L., and Frayn, K. N. (2002). *Lipid Biochemistry*. Oxford: Blackwell Science.

Guschina, I. A., and Harwood, J. L. (2009). *Lipids in Aquatic Ecosystems*. New York, NY: Springer. 1–24. doi: 10.1007/978-0-387-89366-2_1

Hansen, H. P., and Koroleff, F (1999). "Determination of nutrients," in *Methods of Seawater Analysis*. 3rd ed. Weinheim: Wiley Blackwell, 159–228.

Harwood, J. L. (1998). "Membrane lipids in algae," in *Lipids in Photosynthesis: Structure, Function and Genetics. Advances in Photosynthesis and Respiration*, Vol. 6. Dordrecht: Springer. doi: 10.1007/0-306-48087-5_3

Henriksen, P., Riemann, B., Kaas, H., Sørensen, H. M., and Sørensen, H. L. (2002). Effects of nutrient-limitation and irradiance on marine phytoplankton pigments. *J. Plankton Res.* 24, 835–858. doi: 10.1093/plankt/24.9.835

Hixson, S. M., and Arts, M. T. (2016). Climate warming is predicted to reduce omega-3, long-chain, polyunsaturated fatty acid production in phytoplankton. *Glob. Change Biol.* 22, 2744–2755. doi: 10.1111/gcb.13295

Huston, M. A., and Wolverton, S. (2009). The global distribution of net primary production: resolving the paradox. *Ecol. Monogr.* 79, 343–377. doi: 10.1890/08-0588.1

IPCC (2014). "Climate change 2014: synthesis report," in *Contribution of Working Groups I, II and III to the Fifth Assessment Report of the Intergovernmental Panel on Climate Change.* eds R. K. Pachauri and L. A. Meyer (Geneva: IPCC), 151.

Jiang, H., and Gao, K. (2004). Effects of lowering temperature during culture on the production of polyunsaturated fatty acids in the marine diatom *Phaeodactylum tricornutum* (*Bacillariophyceae*). *J. Phycol.* 40, 651–654. doi: 10.1111/j.1529-8817.2004.03112.x

Jónasdóttir, S. H. (2019). Fatty acid profiles and production in marine phytoplankton. *Mar. Drugs.* 17:151. doi: 10.3390/md17030151

Jónasdóttir, S. H., Visser, A. W., Richardson, K., and Heath, M. R. (2015). Seasonal copepod lipid pump promotes carbon sequestration in the deep North Atlantic. *Proc. Natl. Acad. Sci. U.S.A.* 112, 12122–12126. doi: 10.1073/pnas.1512110112

Kelly, J. R., and Scheibling, R. E. (2012). Fatty acids as dietary tracers in benthic food webs. *Mar. Ecol. Prog. Ser.* 446, 1–22. doi: 10.3354/meps09559

Khotimchenko, S. V., and Yakovleva, I. M. (2005). Lipid composition of the red alga Tichocarpus crinitus exposed to different levels of photon irradiance. *Phytochemistry* 66, 73–79. doi: 10.1016/j.phytochem.2004.10.024

Komsta, L. (2011). *Package 'Outliers' (Online R Package Version 0.14)*. Lublin: Medical University of Lublin.

Krause, E., Wichels, A., Giménez, L., Lunau, M., Schilhabel, M. B., and Gerdts, G. (2012). Small changes in pH have direct effects on marine bacterial community composition: a microcosm approach. *PLoS ONE* 7:e0047035. doi: 10.1371/journal.pone.0047035

Langen, P. L., Grenier, P., and Brown, R. (2018). "Marine ecosystems," in *Adaptation Actions for a Changing Arctic: Climatic drivers* (Oslo: Arctic Monitoring and Assessment Programme (AMAP)), 39–76

Lemire, M., Kwan, M., Laouan-Sidi, A., Muckle, G., Pirkle, C., Ayotte, P., et al. (2015). Local country food sources of methylmercury, selenium and omega-3 fatty acids in Nunavik, Northern Quebec. *Sci. Total Environ.* 509–510, 248–259. doi: 10.1016/j.scitotenv.2014.07.102

Leu, E., Daase, M., Schulz, K. G., Stuhr, A., and Riebesell, U. (2013). Effect of ocean acidification on the fatty acid composition of a natural plankton community. *Biogeosciences* 10, 1143–1153. doi: 10.5194/bg-10-1143-2013

Leu, E., Falk-Petersen, S., Kwaśniewski, S., Wulff, A., Edvardsen, K., and Hessen, D. O. (2006). Fatty acid dynamics during the spring bloom in a High Arctic fjord: Importance of abiotic factors versus community changes. *Can. J. Fish. Aquat. Sci.* 63, 2760–2779. doi: 10.1139/f06-159

Leu, E., Mundy, C., Assmy, P., Campbell, K., Gabrielsen, T., Gosselin, M., et al. (2015). Arctic spring awakening - Steering principles behind the phenology of vernal ice algal blooms. *Prog. Oceanogr.* 139, 151–170. doi: 10.1016/j.pocean.2015.07.012

Leu, E., Søreide, J. E., Hessen, D. O., Falk-Petersen, S., and Berge, J. (2011). Consequences of changing sea-ice cover for primary and secondary producers in the European Arctic shelf seas: timing, quantity, and quality. *Prog. Oceanogr.* 90, 18–32. doi: 10.1016/j.pocean.2011.02.004

Lewis, E., and Wallace, D. (1998). Program developed for CO_2 system calculations. *Ornl. Cdiac.* 105 1–21. doi: 10.2172/639712

Lewis, K. M., van Dijken, G. L., and Arrigo, K. R. (2020). Changes in phytoplankton concentration now drive increased Arctic Ocean primary production. *Science* 369, 198–202. doi: 10.1126/science.aay8380

Li, W. K. W., McLaughlin, F. A., Lovejoy, C., and Carmack, E. C. (2009). Smallest algae thrive as the arctic ocean freshens. *Science* 326:539. doi: 10.1126/science.1179798

Los, D. A., Mironov, K. S., and Allakhverdiev, S. I. (2013). Regulatory role of membrane fluidity in gene expression and physiological functions. *Photosynth. Res.* 116, 489–509. doi: 10.1007/s11120-013-9823-4

Lovejoy, C., Massana, R., and Pedrós-Alió, C. (2006). Diversity and distribution of marine microbial eukaryotes in the Arctic Ocean and adjacent seas. *Appl. Environ. Microb.* 72, 3085–3095. doi: 10.1128/AEM.72.5.3085-3095.2006

Lund, J. W. G., Kipling, C., and Le Cren, E. D. (1958). The inverted microscope method of estimating algal numbers and the statistical basis of estimations by counting. *Hydrobiologia* 11, 143–170. doi: 10.1007/BF00007865

Lynn, S. G., Kilham, S. S., Kreeger, D. A., and Interlandi, S. J. (2000). Effect of nutrient availability on the biochemical and elemental stoichiometry in the freshwater diatom Stephanodiscus minutulus (*Bacillariophyceae*). *J. Phycol.* 36, 510–522. doi: 10.1046/j.1529-8817.2000.98251.x

Mansour, M. P., Volkman, J. K., Jackson, A. E., and Blackburn, S. I. (1999). The fatty acid and sterol composition of five marine dinoflagellates. *J. Phycol.* 35, 710–720. doi: 10.1046/j.1529-8817.1999.3540710.x

Martin, J., Dumont, D., and Tremblay, J.-É. (2013). Contribution of subsurface chlorophyll maxima to primary production in the coastal Beaufort Sea (Canadian Arctic): a model assessment. *J. Geophys. Res. Oceans* 118, 5873–5886. doi: 10.1002/2013JC008843

Martin, J., Tremblay, J.-É., Gagnon, J., Tremblay, G., Lapoussière, A., Jose, C., et al. (2010). Prevalence, structure and properties of subsurface chlorophyll maxima in Canadian Arctic waters. *Mar. Ecol. Prog. Ser.* 412, 69–84. doi: 10.3354/meps08666

Meier, W. N., Markus, T., and Comiso, J. C. (2018). *AMSR-E/AMSR2 Unified L3 Daily 12.5 km Brightness Temperatures, Sea Ice Concentration, Motion and Snow Depth Polar Grids, Version 1*. Boulder, CA: NASA National Snow and Ice Data Center Distributed Active Archive Center.

Menden-Deuer, S., and Lessard, E. J. (2000). Carbon to volume relationships for dinoflagellates, diatoms, and other protist plankton. *Limnol. Oceanogr.* 45, 569–579. doi: 10.4319/lo.2000.45.3.0569

Milke, L. M., Bricelj, V. M., and Parrish, C. C. (2004). Growth of postlarval sea scallops, Placopecten magellanicus, on microalgal diets, with emphasis on the nutritional role of lipids and fatty acids. *Aquaculture* 234, 293–317. doi: 10.1016/j.aquaculture.2003.11.006

Millero, F. J., Woosley, R., Ditrolio, B., and Waters, J. (2009). Effect of ocean acidification on the speciation of metals in seawater. *Oceanography* 22, 72–85. doi: 10.5670/oceanog.2009.98

Mock, T., and Kroon, B. M. A. (2002). Photosynthetic energy conversion under extreme conditions - II: the significance of lipids under light limited growth in Antarctic sea ice diatoms. *Phytochemistry* 61, 53–60. doi: 10.1016/S0031-9422(02)00215-7

Moore, C. M., Mills, M. M., Arrigo, K. R., Berman-Frank, I., Bopp, L., Boyd, P. W., et al. (2013). Processes and patterns of oceanic nutrient limitation. *Nat. Geosci.* 6, 701–710. doi: 10.1038/ngeo1765

Olenina, I., Hajdu, S., Edler, L., Andersson, A., Wasmund, N., Busch, S., et al. (2006). "Biovolumes and size-classes of phytoplankton in the Baltic Sea," in *HELCOM Baltic Sea Environment Proceedings* (Helsinki), 106.

Parrish, C. C. (1987). Separation of aquatic lipid classes by Chromarod thin-Layer chromatography with measurement by Iatroscan flame ionization detection. *Can. J. Fish Aquat. Sci.* 44, 722–731. doi: 10.1139/f87-087

Parrish, C. C. (1999). In: *Lipids in Freshwater Ecosystems*. New York, NY: Springer. doi: 10.1007/978-1-4612-0547-0_2

Parrish, C. C. (2009). In: *Lipids in Aquatic Ecosystems*. New York, NY: Springer. doi: 10.1007/978-0-387-89366-2_13

Parrish, C. C. (2013). Lipids in marine ecosystems. *Oceanography* 2013:604045. doi: 10.5402/2013/604045

Parrish, C. C., Thompson, R. J., and Deibel, D. (2005). Lipid classes and fatty acids in plankton and settling matter during the spring bloom in a cold ocean coastal environment. *Mar. Ecol. Prog. Ser.* 286, 57–68. doi: 10.3354/meps286057

Parrish, C. C., and Wangersky, P. J. (1987). Particulate and dissolved lipid classes in cultures of *Phaeodactylum tricornutum* grown in cage culture turbidostats with a range of nitrogen supply rates. *Mar. Ecol. Prog. Ser.* 35, 119–128. doi: 10.3354/meps035119

Peltomaa, E., Johnson, M. D., and Taipale, S. J. (2018). Marine cryptophytes are great sources of EPA and DHA. *Mar. Drugs* 16:3. doi: 10.3390/md16010003

Pepin, P., Parrish, C. C., and Head, E. J. H. (2011). Late autumn condition of *Calanus finmarchicus* in the Northwestern Atlantic: evidence of size-dependent differential feeding. *Mar. Ecol. Prog. Ser.* 423, 155–166. doi: 10.3354/meps08952

Pruvost, J., Van Vooren, G., Cogne, G., and Legrand, J. (2009). Investigation of biomass and lipids production with *Neochloris oleoabundans* in photobioreactor. *Bioresour. Technol.* 100, 5988–5995. doi: 10.1016/j.biortech.2009.06.004

R Core Team (2020). *R: A Language and Environment for Statistical Computing*. R Foundation for Statistical Computing, Vienna.

Reitan, K. I., Rainuzzo, J. R., and Olsen, Y. (1994). Effect of nutrient limitation on fatty-acid and lipid-content of marine microalgae. *J. Phycol.* 30, 972–979. doi: 10.1111/j.0022-3646.1994.00972.x

Robert-Baldo, G. L., Morris, M. J., and Byrne, R. H. (1985). Spectrophotometric determination of seawater pH using phenol red. *Anal. Chem.* 57, 2564–2567. doi: 10.1021/ac00290a030

Rodolfi, L., Zittelli, G. C., Bassi, N., Padovani, G., Biondi, N., Bonini, G., et al. (2009). Microalgae for oil: Strain selection, induction of lipid synthesis and outdoor mass cultivation in a low-cost photobioreactor. *Biotechnol. Bioeng.* 102, 100–112. doi: 10.1002/bit.22033

Rossoll, D., Bermúdez, R., Hauss, H., Schulz, K. G., Riebesell, U., Sommer, U., et al. (2012). Ocean acidification-induced food quality deterioration constrains trophic transfer. *PLoS ONE*, 7. doi: 10.1371/journal.pone.0034737

RStudio Team (2020). *RStudio: Integrated Development for R. RStudio,* Boston: PBC.

Schiffrine, N., Tremblay, J.-É., and Babin, M. (2020). Growth and elemental stoichiometry of the ecologically-relevant Arctic diatom *Chaetoceros gelidus*: a mix of polar and temperate. *Front. Mar. Sci.* 6:790. doi: 10.3389/fmars.2019.00790

Siron, R., Giusti, G., and Berland, B. (1989). Changes in the fatty acid composition of *Phaeodactylum tricornutum* and *Dunaliella tertiolecta* during growth and under phosphorus deficiency. *Mar. Ecol. Prog. Ser.* 55, 95–100. doi: 10.3354/meps055095

Sobczuk, T. M., and Chisti, Y. (2010). Potential fuel oils from the microalga *Choricystis minor*. *J. Chem. Technol. Biot.* 85, 100–108. doi: 10.1002/jctb.2272

Sommer, U., Paul, C., and Moustaka-Gouni, M. (2015). Warming and ocean acidification effects on phytoplankton - From species shifts to size shifts within species in a mesocosm experiment. *PLoS ONE* 10:5. doi: 10.1371/journal.pone.0125239

Tatsuzawa, H., and Takizawa, E. (1995). Changes in lipid and fatty acid composition of *Pavlova lutheri*. *Phytochemistry* 40, 397–400. doi: 10.1016/0031-9422(95)00327-4

Tatsuzawa, H., Takizawa, E., Wada, M., and Yamamoto, Y. (1996). Fatty acid and lipid composition of the acidophilic green alga *Chlamydomonas* sp. *J. Phycol.* 32, 598–601. doi: 10.1111/j.0022-3646.1996.00598.x

Thompson, G. A. (1996). Lipids and membrane function in green algae. *Biochim. Biophys. Acta* 1302, 17–45. doi: 10.1016/0005-2760(96)00045-8

Thompson, P. A., Harrison, P. J., and Whyte, J. N. C. (1990). Influence of irradiance on the fatty acid composition phytoplankton. *J. Phycol.* 26, 278–288. doi: 10.1111/j.0022-3646.1990.00278.x

Tremblay, J.-É., Sejr, M., Bélanger, B., Devred, E., Archambault, P., Arendt, K., et al. (2018). "Marine Ecosystems," in *Adaptation Actions for a Changing Arctic: Perspectives from the Baffin Bay/Davis Strait Region.* (Oslo: Arctic Monitoring and Assessment Programme (AMAP)), 139–149.

Tremblay, J. É., Anderson, L. G., Matrai, P., Coupel, P., Bélanger, S., Michel, C., et al. (2015). Global and regional drivers of nutrient supply, primary production and CO_2 drawdown in the changing Arctic Ocean. *Prog. Oceanogr.* 139, 171–196. doi: 10.1016/j.pocean.2015.08.009

Tremblay, J. É., and Gagnon, J. (2009). "The effects of irradiance and nutrient supply on the productivity of Arctic waters: a perspective on climate change," in *Influence of Climate Change on the Changing Arctic and Sub-Arctic Conditions. in NATO Science for Peace and Security Series C: Environmental Security* (Dordrecht: Springer), 6–7. doi: 10.1007/978-1-4020-9460-6_7

Tremblay, J. É., Bélanger, S., Barber, D. G., Asplin, M., Martin, J., Darnis, G., et al. (2011). Climate forcing multiplies biological productivity in the coastal Arctic Ocean. *Geophys. Res. Let.* 38:L18604. doi: 10.1029/2011GL048825

Usup, G., Hamid, S. Z., Chiet, P. K., Wah, C. K., and Ahmad, A. (2008). Marked differences in fatty acid profiles of some planktonic and benthic marine dinoflagellates from Malaysian waters. *Phycologia* 47, 105–111. doi: 10.2216/07-55.1

Utermöhl, H. (1958). Zur Vervollkommnung der quantitativen Phytoplankton-Methodik. Mitteilungen der internationale vereinigung für theoretische und angewandte. *Limnologie* 9, 1–38. doi: 10.1080/05384680.1958.11904091

Vaqué, D., Lara, E., Arrieta, J. M., Holding, J., Sà, E. L., Hendriks, I. E., et al. (2019). Warming and CO_2 enhance arctic heterotrophic microbial activity. *Front. Microbiol.* 10:494. doi: 10.3389/fmicb.2019.00494

Véra, A., Desvilettes, C., Bec, A., and Bourdier, G. (2001). Fatty acid composition of freshwater heterotrophic flagellates: an experimental study. *Aquat. Microb. Ecol.* 25, 271–279. doi: 10.3354/ame025271

Yongmanitchai, W., and Ward, O. P. (1991). Growth of and omega-3 fatty acid production by *Phaeodactylum tricornutum* under different culture conditions. *Appl. Environ. Microb.* 57, 419–425. doi: 10.1128/AEM.57.2.419-425.1991

Zhu, C. J., Lee, Y. K., and Chao, T. M. (1997). Effects of temperature and growth phase on lipid and biochemical composition of *Isochrysis galbana*. *J. Appl. Phycol.* 9, 451–457. doi: 10.1023/A:1007973319348

Conflict of Interest: The authors declare that the research was conducted in the absence of any commercial or financial relationships that could be construed as a potential conflict of interest.

frontiers in Environmental Science

CORRECTION
published: 11 March 2021
doi: 10.3389/fenvs.2021.655241

Corrigendum: Environmental and Biological Determinants of Algal Lipids in Western Arctic and Subarctic Seas

Vincent Marmillot[1], Christopher C. Parrish[2]*, Jean-Éric Tremblay[1], Michel Gosselin[3] and Jenna F. MacKinnon[2]*

[1]Département de Biologie, Université Laval, Québec, QC, Canada, [2]Department of Ocean Sciences, Memorial University of Newfoundland, St. John's, NL, Canada, [3]Institut des Sciences de la mer de Rimouski, Université du Québec à Rimouski, Rimouski, QC, Canada

Keywords: lipids, phytoplankton, ω3 FA, ω6 FA, Arctic, taxonomy, environment

A corrigendum on

Environmental and Biological Determinants of Algal Lipids in Western Arctic and Subarctic Seas

by Marmillot, V., Parrish, C. C., Tremblay, J.-É., Gosselin, M., and MacKinnon, J. F. (2020) Environmental and Biological Determinants of Algal Lipids in Western Arctic and Subarctic Seas. Front. Environ. Sci. 8:538635. doi:10.3389/fenvs.2020.538635

In the original article, there was an error in the Materials and Methods. It was indicated sampling was conducted at Baffin Bay between 26 and 28 August. In fact it was 26–28 September. A correction has been made to the **Materials and Methods** section, subsection **Survey Area.**

"Sampling was conducted with the Canadian icebreaker CCGS Amundsen from 29 July to October 2, 2016. The 44 stations were spread out across Baffin Bay (29 July - 3 August and 26–28 September), Nares Strait (6–16 August), the Northwest Passage (4 August and 17–24 August and 18–25 September), the Beaufort Sea (28 August - 5 September) and the Labrador Sea (1–2 October). According to the general ocean circulation pattern, different water masses influence the overall sampling area. The western parts of Baffin Bay and the Labrador Sea are exposed to cold and relatively fresh waters descending from the high Arctic, such as the Baffin Island Current and the Labrador Current (Tremblay et al., 2018). These two currents carry predominantly Pacific-derived waters that previously transited across the Beaufort Sea and enter the Canadian Archipelago via Nares Strait and the Northwest Passage's Barrow Strait and Lancaster Sound. By contrast, Atlantic waters enter the survey area around the southern tip of Greenland and propagate northward with the West Greenland Current along the eastern edges of the Labrador Sea and Baffin Bay eventually crossing to the west. Most of the sampling stations were located in relatively shallow waters but regional differences in average bottom depths were present, with shelf stations of the Labrador sea (153 ± 13 m) and Northwest Passage (204 ± 26 m) being shallower than stations in the Beaufort Sea (352 ± 70 m), Nares Strait (476 ± 31 m) and Baffin Bay (489 ± 42 m)."

The authors apologize for this error and state that this does not change the scientific conclusions of the article in any way. The original article has been updated.

Approved by:
Frontiers Editorial Office, Frontiers Media SA, Switzerland

****Correspondence:***
Vincent Marmillot
vincent.marmillot.1@ulaval.ca
Christopher C. Parrish
cparrish@mun.ca

Specialty section:
This article was submitted to Biogeochemical Dynamics, a section of the journal Frontiers in Environmental Science

Received: *18 January 2021*
Accepted: *21 January 2021*
Published: *11 March 2021*

Citation:
Marmillot V, Parrish CC, Tremblay J-É, Gosselin M and MacKinnon JF (2021) Corrigendum: Environmental and Biological Determinants of Algal Lipids in Western Arctic and Subarctic Seas. Front. Environ. Sci. 9:655241. doi: 10.3389/fenvs.2021.655241

REFERENCES

Tremblay, J.-É., Sejr, M., Bélanger, B., Devred, E., Archambault, P., and Arendt, K.(2018). Marine ecosystems. *Adaptation actions for a changing Arctic: perspectives from the Baffin Bay/Davis Strait Region* (Oslo: Arctic Monitoring and Assessment Programme (AMAP)139–149.

frontiers in Marine Science

BRIEF RESEARCH REPORT
published: 25 February 2021
doi: 10.3389/fmars.2021.576746

Invariant Gametogenic Response of Dominant Infaunal Bivalves From the Arctic Under Ambient and Near-Future Climate Change Conditions

Adam J. Reed[1†], Jasmin A. Godbold[1†], Martin Solan[1†] and Laura J. Grange[2†]*

[1] School of Ocean and Earth Science, National Oceanography Centre Southampton, University of Southampton, Southampton, United Kingdom, [2] School of Ocean Sciences, Bangor University, Bangor, United Kingdom

OPEN ACCESS

Edited by:
Rui Rosa,
University of Lisbon, Portugal

Reviewed by:
Rejean Tremblay,
Université du Québec à Rimouski, Canada
Sue-Ann Watson,
James Cook University, Australia

***Correspondence:**
Adam J. Reed
adam.reed@noc.soton.ac.uk

†ORCID:
Adam J. Reed
orcid.org/0000-0003-2200-5067
Jasmin A. Godbold
orcid.org/0000-0001-5558-8188
Martin Solan
orcid.org/0000-0001-9924-5574
Laura J. Grange
orcid.org/0000-0001-9222-6848

Specialty section:
This article was submitted to Global Change and the Future Ocean, a section of the journal Frontiers in Marine Science

Received: *26 June 2020*
Accepted: *01 February 2021*
Published: *25 February 2021*

Citation:
Reed AJ, Godbold JA, Solan M and Grange LJ (2021) Invariant Gametogenic Response of Dominant Infaunal Bivalves From the Arctic Under Ambient and Near-Future Climate Change Conditions. Front. Mar. Sci. 8:576746. doi: 10.3389/fmars.2021.576746

Arctic marine ecosystems are undergoing a series of major rapid adjustments to the regional amplification of climate change, but there is a paucity of knowledge about how changing environmental conditions might affect reproductive cycles of seafloor organisms. Shifts in species reproductive ecology may influence their entire life-cycle, and, ultimately, determine the persistence and distribution of taxa. Here, we investigate whether the combined effects of warming and ocean acidification based on near-future climate change projections affects the reproductive processes in benthic bivalves (*Astarte crenata* and *Bathyarca glacialis*) from the Barents Sea. Both species present large oocytes indicative of lecithotrophic or direct larval development after ∼4 months exposure to ambient [<2°C, ∼400 ppm (CO_2)] and near-future [3–5°C, ∼550 ppm (CO_2)] conditions, but we find no evidence that the combined effects of acidification and warming affect the size frequency distribution of oocytes. Whilst our observations are indicative of resilience of this reproductive stage to global changes, we also highlight that the successful progression of gametogenesis under standard laboratory conditions does not necessarily mean that successful development and recruitment will occur in the natural environment. This is because the metabolic costs of changing environmental conditions are likely to be offset by, as is common practice in laboratory experiments, feeding *ad libitum*. We discuss our findings in the context of changing food availability in the Arctic and conclude that, if we are to establish the vulnerability of species and ecosystems, there is a need for holistic approaches that incorporate multiple system responses to change.

Keywords: metabolic plasticity, functional response, oogenesis, life-history, dynamic energy-budget

INTRODUCTION

Ocean acidification and warming are synergistic environmental stressors (Byrne et al., 2013a) that can affect whole animal physiology (Pörtner and Farrell, 2008). However, the extent to which reproduction and life history strategy are vulnerable to environmental change has received comparatively little attention (Ross et al., 2011). Reproduction underpins the success of populations

over time and, regardless of parental survivorship and tolerance capability, negative species responses to novel circumstances at early life cycle stages have the potential to serve as a bottleneck to long-term population survival (Dupont et al., 2010a). Species responses to changing environmental conditions have been shown to carry a high energetic cost in marine calcifiers (Spalding et al., 2017), especially at higher latitudes (Watson et al., 2017), and at earlier stages in the life cycle (Ross et al., 2011; Foo and Byrne, 2017). This is particularly concerning in polar environments where species responses to global climate change and ocean acidification are widely considered to be regionally amplified (Miller et al., 2010). Discerning the direction and generality of effect, however, is frustrated by the effects of transgenerational plasticity (Karelitz et al., 2019; Kong et al., 2019; Byrne and Hernández, 2020; Byrne et al., 2020), as well as intra-specific variations in sensitivity (Przeslawski et al., 2015) and response (Carr et al., 2006; Campbell et al., 2016; Boulais et al., 2017). In addition, maternal environmental history has been shown to affect egg size and volume (Braun et al., 2013) which, in turn, can induce phenotypic responses in larvae (Byrne et al., 2020).

Overall, the combined effects of ocean acidification and temperature on early gamete development are poorly constrained (Boulais et al., 2017) with most available information focused on gamete viability post spawning or larval development in a limited number of taxonomic groups (see review by Ross et al., 2011 and meta-analysis by Kroeker et al., 2010). By focusing on the later stages of a species reproductive cycle, sensitivities of gametogenesis or fertilization mechanisms are missed, stimulating debate about the potential for reproductive cycles to be disrupted (Dupont et al., 2010a; Hendriks and Duarte, 2010). Indeed, empirical evidence for the echinoderms indicates that ocean acidification can result in delayed but normal gametogenesis (Kurihara et al., 2013), reduced sperm volumes (Uthicke et al., 2013), lower gonad indices (Stumpp et al., 2012), or smaller eggs (Suckling et al., 2015). However, experimental manipulation of acidification in other taxa, including corals (Jokiel et al., 2008; Gizzi et al., 2017), annelids (Gibbin et al., 2017), molluscs (Parker et al., 2017), crustaceans (Thor and Dupont, 2015), and several miscellaneous species (for comprehensive list see Foo and Byrne, 2017), reveal no effects on egg size, gametogenesis, or development. Hence, considerable uncertainty exists in understanding the impact of climatic forcing on individual species within the context of the wider ecosystem, but it is clear that the earliest stages of gamete development need to be considered whilst adequately addressing variations within populations and regional environmental change (Dupont and Pörtner, 2013).

While many regionally abundant benthic invertebrate species have shown physiological tolerance to environmental forcing, often explained by, or attributed to, their boreal evolutionary histories (Richard et al., 2012), the viability of Arctic populations through their ability to reproduce is not currently known. Here, we used two abundant and functionally important benthic bivalves, *Bathyarca glacialis* and *Astarte crenata* from the Barents Sea (Cochrane et al., 2009; Solan et al., 2020), a region undergoing rapid change including ice retreat (Polyakov et al., 2012a), increasing sea surface temperatures (Polyakov et al., 2012b), and ocean acidification (Qi et al., 2017), to examine the combined effects of warming and ocean acidification on gamete development. Both species are reported to have large oocytes all year round indicative of lecithotrophic or direct development, and without seasonal or cyclic patterns of oocyte development (Saleuddin, 1965; Von Oertzen, 1972; Oliver et al., 1980). Our *a priori* expectation was that the physiological cost of near future conditions would indirectly affect reproduction, expressed via a trade-off with egg size or increased oocyte reabsorption, with consequences for the long-term viability of the population.

METHODS

Specimens of the infaunal bivalves *Bathyarca glacialis* and *Astarte crenata* were collected in July 2017 and 2018, respectively, by Agassiz trawl in the Barents Sea (74–81°N, along 30°E meridian, 292–363 m depth, JR16006 and JR17007, *RRS James Clark Ross*, **Supplementary Table 1**). Similarly sized individuals of each species (**Supplementary Table 2**) were maintained in aerated seawater (salinity 35, 1.5 ± 0.5°C), and returned to the *Biodiversity and Ecosystem Futures Facility*, University of Southampton. Surficial sediment (less than 10 cm depth: year 2017, mean particle size = 28.06 μm, organic material, 6.74%; 2018, mean particle size = 26.51 μm, organic material, 6.21%; Solan et al., 2020, **Supplementary Table 3** and **Supplementary Figure 1**) was collected using SMBA box cores in the Barents Sea (year 2017, Station B13, 74.4998°N 29.9982°E, 346 m depth; year 2018, Station B16, 80.1167°N 30.0683°E, 280 m depth, and Station B17, 81.2816°N, 29.3269°E, 334 m depth), sieved to remove macrofauna (500 μm mesh), homogenized by stirring, and transported back to the University of Southampton at ambient temperature (1.5 ± 1°C).

We exposed individuals of *Bathyarca glacialis* and *Astarte crenata* to ambient [1–2°C, ∼400 ppm (CO_2)] and near-future [3–5°C, ∼550 ppm (CO_2)] based on IPCC RCP 4.5 and 6.0 future projections for around the year 2050–2080, IPCC, 2013) temperature and atmospheric carbon dioxide scenarios for the Barents Sea. Aquaria (L × W × H: 20 cm × 20 cm × 34 cm, transparent acrylic) were continually aerated by bubbling a treatment-specific air-CO_2 mixture through a glass pipette (Godbold and Solan, 2013) and were filled with 10 cm of homogenized sediment overlain by 20 cm of seawater (∼ 8 L, salinity 34). The aquaria were maintained in the dark and randomly distributed between two insulated water baths within each treatment (Solan et al., 2020). Three *B. glacialis* were introduced to each of twelve aquaria (n = 36) and six *A. crenata* were introduced to each of ten aquaria (n = 60). After acclimation to aquarium conditions at ambient temperature and CO_2 [30 days, 1–2°C, ∼400 ppm (CO_2)], temperature and (CO_2) were adjusted manually (1°C and ∼100 ppm CO_2 week^{-1}) to achieve the near-future treatment conditions. No mortality was recorded during this period. We periodically measured pH [NBS scale, Mettler-Toledo (United States) InLab Expert Pro temperature–pH combination electrode], temperature and salinity (Mettler-Toledo InLab 737 IP67 temperature–conductivity combination

electrode), and total alkalinity (HCl titration by Marianda VINDTA, Canada). Concentrations of bicarbonate (HCO_3^-), carbonate (CO_3^{2-}), and pCO_2 were calculated from measured pH, total alkalinity, temperature, and salinity (Dickson et al., 2007; Dickson, 2010) using CO_2calc (Robbins et al., 2010) with appropriate solubility constants (Mehrbach et al., 1973, refit by Dickson and Millero, 1987) and KSO_4 (Dickson, 1990; **Supplementary Figures 2**, **3**).

The bivalves were fed consistently throughout the acclimation and experiment period *ad libitum* three times per week with 100 ml cultured live phytoplankton (mixed *Isochrysis* sp., *Tetraselmis* sp., and *Phaeodactylum* sp.) at peak culture densities of 15.6×10^6 cells ml^{-1}, 8.6×10^5 cells ml^{-1}, and 14.2×10^6 cells ml^{-1}, respectively. This equates to ∼0.197 g algae per day and represents 9.93 and 6.42% of algal weight/bivalve wet mass in *Astarte* and *Bathyarca*, respectively. Uneaten food was observed settled on the sediment surface which was used as an indicator of feeding *ad libitum*, and overlying sea water was replaced weekly (partial exchange, ∼80%) to prevent the accumulation of excess nutrients. Experiments were run for 120 days (*B. glacialis*, 21/11/2017–20/03/2018) or 135 days (*A. crenata*, 8/10/2018 – 19/02/2019) after which animals were removed and fixed in 4% neutral buffered formaldehyde for approximately 1 month before being prepared for histological examination. No premature mortality was recorded.

Histology

Bivalves were selected for histology within a defined size range (*A. crenata* 25–30 mm shell length; *B. glacialis* 20–25 mm shell length). For each individual [*A. crenata*, $n = 37$ (19 ambient, 18 future); *B. glacialis*, $n = 24$ (12 ambient, 12 future)], maximum shell length, height, and tumidity were measured using a digital caliper (±0.01 mm) (**Supplementary Table 2**), before soft tissue was removed from the shell, wet weighed (±0.001 g), and prepared for histology. Dissection revealed that both species have gonads which infiltrate and partially envelop the digestive diverticula (**Figure 1A**) so, as it was not tractable to perform a dissection of the germinal tissue, we adopted whole animal histology for reproductive analysis.

Soft tissue of each specimen was processed for histology according to the protocols described by Lau et al. (2018). In brief, tissue was dehydrated in isopropanol (70–100%), cleared in XTF (CellPath Ltd., United Kingdom) and embedded in 25 mm × 50 mm paraffin wax blocks. Embedded tissue was cut at 6–7 μm, mounted onto slides and stained using hematoxylin Z (CellPath Ltd., United Kingdom), counter stained with eosin Y (CellPath, United Kingdom), and immediately cover-slipped using a DPX mounting medium (Sigma-Aldrich, United Kingdom). Oocytes were captured using a Nikon D5000 digital SLR camera mounted onto an Olympus (BH-2) stereomicroscope and analyzed using ImageJ v 1.48 (Schneider et al., 2012).

Unique oocytes were measured only when a nucleus was visible to ensure the near maximum cross sectional diameter. The size of each oocyte was standardized to the diameter of a circle with an equal aggregate sectional area to the two dimensional section of the imaged oocyte [Equivalent Circular Diameter (ECD), Lau et al., 2018], comparable to the Oocyte Feret Diameter used in previous studies (Higgs et al., 2009; Reed et al., 2014). For each female with more than 100 sectioned oocytes, we calculated the ECD of 100 oocytes in each female (five females and 500 oocytes per treatment in each species). A Chi-squared test of independence was conducted between individual females in each experiment treatment to determine a statistically significant association in oocyte size frequencies (**Supplementary Figures 4**, **5**). Oocyte length frequency distributions for each treatment were pooled to represent the natural variation within individuals, and were analyzed with a Kolmogorov–Smirnov (K–S) test between treatments. All analyses were conducted in R (R Core Team, 2018 v.1.2.5019) and the *fishmethods* library was used for analysis of the length frequency distribution and K–S test (Nelson, 2019).

RESULTS

Examination of the reproductive organs of *A. crenata* confirmed 16 females and 21 males with no evidence of hermaphroditism, and one specimen with no discernible gonad tissue. Oocytes were developing in reproductive organs infiltrating the digestive diverticula (**Figure 1A**) and consisted of interconnected gonadal alveoli (**Figures 1B,C**). In four specimens in the future climate treatment, oocytes were loosely held within the supra-branchial chamber and reproductive organs simultaneously (**Figure 1D**). Evidence of primary oogenesis was not observed, however, oocytes measured between 46.96 and 185.08 μm (mean ± SD 122.61 ± 22.84 μm, $n = 500$) in the ambient conditions (**Figure 2A**), and 44.61–181.93 μm (mean ± SD 122.48 ± 24.08, $n = 500$) in the future conditions (**Figure 2B**), with no notable evidence of atresia. The oocyte size distributions were not treatment specific (2-tailed K–S test, $D_{(116)} = 0.062$, $p = 0.99$), and showed a distributional peak between 100 and 150 μm.

Histological examination of reproductive organs of *B. glacialis* revealed 10 females and 14 males with no evidence of hermaphroditism. Gonads were positioned partially infiltrating the digestive diverticula (**Figure 3A**) and were observed in densely packed anterior-posterior tubular pouches up to six oocytes across (**Figures 3A,B**). Oocytes measured between 39.60 and 144.77 μm (mean ± SD 96.77 ± 14.36 μm, $n = 500$) in the ambient conditions, and 35.07–144.90 μm (mean ± SD 95.03 ± 18.57 μm, $n = 500$) in the future conditions, with no notable evidence of atresia. The oocyte size distributions were not treatment specific (2-tailed K–S test, $D_{(94)} = 0.122$, $p = 0.81$), but showed a peak at 85 μm following exposure to ambient conditions (**Figure 4A**) and 95 μm following exposure to future conditions (**Figure 4B**).

DISCUSSION

We have demonstrated, for two abundant species of Arctic-boreal bivalve, evidence of gametogenic resilience to projected near-future atmospheric carbon dioxide (550 ppm CO_2) and sea temperature (+3°C), after a 20 week incubation. Our

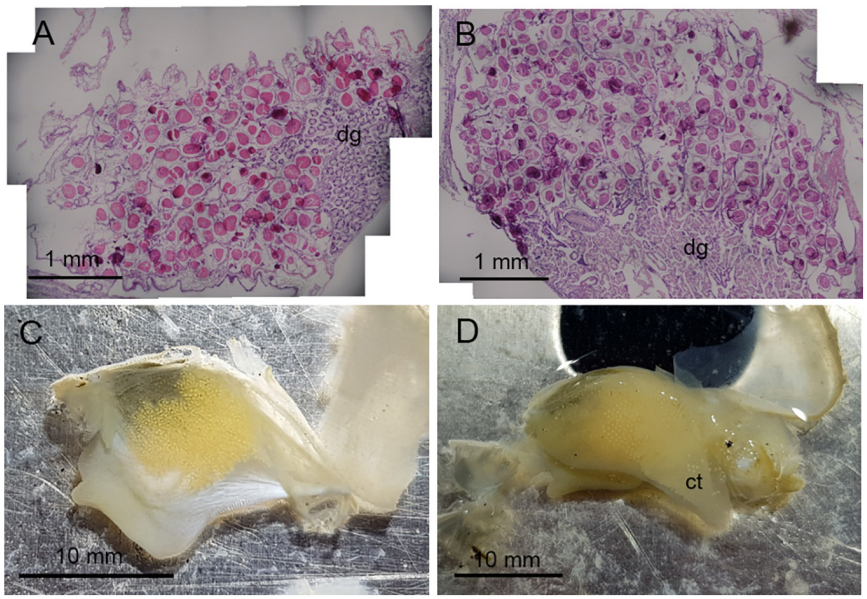

FIGURE 1 | Oocyte development in *Astarte crenata* from the Barents Sea. Transverse histology sections show oocyte development **(A)** surrounding the digestive diverticula under ambient environmental conditions and **(B)** in the gonadal alveoli under representative future environmental conditions. Microphotographs show **(C)** the arrangement of oocytes when within the gonad and **(D)** oocytes loosely held within the supra-branchial chamber on the ctenidia found in the future environmental conditions. dg, digestive diverticula; ct, ctenidia.

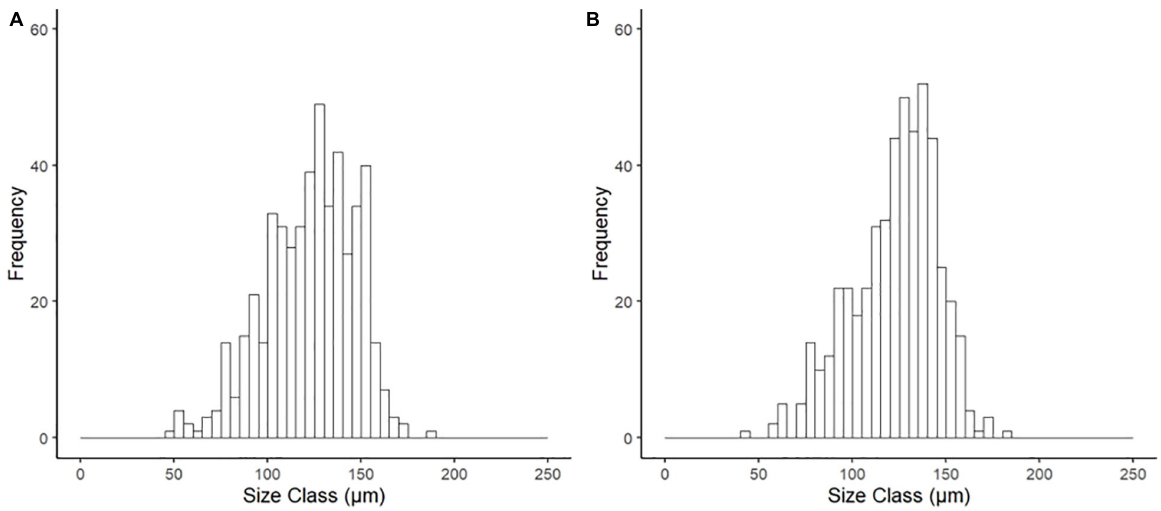

FIGURE 2 | Size frequency of oocytes for *Astarte crenata* from the Barents Sea following incubation (20 weeks) under **(A)** ambient and **(B)** representative future climate conditions. There was no difference in distribution between treatments (2-tailed *K–S* test, $D_{(116)} = 0.062$, $p = 0.99$).

observations show no difference in oocyte size frequency or physical structure, and in this respect are consistent with other studies (Kurihara et al., 2013; Verkaik et al., 2017). However, the interpretation of reproductive resilience based on a gametogenic response risks the generalization of a fundamental physiological output impacting on population dynamics, and does not take into account prolonged developmental cycles in cold water (Peck, 2016; Moran et al., 2019), or the effects on viability, fertilization, and larval development (Dupont et al., 2010a). The maximum oocyte sizes in *A. crenata* and *B. glacialis* are slightly lower than those reported previously (∼200 and 170 µm, respectively, Von Oertzen, 1972; Oliver et al., 1980; see **Supplementary Table 4**), likely representing different stages of maturity, and are consistent with the current understanding of reproduction in these species. Both species have egg sizes which suggest direct development or short pelagic development (i.e., lecithotrophic) (Ockelmann, 1965), and the small variation in oocyte frequency observed within treatments (**Supplementary Figures 4**, **5**) are

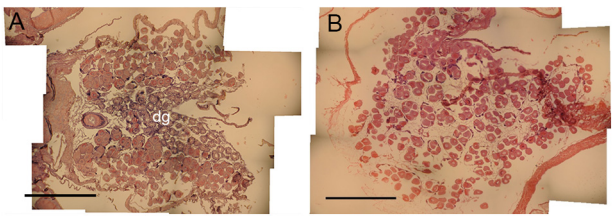

FIGURE 3 | Oocyte development in *Bathyarca glacialis* from the Barents Sea. Transverse histology sections show **(A)** reproductive organs and oocytes infiltrating the digestive diverticula under ambient environmental conditions and **(B)** oocyte development under representative future environmental conditions. dg, digestive diverticula. Scale bars = 1 mm.

akin to continuous spawners with an overlying seasonal intensity in reproduction (Lau et al., 2018), or natural variations in reproductive fitness. However, the presence of eggs in the suprabranchial chamber in four specimens of *A. crenata* exposed to future conditions is indicative of brooding, a previously unreported reproductive trait that is also supported by the large egg sizes, and formally hypothesized by the presence of adherent eggs and observed internal fertilization within Astartidae (Ockelmann, 1958; Marina et al., 2020).

It is tempting to conclude that our findings indicate resilience of the reproductive stage examined to near-term climatic forcing, but our observations of the successful progression of gametogenesis took place under standard laboratory conditions which, following accepted protocols (e.g., Pansch et al., 2018), include a constant supply of food. This may have inadvertently provided a sufficient supply of energy to overcome the metabolic costs of environmental stress (Cominassi et al., 2020) and mitigated the impact on gametogenesis. Increasing temperature and carbon dioxide concentrations affect species physiology through increased metabolism (Parker et al., 2013; Jager et al., 2016; Leung et al., 2020), and sometimes the suppression of feeding (Stumpp et al., 2012; Kurihara et al., 2013; Appelhans et al., 2014), which directly affects per offspring investment (Moran and McAlister, 2009; Pettersen et al., 2019), and gamete behavior post spawning (Verkaik et al., 2016). Energy stored as gametes can also be reabsorbed and act as a trade-off with fecundity (Stumpp et al., 2012; Verkaik et al., 2017; Rossin et al., 2019). However, considerable physiological resilience to ocean acidification has been demonstrated at various life-cycle stages in bivalves (Dell'Acqua et al., 2019), echinoderms (Verkaik et al., 2017), and corals (Gizzi et al., 2017), and during short incubations, appears to show no significant effects on growth and reproduction in benthic invertebrates (Dell'Acqua et al., 2019), even in food limited scenarios (Goethel et al., 2017). Laboratory experiments have shown that higher food quality and availability has a role in buffering the physiological effects of climate change and ocean acidification (Asnaghi et al., 2013), with positive effects reported in *Calanus* copepods (Pedersen et al., 2014), bivalves (Thomsen et al., 2013), and barnacles (Pansch et al., 2014). Further, a recent study has demonstrated that *ad libitum* feeding mediated fish growth rates in ocean acidification and warming scenarios, and suggest that this standard method may not reliably detect the impacts of environmental change in laboratory experiments (Cominassi et al., 2020). In our study, the supply of sufficient and nutrient rich food, common to laboratory experiments, is likely to have moderated the effects of near-future carbon dioxide and temperature controls (Thomsen et al., 2013; Ramajo et al., 2016; Cominassi et al., 2020), and provided the necessary nutrients for successful gamete development. Nevertheless, the physiological fitness of a species and production of gametes does not imply their viability, successful development, or recruitment to the environment (Caroselli et al., 2019).

Environmental change does not only have a direct physical effect on species physiology (Pörtner and Farrell, 2008), but also changes the wider ecosystem, including food-web structures

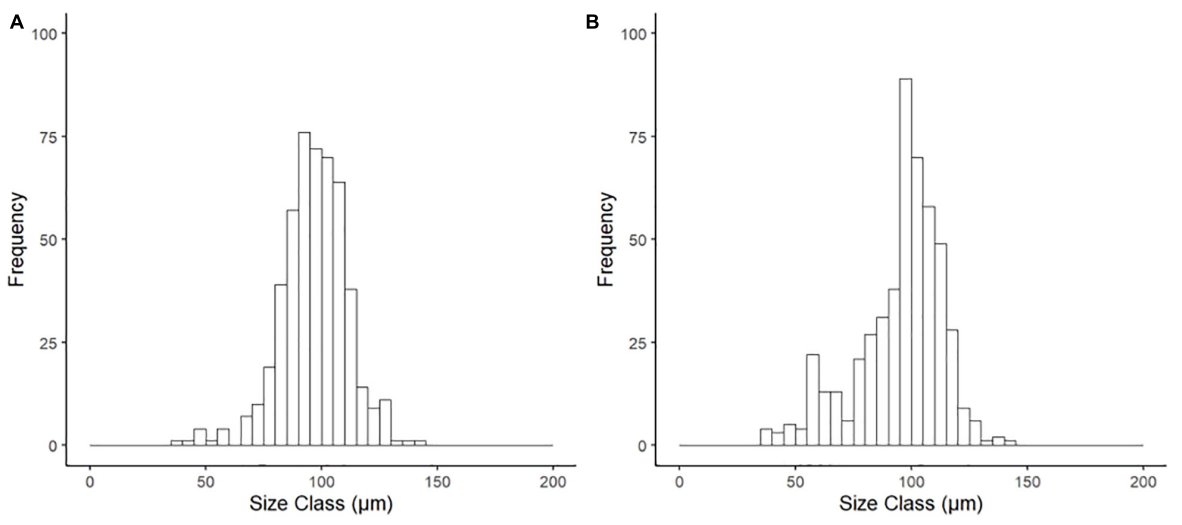

FIGURE 4 | Size frequency of oocytes for *Bathyarca glacialis* from the Barents Sea following incubation (20 weeks) under **(A)** ambient and **(B)** representative future climate conditions. There was no significant difference in distribution between treatments (2-tailed *K–S* test, $D_{(94)} = 0.122$, $p = 0.81$).

(Wassmann et al., 2006). In polar regions, the seasonal input of nutrient rich primary production originating from ice algae contributes an important seasonal input of organic matter to the benthos (Wassmann et al., 2011; Degen et al., 2016), impacting on biomass (Kêdra et al., 2013), growth (Blicher et al., 2010; Carroll et al., 2011a,b, 2014), benthic community physiology (Ambrose et al., 2006; Carroll and Peterson, 2013), and reproduction (Boetius et al., 2013). It has been consistently shown in polar environments that food has a greater impact on invertebrate physiology than temperature (Brockington and Clarke, 2001; Blicher et al., 2010), and can drive multi-decadal scale patterns in growth (Ambrose et al., 2006; Carroll et al., 2009) and recruitment (Skazina et al., 2013; Dayton et al., 2016). Associated with environmental forcing in the Arctic, there is expected to be a shift in the timings and quality of organic matter input to the benthos, from nutrient-rich ice algae to pelagic phytoplankton derived primary productivity (Arrigo and van Dijken, 2015), associated with thinner sea ice (Lange et al., 2019), and the transition to ice free conditions (Grebmeier et al., 2006; Leu et al., 2011; Polyakov et al., 2012a). Arctic phytoplankton assemblages may display resilience to ocean acidification through natural tolerances and intraspecific diversity (Hoppe et al., 2018), but the increasing unpredictability in quality of organic matter input impacts on the tight pelagic-benthic coupling which characterizes the Arctic (Tamelander et al., 2006; Wassmann et al., 2011; Kêdra et al., 2015). However, the observation that benthic species such as *Astarte* spp. and *Bathyarca glacialis* display feeding plasticity also ensures efficient use of available food input throughout the year (Gaillard et al., 2015; De Cesare et al., 2017), which may result in reproductive viability in otherwise unfavorable conditions.

Although gametogenesis may remain unaffected or mediated by food supply as a consequence of near future environmental change, the viability of fertilization and larval development under projected environmental conditions could still compromise successful recruitment (Dupont et al., 2010b; Kroeker et al., 2010; Albright, 2011). Fertilization across taxa has often shown negative responses to increasing carbon dioxide and temperature (e.g., Kurihara et al., 2007; Ericson et al., 2012; Guo et al., 2015; Graham et al., 2015), but results are not always consistent between species (Clark et al., 2009), populations (Thor et al., 2018), sexes (Verkaik et al., 2016), or individuals (Campbell et al., 2016; Boulais et al., 2017). Meanwhile "carry-over" effects and transgenerational plasticity may affect subsequent life cycle stages (Parker et al., 2011; Kong et al., 2019), shifting the development "bottleneck" to later stages, or forcing trade-offs with alternative reproductive traits such as fecundity or egg volume (Chakravarti et al., 2016). Larval development and early life history have also shown inconsistencies in their response to ocean acidification and increasing temperature. The Antarctic urchin *Sterechinus neumayeri* showed no differences in growth of reproductive tissue (Morley et al., 2016), or larval skeletal development (Clark et al., 2009) after exposure to ocean acidification and increased temperature, but a significant decrease in fertilization, developmental success, and increased developmental aberrations in alternative experiments have been recorded (Ericson et al., 2012; Byrne et al., 2013b). Larval type is also considered important, and planktotrophic larvae which are reliant on pelagic food are considered to be more susceptible than direct developing or non-feeding lecithotrophic larvae (Gutowska and Melzner, 2009; Dupont et al., 2010c; Gray et al., 2019). Consequently, biogeographical variations in larval responses to environmental change are likely to follow global and regional patterns of dominant larval types (Marshall et al., 2012). Here, both *A. crenata* and *B. glacialis* have oocyte sizes akin to non-feeding lecithotrophic or direct development (brooding) (Ockelmann, 1965) which is common in Polar species (Marshall et al., 2012), and suggests that food availability will have limited impact on larval development directly.

The lack of consistency between studies demonstrates the complex relationships between ocean acidification and temperature as synergistic stressors on individual reproductive performance (Byrne et al., 2013a; Harvey et al., 2013) and/or natural variations in tolerances within populations (Smith et al., 2019). Recruitment and recovery from disturbance in polar environments is often very slow (years – decades) (Barnes and Kukliński, 2005; Konar, 2013) although our knowledge of Arctic invertebrate reproductive biology remains limited (Kuklinski et al., 2013). The rapid rates of environmental change, however, may be further exacerbated by extreme longevity of organisms at high latitudes (Moss et al., 2016), To understand the effects of environmental change on reproductive ecology it will be important to consider all life history stages (Dupont et al., 2010a), and the role of population variability and plasticity as mechanisms of population resilience to environment change (Byrne et al., 2020). The role of changing food resources in determining reproductive viability in regions experiencing rapid change is presently under appreciated, but will be necessary to understand the links between the environment and reproductive/larval physiology (Goethel et al., 2017). The complex interactions between physiology, the environment, and climate change (Byrne et al., 2013a) will determine future population distributions and local extinction risks (Murdoch et al., 2020). We put forward, therefore, that holistic approaches including projected changes to regional food sources, are required to understand how future conditions may affect reproduction and modify interactions with whole animal physiological characteristics (Pörtner and Farrell, 2008; Dupont and Pörtner, 2013).

DATA AVAILABILITY STATEMENT

The raw data supporting the conclusions of this article will be made available by the authors, without undue reservation. All histology image data are to be made openly available from the Discovery Metadata System (https://www.bas.ac.uk/project/dms/), a data catalogue hosted by The UK Polar Data Centre (UK PDC, https://www.bas.ac.uk/data/uk-pdc/).

AUTHOR CONTRIBUTIONS

AR and LG conceived the idea. AR conducted the laboratory work and image analysis and wrote the manuscript. JG and AR

analyzed the data and produced the figures. MS, LG, and JG reviewed and provided critical comments on the manuscript prior to submission. All of the authors have contributed to the manuscript.

FUNDING

This work was supported by "The Changing Arctic Ocean Seafloor (ChAOS) – how changing sea ice conditions impact biological communities, biogeochemical processes, and ecosystems" project (NE/N015894/1 and NE/P006426/1, 2017-2021) funded by the Natural Environment Research Council (NERC) in the United Kingdom.

ACKNOWLEDGMENTS

We thank the crew of cruise JR16006 and JR17007, *RRS James Clark Ross*, Robbie Robinson (University of Southampton) for assistance with the design of our experimental systems, Tom Williams and Matthew Carpenter-Liquorice for maintaining the experiments, and National Marine Facilities, Southampton and the British Antarctic Survey, Cambridge for logistical support.

SUPPLEMENTARY MATERIAL

The Supplementary Material for this article can be found online at: https://www.frontiersin.org/articles/10.3389/fmars.2021.576746/full#supplementary-material

REFERENCES

Albright, R. (2011). Reviewing the effects of ocean acidification on sexual reproduction and early life history stages of reef-building corals. *J. Mar. Biol.* 2011, 1–14. doi: 10.1155/2011/473615

Ambrose, W. G., Carroll, M. L., Greenacre, M., Thorrold, S. R., and McMahon, K. W. (2006). Variation in *Serripes groenlandicus* (Bivalvia) growth in a Norwegian high-Arctic fjord: evidence for local and large-scale climatic forcing. *Glob. Change Biol.* 12, 1595–1607.1.

Appelhans, Y. S., Thomsen, J., Opitz, S., Pansch, C., Melzner, F., and Wahl, M. (2014). Juvenile sea stars exposed to acidification decrease feeding and growth with no acclimation potential. *Mar. Ecol. Prog. Ser.* 509, 227–239.1.

Arrigo, K. R., and van Dijken, G. L. (2015). Continued increases in Arctic Ocean primary production. *Prog. Oceanogr.* 136, 60–70. doi: 10.1016/j.pocean.2015.05.002

Asnaghi, V., Chiantore, M., Mangialajo, L., Gazeau, F., Francour, P., Alliouane, S., et al. (2013). Cascading effects of ocean acidification in a rocky subtidal community. *PloS one* 8:e61978. doi: 10.1371/journal.pone.0061978

Barnes, D. K. A., and Kukliński, P. (2005). Low colonisation on artificial substrata in arctic Spitsbergen. *Polar Biol.* 29, 65–69.1.

Blicher, M. E., Rysgaard, S., and Sejr, M. K. (2010). Seasonal growth variation in *Chlamys islandica* (Bivalvia) from sub-Arctic Greenland is linked to food availability and temperature. *Mar. Ecol. Progr. Ser.* 407, 71–86. doi: 10.3354/meps08536

Boetius, A., Albrecht, S., Bakker, K., Bienhold, C., Felden, J., Fernández-Méndez, M., et al. (2013). Export of algal biomass from the melting Arctic sea ice. *Science* 339, 1430–1432. doi: 10.1126/science.1231346

Boulais, M., Chenevert, K. J., Demey, A. T., Darrow, E. S., Robison, M. R., Roberts, J. P., et al. (2017). Oyster reproduction is compromised by acidification experienced seasonally in coastal regions. *Sci. Rep.* 7:13276.1.

Braun, D. C., Patterson, D. A., and Reynolds, J. D. (2013). Maternal and environmental influences on egg size and juvenile life-history traits in Pacific salmon. *Ecol. Evol.* 3, 1727–1740. doi: 10.1002/ece3.555

Brockington, S., and Clarke, A. (2001). The relative influence of temperature and food on the metabolism of a marine invertebrate. *J. Exp. Mar. Biol. Ecol.* 258, 87–99.1.

Byrne, M., Foo, S. A., Ross, P. M., and Putnam, H. M. (2020). Limitations of cross- and multigenerational plasticity for marine invertebrates faced with global climate change. *Glob. Chang. Biol.* 26, 80–102.1.

Byrne, M., Gonzalez-Bernat, M., Doo, S., Foo, S., Soars, N., and Lamare, M. (2013a). Effects of ocean warming and acidification on embryos and non-calcifying larvae of the invasive sea star *Patiriella regularis*. *Mar. Ecol. Progr. Ser.* 473, 235–246. doi: 10.3354/meps10058

Byrne, M., and Hernández, J. C. (2020). "Chapter 16 - Sea urchins in a high CO2 world: Impacts of climate warming and ocean acidification across life history stages," in *Developments in Aquaculture and Fisheries Science*, ed. J. M. Lawrence (New York, NY: Elsevier), 281–297. doi: 10.1016/b978-0-12-819570-3.00016-0

Byrne, M., Ho, M. A., Koleits, L., Price, C., King, C. K., Virtue, P., et al. (2013b). Vulnerability of the calcifying larval stage of the Antarctic sea urchin *Sterechinus neumayeri* to near-future ocean acidification and warming. *Glob. Chang. Biol.* 19, 2264–2275.1.

Campbell, A. L., Levitan, D. R., Hosken, D. J., and Lewis, C. (2016). Ocean acidification changes the male fitness landscape. *Sci. Rep.* 6:31250.1.

Caroselli, E., Gizzi, F., Prada, F., Marchini, C., Airi, V., Kaandorp, J., et al. (2019). Low and variable pH decreases recruitment efficiency in populations of a temperate coral naturally present at a CO2 vent. *Limnol. Oceanogr.* 64, 1059–1069. doi: 10.1002/lno.11097

Carr, R. S., Biedenbach, J. M., and Nipper, M. (2006). Influence of potentially confounding factors on sea urchin porewater toxicity tests. *Arch. Environ. Contam. Toxicol.* 51, 573–579.1.

Carroll, J. M., and Peterson, B. J. (2013). Ecological trade-offs in seascape ecology: bay scallop survival and growth across a seagrass seascape. *Landsc. Ecol.* 28, 1401–1413.1.

Carroll, M. L., Ambrose, W. G., Levin, B. S., Locke, W. L., Henkes, G. A., Hop, H., et al. (2011a). Pan-Svalbard growth rate variability and environmental regulation in the Arctic bivalve *Serripes groenlandicus*. *J. Mar. Syst.* 88, 239–251.1.

Carroll, M. L., Ambrose, W. G., Levin, B. S., Ryan, S. K., Ratner, A. R., Henkes, G. A., et al. (2011b). Climatic regulation of *Clinocardium ciliatum* (bivalvia) growth in the northwestern Barents Sea. *Palaeogeogr. Palaeoclimatol. Palaeoecol.* 302, 10–20. doi: 10.1016/j.palaeo.2010.06.001

Carroll, M. L., Ambrose, W. G. Jr., Locke V, W. L., Ryan, S. K., and Johnson, B. J. (2014). Bivalve growth rate and isotopic variability across the Barents Sea Polar Front. *J. Mar. Syst.* 130, 167–180. doi: 10.1016/j.jmarsys.2013.10.006

Carroll, M. L., Johnson, B. J., Henkes, G. A., McMahon, K. W., Voronkov, A., Ambrose, W. G., et al. (2009). Bivalves as indicators of environmental variation and potential anthropogenic impacts in the southern Barents Sea. *Mar. Pollut. Bull.* 59, 193–206. doi: 10.1016/j.marpolbul.2009.02.022

Chakravarti, L. J., Jarrold, M. D., Gibbin, E. M., Christen, F., Massamba-N'Siala, G., Blier, P. U., et al. (2016). Can trans-generational experiments be used to enhance species resilience to ocean warming and acidification? *Evol. Appl.* 9, 1133–1146.1.

Clark, D., Lamare, M., and Barker, M. (2009). Response of sea urchin pluteus larvae (Echinodermata: Echinoidea) to reduced seawater pH: a comparison among a tropical, temperate, and a polar species. *Mar. Biol.* 156, 1125–1137. doi: 10.1007/s00227-009-1155-8

Cochrane, S. K. J., Denisenko, S. G., Renaud, P. E., Emblow, C. S., Ambrose, W. G., Ellingsen, I. H., et al. (2009). Benthic macrofauna and productivity regimes in the Barents Sea — Ecological implications in a changing Arctic. *J. Sea Res.* 61, 222–233. doi: 10.1016/j.seares.2009.01.003

Cominassi, L., Moyano, M., Claireaux, G., Howald, S., Mark, F. C., Zambonino-Infante, J.-L., et al. (2020). Food availability modulates the combined effects of ocean acidification and warming on fish growth. *Sci. Rep.* 10:2338.

Dayton, P., Jarrell, S., Kim, S., Thrush, S., Hammerstrom, K., Slattery, M., et al. (2016). Surprising episodic recruitment and growth of Antarctic sponges:

implications for ecological resilience. *J. Exp. Mar. Biol. Ecol.* 482, 38–55. doi: 10.1016/j.jembe.2016.05.001

De Cesare, S., Meziane, T., Chauvaud, L., Richard, J., Sejr, M. K., Thebault, J., et al. (2017). Dietary plasticity in the bivalve *Astarte moerchi* revealed by a multimarker study in two Arctic fjords. *Mar. Ecol. Progr. Ser.* 567, 157–172. doi: 10.3354/meps12035

Degen, R., Jørgensen, L. L., Ljubin, P. I, Ellingsen, H., Pehlke, H., and Brey, T. (2016). Patterns and drivers of megabenthic secondary production on the Barents Sea shelf. *Mar. Ecol. Progr. Ser.* 546, 1–16. doi: 10.3354/meps11662

Dell'Acqua, O., Ferrando, S., Chiantore, M., and Asnaghi, V. (2019). The impact of ocean acidification on the gonads of three key Antarctic benthic macroinvertebrates. *Aquat. Toxicol.* 210, 19–29. doi: 10.1016/j.aquatox.2019.02.012

Dickson, A. G. (1990). Standard potential of the reaction AgCl(s)+0.5H2 (g)=Ag(s) + HCl(aq) and the standard acidity constant of the ion HSO_4—in synthetic sea water from 273.15 to 318.15 K. *J. Chem. Thermodyn.* 22, 113–127. doi: 10.1016/0021-9614(90)90074-Z

Dickson, A. G. (2010). "The carbon dioxide system in seawater: equilibrium chemistry and measurements," in *Guide to Best Practices for Ocean Acidification Research and Data Reporting*, eds U. Riebesell, V. J. Fabry, L. Hansson, and J.-P. Gattuso (Luxembourg: Publications Office of the European Union), 260.

Dickson, A. G., and Millero, F. J. (1987). A comparison of the equilibrium constants for the dissociation of carbonic acid in seawater media. *Deep Sea Res. A* 34, 1733–1743. doi: 10.1016/0198-0149(87)90021-5

Dickson, A. G., Sabine, C. L., and Christian, J. R. (eds) (2007). *Guide to Best Practices for Ocean CO_2 Measurements*, Vol. 3. Sidney, BC: North Pacific Marine Science Organization, 191.

Dupont, S., Dorey, N., and Thorndyke, M. (2010a). What meta-analysis can tell us about vulnerability of marine biodiversity to ocean acidification? *Estuar. Coast. Shelf Sci.* 89, 182–185. doi: 10.1016/j.ecss.2010.06.013

Dupont, S., Lundve, B., and Thorndyke, M. (2010c). Near Future Ocean Acidification Increases Growth Rate of the Lecithotrophic Larvae and Juveniles of the Sea Star *Crossaster papposus*. *J. Exp. Zool. B Mol. Dev. Evol.* 314, 382–389.1.

Dupont, S., Ortega-Martinez, O., and Thorndyke, M. (2010b). Impact of near-future ocean acidification on echinoderms. *Ecotoxicology* 19, 449–462. doi: 10.1007/s10646-010-0463-6

Dupont, S., and Pörtner, H. (2013). Get ready for ocean acidification. *Nature* 498, 429–429.1.

Ericson, J. A., Ho, M. A., Miskelly, A., King, C. K., Virtue, P., Tilbrook, B., et al. (2012). Combined effects of two ocean change stressors, warming and acidification, on fertilization and early development of the Antarctic echinoid *Sterechinus neumayeri*. *Polar Biol.* 35, 1027–1034. doi: 10.1007/s00300-011-1150-7

Foo, S. A., and Byrne, M. (2017). Marine gametes in a changing ocean: impacts of climate change stressors on fecundity and the egg. *Mar. Environ. Res.* 128, 12–24. doi: 10.1016/j.marenvres.2017.02.004

Gaillard, B., Meziane, T., Tremblay, R., Archambault, P., Layton, K., Martel, A., et al. (2015). Dietary tracers in *Bathyarca glacialis* from contrasting trophic regions in the Canadian Arctic. *Mar. Ecol. Progr. Ser.* 536, 175–186. doi: 10.3354/meps11424

Gibbin, E. M., Chakravarti, L. J., Jarrold, M. D., Christen, F., Turpin, V., and Massamba N'Siala, G. (2017). Can multi-generational exposure to ocean warming and acidification lead to the adaptation of life history and physiology in a marine metazoan? *J. Exp. Biol.* 220, 551–563. doi: 10.1242/jeb.149989

Gizzi, F., de Mas, L., Airi, V., Caroselli, E., Prada, F., Falini, G., et al. (2017). Reproduction of an azooxanthellate coral is unaffected by ocean acidification. *Sci. Rep.* 7:13049.

Godbold, J. A., and Solan, M. (2013). Long-term effects of warming and ocean acidification are modified by seasonal variation in species responses and environmental conditions. *Philos. Trans. R. Soc.Lond. B Biol. Sci.* 368:20130186. doi: 10.1098/rstb.2013.0186

Goethel, C. L., Grebmeier, J. M., Cooper, L. W., and Miller, T. J. (2017). Implications of ocean acidification in the Pacific Arctic: experimental responses of three Arctic bivalves to decreased pH and food availability. *Deep Sea Res. 2 Top. Stud. Oceanogr.* 144, 112–124.1.

Graham, H., Rastrick, S. P. S., Findlay, H. S., Bentley, M. G., Widdicombe, S., Clare, A. S., et al. (2015). Sperm motility and fertilisation success in an acidified and hypoxic environment. *ICES J. Mar. Sci.* 73, 783–790. doi: 10.1093/icesjms/fsv171

Gray, M. W., Chaparro, O., Huebert, K. B., O'Neill, S. P., Couture, T., Moreira, A., et al. (2019). Life history traits conferring larval resistance against ocean acidification: the case of brooding oysters of the genus *Ostrea*. *J. Shellfish Res.* 38, 751–761. doi: 10.2983/035.038.0326

Grebmeier, J. M., Overland, J. E., Moore, S. E., Farley, E. V., Carmack, E. C., Cooper, L. W., et al. (2006). A major ecosystem shift in the Northern Bering Sea. *Science* 311, 1461–1464. doi: 10.1126/science.1121365

Guo, X., Huang, M., Pu, F., You, W., and Ke, C. (2015). Effects of ocean acidification caused by rising CO2 on the early development of three mollusks. *Aqua. Biol.* 23, 147–157. doi: 10.3354/ab00615

Gutowska, M. A., and Melzner, F. (2009). Abiotic conditions in cephalopod (*Sepia officinalis*) eggs: embryonic development at low pH and high pCO2. *Mar. Biol.* 156, 515–519.1.

Harvey, B. P., Gwynn-Jones, D., and Moore, P. J. (2013). Meta-analysis reveals complex marine biological responses to the interactive effects of ocean acidification and warming. *Ecol. Evol.* 3, 1016–1030. doi: 10.1002/ece3.516

Hendriks, I. E., and Duarte, C. M. (2010). Ocean acidification: separating evidence from judgment – a reply to Dupont et al. *Estuar. Coastal Shelf Sci.* 89, 186–190. doi: 10.1016/j.ecss.2010.06.007

Higgs, N. D., Reed, A. J., Hooke, R., Honey, D. J., Heilmayer, O., and Thatje, S. (2009). Growth and reproduction in the Antarctic brooding bivalve *Adacnarca nitens* (Philobryidae) from the Ross Sea. *Mar. Biol.* 156, 1073–1081.1.

Hoppe, C. J. M., Wolf, K. K. E., Schuback, N., Tortell, P. D., and Rost, B. (2018). Compensation of ocean acidification effects in Arctic phytoplankton assemblages. *Nat. Clim. Chang.* 8, 529–533. doi: 10.1038/s41558-018-0142-9

IPCC (2013). "Summary for policymakers," in *Climate Change 2013: The Physical Science Basis. Contribution of Working Group I to the Fifth Assessment Report of the Intergovernmental Panel on Climate Change*, eds T. F. Stocker, D. Qin, G.-K. Plattner, M. Tignor, S. K. Allen, J. Boschung, et al. (Cambridge: Cambridge University Press).

Jager, T., Ravagnan, E., and Dupont, S. (2016). Near-future ocean acidification impacts maintenance costs in sea-urchin larvae: identification of stress factors and tipping points using a DEB modelling approach. *J. Exp. Mar. Biol. Ecol.* 474, 11–17. doi: 10.1016/j.jembe.2015.09.016

Jokiel, P. L., Rodgers, K. S., Kuffner, I. B., Andersson, A. J., Cox, E. F., and Mackenzie, F. T. (2008). Ocean acidification and calcifying reef organisms: a mesocosm investigation. *Coral Reefs* 27, 473–483.1.

Karelitz, S., Lamare, M. D., Mos, B., De Bari, H., Dworjanyn, S. A., and Byrne, M. (2019). Impact of growing up in a warmer, lower pH future on offspring performance: transgenerational plasticity in a pan-tropical sea urchin. *Coral Reefs* 38, 1085–1095. doi: 10.1007/s00338-019-01855-z

Kêdra, M., Moritz, C., Choy, E. S., David, C., Degen, R., Duerksen, S., et al. (2015). Status and trends in the structure of Arctic benthic food webs. *Polar Res.* 34:23775. doi: 10.3402/polar.v34.23775

Kêdra, M., Renaud, P. E., Andrade, H., Goszczko, I., and Ambrose, W. G. (2013). Benthic community structure, diversity, and productivity in the shallow Barents Sea bank (Svalbard Bank). *Mar. Biol.* 160, 805–819.1.

Konar, B. (2013). Lack of recovery from disturbance in high-arctic boulder communities. *Polar Biol.* 36, 1205–1214.1.

Kong, H., Jiang, X., Clements, J. C., Wang, T., Huang, X., and Shang, Y. (2019). Transgenerational effects of short-term exposure to acidification and hypoxia on early developmental traits of the mussel *Mytilus edulis*. *Mar. Environ. Res.* 145, 73–80. doi: 10.1016/j.marenvres.2019.02.011

Kroeker, K. J., Kordas, R. L., Crim, R. N., and Singh, G. G. (2010). Meta−analysis reveals negative yet variable effects of ocean acidification on marine organisms. *Ecol. Lett.* 13, 1419–1434. doi: 10.1111/j.1461-0248.2010.01518.x

Kuklinski, P., Berge, J., McFadden, L., Dmoch, K., Zajaczkowski, M., Nygård, H., et al. (2013). Seasonality of occurrence and recruitment of Arctic marine benthic invertebrate larvae in relation to environmental variables. *Polar Biol.* 36, 549–560. doi: 10.1007/s00300-012-1283-3

Kurihara, H., Kato, S., and Ishimatsu, A. (2007). Effects of increased seawater pCO(2) on early development of the oyster *Crassostrea gigas*. *Aqua. Biol.* 1, 91–98. doi: 10.3354/ab00009

Kurihara, H., Yin, R., Nishihara, G. N., Soyano, K., and Ishimatsu, A. (2013). Effect of ocean acidification on growth, gonad development and physiology

of the sea urchin *Hemicentrotus pulcherrimus*. *Aqua. Biol.* 18, 281–292. doi: 10.3354/ab00510

Lange, B. A., Haas, C., Charette, J., Katlein, C., Campbell, K., Duerksen, S., et al. (2019). Contrasting ice algae and snow−dependent irradiance relationships between first−year and multiyear sea ice. *Geophys. Res. Lett.* 46, 10834–10843. doi: 10.1029/2019gl082873

Lau, S. C. Y., Grange, L. J., Peck, L. S., and Reed, A. J. (2018). The reproductive ecology of the Antarctic bivalve *Aequiyoldia eightsii* (Protobranchia: Sareptidae) follows neither Antarctic nor taxonomic patterns. *Polar Biol.* 41, 1693–1706.1.

Leu, E., Søreide, J., Hessen, D., Falk-Petersen, S., and Berge, J. (2011). Consequences of changing sea-ice cover for primary and secondary producers in the European Arctic shelf seas: timing, quantity, and quality. *Prog. Oceanogr.* 90, 18–32. doi: 10.1016/j.pocean.2011.02.004

Leung, J. Y. S., Russell, B. D., and Connell, S. D. (2020). Linking energy budget to physiological adaptation: how a calcifying gastropod adjusts or succumbs to ocean acidification and warming. *Sci. Total Environ.* 715:136939. doi: 10.1016/j.scitotenv.2020.136939

Marina, P., Urra, J., de Dios Bueno, J., Rueda, J. L., Gofas, S., and Salas, C. (2020). Spermcast mating with release of zygotes in the small dioecious bivalve *Digitaria digitaria*. *Sci. Rep.* 10:12605.

Marshall, D. J., Krug, P. J., Kupriyanova, E. K., Byrne, M., and Emlet, R. B. (2012). The biogeography of marine invertebrate life histories. *Annu. Rev. Ecol. Evol. Syst.* 43, 97–114. doi: 10.1146/annurev-ecolsys-102710-145004

Mehrbach, C., Culberson, C., Hawley, J., and Pytkowicx, R. (1973). Measurement of the apparent dissociation constants of carbonic acid in seawater at atmospheric pressure 1. *Limnol. Oceanogr.* 18, 897–907. doi: 10.4319/lo.1973.18.6.0897

Miller, G. H., Alley, R. B., Brigham-Grette, J., Fitzpatrick, J. J., Polyak, L., Serreze, M. C., et al. (2010). Arctic amplification: can the past constrain the future? *Quater. Sci. Rev.* 29, 1779–1790. doi: 10.1016/j.quascirev.2010.02.008

Moran, A., Harasewych, M., Miller, B., Woods, H., Tobalske, B., and Marko, P. (2019). Extraordinarily long development of the Antarctic gastropod *Antarctodomus thielei* (Neogastropoda: Buccinoidea). *J. Molluscan Stud.* 85, 319–326. doi: 10.1093/mollus/eyz015

Moran, A. L., and McAlister, J. S. (2009). Egg size as a life history character of marine invertebrates: is it all it's cracked up to be? *Biol. Bull.* 216, 226–242.1.

Morley, S. A., Suckling, C. C., Clark, M. S., Cross, E. L., and Peck, L. S. (2016). Long-term effects of altered pH and temperature on the feeding energetics of the Antarctic sea urchin *Sterechinus neumayeri*. *Biodiversity* 17, 34–45.1.

Moss, D. K., Ivany, L. C., Judd, E. J., Cummings, P. W., Bearden, C. E., Kim, W. J., et al. (2016). Lifespan, growth rate, and body size across latitude in marine Bivalvia, with implications for Phanerozoic evolution. *Proc. R. Soc. B Biol. Sci.* 283:7.

Murdoch, A., Mantyka-Pringle, C., and Sharma, S. (2020). The interactive effects of climate change and land use on boreal stream fish communities. *Sci. Total Environ.* 700:134518. doi: 10.1016/j.scitotenv.2019.134518

Nelson, G. A. (2019). *Package "Fish Methods": Fishery Science Methods and Models. Version 11.1-1*. Available online at: https://cran.r-project.org/web/packages/fishmethods/fishmethods.pdf (accessed January, 2020).

Ockelmann, K. W. (1965). "Developmental types in marine bivalves and their distribution along the Atlantic coast of Europe," in *Proceedings of the 1st European Malacological Congress, 1962*, eds L. R. Cox and J. Peake (London: Conchological Society of Great Britain & Ireland), 25–35.

Ockelmann, W. K. (1958). The zoology of East Greenland. *Meddelelser om Grønland* 122, 1–256.

Oliver, G., Allen, J. A., and Yonge, M. (1980). The functional and adaptive morphology of the deep-sea species of the Arcacea (Mollusca: Bivalvia) from the Atlantic. *Philos. Trans. R. Soc. Lond. B Biol. Sci.* 291, 45–76. doi: 10.1098/rstb.1980.0127

Pansch, C., Hattich, G. S. I., Heinrichs, M. E., Pansch, A., Zagrodzka, Z., and Havenhand, J. N. (2018). Long-term exposure to acidification disrupts reproduction in a marine invertebrate. *PLoS One* 13:e0192036. doi: 10.1371/journal.pone.0192036

Pansch, C., Schaub, I., Havenhand, J., and Wahl, M. (2014). Habitat traits and food availability determine the response of marine invertebrates to ocean acidification. *Glob. Change Biol.* 20, 765–777.1.

Parker, L. M., O'Connor, W. A., Byrne, M., Coleman, R. A., Virtue, P., Dove, M., et al. (2017). Adult exposure to ocean acidification is maladaptive for larvae of the Sydney rock oyster *Saccostrea glomerata* in the presence of multiple stressors. *Biol. Lett* 13:20160798. doi: 10.1098/rsbl.2016.0798

Parker, L. M., Ross, P. M., and O'Connor, W. A. (2011). Populations of the Sydney rock oyster, *Saccostrea glomerata*, vary in response to ocean acidification. *Mar. Biol.* 158, 689–697.1.

Parker, L. M., Ross, P. M., O'Connor, W. A., Pörtner, H. O., Scanes, E., and Wright, J. M. (2013). Predicting the response of molluscs to the impact of ocean acidification. *Biology* 2, 651–692.1.

Peck, L. S. (2016). A cold limit to adaptation in the Sea. *Trends Ecol. Evol.* 31, 13–26. doi: 10.1016/j.tree.2015.09.014

Pedersen, S. A., Haåkedal, O. J., Salaberria, I., Tagliati, A., Gustavson, L. M., Jenssen, B. M., et al. (2014). Multigenerational exposure to ocean acidification during food limitation reveals consequences for copepod scope for growth and vital rates. *Environ. Sci. Technol.* 48, 12275–12284. doi: 10.1021/es501581j

Pettersen, A. K., White, C. R., Bryson-Richardson, R. J., and Marshall, D. J. (2019). Linking life-history theory and metabolic theory explains the offspring size-temperature relationship. *Ecol. Lett.* 22, 518–526.1.

Polyakov, I. V., Pnyushkov, A. V., and Timokhov, L. A. (2012b). Warming of the intermediate Atlantic water of the Arctic Ocean in the 2000s. *J. Clim.* 25, 8362–8370. doi: 10.1175/jcli-d-12-00266.1

Polyakov, I. V., Walsh, J. E., and Kwok, R. (2012a). Recent changes of Arctic multiyear sea ice coverage and the likely causes. *Bull. Am. Meteorol. Soc.* 93, 145–151. doi: 10.1175/bams-d-11-00070.1

Pörtner, H. O., and Farrell, A. P. (2008). Physiology and climate change. *Science* 322:690.

Przeslawski, R., Byrne, M., and Mellin, C. (2015). A review and meta-analysis of the effects of multiple abiotic stressors on marine embryos and larvae. *Glob. Chang. Biol.* 21, 2122–2140.1.

Qi, D., Chen, L., Chen, B., Gao, Z., Zhong, W., Feely, R. A., et al. (2017). Increase in acidifying water in the western Arctic Ocean. *Nat. Clim. Chang.* 7, 195–199. doi: 10.1038/nclimate3228

R Core Team (2018). *R: A Language and Environment for Statistical Computing*. Vienna: RFoundation for Statistical Computing.

Ramajo, L., Pérez-León, E., Hendriks, I. E., Marbà, N., Krause-Jensen, D., Sejr, M. K., et al. (2016). Food supply confers calcifiers resistance to ocean acidification. *Sci. Rep.* 6:19374.

Reed, A. J., Morris, J. P., Linse, K., and Thatje, S. (2014). Reproductive morphology of the deep-sea protobranch bivalves *Yoldiella ecaudata*, *Yoldiella sabrina*, and *Yoldiella valettei* (Yoldiidae) from the Southern Ocean. *Polar Biol.* 37, 1383–1392. doi: 10.1007/s00300-014-1528-4

Richard, J., Morley, S. A., Deloffre, J., and Peck, L. S. (2012). Thermal acclimation capacity for four Arctic marine benthic species. *J. Exp. Mar. Biol. Ecol.* 424, 38–43.1.

Robbins, L. L., Hansen, M. E., Kleypas, J. A., and Meylan, S. C. (2010). *CO2calc—A User-Friendly Seawater Carbon Calculator for Windows, Max OS X, and iOS (iPhone)*. US Geological Survey Open-File Report 2010–1280. Reston, VA: U.S. Geological Survey, 17.

Ross, P. M., Parker, L., O'Connor, W. A., and Bailey, E. A. (2011). The impact of ocean acidification on reproduction, early development and settlement of marine organisms. *Water* 3, 1005–1030. doi: 10.3390/w3041005

Rossin, A. M., Waller, R. G., and Stone, R. P. (2019). The effects of in-vitro pH decrease on the gametogenesis of the red tree coral, *Primnoa pacifica*. *PLoS One* 14:e0203976. doi: 10.1371/journal.pone.0203976

Saleuddin, A. (1965). The mode of life and functional anatomy of *Astarte* spp. (Eulamellibranchia). *J. Molluscan Stud.* 36, 229–257.

Schneider, C. A., Rasband, W. S., and Eliceiri, K. W. (2012). NIH Image to ImageJ: 25 years of image analysis. *Nat. Methods* 9, 671–675.1.

Skazina, M., Sofronova, E., and Khaitov, V. (2013). Paving the way for the new generations: *Astarte borealis* population dynamics in the White Sea. *Hydrobiologia* 706, 35–49. doi: 10.1007/s10750-012-1271-1

Smith, K. E., Byrne, M., Deaker, D., Hird, C. M., Nielson, C., Wilson-McNeal, A., et al. (2019). Sea urchin reproductive performance in a changing ocean: poor males improve while good males worsen in response to ocean acidification. *Proc. R. Soc. B* 286:20190785. doi: 10.1098/rspb.2019.0785

Solan, M., Ward, E. R., Wood, C. L., Reed, A. J., Grange, L. J., and Godbold, J. A. (2020). Climate driven benthic invertebrate activity and biogeochemical functioning across the Barents Sea Polar Front. *Philos. Trans. R. Soc. A* 378:20190365. doi: 10.1098/rsta.2019.0365

Spalding, C., Finnegan, S., and Fischer, W. W. (2017). Energetic costs of calcification under ocean acidification. *Glob. Biogeochem. Cycles* 31, 866–877. doi: 10.1002/2016gb005597

Stumpp, M., Trübenbach, K., Brennecke, D., Hu, M. Y., and Melzner, F. (2012). Resource allocation and extracellular acid–base status in the sea urchin *Strongylocentrotus droebachiensis* in response to CO2 induced seawater acidification. *Aqua. Toxicol.* 110-111, 194–207. doi: 10.1016/j.aquatox.2011.12.020

Suckling, C. C., Clark, M. S., Richard, J., Morley, S. A., Thorne, M. A. S., Harper, E. M., et al. (2015). Adult acclimation to combined temperature and pH stressors significantly enhances reproductive outcomes compared to short-term exposures. *J. Anim. Ecol.* 84, 773–784.1.

Tamelander, T., Renaud, P. E., Hop, H., Carroll, M. L., Ambrose, W. G. Jr., and Hobson, K. A. (2006). Trophic relationships and pelagic–benthic coupling during summer in the Barents Sea Marginal Ice Zone, revealed by stable carbon and nitrogen isotope measurements. *Mar. Ecol. Prog. Ser.* 310, 33–46. doi: 10.3354/meps310033

Thomsen, J., Casties, I., Pansch, C., Körtzinger, A., and Melzner, F. (2013). Food availability outweighs ocean acidification effects in juvenile *Mytilus edulis*: laboratory and field experiments. *Glob. Chang. Biol.* 19, 1017–1027.1.

Thor, P., and Dupont, S. (2015). Transgenerational effects alleviate severe fecundity loss during ocean acidification in a ubiquitous planktonic copepod. *Glob. Chang. Biol.* 21, 2261–2271. doi: 10.1111/gcb.12815

Thor, P., Vermandele, F., Carignan, M. H., Jacque, S., and Calosi, P. (2018). No maternal or direct effects of ocean acidification on egg hatching in the Arctic copepod *Calanus glacialis*. *PLoS One* 13:e0192496. doi: 10.1371/journal.pone.0192496

Uthicke, S., Pecorino, D., Albright, R., Negri, A. P., Cantin, N., and Liddy, M. (2013). Impacts of ocean acidification on early life-history stages and settlement of the coral-eating sea star *Acanthaster planci*. *PLoS One* 8:e82938. doi: 10.1371/journal.pone.0082938

Verkaik, K., Hamel, J. F., and Mercier, A. (2016). Carry-over effects of ocean acidification in a cold-water lecithotrophic holothuroid. *Mar. Ecol. Prog. Ser.* 557, 189–206. doi: 10.3354/meps11868

Verkaik, K., Hamel, J.-F., and Mercier, A. (2017). Impact of ocean acidification on reproductive output in the deep-sea annelid *Ophryotrocha* sp. (Polychaeta: Dorvilleidae). *Deep Sea Res. Part II Top. Stud. Oceanogr.* 137, 368–376. doi: 10.1016/j.dsr2.2016.05.022

Von Oertzen, J. A. (1972). Cycles and rates of reproduction of six Baltic Sea bivalves of different zoogeographical origin. *Mar. Biol.* 14, 143–149. doi: 10.1007/bf00373213

Wassmann, P., Duarte, C. M., Agusti, S., and Sejr, M. K. (2011). Footprints of climate change in the Arctic marine ecosystem. *Glob. Chang. Biol.* 17, 1235–1249.1.

Wassmann, P., Reigstad, M., Haug, T., Rudels, B., Carroll, M., Hop, H., et al. (2006). Food webs and carbon flux in the Barents Sea. *Prog. Oceanogr.* 71, 232–287. doi: 10.1016/j.pocean.2006.10.003

Watson, S. A., Morley, S. A., and Peck, L. S. (2017). Latitudinal trends in shell production cost from the tropics to the poles. *Sci. Adv.* 3:8.

Conflict of Interest: The authors declare that the research was conducted in the absence of any commercial or financial relationships that could be construed as a potential conflict of interest.

Advantages of publishing in Frontiers

OPEN ACCESS
Articles are free to read for greatest visibility and readership

FAST PUBLICATION
Around 90 days from submission to decision

HIGH QUALITY PEER-REVIEW
Rigorous, collaborative, and constructive peer-review

TRANSPARENT PEER-REVIEW
Editors and reviewers acknowledged by name on published articles

Frontiers
Avenue du Tribunal-Fédéral 34
1005 Lausanne | Switzerland

Visit us: www.frontiersin.org
Contact us: frontiersin.org/about/contact

REPRODUCIBILITY OF RESEARCH
Support open data and methods to enhance research reproducibility

DIGITAL PUBLISHING
Articles designed for optimal readership across devices

FOLLOW US
@frontiersin

IMPACT METRICS
Advanced article metrics track visibility across digital media

EXTENSIVE PROMOTION
Marketing and promotion of impactful research

LOOP RESEARCH NETWORK
Our network increases your article's readership